# Advances in Physics and Applications of Optically and Thermally Stimulated Luminescence

Reuven Chen
Vasilis Pagonis
editors

World Scientific

# Advances in Physics and Applications of Optically and Thermally Stimulated Luminescence

This page intentionally left blank

# Advances in Physics and Applications of Optically and Thermally Stimulated Luminescence

editors

**Reuven Chen**
Tel Aviv University, Israel

**Vasilis Pagonis**
McDaniel College, USA

World Scientific

NEW JERSEY • LONDON • SINGAPORE • BEIJING • SHANGHAI • HONG KONG • TAIPEI • CHENNAI • TOKYO

*Published by*

World Scientific Publishing Europe Ltd.

57 Shelton Street, Covent Garden, London WC2H 9HE

*Head office:* 5 Toh Tuck Link, Singapore 596224

*USA office:* 27 Warren Street, Suite 401-402, Hackensack, NJ 07601

**British Library Cataloguing-in-Publication Data**
A catalogue record for this book is available from the British Library.

**ADVANCES IN PHYSICS AND APPLICATIONS OF OPTICALLY AND THERMALLY STIMULATED LUMINESCENCE**



ISBN 978-1-78634-578-3

For any available supplementary material, please visit
https://www.worldscientific.com/worldscibooks/10.1142/Q0172#t=suppl

Desk Editor: Christopher Teo

Typeset by Stallion Press
Email: enquiries@stallionpress.com

Printed in Singapore

# Preface

In the present volume, an international group of researchers closely involved in the study of various aspects of thermally stimulated luminescence (thermoluminescence, TL) and optically stimulated luminescence (OSL) has undertaken the endeavor of summing up recent advances in these subjects. This subject, mainly associated with the effects of trapped charge on luminescence processes, started to develop quickly with the work of Randall and Wilkins in 1945, although much earlier accounts on TL can be found in the literature. In fact, as early as 1904, Mme. M. Curie mentioned TL in her doctoral dissertation. In the English translation of her thesis, one can read: "certain bodies, such as fluorite, become luminous when heated; they are thermo-luminescent. Their luminosity disappears after some time, but the capacity of becoming luminous afresh through heat is restored to them by the action of a spark and also by the action of Radium". At the beginning, TL was considered merely as a pure scientific method to study the luminescence effects of imperfections in solids, but rather early on, applications in dosimetry, archaeology and geology developed. At a later stage, the physics as well as the applications of OSL have been studied and implemented. Nowadays, the community of "trapped charge dosimetry and dating" includes several thousands of researches all over the world, publishing hundreds of papers each year describing the advances in the theoretical, experimental and applied aspects of these luminescence and related subjects.

This volume consists of 12 chapters written by leading figures in these fields from all over the world, describing state of the art research. Among other approaches, the use of numerical simulations of these luminescence effects has been considered. Due to the special role of quartz in dating, a chapter is devoted to the properties of this material. Two other chapters deal with thermally assisted OSL and time resolved luminescence. As for the chapters on applications, two chapters deal with TL/OSL archaeological dating and photo- and thermo-chronology dating of geological samples. Regarding dosimetry, a chapter is devoted to retrospective dosimetry based on measurements on ubiquitous materials, another chapter deals with dosimetry of cosmic radiation in space and a third one sums up some medical applications of luminescent materials.

The first chapter has been written by Dr. Reuven Chen and covers recent advances in the theory of delocalized transitions in TL and OSL processes. Dr. Chen is Emeritus Professor at Tel Aviv University. His main research area has been TL and OSL, in particular theoretical studies supported by numerical simulations. He has published about 200 peer-reviewed papers on experimental and theoretical aspects of TL and OSL and is co-author of a number of books and chapters in multi-authored books in the field. His experimental research included luminescence properties of quartz, diamonds, Aluminum Oxide, fluorides and other materials. His theoretical work has covered methods of evaluating trapping parameters from TL curves based on peaks shape and on the heating-rate dependence, and the relation between TL and thermally stimulated conductivity (TSC). In addition, he has made major contributions in the study of dose and dose-rate dependencies of TL and OSL, including superlinear behavior. He has also carried out fundamental studies on the order of kinetics in the TL and OSL processes, including linear-modulated OSL.

The summary of advances in delocalized luminescence processes in Chapter 1, is followed by the complementary review of localized processes by Dr Vasilis Pagonis in Chapter 2. Dr. Pagonis is the co-author of two books in the field of luminescence dosimetry, and his published work of more than 130 papers covers both

experimental and theoretical aspects of TL, OSL, Time-resolved OSL and Thermally-activated OSL. He has developed numerous models for the luminescence mechanisms of quartz, alumina and luminescence materials exhibiting quantum tunneling processes (apatites, feldspars). He has made major contributions in the use of Monte Carlo techniques for describing the luminescence mechanism in dosimetric applications, and especially in the area of nanodosimetric materials. His most recent work includes applications of TL signals from feldspars for temperature sensing and thermochronometry applications. His collaboration with Dr. George Kitis has resulted in the development of new analytical equations describing TL, OSL and IRSL signals from feldspars and apatites, and in a better understanding of the tunneling processes in these materials.

Chapter 3 has been written by Drs. Yigal S. Horowitz, Leonid Oster and Ilan Eliyahu, and covers the very important effects of ionization density in TL mechanisms and dosimetry. Professor Horowitz's main contributions were in his development of the Unified Interaction Model which describes many of the features of thermoluminescence (TL) gamma dose response and the sister model, the Extended Track Interaction Model, describing heavy charged particle fluence response. He was among the first to describe and develop the many possible applications of computerized glow curve analysis to TL phenomena. His more recent contributions are in the unraveling of the mysteries of the LiF:Mg,Ti system via optical absorption (OA) and TL glow curve investigations, which have revealed the composite structure of the main dosimetric peak as arising from a mixture of localized and delocalized recombination. These studies have now been incorporated into increasingly complex and generalized kinetic simulations of TL and OA and have led to a unifying and deep understanding of many of the aspects of the theory of TL systems.

Dr. Leonid Oster has developed mechanisms and applications of exoelectron emission (EEE) from insulating materials, which permit one to propose the experimental criteria for systematization of thermo – and photostimulated exoelectron emission mechanism. He was one of the pioneers in the use of alkali-earth sulphates based

TSEE dosimeters via the development of a $CaSO_4$:Mn,Na material using the precipitation method with a surplus of anion vacancies. His studies of new ultra-sensitive TLD materials allowed to establish the optimal readout procedure and thus removed the final obstacle to the widespread use of LiF:Mg,Cu,P chips in radiation protection dosimetry. Prof. L. Oster is carrying out a multi-pronged investigation of the LiF:Mg,Ti system using a variety of experimental techniques including optical absorption, and spectral emission analysis using an advanced CCD spectrophotometer, heavy charged particles studies, glow curve kinetic analysis as a function of dopant concentration as well as optical bleaching.

Dr. Ilan Eliyahu's research interests are in the broad areas of Radiation Physics with special emphasis on Thermoluminescent Dosimetry, particularly heavy charged particle response, track structure theory, kinetics of thermoluminescent materials, defect studies and Monte Carlo calculations for radiation dosimetry. Additional interests include radiation protection, especially non ionizing radiation, the effects of radiation on human cognitive functions and the development of advanced measurement techniques.

Chapter 4 has been written by Drs. George S. Polymeris and George Kitis, and covers the topic of Thermally Assisted Optically Stimulated Luminescence (TA – OSL), which is of importance in both luminescence dosimetry and luminescence dating.

Dr. George S. Polymeris is a researcher at the Institute of Nuclear Sciences of Ankara University in Turkey. His research interests include the techniques of TL, OSL, Electron Paramagnetic Resonance (EPR) and Fourier Transform Infrared (FTIR) spectroscopy. He has published more than 125 peer-reviewed scientific papers in these fields, covering (a) the analysis of complex experimental curves of TL, OSL and FTIR, (b) the study of athermal fading of signals arising from a mixture of localized and delocalized recombination in feldspars and apatites and (c) several alternative applications of luminescence beside dating and dosimetry. His contributions include the use of luminescence as a probe for archaeo-thermometry in pottery and masonry, solid state bioactivity characterization of bioactive materials and oxidation study of $Mg_2Si$ thermoelectric materials.

Major contributions include the pioneering studies of thermally assisted OSL (TA – OSL) in $Al_2O_3$:C and quartz, towards accessing stable very deep electron traps (VDTs) and thus luminescence age limit extension beyond ages of one million years.

Dr. Kitis is Professor of Physics at Aristotle University of Thessaloniki, Greece. His research work in TL and OSL is both experimental and theoretical, and includes over 200 peer-reviewed publications. He is highly interested in the development of analytical expressions for TL and OSL, which are suitable for application in the analysis of complex experimental curves, through computerized glow curve deconvolution (CGCD) procedures. Recently, he contributed to the analytical solution of the one trap one recombination center (OTOR) model based on the Lambert W function, as well as, to the analytical solution of a localized tunneling recombination model. He studies new alternative natural dosimeters, to be used for dating in archaeology and geology. He was a member of the pioneer research group in the studies of thermally assisted OSL (TA – OSL) in $Al_2O_3$:C and quartz, towards accessing very deep electron traps (VDTs), which are much more stable. He is currently studying TA – OSL in various materials, such as quartz and apatites, thus contributing in efforts to extend luminescence dating limits beyond one million years.

Chapter 5 by Drs. Marco Martini and Mauro Fasoli covers recent developments in our understanding of the luminescence mechanism and related defects in quartz. The early contributions of Prof. Martini concerned the ionic conductivity in quartz and the relationship with its luminescence properties, mainly related to the so-called pre-dose effect of the 110°C TL peak. The development of a model featuring the $[AlO_4]^\circ$ as a luminescence center dates back to 1995. In the last 10 years, together with Prof. Fasoli, his research has focused on a detailed investigation of quartz spectroscopy exploiting the radioluminescence technique coupled to wavelength resolved TL. This investigation allowed the identification of the spectral parameters of quartz emission bands and their dependence on thermal annealing, showing the composite nature of both UV and blue emissions. Recently, by means of EPR technique, the identification

of the $[GeO_4]^-$ point defect as the trap responsible for the 110°C TL peak was achieved.

Chapter 6 by Dr. Alicja Chruścińska summarizes recent experimental and theoretical aspects of OSL. The main area of interest of Alicja Chruścińska was the impact of the trap ionization process on the optically stimulated luminescence and especially on its dependence on measurement temperature and stimulation energy. Including the participation of lattice vibrations in the trap ionization process allowed showing that such effects as the increase in the intensity and the decay rate of the OSL curve, or the optical emptying of traps by photons having energy much below the optical depth of a trap may be explained in the frame of the basic model of OSL. The deeper insight in the trap ionization process resulted in the development of several optical stimulation methods that enable to get more information on traps than just the value of the optical cross-section, which is not uniquely determined and depends on experimental parameters.

Chapter 7 has been written by Dr. Makaiko Chithambo, an expert in the technique and theory of time-resolved luminescence. Makaiko Chithambo is a professor of physics at Rhodes University in South Africa. He has made extensive contributions on theoretical and experimental aspects of time-resolved optical stimulation of luminescence, a method developed for the study of charge-transfer processes in luminescent materials. He also has had a long-standing interest in other allied methods such as thermoluminescence, radioluminescence and 3-D thermoluminescence spectrometry. Chithambo has studied many natural and synthetic materials including quartz, $\alpha$-$Al_2O_3$:C, $\alpha$-$Al_2O_3$:C,Mg and ultra-high molecular weight polyethylene, under the over-arching theme of study of point-defects in insulators using luminescence methods.

Chapter 8 by Dr. Paweł Bilski covers recent developments in TL dosimetry of cosmic radiation in space. Professor Bilski's main area of scientific activity is thermoluminescence and thermoluminescent dosimetry. Among his achievements are works on understanding and optimization of LiF:Mg,Cu,P detectors, as well as on efficiency of TL detectors to various radiation modalities. He also participated in

numerous experiments aimed at measurements of cosmic radiation doses in space. His recent achievement is development of fluorescent nuclear track detectors based on lithium fluoride crystals.

The applications of TL in Chapter 8 are followed by a summary of advances in luminescence measurements for retrospective dosimetry in Chapter 9, written by Drs. Stephen W.S. McKeever and Sergey Sholom. Stephen McKeever is Emeritus Regents Professor at Oklahoma State University. His research career has been in the area of luminescence materials and techniques for radiation dosimetry, especially Thermoluminescence (TL) and Optically Stimulated Luminescence (OSL). He has over 200 peer-reviewed publications in the field and is author or co-author of several leading books in these fields. Areas of particular interest include dosimetry, chronological dating, and solid-state physics. Major accomplishments include the development, with collaborators, of advances in the understanding of TL and OSL kinetics and of pulsed OSL as a primary method for personal dosimetry based on $Al_2O_3$:C. More recent accomplishments concern the application of these methods and electron paramagnetic resonance (EPR) to emergency dosimetry following large-scale radiation exposures.

Sergey Sholom is a Research Assistant Professor in Physics at Oklahoma State University. He is an expert in the application of EPR, TL and OSL techniques in the area of emergency dosimetry following large-scale radiation accidents and exposures. He has over 60 peer-reviewed publications in the general field. Major accomplishments include being part of an international team on the application of EPR to dosimetry of Chernobyl accident victims using teeth and, more recently, the development of EPR of finger nails as personal accident dosimeters. He has also been a leader in the development of TL and OSL techniques from personal electronic devices, such as smart phones, for use as emergency dosimeters.

Chapter 10 has been written by two experts in the field of TL/OSL Dating, Drs. Sheng-Hua Li and Bo Li. Their main contributions were in the methodologies of luminescence dating, particularly to the applications of Quaternary sediments. In this chapter they describe the principles and protocols of luminescence dating techniques,

outlined the prerequisites of the dating applications, and discussed the advantages and limitations of the techniques. They have also described several recent advances mainly in optically stimulated luminescence dating, which have extended either the age range, or the material range of the dating methods.

Chapter 11 has been written by Drs. Benny Guralnik and Reza Sohbati, and covers another major development of luminescence dosimetry applications, namely the fundamentals of luminescence photo- and thermochronometry. Benny Guralnik and Reza Sohbati have, during their concurrent doctoral theses, laid the theoretical and methodological foundations of luminescence thermochronometry and luminescence surface exposure dating, respectively. Both have also played a pivotal role in the initial validation and first applications of these methods in geoscience. The present chapter is, in essence, an organized transcript of a long-standing method developer dialogue, which focuses on the extensive conceptual resemblance between these two novel sub-disciplines, and introduces a joint nomenclature and a fully transferable analytical toolbox across the two for their mutual benefit.

Finally Chapter 12 has been written by Drs. Larry A. DeWerd, Cliff Hammer and Stephen Kry, experts in medical applications of luminescent materials. Professor DeWerd has been working on Thermoluminescence Dosimetry (TLD), mainly the LiF:Mg,Ti system, since the 1960's. He has developed the applications in the realm of radiation therapy and diagnostic radiology. He has worked on the causes of supralinearity and how to use TLD in the higher dose areas. He was among the first to describe and develop the many possible applications and the response of the TLD to various energies. His development of the procedures in handling the materials have resulted in the increased precision and accuracy in the measurement of dose. The applications have extended from the use on phantoms to the use in patients. The applications also have extended from external beam radiations to brachytherapy. Cliff Hammer has also been instrumental in the increased precision for applications. Lately Professor DeWerd has explored some applications using Optically

Stimulated Luminescence (OSL). Professor Stephen Kry has worked extensively with OSL.

We would like to thank our participating colleagues who contributed their professional capabilities and broad knowledge, each in his/her subfield, which enabled the compilation of this volume of up-to-date advances in TL/OSL, some related subjects and main applications.

Reuven Chen
Vasilis Pagonis

This page intentionally left blank

# Contents

# Chapter 1

# Recent Advances in the Theory of Thermoluminescence and Optically Stimulated Luminescence; Delocalized Transitions

Reuven Chen

*Raymond and Beverly Sackler School of Physics and Astronomy*
*Tel Aviv University, Tel Aviv 69978, Israel*
*chenr@tau.ac.il*

Several theories explain different facets of the phenomena of thermoluminescence (TL) and optically stimulated luminescence (OSL). In the present chapter we concentrate on models dealing with processes occurring when charge carriers are moving between traps and centers through the conduction and valence bands. The processes involved include transitions occurring during excitation and during read-out: optical stimulation in OSL and heating in TL. Older theories explaining the basic properties of first-and second-order kinetics as well as the effects of non-linear dose dependence of TL and OSL are briefly mentioned. More recent models, developed in the last decade are described in more detail. The effects of competition between traps and between centers both during excitation and read-out are discussed in some detail, yielding the interpretation of superlinear dose dependence, non-monotonic dose dependence as well as dose-rate dependence. The theories can also explain the experimentally observed concentration quenching and the prevalence of first-order peaks in various materials. A model for explaining an anomalous heating-rate effect and thermal quenching is discussed. The occurrence of anomalously high or low activation energies and frequency factors, sometimes evaluated by standard peak-shape methods is also briefly discussed. Finally, the recently studied subject of two-electron traps or two-hole centers and their effects on TL and OSL phenomena are discussed.

## 1.1. Introduction

The phenomena of thermally stimulated luminescence, usually termed thermoluminescence (TL) and optically stimulated luminescence (OSL) consist of the emission of energy previously absorbed in a solid material in the form of light during thermal or optical stimulation. A prerequisite is that the energy be absorbed, usually by irradiating the sample in hand by ionizing or sometimes non-ionizing radiation. The captured energy may be released in the form of emitted light either by heating the sample, in TL measurements or by illuminating it by some light source. In the latter case, the emitted stimulated light is usually of different wavelength than the stimulating light.

The basic theory of TL and OSL is based on the existence of imperfections, impurities and defects in the otherwise ordered crystals which give rise to allowed discrete energy levels in the forbidden gap of the crystal which may capture electrons or holes. During excitation, electron and hole pairs are produced by the radiation throughout the sample and certain fraction reach the conduction and valence bands, respectively. These carriers may be trapped in electron and hole traps located in the forbidden gap. It is rather conventional to talk about electron traps, located quite close to the conduction band and about hole centers located far from the valence band. Under these conditions, during TL read-out by heating, the trapped electrons may be raised into the conduction band, and following their motion in the conduction band, recombine with a hole in a luminescence center and recombine with it yielding an emitted photon. A schematic energy level diagram with one electron trap and one hole recombination center is shown in Fig. 1. It should be noted that a mirror-image model is just as likely to occur. If the hole trap is located close to the valence band and the electron trap, now referred to as a center, is far from the conduction band, the process taking place during heating includes the thermal release of a trapped hole into the valence band and its recombination with an electron in a center, thus yielding a TL photon. The situation in OSL is the same as far as the excitation is concerned. As for read-out, photons, e.g. infra-red light, raise

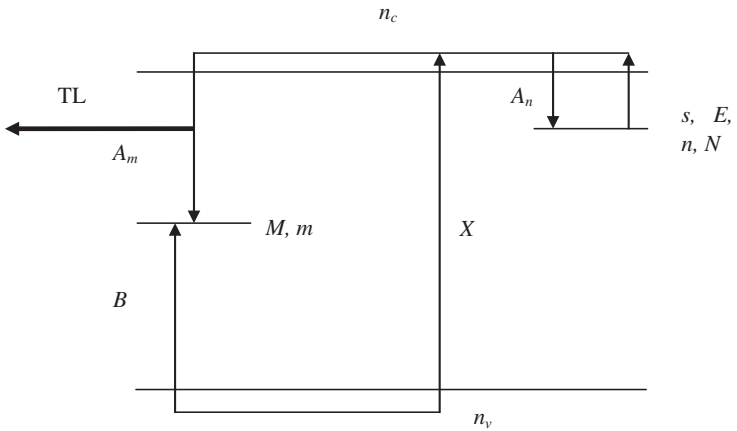


Fig. 1. Schematic energy-level diagram showing an electron trap and a hole center.

electrons from the trap to the conduction band which then find counterpart holes in the center and recombine to yield OSL photons, usually with different wavelength than the stimulating IR light. Like in TL, the inverse picture of hole traps and electron centers can be considered as being relevant also to OSL. It should be mentioned that the models discussed in this chapter assume a homogeneous excitation of the sample which is a good assertion of the situation taking place with UV, X-ray and $\gamma$ excitation and to a lesser extent, for $\beta$ exposure.

The parameters shown in Fig. 1 are as follows: $E$ (eV) is the activation energy for releasing a trapped electron, $s$ ($\mathrm{s}^{-1}$) is the frequency factor, $A_m$ ($\mathrm{cm}^3\mathrm{s}^{-1}$) and $A_n$ ($\mathrm{cm}^3\mathrm{s}^{-1}$) are the recombination and retrapping probability coefficients, $B$ ($\mathrm{cm}^3\mathrm{s}^{-1}$) is the trapping probability coefficient of free holes into centers, $M$ ($\mathrm{cm}^{-3}$) is the concentration of hole centers and $m$ ($\mathrm{cm}^{-3}$) its instantaneous occupancy, $N$ ($\mathrm{cm}^{-3}$) is the concentration of electron traps and $n$ ($\mathrm{cm}^{-3}$) its instantaneous occupancy. $n_c$ ($\mathrm{cm}^{-3}$) and $n_v$ ($\mathrm{cm}^{-3}$) are, respectively, the instantaneous concentrations of free electrons and holes. $X$ ($\mathrm{cm}^{-3}\mathrm{s}^{-1}$) is the rate of production of electron-hole pairs, proportional to the dose rate.

The set of simultaneous differential equations governing the process during excitation is (see e.g. Chen and Pagonis, [1])

$$\frac{dn}{dt} = A_n(N-n)n_c - sn\exp(-E/kT), \tag{1}$$

$$\frac{dm}{dt} = B(M-m)n_v - A_m m n_c, \tag{2}$$

$$\frac{dn_c}{dt} = X - A_n(N-n)n_c - A_m m n_c, \tag{3}$$

$$\frac{dn_v}{dt} = \frac{dn}{dt} + \frac{dn_c}{dt} - \frac{dm}{dt}. \tag{4}$$

At the end of excitation one ends up with a finite concentration of free electrons, $n_c$, and free holes, $n_v$. If one wishes to mimic the experimental procedure of TL or OSL, one has to consider a relaxation time between the end of excitation and the beginning of heating or exposure to stimulating light. This is done by setting $X$ to zero and solving Eqs. (1–4) for a further period of time so that at the end, both $n_c$ and $n_v$ are negligibly small. Obviously, the final values of $n$, $m$, $n_c$ and $n_v$ at the end of excitation are used as initial values for the relaxation stage. Finally, for the read-out stage, we take the final concentrations in the relaxation stage as initial values for the next stage and simulate either the heating in TL or the optical stimulation in OSL. It is worth mentioning that in this, relatively simple case of one trapping state and one kind of recombination center, the final concentrations of traps and centers, which are the initial concentrations $n_0$ and $m_0$ for the read-out stage must be the same. However, when several traps and/or centers are involved, the solutions of the excitation and relaxation stages prior to the read-out stage are crucial in order to get realistic results.

Before moving to the discussion of the heating stage in TL in the one-trap-one recombination center (OTOR) case shown in Fig. 1, let us mention briefly the preceding models given in the earlier literature. Randall and Wilkins [2] developed the first theory for a single TL peak. These authors assumed that once an electron is thermally raised into the conduction band it immediately performs

recombination with a trapped hole in center, and wrote the equation

$$I(T) = -dn/dt = sn \exp(-E/kT). \tag{5}$$

$I$(T) is the intensity of emitted TL and $k$ (eV/K) is the Boltzmann constant. Note that as is, the units of $I(T)$ are $\mathrm{cm}^{-3}\mathrm{s}^{-1}$ and in order to have it in light-intensity units a constant should be added which is arbitrarily set to unity. Equation (5) is a first-order equation and its solution for a linear heating function is an asymmetric glow peak with a fall-off half-intensity width smaller than the half-intensity width in the increasing part. In a later work, Garlick and Gibson [3] took into consideration the possibility of having freed electrons retrap into their initial trapped state and reached a second-order TL peak with nearly symmetrical shape. Halperin and Braner [4] considered the traffic of carriers during the heating of the sample following excitation, taking into account thermal excitation, recombination and retrapping. The set of coupled differential equations governing the process during heating is

$$\frac{dn}{dt} = A_n(N-n)n_c - sn \exp(-E/kT), \tag{6}$$

$$I(T) = -\frac{dm}{dt} = A_m m n_c, \tag{7}$$

$$\frac{dm}{dt} = \frac{dn}{dt} + \frac{dn_c}{dt}. \tag{8}$$

Note that both here and in the simpler first-order case of Fig. 1, in order to simulate a conventional TL curve, one has to use some heating function which in most cases is chosen to be linear with time, i.e., a constant heating rate is used,

$$T = T_0 + \beta t, \tag{9}$$

where $T_0$ (K) and $T$ (K) are the initial and running temperature and $\beta$ (K/s) is the constant heating rate.

This set of coupled differential equations cannot be solved analytically and therefore two different approaches can be applied. In the earlier stages of TL study, simplifying assumptions were made in order to reach possible conclusions. The alternative which has been utilized broadly in more recent studies has been to assume

a plausible set of trapping parameters and solve the equations numerically. Both these approaches will be described here. The same two approaches can be pursued and the results of the two compared also in more complex situations where more trapping levels and/or more recombination centers are involved. Another approach recently developed by Kitis and Vlachos [5] is briefly mentioned. These authors dealt with TL, OSL and linearly modulated OSL (LM-OSL), and found general semi-analytical expressions, using the Lambert W-function.

Halperin and Braner [4] have suggested an approximate expression for the dependence of the emitted light on the relevant occupancies of traps and centers, which also gave a better insight into the question of the effective order of kinetics. They made the simplifying assumptions later termed "quasi-equilibrium" or "quasi-steady" assumptions

$$\left|\frac{dn_c}{dt}\right| \ll \left|\frac{dn}{dt}\right|, \quad \left|\frac{dm}{dt}\right|; \;\; n_c \ll n, m, \tag{10}$$

which state that the rate of change of free carriers is significantly smaller than that of the trapped carriers, and that the concentration of free carriers is significantly smaller than that of trapped carriers. It should be mentioned that Chen and Pagonis [6] suggested a somewhat different way of expressing the conditions leading to the simplified expression given by Halperin and Braner [4], namely

$$\left|\frac{dn_c}{dt}\right| \ll sn\exp(-E/kT), \quad n_c[A_n(N-n) + A_m m], \tag{11}$$

which simply means that the net rate of change of free electrons is significantly smaller than the rates of thermal elevation of electrons into the conduction band and the depletion of free electrons into the trap and center together.

Using either of these sets of simplifying assumptions, one gets

$$I(T) = -\frac{dm}{dt} = sn\exp(-E/kT)\frac{A_m m}{A_m m + A_n(N-n)}. \tag{12}$$

Obviously, this one equation in two unknown functions, $n$ and $m$, cannot be solved without further assumptions. As long as only one

trap and one center are involved, and along with the original quasi-equilibrium assumption, we can assume that $m \approx n$, and one gets an equation in one function, $n$, only (see Kanunnikov [7])

$$I(T) = -\frac{dn}{dt} = sn \exp(-E/kT) \frac{A_m n}{A_m n + A_n(N-n)}. \qquad (13)$$

Further simplifying assumptions would lead to the first- and second-order kinetics equations. If recombination dominates, $A_m m \gg A_n(N-n)$, one gets directly the Randall-Wilkins first-order, Eq. (5). The second-order kinetics suggested by Garlick and Gibson [3] can also be reached from Eq. (13) by making different simplifying assumptions. If we assume that retrapping dominates, $A_n(N-n) \gg A_m m$ and that the trap is far from saturation, $N \gg n$, Eq. (13) reduces to

$$I(T) = -\frac{dn}{dt} = \frac{sA_m}{A_n N} n^2 \exp(-E/kT). \qquad (14)$$

Another less likely possibility is that the retrapping and recombination probability coefficients are equal, $A_m = A_n$. Equation (13) reduces now to

$$I(T) = -\frac{dn}{dt} = \frac{s}{N} n^2 \exp(-E/kT). \qquad (15)$$

Both these last expressions are second-order equations with somewhat different meaning of the effective pre-exponential coefficient.

It is quite obvious that cases intermediate between the first-order case (Eq. 5) and the second order (Eqs. 14, 15) are possible. A very popular approach is using the heuristic "general order" equation (see e.g. Chen [8])

$$I(T) = -\frac{dn}{dt} = s' n^b \exp(-E/kT), \qquad (16)$$

where $b$ is different from 1 or 2. The disadvantage of this approach is that it has no real physical basis where $b \neq 1, 2$ and also that $s'$ has the "strange" units of $\mathrm{cm}^{3(b-1)}\mathrm{s}^{-1}$. The advantage is that the solution of Eq. (16) may yield any symmetry between those of the first- and second-order kinetics.

Another possible way of presenting intermediate cases is that of the mixed-order kinetics (see e.g., Chen *et al.* [9])

$$I(T) = -\frac{dn}{dt} = s'n(n+c)\exp(-E/kT), \tag{17}$$

where here, $s'$, the pre-exponential factor has the same units as in the second-order case, namely, $\mathrm{cm}^3\mathrm{s}^{-1}$.

In the present chapter we elaborate on a number of aspects of TL and OSL that can be explained by models dealing with delocalized transitions taking place during the excitation and read-out stages.

### 1.2. Dose dependence

One of the most important aspects of TL and OSL is the dependence of the signal on the excitation dose. This kind of measurement is of great interest from the pure scientific viewpoint, but also has importance in the applications in dosimetry and in geological and archaeological dating elaborated upon in this volume. It is obvious that for the applications, ideal dose dependence is a linear behavior in the broadest dose range possible. In real life, this is usually not the case and different kinds of non-linear dose dependence are observed. The most common one is that at relatively high doses, saturation effects take place, namely, the dose dependence is sublinear from a certain dose on. More interesting are situations where superlinearity occurs. Nonlinear growth of TL as a function of absorbed $\beta$ or $\gamma$ dose, mainly in the important dosimetry material LiF (TLD-100) has been discussed in some detail by Cameron *et al.* [10]. The characteristic behavior here was a rather broad linear dose dependence followed by more than linear range after which, an approach to saturation was observed. Another kind of superlinearity was discovered in the mid-sixties by Tite [11] in ancient ceramics. Here, the dose dependence curve is linear in a broad range, except for the lowest doses where the TL starts increasing at a small rate with the dose and the rate increases gradually until it reaches a steady value which prevails over a broad dose range. Another sort of superlinearity was reported by Halperin and Chen [12] who studied the dose dependence of UV-irradiated semiconducting diamonds. UV light in the range of

300–400 nm (4–3 eV) excited a TL peak at ∼250 K and the initial dose dependence of the emitted light could be presented as

$$I_{\max} = \alpha D^k, \tag{18}$$

where $I_{\max}$ is the maximum intensity, $D$ the applied dose and $k$ is a factor between 2 and 3 in the mentioned range of 300–400 nm. The superlinearity is expressed by having a $k$ value larger than unity. Two other cases of such very strong superlinearity ($k \sim 3$) of TL have been reported. Chen *et al.* [13] described the effect in $\beta$-excited quartz and reported nearly cubic dose dependence and Otaki *et al.* [14] communicated on slightly more than cubic dose dependence of TL in $CaF_2$:$Tb_4O_7$.

### 1.2.1. *Theory of superlinear dose dependence*

The basic understanding of the superlinear dose dependence of TL and OSL usually includes different kinds of competition. The two main sorts of competition are competition that takes place during excitation and that which occurs during readout (heating in TL and optical stimulation in OSL) or both. The first model explaining superlinearity has been given by Cameron *et al.* [10] (see pp. 168–174). This model proposes the creation of additional traps by radiation and hypothesizes a maximum possible trap density. Another model was given by Suntharalingam and Cameron [15] and further elaborated upon by Bowman and Chen [16]. These authors assumed that the total concentration of traps is not changed by the irradiation and the superlinearity is associated with the competition of electrons being trapped into the active trap and into a competing, usually deeper trap. Intuitively speaking, let us assume a system with concentrations $N_1$ ($cm^{-3}$) active traps and $N_2$ ($cm^{-3}$) competing traps. Let us assume that the trapping probability coefficient $A_2$ is larger than that of the active trap, $A_1$. At low doses, the excitation fills both traps linearly. However, at a certain dose the competing trap saturates and therefore more electrons are made available to the trap of interest $N_1$. This causes faster though linear filling of the trap. However, the transition region from one linear range to the other would appear to be superlinear since this transition

occurs continuously. Bowman and Chen [16] wrote the proper set of differential equations, made the relevant simplifying assumptions and reached an expression that with the appropriate choice of sets of trapping parameters yielded a dose-dependence curve which starts linearly, continues superlinearly and then tends to saturation.

Rodine and Land [17] reported on the dose dependence of some TL peaks in $\beta$-irradiated $ThO_2$ which were found to be quadratic with the dose starting at the lowest doses, and explained the effect qualitatively as being the result of competition during heating. Kristianpoller *et al.* [18] further elaborated on competition during heating (see a more elaborate explanation in Chen and Pagonis [1], pp. 198–205). Without competition, one may expect the area $S$ under a glow peak to be proportional to min $(n_0, m_0)$ where $n_0$ and $m_0$ are, respectively, the concentrations of electrons in traps and holes in centers following excitation and relaxation and prior to readout. The maximum TL intensity is usually more or less proportional to the area under the curve. Thus, if $n_0$ and $m_0$ are linearly dependent on the dose of excitation, the measured TL intensity is also linear with the dose. Kristianpoller *et al.* [18] showed that in the presence of a strong competing trap, the dependence of the area under the curve is, due to competition during heating

$$S \propto n_0 m_0, \tag{19}$$

and if $n_0 \propto D$ and $m_0 \propto D$, then $S \propto D^2$. In a later work, Chen *et al.* [19] have combined the two approaches and showed, using numerical simulation that with a model with two competing traps and one recombination center, more than quadratic dose dependence may be reached, the main effect being related to competition during heating. On the other hand, in a model with two competing centers and one kind of trap, a much weaker superlinearity can be explained, mainly associated with competition during excitation.

In recent years, it has been shown that under the appropriate circumstances, superlinearity of TL and OSL can take place even without competition, which was termed "intrinsic" superlinearity. Chen *et al.* [20] used the simple OTOR energy level diagram, Fig. 1 and considered the situation where relatively high dose rates

are being used. As stated by these authors, the second derivative $d^2n/dD^2$ being positive indicates superlinear dose dependence. Referring to the parameters shown in Fig. 1, the filling of traps with dose can be given as

$$n = aD + bD^2 + O(D^3), \tag{20}$$

where

$$a = \frac{A_n N}{A_n N + A_m m_0}, \tag{21}$$

$$b = \frac{1}{2}\frac{A_m m_0 A_n N}{(A_n N + A_m m_0)^3}(A_m - A_n). \tag{22}$$

The coefficient $b$ governs whether the initial response is superlinear, linear or sublinear. According to Eq. (22), the behavior is superlinear ($b > 0$) if $m_0 > 0$ and $A_m > A_n$. The initial dose dependence is expected to be linear if $m_0 = 0$ or, if $m_0 > 0$ but $A_m = A_n$. Chen *et al.* [20] gave also results of numerical simulations that at the low-dose range coincide with those given by Eq. (20). At higher doses, the $D^3$ and higher terms become important and on the other hand, saturation effects may set in, so that the semi-analytical result and the outcome of the numerical simulation tend to diverge. Another situation that may lead to superlinear dose dependence is associated with two-electron traps and two-hole centers which are explained in subsection 1.2.3.

### 1.2.2. *Non-monotonic dose dependence*

The TL intensity in different materials is usually a monotonically increasing function of the dose, which quite often reaches a saturation value. In several materials, however, non-monotonic dose dependence has been observed. The TL intensity reached a maximum at a certain dose and decreased at higher ones. For some examples, Cameron *et al.* [10] described the non-monotonic dose dependence in LiF:Mg, Ti as a function of $^{60}$Co $\gamma$-ray excitation dose. Jain *et al.* [21] describe a significant decrease of the TL output of peak V in LiF, by a factor of $\sim$2.5 from the maximum, and ascribe it to radiation damage. Yukihara *et al.* [22] described a somewhat superlinear dependence

up to ∼10 Gy of $\beta$ irradiation of the 450 K peak in $Al_2O_3$:C. The peak reached a maximum value and declined at higher doses.

Chen *et al.* [23] suggested a rather general model which does not assume a radiation damage of destruction of trapping states and/or recombination centers. The authors assume the existence of two trapping states and two kinds of recombination centers. The competition over charge carriers during excitation and heating was examined using both numerical simulations and intuitive considerations. The authors chose a physically significant set of trapping parameters and performed the simulation of the three stages of the relevant experiment, namely, excitation, relaxation and heating. An example of the results is shown in Fig. 2. The results show an increase of the TL maximum (solid line) with the dose up to a maximum at a 'dose' of $\sim 7 \times 10^{20}\,\mathrm{m}^{-3}$, followed by a decrease of ∼35% after which the maximum TL intensity tends to level off at higher doses. This behavior is very similar to experimental results reported in some materials, e.g., see Jain *et al.* [21]. A similar behavior is seen in the plot of $m_2$ at the end of the relaxation period (dashed line).

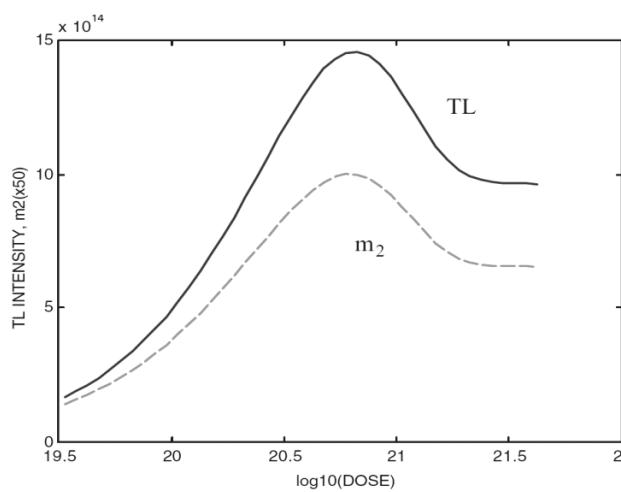


Fig. 2. Simulated dose dependence of the maximum TL (solid line) and radiative-center concentration at the end of irradiation, $m_2$ (dashed line), when competition during irradiation dominates. (After Chen *et al.* [23]).

Pagonis *et al.* [24] used a similar model to account for the non-monotonic dose dependence of OSL. Such results had been observed by Yukihara *et al.* [22], [25].

A later work by Chen *et al.* [26] discussed the time and dose-rate dependence of TL and OSL due to competition between excitation and fading. The authors presented a model of two trapping states and one kind of a recombination center and using simulations, studied the dependence on the time of excitation of the filling of the active trap, to which the TL or OSL signal is proportional. The solution of the relevant set of coupled differential equations has revealed a time dependence of an increase up to a maximum value and then a decrease toward an equilibrium value where the rates of production and decay are equal. This model is more concise since it includes only one kind of recombination center, however, here, the non-monotonic effect occurred only when the dose changed by varying the time of excitation. Here, when the dose rate was varied with constant time of excitation, the curve increased monotonically until it reached the saturation value.

### 1.2.3. *Double-charge traps and centers*

In a recent work, Chen *et al.* [27], [28] have studied the effects of two-electron traps and two-hole centers on the behavior of TL glow curves. The concept of double-electron traps had been established before with regard to different solid state phenomena and also mentioned in connection with TL. Also have been mentioned in the literature two-hole centers and their effect on the TL properties. Mayhugh [29] and Townsend *et al.* [30] explained results of TL in LiF by the existence of $V_3$ centers containing two trapped holes. Böhm and Scharmann [31] mentioned the occurrence of two-electron F' centers in alkali-halides with relation to the general subject of TL dosimetry. Yazici *et al.* [32] who studied TL of LiF:Mg,Ti between 100 and 300 K suggested that their results are related to the $V_3$ two-hole centers. The same $V_3$ centers have been considered as being associated with TL by Horowitz [33] and by Eliyahu *et al.* [34]. Woda and Wagner [35] while explaining non-monotonic dose dependence of Ge- and Ti-centers in quartz, discuss a model of double-electron

capture which can be expressed in both EPR and TL measurements. Chen *et al.* [28] wrote the relevant sets of equations for the excitation, relaxation and heating stages of TL relevant to the two-electron trap model. The model given in Fig. 2 represents the present situation except that the trap can capture either one or two electrons. Let us denote now by $n_1$ ($\mathrm{cm}^{-3}$) the traps with one electron and by $n_2$ ($\mathrm{cm}^{-3}$) the traps with two electrons. Obviously, the instantaneous concentration of empty traps is $N - n_1 - n_2$. The activation energy of a single electron in a trap will be denoted by $E_1$ (eV) and the energy for releasing an electron from a double-occupied trap by $E_2$ (eV). One may assume that $E_1 > E_2$ since with two electrons in a trap there may be Coulombic repulsion whereas with one electron, there may be some Coulombic attraction of the electron to the impurity ion forming the trap. As for the trapping probability coefficients, $A_1$ ($\mathrm{cm}^3\mathrm{s}^{-1}$) is the probability coefficient into an empty trap and $A_2$ ($\mathrm{cm}^3\mathrm{s}^{-1}$) is the trapping probability coefficient into a trap with one electron. In most cases, one would predict that $A_1 > A_2$ since the probability of capturing a free electron is expected to be larger in the empty trap than in a trap holding an electron.

The results of the simulations and the approximate analytical analysis show that the lower-temperature peak has first-order features and is strongly superlinear with the excitation dose. As shown in Fig. 3, the dose dependence is slightly more than cubic with the excitation dose, which may explain the experimentally found strongly superlinear dose dependence mentioned above.

A rather similar situation has been studied by Chen *et al.* [28], namely the case where a recombination center may capture one or two holes. The authors have shown the expected TL behavior using in parallel numerical simulation and approximate analytical treatment. The outcome is two TL peaks and the two-hole center behaves in a sense like two centers with different recombination probabilities. The lower temperature peak has first-order features and is more than quadratically superlinear with the dose. The second peak has a second-order shape and both peaks shift to lower temperature with the dose which is explained by a change in the effective frequency factor with excitation dose.

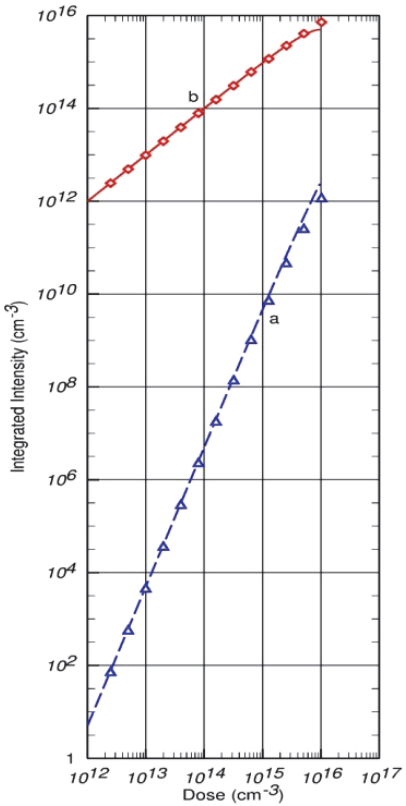


Fig. 3. Dependence of the area under the two simulated TL peaks on dose of excitation plotted on a log-log scale. (a) The lower temperature peak; the dashed line shows the analytical results and the triangles represent the numerical results. (b) The higher temperature peak; the solid line shows the analytical results and the diamonds are the numerical results. (After Chen *et al.* [27]).

### 1.2.4. *Dose-rate dependence*

In the previous sub-section, we discussed the dose dependence of TL and OSL, assuming that it does not matter whether the dose applied on the sample in hand is varied by changing the time of excitation or by changing the dose rate. In fact, dose rate and time of excitation are independent variables and in some cases, the resulting luminescence may depend on the dose rate even when the total dose applied is the same. It should be noted that when

archaeological and geological dating is concerned, the natural dose rate may be as low as $10^{-3}\,\mathrm{Gy}\cdot\mathrm{yr}^{-1}$ ($3\times10^{-11}\,\mathrm{Gy}\cdot\mathrm{s}^{-1}$), whereas the laboratory dose rate applied for calibration may be as high as several $\mathrm{Gy}\cdot\mathrm{s}^{-1}$. One has to distinguish between a dose-rate effect such as that reported by Facey [36], which has to do with the thermal decay during excitation, and "real" dose-rate effect where the TL or OSL signal is stable such that no thermal decay is expected at ambient temperature. Groom *et al.* [37] reported such a significant effect in quartz where no thermal decay takes place. Here, a decrease by up to a factor of ∼5 was observed with increasing dose rate (and constant total dose) in powdered samples of Brazilian crystalline quartz when irradiated by $^{60}$Co $\gamma$-rays at dose rates ranging from $1.4\times10^{-3}$ to $3.3\,\mathrm{Gy}\cdot\mathrm{s}^{-1}$. Also reported on the dose-rate effect in quartz Chawla *et al.* [38]. A smaller effect of the same sort in $CaSO_4$:Dy has been reported by Hsu and Weng [39]. Shlukov *et al.* [40] suggested that in archaeological and geological dating based on TL in quartz, the fact that there is a difference of 8-9 orders of magnitude in the dose rate between natural and calibration irradiations may cause a serious error in the age evaluation. A very interesting dose-rate effect has been reported by Valladas and Ferreira [41]. They distinguish between three components in the emission of TL from quartz, namely UV, blue and green. Applying the same total dose of excitation at two dose rates which are three orders of magnitude apart, they found different behaviors for the three components. The UV component was nearly twice as large with the high dose rate as with the low one. As for the green component, the low dose rate yielded about 10% less emission than in the high one. However, with the blue component, the low dose rate yielded about 50% more TL than the high one.

Chen and Leung [42] have explained by the use of simulations the occurrence of the dose-rate effect. The model they used included one trapping state and two kinds of recombination center and it simulates the mentioned situation reported by Valladas and Ferreira [41], namely that two spectral components in quartz behave in opposite ways, one increases and one decreases with the dose rate. Chen and Leung used the relevant sets of coupled differential equations for the three stages of excitation, relaxation and read-out (heating), and

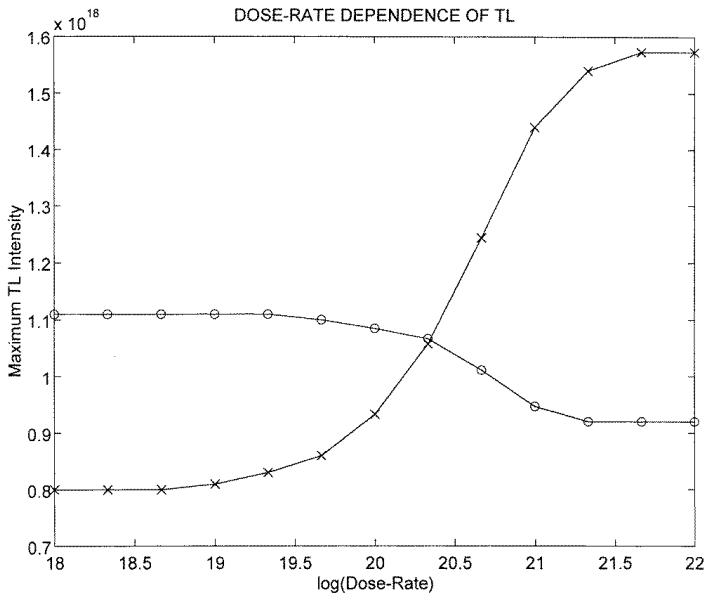


Fig. 4. The dose-rate dependence of the TL maximum intensities of $I_1(T)$ (crosses) and $I_2(T)$ (circles) from the simulations. (After Chen and Leung [42]).

recorded the two emissions, $I_1 = -dm_1/dt$ and $I_2 = -dm_2/dt$, where $m_1$ and $m_2$ are the concentrations of the two recombination centers, respectively.

The dose-rate dependence results of a simulation are given in Fig. 4.

## 1.3. A model for concentration quenching of TL and OSL

All luminescence effects in solids including TL and OSL are directly related to the occurrence of impurities and defects in the host crystal. One would normally expect that when a certain imperfection is responsible for the appearance of TL or OSL, higher imperfections level would mean more emitted luminescence for a given excitation. However, several experiments have shown that a non-monotonic dependence on the impurity concentration may take place. The response to a given irradiation may increase with the

impurity concentration up to a maximum, and then decline for higher concentrations. This effect has been termed concentration quenching (CQ). The first non-monotonic concentration dependence of TL on the relevant impurity concentration has been reported by Medlin [43]. He described the dependence of a TL peak on $Mn^{++}$ impurity in calcite at 350 K and showed that for a given irradiation, a maximum intensity was reached for a certain impurity concentration. Rossiter *et al.* [44] reported on the concentration dependence of peak #5 at 210°C, in LiF:Ti. They found a peak-shaped dependence on the Ti concentration with a maximum efficiency at ∼8 ppm. Nambi *et al.* [45] described the concentration quenching effect of $CaSO_4$, with Dy or Tm impurities. In both cases, the maximum efficiency occurred at ∼0.1 weight percent of the dopant. Lai *et al.* [47] investigated the TL of $ZrO_2$ doped with $Yb_2O_3$ and found concentration quenching with a maximum at 5 mol%, followed by a decrease at higher concentrations. Chen *et al.* [46] proposed a model based on the transitions of electrons and holes between trapping states, the conduction band and the valence band. The model is meant to demonstrate the possibility of explaining the CQ effect for two TL peaks, where the maximum intensity occurs at two different concentrations, similarly to the results by Medlin [43] in $Pb^{++}$ doped calcite. Note that in Medlin's work, the maxima for four peaks in $Mn^{++}$ doped dolomite occurred at different concentrations and one might expect that assuming more trapping states may yield the CQ effect for more than two peaks.

The proposed energy level model includes three electron trapping states, each with $N_i$ ($cm^{-3}$) concentration, $E_i$ (eV) activation energy, $s_i$ ($s^{-1}$) frequency factor and $A_i$ ($cm^3 s^{-1}$) retrapping-probability coefficient, for $i = 1, \ldots, 3$ and a recombination center with concentration $M$ and instantaneous hole concentration of $m$. Chen *et al.* [46] wrote the set of equations governing the excitation stage and relaxation stage (with $X = 0$), analogous to Eqs. (1–4) but with two more equations for the additional two trapping states, and the set analogous to Eqs. (6–8) with the two additional traps. The results of the solution of the equations solved sequentially for excitation, relaxation and heating, in the same way as explained above for

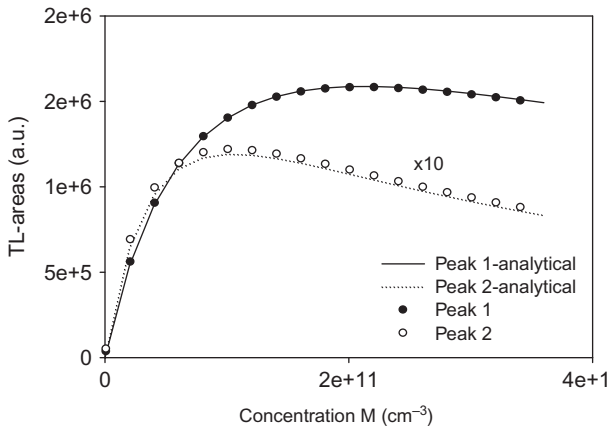


Fig. 5. Simulated results of the concentration dependence of the areas under two TL peaks (After Chen *et al.* [46]).

the simpler OTOR case and for a set of chosen plausible values of the trapping parameters is shown in Fig. 5. The authors state that if one starts the excitation stage with empty centers, the non-monotonic concentration quenching effect is not seen. Instead, if one assumes that the initial occupancy of the centers is a given fraction of the total concentration of the centers, the effect takes place. For the simulation of Fig. 5, the authors chose a fraction $\alpha = 0.1$ of the centers being initially full, which yielded the results shown. The authors emphasize that the underlying reason for the non-monotonic dependence of the TL sensitivity on the concentration is the competition in trapping, both during excitation and read-out between the three traps.

### 1.4. Heating-rate effects in TL and thermal quenching

In practically all known cases, the TL glow peak shifts to higher temperature with increasing heating rate (see e.g. Hoogenstraaten [48]). This can be easily shown for the simple case of first-order kinetics. The solution of Eq. (5) is

$$I(T) = sn_0 \exp(-E/kT) \exp\left[-(s/\beta)\int_{T_0}^{T} \exp(-E/k\tau)d\tau\right]. \quad (23)$$

The well-known condition for the maximum, found by setting the derivative of Eq. (23) to zero, can be written as

$$\beta = (sk/E)T_m^2 \exp(-E/kT_m), \tag{24}$$

where $T_m$ (K) is the temperature at the maximum and $\beta$ (Ks$^{-1}$) the heating rate. When $\beta$ increases, the right-hand side must increase by the same amount. Furthermore, since $T_m^2 \exp(-E/kT_m)$ is an increasing function of $T_m$, the rise in its value implies that $T_m$ must increase. It has been shown (e.g. Chen and Winer [49]) that although in more complex cases Eq. (24) does not hold precisely, it can serve in many instances as a good approximation. Anyway, the shift of a TL peak to higher temperatures with increasing heating rates is a general property.

Chen *et al.* [50] have pointed out that a distinction should be made between two alternative presentations of TL. As an example, one may consider the simple first-order case given by Eqs. (5) and (23). As mentioned above, a dimensional proportionality factor is missing between $I(t)$ and $-dn/dt$ in Eq. (5) which is arbitrarily set to unity. The units of $I(t)$ are cm$^{-3}$s$^{-1}$ whereas the real intensity is given in photons per second or energy per second. As shown before (e.g. Kumar *et al.* [51]), when increasing the heating rate, the maximum intensity increases nearly proportionally. The area under the curve must remain the same for all heating rates and the simple explanation for the increased intensity is that when heating is faster, the peak gets narrower on the time scale. An alternative, quite common presentation is reached by normalizing the intensity as defined in Eq. (5) by dividing it by the heating rate $\beta$. Unfortunately, this is also usually termed in the literature "intensity". This magnitude is usually plotted as a function of temperature rather than time. Thus, the area under the curve remains constant with different heating rates, and this normalized intensity, which is $I(T) = -dn/dT$ (cm$^{-3}$K$^{-1}$) has a slightly decreasing maximum value associated with a slight broadening of the peak with increasing heating rates. The decrease of the normalized intensity with the heating rate is not limited to the first-order case and is observed in many more complicated situations.

Wintle [52] reported on thermal quenching of TL in quartz which is the decrease in luminescence efficiency with the rise in temperature. As reported by several authors (e.g. Subedi *et al.* [53]; Kafadar [54]) the decrease of the maximum of normalized TL with the heating rate is significantly faster than the slight decrease described above. The common explanation has been that since the peak shifts to higher temperature with the heating rate, its intensity decreases due to the thermal quenching. Thus, the area under the normalized curve is not constant but rather, it decreases with increasing heating rates.

In recent years, a number of reports on an inverse, anomalous heating rates effect have been published. Kitis *et al.* [55] have reported on a heating-rate effect in fluorapatite in which the maximum normalized TL intensity and the integral under the curve increased with the heating rate. Bos *et al.* [56] have described a similar effect in $YPO_4$:$Ce^{3+}$,$Sm^{3+}$. Delice *et al.* [57] have described the results of TL in GaS. Two peaks were reported for different heating rates. Whereas the lower-temperature normalized peak decreased with the heating rate $\beta$, the higher-temperature normalized peak increased with $\beta$. Mandowski and Bos [58] explained the effect in $YPO_4$:$Ce^{3+}$,$Sm^{3+}$ by a semi-localized transitions model. Pagonis *et al.* [59] used a simplified semi-localized-transition model to explain the anomalous heating-rate effect.

Chen and Pagonis [50] suggested another model for explaining the anomalous heating-rate effect. The model with one electron trap $N$, one recombination center $M_1$ and one reservoir $M_2$ is shown in Fig. 6. It is assumed that the electron trap is close enough to the conduction band so that electrons are thermally raised into the conduction band during the heating stage. One also assumes that $M_1$, the recombination center is far enough from the valence band so that no holes are thermally released from it into the valence band during heating. Concerning $M_2$, one assumes that it may capture holes from the valence band during excitation and that electrons from the conduction band may recombine with holes both during the excitation and the heating stages. In a sense, this is a Schön-Klasens model (see Schön [60]; Klasens [61]) with an additional reservoir center.

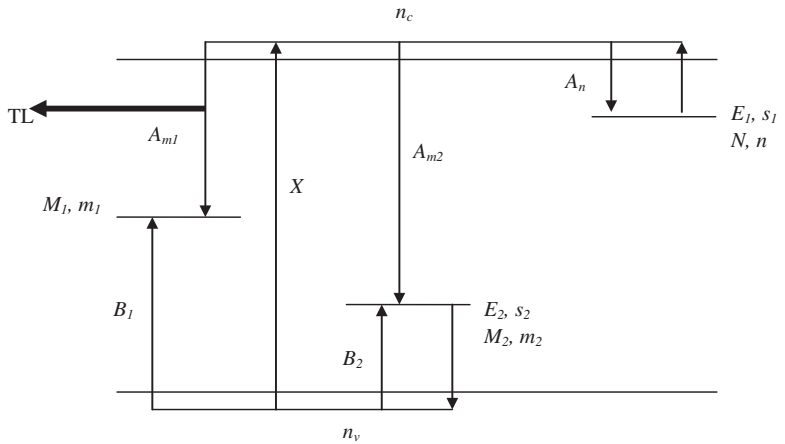


Fig. 6. Schematic energy level diagram describing the model explaining the anomalous heating-rate effect (After Chen and Pagonis [50]).

The instantaneous concentrations of free electrons and holes are $n_c$ and $n_v$, respectively. The activation energy of electrons is $E_1$ and the frequency factor is $s_1$. The activation energy of holes from $m_2$ is $E_2$ and the relevant frequency factor is $s_2$. The trapping probability coefficient of electrons is $A_n$ and of holes into $M_1$ and $M_2$ are $B_1$ and $B_2$, respectively. The recombination probability coefficients into $M_1$ and $M_2$ are $A_{m1}$ and $A_{m2}$, respectively. The rate of production of electron and hole pairs, proportional to the dose rate, is denoted by $X$.

The set of simultaneous differential equations governing the relevant processes is

$$\frac{dn}{dt} = A_n(N-n)n_c - s_1 n \exp(-E_1/kT), \tag{25}$$

$$\frac{dm_1}{dt} = B_1 n_v(M_1 - m_1) - A_{m1} m_1 n_c, \tag{26}$$

$$\frac{dm_2}{dt} = B_2 n_v(M_2 - m_2) - A_{m2} m_2 n_c - s_2 m_2 \exp(-E_2/kT), \tag{27}$$

$$\frac{dn_c}{dt} = X - A_n(N-n)n_c - A_{m1} m_1 n_c - A_{m2} m_2 n_c. \tag{28}$$

$$\frac{dn_v}{dt} = \frac{dn}{dt} + \frac{dn_c}{dt} - \frac{dm_1}{dt} - \frac{dm_2}{dt}. \tag{29}$$

Chen and Pagonis [50] have chosen a reasonable set of trapping parameters and solved numerically the equations in the above mentioned sequence of excitation, relaxation and heating using a linear heating function $T = T_0 + \beta t$ where $\beta$ is the constant rate. One may assume that the emitted light is associated with the recombination of free holes into $M_1$ or into $M_2$. In the former, if transition into $M_1$ is radiative and into $M_2$ is non radiative, the emitted light intensity is given by

$$I(t) = A_{m1} m_1 n_c, \tag{30}$$

and the mentioned normalized intensity is

$$I(T) = A_{m1} m_1 n_c / \beta. \tag{31}$$

The authors note that in more elementary TL models, where valence-band holes are not involved in the read-out process, the way to present the TL intensity is $I(t) = -dm_1/dt$, but since here $m_1$ varies by two channels, recombination with electrons from the conduction band and trapping of holes from the valence band, Eqs. (30) and (31) are the correct way to present the emission of light. By varying the heating rate in the simulation, the authors could show, by using a set of plausible parameters, the anomalous heating-rate effect, namely that with increasing heating rate, the normalized intensity of the TL signal increased. Chen and Pagonis [50] also showed that a strong decrease of the normalized TL intensity with increasing heating rate, similar to that usually explained as the result of thermal quenching, can be reached by nearly the same model. One uses the same set of equations and the same sequence of three stages and the only different assumption made is that now, the transition into $M_2$ is considered to be radiative whereas the transition into $M_1$ is assumed to be non-radiative and therefore, this center acts only as a competitor. The TL intensity is given by

$$I(t) = A_{m2} m_2 n_c, \tag{32}$$

and the normalized intensity is

$$I(T) = A_{m2} m_2 n_c / \beta. \tag{33}$$

By using the same set of parameters and increasing the heating rate, Chen and Pagonis [50] found that the normalized intensity given by

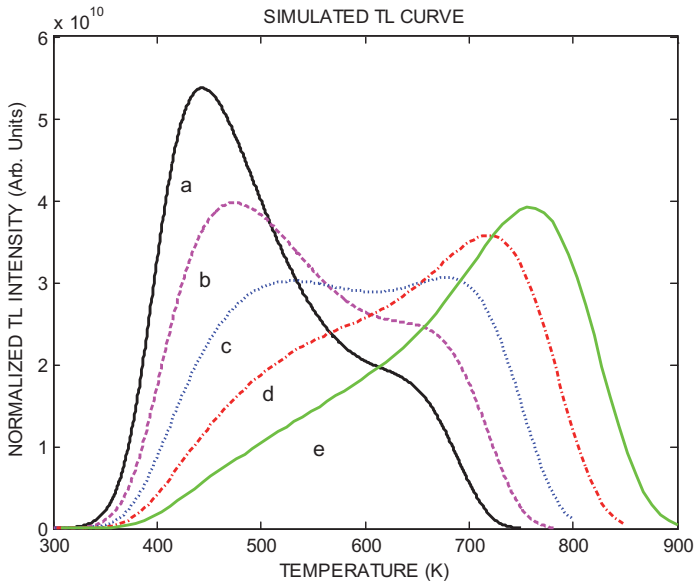


Fig. 7. Simulated TL curves with both transitions into $M_1$ and $M_2$ being radiative. The heating rates vary by a factor of 2 between (a) $0.5\,\mathrm{Ks}^{-1}$ and (e) $8.0\,\mathrm{Ks}^{-1}$ (After Chen and Pagonis [50]).

Eq. (33) reduced significantly with an increase in the heating rate, similarly to the well recognized thermal-quenching effect of TL.

Finally, Chen and Pagonis consider the situation that both trasitions into $M_1$ and $M_2$ are radiative and therefore, the measured (or simulated) curve includes two peaks. With increasing the heating rate, the simulated lower-temperature peak decreases whereas the higher-temperature peak increases. The results of the simulations are shown in Fig. 7. These results are qualitatively similar to the mentioned results in GaS crystals, given by Delice *et al.* [57].

### 1.5. The expected order of kinetics in a series of TL peaks

As can be understood from the discussion in the introduction, single TL peaks may be of first order or second order and obviously, many intermediate possibilities may occur. At first sight, one may think that this should be the case also when peaks which are part of a

series of peaks from the same material are measured. However, in the literature, there is vast evidence that in glow curves consisting of a series of peaks, first-order kinetics is prevalent in natural materials. Lewandowski and McKeever [62] state that first-order processes dominate in nature. Sunta *et al.* [63] suggest that the apparent dominance of first-order kinetics in nature is usually due to slow retrapping, but in multiple-trap-system models, it may occur under fast-retrapping conditions as well. Further statements concerning the dominance of first-order kinetics have been made by Bos [64] and Abd El-Hafez *et al.* [65]. Some authors described the prevalence of first-order shaped peaks in both TL and TSC peaks and mentioned the competition with deep traps as the reason. These include Haering and Adams [66], Dussel and Bube [67], Böhm and Scharmann [68], Simmons and Taylor [69], Agersap Larsen *et al.* [70] and Opanowicz [71]. The same reason of competition with deep traps has been mentioned by Smith and Rhodes [72] and by Bailey *et al.* [73] for the first-order behavior of OSL decay in quartz. Pagonis and Kitis [74] have reported on the prevalence of first-order kinetics of TL based on multiple competition processes. They simulate TL peaks using two models. One is the one-trap-one-center (OTOR) model, which is the same as Eqs. (6–8). These authors solve numerically the set of equations for different values of $A_n/A_m$, and show the gradual transition of the effective kinetic order $b$ from 1 to 2 as well as the dependence of the maximum temperature $T_m$ on this ratio. In the more comprehensive interactive multi-trap system (IMTS) model, they choose sets of parameters at random within the reasonable ranges, solve the equations to get glow curves and determine the effective order of kinetics of the peaks. Running 1000 random variants of the model, they get a distribution of effective kinetic orders weighted strongly toward first order. The distribution has a mean value of $b = 1.08$ and a standard deviation of $\sigma = 0.16$. They ascribe the nearly first-order property to the competition between the traps.

Chen and Pagonis [75] discuss the circumstances under which most of the peaks in a series can be expected to be of first order. In particular, they distinguish between the lower temperature peaks in a series and the highest temperature one. They start with a model with

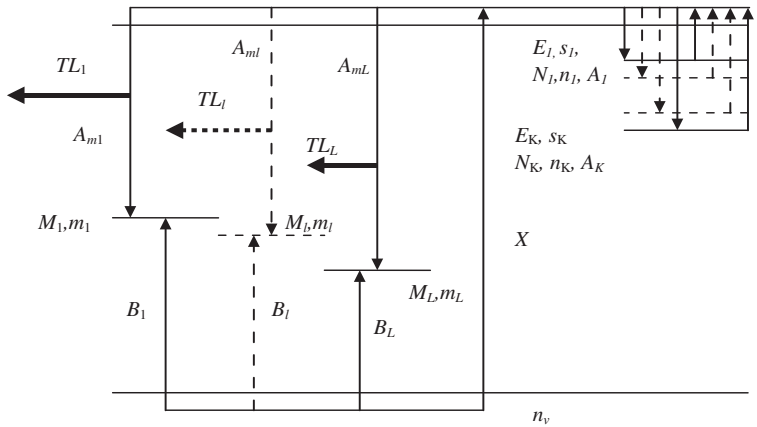


Fig. 8. Schematic energy-level diagram with $K$ trapping states and $L$ kinds of recombination center. Transitions occurring during excitation and during heating are shown. The thick arrows denote the different TL emissions. (After Chen and Pagonis [75]).

multiple trapping states and one recombination center and continue with a more general model with several trapping states and multiple kinds of recombination centers. In the former, simpler case, a series of $K$ traps with different $E_i$ and $s_i$ values and different values of the retrapping probabilities $A_i$ are assumed. For simplicity, the authors also assert that the parameters are such that the peaks are quite well separated. The energy-level diagram is shown in Fig. 8. The set of equations (6–8) now changes into

$$\frac{dn_i}{dt} = A_i(N_i - n_i)n_c - s_i n_i \exp(-E_i/kT), \quad \text{for } i = 1, \ldots, K \tag{34}$$

$$I(T) = -\frac{dm}{dt} = A_m m n_c, \tag{35}$$

$$\frac{dn_c}{dt} = \sum_{i=1}^{K} s_i n_i \exp(-E_i/kT) - \sum_{i=1}^{K} A_i(N_i - n_i)n_c - A_m m n_c. \tag{36}$$

Making the quasi-equilibrium assumption $dn_c/dt \approx 0$, one gets from Eq. (36)

$$n_c = \frac{\sum_{i=1}^{K} s_i n_i \exp(-E_i/kT)}{A_m m + \sum_{i=1}^{K} A_i(N_i - n_i)}. \tag{37}$$

When one considers the $j$-th peak in a series, the traps responsible for lower-temperature peaks can be considered to be empty. Thus, the sum in the denominator of Eq. (37) can be taken only from $i = j$. By inserting Eq. (37) into (35), one gets the expression for TL,

$$I(T) = -\frac{dm}{dt} = \frac{A_m m \sum_{i=1}^{K} n_i s_i \exp(-E_i/kT)}{A_m m + \sum_{i=j}^{K} A_i(N_i - n_i)}. \tag{38}$$

One may consider a peak followed by one or more subsequent peaks. This means that the relevant trap has a number of deeper competing traps. If the concentration of free electrons is small, as is usually the case, the instantaneous concentration of holes in centers must be

$$m = \sum_{i=j}^{K} n_i. \tag{39}$$

As long as the peaks are fairly well separate, since the activation energies are different, the exponents in Eq. (38) are very different from one another, and at the temperature of a certain peak, the contribution of the subsequent peaks is negligible. Therefore, Eq. (39) reduces to

$$I(T) = -\frac{dm}{dt} = \frac{A_m m s_j n_j \exp(-E_j/kT)}{A_m m + \sum_{i=j}^{K} A_i(N_i - n_i)}. \tag{40}$$

If in the range of the $j$-th peak there are still many electrons trapped at traps deeper than the $j$-th, the sum in Eq. (40) changes along the $j$-th peak only slightly, and therefore, $m$ can be considered constant. The amount of change of $m$ can be considered to be relatively small as compared to the area under the higher temperature peaks. If, in addition, the relevant traps with $i > j$ are not too close to saturation, the denominator of Eq. (40) is rather close to be constant. The observation that glow peaks tend to be of first order at low occupancies has been made by Sunta *et al.* [63]. It should be noted that if the peaks are rather separate, and if the traps are saturated, within the range of the $j$-th peak, $dm/dt \approx dn_j/dt$. If, however, the traps from the $j$-th and deeper are not full, they may compete with the center over electrons so that the portion of electrons performing

recombination is

$$\frac{A_m m}{A_m m + \sum_{i=j}^{K} A_i (N_i - n_i)}. \tag{41}$$

This would mean that in this range,

$$\frac{dm}{dt} = \frac{dn_j}{dt} \frac{A_m m}{A_m m + \sum_{i=j}^{K} A_i (N_i - n_i)}. \tag{42}$$

Comparing the right-hand side of Eqs. (40) and (42) results in

$$-\frac{dn_j}{dt} = s_j n_j \exp(-E_j/kT). \tag{43}$$

The solution of this equation is a first-order peak-shaped curve, with the original activation energy and frequency factor of the $j$-th trap. The solution of the rate of change of $n_j$ is

$$-\frac{dn_j}{dt} = n_{j0} s_j \exp(-E_j/kT) \exp\left[-(s_j/\beta) \int_{T_i}^{T_f} \exp(-E_j/k\theta) d\theta\right]. \tag{44}$$

This first-order expression is not the TL intensity, but using Eq. (43) we can get the TL expression

$$\begin{aligned} I(T) = -\frac{dm}{dt} &= n_{j0} s_j \exp(-E_j/kT) n_{j0} s_j \exp(-E_j/kT) \\ &\quad \times \exp\left[-(s_j/\beta) \int_{T_i}^{T_f} \exp(-E_j/k\theta) d\theta\right] \\ &\quad \times \frac{A_m m}{A_m m + \sum_{i=j}^{K} A_i (N_i - n_i)}. \end{aligned} \tag{45}$$

As long as the last term in Eq. (45) is approximately constant along the $j$-th peak, the function looks like a first-order peak and the analysis should yield the inserted $E$ and $s$ values. The approximate constancy of this term can be expected as long as $m$ is not varying significantly along the $j$-th peak. This is usually the case for the lower temperature peaks in a series and ceases to be so for the last peak in a series. Chen and Pagonis [75] show that under these circumstances, the last peak in such a series tends to be of second order.

Chen and Pagonis [75] have demonstrated the properties of a glow curve resulting from a model of five traps and one recombination

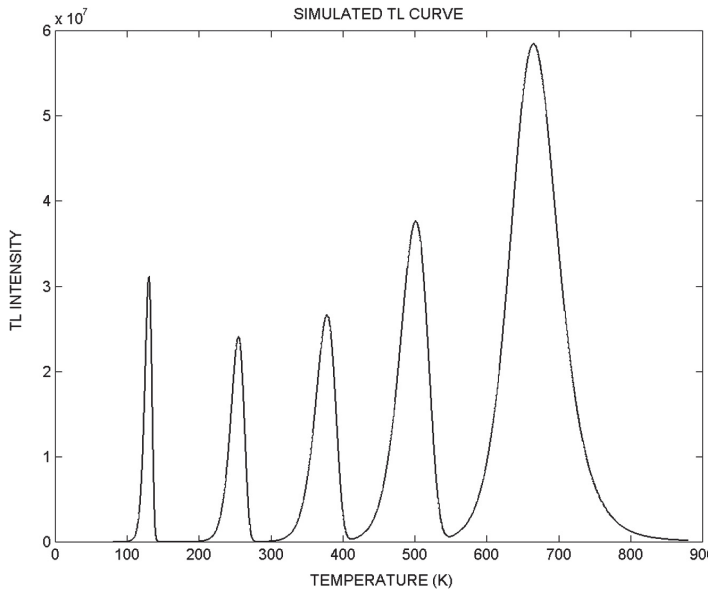


Fig. 9. A simulated five-peak TL curve (After Chen and Pagonis [75]).

center by solving sequentially the set of equations which are the extension of Eqs. (1–4) for excitation and relaxation ($X = 0$), followed by Eqs. (34–36). The results are shown in Fig. 9 and, indeed, the symmetry of the first four peaks is characteristic of first order and the 5-th peak looks like a second-order peak. The authors also discuss cases where the last peak in a series has a long high-temperature tail, which is associated with the failure of the quasi-equilibrium assumption in this range. Finally, the authors show that even in the more general situation, where several traps and several recombination centers take part in the process, all TL peaks except for the last in a series tend to be of first order.

## 1.6. Anomalous evaluated trapping parameters from TL curves

Several methods have been developed for the evaluation of the activation energy and frequency factor from TL curves (see e.g. Chen [76]). As an example, a simple method for finding the activation

energy of a first-order peak is given by

$$E = 2.29kT_m^2/\omega, \tag{46}$$

where $T_m$ is the maximum intensity temperature and $\omega = T_2 - T_1$ and $T_1$ and $T_2$ are the low and high half-intensity temperatures. Equation (46) shows immediately the inverse relation between the width of the peak, $\omega$, and the activation energy.

Once $E$ is known, inserting $T_m$, $E$ and the heating rate $\beta$ into Eq. (24) yields the frequency factor $s$. One should note that the usually acceptable values of $s$ are between $10^8$ and $10^{13}\,\mathrm{s}^{-1}$ (e.g., Chen [76]). In the literature, there are reports on evaluated frequency factors many orders of magnitude larger or smaller than the mentioned range. For example, Taylor and Lilley [77] reported an activation energy of 2.06 eV and frequency factor of $2 \times 10^{20}\,\mathrm{s}^{-1}$ in LiF:Mg,Ti (TLD-100) and other authors reported even higher values. On the other hand, very low values of evaluated $s$ have been reported such as by Haake [78] who determined for ZnS·ZnO-Cu,Cl and ZnS-Cu, Cl as low values as $1\,\mathrm{s}^{-1}$ to $2000\,\mathrm{s}^{-1}$. Chen and Hag-Yahya [79] presented a model with three recombination centers, one radiative and two non-radiative (or radiative in a different range of the spectrum). The model yields a very narrow glow peak which gives by using Eq. (46) a very high effective activation energy and, in turn, using Eq. (24), an effective frequency factor many orders of magnitude higher than usually acceptable. It is worth mentioning that Chen and Hag-Yahya [80] used a very similar model to explain anomalous fading of TL as being normal fading in disguise. As for the very low frequency factors reported in the literature, Chen *et al.* [81] have studied a model with two trapping states and one recombination center which yield two neighboring TL peaks that may appear as a very broad single peak. This yields in the analysis very low effective activation energy and a very low frequency factor. The authors use simulations by solving the relevant differential equations to demonstrate this possibility and suggest that it should be considered in particular when a complex glow curve with overlapping peaks is studied, e.g. by deconvolution, when the number of individual peaks is not always known.

## 1.7. Conclusion

In this chapter, some models of thermoluminescence (TL) and optically stimulated luminescence (OSL), associated with delocalized transitions during excitation and read-out have been discussed. The analytical results reached by making plausible approximation have been considered and compared to experimental results in different materials. These were accompanied by the results of numerical simulations consisting of the solution of the relevant set of simultaneous differential equations in the sequence of excitation, relaxation and read-out, namely heating in TL and optical stimulation in OSL. The effects covered included different kinds of dose dependence, linear, sublinear and superlinear as well as non-monotonic dose dependence. Also the possibility of dose-rate dependence sometimes mentioned in the literature has been considered. Other effects discussed have been the concentration-quenching effect, the predominance of the occurrence of first-order TL peaks and an anomalous heating-rate effect. The model for the latter may be associated with an alternative explanation to the well-known thermal quenching effect, as seen in TL measurements at various heating rates. Also are briefly discussed the reasons for anomalously high or low evaluated activation energies and frequency factors.

## References

[1] R. Chen and V. Pagonis, Thermally and Optically Stimulated Luminescence: A Simulation Approach, Chichester: John Wiley & Sons Ltd., 2011.

[2] J.T. Randall and M.H.F. Wilkins, "The phosphorescence of various solids," *Proc. Roy. Soc. London*, vol. A184, pp. 347–365, 1945.

[3] G.F.J. Garlick and A.F. Gibson, "The electron trap mechanism of luminescence in sulphide and silicate phosphors," *Proc. Phys. Soc.*, vol. 60, pp. 574–590, 1948.

[4] A. Halperin and A.A. Braner, "Evaluation of thermal activation energies from glow curves," *Phys. Rev.*, vol. 117, pp. 408–415, 1960.

[5] G. Kitis and N.D. Vlachos, "General semi-analytical expressions for TL, OSL and other luminescence stimulation modes from OTOR model using Lambert W-function," *Radiat. Meas.*, vol. 48, pp. 47–54, 2013.

[6] R. Chen and V. Pagonis, "On the quasi-equilibrium assumptions in the theory of thermoluminescence (TL)," *J. Lumin.*, vol. 143, pp. 734–740, 2013.

[7] I.A. Kanunnikov, "Reaction order of thermally stimulated recombination," *J. Appl. Spect.*, vol. 28, pp. 597–599, 1978.
[8] R. Chen, "Glow curves with general-order kinetics," *J. Electrochem. Soc.*, vol. 116, pp. 1254–1257, 1969.
[9] R. Chen, N. Kristianpoller, Z. Davidson and R. Visocekas, "Mixed first and second order kinetics in thermally stimulated processes," *J. Lumin.*, vol. 23, pp. 293–303, 1981.
[10] J.R. Cameron, N. Suntharalingam and G.N. Kenney, Thermoluminescent Dosimetry, Madison, USA: The University of Wisconsin Press, 1968.
[11] M.S. Tite, "Thermoluminescent dating of ancient ceramics: A reassessment," *Archaeometry*, vol. 9, pp. 155–169, 1966.
[12] A. Halperin and R. Chen, "Thermoluminescence in semiconduting diamonds," *Phys. Rev.*, vol. 148, pp. 839–845, 1966.
[13] R. Chen, X.H. Yang and S.W.S. McKeever, "The strongly superlinear dose dependence of thermoluminescence in synthetic quartz," *J. Phys. D: Appl. Phys.*, vol. 21, pp. 1452–1457, 1988.
[14] H. Otaki, H. Kido, A. Hiratsuka and N. Takeuchi, "Estimation of UV radiation dose using $CaF_2$:$Tb_4O_7$ as a thermoluminescence dosimeter," *J. Mater. Sci. Lett.*, vol. 13, pp. 1267–1269, 1994.
[15] N. Suntharalingam and J.R. Cameron, "Thermoluminescence response of lithium fluoride to radiations with different LET," *Phys. Med. Biol.*, vol. 14, pp. 397–410, 1969.
[16] S.G.E. Bowman and R. Chen, "Superlinear filling of traps in crystals due to competition during irradiation," *J. Lumin.*, vol. 18, pp. 345–348, 1979.
[17] E.T. Rodine and P.L. Land, "Electronic defect structure of single crystal $ThO_2$ by thermoluminescence," *Phys. Rev. B*, vol. 4, pp. 2701–2724, 1971.
[18] N. Kristianpoller, R. Chen and M. Israeli, "Dose dependence of thermoluminescence peaks," *J. Phys. D: Appl. Phys.*, vol. 7, pp. 1063–1074, 1974.
[19] R. Chen, G. Fogel and C.K. Lee, "A new look at the models of the superlinear dose dependence of thermoluminescence," *Radiat. Prot. Dosim.*, vol. 65, pp. 63–68, 1996.
[20] R. Chen, J.L. Lawless and V. Pagonis, "Intrinsic superlinear dose dependence of thermoluminescence and optically stimulated luminescence at high dose rates," *Radiat. Meas.*, vol. 71, pp. 220–225, 2014.
[21] V.K. Jain, S.P. Kathuria and A.K. Ganguly, "Radiation damage in thermoluminescent LiF TLD-phosphor," *J. Phys. C: Sol. St. Phys.*, vol. 8, pp. 2191–2197, 1975.
[22] E.G. Yukihara, V.H. Whitley, J.C. Polf, D.M. Klein, S.W.S. McKeever, A.E. Akselrod and M.S. Akselrod, "The effect of deep trap population on the thermoluminescence of $Al_2O_3$:C," *Radiat. Meas.*, vol. 37, pp. 627–638, 2003.
[23] R. Chen, D. Lo and J.L. Lawless, "Non-monotonic dose dependence of thermoluminescence," *Radiat. Prot. Dosim.*, vol. 119, pp. 33–36, 2006.
[24] V. Pagonis, R. Chen and J.L. Lawless, "Nonmonotonic dose dependence of OSL intensity due to competition during irradiation and readout," *Radiat. Meas.*, vol. 41, pp. 903–906, 2006.

[25] E.G. Yukihara, V.H. Whitley, S.W.S. McKeever, A.E. Akselrod and M.S. Akselrod, "Effect of high-dose irradiation on the optically stimulated luminescence of $Al_2O_3$:C," *Radiat. Meas.*, vol. 38, pp. 317–333, 2003.

[26] R. Chen, V. Pagonis and J.L. Lawless, "Time and dose-rate dependence of TL and OSL due to competition between excitation and fading," *Radiat. Meas.*, vol. 82, pp. 115–221, 2015.

[27] R. Chen, J.L. Lawless and V. Pagonis, "Thermoluminescence associated with two-electron traps," *Radiat. Meas.*, vol. 99, pp. 10–17, 2017.

[28] R. Chen, J.L. Lawless and V. Pagonis, "Thermoluminescence associated with two-hole recombination centers," *Radiat. Meas.*, vol. 115, pp 1–6, 2018.

[29] M.R. Mayhugh, "Color centers and thermoluminescence mechanism in LiF," *J. Appl. Phys.*, vol. 41, pp. 4776–4782, 1970.

[30] P.D. Townsend, G.C. Taylor and M.C. Wintersgill, "An explanation of the anomalously high activation energies of TL in LiF (TLD 100)," *Radiat. Eff.*, vol. 41, pp. 11–16, 1979.

[31] M. Böhm and A. Scharmann, "Theory," in *Applied Thermoluminescence Dosimetry*, M. Oberhofer and A. Scharmann, Eds., Bristol, Adam Hilger Ltd., 1981, pp. 11–38.

[32] A.N. Yazici, T. Karali, P.D. Townsend and M. Ari, "Thermoluminescence studies of LiF:Mg,Ti between 100 and 300 K," *J. Phys. D: Appl. Phys.*, vol. 37, pp. 3165–3173, 2004.

[33] Y. Horowitz, "A unified comprehensive theory of the TL dose response of thermoluminescence systems applied to LiF:Mg,Ti," in *Macrodosimetric Response of Physical and Biological Systems applied to LiF:Mg,Ti Radiations*, Y. Horowitz, Ed., Amsterdam, Elsevier, 2006, pp. 75–202.

[34] I. Eliyahu, S. Druzhyna, Y. Horowitz, G. Reshes and L. Oster, "Kinetic simulation of charge transfer following 5.08 eV (F band) optical excitation of irradiated LiF:Mg,Ti (TLD-100): Participation of holes released via $V_3$-$V_k$ transformation," *Radiat. Meas.*, vol. 90, pp. 27–32, 2016.

[35] C. Woda and G.A. Wagner, "Non-monotonic dose dependence of the Ge- and Ti- centers in quartz," *Radiat. Meas.*, vol. 42, pp. 1441–1452, 2007.

[36] R.A. Facey, "Heating-rate effects in glow peak measurements for thermoluminescence dosimetry," *Health Phys.*, vol. 12, pp. 717–720, 1966.

[37] P.J. Groom, S.A. Durrani, K.A. Khazal and S.W.S. McKeever, "The dose-rate dependence of thermoluminescence and sensitivity in quartz," *Europ. PACT J.*, vol. 2, pp. 200–210, 1978.

[38] S. Chawla, T.K. Gundu Rao and A.K. Singhvi, "Quartz thermoluminescence: Dose and dose-rate effects and their implications," *Radiat. Meas.*, vol. 29, pp. 53–63, 1998.

[39] P.C. Hsu and P.S. Weng, "Reaffirmation on the low exposure rate dependence of the $CaSO_4$:Dy thermoluminescence dosimeter," *Nucl. Instrum. Meth.*, vol. 174, pp. 73–76, 1980.

[40] A.I. Shlukov, A.I. Shakhovets and M.G. Lyashenko, "A criticism of standard TL dating technology," *Nucl. Instrum. Meth. Phys. Res. Sect. B*, vol. 73, pp. 373–381, 1993.

[41] G. Valladas and J. Ferreira, "On the dose-rate dependence of the thermoluminescence response of quartz," *Nucl. Instrum. Meth.*, vol. 175, pp. 216–218, 1980.
[42] R. Chen and P.L. Leung, "A model for dose-rate dependence of thermoluminescence intensity," *J. Phys. D: Appl. Phys.*, vol. 33, pp. 846–850, 2000.
[43] W.L. Medlin, "Thermoluminescence properties of calcite," *J. Chem. Phys.*, vol. 30, pp. 451–458, 1974.
[44] M.J. Rossiter, D.B. Rees-Evans, S.C. Ellis and J.M. Griffiths, "Titanium as a luminescence centre in thermoluminescent lithium fluoride," *J. Phys D: Appl. Phys.*, vol. 4, pp. 1245–1251, 1971.
[45] K.S.V. Nambi, V.N. Bapat and A.K. Ganguly, "Thermoluminescence of $CaSO_4$ doped with rare earths," *J. Phys. C: Sol. St. Phys.*, vol. 7, pp. 4403–4415, 1974.
[46] R. Chen, J.L. Lawless and V. Pagonis, "A model for explaining the concentration quenching of thermoluminescence," *Radiat. Meas.*, vol. 46, pp. 1380–1384, 2011.
[47] L.J. Lai, H.S. Sheu, Y.K. Lin and T.C. Chu, "Thermoluminescence of $ZrO_2$ doped with $Yb_2O_3$ following excitation with X rays," *J. Appl. Phys.*, vol. 100, p. 103508 (5pp), 2006.
[48] W. Hoogenstraaten, "Electron traps in ZnS phosphors," *Philips Res. Repts.*, vol. 13, pp. 515–693, 1958.
[49] R. Chen and S.A.A. Winer, "Effects of various heating rates on glow curves," *J. Appl. Phys.*, vol. 41, pp. 5227–5232, 1970.
[50] R. Chen and V. Pagonis, "A model explaining the anomalous heating-rate effect in thermoluminescence as an inverse thermal quenching based on simultaneous thermal release of electrons and holes," *Radiat. Meas.*, vol. 106, pp. 20–25, 2017.
[51] M. Kumar, G. Chourasiya, B.C. Bhatt and C.M. Sunta, "Dependence of peak height of glow curves on heating rate in thermoluminescence," *J. Lumin.*, vol. 130, pp. 1216–1220, 2010.
[52] A.K. Wintle, "Thermal quenching of thermoluminescence in quartz," *Geophys. J.R. Soc.*, vol. 41, pp. 107–113, 1975.
[53] B. Subedi, G. Kitis and V. Pagonis, "Simulation of the influence of thermal quenching on thermoluminescence glow peaks," *Phys. Stat. Sol. (a)*, vol. 207, pp. 1216–1226, 2010.
[54] V.E. Kafadar, "Thermal quenching of thermoluminescence in TLD-200, TLD-300 and TLD-400 after beta irradiation," *Phys. B*, vol. 406, pp. 537–540, 2011.
[55] G. Kitis, G.S. Polymeris, V. Pagonis and N.C. Tsirliganis, "Thermoluminescence response and apparent anomalous fading factor of Durango fluorapatite as a function of the heating rate," *Phys. Stat. Sol. (a)*, vol. 203, pp. 3816–3823, 2006.
[56] A.J.J. Bos, N.R.J. Poolton, J. Bessière and P. Dorenbos, "Energy levels in $YPO_4$:$Ce^{3+}$,$Sm^{3+}$ studied by thermally and optically stimulated luminescence," *Radiat. Meas.*, vol. 45, pp. 343–346, 2010.

[57] S. Delice, E. Bulur and N.M. Gasanly, "Thermoluminescence in gallium arsenide crystals: an unusual heating rate dependence," *Phil. Mag.*, vol. 95, pp. 998–1006, 2015.

[58] A. Mandowski and A.J.J. Bos, "Explanation of the anomalous heating rate dependence of thermoluminescence in $YPO_4$:$Ce^{3+}$,$Sm^{3+}$ based on the semi-localized transition (SLT) model," *Radiat. Meas.*, pp. 1376–1379, 2011.

[59] V. Pagonis, L. Blohm, M. Brengle, G. Mayonado and P. Woglam, "Anomalous heating rate effect in thermoluminescence intensity using simplified semi-localized transition (SLT) model," *Radiat. Meas.*, Vols. 51–52, pp. 40–47, 2013.

[60] M. Schön, "Zum Leuchtmechanismus der Kristallophore," *Z. Phys.*, vol. 19, pp. 463–471, 1942.

[61] H.A. Klasens, "Transfer of energy between centers in zinc sulphide phosphors," *Nature*, vol. 158, pp. 306–307, 1946.

[62] A.C. Lewandowski and S.W.S. McKeever, "Generalized description of thermally stimulated processes without quasiequilibrium approximation," *Phys. Rev. B*, vol. 43, pp. 8163–8178, 1991.

[63] C.M. Sunta, W.E.F. Ayta, J.F.D. Chubaci and S. Watanabe, "A critical look at the kinetic models of thermpluminescence: I. First-order kinetics," *J. Phys. D: Appl. Phys.*, vol. 34, pp. 2690–2698, 2001.

[64] A.J.J. Bos, "On the energy conversion in thermoluminescence dosimetry materials," *Radiat. Meas.*, vol. 33, pp. 737–744, 2010.

[65] A.I. Abd El-Hafez, M.N. Yasin and A.M. Sadek, "GCAFIT-A new tool for glow curve analysis in thermoluminescence nanodosimetry," *Nucl. Inst. Meth. Phys. Res. A*, vol. 637, pp. 158–163, 2011.

[66] R.H. Haering and E.N. Adams, "Theory and applications of thermally stimulated centers in photoconductors," *Phys. Rev.*, vol. 117, pp. 451–454, 1960.

[67] G.A. Dussel and R.H. Bube, "Theory of thermally stimulated conductivity in previously photoexcited crystal," *Phys. Rev.*, vol. 155, pp. 764–779, 1967.

[68] M. Böhm and A. Scharmann, "First-order kinetics in thermoluminescence and thermally stimulated conductivity," *Phys. Stat. Sol. (a)*, vol. 4, pp. 99–104, 1971.

[69] J.G. Simmons and G.W. Taylor, "High-field isothermal currents and thermally stimulated currents in insulators having discrete trapping levels," *Phys. Rev. B*, vol. 5, pp. 1619–1629, 1972.

[70] N. Agersap Larsen, L. Bøtter-Jensen and S.W.S. McKeever, "Thermally stimulated conductivity and thermoluminescence from $Al_2O_3$," *Radiat. Prot. Dosim.*, vol. 84, pp. 87–90, 1999.

[71] A. Opanowicz, "Analysis of thermally stimulated luminescence and conductivity without quasi-equilibrium approximation," *J. Phys. D: Appl. Phys.*, vol. 40, pp. 4980–4990, 2007.

[72] B.W. Smith and E.J. Rhodes, "Charge movements in quartz and their relevance to optical dating," *Radiat. Meas.*, vol. 23, pp. 329–333, 1994.

[73] R.M. Bailey, B.W. Smith and E.J. Rhodes, "Partial bleaching and the decay from characteristics of quartz OSL," *Radiat. Meas.*, vol. 27, pp. 123–126, 1997.

[74] V. Pagonis and G. Kitis, "Prevalence of first-order kinetics in TL materials: an explanation based on multiple competition processes," *Phys. Stat. Sol. (a)*, vol. 249, pp. 1590–1601, 2012.

[75] R. Chen and V. Pagonis, "On the expected order of kinetics in a series of thermoluminescence (TL) and thermally stimulated conductivity peaks," *Nucl. Inst. Meth. Phys. Res. B*, vol. 312, pp. 60–69, 2013.

[76] R. Chen, "On the calculation of activation energies and frequency factors from glow curves," *J. Appl. Phys.*, vol. 40, pp. 570–585, 1969.

[77] G.C. Taylor and E. Lilley, "The analysis of thermoluminescence glow peaks in LiF (TLD-100)," *J. Phys. D: Appl. Phys.*, vol. 11, pp. 567–581, 1978.

[78] C.H. Haake, "Critical comment on a method for determining electron trap depths," *J. Opt. Soc. Am.*, vol. 47, pp. 649–652, 1957.

[79] R. Chen and A. Hag-Yahya, "Interpretation of very high activation energies and frequency factors in TL as being due to competition between centres," *Radiat. Prot. Dosim.*, vol. 65, pp. 17–20, 1996.

[80] R. Chen and A. Hag-Yahya, "A new possible interpretation of the anomalous fading in thermoluminescent material as normal fading in disguise," *Radiat. Meas.*, vol. 27, pp. 205–210, 1997.

[81] R. Chen, V. Pagonis and J.L. Lawless, "Evaluated thermoluminescence trapping parameters-What do they really mean?," *Radiat. Meas.*, vol. 91, pp. 21–27, 2016.

## Chapter 2

# Recent Advances in the Theory of Quantum Tunneling for Luminescence Phenomena

Vasilis Pagonis

*McDaniel College, Department of Physics*
*Westminster, MD 21157, USA*
*vpagonis@mcdaniel.edu*

Although quantum tunneling models for luminescence phenomena have been developed over the last 40 years, interest in these models has been revived recently in two applied areas: dosimetry/dating applications, and development of luminescence nanomaterials with many practical applications. This chapter summarizes luminescence models for random distributions of electrons and positive ions in solids. Two different approaches have been developed within the context of these models. The first approach is a macroscopic point of view which uses differential equations, and this chapter reviews some of the available analytical equations in the literature. The second approach uses a microscopic description based on Monte Carlo simulations, which allow for spatial correlations between the charges. Monte Carlo methods have not been used extensively for this type of study. We will review recent work, and where applicable will compare the solutions of differential equations with the Monte Carlo simulations. Strengths and weaknesses of the two approaches will be presented. A third approach which bridges the first two approaches is also described, in which the differential equations are solved computationally using a Monte Carlo method. In the final part of this chapter we present simulations of luminescence phenomena for nanomaterials, with emphasis on the effect of crystal size on the experimentally measured luminescence signals.

## 2.1. Introduction

This chapter is a review of recent research on quantum tunneling models associated with luminescence phenomena in solids. More specifically, the models considered here are applicable to tunneling phenomena in systems of randomly located defects in a solid. There have been several efforts during the past 40 years to develop models for luminescence signals in solids originating in a random distribution of donor-acceptor pairs, especially in connection with kinetics of chemical reactions (see for example the book by Chen and Pagonis [1]; and references therein).

There are two major areas of applied research which provide the motivation for developing such models.

The first broad applied research area is in luminescence dosimetry and luminescence dating. From a dosimetry point of view, it is important to understand the tunneling mechanisms and the associated luminescence signals, with a view towards improving dosimetry and dating techniques. Quantum mechanical tunneling and the associated phenomena of "anomalous fading" and "long afterglow" of luminescence signals are now well established as dominant mechanisms in feldspars, apatites, rare earth doped materials and other important luminescent dosimetric materials (see for example the review paper, by Pagonis *et al.* [2]).

The second major experimental thrust for these types of models is for luminescence nanomaterials which find many practical applications. Recently luminescent materials consisting of nanoclusters with only a few atoms have attracted significant attention. The synthesis and characterization of such nanodosimetric materials has become an increasingly active research area, and it has been shown that their physical properties can be different from those of similar conventional microcrystalline phosphors (see for example Salah [3]; Sun and Sakka [4]; Eliyahu *et al.* [5]; and references therein). It has been suggested that traditional energy band models may not be applicable for some of these nanodosimetric materials, because of the existence of strong spatial correlations between traps and recombination centers. Such spatially correlated systems are also likely to be found in polycrystalline and low-dimensional structures, as well as in materials

which underwent high energy/high dose irradiations which create groups of large defects.

Two possible complementary modeling approaches have been used in the literature to simulate tunneling in random distributions of defects: a macroscopic description using differential equations, and a microscopic description based on Monte Carlo simulations. These two approaches are discussed in sections 2.2 and 2.3, together with an alternative third approach, in which the differential equations are solved computationally by using a different type of Monte Carlo method. Section 2.4 presents simulations of luminescence phenomena for nanomaterials, with emphasis on the effect of crystal size on the experimentally measured luminescence signals.

## 2.2. The macroscopic differential equation approach

In this section we will consider four different types of tunneling phenomena, all of which can be described with differential equations. Section 2.2.1 describes tunneling taking place from the ground state of the electron trap directly into the recombination center. Three approximate analytical equations are available in the literature, which are applicable under different relative concentrations of electrons and positive ions. Section 2.2.2 extends the work in section (2.2.1), to include the possibility of simultaneous irradiation and ground state tunneling of the material. Two analytical equations are available for such cases, which are applicable under the assumption that the concentration of electrons is much smaller than the corresponding concentration of positive ions.

Section 2.2.3 reviews extensive modeling work carried out during the past 10 years, which is based on tunneling taking place from the excited state of the electron trap. Several analytical equations are reviewed, which are again based on the assumption of the concentration of electrons being much smaller than the concentration of positive ions.

Figure 1 shows three previously proposed relatively simple models for luminescence signals in feldspars. Figure 1a and 1b show two ground state tunneling models considered by Tachiya and Mozumder

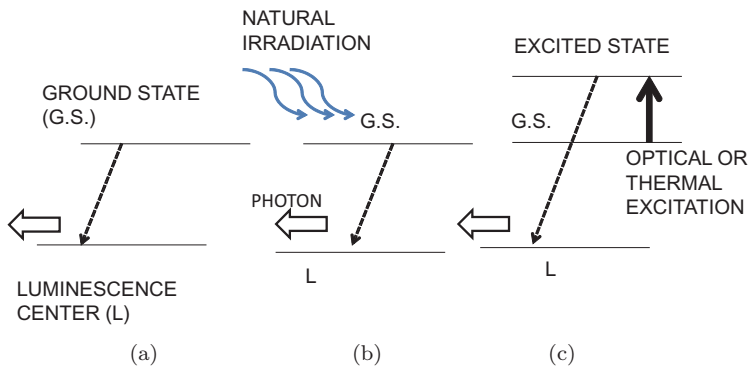


Fig. 1. Schematic depiction of the three luminescence models considered in this paper: (a) The ground state tunneling model. (b) The more general ground state tunneling model, in which anomalous fading and natural irradiation are taking place simultaneously. (c) The excited state tunneling model. (After Pagonis and Kitis [12]).

[6] and by Li and Li [7] respectively. Figure 1c shows an excited state tunneling model considered by Avouris and Morgan [8], Thioulouse and Chang [9], Jain *et al.* [10] and Kitis and Pagonis [11].

### 2.2.1. *Ground state tunneling models*

Several authors discussed the tunneling mechanism for a random distribution of donors and acceptors in a luminescent material, based on recombination taking place directly from the ground state of the system into the recombination center. The recombination of trapped charge is assumed to take place by quantum mechanical tunneling with a lifetime $\tau_{FADING}$ given by:

$$\tau_{FADING} = (1/s)\exp[\alpha r] \tag{1}$$

where $\alpha$ ($\mathrm{m}^{-1}$) is the potential barrier penetration constant, $r$(m) is the separation distance between donor and acceptor and $s$ ($\mathrm{s}^{-1}$) is the attempt-to-tunnel frequency. The instantaneous concentration $n(r,t)$ of trapped electrons in the ground state depends on both the elapsed time $t$ and on the separation distance $r$ between donor and acceptor.

We will now consider three different cases, depending on the relative concentration of electrons/donors ($n_o$) and acceptors ($m_o$).

We first consider the situation where the concentration of electrons is much smaller than the concentration of acceptors, so that the system can be characterized by a *constant* number density of acceptors per unit volume $\rho$ ($\mathrm{m}^{-3}$). In such cases one can define a dimensionless distance parameter $r'$, such that:

$$r' = (4\pi\rho/3)^{1/3} r \tag{2}$$

In addition one defines a *constant* dimensionless parameter $\rho'$ proportional to $\rho$, by:

$$\rho' = (4\pi\rho/3)\alpha^{-3} \tag{3}$$

In order to maintain charge neutrality in this system of constant $\rho$, it is assumed that there is a large number of additional filled electron traps in the system, which do not participate in the tunneling process. This is a common situation in many dosimetric materials, in which several different types of electron traps are present. A second common assumption made in these tunneling models is that tunneling takes place only to the nearest neighbor in the system; this is known as the *nearest neighbor approximation*, and has been shown to be a reasonable approximation in most situations, except at very high charge densities. It can be shown from geometrical arguments that the nearest neighbor distribution of distances between electrons and acceptors is given by the following normalized distribution:

$$g_{NN}(r) = 4\pi\rho r^2 \exp[-(4\pi/3)\rho r^3] \tag{4}$$

In terms of the radius $r'$ this equation becomes dimensionless:

$$g_{NN}(r') = 3(r')^2 \exp[-(r')^3] \tag{5}$$

As the tunneling process proceeds over time, the distribution of electrons in the ground state $n(r', t)$ varies with the distance parameter $r'$ and with time $t$ according to:

$$n(r', t) = 3n_o(r')^2 \exp[-(r')^3] \exp[-st \exp(-(\rho')^{-1/3} r')] \tag{6}$$

where $n_o$ is the total initial number of donors in the system.

Figure 2a shows a plot of Eq. (6) at a time $t = 1000\,\mathrm{s}$ after the start of the tunneling process (dashed line). The solid line in Fig. 2a indicates the initial peak-shaped symmetric distribution $g_{NN}(r')$ obtained using Eq. (5), and the values of the parameters used in this simulation are typical for feldspars, $\rho' = 3 \times 10^{-6}$, $s = 3 \times 10^{15}\,\mathrm{s}^{-1}$. The dashed line in Fig. 2a represents the "moving tunneling front" in the tunneling process. The characteristic shape of this tunneling front is the product of the two functions appearing in Eq. (6), namely of the sharply rising double exponential function $\exp[-st\exp[-(\rho')^{-1/3}r']$, and of the symmetric distribution $g_{NN}(r')$.

The instantaneous total concentration of *remaining* carriers $n(t)$ is calculated by integrating Eq. (6) over all possible distances $r'$:

$$n(t) = n_o \int_0^\infty 3(r')^2 \exp[-(r')^3] \exp[-t/\tau] dr' \tag{7}$$

In the approximate semi-analytical version of the model, one introduces a critical lifetime $\tau_c$ and a corresponding critical radius $r'_c$, which describe the behavior of the physical system. Geometrically, this approximation corresponds to replacing the dashed lines in Fig. 2a by a vertical line at $r' = r'_c$. Mathematically the value of the critical distance can be estimated from the *inflection point* of the double exponential function in Eq. (6) ([10, 12, 13]), and is given by:

$$r'_c = (\rho')^{1/3} \ln(st). \tag{8}$$

Using this approximation we can now evaluate the integral in Eq. (7), by replacing the exponential $\exp(-t/\tau)$ with a value of 0 for $t < \tau$, and with a value of 1 for $t > \tau$. By carrying out the integration we obtain the electron survival probability $S(t)$:

$$S(t) = n(t)/n_o = \exp[-\rho' \ln(st)^3] \tag{9}$$

A more accurate numerical approximation is obtained at all values of $st$ by using the following slightly modified version of Eq. (9) (Kitis and Pagonis [11]):

$$S(t) = n(t)/n_o = \exp[-1.8\rho' \ln(st)^3] \tag{10}$$

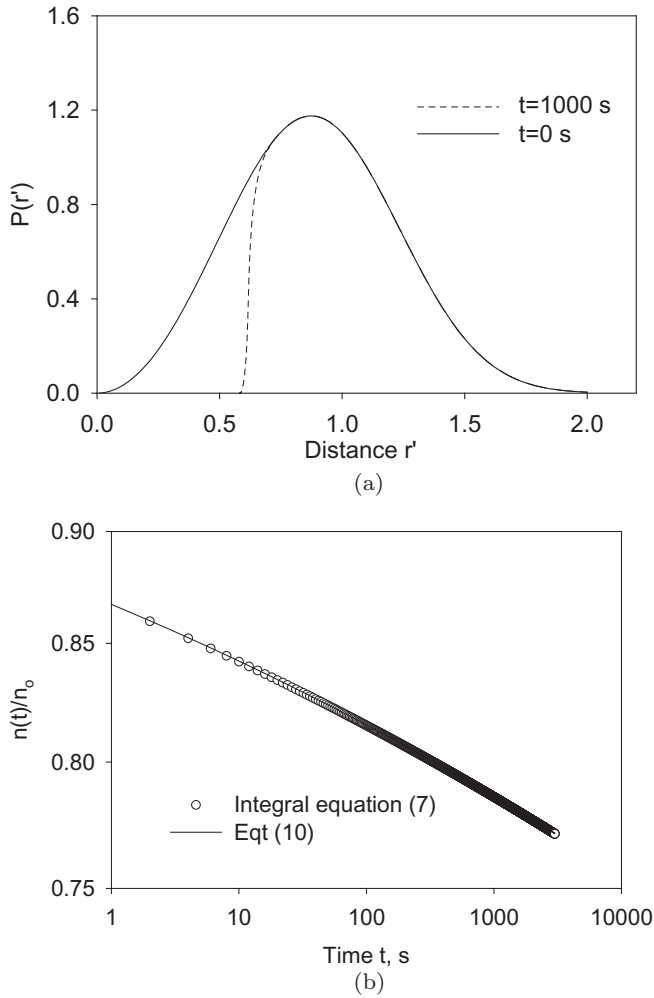


Fig. 2. (a) An example of the distribution of distances obtained using Eq. (6) as a function of the dimensionless distance $r'$, and at a two times $t = 0\,\mathrm{s}$ (solid line), and at $t = 1000\,\mathrm{s}$ after the start of the tunneling process (dashed line). The critical radius corresponds to the approximation of replacing the dashed line by a vertical line. (b) Comparison of the concentration n(t) obtained by numerically integrating Eq. (7) over the possible range of values of distances, with the analytical expressions in Eq. (10). (After Pagonis *et al.* [13]).

Figure 2b shows a comparison of the concentration $n(t)$ obtained by numerically integrating Eq. (7) over the possible range of values of distances $r'$, with the analytical expressions in Eq. (10), showing good agreement between the two approaches.

In summary, Eq. (7) is derived by assuming (a) a random distribution of defects (b) nearest neighbor interaction and (c) that the concentration of electrons is much smaller than the concentration of acceptors. Furthermore, Eq. (10) provides a good analytical approximation of Eq. (7).

Pagonis *et al.* [14] developed the following new analytical equation for the electron survival probability $S(t)$ for a random distribution of electrons and positive ions. This equation is derived on the assumption of *equal initial* concentrations $n_o = m_o$ of donors and acceptors correspondingly:

$$P(t) = 1/\{1 + (4\pi/3)n_o a^3[ln(st)]^3\} \tag{11}$$

Where $a = 1/\alpha$ ($\mathrm{m}^{-1}$) is the tunneling length parameter, $s$ ($\mathrm{s}^{-1}$) is the tunneling frequency, and $n_o$, $m_o$ are the initial equal concentrations of donors/acceptors at time $t = 0$.

Pagonis *et al.* [15] also considered cases of unequal initial concentrations of electrons and positive ions. They derived the following analytical equation for the electron survival probability:

$$P(t) = 1/\{-[n_o/\Delta m] + [m_o/\Delta m]\exp[(4\pi/3)\Delta m\ a^3[ln(st)]^3\} \tag{12}$$

Figure 3a shows graphs of Eq. (11) for different values of the dimensionless parameter $n'_o = n_o a^3$. Figure 3b shows graphs of Eq. (12) for different relative concentrations $n_o/m_o$ and for $n_o < m_o$. In the limiting case where $n_o \ll m_o$, Eq. (12) becomes the same as Eq. (9) with $\rho' = 4\pi m_o a^3/3$.

### 2.2.2. *Irradiation and ground state tunneling*

Huntley and Lian [16] suggested an extension of the model in Fig. 1a, which uses a differential equation to describe simultaneous natural irradiation and anomalous fading effects on the luminescence of feldspars. Li and Li [7] applied the model of Huntley and Lian [16]

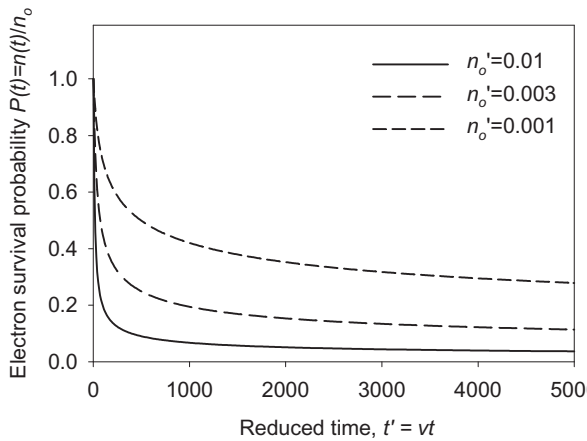


(a)

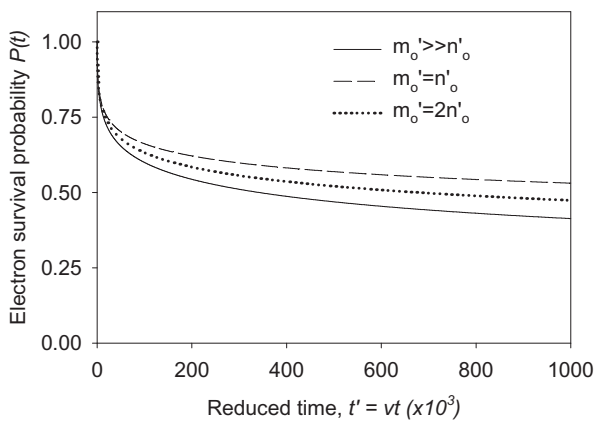


(b)

Fig. 3. (a) Plots of Eq. (11) for different values of the dimensionless parameter $n_o' = n_o a^3$. (b) Plots of Eq. (12) for different relative concentrations $n_o/m_o$ and for $n_o < m_o$. (After Pagonis *et al.* [14]).

in an extensive experimental and modeling study of both laboratory-irradiated and naturally irradiated feldspars. These authors studied the decay of IRSL signals, the effects of anomalous fading on the shape of dose response curves (DRCs), the probability distribution of trap-to-center distance and the dependence of anomalous fading on the parameters of the model. They reported that the fading rates

depend strongly on the radiation dose previously received by the samples.

Li and Li [7] developed a single differential equation, whose solution for a constant distance $r'$, is given by:

$$\frac{n(r')}{N(r')} = \frac{D_R\tau(r')}{D_R\tau + D_o}\left(1 - \exp\left[-\frac{D_R\tau(r') + D_o}{D_o\tau}t\right]\right) \tag{13}$$

where $D_R$ is the natural irradiation dose rate, $D_o$ is the characteristic unfaded dose, $n(r')$ and $N(r')$ are the instantaneous and maximum possible concentrations of carriers corresponding to a given distance $r'$, and the tunneling lifetime $\tau(r')$ is found from Eq. (1) as before. Using $t = D_n/D_R$ where $D_n$ is the paleodose and by defining an effective characteristic dose $D'_o(r')$:

$$D'_0(r') = \frac{D_R\tau(r')D_o}{D_R\tau + D_o} \tag{14}$$

Eq. (13) becomes:

$$\frac{n(r')}{N(r')} = \frac{D'_0}{D_o}\left(1 - \exp\left[-\frac{D_n}{D'_0}\right]\right) \tag{15}$$

This is the saturating exponential function derived by Li and Li [7], which expresses how $n(r')$ fills up with the paleodose $D_n = D_R t$. Both the lifetime $\tau(r')$ and the effective characteristic dose constant $D'_o\,(r')$ depend on the distance $r'$. As time progresses, the probability distribution of distances $r'$ for the system changes with the paleodose $D_n$ according to the equation:

$$P_n(r') = \frac{P(r')n(r')}{N(r')} = 3(r')^2\exp(-(r')^3)\frac{D'_0}{D_o}\left(1 - e^{-\frac{D_n}{D'_0}}\right) \tag{16}$$

where $P(r') = 3(r')^2\exp(-(r'))^3$ is the unfaded nearest neighbor probability distribution function.

Figure 4a shows an example of the probability distribution function (PDF) $P_n\,(r')$ from Eq. (16), with the numerical values $\rho' = 3\times10^{-6}$, $s = 3\times10^{15}\,\mathrm{s}^{-1}$, $D_n = 500\,\mathrm{Gy}$, $D_R = 3\,\mathrm{Gy\ ka}^{-1}$ and $D_o = 538\,\mathrm{Gy}$. The solid curve in Fig. 4a represents the symmetric unfaded PDF, and the dashed curve represents the faded distribution $P_n\,(r')$. Physically this $P_n\,(r')$ function represents a "tunneling front"

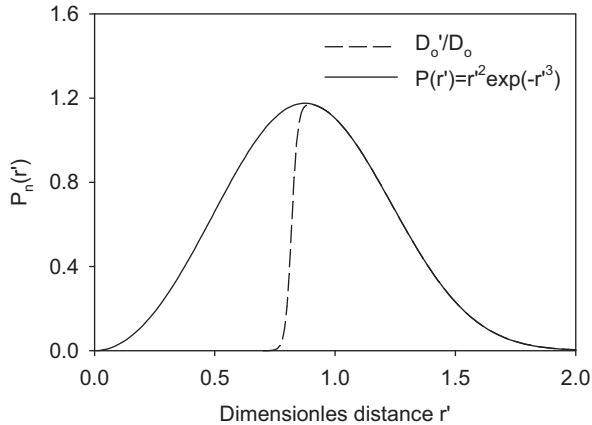


(a)

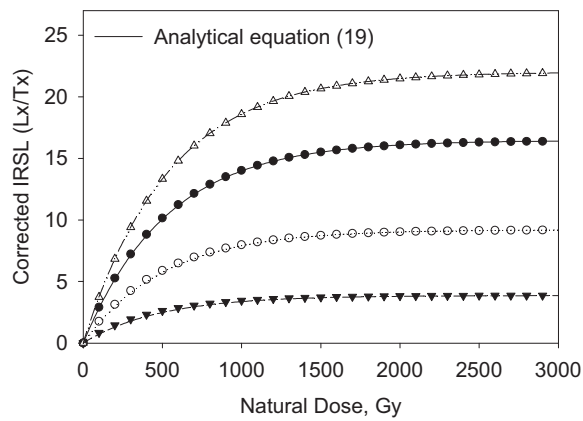


(b)

Fig. 4. (a) An example of the probability distribution $P_n(r')$ from Eq. (16). The solid line represents the symmetric unfaded PDF, and the dashed line represents the faded distribution $P_n(r')$, similar to the tunneling front shown in Fig. 2a for ground state tunneling. (b) Comparison of the DRC analytical Eq. (20) with the results obtained by the numerical integration of equations in the model. (After Pagonis and Kitis [12]).

which is mathematically similar to the front shown in Fig. 2a for ground state tunneling.

The modeling results of Li and Li [7] were expressed in terms of integral equations which require numerical integration over the

donor-acceptor distances in the model. Pagonis and Kitis [12] showed that the integral equations for DRCs in the model of Li and Li [7] can be replaced with analytical equations. These authors demonstrated the mathematical similarities between the two ground state tunneling models shown in Fig. 1ab, and introduced a critical radius approximation:

$$r'_c = (\rho')^{1/3} \ln\left(\frac{D_o s}{D_R}\right) \tag{17}$$

Using this value of the critical radius, one can now numerically evaluate the integrals in the work of Li and Li [7], to obtain this equation for the faded luminescence signal as a function of the natural dose $D_n$:

$$L_n(D_n) = \left(1 - \exp\left[-\frac{D_n}{D_0}\right]\right) M \exp\left\{-\rho' \ln\left[\frac{D_o s}{D_R}\right]^3\right\} \tag{18}$$

This is the desired analytical expression for the luminescence $L_n$ as a function the natural dose $D_n$. For the unfaded signal, the corresponding expression is:

$$L_{unfaded} = M\left\{1 - \exp\left[-\frac{D_n}{D_0}\right]\right\} \tag{19}$$

Eqs. (18) and (19) are the important analytical equations for the faded and unfaded signals $L_n$ and $L_{unfaded}$ and both equations are simple saturating exponentials of the natural dose $D_n$. The saturation level reached by the unfaded signal is equal to the total number of traps $M$, and the saturation level reached by the faded signal is equal to the second exponential term in Eq. (18). The ratio of the faded over the unfaded signal is then equal to $k = \exp(-\rho' \ln[(D_o s)/D_R]^3)$ and depends on the parameters $\rho'$, $s$, $D_R$ and $D_o$ in the model. By using the previously stated values of these parameters, we obtain the fading ratio $k = 0.438 = 43.8\%$ of the original signal remaining in the sample, in agreement with experimental data.

Experimentally one usually measures a sensitivity corrected signal, by using the response of the material to a test dose. For a small

test dose of $D_{test}$ the sensitivity corrected signal $L/T$ is given by the analytical expression:

$$\frac{L_n}{T_n} = \frac{\left(1 - \exp\left\{-\frac{D_n}{D_0}\right\}\right) \exp\left\{-\rho' \ln\left[\frac{D_\rho s}{D}\right]^3\right\}}{\left(1 - \exp\left\{-\frac{D_{test}}{D_0}\right\}\right)} \tag{20}$$

Figure 4b compares the results from the DRC analytical Eq. (20) with the corresponding results obtained by the numerical integration of the equation in the model of Li and Li [7]. Very good agreement is seen at all values of the natural dose $D_n$.

Guralnik *et al.* [18] used a different approach based on a general-order kinetics model, to describe both the DRC's and the isothermal process in feldspars. They compared their model with experimental data for different materials by using a minimum of model parameters. These authors also compared their model with experimental data from a multi-elevated temperature post-IR IRSL (MET-pIRIR) dataset.

The empirical equation used by Guralnik *et al.* [18] to fit the DRCs is:

$$f(D) = a[1 - (1 + bcD)^{(-1/c)}] + d \tag{21}$$

where $D$ is the dose and $a, b, c, d$ are constants.

### 2.2.3. *Excited state tunneling*

Early modeling work was carried out by Avouris and Morgan [8] and Thioulouse *et al.* [9]. Jain *et al.* [10] presented a mathematical description of the model in Fig. 1c. The main assumptions of the model are the presence of a random distribution of electron-hole pairs, in which the concentration of holes (acceptors) is much larger than the concentration of electrons (donors). Thermal or optical excitation raises the electrons from the ground into the excited state of the system. Tunneling takes place from the excited state of the electron trap into the recombination center, and to the nearest neighbors only. Kitis and Pagonis [11] quantified the semi-analytical model of Jain *et al.* [10] by deriving analytical expressions for different experimental stimulation modes.

In additional work Pagonis *et al.* [13] examined the exact version of the model by Jain *et al.* [10] and showed that these equations for excited state tunneling are a direct generalization of the equations previously derived by Tachiya and Mozumder [6] for the case of ground state tunneling. These authors showed that the system of equations in Jain *et al.* [10] can be replaced with the following single differential equation:

$$\frac{dn(r',t)}{dt} = -\frac{As_{tun}}{B\exp[(\rho')^{-1/3}r']}n(r',t) \tag{22}$$

where $n(r',t)$ represents the concentration of electrons in the ground state, and $n_o$ is the total initial number of donors in the system, as in the previous sections. In addition, $A$ is the rate of excitation of the electron from the ground into its excited state, $B$ is the transition rate from the excited into the ground state, and $s_{tun}$ is the frequency factor characterizing the tunneling process taking place from the excited state of the system. In previous modeling work by Jain *et al.* [10] and Kitis and Pagonis [11], it was assumed for simplicity in the model that $s_{tun} = B$, which led to a simplified form of Eq. (22). However, from a physical point of view, there is no relationship between the two parameters $s_{tun}$ and $B$, so one should not assume that they are equal.

The total remaining number of electrons in the ground state at time $t$ is given by:

$$n(t) = \int_0^\infty 3n_0(r')^2\exp[-(r')^3]\exp\left[-\frac{s_{tun}}{B\exp[(\rho')^{-1/3}r']}\int_0^t Adt'\right]dr' \tag{23}$$

Eq. (23) allows a numerical calculation of $n(t)$, by numerical integration.

The value of the parameter $A$ in the above equation depends on the stimulation mode used in the experiments. In the case of continuous wave infrared stimulated (CW-IRSL) experiments, the parameter $A$ represents the constant rate of infrared excitation $A_{IR}$,

and the integral in this equation can be replaced by $A_{IR}t$, where $t$ is the time elapsed from the beginning of the IR-excitation. In an isothermal decay experiment, the temperature $T_{ISOTH}$ of the sample is kept constant and the parameter $A$ is replaced by the constant rate of thermal excitation $A_{ISOTH} = s_{th} \exp(-E/k_B T_{ISOTH})$, where $E$ is the thermal activation energy and $s_{th}$ is the pre-exponential factor for the thermal excitation process, which is proportional to the lattice vibration frequency. In this case the integral can be replaced by $A_{ISOTH}t$, where $t$ is the elapsed time from the isothermal experiment. In a TL experiment, the sample is heated with a linear heating rate $\beta$, from a starting temperature $T_o$ up to a high temperature around 500°C. In this case parameter $A$ is replaced by time-dependent probability of thermal excitation $A_{TL} = s_{th} \exp[-E/kT(t)]$ where $k$ is the Boltzmann constant and the integral can be approximated to any desired degree of accuracy by using the exponential integral function $E_i(T)$ (Chen and Pagonis [1]). During linearly modulated IRSL (LM-IRSL) experiments, the probability of optical excitation is varied linearly with time in the form $A = bt/T$, where $T =$ total excitation period and $b$ is an experimental constant. The integral can now be replaced by $bt^2/2T$, where $t$ is the time elapsed in the LM-IRSL excitation.

The analytical solution of Eq. (23) for excited state tunneling was developed by Kitis and Pagonis [11]:

$$n(t) = n_o \exp[-\rho' F(t)^3] \tag{24}$$

$$F(t) = \ln\left(1 + 1.8 \int_0^t A dt'\right) \tag{25}$$

$$L(t) = -\frac{dn}{dt} = \frac{AF(t)^2 \exp[-\rho'[F(t)]^3]}{1 + 1.8 \int_0^t A dt'} \tag{26}$$

Where $L(t)$ represent the luminescence intensity observed during these different types of experiments. Figure 5 shows examples of 2 different types of experimental data, which was analyzed using Eqs. (24)–(26).

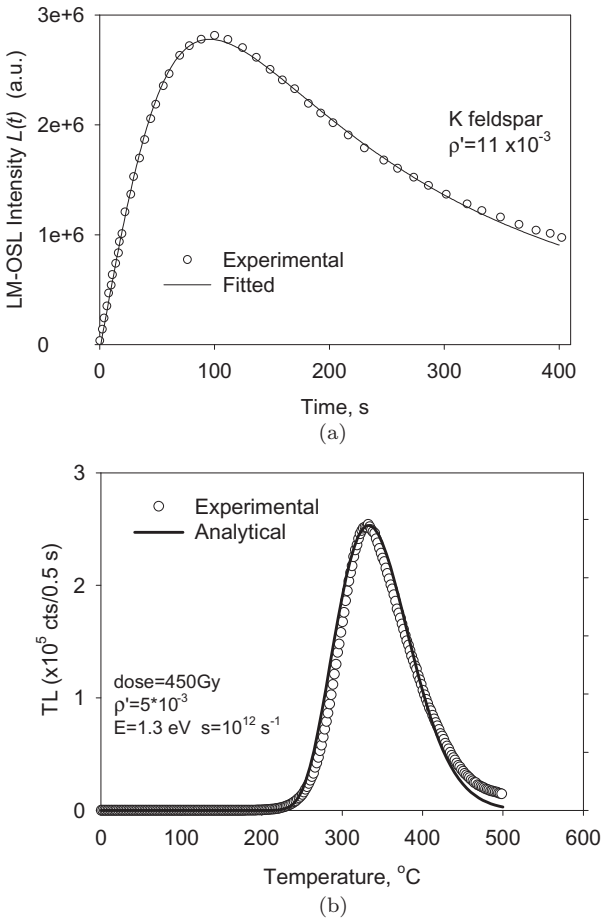


Fig. 5. (a) LM-OSL data (b) TL data analyzed using Eqs. (24)–(26) in the text (After Kitis and Pagonis [11]).

## 2.3. The microscopic Monte Carlo approach

The Monte Carlo simulations can provide valuable insight into the various factors which affect the luminescence mechanism in these materials. The advantages of using a Monte Carlo method, as opposed to the differential approach, are (Pagonis and Kulp, [18]):

- Monte Carlo methods are fast, efficient and avoid numerical integrations required in the differential equation approach.

- MC methods can be used to produce accurate results in cases of low stimulation probability, in which it is known that the analytical equations of Kitis and Pagonis [11] fail.
- They can be used for both freshly irradiated samples, and for irradiated samples which underwent thermal or optical pre-treatments.
- They can also be used to describe time-resolved experiments based on Mott hopping processes.

Section 2.3.1 summarizes earlier Monte Carlo work on luminescence clusters, and reviews the recent work by Pagonis *et al.* [19] which is based on the general one trap (GOT) model. Sections 2.3.2 describes the recent work by Pagonis and Kulp [17], who simulated the loss of charge due to ground state tunneling, as well as the charge creation by natural irradiation of the samples.

Section 2.3.3 considers the simultaneous processes of irradiation and charge loss due to ground state tunneling, and compares the Monte Carlo simulations with analytical expressions in the literature. Section 2.3.4 presents a hybrid Monte Carlo method, which is based on the solution of differential equations for a finite number of charge carriers in a solid.

### 2.3.1. *Monte Carlo under QE conditions*

Early Monte-Carlo methods for the study of thermoluminescence (TL) were presented in the papers by Kulkarni [20], Mandowski [21–23] and Mandowski and Świątek ([24–27]). These authors suggested that usually the number of carriers in a sample is large and the differential equations used in traditional kinetic models describe the system properly. However, in some solids one must consider clusters of traps as separate systems, since the continuous differential equations are not valid. Typically the Monte Carlo calculations are performed with the total population of carriers simultaneously, and in each step of the Monte-Carlo simulation one finds the lowest transition time for all possible transitions, and this is the only transition which is executed. These studies of TL showed that spatially correlated effects become prominent for low concentrations of thermally disconnected traps and for high recombination situations.

In additional Monte Carlo applications in luminescence, Pagonis and Kitis [28] studied several popular luminescence models using random combinations of variables, while Pagonis *et al.* [29] applied the same technique in simulating several dating protocols for quartz. Adamiec *et al.* ([30, 31]) used a method of random variation of kinetic parameters to develop a genetic algorithm for luminescence models.

The above mentioned studies have focused on the properties of TL glow curves using Monte Carlo simulations. Pagonis *et al.* [19] used a simple technique based on the general one trap (GOT) model of luminescence, and obtained physical insight into the nature of the simulated multi-peak TL and linearly modulated OSL signals (LM-OSL), by varying the parameters in the model. The physical picture in the simple model of these authors is that the system consists of many independent clusters of electron-hole pairs. Electrons are released from the traps and into the conduction band by either thermal or optical stimulation. Subsequently they are either recombined radiatively or are retrapped, with both retrapping and recombination taking place *within the same cluster*. The simplified model is based on the differential equation:

$$I_{TL}(t) = -\frac{dn}{dt} = \frac{n^2 p(t)}{(N-n)r + n} \tag{27}$$

where $N$ ($\mathrm{cm}^{-3}$) is the total concentration of dosimetric traps, $n(\mathrm{cm}^{-3})$ is the concentration of filled dosimetric traps. $r$ is the ratio of the capture coefficients $A_n$ and $A_m$ ($\mathrm{cm}^3\mathrm{s}^{-1}$) of the trap and recombination center respectively, and $p(t)$ is the experimental rate of excitation of the electrons in the trap. In the case of TL, the rate of thermal excitation is $p(T) = s\exp(-E/kT)$ where $E$ (eV) and $s$ ($\mathrm{s}^{-1}$) represent the thermal activation energy and the frequency factor of the dosimetric trap, correspondingly, $T$ is the absolute temperature and $k$ the Boltzmann constant. The initial concentrations of filled traps at time $t = 0$ are denoted by the symbol $n_0$, and a linear heating rate is assumed during the TL experiment. In the case of continuous-wave OSL signals (CW-OSL), $p(t) = \lambda(\mathrm{s}^{-1})$ is the constant rate for optical excitation and in the case of LM-OSL experiments, $p(t) = bt$, where $b$ is a parameter which depends on

the experimental conditions and on the optical cross section for the traps under consideration. In the "brute force" Monte Carlo method presented by Pagonis *et al.* [19], this becomes a difference equation for the discrete variable $n$:

$$\Delta n = -\frac{n^2 p(t)}{(N-n)r+n}\Delta t \tag{28}$$

The dimensionless time-dependent probability $P$ for an electron to recombine within a time interval $\Delta t$ is $P = p(t)Dt$, and a suitable value of $\Delta t$ is chosen so that $P \ll 1$. A random number $r$ uniformly distributed in the unit interval $0 \leq r < 1$ is generated; if $r \leq P$ the recombination takes place, otherwise it does not. The value of the remaining electrons $n$ is updated at the end of each time interval $\Delta t$, and the process is continued until there are no electrons left. These authors used local variables to describe the internal structure of each cluster, and global variables which describe the whole group of clusters. A double iterative loop is used, with the inner loop simulating a single cluster using local variables, and with the outer loop simulating the whole group of clusters using global variables. A third iterative loop advances the time $t$ by increments of $\Delta t$, simulating the thermal/optical stimulation of the system.

Figure 6a shows a typical simulated system of small trap clusters, in which there are 4 traps in each cluster (shown as both open and solid circles), with only 3 of them being initially filled (shown as solid circles). One ensures the charge balance in the system, by assuming the existence of an equal number of 4 luminescence centers (shown as both open and solid stars), 3 of which have been activated (shown as solid stars). Figure 6b shows the results of a Monte Carlo simulation for the TL signal, with the kinetic parameters $s = 10^{10}\,\mathrm{s}^{-1}$, $E = 0.9\,\mathrm{eV}$, a linear heating rate $1K/s$ and the retrapping ratio $r = A_n/A_m = 10^3$. The system consists of two initially filled traps per cluster, and a large number of $n_o = 2 \times 10^5$ initially filled traps. The TL glow curve in Fig. 6b consists of 2 peaks; this is consistent with the work of Mandowski and Świątek [26], who showed that the number of constituent TL peaks should be equal to the number of filled traps per cluster.

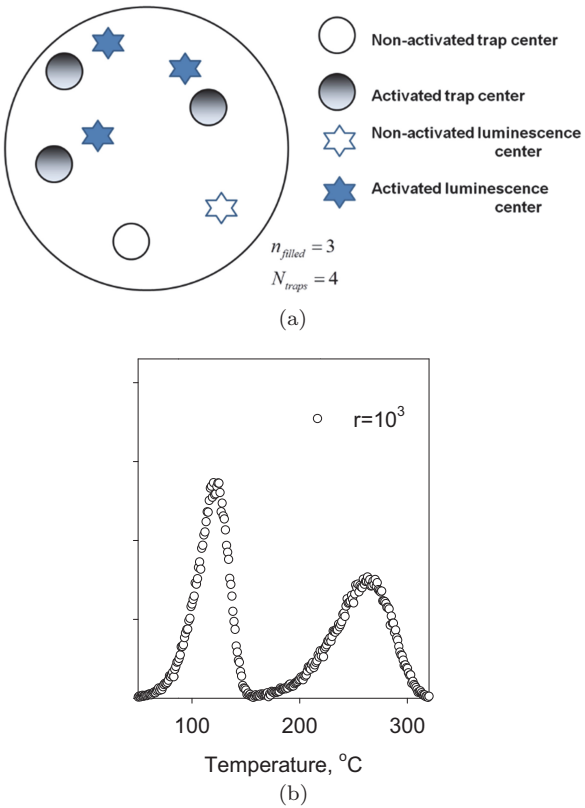


Fig. 6. (a) The model of Pagonis *et al.* [19] based on the GOT model (b) Simulated TL glow curve based on the model shown in (a).

Pagonis and Chen [32] applied the same simple Monte Carlo method to the semi-analytical version of the model by Jain *et al.* [10], in which the system of simultaneous differential equations can be approximated to a very good precision by the difference equation.

$$\Delta n = -3\rho'^{1/3} Az \exp\left[\left(\frac{1}{\rho'}\ln\frac{n_{filled}}{n}\right)^{1/3}\right]\left(\ln\frac{n_{filled}}{n}\right)^{2/3} n\Delta t \tag{29}$$

where $z = 1.8$, $n_{filled}$ is the local parameter for the initially filled traps in the cluster, and the rest of the parameters were defined previously.

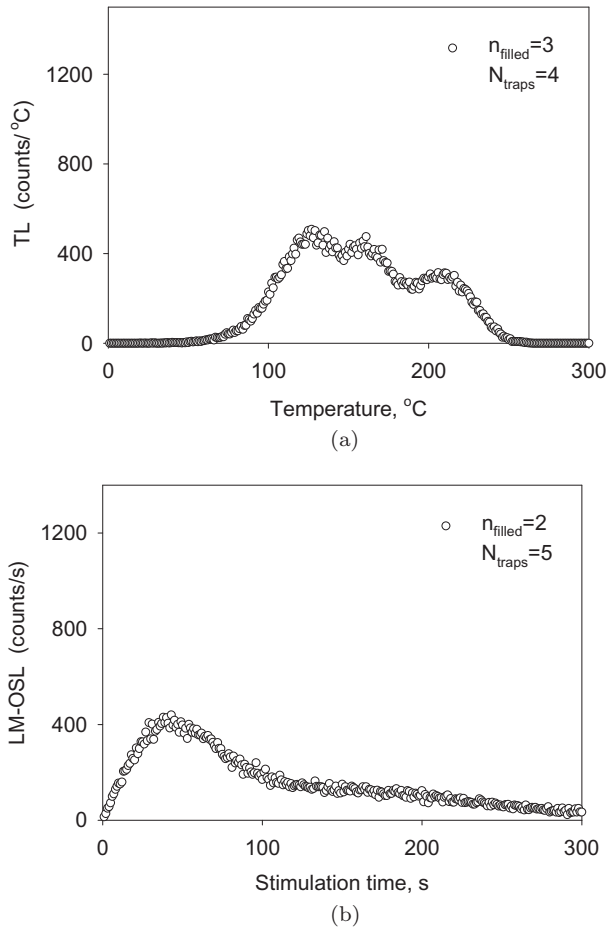


Fig. 7. (a) Simulation of TL glow curve (b) Simulation of LM-OSL curve (from Pagonis and Chen [32]).

Figures 7a and 7b show typical results from Eq. (29), for a simulated TL and LM-OSL experiment correspondingly.

### 2.3.2. *Monte Carlo simulations of ground state tunneling*

Larsen *et al.* [33] presented a numerical Monte Carlo model that simulated the processes of charge loss, charge creation and charge

recombination in feldspar. Their main assumptions were that the number densities of electrons and holes are equal at all times, and that nearest neighbor interactions take place. The focus of their study was to reproduce the experimentally observed values of the well-known g-factor describing anomalous fading effects. These authors were not able to get reliable results for bulk crystals, and obtained good agreement with experiment only when they assumed that the material consisted of small nanocrystals, and that charge carriers were allowed to recombine only within these smaller volumes.

Pagonis and Kulp [17] presented a different version of the model by Larsen *et al.* [33], in which the number density of acceptors far exceeds that of donors. The new version of the model was used to simulate the loss of charge due to ground state tunneling, as well as the charge creation by natural irradiation of the samples. The results from the model compared well with the analytical equations (24–26) presented in the previous subsection. The simulations can describe the loss of charge on a wide variety of time scales, from microseconds to thousands of years. The effect of crystal size, charge carrier density, natural irradiation dose rate and total number of charge carriers were studied in a quantitative manner.

Figure 8 shows typical simulation results obtain by Pagonis and Kulp [17]. During the simulation each of the electrons in the volume is examined, and the distances of this electron from all holes are calculated. The minimum distance $r_{MIN}$ to the nearest neighbor is found, and the Monte Carlo algorithm generates $i = 1 \ldots n_{DONORS}$ possible random fading times $t^i_{FADING}$ given by:

$$t^i_{FADING} = -s^{-1} \exp(\alpha\, r_{MIN}) \ln(1 - P_i) \tag{30}$$

where $P_i$ is a random number between 0 and 1, representing the probability of recombination for each surviving electron. These possible times $t^i_{FADING}$ depend on the tunneling frequency $s$, on the barrier penetration parameter $\alpha$, and on the instantaneous distribution of distances $r_{MIN}$ in the system. Close-by pairs are more likely to recombine first, and further away pairs are likely to recombine later. Only the event corresponding to the shortest of all

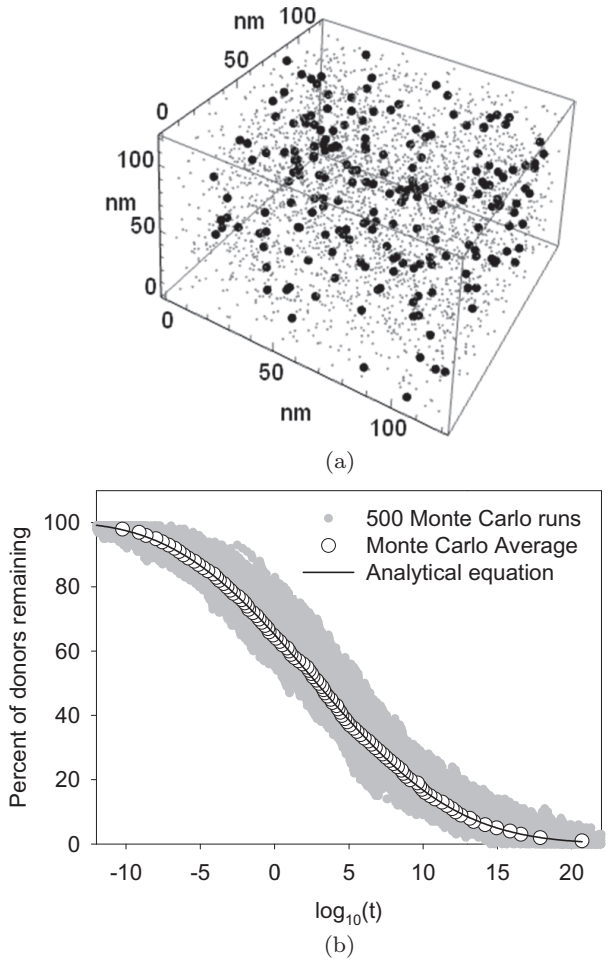


Fig. 8. (a) A cube containing random distributions of electrons and positive ions (b) Monte Carlo simulation of the charge loss in the distribution shown in (a) (After Pagonis and Kulp [17]).

the possible times in Eq. (30) happens, i.e. the donor-acceptor pair corresponding to this shortest time is allowed to recombine. After this pair is removed from the system in the simulation, the distances between each donor and each acceptor are re-evaluated, and the minimum $t^i_{FADING}$ time is used to update the total time elapsed from

the beginning of the simulation. This process is repeated until there are no more donors left in the system.

The Monte Carlo simulations average the results from 500 such random cubes of the same size shown in Fig. 8a, with typical results shown in Fig. 8b. The parameters used for the simulation in Fig. 8 are $\rho' = 10^{-5}$, $s = 3 \times 10^{15}\,\mathrm{s}^{-1}$, $n_{DONORS} = 100$ and $n_{ACCEPTORS} = 1222$, the potential barrier penetration constant $\alpha = 4 \times 10^{9}\,\mathrm{m}^{-1}$ and the size of the cube $d = 200\,\mathrm{nm}$. The solid line in Fig. 8b represents the analytical Eq. (10) for the loss of charge due to ground state tunneling. Very good agreement is obtained between the analytical equation and the results of the Monte Carlo simulation. Finally, Pagonis and Kulp [17] extended their version of the model to describe luminescence signals originating in the nearest neighbor hopping mechanism in feldspars, and compared with experimental data from time-resolved infrared stimulated luminescence (TR-IRSL) in these materials.

### 2.3.3. *Monte Carlo simulations of simultaneous irradiation and tunneling*

Pagonis and Kulp [17] simulated the simultaneous processes of charge loss by tunneling, and charge creation by irradiation in nature, and compared the results of the Monte Carlo simulations with previously derived analytical equations. The simulations were compared with analytical expressions over a wide variety of time scales, from microseconds to thousands of years. These authors were able to produce quantitative agreement of the Monte Carlo model with experimental data for both bulk and nano-sized crystals. They studied quantitatively the influence of various parameters in the model, such as the crystal size, charge carrier density, natural irradiation dose rate and total number of charge carriers.

Figure 9a shows the results of the acceptor density on the loss of charge due to tunneling. Figure 9b shows the dose response of a feldspar sample under the simultaneous effect of tunneling and natural irradiation. The solid line represents the analytical Eq. (18) derived by Pagonis and Kitis [12].

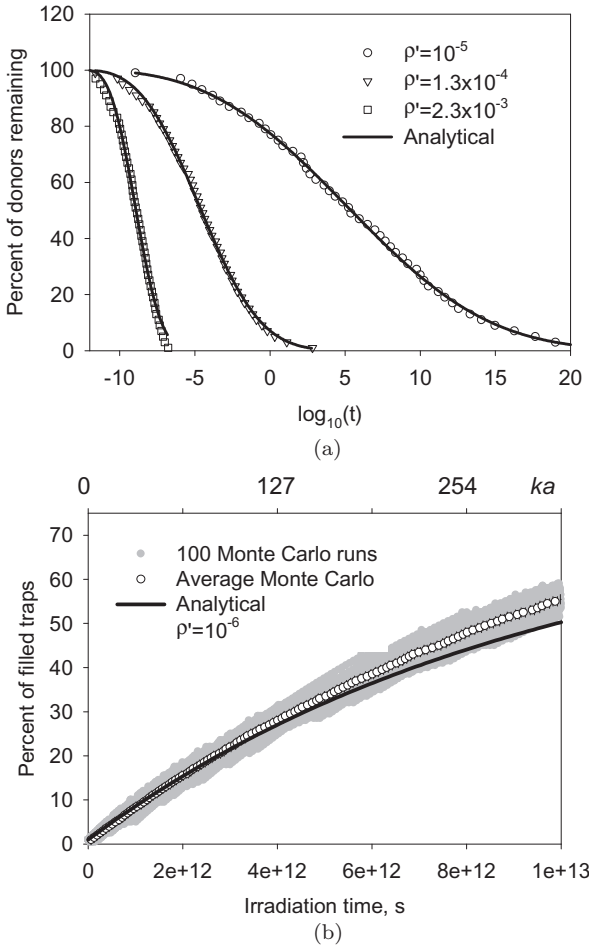


Fig. 9. (a) Effect of density on the loss of charge by tunneling (b) dose response under simultaneous irradiation and tunneling (After Pagonis and Kitis [12]).

### 2.3.4. *Monte Carlo simulations of tunneling from the excited state*

In this section we present a different Monte Carlo technique which can be used to study tunneling from the excited state of a trap, as shown schematically in Fig. 1c. This alternative computational approach has the advantage that it can be applied to any of the different situations presented in sections 2.2 and 2.3. Furthermore,

this method can be used for both freshly irradiated samples, and for irradiated samples which underwent thermal or optical pre-treatments before measurement of their luminescence signal.

The method is based on Eq. (22), which is written as a difference equation for the discrete variable $n(r',t)$ characterizing the number of electrons in the material:

$$\Delta n(r',t) = -\frac{As_{tun}}{B\exp[(\rho')^{-1/3}r']} n(r',t)\Delta t. \tag{31}$$

The total number $n(t)$ of remaining electrons at time $t$, and the luminescence intensity $I(t)$ are evaluated from the finite sums:

$$n(t) = \sum_{r'=0}^{2} n(r',t)\Delta r' \tag{32}$$

$$L(t) = -\sum_{r'=0}^{2} \frac{\Delta n(r',t)}{\Delta t}\Delta r'. \tag{33}$$

For pretreated samples one can approximate the nearest neighbor distribution with a *truncated* distribution function which extends from a minimum critical radius $r'_c$ up to infinity (Pagonis *et al.* [13]; Jain *et al.* [34]). This critical radius can be treated as an adjustable modeling parameter when fitting experimental data. For such samples the summations in Eqs. (32)–(33) start at $r = r'_c$, instead of starting at $r' = 0$. In these equations $\Delta r'$ is an appropriate distance interval, e.g. $\Delta r' = 0.02$. The overall evolution of the system must be followed for *both* the time variable $t$, and for each value of the dimensionless distance $r'$, by using two iterative loops. The inner loop is executed using a time variable $t$, and for a constant value of the distance parameter $r'$. The outer loop repeats the inside loop for all possible discrete values of the parameter $r' = r' + \Delta r'$. At time $t = 0$ there are $n_o$ filled traps, and the distribution of nearest neighbors is given by the peak shaped function. The rate $P$ for an electron to recombine radiatively within the time interval $\Delta t$ and for certain distance $r'$ is given by the function on the right hand side of Eq. (31). By following the same method as in Pagonis *et al.* [19], and Pagonis and Chen [32], one chooses a suitable value

of $\Delta t$ so that $P\Delta t \ll 1$, and a random number $r$ is generated, which is uniformly distributed in the unit interval $0 \leq r < 1$. If $r \leq P$ the electron recombines radiatively, otherwise it does not; all non-recombined remaining electrons in the system are tested in this manner during each time interval $\Delta t$, and at the end of each time interval $\Delta t$, the program stores the values of $n(r', t)$ and $\Delta n(r', t)/\Delta t$. This process is now repeated for the next value of the

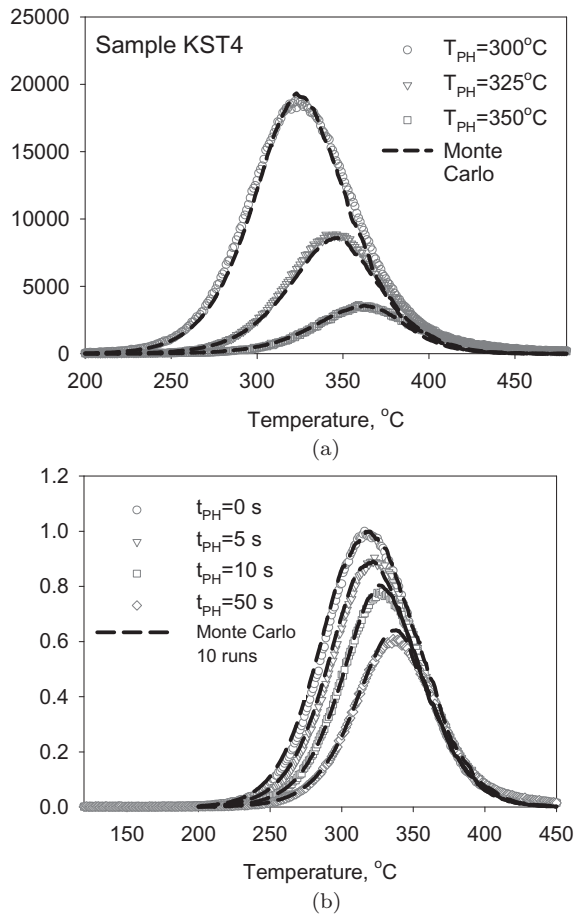


Fig. 10. (a) Comparison of model with experimental TL glow curves of irradiated sample preheated at different temperatures (b) Same as (a), for a sample preheated at different times for a fixed preheating temperature (After Polymeris *et al.* [35]).

distance $r'$ in the outer software loop. Finally the contributions from all distances $r'$ are added according to Eqs. (32) and (33), resulting in the simultaneous evaluation of the discrete-value functions $n(t)$ and $L(t)$. Both iterative loops are executed until there are no particles left in the system. Figure 10 shows how the results of this method compare with experimental data.

## 2.4. Monte Carlo simulations of luminescence phenomena in nanodosimetric materials: ground state tunneling

In this section we present simulations of luminescence phenomena for nanomaterials based on ground state tunneling, with emphasis on the effect of crystal size on the experimentally measured luminescence signals.

Pagonis *et al.* [15] simulated the effect of crystal size on quantum tunneling phenomena in nanocrystals, based on the assumption of a random distribution of electrons and positive ions. They found a rather complex behavior of such random distributions, which is determined by three characteristic lengths: the radius of the crystal $R$, the tunneling length $a$, and the initial average distance $\langle d \rangle$ between electrons and positive ions (which is directly related to the density of charges in the material). Two different cases were examined, depending on the relative concentrations of electrons and ions. In the first case described in section 2.4.1, the concentration of electrons was assumed to be much smaller than the concentration of positive ions, and an analytical equation is available to describe the effect of varying crystal size. In the second situation presented in section 2.4.2, the concentrations of electrons and positive ions were equal at all times, and no analytical equation is available to describe the process. As a consequence, crystal size effects in this situation must be simulated using Monte Carlo techniques.

### 2.4.1. *Case #1: Concentration of electrons much smaller than concentration of positive ions*

When the concentration of positive ions $\rho$ far exceeds the concentration of electrons in the system, then $\rho$ can be considered

to stay almost constant during the tunneling process. Tachiya and Mozumder [6] developed the following analytical equation to describe the electron survival probability $P(t)$ in a spherical random distribution of electrons and positive ions with radius $R$:

$$P(t) = \left[ \frac{1}{(4/3\pi R^3)} \int_0^R \exp\left[ \frac{-t}{\tau_{FADING}(r)} \right] 4\pi r^2 dr \right]^{\rho(4/3\pi R^3)}, \quad (34)$$

where the lifetime $\tau_{FADING}$ is given by Eq. (1). It is noted that Eq. (34) has been available for more than 40 years in the literature, but was used only recently to describe crystal size effects on tunneling phenomena.

In the limit of bulk large crystals $R \to \infty$, Tachiya and Mozumder [6] showed that Eq. (34) has the following analytical expression:

$$P(t) = \exp\left[ -\rho \left( \frac{4}{3}\pi a^3 \right) g(st) \right], \quad (35a)$$

$$g(st) = \ln(st)^3 + 1.7316 \ln(st)^2 + 5.9343 \ln(st) + 5.4449. \quad (35b)$$

Pagonis *et al.* [15] studied the behavior of Eq. (34) as a function of the radius $R$, and with a constant density of positive ions $\rho$, and found two opposite behaviors as a function of the crystal size. When the tunneling length $a$ is much smaller than both $R$ and $\langle d \rangle$, the analytical equations show that smaller crystals exhibit a faster tunneling recombination rate, as shown in Fig. 11a.

However, when the tunneling length $a$ is of the same order of magnitude as both $R$ and $\langle d \rangle$, the opposite effect is observed in Fig. 11b, with smaller crystals exhibiting a slower tunneling recombination rate. As the crystal size increases, the rate of tunneling in both cases reaches the limit expected for bulk materials, given by Eq. (35).

In the second situation presented in section 2.4.2, the concentrations of electrons and positive ions were equal at all times, and no analytical equation is available to describe the process. As a consequence, crystal size effects in this situation must be simulated using Monte Carlo techniques.

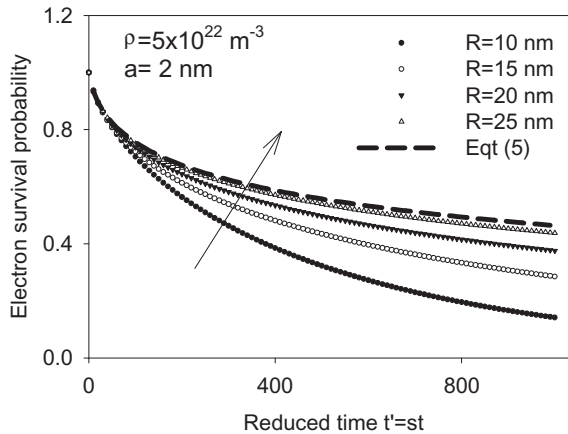


(a)

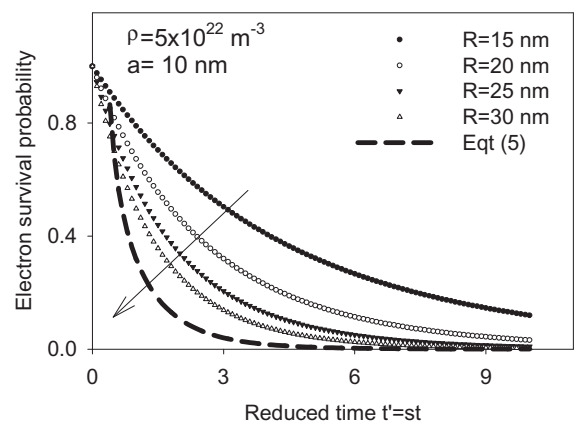


(b)

Fig. 11. (a) The results of integrating Eq. (34) numerically for a positive ion density $\rho = 5 \times 10^{22}\,\mathrm{m}^{-3}$, tunneling length $a = 2\,\mathrm{nm}$, and for crystal sizes $R = 10 - 25\,\mathrm{nm}$. The dashed line shows the limit described by the analytical equation (24). (b) Same as (a), for a longer tunneling length $a = 10\,\mathrm{nm}$, and for a radius in the range $R = 15$–$30\,\mathrm{nm}$. (After Pagonis *et al.* [15]).

### 2.4.2. *Case #2: Equal concentrations of electrons and positive ions at all times*

Pagonis *et al.* [15] discussed the situation when the concentrations of electrons and positive ions are equal at all times. In this case crystal size effects must be simulated using Monte Carlo techniques. These

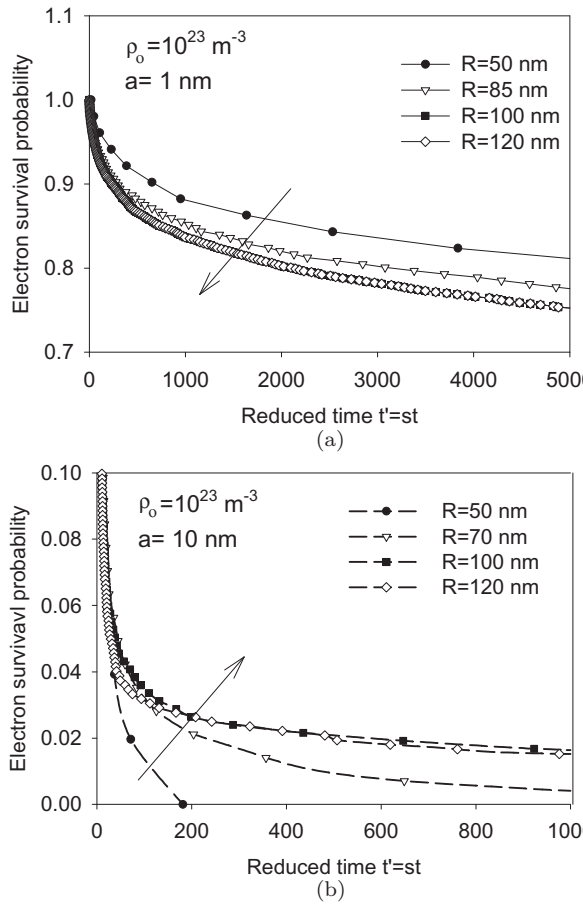


Fig. 12. (a) The results of Monte Carlo simulations of a spherical distribution, for an *initial* positive ion density $\rho = 10^{23}\,\mathrm{m}^{-3}$, tunneling length $a = 1\,\mathrm{nm}$, and for crystal sizes $R = 50 - 120\,\mathrm{nm}$. (b) Same as (a), for a longer tunneling length $a = 10\,\mathrm{nm}$. (After Pagonis *et al.* [15]).

authors employed the Monte Carlo method described in Pagonis and Kulp [17], and examples of the results of their simulations are shown in Fig. 12.

The Monte Carlo simulations of Figs. 12ab show the same effect of crystal size on the tunneling rate as the results of the analytical Eq. (34) shown in Fig. 11.

Pagonis *et al.* [15] also studied the effect of sample temperature, by extending the Monte Carlo simulations to include thermal characteristics of the defects. By following the suggestion by Larsen *et al.* [33], these authors included the thermal time constant $\tau_{THERMAL} = (1/s)\exp(E/kT)$, which is assumed to be constant and the same for all traps. This Arrhenius-type thermal time constant $\tau_{THERMAL}$ is

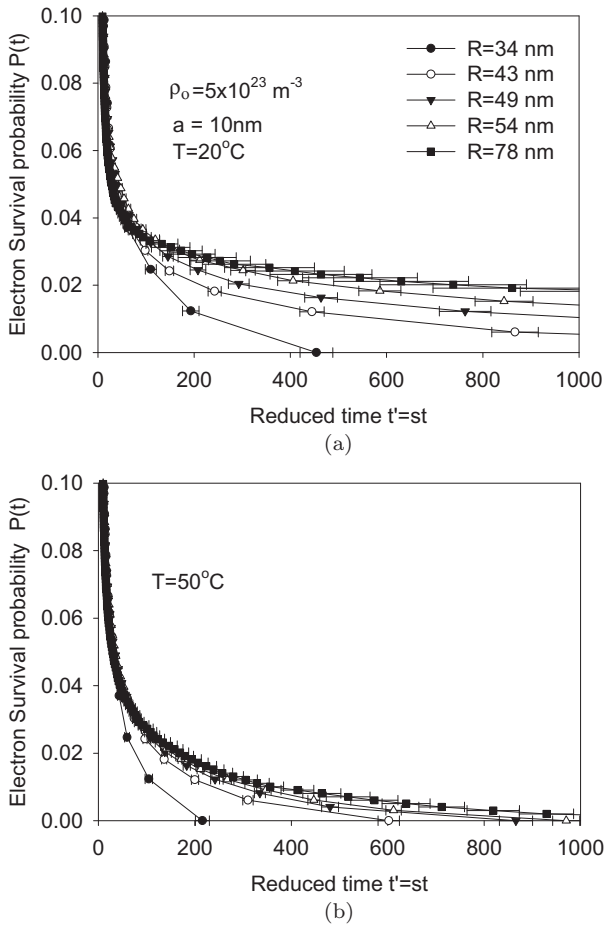


Fig. 13. (a) The results of Monte Carlo simulations of a spherical distribution, for an *initial* positive ion density $\rho = 10^{23}\,\mathrm{m}^{-3}$, tunneling length $a = 1\,\mathrm{nm}$, and for crystal sizes $R = 50$–$120\,\mathrm{nm}$. (b) Same as (a), for a longer tunneling length $a = 10\,\mathrm{nm}$. (After Pagonis *et al.* [15]).

characterized by the thermal activation energy $E$ and the thermal frequency factor $s$, $k$ is the Boltzmann constant and $T$ is the temperature of the sample.

The results of the simulations are shown in Fig. 13 with the parameters $E = 1\,\text{eV}$, $s = 10^{12}\,s^{-1}$, initial charge density $\rho_o = 5 \times 10^{23}\,\text{m}^{-3}$, $a = 1\,\text{nm}$ and crystal sizes $R = 34$–$78\,\text{nm}$. The simulations are shown at two different sample temperatures $T = 20, 50°\text{C}$.

As the temperature of the sample increases in Fig. 13b, the electron survival probability curves $P(t)$ become steeper and closer together, i.e. the recombination takes places faster.

## 2.5. Monte Carlo simulations of luminescence phenomena in nanodosimetric materials: excited state tunneling

TL signals from nanodosimetric materials have been studied extensively during the past twenty years, especially in the area of nanomaterials doped with rare earths. One of the primary effects being studied experimentally have been possible correlations between the nanocrystal size and the shape and magnitude of TL signals. While there is an abundance of experimental studies attempting to establish such correlations, the underlying mechanism is not well understood. In this section we present the simulations of TL glow curves by Pagonis and Truong [36], which are based on tunneling taking place from the excited state of the system.

In general, Fig. 14 shows three types of kinetic models which have been studied using Monte-Carlo methods. Fig. 14a shows the energy scheme in the well-known one trap one recombination center model (OTOR), which is commonly used to describe delocalized luminescence phenomena in crystalline solids ([1]). Several energy transitions are shown schematically: thermal or optical excitation of a carrier from the ground state of the electron trap into the conduction band (solid arrow D), retrapping from the conduction band into the trap (solid arrow T), and direct recombination transition of electrons from the conduction band into a recombination center (L) resulting in the emission of photons (dashed arrow R). It is noted

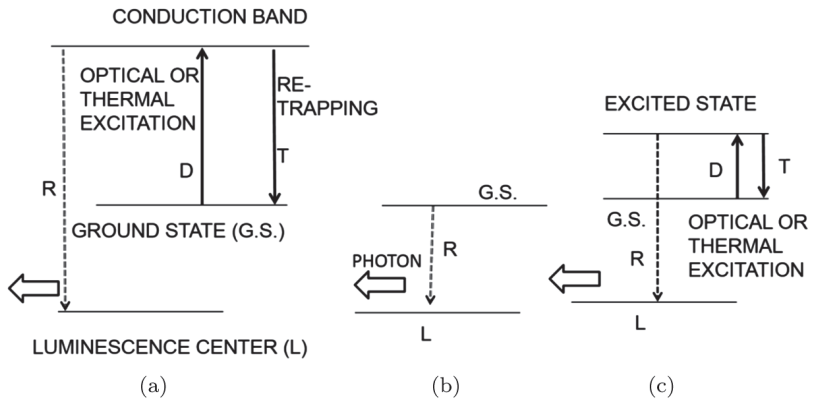


Fig. 14. (a) The energy scheme in the *delocalized* OTOR model, used for describing luminescence phenomena in crystalline solids. (b) The *localized* transition model for tunneling processes taking place from the ground state of the trap. (c) The *localized* transition model for tunneling processes taking place from the excited state of the trap. The various transitions are discussed in the text. (After Pagonis and Truong [36]).

that all transitions shown in Fig. 14a represent delocalized transition processes, as opposed to the models in Fig. 14b and Fig. 14c which are based on localized energy transitions. Previous TL Monte Carlo work based on Fig. 14a were presented in the papers by Mandowski and collaborators, and are summarized in Pagonis and Truong [36].

Typically the Monte Carlo calculations in Fig. 14a are performed with the total population of carriers simultaneously, and in each step of the Monte-Carlo simulation one finds the lowest transition time for all possible transitions, and this is the only transition which is executed. Mandowski and collaborators demonstrated how to perform Monte Carlo calculations in a solid consisting of a number of *separate* systems. Each transition in this scheme is represented mathematically by a transition rate $\lambda(t)(\mathrm{s}^{-1})$ as follows. The rate for thermal excitation (transition $D$) from the trap into the conduction band is $\lambda_{THERMAL}(t) = \mathrm{s}\exp(-E/kT)$ where $E, s$ are the thermal activation energy and frequency factor characterizing the thermal properties of the electron trap. The corresponding optical excitation

rate (also transition $D$) is given by $\lambda_{OPTICAL} = \sigma I$ where $\sigma$ ($\mathrm{cm}^2$) is the optical cross section of the trap and $I$ is the photon flux (*photons* $\mathrm{cm}^{-2}\,\mathrm{s}^{-1}$). The retrapping rate for transition $T$ from the conduction band into the trap is given by the product $T = A_n(N - n)$ where $n$, $N$ are the number of trapped electrons and total number of traps correspondingly, and $A_n$ is the constant retrapping coefficient for a single carrier into a single trap. The recombination rate (transition $R$) from the conduction band into the luminescence center ($L$) is given by the product $R = A_m m$, where $m$ is the number of trapped holes in recombination centers, and $A_m$ is the constant recombination coefficient for a single carrier into a single center.

In each step of the Monte Carlo simulation, the times $t_i$ of each allowed transition are generated for all carriers in the system, and can be evaluated from the integral equation (Mandowski and Świątek [24], their Eq. 5):

$$\int_0^{t_i} \lambda(t')dt' = -\ln(a_i) \tag{36}$$

where $a_i$ is a homogeneous normalized random variable from the interval (0, 1) and $\lambda(t)$ (in $\mathrm{s}^{-1}$) is the appropriate transition rate ($T$, $R$, or $D$) for the transition under consideration, as described above. Eq. (36) has simple analytical solutions for the transitions $R$, $T$ in Fig. 14a, since these transitions do not depend on time. However, in the case of TL experiments Eq. (36) must be solved numerically, as described below.

Fig. 14b shows a ground state tunneling model which is based on localized energy transitions; recent Monte Carlo work using this type of model was presented in previous sections of this chapter.

In the third type of model shown in Fig. 14c, electrons can tunnel from the excited state of the electron trap to the luminescence center. During a typical laboratory experiment, one uses optical or thermal excitation, and the dominant process is the recombination process taking place from the excited state of the trapped electron to the recombination center. The relevant *localized* transitions are shown as $D$, $T$, $R$ in Fig. 1c; although these transitions have some

mathematical similarity to the transitions of the delocalized model of Fig. 1a, the important difference is that they involve the excited state of the trap, instead of taking place via the conduction band.

In a typical TL experiment, the sample is heated with a constant heating rate $\beta(K/s)$ from a starting temperature $T_o$ up to a high temperature around 500°C, so that the temperature varies with time $t$ as $T(t) = T_o + \beta t$. Jain *et al.* [25] and previously Thioulouse *et al.* [9] and Chang and Thioulouse [37], demonstrated that for this type of experiment Eq. (36) must be replaced by the following Arrhenius type of expression (Jain *et al.* [34], their Eqs. 3 and 6):

$$\lambda(r,t) = s \exp[-r/a] \exp[-E/\{k_B(T_o + \beta t)\}] \tag{37}$$

where $E$ is the thermal activation energy between the ground state and the excited state of the trapped electron, $k_B$ is the Boltzmann constant and $s$ is the frequency factor characterizing tunneling taking place from the excited state of the system. It is noted that Eq. (37) is derived by assuming quasi-static equilibrium conditions (QE) in the excited state tunneling model of Fig. 14c.

By combining Eqs. (36) and (37) we obtain:

$$s \exp[-r/a] \int_0^{t_i} \exp[-E/\{k_B(T_o + \beta t')\}] dt' = -\ln(a_i) \tag{38}$$

Pagonis and Truong [36] presented a Monte Carlo simulation study of the effect of nanocrystal size on the TL signals from a random distribution of electrons and positive ions, based on Eq. (38). These authors varied the following parameters in the model: the radius of the crystal R, the tunneling length a, and the relative concentrations of electrons and ions.

Typical results from the simulations of Pagonis and Truong [36] are shown in Fig. 15. As the radius of the nanocrystals becomes larger, the peaks of the TL glow curves shift towards lower temperatures and changes occur in both peak intensity and peak width. For large crystals with a constant density of positive ions, the TL glow curves reach the analytical limit expected for bulk materials.

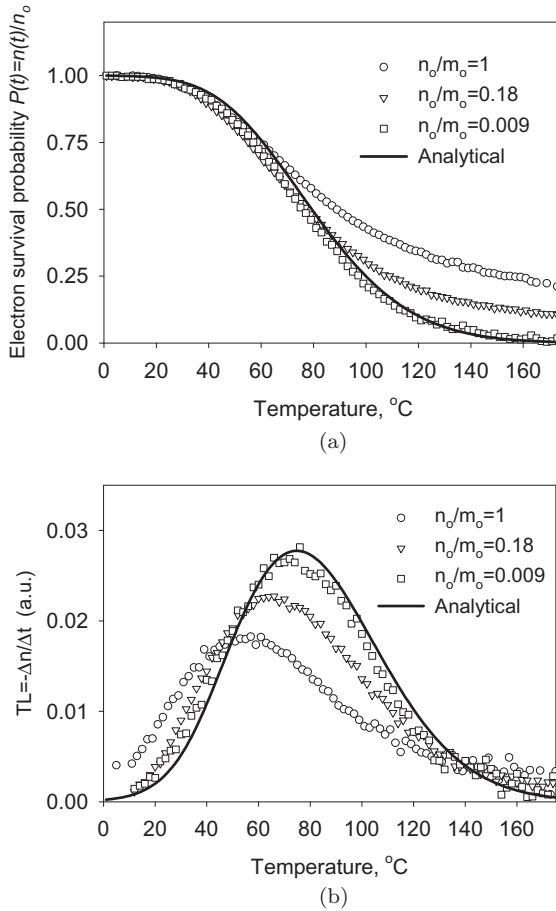


Fig. 15. Monte Carlo simulation for a spherical distribution, by varying the relative initial concentrations of electrons and positive ions in the system. The initial number of positive ions inside the sphere is kept constant at $m_o = 1100$, while the initial number of electrons is varied. The solid lines correspond to the analytical equation, which is valid for very low values of the ratio $n_o/m_o$. (a) The electron survival probability and (b) the corresponding TL glow curve (After Pagonis and Truong [36]).

Figure 16 shows simulations of TL glow curves in crystals with *equal* number of electrons and positive ions at all times. Figure 16a shows that at low temperatures the tunneling process for small crystals is *slower* than in large crystals, with the arrows indicating

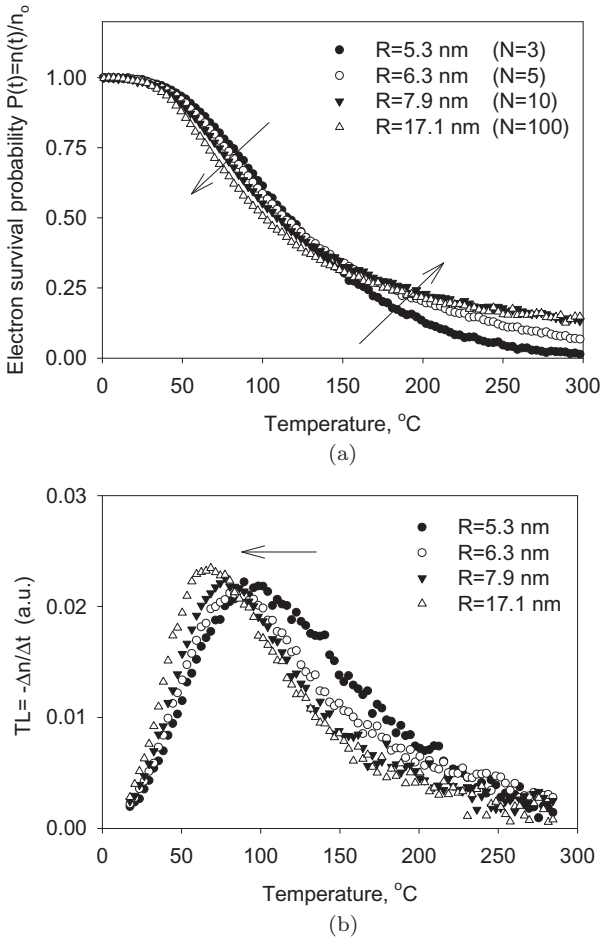


Fig. 16. Simulations for crystals with *equal* number of electrons and positive ions at all times. (a) At low temperatures the tunneling process for small crystals is *slower* than in large crystals, with the arrows indicating the direction of increasing radius $R$. At higher temperatures the order of the curves is reversed. (b) The corresponding simulated TL curves. (After Pagonis and Truong [36]).

the direction of increasing radius $R$. At higher temperatures the order of the curves is reversed. Fig. 16b shows the corresponding simulated TL curves.

Figure 17 shows the same type of simulations as Fig. 16, for a smaller tunneling length $a = 1\,\text{nm}$ while keeping all the other

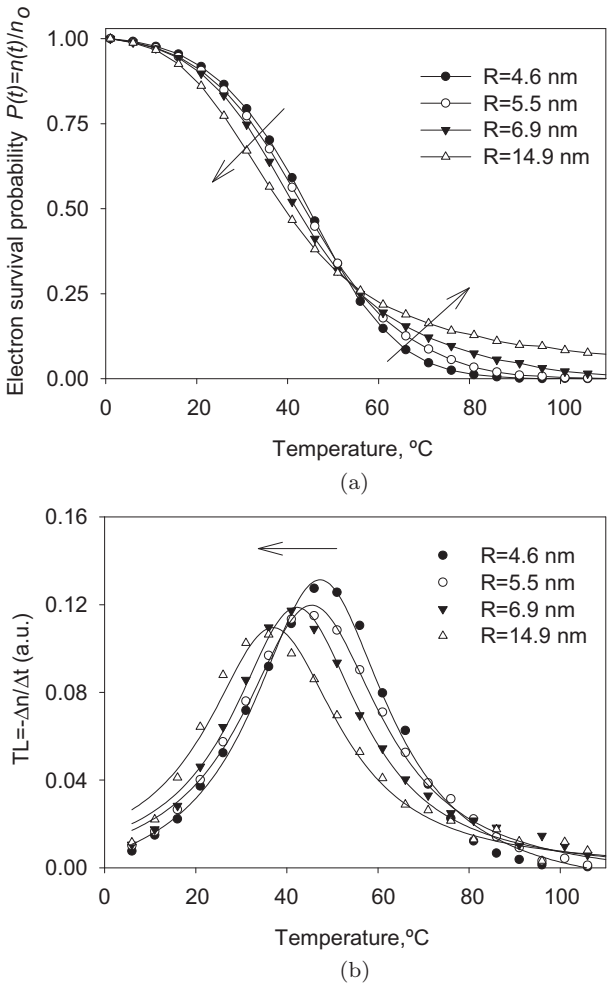


Fig. 17. The simulations in Fig. 16 are repeated for a smaller tunneling length. The TL height shows the opposite behavior than in Fig. 16b. (After Pagonis and Truong [36]).

parameters fixed. The TL height as a function of the radius $R$ in Fig. 17 shows the opposite behavior than the corresponding curves in Fig. 16. The solid lines are again a guide to the eye.

As the radius of the nanocrystals becomes larger, the peaks of the TL glow curves shift towards lower temperatures and changes

occur in both peak intensity and peak width. For large crystals with a constant density of positive ions, the TL glow curves reach the analytical limit expected for bulk materials.

Pagonis and Truong [36] compared the results from the Monte Carlo simulations with experimental data for Durango apatite, a material which is known to exhibit strong anomalous fading due to tunneling. Specifically Polymeris *et al.* [38] found that ball milling of Durango apatite powders for up to 48 hours, resulted in significant changes in the TL and OSL luminescence signals in this material. Figure 18 shows some of their experimental TL glow curves for the same Durango apatite sample which has undergone ball milling for 2 hours (dark circles) and 24 hours (open circles). The sample was irradiated with a small test dose after the end of the ball milling process, and its prompt TL signal was measured immediately after. Figure 18a shows the complete normalized TL glow curves for the two ball milling times, while Fig. 18b shows details of the same data between 200 and 400°C. The main peak in the TL glow curve for the smaller crystals with an average grain size $R = (0.4 \pm 0.2)\mu$m, is shifted towards higher temperatures than the TL for larger crystals with average grain size $R = (5.0 \pm 1.0)\mu$m. The *qualitative* behavior of the TL glow curves in Fig. 18 is very similar to the simulated behavior shown in Fig. 17, although the temperature and radius scales are very different. The grain sizes in Polymeris *et al.* [38] were obtained by analyzing scanning electron microscope images (SEM) of the ball milled sample. This comparison of experimental data with the Monte Carlo model in this chapter is very encouraging, and prompts the need for additional work to produce quantitative agreement between experiment and theory.

Pagonis and Truong [36] also examined the commonly used assumption of nearest neighbor interactions within the model, and presented simulated examples at very high charge densities, in which this assumption breaks down. Finally these authors also demonstrated that the Monte Carlo method presented in their paper can also be used for linearly modulated infrared stimulated luminescence (LM-IRSL) signals, which are of importance in luminescence dosimetry and luminescence dating applications.

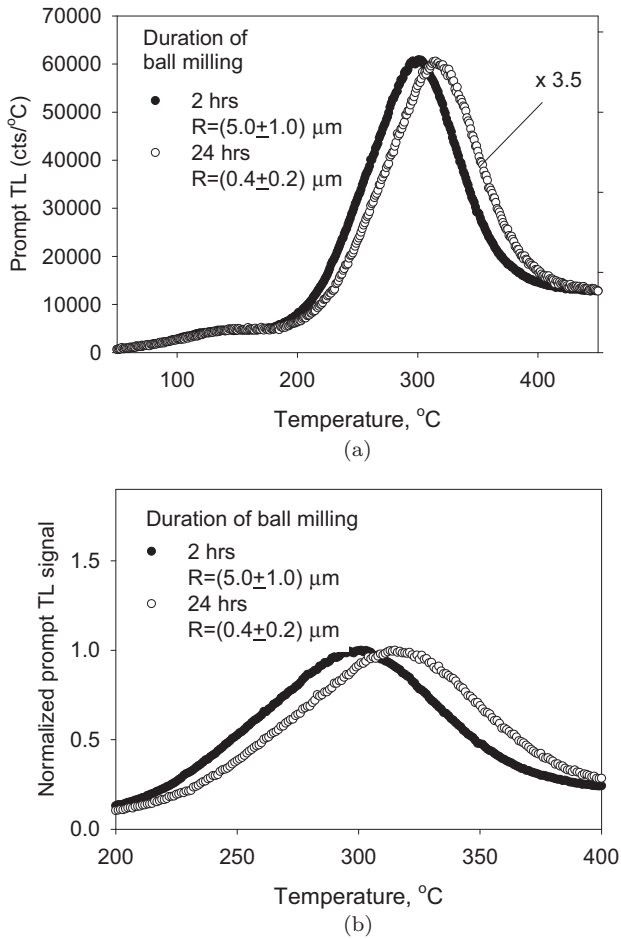


Fig. 18. Experimental TL glow curves for a Durango apatite sample which has undergone ball milling for 2 hours (dark circles, larger crystals) and 24 hours (open circles, smaller crystals). (a) The complete TL glow curves (b) Detailed view of the normalized signals from (a), between 200 and 400°C. (After Pagonis and Truong [36] and Polymeris *et al.* [38]).

## 2.6. Conclusions

In this chapter, two approaches were discussed for calculating tunneling phenomena in random distributions of electrons and positive ions. The differential equation approach is useful for large crystals, and

several analytical equations are available in the literature. Several of these analytical equations have been developed by assuming that the concentrations of electrons is much smaller than the concentration of positive ions, which allows the system to be described by the constant density of positive ions. The model by Jain *et al.* [10] and the analytical equations developed by Kitis and Pagonis [11] have been a major recent development, and have contributed in the understanding of tunneling phenomena in a random distribution of electron-hole pairs. Specifically the analytical equations by Kitis and Pagonis [11] have now been used to describe luminescence signals from a variety of feldspars and apatites (Polymeris *et al.* [39]; Sahiner *et al.* [40]; Sfampa *et al.* [41]; Kitis *et al.* [42]).

The Monte Carlo approach is useful for crystals of any size, especially in cases where analytical equations are not available in the literature. The rate of quantum tunneling in random distributions of electrons and positive ions was shown to depend in a complex manner on three fundamental lengths in the system: the radius of the crystal $R$, the tunneling length $a$, and the initial average distance $\langle d \rangle$ between electrons and positive ions (which is directly related to the density of charges in the material).

Both the differential equation and Monte Carlo approaches can be used to describe the ground state tunneling phenomena, as well as tunneling taking place from the excited state of the electron trap. Further modeling work will need to combine the localized transition models in this chapter with delocalized transitions involving the conduction and valence band, as well as transitions taking place via the band tail states.

## References

[1] R. Chen and V. Pagonis, 2011. *Thermally and Optically Stimulated Luminescence: A Simulation Approach* (Chichester: Wiley and Sons).

[2] V. Pagonis, R. Chen, C. Kulp and G. Kitis, "An overview of recent developments in luminescence models with a focus on localized transitions," *Radiat. Meas.*, vol. 106, pp. 3–12, 2017.

[3] N. Salah, "Nanocrystalline materials for the dosimetry of heavy charged particles: A review," *Radiat. Phys. Chem.*, vol. 80, pp. 1–10, 2011.

[4] H.T. Sun and Y. Sakka, "Luminescent metal nanoclusters: Controlled synthesis and functional applications," *Sci. Technol. Adv. Mater.*, vol. 15, p. 014205, 2014.

[5] I. Eliyahu, Y.S. Horowitz, L. Oster, S. Druzhyna and I. Mardor, "Nanodosimetric kinetic model incorporating localized and delocalized recombination: Application to the prediction of the electron dose response of the peak 5a/5 ratio in the glow curve of LiF:Mg,Ti (TLD-100)," *Radiat. Meas.*, vol. 71, pp. 226–231, 2014.

[6] M. Tachiya and A. Mozumder, "Decay of trapped electrons by tunnelling to scavenger molecules in low temperature glasses," *Chemical Physics Letters*, vol. 28, pp. 87–89, 1974.

[7] B. Li and S.H. Li, "Investigations of the dose-dependent anomalous fading rate of feldspar from sediments," *J. Phys. D: Appl. Phys.*, vol. 41, p. 225502, 2008.

[8] P. Avouris and T.N. Morgan, "A tunneling model for the decay of luminescence in inorganic phosphors: The case of $Zn_2SiO_4$:Mn," *J. Chem. Phys.*, vol. 74, p. 4347, 1981.

[9] P. Thioulouse, E.A. Giess and I.F. Chang "Investigation of thermally stimulated luminescence and its description by a tunneling model," *J. Appl. Phys.*, vol. 53, p. 9015, 1982.

[10] M. Jain, B. Guralnik and M.T. Andersen, "Stimulated luminescence emission from localized recombination in randomly distributed defects," *J. Phys.: Condens. Matter*, vol. 24, 385402 (12pp), 2012.

[11] G. Kitis and V. Pagonis, "Analytical solutions for stimulated luminescence emission from tunneling recombination in random distributions of defects," *J. Lumin.*, vol. 137, pp. 109–115, 2013.

[12] V. Pagonis and G. Kitis, "Mathematical aspects of ground state tunneling models in luminescence materials," *J. Lumin.*, vol. 168, pp. 137–144, 2015.

[13] V. Pagonis, H. Phan, D. Ruth and G. Kitis, "Further investigations of tunneling recombination processes in random distributions of defects," *Radiat. Meas.*, vol. 58, pp. 66–74, 2013.

[14] V. Pagonis, C. Kulp, C. Chaney and M. Tachiya, "Quantum tunneling recombination in a system of randomly distributed trapped electrons and positive ions," *J. Phys. Condens. Matter*, vol. 29, no. 36, p. 365701, 2017, 2017c.

[15] V. Pagonis, S. Bernier, F.M. Vieira and S. Steele, "The effect of crystal size on tunneling phenomena in luminescence dosimetric materials," *Nucl. Inst. Methods Phys. Res. B*, vol. 412, pp. 198–206, 2017.

[16] D.J. Huntley and O.B. Lian, "Some observations on tunnelling of trapped electrons in feldspars and their implications for optical dating," *Quat. Sci. Rev.*, vol. 25, p. 2503, 2006.

[17] V. Pagonis and C. Kulp "Monte Carlo simulations of tunneling phenomena and nearest neighbor hopping mechanism in feldspars," *J. Lumin.*, vol. 81, pp. 114–120, 2017.

[18] B. Guralnik, B. Li, M. Jain, R. Chen, R.B. Paris, A.S. Murray, S.H. Li, V Pagonis, P.G. Valla and F. Herman, "Radiation-induced growth and

isothermal decay of infrared-stimulated luminescence from feldspar," *Radiat. Meas.*, pp. 224–23, 2015.

[19] V. Pagonis, E. Gochnour, M. Hennessey and C. Knower, "Monte Carlo simulations of luminescence processes under quasi-equilibrium (QE) conditions," *Radiat. Meas.*, vol. 67, pp. 67–76, 2014.

[20] R.N. Kulkarni, "The development of the Monte Carlo method for the calculation of the thermoluminescence intensity and the thermally stimulated luminescence," *Radiat. Prot. Dosim.*, vol. 51, pp. 95–105, 1994.

[21] A. Mandowski, "Modelling of charge carriers' transport and trapping phenomena in one-dimensional structures during thermal stimulation," *J. Electr.*, vols. 51-51, pp. 585–589, 2001.

[22] A. Mandowski, "Calculation and properties of trap structural functions for various spatially correlated systems," *Radiat. Prot. Dosim.*, vol. 119, pp. 85–88, 2006.

[23] A. Mandowski, "How to detect trap cluster systems?" *Radiat. Meas.*, vol. 43, pp. 167–170, 2008.

[24] A. Mandowski and J. Świątek, "Monte Carlo simulation of thermally stimulated relaxation kinetics of carrier trapping in microcrystalline and two-dimensional solids," *Phil. Mag. B*, vol. 65, pp. 729–732, 1992.

[25] A. Mandowski and J. Świątek, "On the influence of spatial correlation on the kinetic order of TL," *Radiat. Prot. Dosim.*, vol. 65, pp. 25–28, 1996.

[26] A. Mandowski and J. Świątek, "Thermoluminescence and trap assemblies — results of Monte Carlo calculations," *Radiat. Meas.*, vol. 29, pp. 415–419, 1998.

[27] A. Mandowski and J. Świątek, "The kinetics of trapping and recombination in low dimensional structures," *Synth. Metals*, vol. 109, pp. 203–206, 2000.

[28] V. Pagonis and G. Kitis, "Prevalence of first order kinetics in thermoluminescence materials: An explanation based on multiple competition processes," *Phys. Status Solidi B*, pp. 1–12, 2012.

[29] V. Pagonis, R. Chen and G. Kitis, "On the intrinsic accuracy and precision of luminescence dating techniques for fired ceramics," *J. of Arch. Science*, vol. 38, pp. 1591–1602, 2011.

[30] Adamiec, "Investigation of a numerical model of the pre-dose mechanism in quartz," *Radiat. Meas.*, vol. 39, pp. 175–189, 2005.

[31] G. Adamiec, A. Bluszcz, R. Bailey and M. Garcia-Talavera, "Finding model parameters: Genetic algorithms and the numerical modelling of quartz luminescence," *Radiat. Meas.*, vol. 41, pp. 897–902, 2006.

[32] V. Pagonis and R. Chen, "Monte Carlo simulations of TL and OSL in nanodosimetric materials and feldspars," *Radiat. Meas.*, vol. 81, pp. 262–269, 2015.

[33] A. Larsen, S. Greilich, M. Jain and A.S. Murray, "Developing a numerical simulation for fading in feldspar," *Radiat. Meas.*, vol. 44, p. 467, 2009.

[34] M. Jain, R. Sohbati, B. Guralnik, A.S. Murray, M. Kook, T. Lapp, A.K. Prasad, K.J. Thomsen and J.P. Buylaert, "Kinetics of infrared stimulated luminescence from feldspars," *Radiat. Meas.*, vol. 81, pp. 242–250, 2015.

[35] G.S. Polymeris, V. Pagonis and G. Kitis, "Thermoluminescence glow curves in preheated feldspar samples: An interpretation based on random defect distributions," *Radiat. Meas.*, vol. 97, pp. 20–27, 2017.

[36] V. Pagonis and P. Truong, "Thermoluminescence due to tunneling in nanodosimetric materials: A Monte Carlo study," *Physica B: Condensed Matter*, vol. 531, pp. 171–179, 2018.

[37] I.F. Chang and P. Thioulouse, "Treatment of thermostimulated luminescence, phosphorescence, and photostimulated luminescence with a tunneling theory," *J. Appl. Phys.* vol. 53, p. 5873, 1982.

[38] G.S. Polymeris, I.K. Sfampa, M. Niora, E.C. Stefanaki, L. Malletzidou, V. Giannoulatou, V. Pagonis and G. Kitis, "Anomalous fading in TL, OSL and TA – OSL signals of Durango apatite for various grain size fractions; from micro to nano scale," *J. Lumin.*, vol. 195, pp. 216–224, 2018.

[39] G.S. Polymeris, V. Giannoulatou, I.K. Sfampa, N.C. Tsirliganis and G. Kitis, "Search for stable energy levels in materials exhibiting strong anomalous fading: The case of apatites," *J. Lumin.*, vol. 153, pp. 245–251, 2014.

[40] E. Şahiner, G. Kitis, V. Pagonis, N. Meriç and G.S. Polymeris, "Tunnelling recombination in conventional, post-infrared and post-infrared multi-elevated temperature IRSL signals in microcline K-feldspar," *J. Lumin.*, vol. 188, pp. 514–523, 2017.

[41] I.K. Sfampa, G.S. Polymeris, N.C. Tsirliganis, V. Pagonis and G. Kitis, "Prompt isothermal decay of thermoluminescence in an apatite exhibiting strong anomalous fading," *Nucl. Instr. Meth. B*, vol. 320, pp. 57–63, 2014.

[42] G. Kitis, G.S. Polymeris, I.K. Sfampa, M. Prokic, N. Meriç and V. Pagonis, "Prompt isothermal decay of thermoluminescence in $MgB_4O_7$:Dy,Na and $LiB_4O_7$:Cu,In dosimeters," *Radiat. Meas.*, vol. 84, pp. 15–25, 2016.

This page intentionally left blank

# Chapter 3

# Modeling the Effects of Ionization Density in Thermoluminescence Mechanisms and Dosimetry

Yigal S. Horowitz*, Leonid Oster† and Ilan Eliyahu‡

*Physics Department, Ben Gurion University of the Negev
Beersheva, Israel
yigalho@gmail.com
†Physics Unit, Sami Shamoon College of Engineering
Beersheva, Israel
‡Soreq Nuclear Research Center
Yavneh, Israel

The current state of knowledge concerning the effects of ionization density (ID) in the thermoluminescence (TL) of LiF:Mg,Ti — possibly the most prominent passive TL dosemeter in world-wide use — is reviewed. Other materials touched upon and demonstrating ID dependent characteristics are $CaF_2$:Tm in its application as a linear-energy-transfer discriminator. Mechanisms discussed in depth in LiF:Mg,Ti are the preferential population of a nano-sized trapping center-luminescent center (TC/LC) complex following high-ionization density (HID) relative to low-ionization density (LID) irradiation. The presence of these TC/LC complexes leads to important changes in the relative efficiency of TL production for various types of radiation and levels of dose. The most dramatic example is the linear/supralinear dose response observed in many TL materials which is now recognized as the signature of spatially correlated TCs and LCs. The linear/supralinear dose response is modeled in the framework of a nanoscopic TC/LC model — the Unified Interaction Model (UNIM). Kinetic analyses based on conduction band/valence band charge carrier migration and spatially correlated TCs/LCs are also shown to be capable of simulating many of the effects of ID on efficiency, but only with the addition of hitherto relatively unknown radiation

mechanisms in TL phenomena. Even though the focus of this chapter is on LiF:Mg,Ti, the discussion is of relevance to most other TL materials, since ID-dependent behavior is a common phenomenon observed in many materials.

## 3.1. Introduction

### 3.1.1. *Ionization density non-uniformity*

Radiation action mechanisms in solid state systems are extremely diverse and complex. Ionization density affects the following characteristics of LiF:Mg,Ti:

(i) The structure of the glow curve (i.e., the relative intensity and shape of the various glow peaks) as a function of dose and the type of radiation [1] (ii) the dose onset of supralinearity, $D_{\mathrm{th}}$, indicating the departure from linear response and the maximum value of the supralinearity, $f(D)_{\max}$, following irradiation by electrons and photons [1] and heavy charged particles (HCPs) [2] (iii) the relative TL efficiency (the TL intensity per unit dose relative to the TL intensity per unit dose induced by $^{60}$Co or $^{137}$Cs gamma rays or electrons of equivalent energy) as a function of X-ray energy [3] and (iv) the HCP relative TL efficiency [4].

### 3.1.2. *Electron/photon tracks*

The tortuous electron tracks following irradiation by photons and electrons of various energies are shown in Fig. 1, which illustrates their great variation in ID.

The lines and dots indicate areas of ionization which release electrons and holes of various energies. These lose energy via elastic and inelastic scattering with the surrounding atoms. It is generally assumed that capture of the electrons into traps occurs primarily at thermal energies (25.3 meV) corresponding to a de Broglie wavelength of $\sim$8 nm. A lifetime before capture of $\sim 10^{-12}$ s and a velocity of $\sim 10^{14}\,\mathrm{nm\,s^{-1}}$ implies that the thermalized electron will traverse a volume of dimensions ranging from tens to possibly hundreds of nm before capture. Similar considerations apply to the

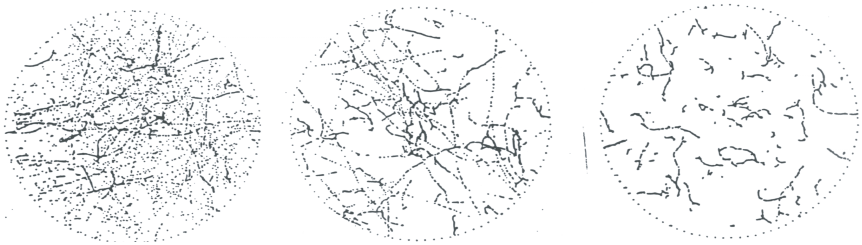


Fig. 1. Ionization tracks of photons and electrons in PMMA. Reproduced from the web-site of the Henderson Research Group, Intro. To E-beam Lithography; https://sites.google.com/site/hendersonresearchgroup/helpful-primers-introductions/intro-to-ebeam-litho.

holes. The distribution of occupied TCs and LCs will therefore be more uniform than the distribution of ionization events shown in Fig. 1 but still non-uniform to an extent difficult to evaluate. The liberated electron and hole can also migrate in the material as a bound pair (exciton) and be captured or recombine and annihilate.

### 3.1.3. *Heavy charged particle tracks*

The radiation induced mechanisms in HCP tracks are of fundamental interest due to their greatly increased radio-biological-effectiveness (RBE). The RBE of 1 MeV neutrons can be as high as 20, as well as that of alpha particles, fission products and heavy ions. Even the lighter protons have an RBE of 2. A Monte Carlo calculated version [5] of the track (irradiated volume) of a 1.43 MeV proton stopping in LiF is shown in Fig. 2 and the energy spectrum of released secondary electrons in Fig. 3.

The details of the radial dose and track extension depend on the HCP mass and energy and cannot be determined experimentally in the condensed phase. The importance of track dimensions/beam geometry in TL was demonstrated experimentally by Horowitz *et al.* [6] who showed that alpha particle TL fluence response was dependent on the vector properties of the radiation field.

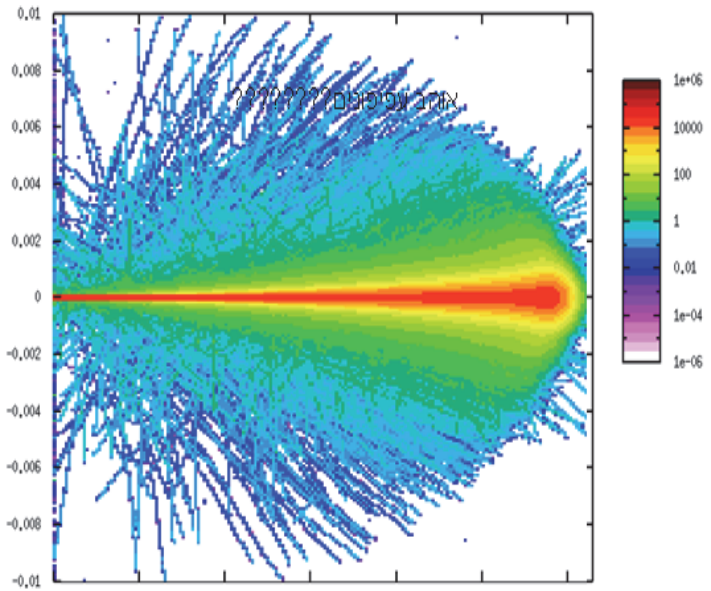


Fig. 2. Schematic representation of the ionization track of a 1.43 MeV proton. The colored regions indicate the level of dose (after Salvat [5]).

Parallel beam geometry, led to decreased supralinearity than in near-isotropic geometry due to decreased track overlap/interaction. The observation that the HCP track maintains a highly non-uniform charge-carrier-populated-defect distribution in the irradiation stage in significant amounts (electrons and holes apparently do not reach the CB/VB), requires an explanation. It has been suggested that the HCP track of radiation damage/effects may create a potential barrier (distorted lattice structure) which limits the range of migration of the charge carriers [7]. In addition to the extreme dose-non-uniformity, the local heating and enhanced creation of defects in HCP tracks creates an environment in which the ability of current track structure theories to predict HCP relative TL efficiencies is severely limited [8–10]. A similar situation exists in the simulations of the complex DNA damage induced by ions. Surdutovich *et al.* [11] reported that the radial distribution of the complex damage is different from that of the radial dose.

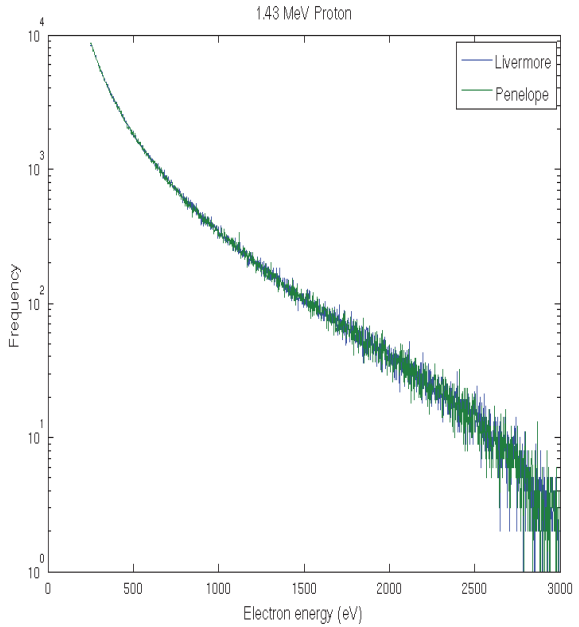


Fig. 3. Energy spectrum of released secondary electrons calculated by Monte Carlo (after Salvat [5]).

## 3.2. The effects of ionization density on TL characteristics

### 3.2.1. *The glow curve*

The detected photon intensity, I(T), as a function of the temperature of the sample is referred to as the glow curve. In TL dosimetric applications calibration procedures are required which mimic as closely as possible the properties and environment of the radiation field under investigation. It is widely believed that the TL signal intensity, although an increasing function of dose, is not dose-rate dependent in LiF:Mg,Ti (TLD-100) although there have been reports on dose-rate effects of TL (and one of optically stimulated luminescence, or OSL) in different kinds of quartz, as well as calcite and diamonds. Recently, the dose-rate independence in the response of LiF:Mg,Ti has been criticized as unsubstantiated [12]. The glow curve usually consists of a number of individual glow peaks which

almost always overlap. It is rare indeed for the glow curve to consist of a single glow peak or well-separated glow peaks. Each glow peak can be correlated with a trapping structure with different trapping and excitation characteristics, so that in principle a great deal of information might be extracted from the behavior of the individual peaks [13, 14]. However, the reliable deconvolution of the glow curve into glow peaks for the extraction of physical or additional dosimetric information is often no simple matter [15]. Even the shape of a single glow peak can change due to various instrumental, physical and radiation field parameters such as heating rate, ID, dose and competition between the various trapping centers (TCs). The shape of the individual glow peaks is usually discussed in terms of the thermal activation energy E, the attempt-to-escape-frequency s, the order of kinetics b, and the heating rate. However, in an interacting system (the usual case) the shape may well be influenced by the action of competitive centers [16], so that the extraction of meaningful physical parameters from glow peak shapes should be regarded with caution. The extraction of dosimetric information from the behavior of the individual peaks can, however, be usually achieved by a phenomenological approach coupled with calibration. The influence of ID is reflected in the differences in the shape of the glow curves following irradiation by different particle types as shown in Figs. 4 and 5.

Due to its large band gap of 13.6 eV a great variety of trapping centers exist in LiF:Mg,Ti, leading to as many as fifteen glow peaks in the glow curve. At low levels of dose, the glow curve is far simpler (Fig. 4). The maximum intensity of the main glow peak occurs at a temperature of 200–205°C when a heating rate of $1°C\,s^{-1}$ is employed. The low temperature shoulder of glow peak 5 is also affected by ID, indicating a difference in the relative intensity of glow peak 5a (a low temperature satellite of composite glow peak 5). Peak 5a arises from a locally trapped electron-hole, whereas glow peak 5 arises from the capture of an electron only. On the other hand, peak 4 is considered to arise from the same basic TC/LC configuration which has captured a hole only. The ratio of peak 5a to peak 5 increases with increasing ID, since there is a greater probability of capturing

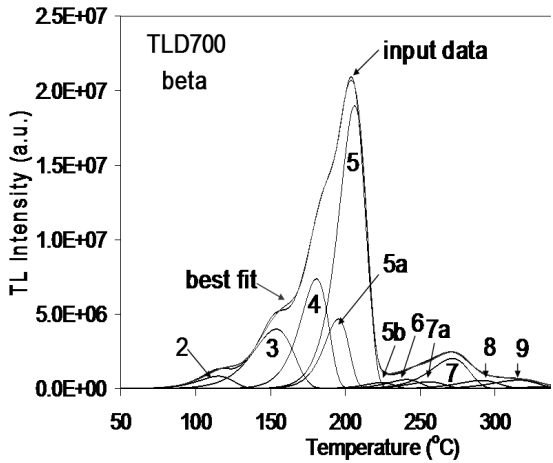


Fig. 4. The glow curve of LiF:Mg,Ti following low dose LID radiation (After Horowitz [1]).

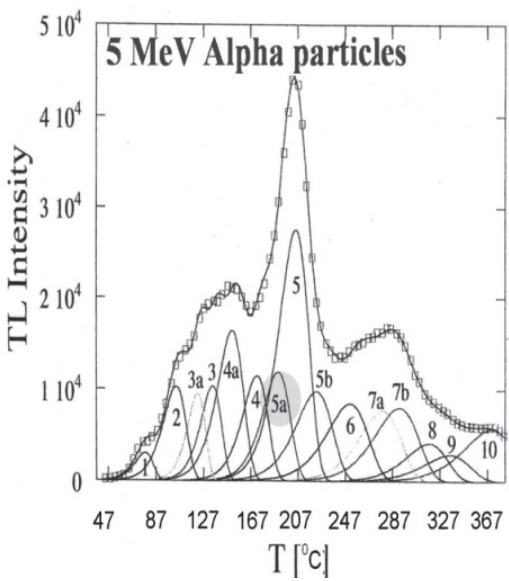


Fig. 5. The glow curve of LiF:Mg,Ti following alpha particle irradiation (After Horowitz *et al.* [2]).

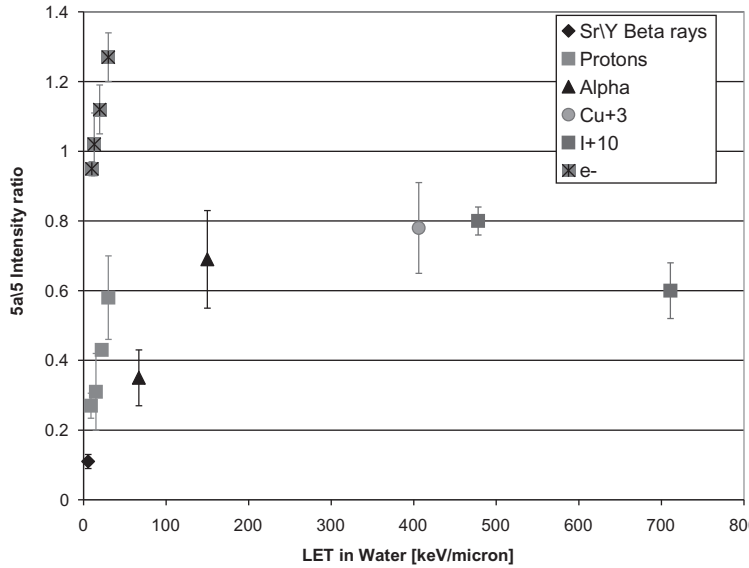


Fig. 6. The ratio of the intensities of glow peak 5a to glow peak 5 for various radiations of different linear energy transfer (LET). The LET correlates strongly with ID. (After Fuks *et al.* [17]).

both an electron and a hole at higher ID. This has suggested its use as an ID discriminator in mixed radiation fields [17] as shown in Fig. 6. Practical implementation of the ratio 5a/5 has been hindered by difficulties in the reproducible deconvolution of the complex glow curve.

This complexity of the LiF:Mg,Ti glow curve, however, has not significantly hindered the dosimetric use of this material. Applications which require high throughput simply integrate the TL signal between previously determined temperatures (region-of-interest (ROI) analysis). Others use the peak-height of composite glow peak 5 or the integral of peaks 4, 5a, 5, and 5b.

In most applications the glow peaks above 225°C can be ignored due to their very low intensity relative to peak 5. In addition, the presence of peak 5a shown in Figs. 4 and 5 can be ignored unless the application involves ID-behavior. It deserves mention that the relative intensity of the various glow peaks can be influenced by many parameters, including even the cooling rate following the

pre-irradiation 400°C high temperature anneal. For example, in rapidly cooled material the ratio of 5a/5 is $0.05 \pm 0.015$ (1 SD) compared to $0.15 \pm 0.03$ in slow-cooled material. With increasing dose the glow curve following LID irradiation more and more resembles the complex glow curve following HCP irradiation. This phenomenon is due to the very high levels of secondary electron dose in the HCP irradiated volumes.

There are certain important differences in the radiation action of HCPs compared to electrons and photons, such as local heating and enhanced creation of defects via nuclear scattering leading to atomic displacements. If these were ignored, the HCP-induced glow curve might be estimated by a mass-weighted integration over the volume of the track of the glow curves induced by LID electron at different levels of dose. But such a calculation has never been carried out. In any event, it is clear that at greater levels of dose the low ID-radiation glow curve increasingly mimics the HCP induced glow curve.

### 3.2.2. *Relative TL response of photons and electrons*

The relative TL response of photons and electrons departs from the mass-energy absorption coefficients of the material, due to the effects of ID (Fig. 7).

In LiF:Mg,Ti the relative response below energies of a few hundred keV is greater than that predicted by the mass-energy absorption coefficients, whereas the opposite is true for LiF:Mg,Cu,P. The deviation from the mass-energy absorption coefficients in these materials is due to the dependence of the relative TL response on ID at lower photon energies, and is a significant nuisance in personnel dosimetry. This behavior of the relative TL response befuddled the dosimetric community for many years. Experts in Monte Carlo radiation transport refused to believe that their calculations (which could not and did not include the effects of ID) were not correct. The experiments were somehow at fault. In fact, the opposite behavior of the two materials of essentially identical $Z_{\text{eff}}$ can be correlated with the macroscopic linear/supralinear dose response of LiF:Mg,Ti contrasted to the linear-sublinear behavior of LiF:Mg,Cu,P as shown in Fig. 8. The figure demonstrates that over certain levels of ID (dose)

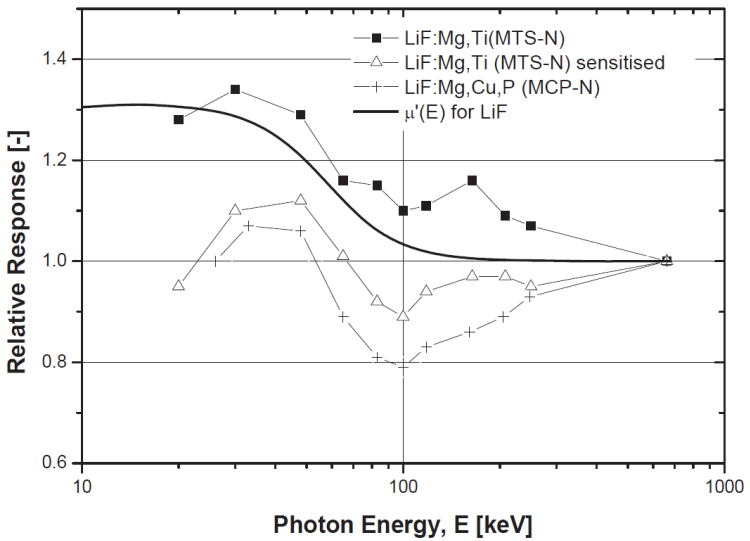


Fig. 7. The relative response of LiF based materials as a function of energy. $\mu'(E)$ are the calculated mass-energy absorption coefficients (After Olko *et al.* [3]).

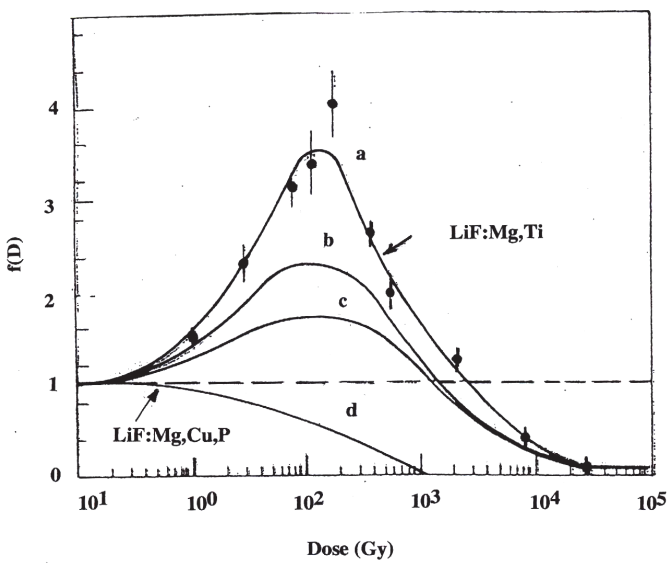


Fig. 8. The normalized TL dose response, $f(D)$, of LiF:Mg,Ti (TLD-100) and LiF:Mg,Cu,P. (a) 1.25 MeV gamma rays, (b) 50 kVp x-rays, (c) 20 kVp x-rays, (d) LiF:Mg,Cu,P. (After Horowitz [19]).

the relative TL efficiency of LiF:Mg,Ti is greater than unity, whereas in LiF:Mg,Cu,P, over the same levels of ID, it is always less than unity [18]. These same levels of ID exist in single electron tracks.

A phenomenological model has been developed to simulate the photon energy dependence of doped LiF materials based on Monte Carlo calculations of energy deposition in nanovolumes of various dimensions [3]. The dependence of TL characteristics on ID has led to many attempts to use TL detectors as ID discriminators (average linear-energy-transfer estimators) [19–21]. Additional research and development should lead to further improvements [22–24].

### 3.2.3. *HCP relative efficiencies*

The TL efficiency, $\alpha$, is defined as the ratio of the total energy emitted as TL light $\varepsilon_o$ to the energy imparted to the material by the radiation field $\varepsilon$.

$$\alpha = \varepsilon_o/\varepsilon \tag{1}$$

The relative TL efficiency measures the TL signal produced per unit dose and unit mass by the radiation under study, with respect to the TL signal per unit dose and unit mass produced by the reference radiation:

$$\eta_{k,\gamma} = \frac{R_k}{D_k} \Big/ \frac{R_\gamma}{D_\gamma} \tag{2}$$

Here $R_k$ and $R_\gamma$ are the TL responses per unit mass for the radiation under study ($k$) and the reference radiation ($\gamma$) at dose levels of $D_k$ and $D_\gamma$ respectively. The dose levels $D_k$ and $D_\gamma$ must be low doses where $R_k$ and $R_\gamma$ fall in the linear region of the TL dose/fluence response. Even relative efficiencies are influenced by a large number of experimental factors, e.g., annealing parameters, readout parameters and sample temperature (the glow peak under consideration). The relative TL efficiencies show a general tendency to decrease with increasing LET, due to the effects of ionization density; however, the situation is complicated since different particles of the same LET can possess very different relative TL efficiencies. This arises because the radial dose deposition profiles which determine the levels

of occupation of the TCs, LCs and CCs in the track do not uniquely depend on LET. Particles of the same LET but of different charge and mass can possess significantly different radial dose profiles and different modes of lattice interactions.

3.2.3.1. *TL-TST calculations*

Track Structure Theory (TST) attempts to describe the differences in the radiation end effects, via the differences in the microscopic distribution of energy deposition of two types of radiation. Typically, these are HCP efficiencies relative to those of gammas and electrons, usually $^{60}$Co or $^{137}$Cs. TST has been used to estimate the HCP relative TL efficiency of several materials of dosimetric importance with varying degrees of success compared with experimentally measured values [25–27]. These earlier calculations were based on the premise that the radiation effect is induced exclusively by the released secondary electrons, and that it can be estimated by measurement of the same radiation effect generated by electrons of any energy. In addition, it was assumed that there was no need to match the secondary electron energy spectrum generated by the HCP slowing down, with the low ionization density (LID) induced secondary electron spectrum. Other possible HCP induced radiation mechanisms, e.g., enhanced creation of various defects due to their heavier mass or the short time scale of energy deposition were ignored entirely. A modified form of TST [MTST] was developed [28] for the calculation of relative HCP TL efficiencies $\eta_{\mathrm{HCP},\gamma}$, in a solid state system such as LiF:Mg,Ti in which the normalized dose response, $f_\delta(D)$ following LID radiation is energy dependent. MTST requires matching of the secondary electron energy spectrum created by the HCP with the electron energy spectrum used to experimentally measure $f_\delta(D)$. The method of calculation of $\eta_{\mathrm{HCP},\gamma}$ is shown below in equation (3).

$$\eta_{\mathrm{HCP},\gamma} = \eta_{\delta,\gamma} \times \frac{W_\gamma \int_0^{R_{\max}} \int_0^{r_{\max}} f_\delta(D) D(r,z) 2\pi r dr dz}{W_{\mathrm{HCP}} \int_0^{R_{\max}} \int_0^{r_{\max}} D(r,Z,E) 2\pi r dr dz} \qquad (3)$$

$D(r,z)$ is the radial dose at penetration distance $z$ and $f_\delta(D)$ has been previously defined. $\eta_{\mathrm{HCP},\gamma}$ is the relative efficiency averaged over

the entire HCP track. $W_\gamma$ and $W_{\mathrm{HCP}}$ are the average energy required to produce an e-h pair by gamma and HCP radiations and their ratio has been estimated at ∼1.1 for low energy protons and He ions. $\eta_{\delta\gamma}$ is usually taken to approximately equal unity. The requirement of energy matching is difficult to carry out for low energy protons and He ions, since the maximum energy of the secondary electrons generated by these HCPs is 2–3 keV and the average energy is ∼1 keV as shown in Fig. 3.

Kalef-Ezra and Horowitz [28] reported agreement between TST calculations and experimental measurements. However, several difficulties (e.g., scaling to estimate $D(r)$ in condensed phase LiF, inadequate matching of the spectra used to measure $f_\delta(D)$ to the HCP generated secondary electron spectra and near-isotropic geometry of the incident alpha particle fluence) suggests in retrospect that the agreement was largely coincidental and due to a cancellation of errors. Later calculations of $D(r)$ (Fig. 9) in condensed phase LiF using a track segment Monte Carlo approach were carried out using TRIPOS-E, a coupled electron-ion transport code [27] for low energy protons and He ions.

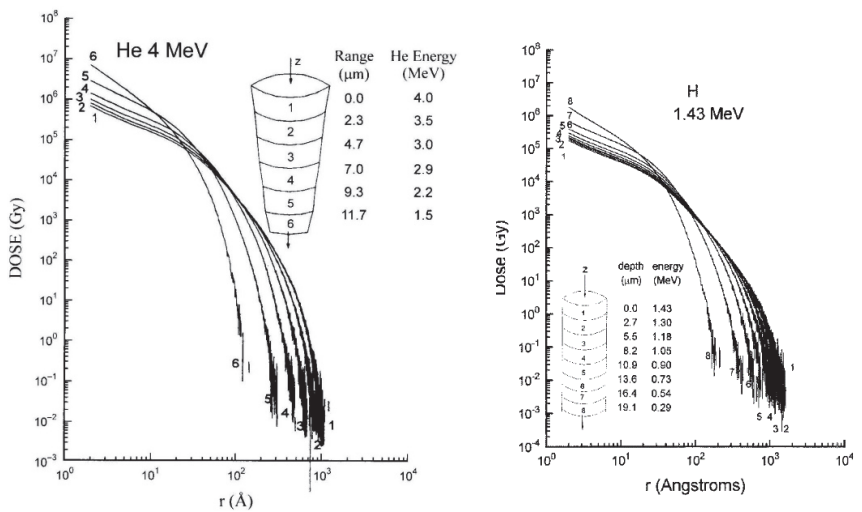


Fig. 9. Left: Monte Carlo track segment calculations of $D(r)$ for 4 MeV He ions in LiF; Right: 1.43 MeV protons. (After Avila *et al.* [27]).

Although there were approximations in this approach, especially in the high cut-off energies of the secondary electron tracks, they allowed a more realistic comparison of TST calculations with experimental measurements. In LiF:Mg,Ti the values of $f_\delta(D)$ at the required average electron energy of ∼1 keV were estimated by extrapolation from experimental measurements at higher energies using the Unified Interaction Model (UNIM)[1]. For the 1.4 MeV protons a calculated value of 0.15 for composite peak 5 was obtained compared to the experimental value of 0.3, a 50% discrepancy. For the He ions a somewhat smaller discrepancy of ∼35% was obtained. The relative efficiency of the strongly supralinear high temperature glow peaks 7–9 were under-estimated by an order of magnitude. Extrapolation of the values of $f_\delta(D)$ to the ultra-low electron energies required by MTST introduces a degree of uncertainty in the results which is difficult to evaluate. Unfortunately, the option of electron irradiation at keV energies is also problematic, due to the likelihood of dead layers/surface effects in the shallow penetration depths of such low energy electrons. An additional effort studied the situation in LiF:MCP which does not exhibit energy-dependent-supralinearity in the dose response, so that matching of the electron spectra is unnecessary. Again it was demonstrated that there was significant disagreement between calculations and experimental values [8]. The results showed that the values of the TST calculated relative efficiencies for 1.43 MeV protons were between 0.056 to 0.087 (the spread in values arising from uncertainty in the measurement of $f_\delta(D)$) compared to 0.15 measured experimentally. For the alpha particles even greater discrepancies were observed. Here also, however, problems of accuracy were encountered. Due to the opaque nature of the LiF:MCP samples, self-absorption and planchet reflection corrections are necessary but are difficult to estimate accurately. In addition, at high levels of dose, the glow curve becomes increasingly complex with the appearance of intense high temperature peaks which strongly overlap with the main dosimetric peak, leading to possibly significant deconvolution-related errors in the estimate of the glow peak intensities.

These uncertainties in the TL measurements, coupled with possible uniquely HCP induced reactions in the recombination/heating stage, motivated an optical absorption (OA) study in LiF:Mg,Ti as a stringent test of the applicability of TST to HCP radiation effects.

3.2.3.2. *TST OA calculations*

In the evaluation of the reliability of TST, OA has several important advantages over TL in LiF:Mg,Ti: (i) The dose response of the OA bands does not depend on photon energy [30], so that matching of the electron spectra is not required. (ii) The dose response of many of the OA bands is linear/exponentially saturating with no hint of supralinearity. The experimental measurement of $f_\delta(D)$ is therefore simpler and can be carried out with greater precision. This reduces the error in the calculation of $\eta$. (iii) Application of TST to the irradiation stage avoids likely complications in the heating/recombination stage. In the course of heating the TL may be accompanied by association-dissociation reactions between the various centers in the ionic sub-system. Thus one circumvents the possibility that reactions during heating are not the same following HCP and electron/photon irradiation. In OA one measures the absorption coefficient, $\alpha(D)$, in units of $\mathrm{cm}^{-1}$ defined in the Beer–Lambert law as

$$\alpha = \mathrm{OD}/[\log e \times d] \tag{4}$$

The optical density (OD) is given by $\log (I_{\mathrm{in}}/I_{\mathrm{out}})$ where $I_{\mathrm{in}}$ and $I_{\mathrm{out}}$ represent the light intensity impinging on and exiting the sample. The irradiation depth of penetration $d$, is given by the thickness of the sample for high energy LID irradiations. For the proton and He irradiations, $d$ is the range. The TST calculation of $\eta$ requires the measurement of $f(D)$ following gamma ray irradiation, and the experimental measurement requires a measurement of the OA energy spectrum in the linear fluence and dose response region for the HCPs and gammas respectively.

3.2.3.2.1. *The OA spectrum of irradiated LiF:Mg,Ti*

Typical deconvoluted OA spectra following $^{60}$Co irradiation (800 Gy) and He ion irradiation in the linear fluence response regime of LiF:Mg,Ti (TLD-100) are shown in Figs. 10 and 11 respectively.

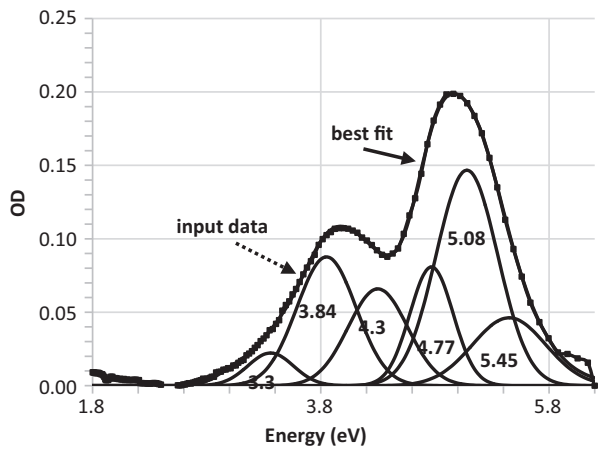


Fig. 10. OD energy spectrum of LiF:Mg,Ti following $^{60}$Co gamma irradiation to 0.8 KGy. (After Druzhyna *et al.* [31]).

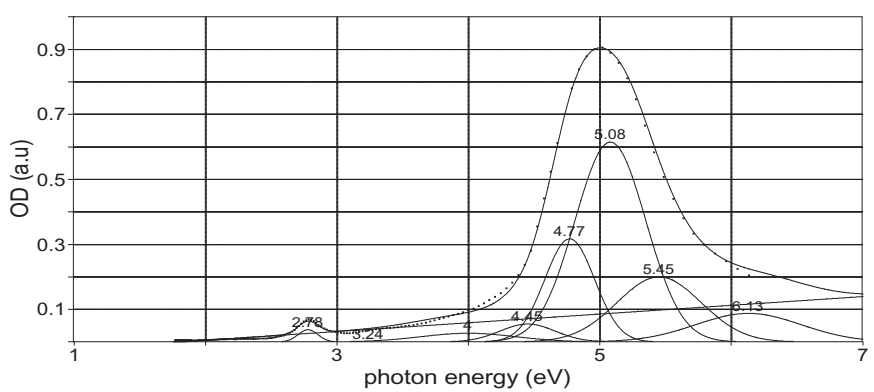


Fig. 11. OD energy spectrum following He ion irradiation in the no-overlap-track-fluence regime. (After Biderman *et al.* [32]).

Note the very weak relative intensity of the 4 eV OA band in Fig. 11. The 4.0 eV band is the summed intensity of the 3.8 eV and 4.3 eV OA bands shown in Fig. 10 following gamma irradiation. The 3.8 eV and 4.3 eV are the sub-bands of the 4.0 eV OA band associated with the trapping center of composite glow peak 5 [31]. Following proton and He ion irradiation the 4.0 eV band is too weak to allow accurate deconvolution into its two sub-bands. The major OA bands are at 5.08 eV (F center), 4.77 eV (unknown structure but sometimes suggested as F center-related) and 5.45 eV (associated with the recombination stage competitor to the glow peak 5 TC). The maximum F center concentration, $N_{Fmax}$, at saturation following LID irradiation is $\sim 6 \times 10^{23}\,\mathrm{m}^{-3}$ [32]. Following HCP irradiation $N_{Fmax}$ is significantly greater, reaching values of approximately $3.16 \times 10^{24}\,\mathrm{m}^{-3}$ and $5.50 \times 10^{24}\,\mathrm{m}^{-3}$ for 1.4 MeV protons and 4 MeV He ions respectively [9]. The enhanced production of vacancies/F centers following HCP irradiation is discussed in detail elsewhere [34, 35].

### 3.2.4. *F band optical absorption dose response in LiF*

The F band is the most intense band in the OA spectrum. Due to its possible participation in the TL process, its behavior is of special importance. The OA dose response of LiF:Mg,Ti gamma irradiated samples has been measured over an extended dose-range from 10 Gy–$10^5$ Gy [31, 32] as shown in Fig. 12.

The dose response of the absorbance, $\alpha$, of the 5.08 eV OA band is linear/exponentially saturating with

$$\alpha = (\alpha_{\max})_{\mathrm{sat}}[1 - \exp(-\beta_{\mathrm{F}}\,\mathrm{D})] \tag{5}$$

where $\beta_{\mathrm{F}}$ is the "dose-filling constant" and $(\alpha_{\max})_{\mathrm{sat}}$ is the maximum value of $\alpha$ at saturation in the dose response. Figure 12 shows the F band dose response with $\beta_{\mathrm{F}} = 6.1 \pm 0.6 \times 10^{-5}\,\mathrm{Gy}^{-1}$.

#### 3.2.4.1. *Experimental Measurement of* $\eta_{HCP,\gamma}$

At levels of fluence, $f_{fL} \leq \sim 10^{11}\,\mathrm{cm}^{-2}$, for which track overlap/saturation effects are not significant for low energy protons and He ions, the fluence response is linear and $\eta_{\mathrm{p}\gamma}$ and $\eta_{\mathrm{He}\gamma}$ can be experimentally measured using Eq. (5). The number of F centers

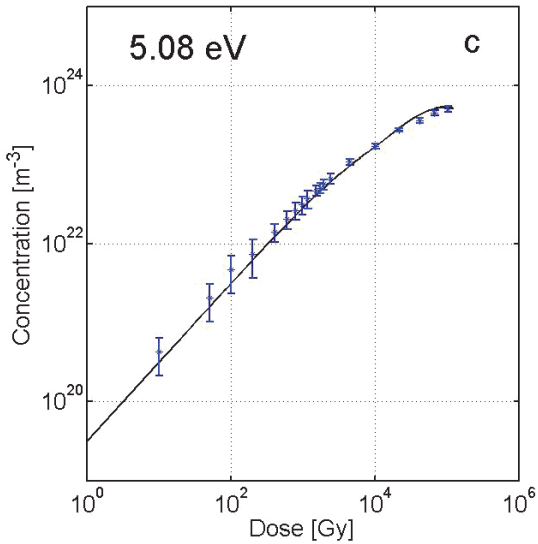


Fig. 12. Concentration of F centers as a function of $^{60}$Co gamma dose. The solid line is a fit from the kinetic simulations. (After Biderman *et al.* [32]).

in the HCP track, $N_{HCP}$ ($N_{He}$, $N_P$), can also be estimated from the value of the OD at saturation.

$$\eta_{\mathrm{HCP},\gamma} = \frac{\frac{I_{\mathrm{HCP}}}{E_{tot}}}{\frac{I_\gamma}{E_\gamma}} = \frac{\frac{I_{\mathrm{HCP}}}{f_{fL}\cdot A\cdot E_{\mathrm{HCP}}\cdot C}}{\frac{I_\gamma}{D_\gamma\cdot m}} = \frac{\frac{I_{\mathrm{HCP}}}{f_{fL}\cdot A\cdot E_{\mathrm{HCP}}\cdot C}}{\frac{I_\gamma}{D_\gamma\cdot\rho\cdot A\cdot d}}$$

$$= \frac{I_{\mathrm{HCP}}\cdot D_\gamma\cdot\rho\cdot d}{I_\gamma\cdot f_{fL}\cdot E_{\mathrm{HCP}}\cdot C} \tag{6}$$

$I_{\mathrm{HCP}}$ is the measured intensity of the radiation effect following irradiation by the HCPs to a particle fluence $f_{\mathrm{fL}}$. $E_{\mathrm{tot}}$ is the total energy deposited by the HCPs. For OA measurements, I is the OD given by $\log(I_{\mathrm{in}}/I_{\mathrm{out}})$. $E_{\mathrm{HCP}}$ is the HCP energy [eV], $I_\gamma$ the measured intensity of the radiation effect following beta or gamma irradiation to a dose level $D_\gamma$[J/kg], $m$ is the sample mass, $d$ is the sample thickness [cm], $A$ is the irradiated area of the sample equal ideally to the geometric area [cm$^2$] and $C$ is the conversion factor from eV to Joule. It is important to point out that since the measured values of $I_{\mathrm{HCP}}$ and $I_\gamma$ are normalized to absorbed energy (and not to dose)

the calculation of $\eta_{\mathrm{HCP},\gamma}$ does not require estimation of the HCP penetration depth.

The response curves for the F band are linear up to fluences of $\sim 4.10^{11}\,\mathrm{cm}^{-2}$ and $\sim 5.10^{10}\,\mathrm{cm}^{-2}$ for the 1.4 MeV protons and 4 MeV He particles respectively. Using the calculated ranges of 23 $\mu$m and 14 $\mu$m, the "equivalent" or average dose at a fluence of $10^{11}\,\mathrm{cm}^{-2}$ is 3.6 KGy and 17 KGy for the protons and He ions respectively. Using the Smakula formula [36] with an oscillator strength of $f = 0.82$ yields $\mathrm{N_{He}} = 5900$ and $\mathrm{N_p} = 3930$, or 1475 and 2800 F centers per MeV for the He ions and protons tracks respectively. The higher value per unit dose for the protons is unexpected and may be due to the greater frequency of vacancy-interstitial recombination and defect agglomeration in the He track due to the higher levels of radial dose [37]. These values of $d_c$ (the critical distance below which vacancy-interstitial recombination becomes significant) in the HCP tracks would strongly limit F center production in the track cores. Van der Lugt *et al.* [38] estimated that 4500 F centers are generated in a 3 MeV He track in LiF using $f = 1$ and $W = 0.7$ eV. Using the values adopted herein of $f = 0.82$ and $W = 0.64$ eV would increase this value to $\mathrm{N_{He}} = 5150$. Since the He energies are different by $\sim 25\%$, the two estimates are in good agreement.

3.2.4.2. *Comparison of $\eta_{TST}$ with $\eta_{p\gamma}$ and $\eta_{He\gamma}$*

The experimental values of $\eta_{\mathrm{p}\gamma}$ and $\eta_{\mathrm{He}\gamma}$ have been calculated from Eq. (5) using the ratio $\mathrm{OD_{HCP}}/\mathrm{OD}_\gamma$ normalized to deposited energy in the low fluence no–track-overlap regime. $\eta_{\mathrm{TST}}$ is calculated from Eq. (3) via integration of $f_\delta(D)D(r)$ over the volume of the various HCP track segments. It is assumed that the measured ODs continue at saturation levels even beyond $10^5$ Gy. In any event the contribution to the OA/TL signal is insignificant at higher levels of dose, due to the very small volume involved with radial extension of $\sim 5$ Å compared to the overall track radial extension of $\sim 1000$ Å.

The values of $\eta_{\mathrm{p}\gamma}$ and $\eta_{\mathrm{He}\gamma}$ compared with $\eta_{\mathrm{TST}}$ are shown below in Table 1. As can be seen the experimental values for the F band

Table 1. Calculated and experimental values of $\eta$.

| Particle | OA bands (eV) | $\eta_{\text{expt Experimental}}$ | $\eta_{\text{TST}}$ | $\eta_{\text{m}}/\eta_{\text{TST}}$ |
|---|---|---|---|---|
| Protons | 5.08 | $1.47 \pm 0.14$ | $0.56 \pm 0.020$ | $2.6 \pm 0.3$ |
| He | 5.08 | $0.75 \pm 0.07$ | $0.38 \pm 0.015$ | $2.0 \pm 0.2$ |
| Protons | 4.77 | $0.65 \pm 0.06$ | $0.75 \pm 0.03$ | $0.86 \pm 0.09$ |
| He | 4.77 | $0.43 \pm 0.04$ | $0.52 \pm 0.03$ | $0.82 \pm 0.01$ |
| Protons | 4.0 | $0.06 \pm 0.02$ | $0.33 \pm 0.018$ | $0.18 \pm 0.05$ |
| He | 4.0 | $<0.02$ | $0.16 \pm 0.012$ | $<0.12$ |

are $2.6 \pm 0.3$ and $2.0 \pm 0.2$ times greater than the TST calculated values.

The quoted errors in $\eta_{\text{TST}}$ arise almost entirely from the uncertainty in the determination of the dose filling constants of $\sim$10% (1SD). The calculation of $\eta_{\text{TST}}$ is not very sensitive to the details of the Monte Carlo calculated values of $D(r)$. For example, reducing the value of $D(r)$ to $1.5 \times 10^5$ Gy near the track axis and extending $D(r)$ to higher values of $r$ to conserve the deposited energy in each segment, increases $\eta_{\text{TST}}$ for the He ions by only 10% from 0.38 to 0.42. The large differences between $\eta_{\text{expt}}$ and $\eta_{\text{TST}}$ cannot therefore be due to uncertainties in the evaluation of $D(r)$, unless these are very large indeed. It is interesting to note that for the 4.77 eV band the ratio of $\eta_{\text{expt}}/\eta_{\text{TST}}$ is $0.86 \pm 0.09$ and $0.82 \pm 0.08$ indicating fairly good agreement for the protons and He ions respectively. The poorest agreement is for the 4.0 eV band (the summed ODs of the 3.8 eV and 4.3 eV bands) with $\eta_{\text{expt}}/\eta_{\text{TST}} = 0.18 \pm 0.05$ and $<0.12$ for the protons and He ions respectively.

### 3.2.4.3. *Conclusions*

The values of $\eta_{\text{expt}}$ are greater than $\eta_{\text{TST}}$ for the F band because the TST calculations do not take into account enhanced creation of vacancies/F centers by the protons and He ions relative to LID radiation. This enhanced creation occurs even though there is very significant annihilation of Fluorine vacancies due to vacancy-interstitial

recombination in the HCP tracks. These results of the proton and alpha particle induced OA F band relative efficiencies thus consolidate and finalize the conclusion that enhanced creation of Fluorine vacancies by the HCPs cannot be ignored in the conventional TST formalism.

On the other hand, with respect to the summed intensity of the 3.8 eV and 4.3 eV bands, (the sub-bands belonging to the TC giving rise to composite peak 5), the very low values of 0.18 and $\leq$0.12 indicate that certain mechanisms are active in the HCP tracks which either destroy this center and/or depopulate it during irradiation. Local heating during irradiation (thermal spike [39, 40]) could be one possibility. The OA values of $\eta_{\mathrm{p}\gamma} = 0.06$ and $\eta_{\mathrm{He}\gamma} \leq 0.02$ are significantly lower by $\sim$ a factor 5 than the TL values for composite peak 5 of 0.3 and 0.1 respectively. This tends to support the conclusion that the "thermal spike", if indeed it is the responsible mechanism, is de-populating the peak 5 center during irradiation rather than permanently destroying it.

The value of $\eta_{\mathrm{expt}}/\eta_{\mathrm{TST}} \approx 0.8$ for the 4.77 eV band requires an explanation/speculation which combines the opposite effects of defect creation and thermal de-population. The increased values of $N_{Fsat}$ following HCP irradiation compared to LID irradiation indicate that, like the 5.08 eV band, it is being created by the irradiation. The observed value of 0.8 might then be explained by a greater sensitivity to thermal de-population during irradiation than the F center.

In summary, conventional TST which assumes that the HCP radiation effect is created entirely by the secondary electrons liberated by the HCP, fails significantly in the calculation of HCP F band induced OA, due to the enhanced vacancy/defect creation by the HCPs. Other mechanisms (e.g., thermal spikes/Coulomb explosion leading to greater track radial extension) influencing HCP irradiation but not LID irradiation lead to underestimation of factors of 6 and >8 in the proton/He particle intensity of the combined 3.8 eV and 4.3 eV OA bands. In this case, therefore, conventional TST fails miserably. One can only wonder about the underlying reasons leading

to somewhat better agreement between theory and experiment in TL. The Physics of low energy radiation action of protons and He ions remains, therefore, an intractable problem.

## 3.3. Selected applications to mixed-field dosimetry

### 3.3.1. *$\alpha/\gamma$ separation using the shape of composite peak 5*

Some success has been achieved in the separation of $\alpha/\gamma$ dose components by very careful attention to read-out and deconvolution protocols [23]. The increased percentage of TL from alpha particle irradiation results in a greatly increased presence of peaks 4 and 5a in the glow curve, which allows the separation of the alpha particle and beta particle induced TL.

### 3.3.2. *Proton microdosimetry using peak-height ratios in $CaF_2$:Tm*

The ratio of the peak heights in the glow curve of $CaF_2$: Tm has been used in a study of the microdosimetric characteristics of the 175 MeV pre-therapeutic beam at the COSY synchrotron [41, 42]. Both the dose and the average linear energy could be measured to an accuracy of $\pm 4\%$ and $\pm 5$ keV $\mu m^{-1}$, respectively. In this case, extraction of the information from the glow curve is far more reliable than in the case of 5a/5 ratios where 5a is imbedded between glow peaks 4 and 5 and its measurement is susceptible to deconvolution uncertainties. The dependence of the peak-height-ratio on linear energy is shown in Fig. 13. Deconvolution of the glow curve is unnecessary in this application due to the excellent separation of the high and low temperature structures.

The downside of this particular application of $CaF_2$:Tm is, of course, its non-tissue equivalence to photon/electron radiation due to the high Z-value of Ca. Although this can be partially corrected by entrance filter combinations, the resulting angular dependence significantly influences the dosemeter response and remains problematic.

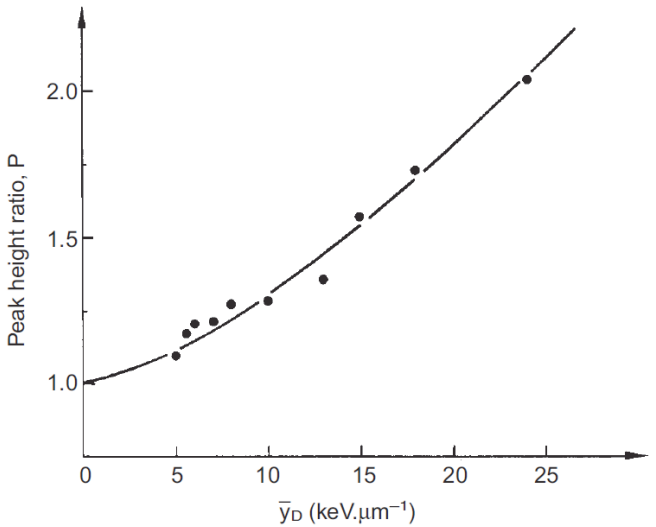


Fig. 13. The behavior of the peak–height-ratio with linear energy (after Hoffman *et al.* [41]).

### 3.4. TL dose response

An ideal dosimeter would show a linear response spanning all the relevant levels of dose. This would vastly simplify calibration procedures and improve accuracy and precision. Unfortunately in most TL materials the dose response is linear only at low dose followed by supralinearity, saturation and finally radiation damage leading even to decreased TL intensity with increasing dose. In some materials, e.g., highly sensitive LiF:Mg,Cu,P, supralinearity is not observed but this material is sub-linear above approximately 5 Gy. From a dosimetric standpoint, sublinearity and supralinearity are equally bothersome. Nonetheless the dose response linearity of this material covers the range of dose levels important in the main areas of applications in environmental and personnel dosimetry, with the exception of clinical dosimetry and accident dosimetry. However, certain disadvantage lies in its loss of sensitivity when annealed above a temperature of 240°C, although annealing procedures which can regain the loss in sensitivity have been reported [43]. It deserves mention that the characteristics of TL materials can be notoriously

non-universal due to the dependence on impurity concentrations, growth parameters, annealing protocol etc. The glow curve and dose response may be manufacturer dependent and can vary over the months and years, even when supplied from the same manufacturer.

The normalized TL dose response $f(D)$, which is a measure of the TL efficiency per unit dose, can be defined in the following manner for materials exhibiting linear response at low levels of dose.

$$f_{\mathrm{i}}(D) = [F_{\mathrm{i}}(D)/D]/[F_{\mathrm{i}}(D_1)/D_1] \tag{7}$$

where $F_i(D)$ is the TL signal intensity of the $i$'th glow peak at dose $D$ and $F_{\mathrm{i}}(D_1)$ is the TL signal of the $i$'th glow peak at a low dose in the region of linear dose response. The normalized dose response can be characterized by the dose-onset of supralinearity, $D_{\mathrm{c}}$, the maximum value of the supralinearity $f(D)_{\max}$, and the level of dose $D_{\max}$, at which $f(D)_{\max}$ occurs.

Following photon/electron irradiation at energies above approximately 100 keV and readout at low heating rates ($1^{\circ}\mathrm{C\,s^{-1}}$), the TL efficiency of peak 5 in TLD-100 is constant [$f(D) = 1$] from the lowest measurable dose levels of $\sim$3 $\mu$Gy up to $D_{\mathrm{c}} \approx 1$ Gy. At higher levels of dose $f(D) > 1$ with $f(D)_{\max} \approx 3$–4 for $200 < D_{\max} < 400$ Gy. The values of $D_{\mathrm{c}}$, $f(D)_{\max}$ and $D_{\max}$ are dependent on the ID characteristics of the radiation field, as well as material and readout parameters which explains the range of values reported in the literature. The supralinearity is dependent on photon energy with $f(D)_{\max}$ decreasing with decreasing energy [44] as shown in Fig. 14. This unusual ID-behavior has also dumfounded radiation scientists [45].

The details of $f(D)$ are also dependent on recombination temperature [46, 47] so that each glow peak can have significantly different values of $D_{\mathrm{c}}$, $D_{\max}$ and $f(D)_{\max}$. In general, the supralinearity increases with increasing temperature. For example, $f(D)_{\max}$ reaches values of 20 and 140 for glow peaks 7 and 8 at temperatures of 270°C and 310°C respectively in TLD-100 [47]. The supralinearity is greatly suppressed following low energy heavy charged particle (HCP) irradiation, due to the inter-play between increased efficiency (arising from charge migration between neighboring tracks) and

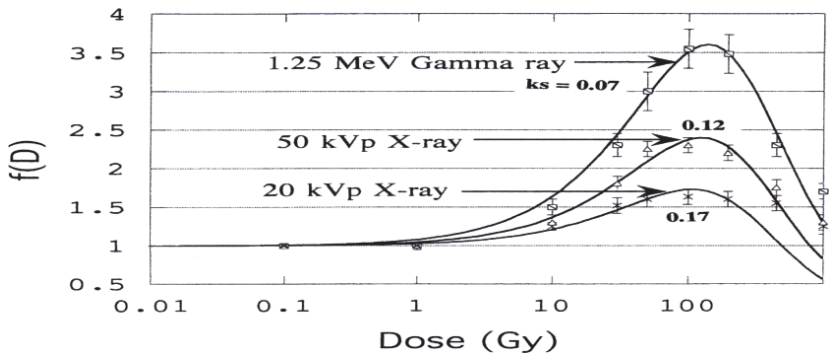


Fig. 14. The dependence of $f(D)$ on photon energy in LiF:Mg,Ti (TLD-100). The solid line is a fit using the UNIM. ks describes the concentration of the $e-h$ populated TC/LC complex relative to the $e$-only. (After Mahajna *et al.* [44]).

decreased efficiency (arising from full population of available centers due to overlapping tracks) [48]. The following section describes how many of the characteristics of $f(D)$ can be simulated in a nanoscopic model, based on spatially correlated trapping centers (TCs) and luminescent centers (LCs).

## 3.5. The Unified Interaction Model

### 3.5.1. *TC/LC spatially correlated configurations*

Kinetic models based purely on delocalized charge migration in the valence and conduction bands during heating ignore the effects of non-uniform ID in particle tracks and the effects of interacting or overlapping tracks [49]. In order to address this issue, the Unified Interaction Model (UNIM) was developed to simulate TL dose response and the dependence of the supralinearity on ID [1, 2]. The UNIM is based on spatially correlated/coupled trapping centers (TCs) and luminescent centers (LCs) which can lead to localized (geminate) recombination. In LiF:Mg,Ti the TC/LC pair is believed to arise from Mg-$Li_{vac}$ trimers in close proximity to Ti-OH. The lattice constant of LiF is 0.4 nm so the physical size of the suggested TC/LC structure is ∼2 nm. Following irradiation the four possible configurations of the TC/LC pair are shown in Fig. 15.

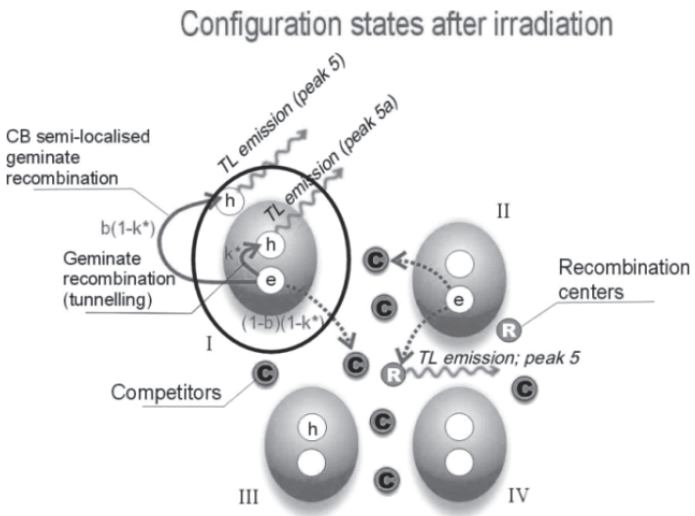


Fig. 15. Four possible configurations of the TC/LC pair following irradiation (after Horowitz [19]).

The basic idea of the UNIM is that the linear response at low dose arises from geminate recombination in a localized entity via a tunneling process [50, 51] in complex molecules with internal localized transitions, which may extend over many lattice sites. Particularly compelling is the evidence from TL emission spectra [51, 52] and the dependence of the glow peak 5 shape parameters on Ti concentration [53] which demonstrated that the TC and LC structures interact directly. Close donor-acceptor pairs and energy transfer from F centers to the dopant ions in alkali-halide systems have been discussed by Vale [54]. The dependence on dose of the delocalized conduction-band-mediated luminescence recombination gives rise to the supralinearity in the following manner.

As the dose increases, the average of the distance distribution between occupied/active neighboring TC/LC entities decreases, and the luminescence recombination efficiency increases, due to the greater probability of charge carrier migration between neighboring TC/LC complexes without interception by the competitive centers (CCs).

In addition, if the CCs capture charge of the same sign as the TCs, their ‘competitive efficiency’ is decreased as the dose level increases,

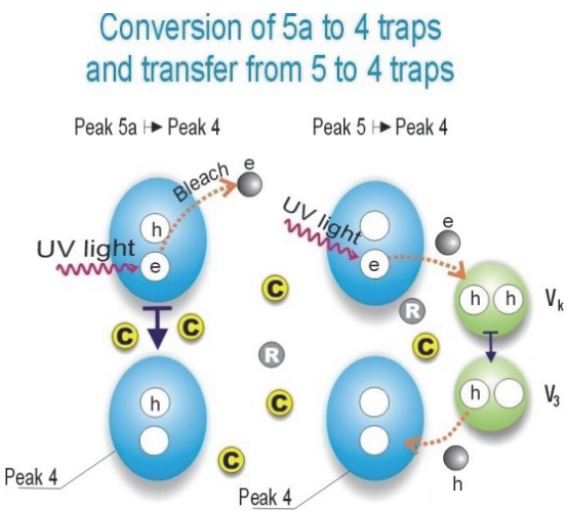


Fig. 16. The effect of 4 eV (310 nm) optical bleaching on the e-h and e-only configurations (After Horowitz [19]).

since an occupied CC no longer serves as an active CC for the charge carrier liberated by the TC.

Compelling evidence for the TC/LC entity of composite peak 5 in LiF:Mg,Ti was reported by Weizman *et al.* [55]. During 310 nm optical bleaching following irradiation (Fig. 16), the light expels the electron from the e-h occupied complex and the remaining hole transforms the TC/LC configuration into an occupied peak 4 trap. This transformation explains the very highly increased intensities of peak 4 following the 310 nm bleach.

### 3.5.2. *Mathematical formulation of the UNIM*

In the UNIM the number of TL photons, $F(D)$, created in the sample due to e-h recombination is given by Eq. (8) (the parameters are defined below):

$$\mathrm{F(D)} = ksn_e(D) + (1 - ks)n_e \times \sum_{i=1}^{3} \int_{r_0}^{r_{\max}} g(R_i) \cdot e^{-\frac{R_i}{\lambda(D)}} \cdot P_i(n_h, R_i, D) dR_i \qquad (8)$$

The overall reader detection efficiency combining the effects of photocathode efficiency, solid angle, etc. can be denoted by a constant, $c$, so that $cF(D)$ is the detected TL signal intensity. In charge integration readers $c$ cancels out in Eq. (7), as it appears in both the numerator and denominator. In single photon counting systems $c$ may be dose dependent due to signal pile-up at high levels of dose.

The first term, $ksn_e$, determines the contribution of the e-h populated TC to the total TL intensity and is expected to be near-linear at low levels of dose and then to increase at higher dose levels, due to the increased statistical probability of the multiple capture of the charge carriers. The second term estimates the increased TL signal at higher dose levels due to charge carriers reaching neighboring tracks and recombining with luminescent centers. The decrease in $f(D)_{\max}$ with decreasing photon energy occurs due to the increasing value of $ks$ leading to geminate recombination as the ID increases. This increase in the e-h populated TC/LC is expected due to increased average ID of single electron tracks with decreasing photon energy.

The parameters in Eq. (8) are defined as follows:

— $k$ is the relative probability of geminate/localized recombination in the TC/LC complex giving rise to luminescence.
— $s$ is the fraction of TC/LC complexes which have captured an e-h pair following irradiation.
— $r_o$ is the "effective" radius of the TC/LC complex for which geminate recombination exists
— $g(r_h.R_i)$ is a two dimensional solid angle factor between two neighboring TC/LC pairs given approximately by $\pi r_h^2/4\pi R_i^2$.
— $S_{LC} = \pi r_h^2$ is the cross-section for capture of an electron by the LC. $\pi r_h^2$ is a geometrical interpretation of the cross section, $S_{LC}$.
— $R_i$ is the distance between neighboring TC/LC pairs.
— $P_i(n_{LC}, R_i)dR_i$ is the nearest neighbor probability distribution function.
— $r_{\max}$ is the maximum distance over which charge carriers reach neighboring centers.

— $\lambda$ is the mean free path of the electrons between the TC/LC pairs. $\lambda$ is an increasing function of dose (due to the filling (de-activation) of the competitors with increasing dose) and is given by:

$$\lambda(D) = \lambda_0 e^{\beta_{cc} D} \tag{9}$$

– $\lambda_o$ is the mean free path for charge carrier diffusion in the inter-track unirradiated region and is given by $(N_{cc} S_{cc})^{-1}$.
– $S_{cc}$ is the capture cross section of the unoccupied competing center.
– $n_{LC}(n_h)$, $n_{cc}$ and $n_{\mathrm{e}}$ represent the concentration of occupied luminescent centers, competitive centers and trapping centers.
– $\beta_{CC}$ is the dose filling constants of the CCs.

Many of the parameters of the UNIM cannot be estimated from ab-initio principles. Ancillary measurements such as optical absorption, HCP fluence response, other known material characteristics, e.g., dopant levels, etc. can be used to restrict the range of allowed values. The UNIM can also describe fluence response for HCPs in the framework of the Extended Track Interaction Model (ETIM).

The nearest neighbor probability distribution functions, $P_i(n_{LC}, R_i)dR_i$, are a crucial element, since it is over these distances that the electron must migrate before recombination with a hole trapped in an LC. The derivation of $P_{i=1\text{-}3}$ is quite straight forward [1]. For typical values of $n_h$, the probabilities are non-zero over distances from a few nm to a few hundred nm as shown in Fig. 17.

3.5.2.1. *The dependence of $f(D)$ on the values of $\beta$*

The $\beta$-values of the dose response of the TC and LC strongly affect both $f(D)_{\max}$ and $D_{\max}$. On the other hand, $f(D)$ is barely affected by $\beta_{\mathrm{cc}}$. The possible effects of radiation damage are shown in Eq. (10). In LiF:Mg,Ti a decreasing TL signal intensity of 40% for composite peak 5 has been measured at 3000 Gy. The choice of LCs in the radiation damage mechanism is dictated by the results of optical absorption measurements, which show no decrease in the optical density of the 4 eV (TC) or 5.45 eV (CC) bands at high levels of

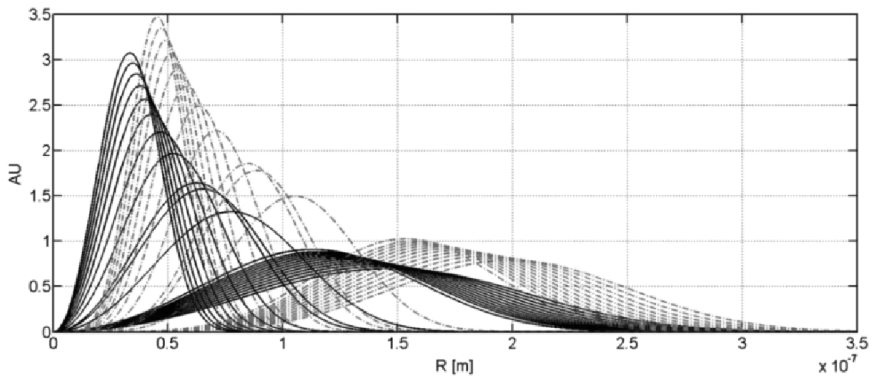


Fig. 17. First and second nearest-neighbor-distance probability distribution functions as a function of dose from 1 mGy to 10,000 Gy (after Lavon *et al.* [56]).

dose reaching 30,000 Gy [32].

$$N_{LC}{}^{*} = N_{LC} \cdot e^{-\beta_{RD} \times D} \tag{10}$$

$N_{LC}$ represents the density of available LCs in un-irradiated samples. Without the assumption of radiation damage to the LCs, the UNIM over-estimates $f(D)$ at very high levels of dose above approximately 1000 Gy. Of course, other reasons may also exist, for example, inaccuracy in the calculation of the nearest-neighbor distance probability functions which are based on uniform ionization density.

The values of $\lambda_{\mathrm{o}}$ related to the action/population of the competitive centers strongly affect $f(D)_{\max}$ but have little effect on $D_{\max}$. Very small values of $\lambda_{\mathrm{o}}$ (related to unoccupied CCs) reduce $f(D)_{\max}$ to unity since the migrating charge carriers cannot reach neighboring tracks [57].

### 3.5.2.2. *The dependence of $f(D)$ on the ID behavior of ks ($n_{e\text{-}h}/n_T$)*

TC/LC complexes and localized/delocalized (LDL) recombination in conduction band/valence band modeling has been recently incorporated in the kinetic simulation of the dose dependence of the 3.8 eV and 4.3 eV optical absorption bands in LiF:Mg,Ti (TLD-100) [58]. The 3.8 eV and 4.3 eV bands are the components of the 4.0 eV

band referred to previously. Track structure considerations are used to describe the relative concentration of the TC/LC complexes by an electron-hole, $n_{e\text{-}h}$, (4.3 eV OA band) or by an electron-only, $n_e$, (3.8 eV OA band) as a function of dose. In addition, a similar model has been shown to successfully simulate the dependence of the supralinearity of composite peak 5 on photon energy [59].

In this modeling, the total population of trapping centers, $N_{TC}$, giving rise to peak 5, is composed of a certain fraction of trapping centers, $N_{e-h}$, which are spatially correlated/coupled to the luminescent centers. The remaining fraction of TCs is denoted by $N_e$. The fraction, $N_{e-h}/N_{TC}$, may be influenced by various factors including methods of crystal growth and thermal treatments such as the cooling rate following the 400°C pre-irradiation anneal [60].

The fraction, $n_{e-h}/n_e$, of the density of $e-h$ to e-only populated complexes following irradiation is assumed to be given by:

$$\frac{n_{e-h}}{n_e} = a \cdot (1 - e^{-\beta_{e-h} \cdot D}) + b \tag{11}$$

The combined densities must, of course, yield the total density of occupied peak 5-TCs as given below:

$$n_{tot} = N_{\mathrm{TC}}(1 - e^{-\beta_{\mathrm{TC}} D}) = n_{e-h} + n_e \tag{12}$$

The parameters $a, b$ and $\beta_{e-h}$ are postulated to depend on photon/electron energy. These equations are employed to yield values of $n_{e\text{-}h}/n_e$ which increase slowly up to a threshold dose of 1 Gy where supralinearity begins to appear in the dose response of peak 5. Above this level of dose, the ratio increases rapidly and is governed by $\beta_{e\text{-}h}$. The parameter "$b$" determines the ratio of $n_{e\text{-}h}/n_e$ at the lowest dose–levels; the dose filling factor $\beta_{e\text{-}h}$ is expected to decrease with decreasing photon energy, due to the onset of track interaction at higher levels of dose for the lower photon energies. The parameter "$a$" determines the relative importance of the two terms. The values of the parameters to simulate $f(D)$ following photon irradiation of 100 keV ($f(D)_{\max} = 3.3$) and 8 keV ($f(D)_{\max} = 1.7$) are given in Eliyahu *et al.* [61]. Incorporation of $n_{e\text{-}h}/n_e$ into the UNIM requires

the calculation of $s = n_{e\text{-}h}/n_{tot}$. It can be easily shown that:

$$s = \frac{n_{e-h}}{n_{tot}} = \frac{a \cdot (1 - e^{-\beta_{e-h} \cdot D}) + b}{1 + a \cdot (1 - e^{-\beta_{e-h} \cdot D}) + b} \tag{13}$$

so that at low dose:

$$s|_{\substack{D<0.1 \\ \beta \ll 0.01}} = \frac{b}{1+b} \tag{14}$$

and at high dose:

$$s|_{D \cdot \beta > 10} = \frac{a+b}{1+a+b} \tag{15}$$

The dependence of $f(D)$ on $\beta_{e-h}$ is shown below in Fig. 18. The values of the parameters are listed in Table 2.

Variation in the value of "$a$" leads to a moderate decrease of $f(D)_{\max}$ from 3.3 to 2.8 but $D_{max}$ is unaffected. Variations in "$b$", however, lead to large changes in $f(D)_{\max}$ reaching values as high as 75. Very low values of "$b$" reflect very low values of $n_{e\text{-}h}/n_T$ at low dose, which implies a TL signal which is based almost completely on

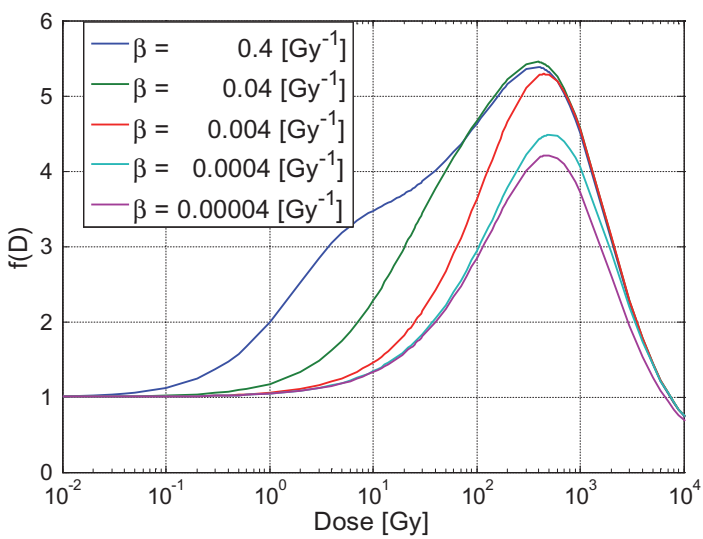


Fig. 18. The behavior of $f(D)$ for values of $\beta_{\text{e-h}}$ (after Lavon *et al.* [56]).

Table 2. Values of the TC/LC e-h filling parameters.

| | Symbol | Parameter value $f(D)_{\max} = 1$ photon energy 2 keV | Parameter value $f(D)_{\max} = 1.8$ photon energy 8 keV | Parameter value $f(D)_{\max} = 2.4$ photon energy 50 keV | Parameter value $f(D)_{\max} = 3.5$ photon energy 500 keV |
|---|---|---|---|---|---|
| The ratio | a | $620 \cdot 10^{-3}$ | $620 \cdot 10^{-3}$ | $700 \cdot 10^{-3}$ | $800 \cdot 10^{-3}$ |
| $n_{e-h}/n_e$ | b | $350 \cdot 10^{-3}$ | $300 \cdot 10^{-3}$ | $220 \cdot 10^{-3}$ | $150 \cdot 10^{-3}$ |
| | $\beta_{e-h}[\mathrm{Gy}^{-1}]$ | $2 \cdot 10^{-4}$ | $40 \cdot 10^{-4}$ | $70 \cdot 10^{-4}$ | $110 \cdot 10^{-4}$ |

delocalized recombination, leading to very high values of $f(D)_{\max}$ due to the dependence on the product of $n_e$ and $n_h$, i.e., to $n^2$. Very high values of $\beta_{e\text{-}h}$ give rise to very broad (double-peaked) values of $f(D)$.

#### 3.5.2.3. *UNIM simulation of $f(D)$ at photon energies >100 keV and 8 keV*

The variable parameters in the UNIM are: $k, a, \beta_{e-h}, b, \beta_{\mathrm{TC}}, \beta_{\mathrm{LC}}$, $\beta_{\mathrm{CC}}, \beta_{\mathrm{RD}}, \lambda_{\mathrm{O}}$, $S_{\mathrm{LC}}$, $N_{\mathrm{LC}}$ and $r_o$, twelve parameters in all. An additional parameter, $N_{\mathrm{TC}}$, cancels out since $f(D)$ is normalized. Only $a, \beta_{e-h}$ and $b$ are expected to depend strongly on photon energy. Some values of the parameters can be estimated from ancillary experiments [62]. $N_{\mathrm{LC}}$ has been estimated approximately from the concentration of Ti in the LiF:Mg,Ti sample [63]. Table 3 shows the values of the parameters following 100 keV photon irradiation. A good fit to the experimental data (Fig. 19) could not be achieved without changing the e-h dose-filling-rate parameters, $a, b$ and $\beta_{e-h}$ employed in the LDL kinetic modeling (Section 3.6). However, there is no compelling reason to expect that these values are appropriate to the UNIM, since the two models simulate supralinearity in two very different theoretical frameworks. The dependence of the ID parameters on photon/electron energy deserves special comment. The value of $s$ at low dose levels is given by the value of $b/(1+b)$. This would be expected to be higher for the lower photon/electron

Table 3. UNIM parameters for the major glow peaks in TLD-100 following 100 keV photon irradiation.

| | Glow peak | | | | |
|---|---|---|---|---|---|
| Parameter | 4 | 5 | 5b | 7 | 8 |
| $\beta_{TC}$ ($10^{-3}$ $Gy^{-1}$) | 1.1 | 1.1 | 1.1 | 0.4 | 0.1 |
| $\beta_{LC}$ ($10^{-3}$ $Gy^{-1}$) | 9.0 | 9.0 | 9.0 | 9.0 | 3.0 |
| $\beta_{CC}$ ($10^{-3}$ $Gy^{-1}$) | 0.1 | 0.1 | 0.1 | 0.1 | 0.1 |
| ks | 0.14 | 0.11 | 0.07 | 0.038 | 0.009 |
| $r_o$ (Å) | 20 | 20 | 20 | 20 | 20 |
| $S_{LC}$ ($10^{-16}$ $m^2$) | 9.6 | 9.6 | 9.6 | 9.6 | 9.6 |
| $\lambda_o$ (Å) | 475 | 475 | 475 | 475 | 475 |
| $N_{LC}$ ($10^{22}$ $m^{-3}$) | 1.95 | 1.95 | 1.95 | 1.95 | 1.95 |
| $\beta_{RD}$ ($10^{-3}$ $Gy^{-1}$) | 0.5 | 0.5 | 0 | 0.025 | 0.02 |

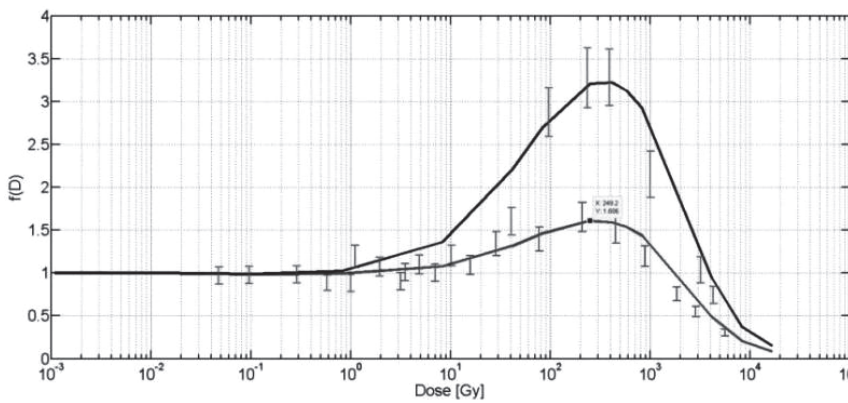


Fig. 19. UNIM simulation of the experimentally measured values of $f(D)$ for 100 keV electrons and 8 keV photons. A similar fit has been obtained using the LDL kinetic modeling (after Eliyahu *et al.* [61]).

energies due to the higher ID at lower energy, and as shown in Table 2 these values are 0.44 and 0.23 for the 8 keV and 500 keV energies respectively.

The UNIM fits to the experimental data for 100 keV electrons and 8 keV photons [56] are shown in Fig. 19 using the values of the parameters shown in Table 3.

### 3.6. Conduction band/valence band kinetic simulations

Following the development of the UNIM, kinetic simulations by various groups focused on the inclusion of localized transitions between spatially correlated TCs and luminescent centers (LCs) [64, 65]. The emphasis remained on glow peak shapes and tunneling/recombination in randomly distributed defects [66, 67]. In the following (Fig. 20) a kinetic model combining both localized and delocalized mechanisms is described which is capable of simulating (i) the OA dose response of all the major OA bands [32, 68], (ii) the dose response of peak 5 as a function of photon energy [61] and (iii) the ratio of the intensity of glow peak 5a/5 as a function of dose [59].

$N_{2e-h}$ and $N_{2e}$ represent the relative number of TC/LC spatially correlated and randomly distributed configurations respectively. The value of $N_{e-h}/N_2$ chosen in the irradiation stage is consistent with the population densities, $n_{e-h}$ and $n_e$ at saturation (full population) calculated from OA dose response. The values of the parameters are shown in Table 4.

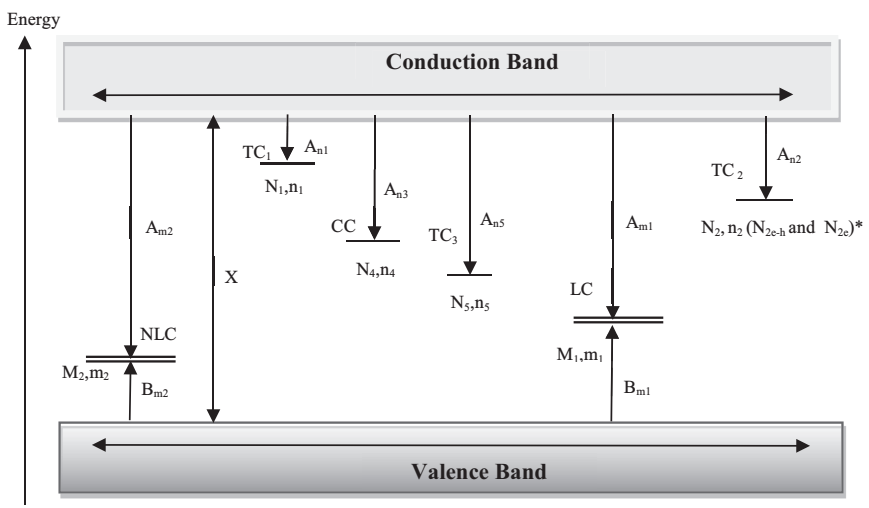


Fig. 20. CB/VB model for the irradiation stage (After Eliyahu *et al.* [59]).

Table 4. Parameters of the irradiation stage.

| Center Name | Symbol | Center parameters | Parameter value |
|---|---|---|---|
| LC — Luminescent Center | $M_1$ | Center concentration | $5 \cdot 10^{22}[\mathrm{m}^{-3}]$ |
| | $A_{m1}$ | Electron trapping probability | $5 \cdot 10^{-24}[\mathrm{m}^3\mathrm{s}^{-1}]$ |
| | $B_{m1}$ | Hole trapping probability | $2 \cdot 10^{-21}[\mathrm{m}^3\mathrm{s}^{-1}]$ |
| $N_{LC}$ — Non Luminescent hole Center | $M_2$ | Center concentration | $8 \cdot 10^{25}[\mathrm{m}^{-3}]$ |
| | $A_{m2}$ | Electron trapping probability | $1 \cdot 10^{-25}[\mathrm{m}^3\mathrm{s}^{-1}]$ |
| | $B_{m2}$ | Hole trapping probability | $2 \cdot 10^{-24}[\mathrm{m}^3\mathrm{s}^{-1}]$ |
| $TC_1$ — Trapping Center low temperature | $N_1$ | Center concentration | $1 \cdot 10^{24}[\mathrm{m}^{-3}]$ |
| | $A_{n1}$ | Electron trapping probability | $5 \cdot 10^{-24}[\mathrm{m}^3\mathrm{s}^{-1}]$ |
| $TC_2$ — peak 5 Trapping Center | $N_2$ | Center concentration | $1 \cdot 10^{23}[\mathrm{m}^{-3}]$ |
| | $A_{n2}$ | Electron trapping probability | $1.5 \cdot 10^{-22}[\mathrm{m}^3\mathrm{s}^{-1}]$ |
| CC — Competitive Center | $N_4$ | Center concentration | $5 \cdot 10^{24}[\mathrm{m}^{-3}]$ |
| | $A_{n4}$ | Electron trapping probability | $1 \cdot 10^{-23}[\mathrm{m}^3\mathrm{s}^{-1}]$ |
| $TC_3$ — Catch all trapping center | $N_5$ | Center concentration | $5 \cdot 10^{24}[\mathrm{m}^{-3}]$ |
| | $A_{n5}$ | Electron trapping probability | $7 \cdot 10^{-25}[\mathrm{m}^3\mathrm{s}^{-1}]$ |
| X | | Production rate of electrons and holes | $3.7 \cdot 10^{20}[\mathrm{m}^{-3}\mathrm{s}^{-1}]$ |

$TC_2$ is intended to correspond to the 4 eV optical absorption (OA) band identified with composite glow peak 5, and CC is identified with the 5.45 eV electron trapping competitive center. The differential equations governing the traffic of charge carriers in the irradiation stage are shown below.

$$\frac{dm_1}{dt} = -A_{m1} \cdot m_1 \cdot n_c + B_{m1}(M_1 - m_1) \cdot n_v \tag{16}$$

$$\frac{dm_2}{dt} = -A_{m2} \cdot m_2 \cdot n_c + B_{m2}(M_2 - m_2) \cdot n_v \tag{17}$$

$$\frac{dn_1}{dt} = A_{n1} \cdot (N_1 - n_1) \cdot n_c \tag{18}$$

$$\frac{dn_2}{dt} = A_{n2} \cdot (N_2 - n_2) \cdot n_c \tag{19}$$

$$\frac{dn_4}{dt} = A_{n4} \cdot (N_4 - n_4) \cdot n_c \tag{20}$$

$$\frac{dn_5}{dt} = A_{n5} \cdot (N_5 - n_5) \cdot n_c \tag{21}$$

$$\frac{dn_v}{dt} = X - n_v \cdot [B_{m1} \cdot (M_1 - m_1) + B_{m2} \cdot (M_2 - m_2)] \tag{22}$$

$$\begin{aligned}\frac{dn_c}{dt} = {} & X - n_c \cdot [A_{m1} \cdot m_1 + A_{m2} \cdot m_2 + A_{n1} \cdot (N_1 - n_1) \\ & + A_{n2} \cdot (N_2 - n_2) \ldots + A_{n4} \cdot (N_4 - n_4) + A_{n5} \cdot (N_5 - n_5)\end{aligned} \tag{23}$$

### 3.6.1. *Recombination stage*

The conduction band/valence band model for the recombination stage is shown in Fig. 21 and the parameters and their values in Table 5. Figure 21 shows explicitly the separate population levels of the TC/LC complex via joint e-h capture and e-only capture.

Electron de-trapping leading to peak 5a proceeds via (i) an excited state leading to geminate recombination ($h\nu_2$) and (ii) via the conduction band leading to de-localized recombination ($h\nu_1$). Retrapping to the ground state is allowed but it is assumed that it is negligible into the excited state. The values of $E_1$ and $S_{n1}$ for $TC_1$ were chosen to simulate the low temperature peaks (commonly labeled 2–4). This means that this one level is responsible for all three traps. The value of $E_g = 1.08\,\text{eV}$ for the activation energy governing geminate recombination was chosen to be somewhat lower than the activation energy leading to thermal elevation of the electrons to the conduction band. It is well known that the competitive center (CC) in LiF:Mg,Ti is a "deep-trap" which is not depopulated at the temperatures corresponding to the readout of peak 5 (e.g., <250°C) and for this reason during the recombination stage thermal elevation

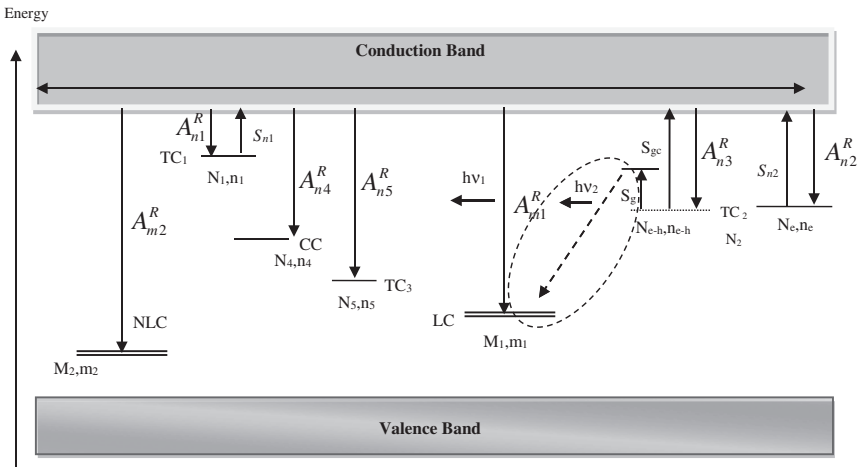


Fig. 21. CB/VB model for the recombination stage (After Eliyahu *et al.* [61]).

Table 5. Trap parameters of the recombination stage.

| Center Name | Symbol | Center parameters | Parameter value |
|---|---|---|---|
| LC — Luminescent Center | $A^R_{m1}$ | Electron trapping Probability | $5 \cdot 10^{-24}[\mathrm{m^3 s^{-1}}]$ |
| $N_{\mathrm{LC}}$ — Non Luminescent hole Center | $A^R_{m2}$ | Electron trapping Probability | $1 \cdot 10^{-25}[\mathrm{m^3 s^{-1}}]$ |
| $TC_1$ — Trapping Center low Temperature | $S_{n1}$<br>$E_1$<br>$A^R_{n1}$ | frequency factor<br>activation energy<br>Electron trapping Probability | $5 \cdot 10^{12}[\mathrm{s^{-1}}]$<br>1.15[eV]<br>$5 \cdot 10^{-24}[\mathrm{m^3 s^{-1}}]$ |
| $TC_2$ — Peak 5 Trapping Center* | $S_{n2}$<br>$E_2$<br>$A^R_{n2}$ | frequency factor<br>activation energy<br>Electron trapping Probability | $1 \cdot 10^{13}[\mathrm{s^{-1}}]$<br>1.39[eV]<br>$1.5 \cdot 10^{-23}[\mathrm{m^3 s^{-1}}]$ |
| CC — Competitive Center | $A^R_{n4}$ | electron trapping Probability | $1 \cdot 10^{-23}[\mathrm{m^3 s^{-1}}]$ |
| $TC_3$ — Catch all Trapping Center | $A^R_{n5}$ | electron trapping Probability | $7 \cdot 10^{-25}[\mathrm{m^3 s^{-1}}]$ |

of electrons from the CC is not allowed. The geminate recombination governed by $S_g$ may occur via ground state tunneling or via an excited state similar to the "band-tail states" [69].

The differential equations governing the traffic of charge carriers in the recombination stage are shown below.

$$\frac{dm_1}{dt} = -A^R_{m1} \cdot m_1 \cdot n_c - n_{e-h} \cdot S_g \cdot e^{(-E_g/kT)} \tag{24}$$

$$\frac{dm_2}{dt} = -A^R_{m2} \cdot m_2 \cdot n_c \tag{25}$$

$$\frac{dn_1}{dt} = -n_1 \cdot S_{n1} \cdot e^{(-E_{LT}/kT)} + A^R_{n1} \cdot (N_1 - n_1) \cdot n_c \tag{26}$$

$$\frac{dn_e}{dt} = -n_e \cdot S_{n2} \cdot e^{(-E_{TC}/kT)} + A^R_{n2} \cdot (N_e - n_e) \cdot n_c \tag{27}$$

$$\begin{aligned}\frac{dn_{e-h}}{dt} = &-n_{e-h} \cdot S_g \cdot e^{(-E_g/kT)} - n_{e-h} \cdot S_{gc} \cdot e^{(-E_{gc}/kT)} \\ &+ A^R_{n3} \cdot (N_{e-h} - n_{e-h}) \cdot n_c\end{aligned} \tag{28}$$

$$\frac{dn_4}{dt} = A^R_{n4} \cdot (N_4 - n_4) \cdot n_c \tag{29}$$

$$\frac{dn_5}{dt} = A^R_{n5} \cdot (N_5 - n_5) \cdot n_c \tag{30}$$

$$\begin{aligned}\frac{dn_c}{dt} = &\, n_1 \cdot S_{n1} \cdot e^{(-E_{LT}/kT)} + n_e \cdot S_{n2} \cdot e^{(-E_{TC}/kT)} \\ &+ n_{e-h} \cdot S_{gc} \cdot e^{(-E_{gc}/kT)} \ldots \\ &- n_c \cdot [A^R_{m1} \cdot m_1 + A^R_{m2} \cdot m_2 + A^R_{n1} \cdot (N_1 - n_1) \\ &+ A^R_{n2} \cdot (N_e - n_e) \ldots \\ &+ A^R_{n3} \cdot (N_{e-h} - n_{e-h}) + A^R_{n4} \cdot (N_4 - n_4) + A^R_{n5} \cdot (N_5 - n_5)\end{aligned} \tag{31}$$

The values of the parameters governing geminate recombination are as follows:

$S_g = 10^{10}\,\mathrm{s}^{-1}$, $E_g = 1.08\,\mathrm{eV}$, $S_{gc} = 10^{13}\,\mathrm{s}^{-1}$, $E_{gc} = 1.37\,\mathrm{eV}$ and $A^R_{n3} = 5.10^{-24}\,\mathrm{m}^3\,\mathrm{s}^{-1}$. In order to describe the dependence of the

peak ratio 5a/5 on dose, different electron trapping probabilities in the irradiation and recombination stages were used due to the dependence of the cross-sections on temperature. The simulation of dose response linearity from approximately $10^{-5}$ Gy to 1 Gy, required the introduction of band-tail states in the recombination process of peak 5. These band-tail states allow semi-localized recombination via thermally activated hopping, without competitive conduction band–related effects which lead to non-linear dose response.

### 3.6.2. *Results of the simulations*

Figure 22 shows the dependence of $n_{e-h}/n_e$ as a function of dose for various values of $f(D)_{\max}$

Figure 23 shows the values of $f(D)_{\max}$ of 3.5, 2.4, 1.8 and 1 which correspond approximately to photon energies above 100 keV, ∼50 keV, ∼10 keV and ∼2 keV respectively. The significant increase of $n_{e\text{-}h}/n_e$ with increasing dose has been chosen to begin at a level of dose corresponding approximately to the onset of supralinearity for glow peak 5 in LiF:Mg,Ti.

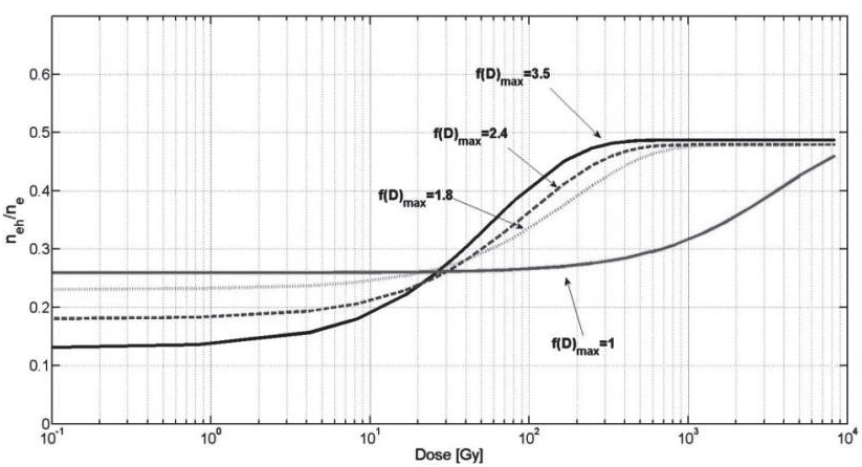


Fig. 22. The dependence of $n_{eh}/n_e$ on dose for various values of $f(D)_{\max}$. (After Eliyahu *et al.* [61]).

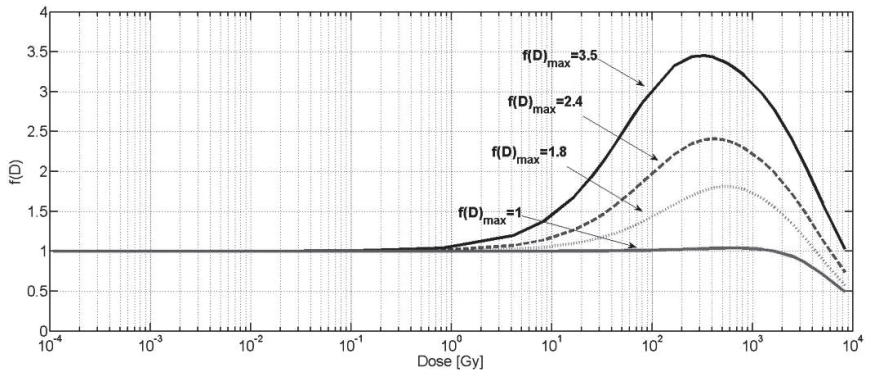


Fig. 23. The values of $f(D)$ corresponding to Figure 22 (After Eliyahu *et al.* [61]).

### 3.7. Summary

This chapter has reviewed many of the ionization density characteristics of TL materials with special emphasis on LiF:Mg,Ti. The ID characteristics arise from the presence of spatially correlated TC/LC complexes which give rise to localized transitions. Linear/supralinear dose response and its dependence on ID is the most important of the characteristics, as it affects all dosimetric applications and is also of fundamental theoretical importance. The model adopts a nanodosimetric approach to the $e-h$ filling rates and $e$-only filling rates of the coupled TC/LC. A close to linear and then exponential filling rate was adopted for the $e-h$ and $e$-only trapping configurations. Ab–initio calculations of the behavior of $n_{e-h}/n_e$ as a function of dose and energy, and based on physical/nanoscopic principles, would of course be highly desirable. These, however, would require detailed knowledge of the structure of the TC/LC complex as well as of the low electron energy cross-section interactions with the constituents of the complex. The simulations demonstrate the importance of attempting the description of several characteristics in both the absorption and recombination stages with essentially the same set of variables. In the case described herein, this approach forced the adoption of the presence of band-tail states in the TL mechanisms of LiF:Mg,Ti.

The UNIM and the LDL kinetic model are both successful in simulating the linear/supralinear behavior of $f(D)$ and its dependence on photon energy. However, the values of the dose-filling characteristics, $a$, $b$ and $\beta_{e\text{-}h}$ used in the two models are different since the two models approach the problem from very different perspectives. Further refinement of the models may discover a single set of parameters describing the filling rates of the TC/LC complex, however, this appears an imposing challenge considering their very different theoretical frameworks. In the meantime, the importance and role of TC/LC localized population and recombination, as well as the simultaneous simulation of both the irradiation and recombination stages in kinetic CB/VB modeling are conclusively demonstrated. The dependence of TL characteristics on ID still presents interesting theoretical and dosimetric challenges. For example, it has been suggested that the cross-sections for charge carrier capture may be dose-dependent, related to the build-up of Coulombic charge in neighboring TCs and LCs [70].

## References

[1] Y.S. Horowitz, "Theory of thermoluminescence gamma dose response: The unified interaction model," *Nucl. Instrum. Meths.*, vol. B184, pp. 68–84, 2001.

[2] Y.S. Horowitz, O. Avila and M. Rodríguez-Villafuerte, "Theory of heavy charged particle (efficiency and supralinearity) in TL materials," *Nucl. Instrum. Meths.*, vol. B184, pp. 85–122, 2001.

[3] P. Olko, P. Bilski and J.L. Kim, "Microdosimetric interpretation of the photon energy response of LiF:Mg,Ti detectors," *Radiat. Prot. Dosim.*, vol. 100, pp. 119–122, 2002.

[4] O. Avila, M. Rodríguez-Villafuerte, I. Gamboa-deBuen, P. Aviles, D. Estrada, A.E. Buenfil, C. Ruiz-Trejo, M.E. Brandan and Y.S. Horowitz, "On the correct measurement of relative HCP to gamma TL efficiencies," *Radiat. Prot. Dosim.*, vol. 100, pp. 87–90, 2002.

[5] F. Salvat, PENELOPE-2006: "A Code System for Monte Carlo Simulation of Electron and Photon Transport" Workshop Proceedings, Barcelona, Spain, July 2006.

[6] Y.S. Horowitz, M. Rosenkrantz, S. Mahajna and D. Yossian, "The track interaction model for alpha particle induced thermoluminescence supralinearity: Dependence of the supralinearity on the vector properties of the alpha particle radiation field," *J. Phys. D. Appl. Phys.*, vol. 29, pp. 205–214, 1996.

[7] S.W.S. McKeever, private communication, 1995.
[8] Y.S. Horowitz, D. Sibony, L. Oster, J. Livingstone, S. Guatelli, A. Rosenfeld, D. Emfietzoglou, P. Bilski and B. Obryk, "Alpha particle and proton relative thermoluminescence efficiencies in LiF:Mg,Cu,P: Is track structure theory up to the task?" *Radiat. Prot. Dosim.*, vol. 150, pp. 359–374, 2012.
[9] I. Eliyahu, Y.S. Horowitz, L. Oster, I. Mardor, S. Biderman, S. Druzhyna and S. Marino, "Probing the defect nanostructure of Helium and proton tracks in LiF:Mg,Ti using optical absorption: Implications to track structure theory calculations of heavy charged particle relative efficiency," *Nucl. Instrum. Meths.*, vol. B349, pp. 209–220, 2015.
[10] D. Emfietzoglou, "Modelling the energy loss mechanism of charged particles in organic solids," *Radiat. Prot. Dosim.*, vol. 100, pp. 153–158, 2002.
[11] E. Surdutovich, D.C. Gallagher and A.V. Solov'yov, "Calculation of complex DNA damage induced by ions," *Phys. Rev.*, vol. E84, pp. 051918, 2011.
[12] Y.S. Horowitz, L. Oster and I. Eliyahu, "Review of dose-rate effects in the thermoluminescence of LiF (Harshaw)," *Radiat. Prot. Dosim.*, vol. 179, pp. 184–188, 2018, doi:10.1093/rpd/ncx248.
[13] Y.S. Horowitz and D. Yossian, "Computerized glow curve deconvolution: Application to thermoluminescence dosimetry," *Radiat. Prot. Dosim.*, vol. 60, pp. 1–114, 1995.
[14] Y.S. Horowitz, E. Fuks, L. Oster, L. Podpalov, Y. Belaish and B. Ben Shachar, "Advanced multistage deconvolution applied to composite glow peak 5 in LiF:Mg,Ti (TLD-100)," *Radiat. Prot. Dosim.*, vol. 126, pp. 322–325, 2007.
[15] Y.S. Horowitz and M. Moscovitch, "Highlights and pitfalls of 20 years of application of computerized glow curve analysis to thermoluminescence research and dosimetry," *Radiat. Prot. Dosim.*, vol. 153, pp. 1–22, 2013.
[16] R. Chen and A. Hag-Yahya, "Interpretation of very high activation energies and frequency factors as being due to competition between centres," *Radiat. Prot. Dosim.*, vol. 65, pp.17–20, 1996.
[17] E. Fuks, Y.S., Horowitz, A. Horowitz, L. Oster, S. Marino, M. Rainer, A. Rosenfeld and H. Datz, "Thermoluminescence solid state nanodosimetry-the peak 5a/5 dosemeter," *Radiat. Prot. Dosim.*, vol. 143, pp. 416–426, 2011.
[18] Y.S. Horowitz, "Queer, quaint, quirky and quizzical thermoluminescent Lithium Fluoride: The $^{137}Cs/^{60}Co$ calibration anomaly — a challenge for nanodosimetry," *Radiat. Prot. Dosim.*, vol. 69, pp. 83–84, 1997.
[19] Y.S. Horowitz, "A unified and comprehensive theory of the TL dose response of thermoluminescent systems applied to LiF:Mg,Ti," In: "Microdosimetric response of physical and biological systems to low-and high-LET radiations: Theory and applications to dosimetry": Ed. Y.S. Horowitz, Elsevier, The Netherlands, 2006.
[20] T.M. Piters, A.J.J. Bos and J.L., Zoetelief, "TL dosimetry in mixed neutron-gamma radiation fields using glow curve superposition," *Radiat. Prot. Dosim.*, vol. 44, pp. 305–308, 1992.

[21] P. Meissner, U. Bienek and J. Rassow, "Applicability of TLD-700 detectors for dosimetry in d(14)+Be neutron field," *Radiat. Prot. Dosim.*, vol. 23, pp. 421–424, 1988.

[22] M. Skopec, M. Loew, J.L. Price and M. Moscovitch, "Classification of mixed radiation fields using the vector representation of thermoluminescence glow curves," *Radiat. Meas.*, vol. 41, pp. 410–413, 2008.

[23] D. Sibony, Y.S. Horowitz, L. Oster, A. Wojcik and A. Sollazzo, "Combined measurement of dose and $\alpha/\gamma$ radiation field components using the shape of composite peak 5 in the glow curve of LiF:Mg,Ti," *Radiat. Meas.*, vol. 71, pp. 86–89, 2014.

[24] Y.S. Horowitz, "Thermoluminescence dosimetry: State-of-the-art and frontiers of future research," *Radiat. Meas.*, vol. 71, pp. 2–7, 2014.

[25] M.E. Brandan, I. Gamboa deBuen and M. Rodríguez Villafuerte, "Thermoluminescence induced by heavy charged particles," *Radiat. Prot. Dosim*, vol. 100, pp. 39–44, 2002.

[26] M. Rodríguez-Villafuerte and M.E. Brandan, "Comparison of track structure calculations with experimental results," *Radiat. Prot. Dosim*, vol. 84, pp. 73–76, 1999.

[27] O. Avila, I. Gamboa-deBuen and M.E. Brandan, "Study of the energy deposition in LiF by heavy charged particle irradiation and its relation to the thermoluminescent efficiency of the material," *J. Phys. D. Appl. Phys.*, vol. 32, pp. 1175–1181, 1999.

[28] J. Kalef-Ezra and Y.S. Horowitz, "Heavy charged particle thermoluminescence dosimetry: Track structure theory and Experiments," *Int. J. Appl. Radiat. Isot.*, vol. 33, pp. 1085–1100, 1982.

[29] Y.S. Horowitz, E. Fuks, H. Datz, L. Oster, J. Livingston and A. Rosenfeld, "Mysteries of LiF TLD response following high ionization density irradiation: Glow curve shapes, dose response, the Unified Interaction Model and Modified Track Structure Theory," *Radiat. Meas.*, vol. 46 pp. 1342–1348, 2011.

[30] I. Nail, Y.S. Horowitz, L. Oster, M.E. Brandan, M. Rodríguez-Villafuerte, A.E. Buenfil, C. Ruiz-Trejo, I. Gamboa-deBuen, O. Avila, A.M. Tovar, P. Olko and N. Ipe, "Search for ionization density effects in the radiation absorption stage in LiF:Mg,Ti," *Radiat. Prot. Dosim.*, vol. 119, pp. 180–183, 2006.

[31] S. Druzhyna, I. Eliyahu, L. Oster, Y.S. Horowitz, S. Biderman, G. Reshes and I. Orion, "Investigation of the optical absorption dose response of LiF:Mg,Ti(TLD-100) and the role of V centers in F center (5.08 eV) bleaching," *Radiat. Meas.*, vol. 90, pp. 113–116, 2016.

[32] S. Biderman, S. Druzhyna, G. Reshes, I. Eliyahu, L. Oster and Y.S. Horowitz, "Investigation of the energy spectrum and dose response of optical absorption bands in 4N single crystal LiF and LiF:Mg,Ti (TLD-100)," *Radiat. Meas.*, vol. 106, pp. 30–34, 2017.

[33] A. Perez, J. Davenas and C.H.S. Dupuy, "Ionization induced defects in Alkali Halide single crystals," *Nucl. Instrum. Meths.*, vol. 132, pp. 219–227, 1976.

[34] C. Trautman, M. Toulemonde, K. Schwartz, J.M. Constantin and A. Müller, "Damage structure in the ionic crystal LiF irradiated with swift heavy ions," *Nucl. Instrum. Meths.*, vols. B164–165, pp. 365–376, 2000.

[35] K. Schwartz, C. Trautmann, A. S. El-Said, R. Neumann, M. Toulemonde and W. Knolle, "Color-center creation in LiF under irradiation with swift heavy ions: Dependence on energy loss and fluence," *Phys. Rev.*, vol. B70, pp. 184104, 2004.

[36] A.Z. Smakula, "Uber erregung und entfarbung lichtelekrisch leitender alkalihalogenide," *Physik*, vol. 59, p. 603, 1930.

[37] I. Eliyahu, Y.S. Horowitz, L. Oster, I. Mardor, S. Druzhyna and S. Biderman, "Kinetic modeling of Fluorine vacancy/F center creation in LiF:Mg,Ti including vacancy interstitial recombination: Evaluating the factors leading to the lack of supralinearity in the optical absorption F center concentration dose response," *Nucl. Instrum. Meths.*, vol. B143 pp. 15–25, 2015.

[38] K.L. Van der Lugt, J. Comas and E.A. Wolicki, "Coloration of LiF by 3.0 MeV $^{3}$He, $^{40}$Ar, $^{84}$Kr and 2.0 MeV $^{129}$Xe ions," *J. Phys. Chem. Solids*, vol. 31, pp. 1361–1373, 1970.

[39] M. Toulemonde, E. Paumier and C. Dufour, "Thermal spike model in the electronic stopping power regime," *Radiat. Eff. Defects in Solids*, vol. 126, pp. 201–206, 1993.

[40] S. Klaumunzer, "Thermal spike models for ion track physics: A critical examination," in Ion Beam Science: Solved and Unsolved Problems, Ed. P. Sigmund, Matematisk-Fysiske Meddelelser, Copenhagen, vol. 52, pp. 293–328, 2006.

[41] W. Hoffman, J. Bienen, D. Filgers and Th. Schmitz, "TLD-300 dosimetry in a 175 MeV proton beam," *Radiat. Prot. Dosim.*, vol. 85, pp. 341–343, 1999.

[42] Th. Loncol, S. Vynkier and A. Wambersie, "Thermoluminescence in proton and fast neutron therapy beams," *Radiat. Prot. Dosim.*, vol. 66, pp. 299–304, 1996.

[43] B. Obryk, K. Skowro, A. Sas-Bieniarz, L. Stolarczyk and P. Bilski, "High dose, high-temperature emission of LiF:Mg,Cu,P: Thermally and radiation induced loss and recovery of its sensitivity," *Radiat. Meas.*, vol. 56, pp. 171–178, 2013.

[44] S. Mahajna and Y.S. Horowitz, "The Unified Interaction Model applied to the gamma ray induced supralinearity and sensitization of peak 5 in LiF:Mg,Ti (TLD-100)," *J. Phys. D: Appl. Phys.*, vol. 30, pp. 2603–2619, 1997.

[45] R. Katz, private communication.

[46] Y.S. Horowitz, D. Satinger and L. Oster, "The dependence of the dose response supralinearity of peak 5 in TLD-100 on recombination temperature," *Radiat. Prot. Dosim.*, vol. 84, pp. 99–102, 1999.

[47] H. Datz, Y.S. Horowitz, L. Epstein, L. Oster, J. Livingstone, A. Horowitz, M. Kol and M. Margaliot, "Energy dependence of the supralinearity, $(f(D)_{\max})$, of peaks 7 and 8 in the high temperature thermoluminescence of LiF:Mg,Ti (TLD-100): interpretation using the Unified Interaction Model," *Radiat. Meas.*, vol. 46, pp. 1436–1439, 2011.

[48] M. Rodríguez-Villafuerte, A.E. Buenfil, I. Gamboa-deBuen, C. Ruiz-Trejo, M.E. Brandan, D. Yossian, D. Satinger and Y.S. Horowitz, "Study of the TL response of LiF:Mg,Ti to 3 and 7.5 MeV He ions: Measurements and interpretation in terms of the track interaction model," *Nucl. Instrum. Meths.*, vol. B160, pp. 377–386, 2000.

[49] Y.S. Horowitz, I. Eliyahu and L. Oster, "Kinetic simulations of thermoluminescence dose response: Long overdue confrontation with the effects of ionization density," *Radiat. Prot. Dosim.*, vol. 172, pp. 524–540, 2016.

[50] R.H. Templer, "The localized transition model of anomalous fading," *Radiat. Prot. Dosim.*, vol. 17, pp. 493–497, 1986.

[51] P.D. Townsend, K. Ahmed, P.J. Chandler, S.W.S. McKeever and H.J. Witlow, "Measurements of the emission spectra of LiF during thermoluminescence," *Radiat. Eff.*, vol. 72, pp. 245–257, 1983.

[52] S. Biderman, Y.S. Horowitz and L. Oster, "Investigation of the emission spectra of LiF:Mg,Ti (TLD-100) during thermoluminescence," *Radiat. Prot. Dosim.*, vol. 100, pp. 369–372, 2002.

[53] Y. Weizman, Y.S. Horowitz, L. Oster, D. Youssian and A. Horowitz, "Mixed-order kinetic analysis of the glow curve characteristics of single crystal LiF:Mg,Ti as a function of Ti concentration," *Radiat. Prot. Dosim.*, vol. 84, pp. 47–50, 1999.

[54] G. Vale, "Energy transfer from colour centres to the dopant in alkali halides," *J. Lumin.*, vols. 72–74, pp. 726–728, 1997.

[55] Y. Weizman, Y.S. Horowitz and L. Oster, "Investigation of the composite structure of peak 5 in the thermoluminescence glow curve of LiF:Mg,Ti (TLD-100) using optical bleaching," *J. Phys. D: Appl. Phys.*, vol. 32, pp. 2118–2127, 1999 [cited as an article of high interest by the Editors of the J. Phys. D.]

[56] A. Lavon, I. Eliyahu, L. Oster and Y.S. Horowitz, "The modified unified Interaction model:incorporation of dose-dependent localized recombination," *Radiat. Prot. Dosim.*, vol. 163, pp. 362–372, 2015.

[57] Y.S. Horowitz, S. Mahajna and M. Rosenkrantz, "Unified approach to gamma and heavy charged particle supralinearity: The Track Defect Interaction Model, *Radiat. Prot. Dosim.*, vol. 65, pp. 7–12, 1996.

[58] I. Eliyahu, S. Biderman, L. Oster and Y.S. Horowitz, "Kinetic simulation of the optical absorption dose response of LiF:Mg,Ti (TLD-100) incorporating spatially correlated electron and hole trapping centers," *Nucl. Instrum. Meths.*, vol. B407, pp. 282–290, 2017.

[59] I. Eliyahu, Y.S. Horowitz, L. Oster, S. Druzhyna and I. Mardor, "Nanodosimetric kinetic model incorporating localised and delocalised recombination: application to the prediction of the electron dose response of the peak 5a/5 ratio in the glow curve of LiF:Mg,Ti (TLD-100)," *Radiat. Meas.*, vol. 71, pp. 226–231, 2014.

[60] E. Fuks, Y.S. Horowitz and L. Oster, "Investigation of the properties of composite glow peak 5 in slow-cooled TLD-100," *Radiat. Meas.*, vol. 43, pp. 249–253, 2008.

[61] I. Eliyahu, Y.S. Horowitz, L. Oster and I. Mardor, "A kinetic model incorporating both localized and delocalized recombination: Application to the dependence of the TL dose response on photon energy," *J. Lumin.*, vol. 145, pp. 600–607, 2014.

[62] I. Gamboa deBuen, A.E., Buenfil, M. Rodríguez Villafuerte, C.G. Ruiz, A. Zarata-Morales and M.E. Brandan, "Supralinearity in the response of TLD-100 to 5.3 MeV alpha particles," *Radiat. Prot. Dosim.*, vol. 65, pp. 13–16, 1996.

[63] Y.S. Horowitz, "A note on the average distance between Mg-based trapping structures in LiF:Mg,Ti and LiF:Mg,Cu,P and the relevance to microdosimetry," *Radiat. Prot. Dosim.*, vol. 82, pp. 51–54, 1998.

[64] A. Mandowski, "Semi-localized transitions model for thermoluminescence," *J. Phys. D: Appl. Phys.*, vol. 38, pp. 17–21, 2005.

[65] M. Kumar, R.K. Kher, B.C. Bhatt and C.M. Sunta, "A comparative study of the models dealing with localized and semi-localized transitions in thermally stimulated luminescence," *J. Phys. D: Appl. Phys.*, vol. 40, pp. 5865–5872, 2007.

[66] V. Pagonis, "Evaluation of activation energies in the semi-localized transition model of thermoluminescence," *J. Phys. D: Appl. Phys.*, vol. 38, pp. 2179–2186, 2005.

[67] V. Pagonis, R. Chen, C. Kulp and G. Kitis, "An overview of recent developments in luminescence models with a focus on localized transitions," *Radiat. Meas.*, vol. 106, pp. 3–12, 2017.

[68] S. Biderman, I. Eliyahu, Y.S. Horowitz and L. Oster, "Dose response of F center optical absorption in LiF:Mg,Ti, *Radiat. Meas.*, vol. 71, pp. 237–241, 2014.

[69] N. Poolton, R. Kars, J. Wallinga and A.J.J. Bos, "Direct evidence for the participation of band-tails and excited-state tunneling in the luminescence of irradiated feldspars," *J. Phys. C: Condens. Matt.*, vol. 21, pp. 485–505, 2009.

[70] C.T. Sune, A. Reisman and C.K. Williams, "A new electron trapping model for the gate insulator of insulated gate filed-effect transistors," *J. Electronic Materials*, vol. 19, pp. 651–656, 1990.

This page intentionally left blank

# Chapter 4

# Thermally Assisted Optically Stimulated Luminescence (TA – OSL)

George S. Polymeris* and George Kitis†

*Institute of Nuclear Sciences, Ankara University
06100-Beşevler, Ankara, Turkey
gspolymeris@ankara.edu.tr, polymers@auth.gr
†Nuclear Physics Laboratory, Physics Department
Aristotle University of Thessaloniki
54124-Thessaloniki, Greece
gkitis@auth.gr

The current status of knowledge concerning the thermally assisted optically stimulated luminescence (TA – OSL) signal in various naturally occurring as well as artificial luminescent phosphors is described. TA – OSL stands as an effective experimental tool for stimulating electrons from very deep traps (VDTs). Basic TA – OSL features, such as stability, dose response, thermal assistance and TA – OSL curve shapes, along with the prevalence and the ubiquity of these features are presented, from both an experimental and a simulation approach. TA – OSL from anion deficient alumina doped with carbon and also from quartz has been effectively used towards dosimetry purposes, especially for large accumulated doses.

## 4.1. Definition of very deep traps — nomenclature

The temperature dependence of the thermoluminescence (hereafter TL) emission appears as a set of peaks, with each one corresponding to an electron-trapping defect; this is the definition of the TL glow curve [1]. In order to distinguish between the different components that make up the TL glow curves, the knowledge of trap depth $E$ of each electron-trapping defect becomes mandatory. The peak position

or peak maximum temperature, $T_{max}$, for a given heating rate is controlled by two parameters, the trap depth and the probability of detrapping; the latter relates to the frequency factor. These two parameters also control the long term stability of the electrons in the trap when the crystals are stored at ambient temperature. In the absence of retrapping and anomalous fading, the electron lifetime $\tau$ in a trap is commonly expressed using the following formula:

$$\tau = s^{-1} \cdot e^{\frac{E}{kT}} \tag{1}$$

where $s$ is the frequency factor (in $s^{-1}$), $E$ is the activation energy required to release the electron from the trap (in eV), $k$ is the Boltzmann constant (in $eV \cdot K^{-1}$) and $T$ is the absolute temperature (in K).

Based on the number of available TL peaks and their corresponding peak positions, an experimental TL glow curve is usually divided into three main temperature regions, based on the stability of the corresponding peaks:

*Region I:* Starting from room temperature up to around 150°C, this region is considered the low temperature region, including shallow traps. These traps are thermally unstable at ambient temperatures and thus inappropriate for dosimetric applications, as their lifetime according to Eq. (1) does not exceed several hours. Consequently, the electron traps giving rise to these low temperature peaks are not stable in time, and hence such TL peaks are monitored only in artificially irradiated samples. A typical example of a TL peak at this specific region is the so-called "110°C TL peak" in quartz [2, 3].

*Region II:* Ranging between 150 and 300°C, this specific temperature region is considered the main dosimetric region. The traps are thermally stable at ambient temperatures and thus appropriate for dosimetry applications. All commercially available TL dosimeters, such as aluminum oxide ($Al_2O_3$:C, 185°C) and beryllium oxide (BeO, 210°C) yield TL peaks at this specific temperature region [4] (with peak positions $T_{max}$ measured for a heating rate of 1°C/s).

*Region III:* The temperature region ranging between 300 and 500°C is called the high temperature region, corresponding to relatively deeper traps. These traps yield lifetimes according to

Eq. (1) much prolonged and consequently more appropriate for dosimetry using natural phosphors, especially for dating applications. A typical example of a TL peak at this specific region is the so-called "325°C TL peak" in quartz [2, 5].

The range of temperatures of these three regions is relevant to dating and dosimetry. For many TL dosimeters and other materials in general, traps with TL peak temperatures lower than room temperature (RT hereafter) also exist; these are much shallower traps that can be accessible only by performing TL measurements below room temperature. Besides these three regions, it is necessary to consider an additional region (region *IV*) for temperatures above 500°C, corresponding to much deeper traps. Most of TL phosphors are wide band gap materials, and contain many deep energy level defects in this temperature range [6]. Consequently, there are traps lying well within the band gap that are thermally inaccessible when a luminescent material is heated from room temperature to 500°C, as is usual with commonly used TL measurement systems. These traps will be termed as Very Deep Traps or VDTs hereafter, and they correspond to TL glow peaks having their peak maximum temperature, $T_{max}$, above 500°C.

In common practice and applications, two experimental parameters should be defined for every TL glow curve, namely the maximum temperature to which the sample will be heated, as well as the heating rate. For artificial luminescent dosimeters, such as lithium fluoride (LiF:Mg,Ti), aluminum oxide ($Al_2O_3$:C) and others, the maximum heating temperature is strictly suggested by the manufacturers and never exceeds 350°C–400°C ([4] and references therein). Heating at higher than this recommended temperature will possibly result in undesirable sensitivity changes of the luminescent phosphor [4]. For naturally occurring materials, such as quartz, feldspars, calcium carbonate and apatites, heating from RT up to 500°C has been a common practice [2, 3, 5], since most of dosimetric peaks are observed below 425°C. Moreover, while applying OSL dating protocols for quartz samples, a fast OSL component is extensively used. Prior to OSL measurements, preheating is required; however, this preheating temperature usually does not exceed 260–280°C,

as the signal from this fast OSL component is directly related to an electron trap responsible for the TL glow-peak with maximum temperature at 325°C [7, 8]. For the case of infrared stimulation, it was demonstrated that IRSL measurements at high temperatures could isolate a more stable luminescence signal [9]. Among the promising techniques to address this issue are, (a) post-IR IRSL dating, being a two-step protocol that uses an IRSL signal measured at elevated temperatures and (b) a multi-step protocol, which includes IRSL measurements at sequentially increasing temperatures (termed multi-elevated-temperature post-IR IRSL). Both these techniques have been extensively tested using different temperature combinations [9–12]; however, the maximum measurement temperature in these techniques does not exceed 300–350°C.

Currently, the electron trapping defects used for all applications are exclusively those levels that can be thermally excited at moderate temperatures, namely below 400°C. Even though the temperature of 500°C was arbitrarily selected by Polymeris *et al.* [13] for the definition of VDT, it reflects the maximum attainable operational temperature on a number of commercially available luminescence readers. Traps corresponding to peak positions higher than 500°C are very difficult to observe for many reasons. Most of the available commercial systems do not support TL measurements at this high temperature region. Moreover, heating to such high temperatures causes permanent changes to the sensitivity of almost all materials, with rare exceptions. Furthermore, such VDTs are very difficult to observe in various natural and artificial luminescence phosphors using conventional luminescence techniques, mostly because at such high temperatures the interference from a high infrared background makes TL measurements up to temperatures higher than 600°C quite problematic [14]. Moreover, these traps have large thermal trap depth and thus are not accessible by using commercially available TL readers. Conventional OSL using visible stimulation sources of various wavelengths at ambient temperatures is also incapable of accessing such VDTs, as the photo-ionization cross section of these traps is expected to be very low at ambient temperatures. Finally, possible thermal quenching of the luminescence centers that has been

monitored for luminescence dosimeters such as aluminum oxide [15] and quartz [16] imposes another difficulty.

## 4.2. Monitoring the presence of very deep traps

### 4.2.1. *Indirect luminescent probes and non – luminescence oriented measurements*

Because of all the reasons stated above, mostly indirect ways/ techniques were applied in order to monitor and study these VDTs, including mainly thermally stimulated exo-electron emission (TSEE). Besides TSEE, much deeper traps could be observed in thermally stimulated conductivity measurements (TSC), since these do not suffer from thermal quenching [17]. Nevertheless, the active interest expressed in VDTs was initiated for anion deficient alumina doped with carbon ($Al_2O_3$:C), due to the pronounced impact that these traps have on the parameters of the main dosimetric TL peak around 185°C. The pioneering work dealing with these traps is dated back to the 1990's, when Akselrod and Kortov provided evidence of traps with a delocalization temperature above 650°C, based mostly on TSEE of $Al_2O_3$:C crystals at large doses [18]. A number of experimental properties such as the (a) decrease in the mean activation energy within the main peak [19, 20], (b) dependence of the TL output on the heating rate [20, 21], (c) variations in the sensitivity [19, 21, 22], temperature position, width and shape of main TL peak [19, 21–25] as well as (d) nonlinear TL dose response [22, 23, 26] were already reported in the literature by the research group from the Ural State Technical University, Russia. These features have been attributed to the degree of VDT filling in this material. A large population of charges trapped at deep trapping states was also inferred from their influence on the OSL sensitivities after high dose irradiation using step annealing [27], identifying the importance of these much deeper traps in dictating the high-dose OSL characteristics of this material. All these experimental features have been used as indirect probes for very deep traps. Some of these effects were interpreted as due to sensitivity changes introduced by competition mechanisms involving deeper electron and hole traps,

and also by the multiple component nature of the main TL peak. Both the dose response of the TL signal and the TL sensitivity were shown to be influenced by sensitization and desensitization processes caused by the filling of deeper electron and hole traps, respectively [23]. The development of a model based on a mechanism which involves interactive competition between shallow, deep and very deep traps permitted description in a common frame of the totality of the main experimentally observed features in this material [19, 21, 22, 28, 29].

### 4.2.2. *Direct TL measurements*

Due to the previously reported instrumental limitations imposed by the commercially available luminescence readers, only a scarce number of studies were focused on direct TL observations of these VDTs. The first direct TL observations of their existence were reported by Milman *et al.* [19] as well as Kortov *et al.* [22] for the case of $\alpha$-$Al_2O_3$:C. After irradiating the samples with UV irradiation at various high temperatures and subsequent heating to temperatures up to 900°C, TL peaks associated with these traps were monitored. Figure 1 shows glow curves for anion-defective $\alpha$-$Al_2O_3$ crystals excited at 460 K (curve 1), 620 K (curve 2) and 720 K (curve 3) after UV radiation [19].

In addition to the main dosimetric peak A ($T_{max}$ = 450 K) and the peak B ($T_{max}$ = 570 K), the glow curves indicate two more peaks C and D, with peak positions $T_{max}$ = 730 K and $T_{max}$ = 880 K respectively. These two are identified as deep trap and VDT respectively, with delocalization temperatures around 490 and 610°C. Later on, Molnár *et al.* [30] reported TL peaks in $Al_2O_3$:C at 310, 460 and 675°C for a heating rate of 2°C/s using UV interference filters. Similar results have also been reported using direct TL measurements after irradiation at elevated temperatures [29, 31, 32].

### 4.2.3. *Photo-transferred TL (PTTL)*

Photo-transferred TL (PTTL) is thermoluminescence produced due to transfer of electrons, by light, from a deeper electron trap to a previously empty shallower trap. This is in contrast to conventional

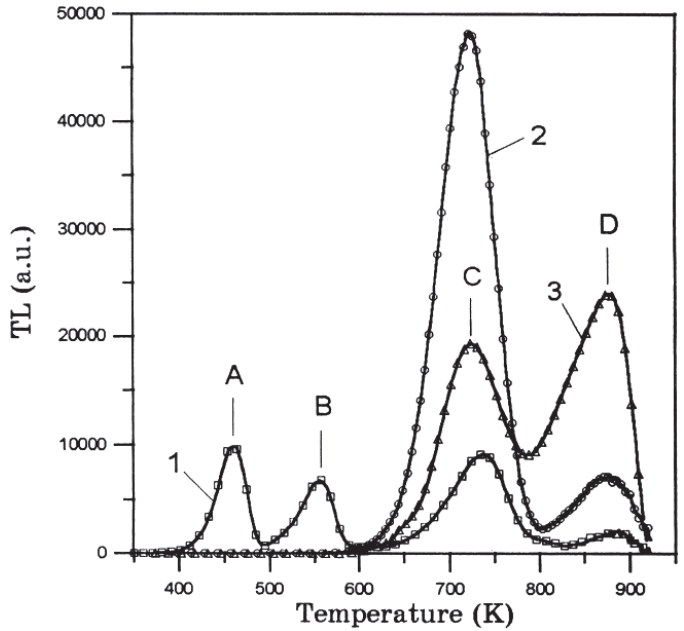


Fig. 1. Glow curves of $\alpha$-$Al_2O_3$ crystals excited by UV radiation at the heating rate of 2 K/s. The excitation temperatures: 1:460 K; 2:620 K; 3:720 K. While peak C is attributed to a deep trap with delocalization temperature of 490°C, peak D corresponds to a VDT with peak position at 610°C. The figure, which is reprinted from Milman *et al.* [19], stands as the first direct experimental verification for the presence of VDT in the literature.

TL, where the signal is an immediate result of radiative recombination of free electrons generated by ionizing radiation the sample is exposed to [33]. PTTL appears in a wide variety of materials, so it was studied extensively; moreover, it was suggested as an alternative method for both radiation dosimetry and dating applications [34]. Chen and McKeever [35] had reviewed in detail previous related literature.

Up to 2010, PTTL was traditionally the most trustworthy and the unique indirect luminescence-oriented method to quantitatively measure part of the signal stored at VDTs. Akselrod and Gorelova [36] investigated the optical absorption and PTTL responses of $\alpha$-$Al_2O_3$:C crystals after isochronous annealing in air at 180–1080°C. These researchers concluded that at least three main types of

charge-carrier traps exist, which affect specific dosimetric parameters of $Al_2O_3$:C, such as their sensitivity to light and ionizing radiation and the linear dose dependence. Besides the main dosimetric hole trap, they monitored a deep hole trap annealed at 550–650°C, along with a deep electron trap with delocalization temperatures of 800–900°C. These results stand in excellent agreement with the results by Milman *et al.* [19] as well as Kortov *et al.* [22]. Bulur and Göksu [6] have also successfully measured PTTL from $\alpha$-$Al_2O_3$:C single crystals, by using a blue light emitting diode in order to induce photo-transfer of charges from deeper traps into the main dosimetric trap.

### 4.3. Thermally Assisted OSL (TA – OSL); the technique

Recently, Polymeris *et al.* [13] and later Soni *et al.* [37] have independently suggested an alternative experimental technique in order to not only measure the signal of VDT in $\alpha$-$Al_2O_3$:C without heating the sample at temperatures greater than 500°C, but also use this signal for high-dose-level dosimetry as well. The access to the OSL signal originating from VDTs is achieved by an experimental technique which comprises combined action of thermal and optical stimulation, termed Thermally Assisted OSL (TA – OSL).

According to TA – OSL, an irradiated sample is exposed to intensive light from blue LEDs at elevated temperature. This leads to carrier photo-transfer from VDTs to shallower traps. This experimental procedure is also termed photo-thermostimulation luminescence (PTSL) method [38]. The methodology is similar to that proposed earlier by Bulur and Göksu [6] for PTTL instead of OSL. However, in the case of TA – OSL, only the OSL signal is used instead of TL. In both techniques the phosphor is preliminarily heated to empty the shallow, main and deep traps. The phosphor is then exposed to intensive blue light for optical emptying of the traps, and for transferring of the charge carriers delocalized from VDT through the conduction band to the empty shallow traps, mostly at ambient temperatures. A subsequent TL measurement allows one to measure PTTL. The quite

long measuring procedure is a major drawback of the PTTL method. Moreover, not all the VDTs can be emptied with photo-stimulation.

The TA – OSL technique makes the elimination of these disadvantages possible. Simultaneous thermal and optical stimulation is an extremely complicated procedure, mostly due to being highly interactive. Besides thermal and optical stimulation, it could potentially give rise to another two simultaneous effects, namely the optically assisted thermal stimulation and the thermally assisted OSL [39]. However, these phenomena are usually negligible, since TA – OSL is registered after the sample was previously heated up to 500°C, emptying thus all TL traps within regions *I–III*.

### 4.3.1. *Isothermal TA – OSL*

The so-called isothermal TA – OSL technique was introduced by Polymeris *et al.* [13]. These authors have suggested an experimental protocol which involves the measurement of TA – OSL at a steady elevated temperature, similarly to isothermal TL. The protocol, which was initially suggested for $Al_2O_3$:C but later on was implemented to other materials as well, includes the following steps [14]:

- *Step 0:* Apply a low test dose to the (preferably previously annealed) sample,
- *Step 1:* TL measurement up to a specific maximum temperature between 400–500°C at 1°C/s ($TL_i$),
- *Step 2:* Apply a large dose $\mathbf{D_i}$ (Gy) to the sample,
- *Step 3:* TL measurement with parameters as in step 1 ($TL_d$),
- *Step 4:* Isothermal TL ($ITL$) at RT for 60 s,
- *Step 5:* Increase and hold temperature at $\mathbf{T_i}$ (°C); measure CW-OSL at this temperature for some preselected stimulation time t(s), in order to obtain the TA – OSL signal using optical stimulation intensity $\varphi$ ($\mathrm{mWcm^{-2}}$),
- *Step 6:* Residual TL ($RTL$) measurement with parameters as in steps 1 and 3,
- *Step 7:* Apply the same test dose as in step 0,
- *Step 8:* TL measurement with parameters as in steps 1, 3 and 6 ($TL_f$).

The term isothermal indicates that the main measurement of TA – OSL, being incorporated at step 5, is measured at steady elevated temperature. However, all the other steps are also important. The TL of step 1 measures the TL sensitivity of the phosphor before TA – OSL and the TL of step 3 depletes all shallow and deeper traps responsible for glow-peaks within regions *I–III*, so that only VDTs remain available for TA – OSL. The aim of step 4 is twofold [40], as well as mandatory when the TA – OSL measurements take place in Risø readers. This step ensures that the temperature of the hot plate is decreased to RT, since these readers are configured so that the next measurement will not take place until the hotplate temperature is 60°C or less. In addition, this step helps to check whether the PM tube suffers from saturation effects, and this control step is extremely useful while applying high doses to sensitive materials. The measurement of RTL in step 6 monitors the presence of possible residual TL signal; this helps to investigate whether the main measurement of step 5 is able to create PTTL by liberating electrons from VDT and to photo-transfer them via the conduction band into shallower traps. Finally, the TL glow curve of step 8 is used in order to monitor possible changes in sensitivity as well as in TL glow curve shape, by comparing it with the corresponding TL obtained during step 1. The maximum TL measured temperatures, as well as the test dose in steps 0 and 7, depend strongly on the materials studied as well as on the instrumentation used.

Two different experimental parameters of the protocol are highlighted in bold, namely the large dose applied during step 2 ($\mathbf{D_i}$) as well as the stimulation temperature ($\mathbf{T_i}$) of step 5. Both parameters are quite important; the dose $\mathbf{D_i}$ should be sufficient so that the VDTs are being populated, while the temperature $\mathbf{T_i}$ is the temperature at which the combined thermal and optical stimulation will take place. When the temperature increases up to $\mathbf{T_i}$, the stimulation light source is off. Nevertheless, the acquisition time for the TA – OSL signal in step 5 should be large enough, ranging between 500 and 2000 s at elevated temperature, which may lead to heating of the reader assembly. This is an additional limitation for adoption of this technique for routine dose measurements.

### 4.3.2. *TA – OSL under linear heating*

Due to the long acquisition duration, Soni *et al.* [37] suggested that TA – OSL should be measured by stimulating simultaneously with blue light and temperature using linear heating, so that the different components of this signal could be easily resolved. According to these authors, the maximum heating temperature was limited to 400°C, while the readout time was up to 120 s. The following experimental protocol which gives access to VDTs was formulated [37, 41]:

- *Step 1:* Apply a large dose $\mathbf{D_i}$ (Gy) to the (preferably previously annealed) sample,
- *Step 2:* TL measurement up to a specific maximum temperature between 400–500°C at 1°C/s,
- *Step 3*: Blue OSL at the continuous wave mode, and simultaneous TL measurement at a constant heating rate $\boldsymbol{\beta_i}$ (K/s) up to the same temperature as in step 2; optical stimulation intensity $\boldsymbol{\varphi_i}$ ($\mathrm{mWcm^{-2}}$),
- *Step 4:* Residual TL (RTL) measurements with parameters as in step 2.

Step 3, involving combined TL and OSL measurements, stands as the main innovation of the specific TA – OSL protocol. The basic role of TL measurement of this step is to provide thermal assistance to the OSL as a function of temperature. However, since all peaks up to 400–500°C have been drained out previously in step 2, the TL measurement records also the PTTL from VDT. The TA – OSL measurement of step 3 resembles closely the thermally modulated optically stimulated luminescence (TM-OSL) technique [42], especially if step 2 is omitted; then the protocol becomes a protocol for combined thermal and optical stimulation of an electron trap within regions *II–III* [42].

For this protocol, three different experimental parameters are highlighted in bold, namely the given dose ($\mathbf{D_i}$) as well as the linear heating rate $\boldsymbol{\beta_i}$ and the stimulation intensity $\varphi_i$ of the TA – OSL measurement. As the main goal of the TA – OSL under linear heating

is to resolve the various components of the TA – OSL signal, the selection of these two stimulation parameters is very important.

### 4.3.3. *Thermal quenching and correction*

The decrease of luminescence efficiency with increasing temperature due to the increased probability of non-radiative transitions is known as thermal quenching [43]. Thermal quenching is attributed to the so-called Mott-Seitz mechanism, which takes into account the competition between the radiative and non-radiative recombination [16, 43]. According to this model, the thermal quenching internal efficiency versus temperature, $\eta(T)$ is given by the following equation [43]:

$$\eta(T) = \frac{1}{1 + Ce^{-\frac{W}{k\,T}}} \tag{2}$$

where $C$ and $W$are called the "quenching parameters" and $T$ is the absolute temperature in units of K. $C$ is a dimensionless constant which is the ratio of the non-radiative transition probability to the radiative transition probability [44]. The physical meaning of the $W$(eV) parameter depends on the specific model adopted for explanation [43, 44].

As TA – OSL measurements include the combined action of thermal and optical stimulation, the presence of the thermal quenching effect is expected to substantially suppress the TA – OSL intensity. Therefore, in luminescence dosimeters such as aluminum oxide [15] and quartz [16], for which thermal quenching has been reported, the appropriate correction is required. This correction, also known as reconstruction [45], is different for the two TA – OSL protocols. For the case of isothermal TA – OSL, as the entire measurement takes place at a steady temperature $T_{meas}$, the unquenched integrated TA – OSL intensity $I_{uq}(T_{meas})$ can be identified using the following formula:

$$I_{uq}(T_{meas}) = \frac{I_q(T_{meas})}{\eta(T_{meas})} \tag{3}$$

where $I_q(T_{meas})$ and $I_{uq}(T_{meas})$ are the integrated TA – OSL intensities which are quenched and unquenched respectively, and

$\eta(T_{meas})$ corresponds to a single value of the thermal quenching efficiency at the specific measurement temperature. For the case of TA – OSL measured with linear heating, a glow curve is measured throughout a wide temperature range. This unquenched glow curve $I_{uq}(T)$ can be identified using the following formula [45]:

$$I_{uq}(T) = \frac{I_q(T)}{\eta(T)} \tag{4}$$

Unlike Eq. (3), the entire glow curve is used instead of the integrated intensity of the TA – OSL. This is the reason why the notation is somehow different for Eq. (4), namely all three physical quantities $I_{uq}$, $I_q$ and $\eta$ are expressed as a function of $T$ instead of $T_{meas}$. According to the reconstruction procedure, each experimental data point of the glow curve corresponding to a specific temperature, is divided by the corresponding thermal quenching efficiency which also depends on the temperature through the $W$ and $C$ values.

### 4.4. TA – OSL decay curve shapes and dependence on the stimulation parameters

TA – OSL under linear heating was suggested by Soni *et al.* [37] since the corresponding TA – OSL curve is expected to resemble the shape of a typical TL glow curve, consisting of various prominent peaks. Typical experimentally obtained TA – OSL curves under linear heating are presented in Fig. 2 for two different cases, namely $Al_2O_3$:C, and Durango apatite (plots a and b respectively); these materials were selected since they yield intense TA – OSL signals. In addition to the TA – OSL curves, this figure also shows the TL glow curves measured from step 2, and the RTL signal from step 4 of the protocol. The TA – OSL curve of $Al_2O_3$:C indeed yields at least three overlapping peaks, similar to Ref. [37].

In addition to the original experimental data, Fig. 2a presents examples of both reconstructed TL and RTL, as well as reconstructed TA – OSL glow curves for $Al_2O_3$:C. Reconstruction was performed according to Eq. (4) throughout the entire curve, using the values of the thermal quenching parameters suggested by Dallas *et al.* [45], namely $W = 1.085\,\text{eV}$ and $C = 3.71 \cdot 10^{12}$. The comparison between

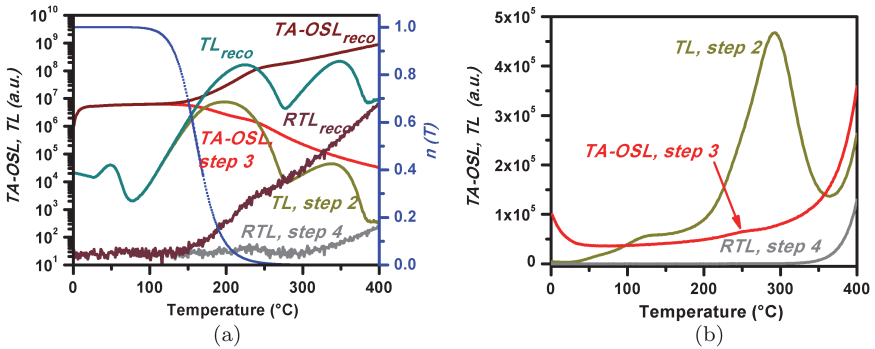


Fig. 2. Experimental TL glow curves (step 2), TA – OSL curves under linear heating (step 3) and RTL glow curves (step 4) according to the corresponding measurement protocol for (a) $\alpha$-$Al_2O_3$:C single crystal and (b) Durango apatite. For the former case, reconstructed TL and TA – OSL curves according to Eq. (4) (with the index *reco*) are also presented. The blue dotted line corresponds to the thermal quenching efficiency $\eta(T)$ according to Eq. (2), using the values for the thermal quenching parameters $W$ and $C$ reported by Dallas *et al.* [45].

the unquenched and quenched TA – OSL glow curves reflects clearly the strong influence of thermal quenching on the shape as well as the intensity of the corresponding curves. Reconstruction does not change the number of prominent TA – OSL components. The most important piece of information that the reconstructed glow curve provides, deals with the huge difference between the quenched and the reconstructed TA – OSL intensity, especially in the high temperature region.

Figure 2b shows that in the case of Durango apatite the shape of the TA – OSL under linear heating does not yield prominent peaks; instead, a smooth continuum is observed. Optical stimulation becomes dominant at ambient temperatures; this is the reason why an initial rapidly decaying part is monitored, corresponding to a fast TA – OSL signal. Nevertheless, as the heating further proceeds, thermal stimulation becomes more intense and the signal shape changes further, yielding indications for a TA – OSL peak centered around 530 K and an intense rising part of a TA – OSL peak having its maximum above 700 K. Similar TA – OSL features were also obtained for the case of quartz with one notable exception; the

TA – OSL of quartz yields a smooth continuum, without any obvious indication for the presence of a TA – OSL peak within the measurement temperature range.

Figures 3 and 4 show the dependence of the shape of TA – OSL signals under linear heating on two stimulation parameters, namely the heating rate $\boldsymbol{\beta_i}$ as well as the intensity of the optical stimulation $\boldsymbol{\varphi}_i$, for $Al_2O_3$:C and sedimentary quartz respectively. In both figures, plot (a) shows the decay curves of TA – OSL under linear heating

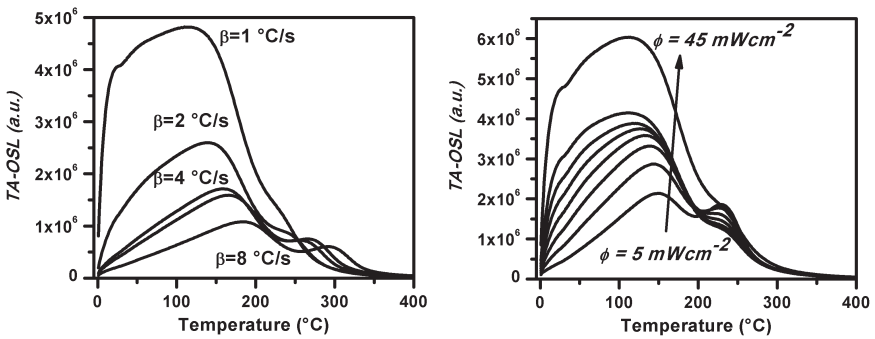


Fig. 3. Experimental TA – OSL curves under linear heating for $Al_2O_3$:C, versus (a) the heating rate and (b) the stimulation power from 5 to 45 $\mathrm{mWcm^{-2}}$ in steps of 5 $\mathrm{mWcm^{-2}}$.

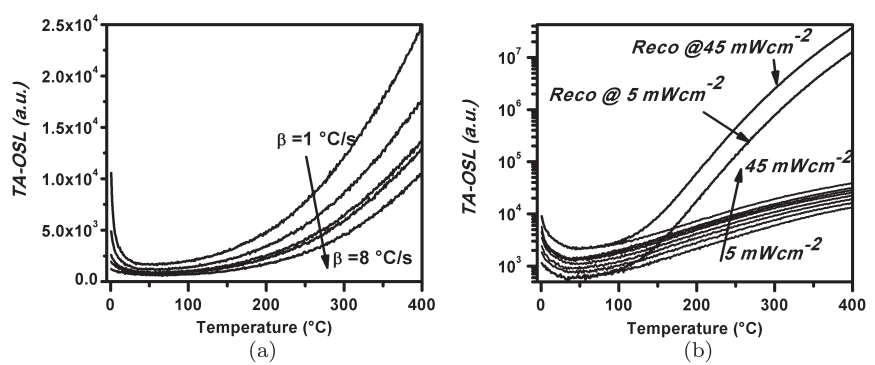


Fig. 4. As in Fig. 3, but for the case of sedimentary quartz. For this case, reconstructed TA – OSL curves according to Eq. (4) (labeled *Reco*) are also presented for the extreme values of optical stimulation intensities.

for heating rates of 1, 2, 4, 5 and 8°C/s, while plot (b) shows TA – OSL measured using various optical stimulation intensities ranging between 10% and 90% of the maximum stimulation intensity ($50\,\mathrm{mWcm^{-2}}$) in steps of 10% ($5\,\mathrm{mWcm^{-2}}$). Similar features are observed for both phosphors, such as the increase of the TA – OSL intensity as the optical stimulation intensity increases. For the cases where prominent TL peaks are seen, the TA – OSL glow peaks shift to higher temperatures as the heating rate increases. In the case of $Al_2O_3$:C, the two TA – OSL lower temperature peaks overlap as the heating rate increases, providing indications for the presence of two prominent TA – OSL peaks. This feature is in good agreement with the experimental data of Ref. [37]. In this latter publication only two TA – OSL components were reported, since the very low temperature peak around 300 K is not observed. This is because the measurements by these authors begin at 323 K, and a heating rate of 4°C/s was used. A one-to-one correlation was established between these two TA – OSL components and the corresponding VDTs; it was reported by Soni *et al.* [37] that these two peaks correspond to the two different deep traps being emptied at about 650°C and 900°C respectively [36].

Figure 4b also presents, for the case of quartz, the reconstructed TA – OSL curves under linear heating for the minimum and the maximum stimulation intensities. Once again, reconstruction was performed according to Eq. (4) using the values of the thermal quenching parameters suggested by Subedi *et al.* [16], namely $W = 0.67\,\mathrm{eV}$ and $C = 2.71 \cdot 10^7$. The reconstruction reveals the real shape of the TA – OSL curve. Nevertheless, even in the reconstructed TA – OSL curve, there is no indication for the presence of any prominent peak, despite the numerous TL peaks of the corresponding TL glow curve. Finally, it is worth mentioning the decrease of the TA – OSL integrated intensity as the thermal assistance heating rate increases, for both cases of luminescence phosphors. For $Al_2O_3$:C and quartz, this decrease could also be attributed to the thermal quenching effect [15, 16]. It is safe to conclude that the shape of the TA – OSL decay curves under linear heating does not change. Figures 3 and 4

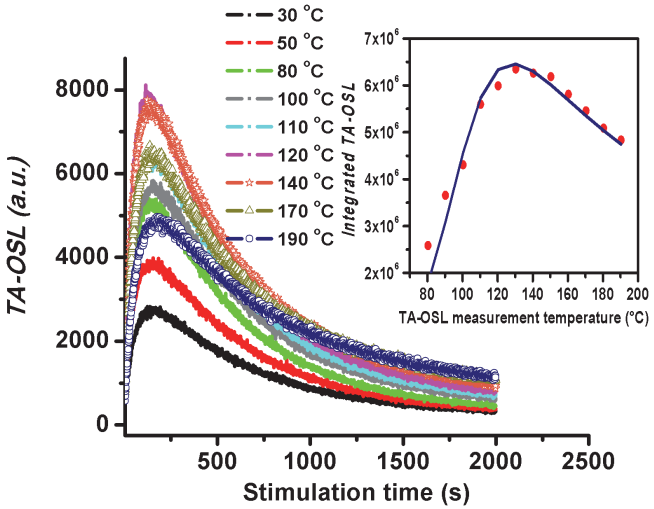


Fig. 5. A selection of isothermal TA – OSL curves for $Al_2O_3$:C grains with double main TL peak structure; reprinted from Polymeris and Kitis [14]. Inset: Integrated TA – OSL signal intensity versus stimulation temperature for double-peak-structure samples corresponding to 500 Gy. The solid line through the data points is the best fit of Eq. (6).

highlight the importance of the stimulation parameters $\boldsymbol{\beta_i}$ and $\boldsymbol{\varphi}_i$ on the deconvolution of the various TA – OSL peaks.

Figure 5 presents the isothermal TA – OSL curves for $\alpha$-$Al_2O_3$:C grains reported by Polymeris and Kitis [14], for various increasing measurement temperatures between RT and 190°C. As this measurement temperature increases, the signal forms a narrow peak for short stimulation times, rather than resembling the decaying shape of an ordinary CW-OSL curve. The rather unusual peak shaped TA – OSL curves measured at the continuous wave configuration, resemble both typical linearly modulated OSL (LM-OSL) curves, as well as the plot in Fig. 2 of Ref. [6], where the integrated PTTL intensity (in the region 140–240°C) is plotted as a function of illumination time. This specific peak shape of the isothermal TA – OSL curve for the case of $\alpha$-$Al_2O_3$:C was also verified by time-resolved TA – OSL measurements (TA – TR – OSL, [46]). Similar peak or bell shaped

TA – OSL curves were obtained for the cases of $CaF_2$:N throughout a range of measuring temperatures [47], and for BeO at two different measurement temperatures of 200°C and 220°C [39]. However, a thorough TA – OSL study still lacks from the literature for this latter material. At the same time, peak-shaped TA – OSL curves have been reported as being typical for charge transfer effects [35, 47].

In most luminescence phosphors, including various types of quartz, feldspars, salt and apatites, isothermal TA – OSL yields a typical featureless decaying OSL curve shape, similar to that reported for the cases of conventional OSL. Figure 6 presents such TA – OSL curves obtained for Durango apatite (plot 6a, [48]), for salt (plot 6b) as well as for quartz (plot 6c, [40]) for a selection of stimulation temperatures. These figures show that the featureless decaying shape of the isothermal TA – OSL curves does not change significantly with stimulation temperature. Only the intensity is dramatically changing in both cases with increasing stimulation temperature. Moreover, after 300s of stimulation at the optimum temperature, the signal becomes flat with stable intensity almost one order of magnitude higher than the ordinary OSL dark count background level of ∼40–60 counts/s.

This feature is prominent in the case of quartz and salt samples, providing thus experimental hints towards the presence of a second TA – OSL component, especially in quartz. The stimulation time after which the signal becomes flat depends strongly on the phosphor. In order to study further this specific flat signal, sequential TA – OSL measurements applied to the same aliquot were reported after the typical TA – OSL measurement at 180°C [40]. These curves were obtained for the temperature range between 200 and 280°C. All curves exhibit similar features, such as the absence of any initial and fast decaying part; instead, a very slowly decaying signal was observed, the shape of which is extremely flat with very large intensity. It is worth emphasizing that with increasing stimulation temperature the intensity of this flat TA – OSL component is also increased, reaching the level of 2000 counts/s for stimulation at 280°C, further supporting the fact that this signal corresponds to a very slowly decaying TA – OSL component.

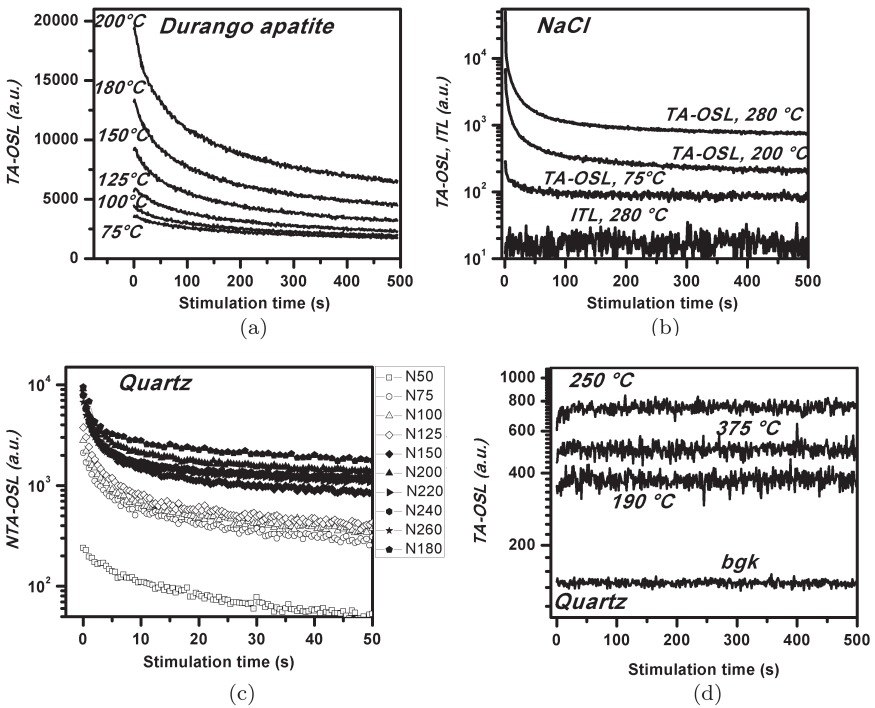


Fig. 6. Isothermal TA – OSL curves measured at a selection of stimulation temperatures ranging between 50°C up to 280°C for the cases of (a) Durango apatite after artificial irradiation [48]; (b) salt after artificial irradiation; (c) sedimentary quartz naturally irradiated, NTA - OSL [40] and (d) sedimentary quartz after artificial irradiation [49]. Plot (b) presents also, among others, an ITL measurement at 280°C according to step 5 without optical stimulation.

Similar, very slowly decaying TA – OSL signals without an initial and fast decaying part, were so far reported only for the cases of quartz and geological $CaCO_3$ [49–51], even for lower stimulation temperatures. A selection of such TA – OSL curves from quartz is presented in Fig. 6d. The experimental features of the TA – OSL signal in the case of polymineral samples resemble closely the corresponding TA – OSL features of pure quartz in terms of glow-curve shape, as well as the signal intensity and its dependence on the stimulation temperature [52]. Finally, it is worth emphasizing that, while for the case of $\alpha$-$Al_2O_3$:C, peak shaped isothermal TA – OSL

curves are observed, for the case of $\alpha$-$Al_2O_3$:C,Mg the corresponding isothermal TA – OSL curves have a featureless decaying shape [53].

### 4.5. Residual TL, PTTL and changes in sensitivity and glow curve shapes

The presence of RTL signals in both TA – OSL protocols indicates that the main measurement in TA – OSL protocols is able to create PTTL, by liberating electrons from VDTs. PTTL then becomes of great interest in TA – OSL studies. When PTTL is absent, then the TA – OSL signal is attributed to direct stimulation of electrons from VDTs and to their subsequent recombination. In this case TA – OSL is considered as a one-step effect. On the other hand, when PTTL is observed, then the TA – OSL possibly originates either directly from the VDT, or indirectly from the shallower trap, to which electrons are photo-transferred from the VDT. Therefore, PTTL should be always taken under consideration in the interpretation of the TA – OSL results, and its role will be crucial for any future modeling and simulations of TA – OSL phenomena. Furthermore, PTTL is the only experimental verification of the theoretical prediction that electrons released from one trap can be re-trapped into another electron trap active at lower temperatures. It must be noted, however, that there is no experimental verification of the opposite effect, i.e. that electrons released from a shallow trap can be re-trapped into a deeper trap.

For the majority of the phosphors that yield intense TA – OSL, the RTL glow curves do not yield TL peaks; instead, independent of dose, stimulation temperature and TA – OSL stimulation mode, the RTL curves resemble much a typical background noise signal. This feature can be seen in Fig. 2b. At the same time, in all these materials the shape of a typical isothermal TA – OSL curve is similar to conventional decaying CW-OSL curve. In addition, in the corresponding TA – OSL under linear heating, no obvious peaks are seen and a smooth continuum is observed instead.

A notable exception is $Al_2O_3$:$C$ where intense RTL glow curves are observed, independent of the TA – OSL stimulation mode (i.e. in both isothermal or linear heating TA – OSL). In general, the features

of the RTL glow curve are sample dependent, as three different types of glow curves were reported for the main dosimetric peak of $Al_2O_3$:C, namely "narrow", "wide" and "double" TL glow-peak structures [14, 25, 45, 54].

Three ubiquitous features have been reported. First, almost all RTL glow curves after isothermal TA – OSL appear as double TL peaks, composed of TL peaks at 185°C and ∼250°C. This feature can be seen in Fig. 7a, where typical TL and RTL glow curves of $Al_2O_3$:C are presented, according to the protocol for isothermal TA – OSL. This feature is independent of the TL shape of the main dosimetric peak. As the TL peak of $Al_2O_3$:C with peak position at ∼250°C is associated with a hole trap [14, 55], this experimental feature highlights the presence of free holes, besides electrons. Second, despite the fact that the RTL integrated intensity depends strongly on the initially applied dose, it increases sub linearly with the dose up to 250–300 Gy. At larger doses the signal is almost stable for the dose region between 250 and 2000 Gy as seen in Fig. 7b. Third, the integrated RTL intensity is large, even though it is at least 2–3

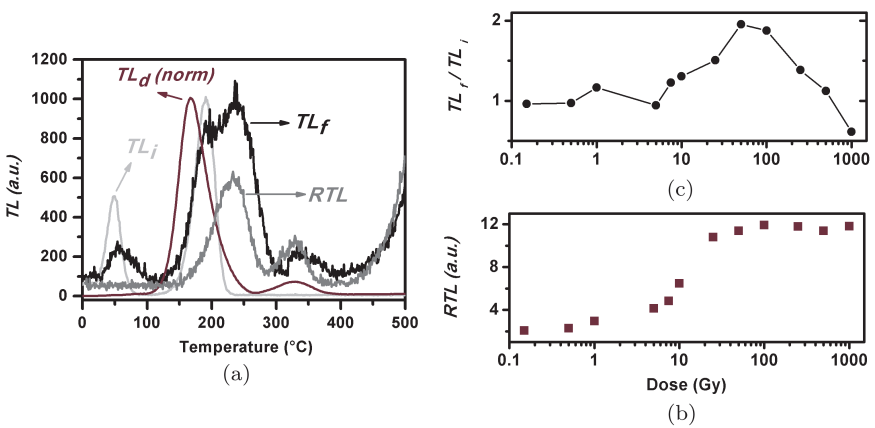


Fig. 7. (a) A selection of TL and RTL glow curves for $Al_2O_3$:C grains after isothermal TA – OSL, measured for 1000 Gy; step 1 ($TL_i$), step 3 ($TL_d$), step 6 ($RTL$) and step 8 ($TL_f$). Plot (b) presents the dose response curve for the case of integrated RTL after isothermal TA – OSL, while plot (c) presents the sensitivity changes in terms of the ratio $TL_f/TL_i$ versus dose $\mathbf{D_i}$ of step 2. Reprinted from Polymeris and Kitis [14].

orders of magnitude lower than the corresponding TA – OSL. It is important to note that the RTL signal measured after the TA – OSL in the framework of both protocols, includes the afterglow emission due to radiative relaxation of unstable centers, in addition to the high temperature blue stimulated OSL component.

A careful comparison between Figs. 2a and 7a indicates that the positions of the TL and PTTL glow curve peaks and those of the TA – OSL peaks coincide. However, this conclusion contradicts the results of Soni *et al.* [37]. The presence of the hole trap responsible for the 250°C peak is unambiguous to all PTTL curves, both in $Al_2O_3$:C grain or single crystal samples, regardless of the type of glow peak structure. This peak was also linked to the occupancy of VDTs by Nikiforov *et al.* [56]. Initially, the optical stimulation liberates electrons from VDTs, with a fraction of them being re-captured to electron traps instead of recombining. Under linear heating and as long as the temperature is lower than 185°C, which represents the peak position of the main dosimetric peak, electrons are re-captured into the main dosimetric trap. However, during isothermal TA – OSL measurements, electrons are re-trapped in other traps besides the dosimetric trap. Subsequently these trapped electrons are thermally stimulated giving rise to PTTL. Therefore, TL, PTTL and TA – OSL use the same traps besides the main dosimetric one. The strong RTL and PTTL signals provide a clear indication regarding the recombination pathway of TA – OSL in the case of $Al_2O_3$:C where electrons recombine through the conduction band. Nyirenda *et al.* [46] have compared the luminescence lifetimes for OSL and TA – OSL, which were evaluated by fitting the decay component of the time resolved signal. Their results agree with the proposition that following optical stimulation from VDTs, electrons redistribute via the conduction band into the shallow and intermediate energy electron traps of regions *I–III*.

Unfortunately, this conclusion has been verified only for the case of $Al_2O_3$:C via TA – TR – OSL. According to Ref. [39], the shape of the TA – OSL curves could be used as a probe in order to distinguish the recombination pathways of these signals. The presence of the peak-shaped TA – OSL curve, in either stimulation

mode, in conjunction with a strong PTTL signal, could be considered as being typical of transfer effects taking place via the conduction band. This conclusion is further supported by the model adopted for the fitting of these curves in the case of $CaF_2$:N [47]. The typical featureless decaying isothermal TA – OSL curve shape could possibly correspond to recombination pathways which do not take place via the conduction band, such as tunneling recombination.

The majority of studies on TA – OSL signal originating from VDTs have been devoted to $Al_2O_3$:C, in both forms of powder (Landauer Inc.) and single crystals (The Ural State Technical University, Russia) [13, 14, 37, 41, 57, 58]. The active interest in VDTs was initiated for this material due to the pronounced effect that these traps have on the trapping parameters of the main dosimetric TL peak. Changes in sensitivity, sensitization and TL shape induced by TA – OSL were studied only for $Al_2O_3$:C. The changes in sensitivity and TL shape were investigated using the TL glow curves measured at step 8 of the isothermal TA – OSL protocol, by comparing them with the TL glow curves obtained at step 1 of the same protocol and for each dose. The glow curve shape was altered after TA – OSL, and the peak at ∼250°C became ubiquitous. Due to the presence of this latter TL peak, sensitization could be expressed in terms of the ratio $TL_f/TL_i$ solely for the 185°C TL peak, with $TL_f$ corresponding to the de-convolved signal of this aforementioned TL peak. The results are presented in Fig. 7c. TA – OSL in conjunction with heavy irradiations induces sensitization as well as de-sensitization; these features are both material and dose dependent. Similar results were also reported by Polymeris and Kitis [14].

An increasing sensitivity for the main dosimetric TL peak of $Al_2O_3$:C dosimeters due to previous TA – OSL measurements was also reported by Meriç *et al.* [58]. However, no change has been observed for the shapes of either the TL or the TA – OSL curves. Ref. [58] has provided further experimental evidence towards establishing the dependence of both TL and TA – OSL sensitivity and sensitization on the occupancy of these VDTs, in excellent agreement with previous published results [59]. The sensitivity changes which

are induced after long-term use for TLD 500 dosimeters, are directly attributed to the occupancy of VDTs. The application of TA – OSL is highly suggested for these materials after long-term use, as it minimizes the induced sensitization [58].

### 4.6. Thermal assistance

During the simultaneous photo-thermostimulation process, heating enhances electron energy in the traps, so that photons of lower energy succeed in emptying the very deep traps sufficiently. This is the reason why the method was termed thermally assisted OSL. In all thermally assisted processes, the signal intensity is expected to rise with increasing stimulation temperature [35]. This feature is the main experimental difference between the TA – OSL and the conventional OSL signal. Measuring isothermal TA – OSL for various increasing stimulation temperatures has been a standard approach in isothermal TA – OSL studies of various materials.

The reason for these studies is threefold, as follows. The first goal of these studies is to verify the thermally assisted nature of the signal, by monitoring the increase of the signal versus increasing stimulation temperature. Even though this increase has been observed in the majority of the experimental studies in the literature [47–49, 60, 61], in some cases, such as $Al_2O_3$:C yielding double-structured main TL peak [14] and quartz [40], this increase is not monotonic throughout the entire temperature region, yielding a decreasing signal intensity especially for higher stimulation temperatures. Figures 5, indicate this feature, where the isothermal TA – OSL signal intensity is presented for $Al_2O_3$:C. TA – OSL is increasing for stimulation temperatures up to 140°C, but decreasing for higher temperatures. This feature is attributed to the effect of thermal quenching [15]. As each isothermal TA – OSL of Fig. 5 was measured at a steady temperature, reconstruction is required according to Eq. (3), using the values of the thermal quenching parameters suggested in Ref. [45]. After correction, the intensity is monotonically increasing with stimulation temperature throughout the entire temperature region studied, yielding an exponential behavior.

The second goal of these studies is to identify the optimum stimulation temperature $\mathbf{T_i}$ of isothermal TA – OSL in step 5; this stimulation parameter needs to be experimentally defined for each phosphor. The criterion for such a selection includes the presence of a signal with enhanced signal to noise ratio. Special care should be taken in order to prevent retrapping of charge evicted from the VDT into shallow or main dosimetric TL peaks. This feature was taken under consideration in selecting the measurement temperatures for quartz. The experimentally selected values for the stimulation temperature $\mathbf{T_i}$ of TA – OSL lie within the 180–220°C temperature range for all materials. Special emphasis should be placed on the fact that while measured at RT or ambient temperatures, TA – OSL could still indicate a measurable signal, as both Figs. 5 and 6c clearly indicate.

The third goal in these studies is to study the rate of such thermally assisted processes. This rate is usually expressed by the Arrhenius equation which leads to the concept of the thermal activation energy (or alternatively thermal assistance energy), $E_A$ (in eV). In all cases, the TA – OSL signal originates from VDTs with activation energy values well above 2 eV. Due to the simultaneous thermal and optical stimulation, $E_A$ indicates the quantity of energy supplied in the form of pure thermal energy so that trapped charges can be released from a VDT. This $E_A$, is nothing but the sum of the series of quanta of all possible vibrational energy states associated with the ground state of the VDT, at the elevated temperature of TA – OSL measurement.

The theoretical formulation for determining the thermal assistance energy has been very helpful in explaining the mechanism of TA – OSL stimulation. At high temperatures, the activation type dependence $e^{(-E_A/kT)}$ plays an important part, with the activation energies $E_A$ depending on the actual structure of the given traps. According to this approach, the decay constant of OSL curve was observed to follow Arrhenius law, which may be interpreted as a temperature dependence of the photo-ionization cross-section $\sigma$ (in $cm^2$), and the decay constant is the product of $\sigma$ and the stimulation flux $\varphi$. It has been suggested that the photo-ionization

cross-section consists basically of two parts, one being temperature independent and the second is a temperature dependent exponential term, described by the equation [8, 62]:

$$\sigma(T,\lambda) = \sigma_0(T,\lambda)e^{-E_A/kT} \tag{5}$$

where $\sigma(T,\lambda)$ is the photo-ionization cross-section at temperature $T(K)$ and stimulation wavelength $\lambda$, which is not influenced by thermal perturbations, $k$ is Boltzmann's constant and $\sigma_0(\lambda)$ is the pre-exponential photo-ionization cross section. This cross section is independent of measurement temperature and could be considered as the value of photo-ionization cross-section with thermal assistance of energy from 0 K to room temperature [37, 63]. According to this equation, the values of this $\sigma$ parameter are expected to increase with increasing measurement temperature. The photo-ionization cross-section is a parameter of major interest in the OSL phenomenon, since it is related to the electron eviction probability while applying optical stimulation. This parameter attains values of the order of $10^{-20}$–$10^{-16}\,\mathrm{cm}^2$ or even lower.

The same activation type dependence $e^{(-E_A/kT)}$ holds for the TA – OSL intensity as well. In all thermally assisted processes, the plot of *ln(TA – OSL)* versus $1/kT_{meas}$ (where $T_{meas}$ stands for the measurement temperature and $k$ is the Boltzmann constant) yields a linear part with a slope corresponding to the thermal assistance energy, $E_A$. Typical thermal assistance activation energies reported so far in the literature are $0.37 \pm 0.02\,\mathrm{eV}$ for $CaF_2$:N [47], $0.28 \pm 0.01\,\mathrm{eV}$ for apatites [48], $0.32 \pm 0.06\,\mathrm{eV}$ for K-feldspars [52], $0.667 \pm 0.006\,\mathrm{eV}$ for $Al_2O_3$:C,Mg [53], $0.21 \pm 0.02\,\mathrm{eV}$ for enamel [64] and $0.47 \pm 0.03\,\mathrm{eV}$ for salt. These values were reported to be prevalent for 3 different samples of halites, as well as 5 different samples of apatites [48]. For the cases of quartz and aluminum oxide, the reported values were calculated by incorporating a correction for thermal quenching, enabling thus the evaluation of the unbiased thermal assistance energy $E_A$ values for these samples. Polymeris *et al.* [40] have demonstrated that the thermal quenching effect results in a severe underestimation of the thermal assistance activation energy of quartz, being calculated as $0.28 \pm 0.02\,\mathrm{eV}$ and $0.47 \pm 0.03\,\mathrm{eV}$ without

and with thermal quenching correction respectively. In addition to the thermal quenching correction shown in Eq. (3), another alternative methodology for evaluating the $E_A$ has been proposed very recently [65]. As thermal assistance and thermal quenching are geminate and thermodynamically separable effects, the luminescence emission which is subject to both effects, can be expressed by the following formula:

$$I_{TA-OSL}(T) = \frac{I_0 \prod_i^n exp\left(\frac{-E_{Ai}}{kT}\right)}{1 + Cexp\left(\frac{-W}{kT}\right)} \tag{6}$$

where $I_0$ is the initial TA – OSL intensity and $E_{Ai}$ is the activation energy for thermal assistance of the i$^{\text{th}}$ electron trap. The use of this expression implies that, beside $E_{Ai}$, more parameters are also included within the list of the fitting parameters, namely $W$ and $C$.

The maximum value of thermal assistance energy was monitored for the case of $Al_2O_3$:C grains with a single main TL peak, being around $1.21 \pm 0.03$ eV [13]. Moreover, the TA – OSL isothermal curves of Fig. 5 fitted using Eq. (6) and presented at the inset of Fig. 5, indicated the presence of two VDTs, with $E_{A1} = 0.196 \pm 0.007$ eV and $E_{A2} = 0.898 \pm 0.011$ eV, along with the values $W = 0.976$ eV and $C = 4.5 \cdot 10^{12}$ for the thermal quenching parameters. Finally, it is worth mentioning that the slowly decaying component in quartz yielded a corresponding Arrhenius plot which is also linear. $E_A$ value of almost 1 eV was obtained after incorporating correction for thermal quenching, further supporting thus the presence of two different TA – OSL components for the case of quartz; this result was obtained for 7 different quartz samples in two different reports [40, 49].

For the case of TA – OSL under linear heating, calculation of $E_A$ does not require multiple measurements. Since the initial-rise part of the TA – OSL curve is governed by the Arrhenius type dependence $e^{(-E_A/kT)}$, the plot of ln (TA – OSL) vs. 1/kT for the initial part of the curve, gives a linear plot with the slope of the thermal assistance energy $E_A$. Soni *et al.* [37] have adopted this methodology towards estimating the photo-ionization cross section for each one of their two components in $Al_2O_3$:C.

The TA – OSL parameters for their 232°C peak were found to be $E_{A2} = 0.485\,\text{eV}$, with corresponding $\sigma_2\,(300\,\text{K}, \lambda) = 3.70 \cdot 10^{-22}\,\text{cm}^2$, while that of the dosimetric traps $\sigma\,(300\,\text{K}, \lambda)$ was $1.80 \cdot 10^{-18}\,\text{cm}^2$. For the corresponding peak observed at 121°C, $E_{A1} = 0.265\,\text{eV}$, with corresponding $\sigma_1\,(300\,\text{K}, \lambda) = 5.82 \cdot 10^{-20}\,\text{cm}^2$. It is worth emphasizing that the value of 0.485 eV is quite underestimated compared to the values of 0.898 eV according to Eq. (6), as well as compared with the value 1.2 eV of Ref. [13] from isothermal TA – OSL data; this discrepancy could be attributed to the fact that $E_{A2}$ was calculated without incorporating a correction for thermal quenching. The photo-ionization cross-section of the trap becomes $7.64 \cdot 10^{-19}\,\text{cm}^2$ at 232°C, a value comparable to that of the main dosimetric trap at room temperature [37]. For the case of quartz, preliminary results indicated that $\sigma_q\,(300\,\text{K}, \lambda) = 1 \cdot 10^{-23}\,\text{cm}^2$ and $\sigma_q\,(480\,\text{K}, \lambda) = 3 \cdot 10^{-18}\,\text{cm}^2$, while the corresponding value or the fast component of the conventional OSL signal was of the order of $10^{-17}$–$10^{-18}\,\text{cm}^2$.

### 4.7. Numerical simulations of TA – OSL process using the OTOR model

Detailed simulations of TA – OSL have been carried out, in both the constant heating rate method and in the isothermal stimulation modes, by using the well-known OTOR model. The differential equations governing the traffic of electrons between one trapping level, the recombination center and the conduction band in the OTOR model are [35]:

$$\frac{dn}{dt} = -np(t) + n_c(N - n)A_n \tag{7}$$

$$\frac{dn_c}{dt} = np(t) - n_c(N - n)A_n - n_c m A_m \tag{8}$$

$$-\frac{dm}{dt} = n_c m A_m \tag{9}$$

where $N\,(\text{cm}^{-3})$ is the total concentration of electron traps in the crystal, $n(T(t))\,(\text{cm}^{-3})$ is the concentration of the filled electron traps in the crystal, $n_c(T(t))\,(\text{cm}^{-3})$ is the concentration of the free

carriers in the conduction band, $m(T(t))\,(\mathrm{cm}^{-3})$ is the concentration of the holes in centers in the crystal, $A_n\,(\mathrm{cm}^3\,\mathrm{s}^{-1})$ is the capture probability coefficient of the electron traps and $A_m\,(\mathrm{cm}^3\,\mathrm{s}^{-1})$ is the capture probability coefficient of the recombination center. The charge neutrality condition is:

$$m = n + n_c \tag{10}$$

In the standard OTOR model the probability rate of escape per second of a trapped electron, $p(t)$, is taken to be equal to the rate of thermal or optical stimulation of the electrons into the conduction band. In our numerical approach of the TA – OSL process in this section another approximation is adopted, by taking into account that the stimulation is neither purely thermal nor optical, but both types of stimulation are present instead [66]. As the thermal stimulation and the optical photo-ionization are entirely different interaction processes, the total stimulation probability can be expressed as:

$$p(t) = se^{-\frac{E}{kT}} + \varphi_0 \cdot \sigma(T,\lambda) = se^{-\frac{E}{kT}} + \varphi_0 \cdot \sigma_0(T,\lambda)e^{-E_A/kT} \tag{11}$$

where $E$ is the activation energy of the VDT and $\varphi_0$ the intensity of the optical stimulation. Two different sets of simulations were carried out. In simulations of the TA – OSL method with constant linear heating rate, the temperature was selected to increase linearly with time. In the simulations of isothermal TA – OSL, the temperature in Eq. (11) is kept constant.

Figure 8 shows the results of the simulations in the case of TA – OSL with a linear heating rate, and Fig. 9 shows the simulation results for the isothermal TA – OSL mode.

The kinetic parameters of the very deep trap in the model were chosen as $\mathrm{E} = 2.5\,\mathrm{eV}$ and $\mathrm{s} = 10^{15}\,\mathrm{s}^{-1}$, corresponding to a TL peak position at 510°C. The thermal activation parameter for the TA – OSL cross section was chosen as $E_A = 0.241\,\mathrm{eV}$, and the optical stimulation parameters as $\varphi_0 = 33.3\,\mathrm{mW{\cdot}cm}^{-2}$, $\sigma_0 = 4 \cdot 10^{-16}\,\mathrm{cm}^2$. The parameters in the OTOR model were: $N = 10^{10}\,\mathrm{cm}^{-3}$, $A_m = 10^{-7}\,\mathrm{cm}^3\,\mathrm{s}^{-1}$, $A_n = 10^{-10}\,\mathrm{cm}^3\,\mathrm{s}^{-1}$, $\beta = 2\,\mathrm{K/s}$. It was assumed that as a result of the irradiation stage the traps are saturated at the beginning of the heating stage, so that

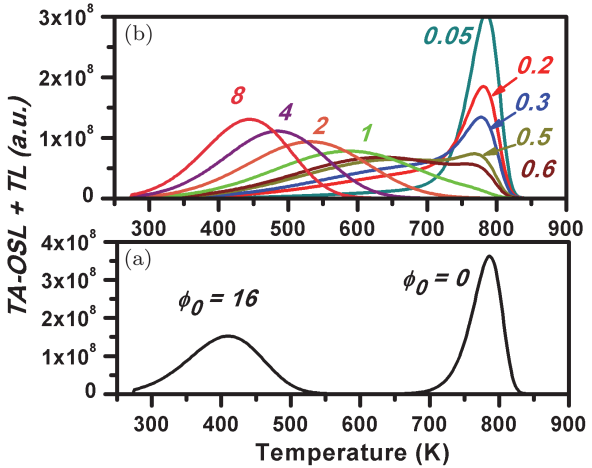


Fig. 8. The relationship between the TA – OSL signal and its origin, which is an electron VDT. The arithmetic values correspond to optical stimulation intensity in $\mathrm{mW{\cdot}cm^{-2}}$. The values of the simulation parameters in the model are given in the text.

$n_0 = 10^{10}\,\mathrm{cm^{-3}}$. By considering that the wavelength of the blue light stimulation of 470 nm corresponds to 2.338 eV, it was calculated that $1\,\mathrm{mW} = 2.369{\cdot}10^{15}$ blue photons/s [47]. This conversion factor allows us to present the simulation results in terms of the variable optical stimulation power $\varphi_0$ in a typical TA – OSL experiment, expressed in units of $\mathrm{mW{\cdot}cm^{-2}}$.

Figure 8a represents the two extreme conditions when only thermal stimulation is used, and when maximum optical stimulation is used. According to Eq. (11), when there is no optical stimulation, $\varphi_0 = 0$, so only the TL peak at 510°C is present. On the other hand, for the maximum value of $\varphi_0 = 16\,\mathrm{mW{\cdot}cm^{-2}}$ the optical stimulation is very strong, and this causes a shift of the TA – OSL signal to much lower temperatures with maximum intensity at a temperature of ∼140°C.

Figure 8b shows the numerically derived TA – OSL signal with a linear heating rate for intermediate cases with $\varphi_0$ values in the range 0.05-14 $\mathrm{mW{\cdot}cm^{-2}}$.

The numerically evaluated results in Fig. 8 are in agreement with the simulation results of Ref. [37], which were obtained using a general-order kinetics model. These are also in agreement with the results reported by Chen and Pagonis [67], who used a different two-stage TA – OSL model based on a modification of the original OTOR model. In addition, the simulated results agree with the experimental TA – OSL peaks presented in Fig. 3.

In a second set of simulations using the OTOR model, the isothermal TA – OSL method was numerically simulated. The same parameters were used as for the TA – OSL simulations with a linear heating rate shown in Fig. 8.

The stimulation temperatures in the isothermal TA – OSL simulations were selected between 30 and 120°C in steps of 10°C, while optical stimulation intensities ranged between 0.1 and 10 $\mathrm{mW{\cdot}cm^{-2}}$. The results are presented in Fig. 9a, which shows the integrated isothermal TA – OSL signal as a function of the measurement temperature. The results are normalized to the TA – OSL signal obtained with a maximum stimulation intensity of $\varphi_0 = 10\,\mathrm{mW{\cdot}cm^{-2}}$ and for a temperature of 120°C. The arithmetic values in Fig. 9a correspond to a variable optical stimulation intensity for values of $\varphi_0 = 10, 5, 2.5, 1, 0.5, 0.25$ and $0.10\,\mathrm{mW{\cdot}cm^{-2}}$.

As the temperature of the isothermal TA – OSL experiment is increased, the integrated TA – OSL signal increases in a non-linear manner. Similarly, when the temperature of the isothermal TA – OSL experiment is kept constant, the integrated TA – OSL increases non-linearly with the intensity of the optical stimulation $\varphi_0$. High optical intensities deplete more effectively the VDT, as the stimulation temperature is further increased.

Figure 9b presents the linear Arrhenius plot from which the value of the thermal assistance activation energy $\mathrm{E_A}$ is obtained as the corresponding slope. The results show a strong dependence of this slope on the optical stimulation intensity. The correct value of the activation energy $\mathrm{E_A}$ is obtained at $\varphi_0$ values less than $1\,\mathrm{mW{\cdot}cm^{-2}}$. However, the Arrhenius plot significantly underestimates the value of $\mathrm{E_A}$ at the higher $\varphi_0$ values of 5 and $10\,\mathrm{mW{\cdot}cm^{-2}}$.

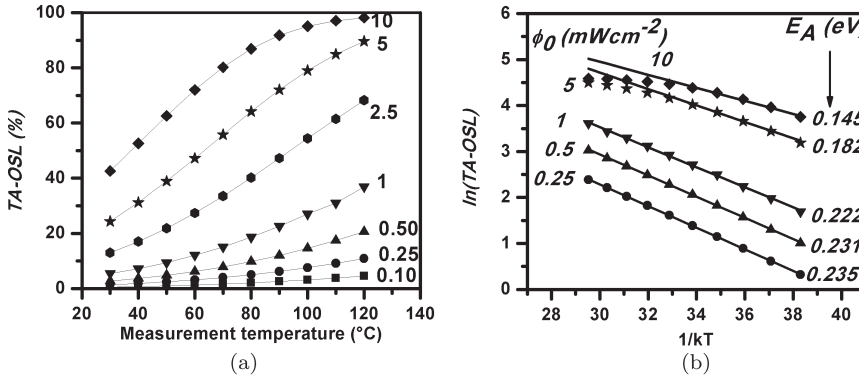


Fig. 9. The dependence of the depleted isothermal TA – OSL signal (plot a) and the $E_A$ calculation using Arrhenius plot (plot b) on the optical stimulation intensity. The arithmetic values correspond to optical stimulation intensity in mW·cm$^{-2}$. The simulation parameters are given in the text.

## 4.8. Stability

Traps that can be thermally stimulated by heating at temperatures beyond 500°C have been rarely used for dosimetric purposes. However, these traps yield outstanding thermal stability.

In order to get an idea about this last statement, the following calculations were performed. Consider a TL peak having peak maximum at 500°C. Assuming first-order kinetics and that the full width half maximum (FWHM) cannot exceed 100°C, it is found that such a peak can be obtained for many $(E, s)$ pairs in the region of $E > 1.5\,\mathrm{eV}$ and $s > 10^8\,\mathrm{s}^{-1}$, having a lifetime of the order of the age of the Earth, according to Eq. (1). Therefore, getting access to the signal from these traps in order to both measure the corresponding signal without heating the sample to temperatures greater than 500°C, as well as use it for high dose level dosimetry and dating purposes, becomes of great interest. It is worth emphasizing the ability of these VDTs to retain the trapped electrons even for storage of the sample in room light conditions, due to the low values of photo-ionization cross-sections at room temperature. An ongoing project with samples exposed to prolonged bleaching attempts to verify that absorbed dose information can be retained, even

for storage of the sample in room light conditions and at ambient temperatures.

Athermal fading (AF hereafter) is the term adopted for the rapid decay of the otherwise stable luminescence at room temperature, instead of the stability expected for it according to the basic luminescence kinetic models. Besides feldspar minerals which yield moderate AF, Durango apatite stands as an example of a material exhibiting very strong athermal fading [48, 61, 68]. Kitis *et al.* [48] as well as Polymeris *et al.* [61] had studied the fading of various luminescence signals from apatites of various types, collected from various origins around the world. AF effect was ubiquitous for all TL and conventional OSL signals of all these apatite samples, and the athermal fading of the TA – OSL signal was strongly differentiated from the athermal fading of electron traps excited at temperatures below 500°C. The TA – OSL signal associated with very deep traps was found to be more stable, showing much slower AF over time. Moreover, the TA – OSL athermal fading rate was reported to be further decreased as a function of grain size, at the edge between the micro- and the nano-scale [68]. Figure 10 presents the residual

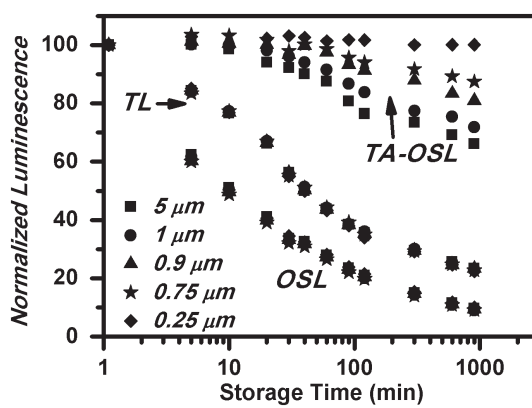


Fig. 10. Normalized residual OSL, TL and TA – OSL signals for Durango apatite, as a function of storage time, for a selection of grain size fractions at the edge between the micro- and the nano-scale. TA – OSL is more stable, while for grains with dimensions lower than 500 nm, TA – OSL yields negligible athermal fading. Arithmetic values correspond to average grain-size value. Reprinted from Polymeris *et al.* [68].

TL, OSL and TA – OSL signals for 5 different grain size fractions, with average values ranging between 5 $\mu$m and 250 nm. While TL and OSL fading rates do not change, the TA – OSL signal yields negligible athermal fading as the grain size is decreased by ball milling below 500 nm. Based on these results, investigating the ubiquity and the fading rates of the TA – OSL of various feldspars becomes of extreme interest. Preliminary TA – OSL fading results on pure K-feldspar samples are quite promising.

### 4.9. Dose response and applications

Currently, the interest in measurements of ionizing radiations is increasingly growing, especially due to development of radiation technologies employing high-dose levels [69]. Besides developing new, improved radiation-resistant materials for high-dose dosimetry, it is also possible to take advantage of the increased capacity of the VDTs in well-established dosimetric phosphors by using TA – OSL.

For $Al_2O_3$:C, a sample-dependent and nonlinear dose dependence of the isothermal TA – OSL output measured up to 2 kGy was reported [13, 14]. Nevertheless, Soni *et al.* [57] reported that using TA – OSL under linear heating, the dose response is linear up to 10 kGy, extending thus the dose response linearity of $\alpha$-$Al_2O_3$:C by almost 3 orders of magnitude. Extension of the maximum detection dose limit was also reported for both cases of quartz [49, 60] as well as natural polymineral sample, consisting mostly of K-feldspar and quartz [60]. In all these publications, a notable feature of the dose response curves is the absence of linearity, especially for the cases of the large applied doses. In all cases the dose response curves were fitted using appropriate saturating exponential functions, with the most interesting fitting parameter being the characteristic dose at which saturation begins to occur, $D_0$. For the latter case, the SAR protocol by employing isothermal TA – OSL signal was applied for the first time in the literature [60]. The isothermal TA – OSL SAR dose response of quartz results in a $D_0$ value of almost 1.5 kGy, which is almost one order of magnitude larger than the

corresponding values for conventional OSL signals [60]. Moreover, recycling ratios and dose recovery tests provide promising hints towards establishing a robust SAR TA – OSL dating protocol. These results were crosschecked by comparing them with the corresponding results obtained by additive dose Electron Spin Resonance (ESR) signals measured at low temperature, resulting from Al and Ti centers. For both ESR and TA – OSL signals, very large equivalent dose values were obtained due to very weak bleaching, associated with large uncertainty values. These common features could possibly imply that the defects associated with TA – OSL in quartz could be correlated with the corresponding Al and Ti centers in ESR; further work is required in order to establish this correlation. The effects of (a) the test dose implemented within the SAR TA – OSL protocol, (b) the TA – OSL stimulation duration and (c) the optimum stimulation temperature, were recently investigated towards decreasing the relative large scattering in the individually obtained equivalent dose values for the SAR TA – OSL approach [70]. In recent review articles, TA – OSL is recognized among the most important modern trends in high-dose luminescent measurements [38, 69], as well as among the most promising recent measurement techniques and new luminescence signals for dating back to a million years, and even before that [7].

## 4.10. Conclusion

TA – OSL, this somehow unconventional technique which efficiently combines both optical and thermal stimulation, appears as a promising tool for stimulating electrons from VDTs. For a number of well-established luminescent phosphors, TA – OSL exhibits a number of interesting properties, including thermal assistance, thermal stability and straightforward dependence on dose; several of them seem to be prevalent, even ubiquitous. TA – OSL of both $Al_2O_3$:C and quartz has been reported to be effectively applied towards extending the maximum detection dose thresholds. The nature of VDTs has not been completely studied yet; further work is required in order to (a)

understand their nature by applying spectroscopy techniques such as ESR, (b) establish their prevalence, especially for many feldspar and quartz samples, and (c) further exploit the applicability of the technique to more luminescent phosphors, such as BeO, MgO, etc. Finally, basic TA – OSL features, such as spectral response, thermal cleaning for high temperatures, bleaching properties, dose response along with sensitization, still require more experimental work over many luminescent phosphors.

## References

[1] S.W.S. McKeever, *Thermoluminescence of Solids*. (Cambridge University Press, Cambridge, 1985).

[2] A.G. Wintle, "Luminescence dating: laboratory procedures and protocols," *Radiat. Meas.*, vol. 27, no. 5/6, pp. 769–817, 1997.

[3] G. Polymeris, G. Kitis and V. Pagonis, "The effects of annealing and irradiation on the sensitivity and superlinearity properties of the 110°C thermoluminescence peak of quartz," *Radiat. Meas.*, vol. 41, pp. 554–564, 2006.

[4] S.W.S. McKeever, M. Moscovitch and P.D. Townsend, *Thermoluminescence Dosimetry Materials: Properties and Uses*. (Nuclear Technology Publishing, 1995).

[5] F. Preusser, M.L. Chithambo, T. Götte, M. Martini, K. Ramseyer, E. Sendezera, G. Susino and A.G. Wintle, "Quartz as a natural luminescence dosimeter," *Earth-Sci. Rev.*, vol. 97, pp. 196–226, 2009.

[6] E. Bulur and H.Y. Göksu, "Phototransferred thermoluminescence from $\alpha$-$Al_2O_3$:C using blue light emitting diodes," *Radiat. Meas.*, vol. 30, pp. 203–206, 1999.

[7] A.G. Wintle and G. Adamiec, "Optically stimulated luminescence signals from quartz: A review," *Radiat. Meas.*, vol. 98, pp. 10–33, 2017.

[8] N.A. Spooner, "On the optical dating signal from quartz," *Radiat. Meas.*, vol. 23, no. 2/3, pp. 693–700, 1994.

[9] B. Li, "The relationship between thermal activation energy, infrared stimulated luminescence and anomalous fading of K-feldspars," *Radiat. Meas.*, vol. 45, pp. 757–763, 2010.

[10] K.J. Thomsen, A.S. Murray, M. Jain and L. Bøtter-Jensen, "Laboratory fading rates of various luminescence signals from feldspar-rich sediment extracts," *Radiat. Meas.*, vol. 43, no. 9, pp. 1474–1486, 2008.

[11] J.P. Buylaert, A.S. Murray, K.J. Thomsen and M. Jain, "Testing the potential of an elevated temperature IRSL signal from K-feldspar," *Radiat. Meas.*, vol. 44, no. 5, pp. 560–565, 2009.

[12] X. Fu, B. Li and S.H. Li, "Testing a multi-step post-IR IRSL dating method using polymineral fine grains from Chinese loess," *Quat. Geochronol.*, vol. 10, pp. 8–15, 2012.

[13] G.S. Polymeris, S. Raptis, D. Afouxenidis, N.C. Tsirliganis and G. Kitis, "Thermally assisted OSL from deep traps in $Al_2O_3$:C," *Radiat. Meas.*, vol. 45, pp. 519–522, 2010.

[14] G.S. Polymeris and G. Kitis, "Thermally assisted photo transfer OSL from deep traps in $Al_2O_3$:C grains exhibiting different TL peak shapes," *Appl. Radiat. Isot.*, vol. 70, pp. 2478–2487, 2012.

[15] M.S. Akselrod, N. Agersnap Larsen, V. Whitley and S.W.S. McKeever, "Thermal quenching of F-center luminescence in $Al_2O_3$:C," *J. Appl. Phys.*, vol. 84, no. 6, pp. 3364–3373, 1998.

[16] B. Subedi, E. Oniya, G.S. Polymeris, D. Afouxenidis, N.C. Tsirliganis and G. Kitis, "Thermal quenching of thermoluminescence in quartz samples of various origin," *Nucl. Instrum. Methods Phys. Res. B*, vol. 269, pp. 572–581, 2011.

[17] N. Agersnap Larsen, L. Bøtter–Jensen and S.W.S. McKeever, "Thermally stimulated conductivity and thermoluminescence from $Al_2O_3$:C," *Radiat. Prot. Dosim.*, vol. 84, pp. 87–90, 1999.

[18] M.S. Akselrod and V. Kortov, "Thermoluminescent and exo-emission properties of new high-sensitivity TLD $\alpha$-$Al_2O_3$:C crystals," *Radiat. Prot. Dosim.*, vol. 33, nos. 1–4, pp. 123–126, 1990.

[19] I.I. Milman, V.S. Kortov and S.V. Nikiforov, "An interactive process in the mechanism of the thermally stimulated luminescence of anion-defective $\alpha$-$Al_2O_3$:C crystals," *Radiat. Meas.*, vol. 29, pp. 401–410, 1998.

[20] V.S. Kortov, S.V. Nikiforov, I.I. Milman and E.V. Moiseykin, "Specific features of luminescence of radiation-colored $\alpha$-$Al_2O_3$:C single crystals," *Radiat. Meas.*, vol. 38, pp. 451–454, 2004.

[21] V.S. Kortov, I.I. Milman and S.V. Nikiforov, "Thermoluminescent and dosimetric properties of anion-defective $\alpha$-$Al_2O_3$ single crystals with filled deep traps," *Radiat. Prot. Dosim.*, vol. 100, pp. 75–78, 2002.

[22] V.S. Kortov, I.I. Milman and S.V. Nikiforov, "The effect of deep traps on the main features of thermoluminescence in dosimetric $\alpha$-$Al_2O_3$ crystals," *Radiat. Prot. Dosim.*, vol. 84, pp. 35–38, 1999.

[23] E.G. Yukihara, V.H. Whitley, J.C. Polf, D.M. Klein, S.W.S. McKeever, A.E. Akselrod and M.S. Akselrod, "The effects of deep trap population on the thermoluminescence of $Al_2O_3$:C," *Radiat. Meas.*, vol. 37, pp. 627–638, 2003.

[24] V.S. Kortov, I.I. Milman, S.V. Nikiforov and E.V. Moiseykin, "The role of deep traps in the luminescence mechanism of anion-defective single crystals of aluminum oxide," *Phys. Status Solidi C*, vol. 2, pp. 515–521, 2005.

[25] A.E. Akselrod and M.S. Akselrod, "Correlation between OSL and distribution of TL traps in $Al_2O_3$:C," *Radiat. Prot. Dosim.*, vol. 100, pp. 217–220, 2002.

[26] V.S. Kortov, I.I. Milman, S.V. Nikiforov, E.V. Moiseykin and S.V. Kondrashov, "Nonlinear dose dependence in TLD-500 detectors

resulting from interactive interference of traps," *Radiat. Meas.*, vol. 42, pp. 590–593, 2007.

[27] E.G. Yukihara, V.H. Whitley, S.W.S. McKeever, A.E. Akselrod and M.S. Akselrod, "Effect of high-dose irradiation on the optically stimulated luminescence of $Al_2O_3$:C," *Radiat. Meas.*, vol. 38, pp. 317–330, 2004.

[28] S.V. Nikiforov, I.I. Milman and V.S. Kortov, "Thermal and optical ionization of F-centers in the luminescence mechanism of anion-defective corundum crystals," *Radiat. Meas.*, vol. 33, no. 5, pp. 547–551, 2001.

[29] V.S. Kortov, I.I. Milman, E.V. Moiseykin, S.V., Nikiforov and M.M. Ovchinnikov, "Deep-trap competition model for TL in $\alpha$-$Al_2O_3$:C heating stage," *Radiat. Prot. Dosim.*, vol. 119, nos. 1–4, pp. 41–44, 2006.

[30] G. Molnár, M. Benabdesselam, J. Borossay, P. Iacconi, D. Lapraz and M. Akselrod, "Influence of the irradiation temperature on the dosimetric and high temperature TL peaks of $Al_2O_3$:C," *Radiat. Prot. Dosim.*, vol. 100, pp. 139–142, 2002.

[31] V.E. Pelenyov, V.S., Kortov and I.I. Milman, "The interaction of deep traps in anion-defective $\alpha$-$Al_2O_3$," *Radiat. Meas.*, vol. 33, no. 5, pp. 629–631, 2001.

[32] I.I. Milman, E.V. Moiseykin, S.V. Nikiforov, S.V. Solovev, I.G. Revkov and E.N. Litovchenko, "The role of deep traps in luminescence of anion-defective $\alpha$-$Al_2O_3$:C crystals," *Phys. Solid State*, vol. 50, no. 11, pp. 2076–2080, 2007.

[33] M.L. Chithambo, C. Seneza and J.M. Kalita, "Phototransferred thermoluminescence of $\alpha$-$Al_2O_3$:C: Experimental results and empirical models," *Radiat. Meas.*, vol. 105, pp. 7–16, 2017.

[34] I.K. Bailiff, S.G.E. Bowman, S.K. Mobbs and M.J. Aitken, "The phototransfer technique and its use in thermoluminescence dating," *J. Electrostat.*, vol. 3, pp. 269–280, 1977.

[35] R. Chen and S.W.S. McKeever, *Theory of Thermoluminescence and Related Phenomena*. (World Scientific, Singapore, 1997).

[36] M.S. Akselrod and E.A. Gorelova, "Deep traps in highly sensitive $\alpha$-$Al_2O_3$:C TLD crystals," *Nucl. Tracks Radiat. Meas.*, vol. 21, no. 1, pp. 143–146, 1993.

[37] A. Soni, D.R. Mishra, B.C. Bhatt, S.K. Gupta, N.S. Rawat, M.S. Kulkarni and D.N. Sharma, "Characterization of deep energy level defects in $\alpha$-$Al_2O_3$:C using thermally assisted OSL," *Radiat. Meas.*, vol. 47, pp. 111–120, 2012.

[38] V.S. Kortov, "Modern trends and development in high-dose luminescent measurements," *J. Phys. Conf. Ser.*, vol. 552, p. 012039, 2014.

[39] G.S. Polymeris, "Thermally assisted OSL (TA – OSL) from various luminescence phosphors; an overview," *Radiat. Meas.*, vol. 90, pp. 145–152, 2016.

[40] G.S. Polymeris, E. Şahiner, N. Meriç and G. Kitis, "Experimental features of natural thermally assisted OSL (NTA – OSL) signal in various quartz samples; preliminary results," *Nucl. Instrum. Methods Phys. Res. B*, vol. 349, pp. 24–30, 2015.

[41] A. Soni, D.R. Mishra, B.C. Bhatt, S.K. Gupta, N.S. Rawat, M.S. Kulkarni and D.N. Sharma, "Improvement in dose threshold of $Al_2O_3$:C using thermally assisted OSL," *Radiat. Meas.*, vol. 49, pp. 67–72, 2013.

[42] A. Chruścińska and N. Kijek, "Thermally modulated optically stimulated luminescence (TM – OSL) as a tool of trap parameter analysis," *J. Lumin.*, vol. 174, pp. 42–48, 2016.
[43] D. Curie, *Luminescence in Crystals.* (Methuen, London, 1963).
[44] V. Pagonis, C. Ankjærgaard, A.S. Murray, M. Jain, R. Chen, J. Lawless and S. Greilich, "Modelling the thermal quenching mechanism in quartz based on time-resolved optically stimulated luminescence," *J. Lumin.*, vol. 130, pp. 902–909, 2010.
[45] G.I. Dallas, D. Afouxenidis, E.C. Stefanaki, N.F. Tsagas, G.S. Polymeris, N.C. Tsirliganis and G. Kitis, "Reconstruction of the thermally quenched glow-curve of $Al_2O_3$:C," *Phys. Status Solidi A*, vol. 205, no. 7, pp. 1672–1679, 2008.
[46] A.N. Nyirenda, M.L. Chithambo and G.S. Polymeris, "On luminescence stimulated from deep traps in $\alpha$-$Al_2O_3$:C," *Radiat. Meas.*, vol. 90, pp. 109–112, 2016.
[47] G.S. Polymeris, G. Kitis and N.C. Tsirliganis, "Correlation between TL and OSL properties of $CaF_2$:N," *Nucl. Instrum. Methods Phys. Res. B*, vol. 251, pp. 133–142, 2006.
[48] G. Kitis, G.S. Polymeris, V. Pagonis and N.C. Tsirliganis, "Anomalous fading of OSL signals originating from very deep traps in Durango apatite," *Radiat. Meas.*, vol. 49, pp. 73–81, 2013.
[49] G. Kitis, N.G. Kiyak, G.S. Polymeris and V. Pagonis, "Investigation of OSL signals from very deep traps in unfired and fired quartz samples," *Nucl. Instrum. Methods Phys. Res. B*, vol. 268, pp. 592–598, 2010.
[50] G.S. Polymeris, G. Kitis, D. Afouxenidis, I.K. Sfampa, N.C. Tsirliganis, A. Rousaki, E. Kouloumpi and K.M. Paraskevopoulos, "On the feasibility of dating portable paintings: preliminary luminescence measurements on ground layer materials," *Mediterr. Archaeol. Archaeom. J.*, vol. 13, no. 3, pp. 93–103, 2013.
[51] Y.K. Kadioğlu, G.S. Polymeris, N. Meriç and E. Şahiner, SAR – TA – OSL dating application on samples of independent chronology with ages larger than 1Ma. *In Proc. 15$^{th}$ International Luminescence and Electron Spin Resonance Dating (L.E.D.) Conference*, Cape Town, South Africa (Sept. 2017).
[52] G.S. Polymeris, E. Şahiner, N. Meriç and G. Kitis, "Thermal assistance in TA - OSL signals of feldspar and polymineral samples; comparison with the case of pure quartz," *Radiat. Meas.*, vol. 81, pp. 270–274, 2015.
[53] M.J. Kalita, M.L. Chithambo and G.S. Polymeris, "Thermally-assisted optically stimulated luminescence from deep electron traps in $\alpha$-$Al_2O_3$:C,Mg," *Nucl. Instrum. Methods Phys. Res. B*, vol. 403, pp. 28–32, 2017.
[54] G.I. Dallas, G.S. Polymeris, E.C. Stefanaki, D. Afouxenidis, N.C. Tsirliganis and G. Kitis, "Sample dependent correlation between TL and LM-OSL in $Al_2O_3$:C," *Radiat. Meas.*, vol. 43, pp. 335–340, 2008.

[55] L.E. Colyott, M.S. Akselrod and S.W.S. McKeever, "Phototransferred Thermoluminescence in Alpha-$Al_2O_3$:C," *Radiat. Prot. Dosim.*, vol. 65, nos. 1–4, pp. 263–266, 1996.

[56] S.V. Nikiforov, V.S. Kortov, S.V. Zvonarev, E.V. Moiseykin and M.G. Kazantseva, "Basic thermoluminescent and dosimetric properties of $Al_2O_3$:C irradiated by pulse intensive electron beam," *Radiat. Meas.*, vol. 71, pp. 74–77, 2014.

[57] A. Soni, D.R. Mishra, B.C. Bhatt, S.K. Gupta, N.S. Rawat, M.S. Kulkarni and D.N. Sharma, "Thermally assisted OSL: a potent tool for improvement in minimum detectable dose and extension of dose range of $Al_2O_3$:C," *Geochronometria*, vol. 40, p. 258, 2013.

[58] N. Meriç, E. Şahiner and G.S. Polymeris, "Thermally assisted OSL (TA – OSL) reproducibility in $Al_2O_3$:C and its implication on the corresponding thermoluminescence (TL) reproducibility," *Radiat. Meas.*, vol. 90, pp. 269–273, 2016.

[59] S.V. Nikiforov and V.S. Kortov, "Effect of deep traps on sensitivity of TLD-500 thermoluminescent detectors," *Radiat. Meas.*, vol. 45, pp. 527–529, 2010.

[60] E. Şahiner, N. Meriç and G.S. Polymeris, "Thermally assisted OSL application for equivalent dose estimation; comparison of multiple equivalent dose values as well as saturation levels determined by luminescence and ESR techniques for a sedimentary sample collected from a fault gouge," *Nucl. Instrum. Methods Phys. Res. B*, vol. 392, pp. 21–30, 2017.

[61] G.S. Polymeris, V. Giannoulatou, I.K. Sfampa, N.C. Tsirliganis and G. Kitis, "Search for stable energy levels in materials exhibiting strong anomalous fading: the case of apatites," *J. Lumin.*, vol. 153, pp. 245–251, 2014.

[62] A. Chruścińska, "On some fundamental features of optically stimulated luminescence measurements," *Radiat. Meas.*, vol. 45, pp. 991–999, 2010.

[63] D.R. Mishra, A. Soni, N.S. Rawat, M.S. Kulkarni, B.C. Bhatt and D.N. Sharma, "Method of measuring thermal assistance energy associated with OSL traps in $\alpha$-$Al_2O_3$:C phosphor," *Radiat. Meas.*, vol. 46, pp. 635–642, 2011.

[64] A. Soni, D.R. Mishra, G.S. Polymeris, B.C. Bhatt and M.S. Kulkarni, "OSL and thermally assisted OSL response in dental enamel for its possible application in retrospective dosimetry," *Radiat. Environ. Biophys.*, vol. 53, pp. 763–774, 2014.

[65] M.L. Chithambo and G. Costin, "Temperature-dependence of time-resolved optically stimulated luminescence and composition heterogeneity of synthetic $\alpha$-$Al_2O_3$:C," *J. Lumin.*, vol. 182, pp. 252–262, 2017.

[66] G.S. Polymeris, "OSL at elevated temperatures: Towards the simultaneous thermal and optical stimulation," *Radiat. Phys. Chem.*, vol. 106, pp. 184–192, 2015.

[67] R. Chen and V. Pagonis, "Modeling TL-like thermally assisted optically stimulated luminescence (TA – OSL)," *Radiat. Meas.*, vol. 56, pp. 6–12, 2013.

[68] G.S. Polymeris, I.K. Sfampa, M. Niora, E.C. Stefanaki, L. Malletzidou, V. Giannoulatou, V. Pagonis and G. Kitis, "Anomalous fading in TL, OSL and TA – OSL signals of Durango apatite for various grain size fractions; from micro to nano scale," *J. Lumin.*, vol. 195, pp. 216–224, 2018.

[69] V. Kortov and Y. Ustyantsev, "Advantages and challenges of high-dose thermoluminescent detectors," *Radiat. Meas.*, vol. 56, pp. 299–302, 2013.

[70] E. Şahiner, N. Meriç and G.S. Polymeris. Modification of Thermally assisted OSL SAR protocols by choosing the appropriate parameters. *In Proc. 18$^{th}$ International Solid State Dosimetry (S.S.D.) Conference*, Munich, Germany (Jul. 2016).

This page intentionally left blank

## Chapter 5

# Luminescence and Defects in Quartz

Marco Martini and Mauro Fasoli

*Dipartimento di Scienza dei Materiali*
*Università di Milano-Bicocca*
*Via Cozzi, 55 Milano 20125, Italy*
*m.martini@unimib.it, mauro.fasoli@unimib.it*

This chapter deals with luminescence in quartz, one of the most widespread minerals on the Earth and, in its synthetic form, the material of choice for electronic clock oscillators. Defects in quartz, whose concentrations cover a very wide range, give the trapping and recombination properties at the basis of delayed luminescence (both TL and OSL), exploited for dosimetry and dating. The various kinds of defects, both intrinsic and impurity related, are described.

It is noted that most luminescence properties are due to the interactions between defects. As a consequence, orders of magnitude variations in the luminescence intensity, after irradiation and thermal treatments, are typical of quartz and are discussed in this chapter. The most cited variation of emission intensity is the well-known "pre-dose" effect, whose mechanisms are still to be clarified. The main centers generally reported as responsible for this effect are reviewed, together with some proposals of their mutual interaction. Radioluminescence, RL, which at a first approximation allows detection of the same emitting centers as TL and OSL, has recently given interesting indications towards the identification of the defects involved. These results, compared with ESR data, are also discussed.

## 5.1. Introduction

Quartz, the crystal form of Silicon Dioxide, $SiO_2$, is the second most abundant mineral in the continental crust of the Earth, the first being feldspars. Its piezoelectric properties make it ideal for use as an

electronic oscillator. It is then industrially synthesized to exploit its properties, and is present in a huge number of electronic devices for high-frequency clocks. Quartz is then widespread both in its natural and synthetic form. It exists in a low temperature form (alpha quartz) and in a high temperature form (beta quartz). A reversible alpha-beta transformation happens at 573°C and has been proposed to play a role in the luminescence modifications of quartz [1].

Like all natural and synthetic materials, quartz contains variable concentrations of defects which can have various effects. In the synthetic form they can interfere with its electronic properties: it has been demonstrated that in quartz electronic oscillators the presence of low concentrations of Al ions, which substitute Si ions, produces an unwanted radiation-induced frequency shift, due to the charge-compensating alkali ions at the Al sites [2]. In both natural and synthetic quartzes the presence of the mentioned defects together with others, is responsible for charge trapping and luminescence recombination that are very useful for dosimetric purposes: based on these properties, radiation dosimetry [3] and ceramics and sediment dating [4, 5] are possible. Trapping and recombination are the basis for Thermoluminescence (TL) and Optically Stimulated Luminescence (OSL) which are practically always present in quartz, even if their intensity varies by many orders of magnitude from quartz to quartz and in a single quartz from zone to zone. Besides, in a single piece of quartz the emission intensity can also vary a lot, as a consequence of repeated irradiation and thermal treatments.

In this chapter we will review the experiments that can give indication about the origin of trapping and luminescence in quartz and the effects of irradiation and thermal treatments.

As a matter of fact, while evidence is given of a role of some impurities and intrinsic defects on the luminescence properties of quartz, the assignment of a given emission band or a trapping center to a specific defect is seldom agreed upon among the various researchers, with few exceptions.

The crystal structure of alpha-quartz is given by $SiO_4$ tetrahedra that are linked by sharing each of their corners with another tetrahedron, giving one of the most relevant features of quartz i.e.

the presence of relatively large channels along the crystallographic c-axis (see Fig. 1). This structure is the basis of the piezoelectric properties, and the channels are responsible for the radiation induced mobility of small ions, typically alkali ions (mainly $Li^+$) and $H^+$, linked to $Al^{3+}$ substituting for $Si^{4+}$ [6]. A number of modifications of the luminescence properties of quartz are due to this mobility that modifies the charge distribution at some defects, typically at the mentioned Al sites. This point will be extensively treated in section 5.3.2.3.

It is to be noted that the emission bands detected in TL and OSL are the same, with few exceptions, as those emitted under continuous irradiation, the so called Radioluminescence, RL [7], or Radiofluorescence, RF [8]. It is evidently much easier to consider RL than TL or OSL, because RL can be studied in a steady state under irradiation, while TL and OSL are transient phenomena, being detectable only as long as filled traps are present. A number of interesting results have recently been obtained in the study of quartz RL [9] and will be reviewed in section 5.4. It is to be noted that the light emissions both in the blue region and in the UV region have been revealed as composite [7, 9]. In particular, after repeated irradiations and specific thermal treatments, the same great variations of the intensities of both the RL and the TL of the so called "110°C peak" have been detected either in the blue emission bands or in the UV emission bands, depending on the activation temperatures [10, 11]. It has been then clarified which luminescence centers participate in the blue and the UV emissions, respectively. However, the identification of the responsible defects are still to be definitely determined. As a matter of fact, only phenomenological studies can be carried out observing the various TL, OSL and RL emissions and their modifications as a consequence of irradiation and thermal treatments.

It is in fact only possible to try to correlate them to the content of specific impurities in quartz; that is not enough to determine the structure of the defect acting as a trap or a luminescence center. It is then necessary to combine the luminescence measurements with other types of studies. A technique that can give useful structural

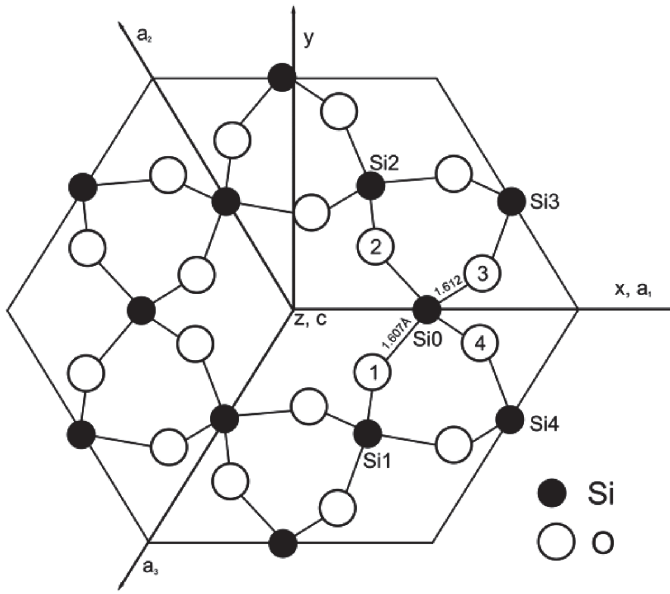


Fig. 1. Projection of alpha quartz atomic position onto the plane perpendicular to the c-crystallographic axis.

details of intrinsic and impurity related defects in solids is Electron Paramagnetic Resonance (EPR), currently known as Electron Spin Resonance (ESR). The limitation of ESR is however due to the possibility of detecting only paramagnetic centers, i.e. defects with unpaired electrons. Besides, generally, the extremely high sensitivity of luminescence measurements can hardly be reached by ESR. All the same, very useful results have been reached in combining luminescence and ESR measurements [12].

### 5.2. Experimental techniques

The identification of defects responsible for either a specific charge trap or a recombination center in quartz is not a straightforward task. Indeed, the joint efforts of investigations carried out using different and complementary techniques are required. In the following, we will shortly review the experimental techniques most used in the study of quartz defects and luminescence.

A huge number of papers have been published on these topics. However, the mentioned difficulties in assigning given emissions or trapping properties to specific defects are related to a number of variables:

1. Even very low concentrations of defects can give rise to relatively intense light emissions.
2. A straightforward correlation between the concentration of impurities and luminescence intensities can rarely occur, because a specific impurity can originate from various centers, only some of them being related to emitting centers.
3. Huge variations of defect concentrations can occur in quartz as a consequence of irradiation and thermal treatments, without modifying the impurity content, but rather changing the charge state of specific traps or emitting centers.
4. A further factor is given by the easy diffusion of monovalent ions, mainly $Li^+$ and $H^+$, which can modify existing defects or create new ones.

Looking at the experimental techniques, given that potentially many defects involved in quartz luminescence are of extrinsic nature, knowing the concentration of contaminants inside the $SiO_2$ matrix is very useful. Inductively coupled plasma mass spectroscopy (ICP-MS), with its variants, is a commonly employed technique to determine the concentration of trace elements in a host [13]. In general, the sensitivity depends on the ion or isotope being investigated and on whether a signal interfering with the ionic signals is present. In favorable conditions, ions at concentrations lower than a part per billion can be detected [14]. ICP-MS can be employed both on liquids (pre-dissolving the investigated material into a solution) and on solids (using laser ablation). It is however important to consider the possible inhomogeneity of extrinsic impurities inside the host matrix, which can be very high in both natural and synthetic quartz. In the case of solutions, the detected concentrations can be considered an average related to the portion of sample being dissolved. Laser ablation ICP-MS, on the other hand, by scanning the laser around the material surface, allows to monitor the inhomogeneity of

impurities down to a scale comparable to the dimension of the spot being vaporized by the laser (about 30 $\mu$m). This inhomogeneity is relevant in natural quartz either polycrystalline or layered, but also in synthetic quartz, where the concentrations of trace elements are known to depend on the specific growing zone [15].

Electron paramagnetic resonance (EPR), also named electron spin resonance (ESR), is certainly one of the most powerful experimental techniques to identify and fully characterize defects in solids [16]. In fact, it allows describing the local environment of uncoupled spins inside the host lattice. However, it has the intrinsic limitation of being sensitive only to paramagnetic centers.

Infrared optical absorption spectroscopy has been effectively employed to investigate the presence of hydrogen inside the quartz matrix, in the spectroscopic range 1500–4000 $\mathrm{cm}^{-1}$. Several absorption lines associated with vibrations of the OH group in different environments (e.g. nearby an Al or an alkali ion) have been in fact identified [17]. This makes this technique particularly useful to monitor the role of hydrogen in quartz submitted to different treatments.

Useful complementary information can be obtained from different luminescence techniques.

Thermally stimulated luminescence (TL) and optically stimulated luminescence (OSL) are the main methods used in dating applications. They provide information on defects acting as charge traps. If the luminescence can be spectrally resolved, then it is also possible to investigate the recombination centers and their possible spatial correlation with traps.

Wavelength resolved luminescence induced by ionizing radiation, like high energy photons for radioluminescence (RL), (also reported as radiofluorescence, RF) [7, 8], electron beams for cathodoluminescence (CL), or protons for ionoluminescence (IL) [18, 19], can also be employed for the investigation of luminescence centers of quartz. Compared to TL and OSL, these techniques have a better overall signal-to-noise-ratio. The spectra can in fact be collected in steady state conditions and are not constrained by a limited number of trapped charges, while for TL and OSL the signal

intensity is dependent on the concentration of both traps and recombination centers. Unlike TL and OSL, RL and CL do not need the presence of traps and the measured intensity is mostly related to the concentration of emitting centers at a first approximation, although the presence of traps competing with the recombination centers can also affect the luminescence intensity. If we compare RL and CL, the former has the advantage of using neutral radiation and therefore does not release any charge in the sample, while CL deposits electrons and it is then necessary to discharge the sample, which locally can alter the charge balance of the investigated area. However, CL can be useful to investigate inhomogeneous samples, considering the fact that the electron beam can scan the surface, providing spatially resolved spectral information on the scale of 30 $\mu$m.

Among the luminescence techniques, photoluminescence emission and excitation (PL/PLE) would be the most powerful one for investigating the spectroscopic features of a luminescent material. Its selective excitation, in fact, would provide full characterization of the luminescent centers available. Unfortunately, in the case of quartz, PL/PLE proved to be unsuccessful for studying the emissions also involved in TL and OSL methods (in the UV and blue region of the spectra). It is possible that the excitation bands of these emissions are in the vacuum UV region of the spectra (below 190 nm), which is inaccessible to common spectrometers [20].

Several factors contribute to the difficulties encountered in combining the information from different techniques (and quartzes) in search of correlations leading to a full understanding of the luminescence mechanisms and dynamics in quartz.

First, one has to consider that the listed techniques are characterized by significantly different sensitivities. It is not straightforward to quantify and compare the sensitivity of each technique, because it is strongly dependent on the specific characteristics of the signal being detected.

In ESR, for example, the sensitivity depends on the width of the signal and on the type of cavity being employed (among other parameters). However, as a rule of thumb, we can state that the

sensitivity is of the order of $10^{12}$–$10^{13}$ unpaired spins inside the magnet cavity. If one can measure 10 mg of quartz, this corresponds to about $10^{14}$–$10^{15}$ paramagnetic centers per gram.

A much higher sensitivity can be reached in luminescence detection. A rough calculation gave an estimate of levels as low as about $10^{10}$–$10^{12}$ centers per gram in TL measurements [21]. Absorption measurements, on the other hand, have a much lower sensitivity, only detecting concentrations orders of higher magnitude [22].

Despite all the available techniques, a possible correlation between two signals from different techniques is then very hard to obtain. Analogously, a comparison between two quartzes with highly different concentrations of a single ion would be in principle very useful, but not easy to interpret. It is possible to modify the presence in quartz of small monovalent ions, mainly $H^+$ and $Li^+$. In fact, as previously mentioned, one of the most interesting features of the structure of quartz is its anisotropy and the presence of channels in the direction of the crystal c-axis: ions can move along these channels and modifications in defect distribution can consequently occur. By applying an electric field parallel to the c-axis of the crystal, while maintaining the temperature in the 450–550°C range, it is possible to "sweep in" specific ions and simultaneously "sweep out" others, depending on the electrodes used and on the sweeping atmosphere [23]. Typically, $H^+$ ions can substitute for existing alkali ions or, alternatively, the concentrations of the latter can be greatly increased. "Swept in" and "swept out" crystals have been widely used to determine the dynamics of Al centers [24] and to compare their luminescence properties [10].

The "sweeping" technique cannot, of course, be useful for all the impurities. In fact, although electro-diffusion allows to "sweep" in or out some interstitial ions, this technique does not work on substitutional ions (like Al, Ge, Ti, etc.) which are known to play an important role in quartz luminescence.

Finally, also some experimental limitations contribute to interference with the comparison of spectroscopic results from different labs. In fact, not all the published emission spectra have been corrected by taking into account the spectral response of the detection system.

Moreover, sometimes the spectra are reported as a function of wavelength and sometimes as a function of energy and, because of the Jacobian conversion required to transform an emission spectrum from wavelength to energy, there is no direct relationship between the wavelength of the emission maximum and its energy [i.e. $E_{max}(eV)$ is never equal to $1240/\lambda_{max}(nm)$]. All these facts contributed to create confusion among spectroscopic data found in the literature, and to the identification of the different and often overlapping, bands.

Similar problems can occur in the identification of TL peaks in glow curves. Besides the well-known and predictable peak shift observed when employing different heating rates, in fact, a more subtle effect is due to thermal lag between the thermocouple and the sample. The use of different sample holders, like cups or disks, often of different material (steel or aluminum) and thickness, produces significantly different glow curves and, consequently, different trap parameters evaluated for the same defect.

### 5.3. Defects in quartz

A large number of studies has been carried out with the aim of understanding the trapping and luminescence properties of defects in quartz, the complex mechanisms governing the various luminescence emissions, and also their modifications as a consequence of irradiation and thermal treatments [3, 25, 26]. Many defects, both intrinsic and impurity related, are known to be present or produced in quartz, having been identified through various spectroscopic techniques. However, so far their trapping properties or the role of these defects in producing luminescence emissions is still under discussion. As already mentioned in the Introduction, only phenomenological studies can be carried out observing the various TL, OSL and RL emissions and their dynamics. The most important contribution to the knowledge of defects in quartz has come from ESR, in the identification of $[AlO_4]^0$, as early as in 1954, followed by E' Oxygen defect center in 1956 ([27] and references therein). Although both of them are known to be involved in the production and modification of luminescence, their dynamics must still be definitely described. In the Introduction, it

has been recalled that only tentative correlations between defects and luminescence emissions have been put forth. Nonetheless a number of assignments of some structural defects have been proposed, mainly through the correlations between the concentrations of paramagnetic centers and the relative intensities of specific emission bands. As an example, the good agreement between the time dependent decay of a Ge paramagnetic center and a specific TL peak (the already mentioned 110°C peak), allowed to definitely identify the center as the electron trap responsible for the peak [12].

While many defects are known to be present both in the crystalline (quartz) and in the amorphous (silica) forms of $SiO_2$, the luminescence properties of quartz and silica are largely different [28].

Some intrinsic or impurity related defects have been proposed as responsible for the luminescence emissions in quartz, and a few proposals of trapping centers are present in the scientific literature so far. It is to be remembered that it happens often that traps and recombination centers are strongly spatially related and some OSL and TL traps/centers have been proposed to be of this kind [29].

The main intrinsic quartz defects are the family of oxygen vacancies, of which the best known is the $E'_1$ center. Si vacancies are also known to be present; they give origin to $H_4O_4$, where the presence of $H^+$ ions balances the $Si^{4+}$ missing charge. A great number of defects related to the presence of extrinsic impurities are known. Among them, the Al centers are surely the most investigated. Both oxygen vacancies and Al centers are directly or indirectly involved in the luminescence properties of quartz. Besides Al, a ubiquitous impurity in quartz, Ge and Ti centers are usually also present and play a role in electron trapping. The presence of channels along the optic c-axis allows the presence and easy migration of small ions, like $H^+$ and $M^+$ ($M^+$ = alkali ions, mainly $Li^+$). They often act as charge compensators where $Al^{3+}$ substitutes for $Si^{4+}$. It is to be noted that an ionic scheme is often used when considering the production and modification of centers, however quartz is surely partly covalent, so the ionic approach can be accepted only as a first approximation. A rough estimate indicates quartz as 60% ionic and 40% covalent [16].

Besides the above cited defects, other impurities, like Fe, Ag, Cu, P ions, give origin to many defects, most of which participate in the trapping-luminescence dynamics.

### 5.3.1. *Intrinsic defects*

Both oxygen and silicon ions can produce vacancies in the quartz lattice. The latter are present as silicon vacancy-hole centers, generally by $H^+$ ions, as described in the following section. Oxygen ions can be displaced from their lattice position, giving origin to oxygen vacancies and peroxides. These latter are well known in the structure of amorphous silica [30], while only few proposals of their presence in crystalline quartz have been reported [31]. As a matter of fact, peroxy defects have been reported only in neutron irradiated quartz. It is then likely that local amorphous micro-zones are created by such irradiation. On the other hand, oxygen vacancies represent the prevalent kind of intrinsic defect in quartz.

#### 5.3.1.1. *Si vacancies*

Unlike oxygen vacancies and many impurity defects, silicon vacancy hole centers in quartz have not been characterized in detail [32]. They have been proposed as responsible for an ultraviolet emission [33].

The lack of the four Si positive charges can be compensated by four $H^+$ ions, resulting in the $[H_4O_4]^0$ center. After trapping a hole, substituting for a hydrogen ion, a Si vacancy can also host three $H^+$ ions creating $[H_3O_4]^0$ proposed as a luminescence center [34]. Nilges *et al.* [32] reported also a center featuring two O atoms related to a Si vacancy and stabilized by an $Al^{3+}$ ion in the neighboring tetrahedron.

#### 5.3.1.2. *O vacancies*

The simplest type of O vacancy is the diamagnetic center resulting from the removal of an O atom from the otherwise perfect $\alpha$-quartz, leaving a direct bond between two Si atoms, the "neutral O vacancy" [35]. As a consequence of the instability of interstitial oxygen in

quartz, it is likely that oxygen vacancies are only present in oxygen deficient quartz.

The neutral O vacancy is generally considered as the precursor of the paramagnetic $E'_1$ center, firstly detected by Weeks [36] and later described by Feigl *et al.* [37], in terms of a positively charged oxygen vacancy in which the two Si atoms relax asymmetrically: $E'_1$ could then be described by a hole trapped at a neutral O vacancy. The resulting defect features an unpaired electron on one of the two Si atoms, while the other Si ion, being positively charged, moves away from the vacancy into a nearby plane configuration [38]. Jani *et al.* [39] showed that the production of $E'_1$ centers in quartz is strongly dependent on prior sample treatments: the $E'_1$ centers are produced by a 15-min anneal at 300°C, provided the sample has been previously irradiated at room temperature. Besides, the presence in quartz of alkali ions is fundamental, because it has been demonstrated by the same authors [39] that a much smaller concentration of $E'_1$ centers is produced in quartz deprived of alkali ions. As will be discussed in section 5.3.3, this is probably due to the correlation between $E'_1$ and $[AlO_4]^0$ centers [39]. A theoretical study by Boero *et al.* [40] demonstrated that an oxygen atom can be displaced away from its equilibrium position without being removed, giving an $E'_1$ center also in the absence of oxygen vacancy.

It is agreed that oxygen vacancies do not participate directly in any luminescence emission in quartz, at least in the visible-UV region. However it is also known that $E'_1$ centers play a role in the emission efficiency of quartz (see section 5.3.3).

Besides the $E'_1$ center, other oxygen-vacancy associated defects involving hydrogen are known to be present in quartz, namely $E'_2$ and $E'_4$. Specifically $E'_4$ contains atomic hydrogen bonded to one of the Si atoms [41]. $E'_2$ was proposed to be a variant of $E'_4$, with a different dangling bond configuration.

A further group of O deficient centers is the E". They are produced by irradiation and are very similar to the E' centers, wherein the number of primes denotes how many unpaired electrons a center possesses. Specifically, $E"_1$, $E"_2$ and $E"_3$ have been reported, characterized by their slightly different ESR signal [42]. They are

all quenched by heating the quartz in the temperature range 50–100°C. It is to be noted that, similarly with E' centers, also E" are present in large concentrations only in quartz containing alkali ions (unswept quartz). They are produced by irradiation at 77 K, provided the sample has been previously irradiated at room temperature. A single 77 K irradiation of a previously un-irradiated sample does not produce E" centers. This indicates that the production of the E" centers is a two-step process [42].

### 5.3.2. *Impurity defects*

Even the purest quartz, either natural or synthetic, contains variable amounts of extrinsic impurities, that contribute to modifying its luminescence properties, even when the concentration is extremely limited, down to levels as low as few parts per million or even less. The ubiquitous Ge and Al ions surely strongly contribute to the trapping and luminescence properties of quartz, but also Ti and Fe have been often indicated as responsible for them. Other impurity-based magnetic defects have been detected: Ag, Ga, Mn, Ni, Cu and P. Furthermore, as already mentioned, alkali and hydrogen ions are practically always present in quartz and play a very important role in the modifications of defects and in the consequent luminescence features.

#### 5.3.2.1. *Ge centers*

Si in quartz can be substituted by Ge. The fundamental $[GeO_4]^-$ paramagnetic center was firstly detected by Mackey [43], by x-ray irradiation at low temperature. Later, various studies detected a number of Ge centers. A large family of them has been proposed as responsible for the role of electron traps. The most investigated Ge centers have been i) the diamagnetic $[GeO_4]^0$ center (a Ge substituting for a Si in the $SiO_4$ tetrahedral unit), ii) the paramagnetic $[GeO_4]^-$ center (a $[GeO_4]^0$ center that has trapped an electron upon irradiation) and iii) the paramagnetic $[GeO_4/M^+]^0$ center, where $M^+$ is an alkaline ion, $Li^+$ or $Na^+$. No $H^+$ compensated Ge centers forming $[GeO_4/H^+]^0$ have been reported.

It is worth highlighting that the $[GeO_4]^-$ center is unstable at room temperature, while $[GeO_4]^0$ and $[GeO_4/M^+]^0$ centers were found to be much more stable.

McKeever *et al.* [44] detected the growth of the concentration of $[GeO_4]^-$ centers upon irradiation and proposed the role of this center as the trap responsible for the 110°C TL peak. Recently, this proposal has been definitely confirmed by Vaccaro *et al.* [12].

McKeever *et al.* [44] detected an increase $[GeO_4/Li^+]^0$ and a corresponding decrease of $[GeO_4]^-$ center concentration, proposing a migration of $Li^+$ ions to $[GeO_4]^-$ centers, while Vaccaro *et al.* reported that all the decrease of the $[GeO_4]^-$ concentration was due to electron-hole recombination and observed a stable concentration of radiation induced $[GeO_4/Li^+]^0$ at room temperature. McMorris [45] observed that a TL peak at 300°C (heating rate 0.17°C/s) decreases in the same fashion as the concentration of $[GeO_4/M^+]^0$ (where $M^+ = Li^+$ or $Na^+$) center as a function of thermal annealing up to 400°C. It is then possible that electron de-trapping from $[GeO_4/Li^+]^0$, and its corresponding annealing, can happen at higher temperature, being accompanied by a TL peak.

#### 5.3.2.2. *Ti centers*

Titanium is generally reported as the main impurity in rose quartz. Similarly to germanium, titanium is substitutional for Al giving $[TiO_4]^0$ and acts as an electron trap yielding $[TiO_4]^-$ [46, 47]. Warming irradiated rose quartz causes the diffusion of $M^+$ ions to $[TiO_4]^-$ giving rise to the charge compensated species $[TiO_4/Li^+]^0$ and $[TiO_4/Na^+]^0$ [16].

The $[TiO_4]^-$ center anneals out at around 300°C, but no blue emission is correlated with the annealing [48].

Unlike germanium, titanium can trap $H^+$ ions and two types of $H^+$ related centers have been detected: $[TiO_4/H^+]^0$ and $[TiO_4/H^+]^+$.

#### 5.3.2.3. *Al centers*

$Al^{3+}$ ion is the main ubiquitous impurity to which many quartz defects are associated. It is present as a substitutional ion for $Si^{4+}$

and is charge compensated by an alkali ion ($M^+$) or by an $H^+$ ion, giving rise to $[AlO_4/M^+]^0$, $[AlO_4/H^+]^0$, respectively. When neither $M^+$ nor $H^+$ is present near a substitutional $Al^{3+}$ ion, this latter can be charge compensated by a positive hole, giving rise to the $[AlO_4]^0$ center, also reported as aluminum-hole center [49].

In a simplified scheme, considering quartz only in an ionic approximation, Halliburton *et al.* [6] concluded that the Al centers are always given by the three mentioned types of defects and the sum of their concentrations is more or less always constant.

The presence of Al ions in quartz, even at low concentrations, creates $[AlO_4]^0$ centers under irradiation at room temperature and a wide absorption band, which gives the quartz the typical grey coloration of the so called smoky quartz. It is to be noted that heating the quartz to $T > 350°C$ anneals out the smoky color. Indeed, the smoky coloration is due to the superposition of a number of absorption bands: some of them have been assigned to Al, others to different impurities, so that different colorations can come out due to the presence of these impurities. Moreover, thermal treatments have been reported to change the quartz coloration, due to the selective annealing of some of these defect centers [48]. Anyway, the dominant absorption band at 2.5 eV has been directly correlated to the ESR signal of Al [50].

The aluminum-hole centers are considered responsible for luminescence in quartz. By sweeping out in vacuum at high temperature, Martini *et al.* [51] could eliminate from quartz crystals both $[AlO_4/Li^+]^0$ and $[AlO_4/H^+]^0$, replacing most of them with $[AlO_4]^0$ centers. They suggested that the 380 nm emission is the result of recombination at $[AlO_4]^0$. Also, the same center has been proposed as the defect responsible for the blue TL at 470 nm [34, 52].

Note that if the irradiation is given at 77 K, no $[AlO_4]^0$ centers are formed, while $[AlO_4/H^+]^+$, $[AlO_4/Li^+]^+$ and $[AlO_4]^+$ are detected. The subsequent heating at temperature $> 200$ K increases the concentration of $[AlO_4]^0$, that can be created directly by irradiating at room temperature.

5.3.2.4. *Fe centers*

Fe is present in quartz mainly as $Fe^{3+}$, similarly to the already mentioned $Al^{3+}$ centers, but iron can also be present in quartz as $Fe^{2+}$ or $Fe^{4+}$ [16]. Three Fe paramagnetic centers, $[FeO_4/Li^+]^0$, $[FeO_4/H^+]^0$ and $[FeO_4/Na^+]^0$, have been reported and their relative concentrations as a function of irradiation and thermal treatments have been studied [53]. As in the corresponding Al centers, irradiation moves $M^+$ ions away from their position near $Fe^{3+}$ and replaces them with $H^+$. This happens if the irradiation is above 130 K, while the corresponding temperature was 200 K for Al centers. Thermal annealing in the temperature range 350–450°C causes the alkali ions to return to the Fe site, restoring the crystal to its pre-irradiation state, in analogy with Al centers.

Many varieties of natural quartz containing iron are known: amethyst and variously brown-colored species.

5.3.2.5. *P centers*

Unlike Ge and Ti, which are present as tetravalent ions, P ions are present in quartz as $P^{5+}$. Upon irradiation, $P^{5+}$ captures an electron and paramagnetic $[PO_4]^0$ centers are created [16]. Pentavalent $P^{5+}$ has been reported, substitutional at Si sites, in rose colored quartz. Unlike Al, monovalent anions are not known to be incorporated for charge compensation, and $P^{5+}$ seems to occur predominantly in coupled substitution with $Al^{3+}$ as a $[O_3POAlO_3]$-defect [54].

5.3.2.6. *$H^+$ ions and other interstitial ions*

As already seen, $H^+$ ions are present in a wide number of defects in quartz. Like alkali ions, also $H^+$ ions can act as charge compensators at Si substitutional sites, mainly $Al^{3+}$, but also $Fe^{3+}$ or $Ti^{3+}$, while, as said, no $[GeO_4/H^+]^0$ have been detected. They can be present since the formation of the crystal, or they can possibly enter the crystal or be eliminated as a consequence of high temperature treatments [51]. In these kinds of centers, the H is present as an $OH^-$ group and is detected by infrared (IR) absorption measurements [17, 55]. Many IR absorption peaks are seen, showing that at the Al site

$OH^-$ groups are linked not only to the simple Al in the $[AlO_4/H^+]^0$, but $M^+$ ions can also be present in more complex configurations, possibly $[AlO_4/H^+/M^+]^+$. $OH^-$ groups are detected also at regular Si sites.

$H^+$ ions can also enter a Si vacancy giving $H_3O_4$ and $H_4O_4$. Both centers can capture a hole by low temperature irradiation, resulting in $[H_3O_4]^0$ and $[H_4O_4]^+$ centers respectively [56]. There are other defects containing H that have been already reviewed, namely $E'_2$ and $E'_4$. A relationship between these H centers and the others mentioned above has not been established, i.e. it has not been clarified if $H^+$ ions move from one type of defect to another.

Besides $H^+$, other monovalent interstitial ions, mainly $Li^+$, $Na^+$, but also $Ag^+$ and $Cu^+$, are weakly bound to their position, generally near a substitutional Al. As already mentioned, they can move along the c-axis channels once they have been freed by radiation or thermal activation. As a consequence, $[AlO_4]^0$ centers can be formed and luminescence emission is observed. At high doses, a variety of coloring is produced. The energy needed to detach an ion from its interstitial position depends on the type of ion: $Ag^+$ can easily be moved away, while $Cu^+$ does not produce luminescence after irradiation, which could be due to the high energy needed to form $[AlO_4]^0$ centers [57].

### 5.3.3. *Defect dynamics*

Even if the concentrations in quartz of ions substitutional for $Si^{4+}$, mainly $Al^{3+}$, are generally very low (in the order of parts per million), they give rise to important effects in the electronic properties and in the luminescence of quartz as well. They are compensated by monovalent ions, very often $H^+$ or $Li^+$. The presence of the cited channels in the direction of the c-axis allows the migration of these small monovalent ions, upon irradiation. It is then possible to modify the distribution of these monovalent ions, by substituting the charge compensation at $Al^{3+}$ sites. Irradiation at room temperature (RT) can give rise to radiation induced ionic conductivity (RIC) that can be explained in terms of detachment of an alkali ion from the

$[AlO_4/M^+]^0$ site. The alkali ion is then free to move along the c-axis channels giving rise to RIC, which decays within hours at RT. The mechanism of this decay has not yet been explained, but it should be based on the trapping of the moving alkali ion at some still unidentified site. It has been proposed that the alkali ions get trapped at $[GeO_4]^-$ centers that would be converted to $[GeO_4/M^+]^0$ center, which is stable at room temperature (RT) for $M^+ = Li^+$ [16] or the titanium analogue [46]. However, upon irradiation Vaccaro *et al.* [12] detected the creation of $[GeO_4]^-$ centers and their decay at RT, but no corresponding increase of $[GeO_4/M^+]^0$ centers that were created as well by irradiation, but whose concentration remained stable in time. RIC due to alkali ion diffusion is strongly temperature dependent [58], and no RIC is detected if the irradiation is given at low temperature: Markes and Halliburton [59] determined that alkali ions are free to move if the irradiation takes place at $T > 200\,K$. Above this temperature the radiation dissociates the $[AlO_4/M^+]^0$ centers and $[AlO_4/H^+]^0$ and $[AlO_4]^0$ centers are formed. The relative proportion of these centers probably depends on other variables such as the concentration of $H^+$ ions at other sites in quartz. At high doses there is possibly an effect also due to the dose-rate [60]. Heating the crystal above 350°C causes the alkali ions to return to the Al site, restoring the crystal to its pre-irradiation state. If other extrinsic defects are present, like Fe, a higher temperature is needed [53].

As already mentioned, it is also possible to change the content in quartz of monovalent ions, by applying an electric field parallel to the c-axis of the crystal in the 450–550°C temperature range. The effect is the so called "sweeping in" of specific ions and simultaneously the "sweeping out" of others, depending on the electrodes used and on the sweeping atmosphere [23]. Typically, if this kind of electro-diffusion is done in air, $H^+$ ions can substitute for existing alkali ions. Alternatively, using alkali compounds as electrodes, the concentrations of the latter can greatly be increased. "Swept in" and "swept out" crystals have been widely used to determine the dynamics of Al centers [24].

The formation of intrinsic defects is also affected by the presence of alkali ions: both E' and E" centers are created only in un-swept

synthetic quartzes [39, 42]. E'$_1$ centers are seen to be created in un-swept quartz by irradiation at RT followed by a thermal anneal to approximately 300°C. Correspondingly, at the same temperature $[AlO_4]^0$ centers are annealed [39]. The E'$_1$ centers are then considered to have a role as hole traps competing with $[AlO_4]^0$ centers, possibly the recombination centers made available after repeated irradiation and heating to around 500°C, the so called "pre-dose" effect [61]. Correspondingly, Benny *et al.* [62] observed an increase of the E'$_1$ center concentration and the desensitization of the TL induced in a quartz after "pre-dose".

Also the production of E" centers in quartz is related to the presence of alkali ions, and is strongly dependent on previous sample treatment: an irradiation of a synthetic quartz at RT, followed by a further irradiation at 77 K produces a great number of E" centers [42], unlike a single irradiation at 77 K in unswept quartz that produces very few E" centers. The production of E" centers is then claimed to be a two-step process, i.e. the initial RT irradiation changes precursor centers into intermediate configurations, which are then converted into E" centers by the subsequent 77 K irradiation. Similarly for E' centers, the initial irradiation is shown to be effective if it is done at $T > 200$ K, the temperature at which $M^+$ ions in Al centers become mobile. Bossoli *et al.* [42] show similar behavior in the production of E"$_1$ and $[AlO_4]^0$ centers as a function of irradiation temperature. Martini *et al.* [63] noted that the E" centers anneal in the temperature region of the 110°C TL peak.

Not only E' and E" centers are produced in quartz by a two-step process: the $[SiO_4/Li]^0$ electron trap centers are produced by a double irradiation, the first one between 150 K and 300 K to release the $Li^+$ ion from $[AlO_4/Li^+]^0$ producing $[SiO_4/Li^+]^0$, and a second irradiation at 77 K to trap an electron [64]. This $[SiO_4/Li]^0$ electron trap center anneals out at a temperature below RT.

### 5.4. Luminescence

In dosimetry and dating applications relying on quartz, TL signal is mostly detected by means of bialkali PMT tubes sensitive in the

wavelength range from the UV to the red regions of the spectrum. The glow curves reported in the literature display a great variety of shapes, evidencing the complexity of the phenomenon. The number of overlapping TL peaks is often so high that a reliable determination of the trap parameters is not feasible. The shape of the glow curves is clearly dependent on quartz type, origin and its annealing and irradiation history [65, 66].

Nevertheless, some peaks seem to be detected in every quartz sample. In particular, this is the case for three peaks that are detected around 110°C, 325°C, and 375°C [4] when 15°C/s heating rate is employed. The lower temperature peak at 110°C is detected only in freshly irradiated samples, because it is unstable at room temperature and its decay time is of the order of tens of minutes. The other two peaks, on the other hand, are stable up to geological scale and thus are suitable for dosimetry purposes. Since the 325°C peak is easily bleached by solar light, it is used for dating geological sediments by means of the OSL technique. Dating of archaeological artifacts exposed to high temperature at the time of their fabrication, relies instead on the 375°C peak for age determination.

Annealing of quartz at high temperature results in an overall luminescence enhancement and in a modification of the glow curve shape. Moreover, the 110°C peak was shown to manifest a peculiar behavior. Its sensitivity enhancement as a consequence of an annealing at about 500°C, was proven (in fired quartz) to be proportional to the dose delivered to the sample before the annealing itself. It is what has been called the pre-dose effect, a phenomenon that was successfully employed for dating relatively recent events, going back up to few hundred years.

Since the first studies, the investigations with wavelength resolving detectors have provided an important insight on the luminescence phenomena in quartz. Over the years, several authors reported the spectra obtained by stimulating different types of quartz with various sources, evidencing several emissions covering the entire detectable spectral range, from the near UV to the near infrared. In TL, in particular, the emissions are typically observed in three specific spectral regions, the UV, the blue and the red one. However, for

each region, the wavelength (or energy) of the emission maximum, reported by different authors, are often significantly different. The maximum of the so called UV emission, for example, as reviewed by Krbetschek [67], has been observed over a broad wavelength range (360–440 nm). Similarly, in the case of the blue emission, despite the fact that most of the times it is observed at 470 nm, again wavelengths ranging from 460 to 500 nm have also been reported. These differences can hardly be ascribed only to experimental issues or to thermal shift [29], and suggest a composite nature of the bands. The relative intensities of quartz emissions were found to be sample dependent, and to be affected by both the thermal and irradiation history of the material [4]. In fact, the extent of the luminescence enhancement induced by annealing at high temperature was found to be different for the various emission regions. In fact, in untreated quartz an emission occurs in the blue (around 470 nm) while after annealing the main emission is in the UV region [51, 68, 69]. The previously described sensitivity enhancement of the so called 110°C peak, when quartz is annealed at 500°C after being delivered a laboratory dose, was found to be related to an increased concentration of recombination centers produced by hole transfer from an unidentified reservoir [61]. The pre-dose effect and the 110°C TL peak were investigated by means of ESR and other spectroscopic techniques [44, 63, 70]. Some authors proposed the $[AlO_4/h^+]^\circ$ [51] as the recombination center responsible for the enhanced UV emission, whereas others indicated the $[H_3O_4]^\circ$ [34] as the possible candidate and a consensus was not achieved.

Annealing at high temperature was found to enhance also the OSL emission [71] that was also shown to occur in the UV region [72], possibly sharing the same recombination centers with TL, as seems to be confirmed by a strong correlation found between OSL sensitivity and that of the 110°C TL peak [73].

Wavelength resolved X-ray induced luminescence, RL, has provided complementary information on quartz luminescence centers. Studies coupling RL to TL have shown that some of the emission bands can be detected with both techniques [74, 75]. Recently, Martini *et al.* investigated different types of quartz (mostly of

Table 1. Spectral parameters of the Gaussian bands detected in quartz radioluminescence [76].

| Band | E (eV) | $-\lambda_{max}$ (nm) | FWHM (eV) |
|---|---|---|---|
| O | 1.92 | 635 | 0.39 |
| A | 2.51 | 490 | 0.46 |
| B | 2.79 | 440 | 0.46 |
| X | 3.06 | 395 | 0.89 |
| C | 3.42 | 360 | 0.58 |
| M | 3.73 | 330 | 0.45 |
| D | 3.93 | 315 | 0.49 |

hydrothermal origin, both synthetic and natural, and a pegmatitic one) exposed to either prolonged irradiation or to thermal annealing. The authors succeeded in decomposing all the RL spectra using the same set of Gaussian components whose parameters were determined, and progressively refined over successive works [7, 9, 10, 76], leading to the values reported in Table 1.

This set does not include the self-trapped exciton (STE) emission, dominating the spectrum below room temperature. In quartz, the STE broad band is centered around 2.6–2.7 eV and it suffers a strong thermal quenching making its contribution at RT negligible [77, 78]. It is important to recall that not all the emissions detected under ionizing radiation do necessarily contribute also to the TL emission. For example, the broad band at 3.06 eV (band X) is observed in RL but not in TL [76]. This happens because, in RL, both hole and electron recombination centers, and excitonic emissions can be simultaneously observed.

It is important to notice that more than one band concur in both the blue and UV emissions. In fact the A and B bands (at 2.51 and 2.79 eV, respectively) emit in the blue region whereas, three components (the C band at 3.42 eV, the M band at 3.73 eV, and the D band at 3.93 eV) contribute to the UV emission.

The relative intensities of these bands, as expected, were found to strongly depend on the specific treatment (irradiation and/or heating) the quartz is submitted to.

A pre-dose-like treatment, consisting of an irradiation followed by heating up to 500°C, resulted in a selective and progressive enhancement of only the C band. After this treatment, exposing the sample to irradiation causes its quenching. The same band (at 3.42 eV) can also be produced in untreated quartz by a single annealing at 500°C for 10 minutes. For lower or higher temperatures, the effect is not observed. Interestingly, annealing quartz at a temperature higher than 800°C produces a different UV band, at 3.73 eV (M band). This band is not detected in untreated samples and its intensity is maximized if the 10 minutes annealing occurs at 1000°C. Figure 2 reports the effect of annealing temperature on the C and M bands for three different types of quartz [9]. The different behavior of the two emission centers is evident and, despite the extent of the effect being sample dependent, the trend is common among all of the samples. The fact that the described phenomena are barely detectable in synthetic quartz and pronounced in the natural ones, clearly suggests the involvement of extrinsic defects in the atomic mechanisms.

As mentioned above, not only the UV emission is composite but also the blue one. When untreated quartz is exposed to prolonged

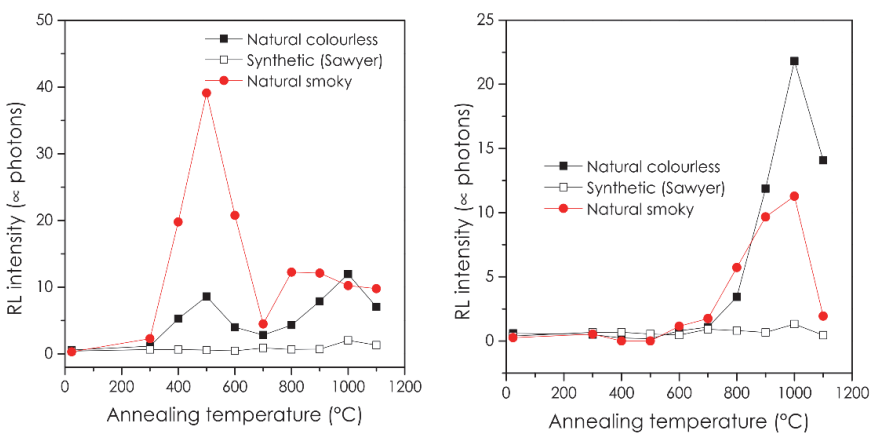


Fig. 2. Effect of annealing temperature on the RL intensity of the 3.42 eV band (C band, left) and the 3.73 eV one (M band, right) [9].

X-ray irradiation the A band at 2.51 eV in the blue region, is progressively enhanced. This behavior is consistent with that observed in [52] in volcanic quartz. The authors report a correlation between the intensity of the blue emission (around 470 nm) with the ESR signal of the $[AlO_4]^\circ$ center. The assignment of the 470 nm emission to such defects was already proposed by McKeever *et al.* [44] who also showed that $[AlO_4]^\circ$ acts as a recombination center for the 110°C peak. Several authors reported that the ESR signal of $[AlO_4]^\circ$ [39] is completely annealed out when quartz is heated at 300°C for 15 minutes. However, TL peaks at higher temperatures (such as the 375°C one) are known to recombine producing a blue emission, possibly contradicting the previously described defect assignment. We must consider, however, that comparing temperature from TL peaks with those found in ESR isochronal annealing can be misleading, since the timing in the two processes is significantly different. It is also important to recall that RL measurements have revealed the presence of a second blue emission band centered at 2.79 eV (B band), which has been clearly detected in samples annealed at 600°C for 5 hours [9]. Whether this band contributes also to the TL emission has yet to be determined.

The effect of irradiation on the two emissions in the blue (the A and B bands) is markedly different. The B band intensity, in fact, progressively decreases becoming negligible whereas the A band has an opposite behavior although no correlation was observed between the two recombination centers [9].

The fact that RL technique can be, indeed, employed to obtain information on the recombination centers involved in TL emission, was verified by comparing the sensitivity of the 110°C TL peak with the intensity of the A and C band for quartz subjected to different treatments. Figure 3 (left) shows the results obtained for quartz exposed to prolonged irradiation, where the RL intensity of the A band is proportional with the 110°C TL peak sensitivity. A similar correlation was observed in this case with the C band, when quartz was subjected to a pre-dose-like treatment in a sequence of successive RL and TL measurements (Fig. 3 right). This evidenced that indeed

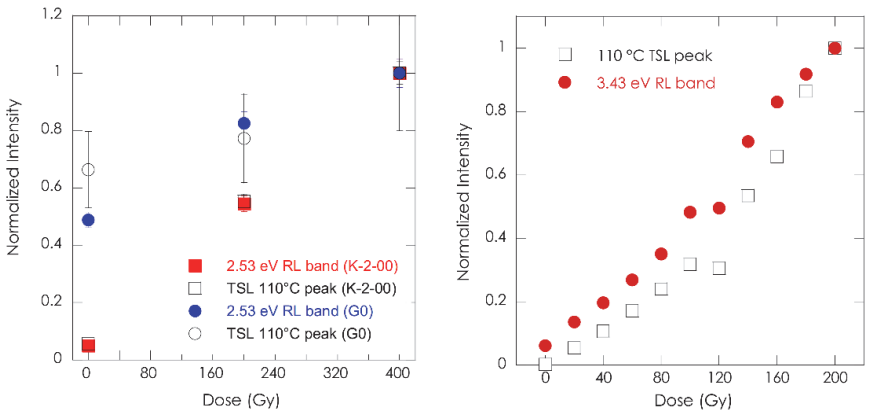


Fig. 3. (Left) Normalized dose response curve of the 2.53 eV RL band (filled markers) and of the 110°C TL peak (open markers) for a pegmatitic (squares) and synthetic (circles) quartz. (Right) Normalized sensitivity of the 110°C TL peak and intensity of the 3.43 eV RL band for a pegmatitic sample subjected to a sequence of alternated RL, at RT, and TL, up to 500°C, measurements [7].

the same A and C bands are involved also in TL emission, as later confirmed by wavelength resolved TL data [7].

### 5.5. Defects assignments

Several works in the literature aimed at identifying the specific defect responsible either for a TL trap or for an emission band. In most cases, unfortunately, it was not possible to achieve a fully convincing evidence of the proposed assignment, and only likely identification (when not plain speculations) were presented. However, by coupling TL and ESR techniques, it was possible to identify some point defects acting as electron trap and giving rise to a specific TL peak. Halperin *et al.* [64] showed that the 190 K peak is to be ascribed to an electron localized close to a $Li^+$ ion near a regular Si atom, $[Si/Li^+]^\circ$. It is interesting to note that the 190 K peak shows a behavior similar to the 110°C peak. In fact, both peaks' sensitivities can be enhanced by a two-stage process, specifically, an irradiation followed by heating.

While for the 110°C peak the heating has to occur at about 500°C, in the case of the 190 K peak, after irradiation at liquid nitrogen temperature, the sample has to be heated up to about 210 K. In both cases, the sensitivity enhancement is due to an increase of a UV emission.

In a similar work, Halperin *et al.* [79] brought evidences that, when $Li^+$ is replaced by $Na^+$, the analogous defect $[Si/Na^+]^\circ$ is the one that, by releasing the trapped electron, produces a TL peak that occurs at a slightly higher temperature, (202 K) compared to the one associated with $[Si/Li^+]^\circ$. In 1995 McKeever *et al.* [44], by monitoring the temperature dependence of various paramagnetic centers and the intensity of the 110°C peak, proposed $[GeO_4]^-$ as the trap responsible for this TL peak. Recently, Vaccaro *et al.* [12] proved this assignment by monitoring the dependence on temperature of the decay time of both the $[GeO_4]^-$ ESR signal and of the 110°C peak TL intensity. The agreement between the two decay times was striking over a broad temperature range. The position of the 110°C TL peak, however, was shown by Yang *et al.* [70] to be dependent on high temperature annealing and on sweeping. Moreover, many authors evidenced that in some samples, the 110°C appears to be composite [80]. Further investigations, therefore, would be useful to clarify these effects.

Other paramagnetic centers have been shown to act as electron traps, although a convincing assignment to a specific TL peak has not been reported up to now. These defects include $[TiO_4]^-$ and $[GeO_4/Li^+]^\circ$ [74, 81].

Concerning recombination centers, unfortunately, no consensus has been achieved yet on any defect assignment proposed insofar. As discussed in the previous section, McKeever *et al.* [44] presented clear evidence that the aluminum hole center, $[AlO_4/h^+]^\circ$, acts as one of the recombination centers for the 110°C peak and proposed that such a defect is responsible for the blue emission around 470 nm. They also proposed that the defect responsible for the recombination center emitting in the UV is the $[H_3O_4]^+$. Martini *et al.* [51], however, by investigating synthetic quartz annealed at 1200°C suggested that $[AlO_4/h^+]^\circ$ is the recombination center associated with the UV

emission. Itoh *et al.* [29] proposed a radically different mechanism for the 110°C peak blue emission, suggesting it could be due to an ionic recombination between $[AlO_4]^-$ and an alkali ion$^+$.

Many other tentative, and often contradictory, assignments have been proposed over the years and some of them were reviewed by Kalceff *et al.* [28]. The composite nature of the UV and blue emission, recently demonstrated, could account for these inconsistent attributions and justify the disagreement between some authors.

## References

[1] N.R.J. Poolton, G.M. Smith, P.C. Riedi, E. Bulur, L. Bøtter-Jensen, A.S. Murray and M. Adrian, "Luminescence sensitivity changes in natural quartz induced by high temperature annealing: a high frequency EPR and OSL study," *J. Phys. D: Appl. Phys.*, vol. 33, pp. 1007–1017, 2000.

[2] P. Pellegrini, F. Euler, A. Kahan, T.M. Flanagan and T.F. Wrobel, "Steady state and transient radiation effects in precision quartz oscillators," *IEEE Trans. Nucl. Sci.*, vol. NS-25, pp. 1267–1273, 1978.

[3] F. Preusser, M.L. Chithambo, T. Götte, M. Martini, K. Ramseyer, E.J. Sendezera, G.J. Susino and A.G. Wintle, "Quartz as a natural luminescence dosimeter," *Earth Sci. Rev.*, vol. 97, pp. 184–214, 2009.

[4] M.J. Aitken, *Thermoluminescence Dating*. (Academic Press, London, 1985).

[5] D.J. Huntley, D.I. Godfrey-Smith and M.L.W. Thewalt, "Optical dating of sediments," *Nature*, vol. 313, pp. 105–107, 1985.

[6] L.E. Halliburton, N. Koumvakalis, M.E. Markes and J.J. Martin, "Radiation effects in crystalline $SiO_2$: the role of aluminum," *J. Appl. Phys.*, vol. 52, pp. 3565–3574, 1981.

[7] M. Martini, M. Fasoli, I. Villa and P. Guibert, "Radioluminescence of synthetic and natural quartz," *Radiat. Meas.*, vol. 47, pp. 846–850, 2012.

[8] C. Schmidt, S. Kreutzer, R. DeWitt and M. Fuchs, "Radiofluorescence of quartz: A review," *Quat. Geochronol.*, vol. 27, pp. 66–77, 2015.

[9] M. Martini, M. Fasoli and I. Villa, "Defect studies in quartz: Composite nature of the blue and UV emissions," *Nucl. Instrum. Meth. B*, vol. 327, pp. 15–21, 2014.

[10] M. Martini, M. Fasoli, A. Galli, I. Villa and P. Guibert, "Radioluminescence of synthetic quartz related to alkali ions," *J. Lumin.*, vol. 132, pp. 1030–1036, 2012.

[11] V. Pagonis, M.L. Chithambo, R. Chen, A. Chruścińska, M. Fasoli, S.H. Li, M. Martini and K. Ramseyer, "Thermal dependence of luminescence lifetimes and radioluminescence in quartz," *J. Lumin*, vol. 145, pp. 38–48, 2014.

[12] G. Vaccaro, L. Panzeri, S. Paleari, M. Martini and M. Fasoli, "EPR investigation of the role of germanium centers in the production of the 110°C

thermoluminescence peak in quartz," *Quat. Geochronol.*, vol. 39, pp. 99–104, 2017.

[13] G.A. Jenner, H.P. Longerich, S.E. Jackson and B.J. Fryer, "ICP-MS — A powerful tool for high-precision trace-element analysis in Earth sciences: Evidence from analysis of selected U.S.G.S. reference samples," *Chem. Geol.*, vol. 83, pp. 133–148, 1990.

[14] B. Flem, R.B. Larsen, A. Grimstvedt and J. Mansfeld, "In situ analysis of trace elements in quartz by using laser ablation inductively coupled plasma mass spectrometry," *Chem. Geol.*, vol. 182, pp. 237–247, 2002.

[15] A.J. Cohen, "Substitutional and interstitial aluminum impurity in quartz, structure and color center interrelationship," *J. Phys. Chem. Solids*, vol. 13, pp. 321–325, 1960.

[16] J.A. Weil, "A review of electron-spin spectroscopy and its application to the study of paramagnetic defects in crystalline quartz," *Phys. Chem. Miner.*, vol. 10, pp. 149–165, 1984.

[17] A. Kats, "Hydrogen in alpha-quartz," *Philips Res. Rep.*, vol. 17, pp. 201–279, 1962.

[18] J. Götze, M. Plötze and D. Habermann, "Origin, spectral characteristics and practical applications of the cathodoluminescence (CL) of quartz — A review," *Miner. Petrol.*, vol. 71, pp. 225–250, 2001.

[19] G.F. King, G.E.A.A. Finch, R.A.J. Robinson and D.E. Hole, "The problem of dating quartz 1: Spectroscopic ionoluminescence of dose dependence," *Radiat. Meas.*, vol. 46, pp. 1–9, 2011.

[20] M. Cannas, M.S. Agnello, F.M. Gelardi, R. Boscaino, A.N. Trukhin, P. Liblik, C. Lushchik, M.F. Kink, M.F.Y. Maksimov and R.A. Kink, "Luminescence of $\gamma$-radiation-induced defects in $\alpha$-quartz," *J. Phys.-Condens. Mat.*, vol. 16, pp. 7931–7939, 2004.

[21] M. Martini, G. Spinolo and A. Vedda, "Thermally stimulated luminescence of thermally grown $SiO_2$ films," *Radiation Effects*, vol. 105, pp. 107–116, 1987.

[22] J.G. Solé, L.E. Bausá and D. Jaque, *An Introduction to the Optical Spectroscopy of Inorganic Solids.* (John Wiley & Sons, Ltd., 2005).

[23] J.J. Martin, "Electrodiffusion (sweeping) of ions in quartz-a review," *IEEE T. Ultrason. Ferr.*, vol. 35, pp. 288–296, 1988.

[24] D.M. Malik, E.E. Kohnke and W.A. Sibley, "Low-temperature thermally stimulated luminescence of high quality quartz," *J. Appl. Phys.*, vol. 52, pp. 3600–3605, 1981.

[25] A.G. Wintle and G. Adamiec, "Optically stimulated luminescence signals from quartz: A review," *Radiat. Meas.*, vol. 98, pp. 10–33, 2017.

[26] K.P. Lieb and J. Keinonen, "Luminescence of ion-irradiated alpha quartz," *Contemp. Phys.*, vol. 47, pp. 305–331, 2006.

[27] J.A. Weil, A demi-century of magnetic defects in $\alpha$-quartz. In G. Pacchioni, L. Skuja and D.L. Griscom (eds.), *Defects in $SiO_2$ and Related Dielectrics: Science and Technology.* (Kluwer, Amsterdam, 197–212, 2000).

[28] M.A. Stevens Kalceff and M.R. Phillips, "Cathodoluminescence microcharacterization of the defect structure of quartz," *Phys. Rev. B*, vol. 52, pp. 3122–3134, 1995.

[29] N. Itoh, D. Stoneham and A.M. Stoneham, "Ionic and electronic processes in quartz: mechanisms of thermoluminescence and optically stimulated luminescence," *J. Appl. Phys.*, vol. 92, pp. 5036–5044, 2002.

[30] D.L. Griscom and E.J. Friebele, "Fundamental defect centers in glass: $^{29}$Si hyperfine structure of the nonbridging oxygen hole center and the peroxy radical in $\alpha$-$SiO_2$," *Phys. Rev. B*, vol. 24, pp. 4896–4898, 1981.

[31] J.M. Baker and P.T. Robinson, "EPR of a new defect in natural quartz: Possibly $O^{2-}$," *Solid State Commun.*, vol. 48, pp. 551–554, 1983.

[32] M.J. Nilges, Y. Pan and R.I. Mashkovtsev, "Radiation-damage-induced defects in quartz. I. Single-crystal W-band EPR study of hole centers in an electron-irradiated Quartz," *Phys. Chem. Miner.*, vol. 35, pp. 103–115, 2008.

[33] S. Botis, S.M. Nokhrin, Y. Pan, Y. Xu, T. Bonli and V. Sopuck, "Natural radiation-induced damage in quartz. I. Correlations between cathodoluminescence colors and paramagnetic defects," *Can. Mineral.*, vol. 43, pp. 1565–1680, 2005.

[34] X.H. Yang and S.W.S. McKeever, "The pre-dose effect in crystalline quartz," *J. Phys. D: Appl. Phys.*, vol. 23, pp. 237–244, 1990.

[35] V.B. Sulimov, P.V. Sushko, A.H. Edwards, A.L. Shluger and A.M. Stoneham, "Asymmetry and long-range character of lattice deformation by neutral oxygen vacancy in $\alpha$-quartz," *Phys. Rev. B*, vol. 66, pp. 024108–14, 2002.

[36] R.A. Weeks, "Paramagnetic resonance of lattice defects in irradiated quartz," *J. Appl. Phys.*, vol. 27, pp. 1376–1381, 1956.

[37] F.J. Feigl, W.B. Fowler and K.L. Yip, "Oxygen vacancy model for $E_1$' center in $SiO_2$," *Solid State Commun.*, vol. 14, pp. 225–229, 1974.

[38] J.K. Rudra and W.B. Fowler, "Oxygen vacancy and the $E_1$' center in crystalline $SiO_2$," *Phys. Rev. B*, vol. 35, pp. 8223–8230, 1987.

[39] M.G. Jani, R.B. Bossoli and L.E. Halliburton, "Further characterization of the $E_1$' center in crystalline $SiO_2$," *Phys. Rev. B*, vol. 27, pp. 2285–2293, 1983.

[40] M. Boero, A. Oshiyama and P.L. Silvestrelli, "E' centers in quartz in the absence of oxygen vacancies: a first-principles molecular-dynamics study," *Phys. Rev. Lett.*, vol. 91, 206401, 2003.

[41] J. Isoya, J.A. Weil and L.E. Halliburton, "EPR and ab initio SCF–MO studies of the Si·H–Si system in the $E_4'$ center of $\alpha$-quartz," *J. Chem. Phys.*, vol. 74, pp. 5436–5448, 1981.

[42] R.B. Bossoli, M.G. Jani and L.E. Halliburton, "Radiation-induced E" centers in crystalline $SiO_2$," *Solid State Commun.*, vol. 44, pp. 213–217, 1982.

[43] H.J. Mackey Jr, "EPR study of impurity-related color centers in germanium-doped quartz," *J. Chem. Phys.*, vol. 39, pp. 74–83, 1963.

[44] S.W.S. McKeever, C.Y. Chen and L.E. Halliburton, "Point-defects and the predose effect in natural quartz," *Nucl. Tracks Rad. Meas.*, vol. 10 489–495, 1985.

[45] D.W. McMorris, "Impurity color centers in quartz and trapped electron dating: electron spin resonance, thermoluminescence studies," *J. Geophys. Res.*, vol. 76, pp. 7875–7887, 1971.

[46] J. Isoya, W.C. Tennant and J.A. Weil, "EPR of the $TiO_4$/Li center in crystalline quartz," *J. Magn. Reson.*, vol. 79, pp. 90–98, 1988.
[47] A.S. Marfunin, *Spectroscopy, luminescence and radiation centers in minerals*. (Springer-Verlag, Berlin, 1979).
[48] E.H. Nunes, V. Melo, F. Lameiras, O. Liz, A. Pinheiro, G. Machado and W. Vasconcelos, "Determination of the potential for extrinsic color development in natural colorless quartz," *Am. Mineral.*, vol. 94, pp. 935–941, 2009.
[49] J.A. Weil, "The aluminum centers in alpha-quartz," *Radiat. Eff.*, vol. 26, pp. 261–265, 1975.
[50] N. Koumvakalis, "Defects in crystalline $SiO_2$: Optical absorption of the aluminum-associated hole center," *J. Appl. Phys.*, vol. 51, pp. 5528–5532, 1980.
[51] M. Martini, A. Paleari, G. Spinolo and A. Vedda, "Role of $[AlO_4]^0$ centers in the 380-nm thermoluminescence of quartz," *Phys. Rev. B*, vol. 52, pp. 138–142, 1995.
[52] C. Woda, T. Schilles, U. Rieser, A. Mangini and G.A. Wagner, "Point defects and the blue emission in fired quartz at high dose: A comparative luminescence and EPR study," *Radiat. Prot. Dosim.*, vol. 100, pp. 261–264, 2002.
[53] M.R. Hantehzadeh, C.S. Han and L.E. Halliburton, "Radiation-induced mobility of interstitial ions in Iron-doped quartz," *J. Phys. Chem. Solids*, vol. 51, 425–429, (1990).
[54] D. Maschmeyer and G. Lehmann, "A trapped-hole center causing rose coloration of natural quartz," *Z. Kristallogr.*, vol. 163, pp. 181–196, 1983.
[55] A.K. Kronenberg, "Hydrogen speciation and chemical weakening of quartz," *Rev. Mineral.*, vol. 29, pp. 123–176, 1994.
[56] R.H.D. Nuttall and J.A. Weil, "Two hydrogenic trapped hole species in alpha-quartz," *Solid State Commun.*, vol. 33, pp. 99–102, 1980.
[57] W. Hohenau, "The influence of silver and copper electrolysis on the radiation-induced optical absorption of natural quartz," *Phys. Status Solidi A*, vol. 83, pp. 119–124, 1984.
[58] M. Martini, G. Spinolo and A. Vedda, "Radiation induced conductivity of as-grown and electrodiffused quartz," *J. Appl. Phys.*, vol. 60, pp. 1705–1708, 1986.
[59] M.E. Markes and L.E. Halliburton, "Defects in synthetic quartz: Radiation-induced mobility of interstitial ions," *J. Appl. Phys.*, vol. 50, pp. 8172–8180, 1979.
[60] M.A. Mondragon, C.Y. Chen and L.E. Halliburton, "Observation of a dose-rate dependence in the production of point defects in quartz," *J. Appl. Phys.*, vol. 63, pp. 4937–4941, 1988.
[61] J. Zimmerman, "The radiation-induced increase of the 100°C thermoluminescence sensitivity of fired quartz," *J. Phys. C: Solid State*, vol. 4, pp. 3265–3276, 1971.

[62] P.G. Benny, T.K. Gundu Rao and B.C. Bhatt, "The $E_1$' center and its sensitization in quartz," *Radiat. Meas.*, vol. 35, pp. 369–373, 2002.
[63] M. Martini, E. Sibilia, G. Spinolo and A. Vedda, "Pre-dose, TSL and AC conductance interrelation un quartz," *Nucl. Tracks Radiat. Meas.*, vol. 10, pp. 497–501, 1985.
[64] A. Halperin, M.G. Jani and L.E. Halliburton, "Correlated ESR and thermoluminescence study of the $[SiO_4/Li]^0$ center in quartz," *Phys. Rev. B*, vol. 34, pp. 5702–5707, 1986.
[65] S.W.S. McKeever, *Thermoluminescence of Solids.* (Cambridge University Press, 2011).
[66] R. Chen and S.W.S. McKeever, *Theory of thermoluminescence and related phenomena.* (World Scientific Publishing Company, 1997).
[67] M.R. Krbetschek, J. Götze, A. Dietrich and T. Trautmann, "Spectral information from minerals relevant for luminescence dating," *Radiat. Meas.*, vol. 27, pp. 695–748, 1997.
[68] R.A. Akber, G.B. Robertson and J.R. Prescott, "The 100°C thermoluminescence emission from high-fired ceramics: a three dimensional view," *Nucl. Tracks Radiat. Meas.*, vol. 14, pp. 21–25, 1988.
[69] H.M. Rendell, P.D. Townsend, R.A. Wood and B.J. Luff, "Thermal treatments and emission spectra of TL from quartz," *Radiat. Meas.*, vol. 23, pp. 441–449, 1994.
[70] X.H. Yang and S.W.S. McKeever, "Characterization of the pre-dose effect using ESR and TL," *Nucl. Tracks Radiat. Meas.*, vol. 14, pp. 75–79, 1988.
[71] L. Bøtter-Jensen, N. Agersnap Larsen, V. Mejdahl, N.R.J. Poolton, M.F. Morris and S.W.S. McKeever, "Luminescence sensitivity changes in quartz as a result of annealing," *Radiat. Meas.*, vol. 24, pp. 535–541, 1995.
[72] J. Lomax, D. Mittelstraß, S. Kreutzer and M. Fuchs, "OSL, TL and IRSL emission spectra of sedimentary quartz and feldspar samples," *Radiat. Meas.*, vol. 81, pp. 251–256, 2015.
[73] A.G. Wintle and A.S. Murray, "Luminescence sensitivity changes in quartz," *Radiat. Meas.*, vol. 30, pp. 107–118, 1999.
[74] T. Schilles, N.R.J. Poolton, E. Bulur, L. Bøtter-Jensen, A.S. Murray, G.M. Smith, P.C. Riedi and G.A. Wagner, "A multi-spectroscopic study of luminescence sensitivity changes in natural quartz induced by high-temperature annealing," *J. Phys. D: Appl. Phys.*, vol. 34, pp. 722–731, 2001.
[75] N. Shimizu, N. Mitamura, A. Takeuchi and T. Hashimoto, "Dependence of radioluminescence on TL-properties in natural quartz," *Radiat. Meas.*, vol. 41, 831–835, (2006).
[76] M. Fasoli and M. Martini, "The composite nature of the thermoluminescence UV emission of quartz," *J. Lumin.*, vol. 173, pp. 120–126, 2016.
[77] K. Tanimura and K.L.F. Halliburton, "Polarization of the x-ray-induced blue luminescence in quartz," *Phys. Rev. B*, vol. 34, pp. 2933–2935, 1986.

[78] A.N. Trukhin, "Self-trapped exciton luminescence in $\alpha$-quartz," *Nucl. Instum. Meth. B*, vol. 91, pp. 334–337, 1994.

[79] A. Halperin and E.W. Sucov, "Single irradiation excitation of the thermoluminescence (TSL) related to the $[SiO_4/Na]^\circ$ center in quartz," *J. Phys. Chem. Solids*, vol. 52, pp. 1039–1040, 1991.

[80] S.A. Petrov and I.K. Bailiff, "The 110°C TL peak in synthetic quartz," *Radiat. Meas.*, vol. 24, pp. 519–523, 1995.

[81] R.V. Lorenze and F.J. Feigl, "Defects in crystalline quartz: electron paramagnetic resonance of multiple-alkali-compensated centers associated with germanium impurities," *Phys. Rev. B*, vol. 8, 4833–4841, 1973.

## Chapter 6

# Recent Experiments and Theory of OSL

Alicja Chruścińska

*Institute of Physics, Faculty of Physics, Astronomy and Informatics*
*Nicolaus Copernicus University, Grudziadzka 5/7*
*87-100 Torun, Poland*
*alicja@fizyka.umk.pl*

Applications of OSL require knowledge about traps existing in the material. The role of traps in OSL is determined by their optical activation energy and the strength of electron-phonon coupling in the process of trap ionization. This chapter shows how taking into account the crystal lattice vibrations in the simple OSL model, allows to explain some thermal effects observed in experiments. It is also shown that the dependence of optical cross-section on the stimulation energy and temperature can be used to change the probability of electron release from a trap during optical stimulation, in such a way that OSL signals from individual traps can be effectively separated. OSL measurement methods consisting of the continuous variation of the stimulation energy or heating the sample during stimulation are discussed, together with results of new experiments. Finally, the effects of changing the shape of the stimulation spectrum on the OSL curve are demonstrated. These effects are the basis of another method of optical stimulation. An advantage of all the introduced methods is that the shape of OSL curves is uniquely determined by the optical depth of the trap and by the strength of electron-phonon coupling.

## 6.1. OSL and crystal lattice vibrations

In material research, the aim of OSL measurements is the determination of traps that are active in the process, and are responsible for the individual OSL curve components. A parameter that is thought to distinguish traps in OSL, in the same way as the thermal

activation energy and the frequency factor characterizing a trap in the thermoluminescence process, is the optical cross-section. It should be remembered, however, that this physical quantity is not a fixed parameter uniquely determined for a trap, as it is, for example, in the case of the thermal depth of traps. The optical cross section depends on the energy of stimulation photons, which seems to be obvious, and on the measurement temperature. A parameter that defines a trap in the OSL process unambiguously is the optical activation energy of the trap (optical depth of the trap, or ionization threshold, $E_0$), which is simply the least energy needed for the ionization of an electron from a trap at 0 K.

Two different general cases in trap photoionization may be considered, just like in every case of electron excitation from the ground state to the excited state in solids. These cases are associated with strong coupling of the defect responsible for the trap when its neighboring ions in the lattice relax to new equilibrium positions after the excitation (so-called displacement recoil), as well as a weak coupling when the difference between the ground state and the excited state equilibrium positions is so small that it can be neglected. A classic example of the first case are F centers in alkali halides, and examples of the second case are rare-earth impurities [1]. However, these differences can be strictly distinguished only at low temperatures. At temperatures significantly higher than 0 K, the electron-phonon coupling is a fundamental effect that is inherent to photo-ionization and should be taken into account. This temperature range is determined individually for the trap center by the strong coupling condition, $S\ coth(\hbar\omega/2kT) \gg 1$, where S is the Huang-Rhys factor, which can be interpreted as the average number of phonons participating in the electron transition, and $\hbar\omega$ is the characteristic phonon energy for the center [2, 3]. This condition is fulfilled with great probability when one detects the OSL in dosimetric applications. Therefore, formulas like those given by Grimmeiss and Ledebo [4] or Lukovsky [5] that result from purely electronic models and neglect the vibrational effects are proper at low temperatures. More advanced formulas should be applied for the description of the OSL dependence on measurement temperature

and stimulation energy, especially in the case of deep OSL traps investigated at temperatures above room temperature [6, 7]. It should also be stressed that, because of the dependence of the phonon energy distribution on temperature, it is obvious that the optical cross-section (OCS) determined by expressions that also take electron-phonon coupling into account must depend on temperature.

In the literature of the 1970s, a number of papers concerned the role of lattice vibrations in the photo-ionization of deep centers in semiconductors. Just as in the case of the F center in alkali halides, a significant broadening and shift of the absorption bands with temperature have been observed. Diverse approaches have been applied in individual cases, in order to incorporate the phonon participation in the transition and to explain the shape of the luminescence bands [8–13].

In the first investigation of the character of OSL changes with stimulation energy and temperature, the simplest model of the electron-phonon interaction proposed by Noras [14] has been used [15, 16]. This leads to the following equation for the OCS ($\sigma$) dependence on stimulation energy:

$$\sigma(h\nu) = \frac{C\kappa}{\nu\sqrt{\pi}} \int_0^\infty x^{a-1} \exp\left\{-\kappa^2[x - (h\nu - E_0)]^2\right\} dx \qquad (1)$$

$$\kappa = \left[2S(h\omega/2\pi)^2 \coth\left(\frac{h}{2\pi}\frac{\omega}{2kT}\right)\right]^{-\frac{1}{2}} \qquad (2)$$

where $h\nu$ is the stimulation energy and $x$ is a bound variable with the dimension of energy. $E_0$ is related to the thermal depth of the trap $E_T$ by the expression: $E_0 = E_T + S\hbar\omega$. Figure 1 presents a configurational coordinate diagram that explains the meaning of the parameters appearing in Eqs. (1) and (2), and also shows the relation between the thermal and optical trap depth. The factor $S\hbar\omega$ in the simple model of optical band shape is a measure of electron-phonon coupling strength. For the derivation of Eq. (1), Gaussian broadening resulting from vibrational interactions has been used for the optical excitation of an electron to a single state in the conduction band, with the assumption of a single configuration-coordinate and equal force constants in the ground and excited states, e.g. [6, 7]. The integral in

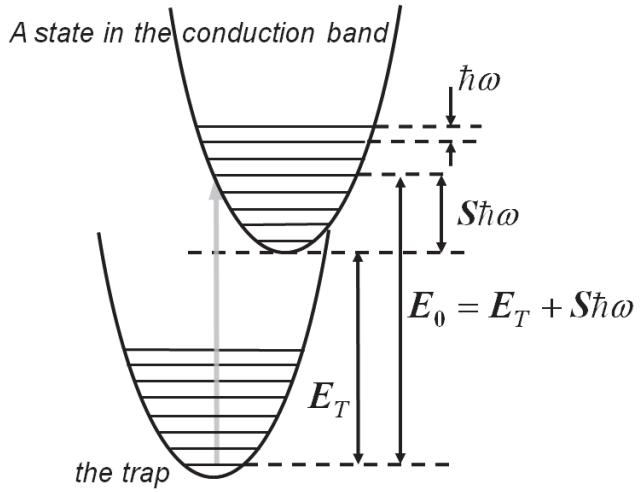


Fig. 1. Illustration of the simplest model of the participation of crystal lattice vibrations in the electron release process from the trap during the optical stimulation — a configurational coordinate diagram for the case of a trap and a state selected from the conduction band states. The derivation of the equation for the OCS dependence on stimulation energy needs to take all the states in the conduction band into account. The simplest model assumes the single vibrational mode and the equal vibrational frequency in the ground and excited states.

Eq. (1) is a consequence of taking into account the transitions to all possible states in the conduction band. A significant simplification while calculating the OCS value, is the fact that the limitation of the integration range in Eq. (1) to a few electron-volts does not change the obtained value noticeably. The pure electronic part of the excitation probability has been assumed to have a particularly simple form of the power law:

$$\sigma_e(h\nu) = \begin{cases} \nu^{-1}(h\nu - E_0)^{a-1}, & h\nu \geq E_0 \\ 0, & h\nu < E_0 \end{cases} \tag{3}$$

where $a = 5/2$ or $3/2$ (for the forbidden and allowed transitions, respectively). The scaling constant $C$ in Eq. (1) has the dimension $\mathrm{cm^2 s^{-1} eV^{-3/2}}$ or $\mathrm{cm^2 s^{-1} eV^{-1/2}}$ corresponding to the $a$ value and is assumed to be equal to 1 in all further considerations. Equation (1) is valid when $S\hbar\omega \ll E_0$. It can be assumed, at least in the first stage

of the investigation, that this condition is fulfilled for OSL traps which are important for dosimetric applications. The middle values of the trap parameters $(S, \hbar\omega)$ from the range satisfying the condition $S\hbar\omega \ll E_0$, have been used in all the calculations presented below.

It is interesting to see how the shape of the $\sigma(h\nu)$ function depends on the trap parameters $E_0$, $S$ and $\hbar\omega$. Figure 2 shows graphs of OCS dependence on stimulation energy calculated by the expressions (1) and (2) for a few values of electron-phonon parameters, and the optical trap depth equal to 2 eV. The most fundamental conclusion that can be drawn from these plots is that electrons can be released by photons with energy far below the optical depth of the trap. This effect has been reported previously by many authors [17–23]. For the range of stimulation energy that is presented in Fig. 2, the character of Eq. (2), which determines the factor $\kappa$, is decisive for the strong variability of $\sigma(h\nu)$ with $S$ and $\hbar\omega$ below the threshold. The stronger the electron-phonon coupling, which means the greater the Huang-Rhys parameter and phonon energy, the higher the OCS

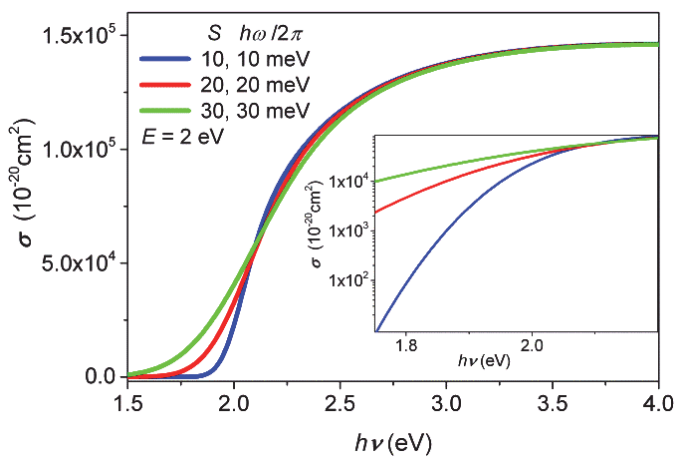


Fig. 2. The OCS dependence on stimulation energy calculated using equations (1) and (2) for the optical trap depth equal to 2 eV and a variety of electron-phonon parameters ($a = 3/2$). The inset shows a part of the main graph, in order to illustrate the significant differences between the OCS values for various electron-phonon coupling parameters below the optical threshold, as well as their dynamic changes in this range of stimulation energy.

values. Above the threshold, these parameters affect the OCS much less and, between the inflection point and the range of saturation level, the tendency is the opposite; the stronger the electron-phonon coupling, the smaller the OCS values.

The $E_0$ value controls the shape of the OCS dependence on the trap parameters to a much lower extent but, obviously, determines its position along the stimulation energy ($h\nu$) axis. As can be seen in Fig. 3, the results obtained for the chosen $E_0$ range also apply to any lower or higher range of energies.

The electron-phonon coupling parameters are rather characteristics of the traps than of the crystal, so they may vary significantly from trap to trap. In this context, it is worth noticing that the common conception that, for a definite stimulation energy, the OCS is higher for traps with lower optical depth can be false. For example, in Fig. 3, in the range below 2.0 eV, the OCS value for $E_0 = 2.1$ eV and $\hbar\omega = 40$ meV is considerably larger than the OCS for $E_0 = 2.0$ eV and $\hbar\omega = 10$ meV. A similar situation is possible when $S$ values are different, but the $\sigma(h\nu)$ variability with this parameter is slightly weaker than in the case of $\hbar\omega$. Such effects take place for stimulation energies below the optical depth of the deeper trap.

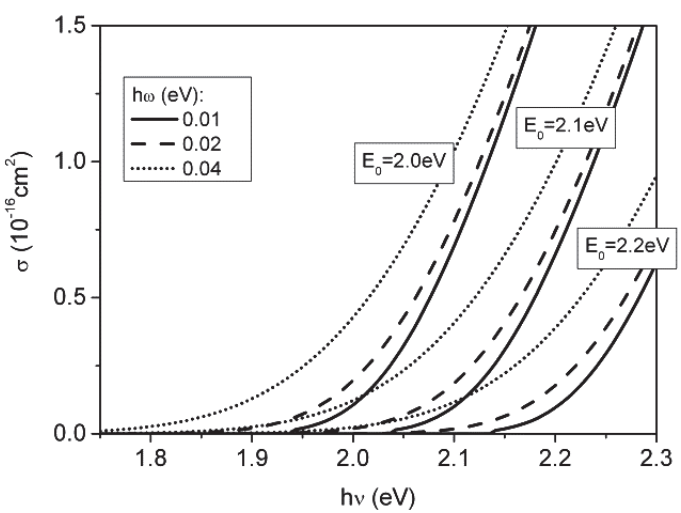


Fig. 3. The OCS dependence on stimulation energy calculated for a few values of the parameters $E_0$ and $\hbar\omega$ ($S = 20$, $a = 5/2$).

Taking into account the lattice vibrations while considering the OSL process, means that a trap is defined by at least the three quantities discussed above. Therefore, interpreting the experimental results that lead to the description of a trap is more difficult in the case of OSL than for TL. However, it will be shown below that knowing an explicit formula for the optical cross-section dependence on the stimulation energy can be a basis for developing new experimental tools. These, on one hand, allow the parameters that uniquely define a trap to be estimated and, on the other hand, are useful for finding methods to better separate the OSL signal components coming from different traps.

So far, two ways of measuring the OSL have been mainly used for investigating the traps participating in OSL processes; the continuous wave OSL (CW-OSL) and linearly modulated OSL (LM-OSL) methods [24, 25]. In both methods, the optical stimulation is performed with constant stimulation energy. In the CW-OSL, the photon flux is constant, whereas in the LM-OSL it is linearly increased. The only trap parameter that can be obtained from these conventional OSL measurements is the OCS. The ability of these methods to separate the signal related to different traps is rather limited. This is a consequence of the fact that, during the stimulation with constant stimulation energy, the OCS of the trap is also fixed. The process of optical emptying of the trap is controlled by the value of the probability (strictly speaking: the density of probability or the probability per time unit) of electron release $\gamma = f(t)\ \sigma$, where $f(t)$ is the photon flux density used for stimulation. During CW-OSL or LM-OSL measurement, for two trap kinds with different OCS ($\sigma_1$, $\sigma_2$), the ratio of probabilities of electron release from different traps is $\gamma_1/\gamma_2 = \sigma_1/\sigma_2$ and is fixed, because the ratio of the OCS is constant. In this case, the change of the photon flux with time $f(t)$ is not important.

The character of trap depopulation during the TL measurements is different. While measuring the glow curve, the ratio of probabilities of the thermal release of electrons from different traps changes in a specific way, making the successive emptying of deeper and deeper traps possible. The shallower traps can be emptied, while

the occupation of deeper traps remains unaffected. This allows the effective separation of TL signals originating from different traps, which is applied successfully in TL analysis using the fractional glow technique or T-stop method [24]. During the CW-OSL or LM-OSL processes, such a favorable situation does not occur for comparable difference between the optical depths of traps. However, there is a way of generating the probability ratio changes and getting a better separation of the OSL signal originating from different traps during the optical stimulation. One should then stimulate suitable changes in OCS; in accordance with Eqs. (1) and (2), this is possible when the stimulation energy or the temperature is changed. The consequences of such changes for the shape of the OSL curve will be presented in the next subsections.

In all the computer simulations, whose results are presented in the next subsections, the following equations have been used:

$$\frac{dn_i}{dt} = -\gamma_i n_i + A_i(N_i - n_i)n_c; \quad i = 1, 2, \tag{4}$$

$$\frac{dm}{dt} = A_m(M - m)m_v - \beta m n_c, \tag{5}$$

$$\frac{dn_c}{dt} = R + \sum_{i=1}^{2} [\gamma_i n_i - A_i(N_i - n_i)n_c] - \beta m n_c, \tag{6}$$

$$\frac{dm_v}{dt} = R - A_m(M - m)m_v \tag{7}$$

where $n_i$ ($\mathrm{cm}^{-3}$) and $N_i$ ($\mathrm{cm}^{-3}$), $i = 1, 2$, are, respectively, the concentrations of trapped electrons and trapping states; $m$ ($\mathrm{cm}^{-3}$) and $M$ ($\mathrm{cm}^{-3}$) are the concentration of holes trapped in recombination centers and the concentration of these centers; $n_c$ ($\mathrm{cm}^{-3}$) and $m_v$ ($\mathrm{cm}^{-3}$) are the concentrations of free electrons and holes in the conduction and valence bands, respectively; $A_i$ ($\mathrm{cm}^3\,\mathrm{s}^{-1}$), $i = 1, 2$, are the probability coefficients of electron trapping in the corresponding traps, $A_m$ ($\mathrm{cm}^3\,\mathrm{s}^{-1}$) is the probability coefficient of hole trapping in the recombination center, $\beta$ ($\mathrm{cm}^3\,\mathrm{s}^{-1}$) is the probability coefficient of a free electron recombination with a hole trapped in the luminescence center; $R$ is the intensity of the excitation irradiation producing pairs

of free electrons and holes (it is taken as $10^8\,\mathrm{cm}^{-3}\mathrm{s}^{-1}$ during the excitation process and 0 for other processes), $\gamma_i$ ($\mathrm{s}^{-1}$) is the time-dependent probability of the release of electrons from the $i$-th trap to the conduction band. $\gamma_i$ has a form suitable for each type of stimulation, and is equal to zero during excitation and relaxation.

Three successive processes have been simulated, namely trap filling during irradiation, relaxation after irradiation and finally optical stimulation. The simulations have been performed using the MATLAB differential equation solver ode23s, which is specially designed for stiff equation sets. The above differential equations have been solved for the case of two traps, as well as in the case of the simpler set (with $i = 1$) for the one-trap model.

### 6.2. Optical cross-section dependence on temperature

The second very important consequence of taking electron-lattice coupling into account while describing the OSL phenomenon, after the possibility of emptying traps by photons with energy much lower than the optical depth of the trap, is including the dependence of OCS on temperature in the basic OSL model, in accordance with the earlier intuition expressed by Spooner [17]: "The temperature dependence observed in the production of OSL is inherent to the photoionization mechanism". This is a direct consequence of Eqs. (1) and (2), but is simultaneously consistent with many experimental observations reported earlier. These observations include: the increase in the initial OSL intensity [17, 18, 26–28] and the OSL decay rate [21, 23, 29–32] with the increase in measurement temperature. In some results, one can clearly see that the increase in the OSL intensity with temperature is more evident for lower stimulation energy [17, 18, 33]. Originally, the changes in OSL intensity with temperature have been explained by thermal assistance, and it should be stressed that these effects can appear simultaneously with the fundamental results of the electron-phonon coupling, especially in such complex systems as quartz or feldspars. However, before one considers the more complex models of OSL for explaining the temperature effect, the fundamental

dependence of OCS on stimulation energy and temperature should be included in the interpretation of OSL measurement results.

It has been demonstrated using OSL simulations, that both the OSL intensity and the decay rate depend on temperature, even if the simplest model of OSL is considered. Figure 4 clearly shows that the value of OCS increases with temperature. The graphs in Fig. 4a are for four different optical trap depths. As one can observe, for a fixed stimulation energy, the changes in $\sigma(h\nu)$ with temperature are more significant for larger optical depths. This effect is more clearly

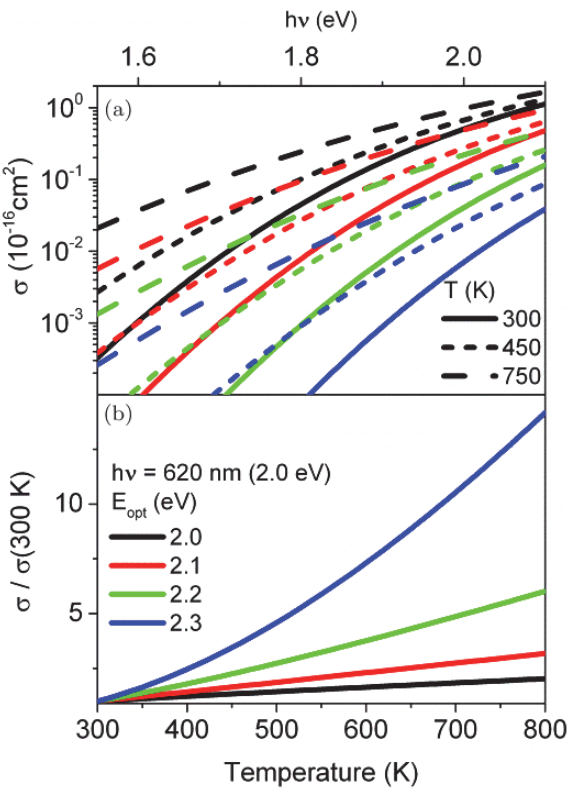


Fig. 4. The OCS dependence on stimulation energy for different temperatures shown for four different optical trap depths $E_0$ (a) and the OCS dependence on temperature for the same optical trap depths drawn for the stimulation energy equal to 2.0 eV (b). The OCS(T) plots are normalized to OCS at 300 K ($S = 20$, $\hbar\omega = 20$ meV, $a = 5/2$).

displayed when the $\sigma - T$ plane is used ( Fig. 4b). A few examples of the OCS(T) plots normalized to OCS at 300 K are given for selected values of the optical trap depth. When $h\nu \geq E_0$ the changes are not large, but they are noticeable. The optical cross-section (OCS) increases by a factor of 2 when the temperature increases from 300 K to 800 K for $E_0 = 2.0\,\text{eV}$ ($h\nu = 2.0\,\text{eV}$). However, in the case of slightly deeper traps with $E_0 = 2.3\,\text{eV}$ and for the same stimulation energy, it increases by a factor of 14 in the same temperature range.

The Noras formulae Eqs. (1) and (2) have been used for modeling OSL measurements carried out at different temperatures [15]. The CW-OSL curve shape changes observed during such experiments are shown in Fig. 5 for a simple one-trap model. These clearly illustrate the scale of shape changes of a single OSL component in a chosen range of temperatures. As can be deduced from the character of $\sigma(T)$, the initial intensity of the CW-OSL curve and the decay rate both increase with the temperature of OSL measurement. A distinct sequence of the OSL curves that cross each other in a relatively small region of the time axis can be seen when the OSL is measured at different temperatures. These changes are particularly intensive for stimulation energy lower than the optical trap depth, as can be observed in Fig. 5a. The optical stimulation with the energy close to the optical trap depth or higher, leads to less significant changes in the OSL curve shape, but the effects can still be clearly observed (Fig. 5b). In the insets of the figure, the normalized OSL curves are shown for better presentation of the increase in decay rate.

Such characteristic behavior of the OSL curves with the temperature may not be observed for more complex models. For example, the slow OSL component observed experimentally may seem not to depend on temperature. Such an effect is clearer when the concentration of deeper traps is larger than those of shallower traps ([15], Figs. 4 and 5). This is due to the higher sensitivity of the OCS of deeper traps to temperature changes. This observation can be of significance for OSL applications in sediment dating, where the most sensitive component of the OSL signal is the best one for age estimation. Increasing the temperature of OSL measurement in dating protocols enhances the OSL intensity but mainly enhances

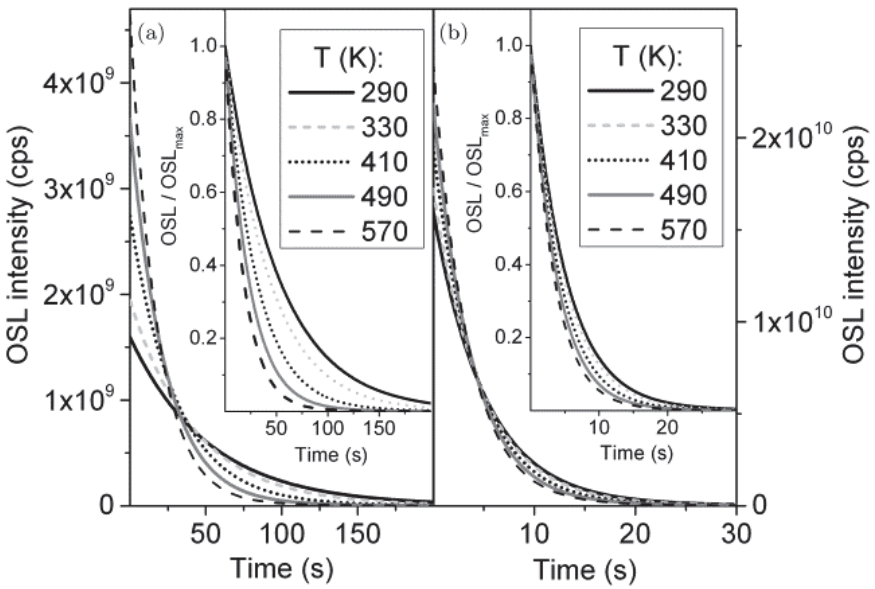


Fig. 5. OSL curve shape dependence on temperature: (a) $h\nu = 1.9\,\mathrm{eV}$, $E_0 = 2.0\,\mathrm{eV}$, $\hbar\omega = 20\,\mathrm{meV}$, $S = 10$; (b) $h\nu = 2.0\,\mathrm{eV}$, $E_0 = 2.0\,\mathrm{eV}$, $\hbar\omega = 20\,\mathrm{meV}$, $S = 10$. The parameters used for simulation: $N = 10^{11}\,\mathrm{cm}^{-3}$, $A = 10^{-10}\,\mathrm{cm}^3\mathrm{s}^{-1}$, $M = 2 \times 10^{12}\,\mathrm{cm}^{-3}$, $A_m = 4 \times 10^{-9}\,\mathrm{cm}^3\mathrm{s}^{-1}$, $\beta = 10^{-8}\,\mathrm{cm}^3\mathrm{s}^{-1}$.

the signal related to traps that are less sensitive to light. This should always be taken into account, especially as the graphs of the function $\sigma(T)$ (Fig. 4b) have different slopes for distinct traps. It may sometimes be hard to notice the pattern of shape changes with temperature in a complex OSL curve and to draw helpful conclusions.

If the kinetics of an apparently simple CW-OSL curve does not resemble the shape of first-order kinetics, it is useful to observe its behavior for different stimulation energies (e.g. [34, 35]), or, which is technically much easier, at different temperatures. The independent observation of the behavior of individual components can be very informative, especially for laboratories that own only one optical stimulation source. The changes with temperature in the OSL curve shape can reveal the complex nature of the OSL signal and possibly the presence of first-order kinetics, at least in the case of certain components. The dependence of the OCS on temperature is the basis

of the OSL measurement method consisting of continuous optical stimulation with fixed stimulation energy during linear heating of the sample. This is described in detail in Section 6.5.

### 6.3. Effective optical cross-section (EOCS)

Usually, in the OSL process simulations, as well as in the interpretation of experimental results, it is assumed that the optical stimulation is carried out using light with a discrete energy spectrum. However, this is not common in experimental practice, especially when luminescence diodes or halogen lamps equipped with optical filters are used. The OCS depends on the stimulation energy, hence using a stimulation band instead of a stimulation line has consequences for the experimentally estimated OCS value. It is important to know how the width and shape of the band used for stimulation influence the shape of the OSL curve.

When the spectral band of stimulation light has a finite width, it should be taken into account in the expression for the probability of the electron release from a trap that in this case can be written as:

$$\gamma(h\nu) = f \int_{h\nu_1}^{h\nu_2} \Phi(h\nu')\sigma(h\nu')d(h\nu') \Big/ \int_{h\nu_1}^{h\nu_2} \Phi(h\nu')d(h\nu') = f\Sigma(h\nu) \tag{8}$$

or

$$\gamma(h\nu) = \phi_{\max} \int_{h\nu_1}^{h\nu_2} \Phi(h\nu')\sigma(h\nu')d(h\nu') \tag{9}$$

where $h\nu_1$ and $h\nu_2$ are the stimulation band limits, OSC ($\sigma$) is expressed by Eqs. (1) and (2) and $\Phi(h\nu)$ ($\mathrm{eV}^{-1}$) is a function of the shape of the spectral band related to the total density of the photon flux $f$ used for stimulation in the following way:

$$f = \int_{h\nu_1}^{h\nu_2} \phi_{\max}\Phi(h\nu')d(h\nu'). \tag{10}$$

The probability of the optical electron release from a trap, which for the stimulation with a spectral line was defined as $f\sigma$, now is expressed by $f\Sigma$. Therefore, the result of analyzing the experimental

data is not the OCS value but another quantity Σ, which may be called the effective optical cross-section (EOCS). Σ is a form of weighted average of the OCS value over the range of the stimulation band, where the weight is controlled by the shape of the stimulation band [36]:

$$\Sigma(h\nu) = \int_{h\nu_1}^{h\nu_2} \Phi\left(h\nu'\right)\sigma(h\nu')d(h\nu') \Big/ \int_{h\nu_1}^{h\nu_2} \Phi(\,h\nu')d(h\nu'). \qquad (11)$$

Basic research has been carried out in order to check the difference between the real OCS of traps and the EOCS obtained by OSL analysis. Results of these tests have been presented in the earlier work [36] for a few examples of spectral band shapes used in practice for OSL measurements.

From Eq. (8) it is clear that the changes in the shape of the stimulation band can cause changes in the probability of electron release from traps. Thus, next to the stimulation energy and the temperature, the shape of the spectral band Φ can also be used for changing the electron release probability and the EOCS, in order to control the shape of the OSL curve. Next, we discuss what can be achieved by means of the stimulation method, by controlling these three factors.

### 6.4. OSL excitation spectra and the VES-OSL

Taking into account the electron-phonon coupling in the electron transition from the trap to the conduction band, admits the possibility of trap emptying by photons with energies much below the threshold energy for optical ionization [15]. As will be shown below, this is of special importance for the advanced methods of OSL measurements that are focused on estimating the optical depth of the trap.

Two such methods have been used previously, measurements of the excitation spectrum of OSL and photoconductivity. Reports concerning these experiments are rather rare in the literature, probably because of the equipment requirements [35, 39–44], and have been conducted in different ways. For example, for the investigation of feldspars in the near infrared range, one has used tunable lasers

and performed the optical stimulation with many breaks for tuning the laser. Sometimes the sample has been irradiated, and then many cycles of the short (e.g. 0.5 or 1 s) OSL measurements, with subsequent breaks for the change in the stimulation energy have been repeated, till the end of the stimulation spectral range [39–41]. In other cases, the excitation spectra have been recorded when using many equally irradiated aliquots of the sample, using a different aliquot for each stimulation energy [42], or by repeating the irradiation of the sample before getting each single point of the spectrum [43]. In a few cases, the OSL has been measured during continuous change of the stimulation energy [44–48].

Although the excitation spectra are achieved in different ways, the researchers always put their main efforts into ensuring the stability of the electron population in the investigated traps to create the excitation spectra that reflect the energy distribution of traps. However, in the case of non-stationary luminescence, it is extremely hard to fulfill this condition, especially when the experiment is not carried out at very low temperatures, and the participation of lattice vibration enables ionization much below the optical depth of the trap. In fact, in such experiments the emission being measured is exactly the result of the changes in the electron population. Thus, the light intensities obtained in such measurements cannot be high. In the case of measurements carried out for a single sample, the proper correction of the trap population should be introduced at the stage of data handling, which is not a trivial task.

The difficulties in meeting the requirement of trap occupation stability is not the only problem while measuring the OSL excitation spectra. Another problem is the shape of the obtained spectra. This is a monotonically growing curve, from which it is difficult to obtain information about the trap distribution, especially when there are significant differences in their concentrations.

Bearing in mind the experimental difficulties connected with recording the excitation spectra, reverse tactics were recently suggested for the experiment aimed at estimating the optical depth of the trap. The variable energy of stimulation optically stimulated luminescence (VES-OSL) method assumes the total emptying of

traps in order to obtain an OSL curve, which then allows the energy distribution of traps to be found as a result of suitable analysis [49]. The basis of the VES-OSL method is that the dependence of the electron release probability on time during the thermal stimulation in TL measurements is of a more favorable shape than this dependence in the case of CW/LM-OSL measurements with constant stimulation energy. It has been also noted that when the electron release probability was calculated using the explicit OCS dependence on the stimulation energy (Eq. (1)), and under linear changes in the energy of photons during stimulation ($h\nu = h\nu_0 + \alpha t$), a promising shape of the dependence of this probability on time can be obtained. The possibility of trap separation seems to be as good as in the case of thermal stimulation ([15], Fig. 6). There is a time range when practically only the shallower traps are depopulated, just like in the case of a glow curve measurement. Computer simulations of VES-OSL experiments and the advantages of this technique have been described earlier [15], and are briefly summarized here.

The VES-OSL curve has the shape of a peak, which is useful for the interpretation of experimental results. Figure 6 presents the outcome of simulations for a one-trap model. As can be seen, the position of a VES-OSL peak depends strongly on many parameters, and usually does not appear at the value of the optical trap depth $E_0$. For this reason, the name "optical stimulation spectrum" is not suitable for the results of experiments carried out with the continuous change of stimulation energy. Two competing tendencies determine the position of the peak maximum, namely the increasing probability of the electron release and the decreasing occupation of traps. Hence, it is controlled by all the parameters determining the value of electron release probability: $E_0, S$ and $\hbar\omega$ which depend on the sample, as well as $f$, $\alpha$ and $T$ which depend on experimental conditions, as is also the case with the shape of the VES-OSL peak. Larger values of stimulation energy increase rate, $\alpha$, similarly to the higher heating rates in the TL process, induce a peak shift into higher energies. The opposite displacement of the peak can be observed for increasing parameters of the electron-phonon coupling $S$ and $\hbar\omega$, and also for higher photon flux $f$ or sample temperature $T$. As the stimulation

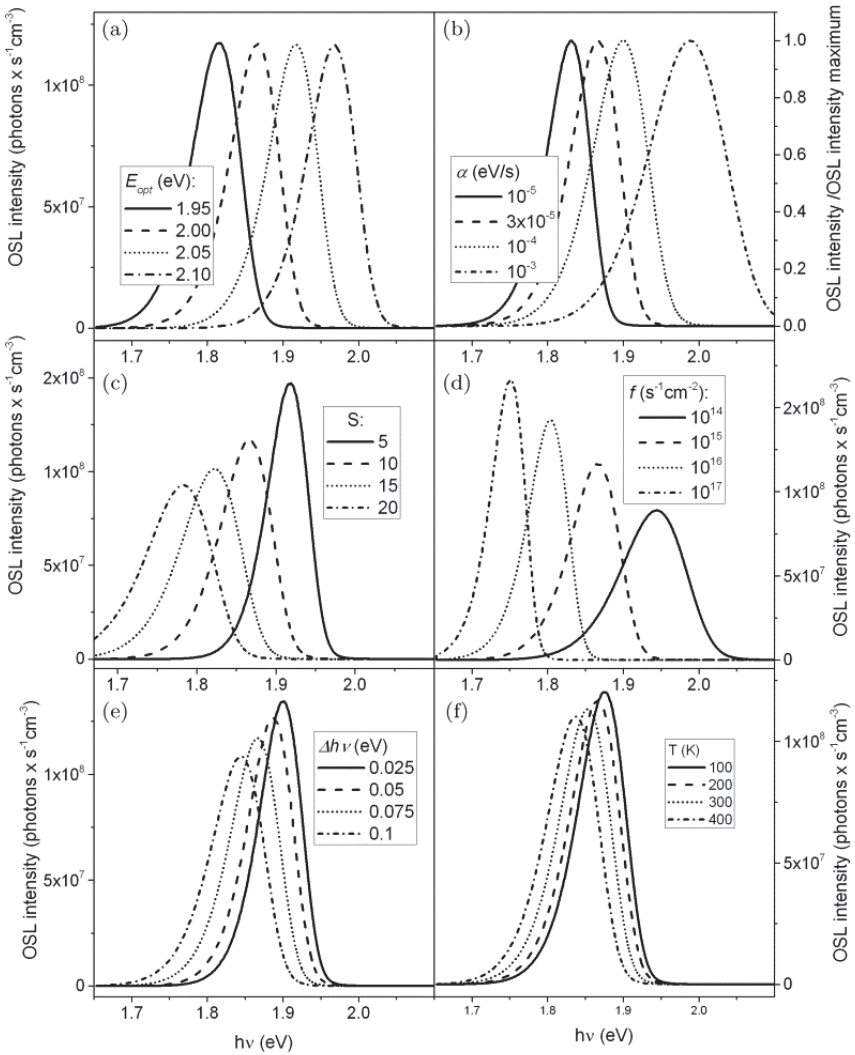


Fig. 6. The dependence of the VES-OSL curve on trap parameters and experimental conditions: $E_0$ (a), the rate of stimulation energy increase $\alpha$ (b), $S$ (c), photon flux density $f$ (d), stimulation bandwidth $\Delta(h\nu)$ (e) and temperature $T$ (f). All parameters which are constant for the individual part of the figure are always the same: $E_0 = 2\,\mathrm{eV}$, $S = 10$, $\hbar\omega = 20\,\mathrm{meV}$, $T = 300\,\mathrm{K}$, $\alpha = 3\times10^{-5}\,\mathrm{eVs}^{-1}$, $f = 10^{15}\,\mathrm{cm}^{-2}\mathrm{s}^{-1}$, $\Delta(h\nu) = 0.05\,\mathrm{eV}$, $N = 10^{11}\,\mathrm{cm}^{-3}$, $A = 10^{-10}\,\mathrm{cm}^3\mathrm{s}^{-1}$, $M = 2\times10^{12}\,\mathrm{cm}^{-3}$, $A_m = 4\times10^{-9}\,\mathrm{cm}^3\mathrm{s}^{-1}$, $\beta = 10^{-8}\,\mathrm{cm}^3\mathrm{s}^{-1}$.

band usually has a finite width, the shape of the VES-OSL peak is also expected to be dependent on the band width $d(h\nu)$. This effect is presented in Fig. 6e for the case of a rectangular band. The shift of the VES-OSL peak into lower energies agrees with the aforementioned increase in the EOCS with the band widening [36].

As has been already stressed, the optical trap depth cannot be read from the position of the VES-OSL peak. It has to be obtained as a result of fitting the theoretical curve to the experimental one. Fortunately, just as in the case of thermoluminescence [24], the shape of the analytical theoretical curve can be obtained under some assumptions imposed on the set of kinetic equations. Under the assumption of the quasiequilibrium and first-order kinetics in Eqs. (4)–(7), the VES-OSL intensity is described by the following analytical expression:

$$I(h\nu) = \gamma(h\nu)n(h\nu) = n_0\gamma(h\nu)\exp\left[-\frac{1}{\alpha}\int_{h\nu_0}^{h\nu}\gamma(h\nu')d(h\nu')\right], \quad (12)$$

where $\gamma(h\nu)$ is determined by Eq. (8) and $n_0$ is the initial trap occupation. It has been confirmed that the quality of fitting the curve determined by Eq. (12) to a single VES-OSL curve is very good, even when the recombination probability coefficient is ten times larger than the retrapping probability coefficient ([15], Fig. 8). The curves in Fig. 6 which were simulated for the model parameters corresponding to the first-order kinetics, have typical asymmetry characteristic also of the first-order TL peaks.

The ability of peak separation in the VES-OSL experiment is demonstrated in Fig. 7. When the parameters used in the simulated experiment are typical of first-order kinetics, the VES-OSL curve for two traps with the optical depths of $E_{01} = 2.00\,\mathrm{eV}$ and $E_{02} = 2.05\,\mathrm{eV}$, respectively, can be satisfactorily approximated by the sum of two first-order peaks. As one can suppose, the matter is not so simple when there are trap coupling effects.

A good example of such complex cases are the results of the VES-OSL measurements that have been carried out so far. The equipment has been specially prepared for the purpose of VES-OSL. Its basis is

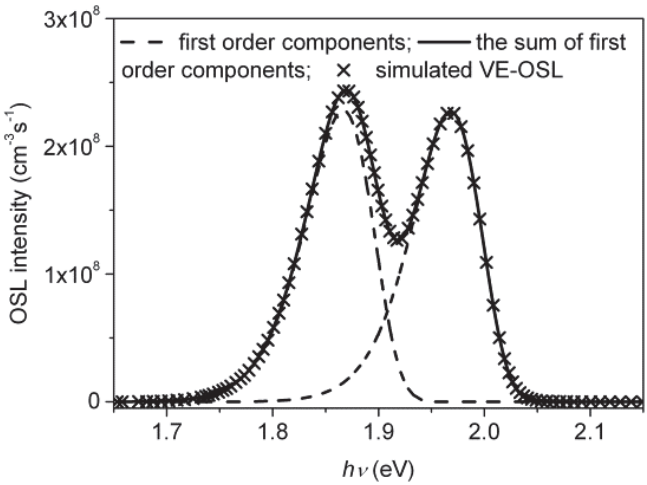


Fig. 7. The simulated VES-OSL curve for two traps with the optical depths $E_{01} = 2.00\,\mathrm{eV}$ and $E_{02} = 2.05\,\mathrm{eV}$, the first-order components and their sum fitted to the simulated curve. The parameters used for simulations: $S = 10$, $\hbar\omega = 20\,\mathrm{meV}$, $T = 300\,\mathrm{K}$, $\alpha = 3 \times 10^{-5}\,\mathrm{eVs}^{-1}$, $f = 10^{15}\,\mathrm{cm}^{-2}\mathrm{s}^{-1}$, FWHM $= 0.05\,\mathrm{eV}$, $N_1 = N_2 = 10^{12}\,\mathrm{cm}^{-3}$, $A_1 = A_2 = 10^{-11}\,\mathrm{cm}^3\mathrm{s}^{-1}$, $M = 2 \times 10^{12}\,\mathrm{cm}^{-3}$, $A_m = 4 \times 10^{-11}\,\mathrm{cm}^3\mathrm{s}^{-1}$, $\beta = 10^{-8}\,\mathrm{cm}^3\mathrm{s}^{-1}$.

an illuminator that can be connected with a Risø TL/OSL System by means of a light guide and a special optical adapter [50].

Quartz samples separated from bricks and sediments for dating purposes have been chosen for the first tests [49], because they usually have low OSL sensitivity. It has been assumed that if the VES-OSL signal can be observed for the less efficient OSL material, the power of the illuminator would be enough to stimulate more efficient materials. In the case of quartz, the photon flux achievable in the system has allowed rather wide curves to be obtained, but required a long time in order to get the signal maximum in the spectral range of the instrument. Nevertheless, it turns out that the analysis of VES-OSL allows the optical depth of traps to be estimated, and some indications concerning the strength of trap coupling with the crystal lattice ($S\hbar\omega$) to be obtained.

More encouraging results have been obtained for $Al_2O_3$:C [51]. It turns out that the photon flux at the sample position of $3 \times 10^{16}$ photons per $\mathrm{cm}^2$ per second during a scan from 800 to 430 nm with

the fixed spectral band of 26 nm, is high enough for emptying the main dosimetric traps in $Al_2O_3$:C, but not equally effective in the case of deeper traps. When the VES-OSL signal related to the main dosimetric traps in $Al_2O_3$:C is recorded during the scan with the rate of wavelength decrease equal to $0.2\,\mathrm{nms}^{-1}$, the signal from the deeper traps can be observed in the same wavelength range for scan rates as low as $0.0125\,\mathrm{nms}^{-1}$. For this rate, the scan in the range 800–430 nm lasts 8 hours.

The analysis of the experimental results for both quartz and $Al_2O_3$:C consists of fitting the sum of the first-order VES-OSL curves (Eq. (12)) to the experimental curve. A fitting procedure is time-consuming hence it has been simplified slightly. The parameter $\kappa$ defined by the Eq. (2) has been used instead of two parameters, $\hbar\omega$ and $S$, and the fitting has been performed for a curve described only by $E_0$ and $\kappa$. Such a simplified procedure does not allow $S$ and $\hbar\omega$ to be established independently, because the parameter $\kappa$ is not unique. However, it is possible to obtain the distribution of the optical depths of traps. This distribution is the first question of interest, just as the distribution of the thermal depths of traps is in TL analysis.

Figure 8b presents the results of the fitting procedure — the initial occupation of traps $n_0$ for the adequate values of optical trap depths. The data are the outcome of scans in the range 800–430 nm with the rate of $0.2\,\mathrm{nms}^{-1}$, as shown in Fig. 8a. A greater number of first-order VES-OSL peaks are required for a satisfactory fit, probably because of fundamental reasons, such as an overly simplistic model assumed for the process of trap ionization, or strictly technical ones connected, for example, with widening of the peaks because of an inhomogeneity in the intensity of stimulation light in the sample volume. There can also be, however, another explanation — a continuous distribution of optical trap depths that has been suggested earlier [35]. Although such a case needs a special approach in the fitting procedure, which has not been taken into account here, one can treat the results as a simplified presentation of the distribution of optical trap depths in $Al_2O_3$:C. The optical depths of the investigated traps are between 2.0 and 2.8 eV with

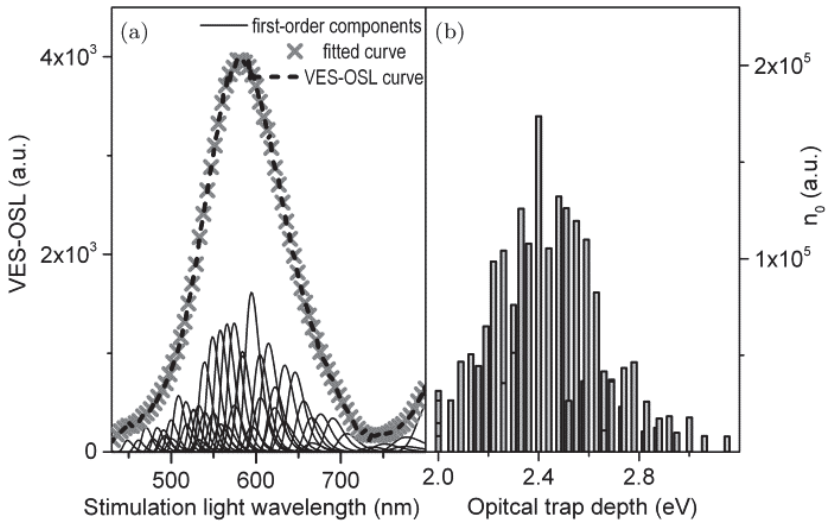


Fig. 8. The experimental VES-OSL curve of $Al_2O_3$:C obtained as a result of the scan in the range 800–430 nm with the rate of 0.2 $nms^{-1}$ as well as the result of fitting the sum of first-order curves (a), and the distribution of optical trap depths estimated by means of the simplified fitting procedure described in the text (b).

the maximum at about 2.5 eV. As has been proved by the TL measurements carried out after the VES-OSL experiments, these traps are responsible for the main TL peak at about 200°C.

The curves obtained with the slower scan rates in Fig. 9 reveal an additional maximum around 3.0 eV. After an initial bleaching of the main VES-OSL maximum made by a single 800–500 nm scan with the rate of 0.2 $nms^{-1}$, the next scan has been performed in order to measure the signal in the range 500–430 nm more accurately with the rate of 0.0064 $nms^{-1}$ (Fig. 9a). The continuous trap distribution in the range 2.8–3.3 eV with the maximum at 3.2 eV can be seen in Fig. 9b. It is interesting here that the signal from the deep traps with the optical depth corresponding to about 387 nm can be detected by VES-OSL much below this wavelength, which falls in the range of the OSL detection window. The TL signal related to these deep traps cannot be detected below 500°C.

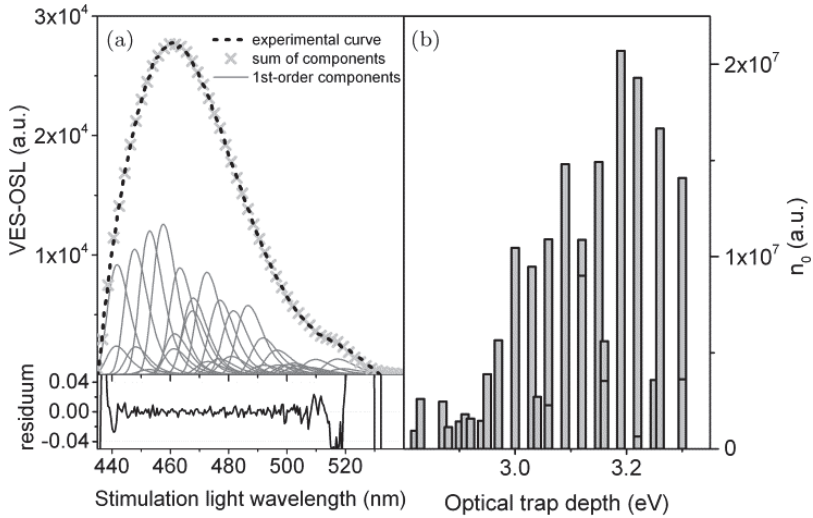


Fig. 9. Results of the VES-OSL curve of $Al_2O_3$:C for a scan in the range 500–430 nm with the rate of 0.0064 $nms^{-1}$ performed after bleaching of the main dosimetric traps. The experimental VES-OSL curve together with the fitting results and the residuals for this procedure (a) and the distribution of the optical depth of traps (b).

Summing up, the VES-OSL measurements provide the possibility of directly estimating the optical depth of the trap ($E_0$) with the fitting procedure. The VES-OSL curve shape and maximum position can be regulated by the density of the stimulation photon flux, the rate of stimulation energy increase (the scan rate) and by the sample temperature. It allows, above all, the traps to be emptied at stimulation energies below their optical depths, which is especially important when they fall within the spectral band of OSL detection. The VES-OSL also enables the investigation of the OSL from deep traps, which provides the estimation of the TL affected by thermal quenching, or overlapping with strong incandescence.

### 6.5. Thermally modulated OSL (TM-OSL)

Optical stimulation with increasing stimulation energy enables the determination of parameters that uniquely specify a trap and the effective separation of the OSL signals of various origins.

The VES-OSL method, however, requires a strong tunable light source, and the stabilization of the density of photon flux. These are significant constraints in the wider application of this kind of stimulation. As is clear from the OCS dependence on stimulation energy described by Eqs. (1)–(2), increasing the sample temperature during the optical stimulation with constant photon energy should also induce the desired changes in the probabilities of the electron release. Such stimulation can be realized using the standard OSL readers.

The method of OSL measurement suggested here may seem similar to a measurement called thermo-optical luminescence (TOL), by which the thermal assistance effects have been investigated [26, 52–55]. In the TOL experiment, the OSL signal is measured during a short (e.g. 0.1 s) light pulse initiated every few degrees (e.g. 10°C) during linear heating (a few degrees per second). Applying the short light pulses is aimed at only slight emptying of traps. The changes in the OSL intensity with temperature are observed, however, the data analysis does not take into account the temperature changes in the OCS, but rather the activity of shallow traps that disturb the OSL process. The method proposed here, which may be called the thermo-modulated OSL (TM-OSL), uses a continuous stimulation in order to efficiently empty the individual kinds of traps and generate a specific OSL curve which can help to estimate the optical depth of the trap and the electron-phonon coupling parameters.

During the TM-OSL measurement there is both the thermal and optical activation of traps, and the probability of electron release from the trap should be written as:

$$\gamma = f\Sigma(T) + s\exp\left(-\frac{E_T}{kT}\right). \tag{13}$$

To simplify matters, it is reasonable to perform the optical stimulation in the temperature region of negligible thermal activation. Therefore, taking the fact that in real materials there are usually many traps of different depths into account, the TM-OSL method is rather suitable for the investigation of deep traps after a preheat that empties shallower traps.

Several features of TM-OSL curves and the potential of the method have been investigated in detail earlier by computer simulations [56]. It has been shown that all three parameters determining the experimental conditions strongly influence the TM-OSL process; these parameters are the stimulation energy, the stimulation photon flux and the heating rate. They have to be suitably chosen in order to obtain the TM-OSL curve related to a specific trap in the desired temperature range. They can also be used for improving the resolution of the TM-OSL method. Figure 10 illustrates the impact of these three parameters on the shape and position of the TM-OSL peak. Figure 10a demonstrates for a fixed photon flux and heating rate, how strongly the stimulation energy influences the position of the TM-OSL peak. The higher the stimulation energy, the lower the temperature of the TM-OSL peak maximum. The TM-OSL peak observed clearly for a stimulation band with the maximum at 600 nm is dominated by the TL signal for a band with the maximum at 620 nm, and only barely falls into the temperature range of measurement for slightly higher stimulation energy (580 nm). The range of optical depth values for which the TM-OSL signal can be measured below the temperatures of the thermal depopulation of traps, and simultaneously have the form of a peak, is very narrow. When the optical depth of 2.2 eV is assumed and for the same values of other parameters, the TM-OSL signal decays quickly just above 300 K, whereas the signal from the deeper trap of 2.6 eV is simply the pure TL signal with the maximum of about 770 K.

For a fixed stimulation band, two other parameters may be used to get the desired position of the TM-OSL peak for a trap of a defined depth: the heating rate and the photon flux. Figure 10b illustrates the effect of the heating rate on the TM-OSL peak shape and position. As can be seen, halving the heating rate shifts the TM-OSL maximum for the 2.4 eV trap into lower temperatures by about 60 K (from 557 K to 495 K). The same change of heating rate in the case of the TL signal for the same trap causes a temperature shift of about 20 K. For the heating rate of 0.2 $\mathrm{Ks}^{-1}$, the maximum of the TM-OSL curve for the 2.4 eV trap is shifted by 60 K, to about 423 K. Significant modification of the TM-OSL curve by the change in the photon flux

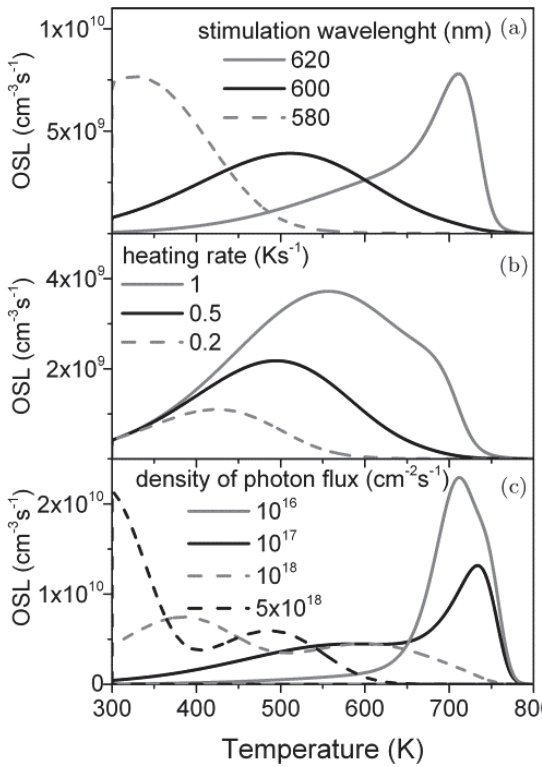


Fig. 10. The simulated TM-OSL curves obtained for different experimental parameters: (a) — the stimulation band maximum, for the one-trap model with a trap having the optical depth of 2.45 eV; (b) the heating rate $\alpha$, for the one-trap model with a trap having the optical depth of 2.4 eV; and (c) — the photon flux density, for the two-trap model with the traps having the optical depths equal to 2.4 and 2.5 eV and the stimulation band maximum at 620 nm. The following model parameters are fixed during the simulations when they are not changed for the individual part of the figure: $N$ (or $N_1 = N_2$) $= 10^{12}\,\mathrm{cm}^{-3}$, $M = 10^{13}\,\mathrm{cm}^{-3}$, $A$ (or $A_1 = A_2$) $= 10^{-10}\,\mathrm{cm}^3\,\mathrm{s}^{-1}$, $A_m$ (or $A_{m1} = A_{m2}$) $= 4 \times 10^{-11}\,\mathrm{cm}^3\,\mathrm{s}^{-1}$, $\beta = 10^{-8}\,\mathrm{cm}^3\,\mathrm{s}^{-1}$, $S = 20$, $\hbar\omega = 0.02\,\mathrm{eV}$, $s = 10^{13}\,\mathrm{s}^{-1}$, $\lambda_{max} = 620\,\mathrm{nm}$, $f = 10^{17}\,\mathrm{cm}^{-2}\,\mathrm{s}^{-1}$, $\alpha = 1\,\mathrm{Ks}^{-1}$.

is demonstrated in Fig. 10c for the OSL model consisting of two traps. The strengthening of the photon flux from the value of $10^{17}$ to $10^{18}\,\mathrm{cm}^{-2}\,\mathrm{s}^{-1}$ shifts the peak maximum for the 2.4 eV trap by about 170 K towards lower temperatures.

Figure 10c shows that at the same time, high densities of the photon flux make the TM-OSL peaks narrower, and increase the resolution of the method. The ratio of the radiative recombination probability coefficient $\beta$ to the probability coefficients of electron trapping in the traps $A_{mi}$ was taken as $10^3$, in order to test the case close to first-order kinetics. For the stimulation photon flux $f = 10^{18}\,\mathrm{cm^{-2}s^{-1}}$, the maxima of the peaks originating from the traps whose optical depths differ by 0.1 eV are shifted with respect to one another by about 215 K, while the maxima of the TL peaks for the same traps differ by no more than 30 K. This confirms the good resolution of the method, and shows the opportunity of applying it for an effective initial cleaning of the shallower traps while keeping constant the occupation of deeper traps.

It should be mentioned that the TM-OSL method provides a unique opportunity to investigate very deep traps for which the TL peaks appear above 800 K. This temperature range is rarely used for TL measurements because of the high incandescence of heaters and the poor capabilities for determining the sample temperature. Applying an adequate stimulation energy and sufficiently large photon flux, as well as a very low heating rate, enables the detection of the TM-OSL peak below 500 K for a trap being the source of the TL peak high above 800 K ([56], Fig. 4).

As can be seen from the relation of the thermal and optical depths of a trap, the parameters determining the strength of the electron-phonon coupling $S$ and $\hbar\omega$ also have to affect the TM-OSL peak position. The higher the $S$ and $\hbar\omega$ values, the lower the temperature of the peak maximum ([56], Fig. 5). These effects are simple consequences of the OCS increase with the parameters determining the strength of electron-phonon coupling (see Fig. 2).

As in the case of the VES-OSL method, the first-order kinetics curve of TM-OSL can be derived from the kinetics equations:

$$I(T) = n_0 \left[ f\Sigma(T) + s \exp\left(-\frac{E_{Ti}}{kT}\right)\right] \times \exp\left[-\frac{1}{\alpha}\int_{T_0}^{T}\left[f\Sigma(T') + s\exp\left(-\frac{E_T}{kT'}\right)\right] dT'\right]. \quad (14)$$

The TM-OSL method has been put into practice for samples of quartz. The comparison of TM-OSL and TL curves measured with the same heating rate and after preheat to the same temperature, can directly reveal the origin of the TM-OSL signal. Quartz has a well-known fast OSL component related to the trap responsible for the TL peak about 325°C (for the heating rate 5 $Ks^{-1}$) [57–59] that in Fig. 11, can be seen clearly between 250 and 350°C. It is interesting to see how the optical stimulation during the heating "transfers" this part of quartz TL to lower temperatures in the form of the TM-OSL peak. Observing the signal originating from the deep trap at much lower temperatures allows higher intensity to be obtained by avoiding the thermal quenching that starts above 100°C in the case of quartz [60–64]. The intensity of the TM-OSL peak is more than 25 times higher than the intensity of the related TL peak. The TM-OSL measurements conducted for quartz allowed three different peaks to be distinguished for stimulation wavelengths 620, 560 (relatively weak) and 460 nm as shown in Fig. 12. Each of them can be erased by fractional bleaching, after which the next peak can be recorded.

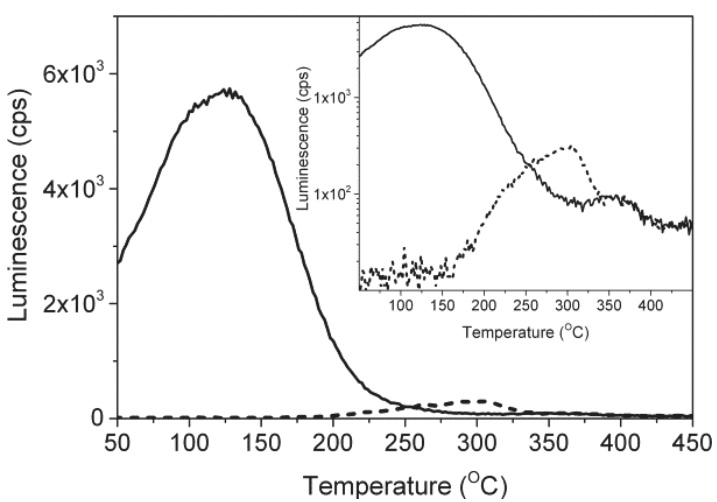


Fig. 11. The TM-OSL (solid line) and TL (dashed line) curves measured for quartz after the preheat to 230°C with the heating rate of 2 $Ks^{-1}$. The stimulation wavelength used in the TM-OSL method was 620 nm and the photon flux 6.5 × $10^{16}$ $cm^{-2}s^{-1}$. The inset presents the same graphs in the logarithmic scale.

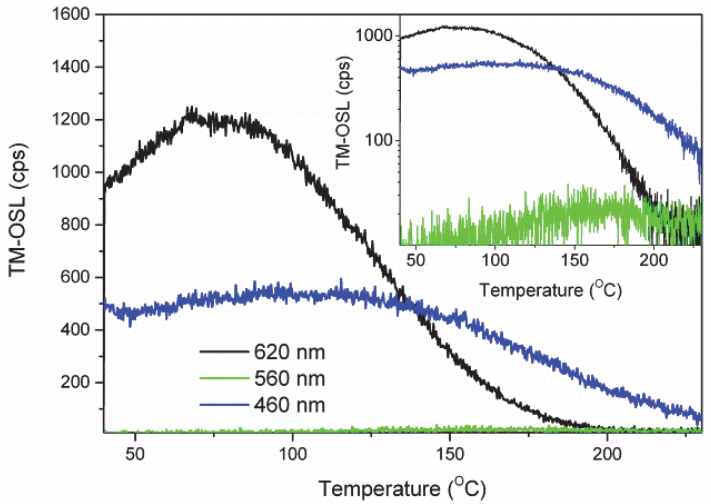


Fig. 12. The TM-OSL peaks of quartz measured after the preheat to 275°C with the heating rate of 0.2 $Ks^{-1}$, the stimulation wavelengths sequentially 620, 560 and 460 nm and photon flux densities respectively of $4.6 \times 10^{16}$, $4.6 \times 10^{16}$ $2.0 \times 10^{16}$ $cm^{-2}s^{-1}$. The inset presents the same data on a logarithmic scale.

Summing up, the stimulation of the OSL during linear heating can be a very useful tool for the investigation of the OSL process. The TM-OSL peaks are mostly rather wide, but their position on the temperature axis depends so strongly on the experimental parameters, such as the heating rate, the stimulation light intensity and the stimulation energy, that it is possible to effectively separate the signals related to different traps. By this kind of stimulation, one can also reach very deep traps that are not detectable by thermoluminescence measurements below 500°C.

### 6.6. Band shape modulation OSL

It was shown in Section 6.3 that the OSL process is governed by the quantity called effective OCS (EOCS). From Eq. (8) it is clear that the changes in the electron release probability $\gamma$ can be caused by modifying the shape of the stimulation band $\Phi$. In order to distinguish this method of optical stimulation from others, it is convenient to call it band shape modulation OSL (BSM-OSL).

This kind of stimulation can be achieved when at least two sources of light are used; the shape of a band that is the sum of bands from both sources can be regulated by changing the emission intensity of the individual sources. The simplest way of generating such changes is by fixing the intensity of the light of the lower photon energy and carefully increasing the intensity of the second source:

$$\Phi(h\nu, t) = \exp(-(h\nu - h\nu_{01})^2/2\delta_1^2) + b\exp(-(h\nu - h\nu_{02})^2/2\delta_2^2)(t/t_{\max})^p, \quad (15)$$

where $h\nu_{01}$ and $h\nu_{02}$ are the energies of the stimulation band maxima (the bands are taken as Gaussian functions) for the first and second source, respectively, $\delta_1$ and $\delta_2$ determine the widths of these bands, $t_{max}$ is the duration of the stimulation, while $b$ and $p$ are the characteristic constants of the function describing the changes in the intensity of the second light source. The bands can be chosen so that the BSM-OSL curve for an individual trap has the shape of a peak. Sample results of such stimulation are presented in Fig. 13. The BSM-OSL curves obtained by simulation of the model consisting of two traps (Eq. 4–7) are shown for a few different pairs of spectral bands of light sources. The energy values of the band maxima strongly influence the shape of the obtained curve. In fact, two factors can be distinguished here: the distance between the maxima of the spectral bands of both sources, and their overall position on the energy axis. In Fig. 13, the first factor is changed, whereas the latter is fixed. The distance between the maxima of the spectral bands is the factor that most strongly affects the resolution of BSM-OSL peaks. The smaller the distance, the better the resolution. The effect is stronger when the overall position of the bands on the energy axis is shifted to lower energies. The lower the photon energy of both sources, the better the separation of the BSM-OSL peaks related to various traps.

This is a result of the more dynamic increase in the OCS with the stimulation energy for lower energy values. However, this same feature of the OCS dependence on the stimulation energy makes at the same time the stimulation of the first source less efficient in comparison with the second source. There is a range where

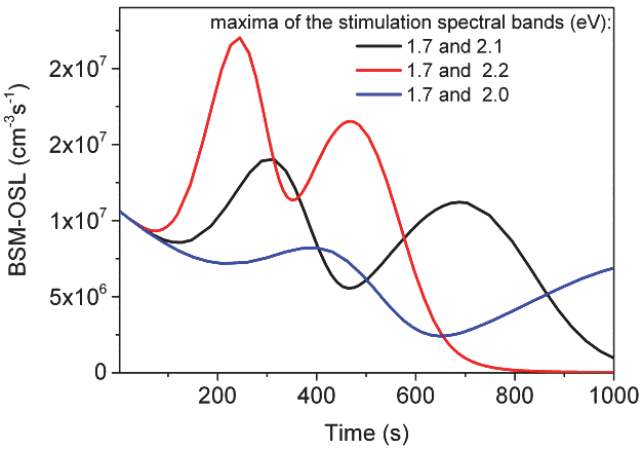


Fig. 13. The BSM-OSL curves obtained as a result of simulations performed using the two-trap OSL model for different distances between the maxima of the spectral bands of the individual sources. In all the presented cases, the function of the intensity changes of the second source is: $(t/1000)^4/10$ ($b = 0.1$, $p = 4$ in Eq. (15)), the optical depth of the traps is $E_1 = 2.5\,\mathrm{eV}$ and $E_2 = 2.7\,\mathrm{eV}$, the electron-phonon coupling parameters are equal for both traps: $S_1 = S_2 = 20$; $\hbar\omega_1 = \hbar\omega_2 = 20\,\mathrm{meV}$ and the photon flux density $4 \times 10^{18}\,\mathrm{cm}^{-2}\mathrm{s}^{-1}$.

the stimulation by the second source dominates so much, that the stimulation by the first source can be omitted. Then, in fact, one deals with a non-linear version of LM-OSL. The advantage of the BSM-OSL method, i.e. the effective separation of the signal from different traps, is then lost. It should also be noted that in the range of very low stimulation energies, effective stimulation requires higher light intensities or adequately low rates of intensity changes.

The distance between the separate BSM-OSL peaks depends, above all, on the energy of the spectral bands, but can also be controlled by other experimental parameters, such as the density of the photon flux $f$ used for stimulation, and the nature and rate of the intensity changes of the second light source. The basis of a good resolution in the BSM-OSL method is the efficient emptying of the shallower traps by the lower energy light source at the initial stages of the stimulation, as well as gradual enhancement of the stimulation by adding photons of higher energy. As a result, the time

of depletion for the shallower traps can be shortened. The number of high energy photons should be increased carefully in order to keep the filling of the deeper traps practically stable. The function of the light intensity changes of the second source used in the simulations, whose results are shown in Fig. 13 is: $(t/1000)^4/10$ ($b = 0.1$, $p = 4$). The effects caused by applying other functions are illustrated in Fig. 14a, which shows that increasing the intensity of the second source more delicately gives better resolution of the peaks. For an established set of light sources, the parameter $p$ controls the shape of the BSM-OSL curve most effectively. The peaks are better separated and the time

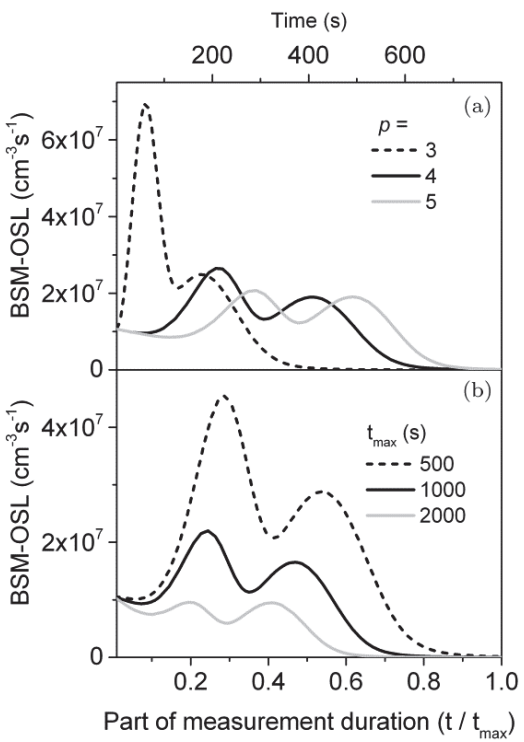


Fig. 14. The simulated BSM-OSL curves for the same model parameters that were used for preparation of Fig. 13 but for various functions of the intensity changes of the second source (different $p$ in Eq. (15)) (a) and for a variety of rates of intensity changes (different $t_{max}$ in Eq. (15)) (b).

range when mainly the shallow trap is emptied is longer for larger values of $p$.

The influence of the density of the photon flux $f$ and of the parameter $b$ determining the mutual relation of the intensities of both sources is much less spectacular. Higher intensities always make the measurement shorter, but slightly better separation of the peaks is obtained with lower intensities, despite the peaks becoming wider.

The rate of the intensity changes is also an important experimental parameter. Figure 14b demonstrates the BSM-OSL curves simulated for the same values of $b$ and $p$ but realized in time intervals of different lengths. The higher rate of intensity changes in the second source results in narrower peaks and slightly better resolution, but above all in much higher signal intensity.

Summing up, optical stimulation with the variable shape of the stimulation band is a method that allows the effective separation of the OSL signal originating from different traps. The range of trap depths that can be covered by a single measurement is rather narrow, and the successful realization of the experiment requires suitable adjustment (matching) of the experimental parameters, especially the stimulation energy. However, the selectivity of the stimulation that can be achieved is very good. This can be regulated by a few different factors. The method can be used for the detailed investigation of the trap parameters that uniquely define the shape of the BSM-OSL curve.

## 6.7. Conclusions

Controlling the probability of electron release from traps by changing the EOCS value, enables the selective optical emptying of individual types of traps. It also enables the direct determination of the optical depth and the parameters defining the strength of the electron-phonon coupling for trap defects. The very simple approach, presented above, of considering the trap ionization process while taking into account the presence of the lattice vibrations, made it possible to show the potential of such stimulation methods. The shape of the obtained OSL curves can be regulated by many experimental

parameters. The first-order curves for each of these methods can be easily derived and are a useful tool for OSL data analysis [49, 56, 65]. However, it should be stressed that in order to make good use of the described methods, the right equation for the dependence of OCS on the stimulation energy and temperature should be applied. In this study, an equation was used which was derived assuming that the process for the optical excitation of an electron from the trap to the conduction band involves only one lattice vibration mode. The participation of more vibration modes in the electron transition requires a more advanced form of OCS dependence on stimulation energy. The fact that an electron which is optically released into the conduction band high above its bottom has a higher mobility than an electron thermally released into the bottom of the conduction band should also be taken into account. In this case, the recombination may proceed in different ways than during TL. These issues need special attention in future investigations of the OSL phenomenon.

The development of effective methods for analyzing the OSL curves obtained by different stimulation techniques is necessary in order to estimate trap parameters. The first attempts have been made in the case of the VES-OSL method [49, 51]. They produced interesting results, and simultaneously showed that taking the lattice vibrations into account in the description of the OSL process may require a more advanced approach, for example, the consideration of more than one vibration mode. Future works should aim to compare the different descriptions of electron-phonon coupling, as well as consider the complications caused by the presence of shallower traps, or the photo-transfer of charge from deeper traps during stimulation.

## References

[1] W.B. Fowler, Physics of Color Centers, New York: Academic Press, 1968.
[2] R. Englman and J. Jortner, "The energy gap law for radiationless transitions in large molecules," *Mol. Phys.*, vol. 18, pp. 145–164, 1970.
[3] D.V. Lang, Deep Centers in Semiconductors, New York: Ed. S.T. Pantelides. Gordon and Breach, 1986.
[4] H.G. Grimmeiss and L.A. Ledebo, "Photo-ionization of deep impurity levels in semiconductors with non-parabolic bands," *J Phys. C*, vol. 8, pp. 2615–2626, 1975.

[5] G. Lukovsky, "On the photoionization of deep impurity centres in semiconductors," *Solid St. Commun.*, vol. 3, pp. 299–302, 1965.
[6] J. Bourgoin and M. Lannoo, Point defects in semiconductors II, Berlin: Springer–Verlag, 1983.
[7] K.W. Böer, Survey of Semiconductor Physics, New York: Van Nostrand Reinhold, 1990.
[8] H. Kukimoto, H.C. Henry and F.R. Merritt, "Photocapacitance studies of the oxygen in GaP. I. Optical cross sections, energy levels, and concentration," *Phys. Rev. B*, vol. 7, pp. 2486–99, 1973.
[9] A.A. Kopylov and A.N. Pikhtin, "Profiles of absorption and luminescence spectra of deep centers in semiconductors (Oxygen in Gallium-Phosphide)," *Sov. Phys. Sem.-USSR*, vol. 8, pp. 1563–1566, 1975.
[10] A.A. Kopylov and A.N. Pikhtin, "Temperature effect on spectra of deep center optical-absorption in semiconductors," *Fiz. Tv. Tela*, vol. 16, pp. 1837–1843, 1974.
[11] M. Jaros, "Wave functions and optical cross sections associated with deep centers in semiconductors," *Phys. Rev. B*, vol. 16, pp. 3694–3706, 1977.
[12] D.V. Lang, R.A. Logan and M. Jaros, "Trapping characteristics and donor-complex (DX) model for the persistent-photoconductivity trapping center in Te-doped $Al_xGa_{1-x}As$," *Phys. Rev. B*, vol. 19, pp. 1015–1030, 1979.
[13] P.M. Mooney, G.A. Northrop, T.N. Morgan and H.G. Grimmeiss, "Evidence for large lattice relaxation at the DX center in Si-doped $Al_xGa_{1-x}As$," *Phys. Rev. B*, vol. 37, pp. 2898–8307, 1988.
[14] J.M. Noras, "Photoionisation and phonon coupling," *J. Phys. C: Solid St. Phys.*, vol. 13, pp. 4779–89, 1980.
[15] A. Chruścińska, "On some fundamental features of optically stimulated luminescence measurements," *Radiat. Meas.*, vol. 45, pp. 991–999, 2010.
[16] A. Chruścińska and K.R. Przegiętka, "The influence of electron-phonon interaction on the OSL decay curve shape," *Radiat. Meas.*, vol. 45, pp. 317–319, 2010.
[17] N.A. Spooner, "On the optical dating signal from quartz," *Radiat. Meas.*, vol. 23, pp. 593–600, 1994.
[18] D.J. Huntley, M.A. Short and K. Dunphy, "Deep traps in quartz and their use for optical dating," *Can. J. Phys.*, vol. 74, pp. 81–91, 1996.
[19] R.M. Bailey, "Depletion of quartz OSL signal using low photon energy stimulation," *Anc. TL*, vol. 16, p. 33–36, 1998.
[20] N.R.J. Poolton, L. Bøtter-Jensen and O. Johnsen, "Thermo-optical properties of optically stimulated luminescence in feldspar," *Radiat. Meas.*, vol. 24, pp. 531–534, 1995.
[21] M. Jain and A.K. Singhvi, "Limits to depletion of blue-green light stimulated luminescence in feldspars: implication for quartz dating," *Radiat. Meas.*, vol. 33, pp. 883–892, 2001.
[22] M. Jain, L. Bøtter-Jensen and A.K. Singhvi, "Dose evaluation using multiple-aliquot quartz OSL: test of methods and a new protocol for improved accuracy and precision," *Radiat. Meas.*, vol. 37, pp. 67–80, 2003.

[23] M. Jain, A.S. Murray, L. Bøtter-Jensen and A.G. Wintle, "A single-aliquot regenerative-dose method based on IR (1.49 eV) bleaching of the fast OSL component in quartz," *Radiat. Meas.*, vol. 39, pp. 309–318, 2005.
[24] R. Chen and S.W.S. McKeever Theory of Thermoluminescence and Related Phenomena, Singapore: World Scientific, 1997.
[25] E. Bulur, "An alternative technique for optically stimulated luminescence (OSL) experiment," *Radiat. Meas.*, vol. 26, pp. 701–709, 1996.
[26] G. Hütt, I. Jaek and J. Tchonka, "Optical dating: K-feldspars optical response stimulation spectr," *Quat. Sci. Rev.*, vol. 7, pp. 381–385, 1988.
[27] B.G. Markey, L.E. Colyott and S.W.S. McKeever, "Time-resolved optically stimulated luminescence from $\alpha$-$Al_2O_3$," *Radiat. Meas.*, vol. 24, pp. 457–463, 1995.
[28] N.R.J. Poolton, L. Bøtter-Jensen and O. Johnsen, "Influence on donor electron energies of the chemical composition of K, Na and C aluminosilicates," *J. Phys.: Condens. Matter*, vol. 7, pp. 4751–4762, 1995.
[29] B.W. Smith and E.J. Rhodes, "Charge movements in quartz and their relevance to optical dating," *Radiat. Meas.*, vol. 23, pp. 329–333, 1994.
[30] S.W.S McKeever, L. Bøtter-Jensen, N. Agersnap Larsen and G.A.T. Duller, "Temperature dependence of OSL decay curves: experimental and theoretical aspects," *Radiat. Meas.*, vol. 27, pp. 161–170, 1997.
[31] R.M. Bailey, B.W. Smith and E.J. Rhodes, "Partial bleaching and the decay form characteristics of quartz OSL," *Radiat. Meas.*, vol. 27, pp. 123–136, 1997.
[32] R.M. Bailey, G. Adamiec and E.J. Rhodes, "OSL properties of NaCl relative to dating and dosimetry," *Radiat. Meas.*, vol. 32, pp. 717–723, 2000.
[33] G.A.T Duller and L. Bøtter-Jensen, "Luminescence from potassium feldspars stimulated by infrared and green light," *Radiat. Prot. Dosim.*, vol. 47, pp. 683–688, 1993.
[34] L. Bøtter-Jensen, S.W.S. McKeever and A.G. Wintle, Optically Stimulated Luminescence Dosimetry, Amsterdam: Elsevier, 2003.
[35] V.H. Whitley and S.W.S. McKeever, "Linearly modulated photoconductivity and linearly modulated optically stimulated luminescence measurements on $Al_2O_3$:C," *J. Appl. Phys.*, vol. 90, pp. 6073–6083, 2001.
[36] A. Chruścińska, "Influence of spectral width of stimulations band on the shape of OSL curve," *Radiat. Meas.*, vol. 56, pp. 18–22, 2013.
[37] A. Chruścińska, "Complex OSL signal and a trap independence assumption," *Radiat. Meas.*, vol. 42, pp. 727–730, 2007.
[38] N. Kijek and A. Chruścińska, "Estimation of OSL trap parameters by the optical "cleaning" — a critical study," *Geochronometria*, vol. 41, pp. 160–167, 2014.
[39] I.K. Bailiff, "Measurements of the stimulation spectrum (1.2–1.7 eV) for a specimen of potassium feldspar using a solid state laser," *Radiat. Prot. Dosim.*, vol. 47, pp. 49–653, 1993.
[40] I.K. Bailiff and S.M. Barnett, "Characteristics of infrared-stimulated luminescence from a feldspar at low temperatures," *Radiat. Meas.*, vol. 23, pp. 541–545, 1994.

[41] D.I. Godfrey-Smith and M. Cada, "IR stimulation spectroscopy of plagioclase and potassium feldspars, and quartz," *Radiat. Prot. Dosim.*, vol. 66, pp. 379–385, 1996.
[42] S.M. Barnett and I.K. Bailiff, "Infrared stimulation spectra of sediments containing feldspars," *Radiat. Meas.*, vol. 27, pp. 237–242, 1997.
[43] L. Trinkler, A.J.J. Bos, A.J.M. Winkelman, P. Christensen, N. Agersnap Larsen and B. Berzina, "Thermally and optically stimulated luminescence of AlN-$Y_2O_3$ ceramics after ionising irradiation," *Radiat. Prot. Dosim.*, vol. 84, pp. 207–210, 1999.
[44] L. Bøtter-Jensen, G.A.T. Duller and N.R.J. Poolton, "Excitation and emission spectrometry of stimulated luminescence from quartz and feldspars," *Radiat. Meas.*, vol. 23, pp. 613–616, 1994.
[45] E. Bulur and H.Y. Göksu, "OSL from BeO Ceramics: New Observations from an old Material," *Radiat. Meas.*, vol. 29, pp. 639–650, 1998.
[46] J.C. Mittania, M. Proki and E.G. Yukiharaa, "Optically stimulated luminescence and thermoluminescence of terbium-activated silicates and aluminates," *Radiat. Meas.*, vol. 43, pp. 323–326, 2008.
[47] Y. Douguchi, H. Nanto, T. Sato, A. Imai, S. Nasu, E. Kusano and A. Kinbara, "Optically stimulated luminescence in Eu-doped KBr phosphor ceramics," *Radiat. Prot. Dosim.*, vol. 84, pp. 143–148, 1999.
[48] A.C. Lewandowski, J.H. Barkyoumb and V.K. Mathur, "Thermoluminescence emission, excitation and stimulation spectra of $CaSO_4$:Dy and $CaSO_4$:Tm," *Radiat. Prot. Dosim.*, vol. 65, pp. 281–286, 1996.
[49] A. Chruścińska, "Estimating parameters of traps in quartz by the variable energy of stimulation OSL method," *Radiat. Meas.*, vol. 81, pp. 205–211, 2015.
[50] A. Chruścińska, "Experimental demonstration of the variable energy of stimulation optically stimulated luminescence (VES-OSL) method," *Radiat. Meas.*, vol. 71, pp. 247–250, 2014.
[51] A. Chruścińska, "Optical depth of traps in $Al_2O_3$:C determined by the variable energy of stimulation OSL (VES-OSL) method," *Radiat. Meas.*, vol. 90, pp. 94–98, 2016.
[52] G.A.T. Duller and A.G. Wintle, "On infrared stimulated luminescence at elevated temperatures," *Nucl. Tracks Radiat. Meas.*, vol. 18, pp. 379–384, 1991.
[53] B.G. Markey, S.W.S. McKeever, M.S. Akselrod, L. Bøtter-Jensen, N. Agersnap Larsen and L.E. Colyott, "The temperature dependence of optically stimulated luminescence from $\alpha$-$Al_2O_3$," *Radiat. Prot. Dosim.*, vol. 65, pp. 185–189, 1996.
[54] U. Rieser, G. Hütt, M.R. Krbetschek and W. Stolz, "Feldspar IRSL emission spectra at high and low temperatures," *Radiat. Meas.*, vol. 27, pp. 273–278, 1997.
[55] G.A.T. Duller, "Behavioural studies of stimulated luminescence from feldspars," *Radiat. Meas.*, vol. 27, pp. 663–694, 1997.

[56] A. Chruścińska and N. Kijek, "Thermally modulated optically stimulated luminescence (TM OSL) as a tool of trap parameter analysis," *J. Lumin.*, vol. 174, pp. 42–48, 2016.

[57] M. Jain, A.S. Murray and L. Bøtter-Jensen, "Characterisation of blue-light stimulated luminescence components in different quartz samples: implications for dose measurement," *Radiat. Meas.*, vol. 37, pp. 441–449, 2003.

[58] A.S. Murray and A.S. Wintle, "Factors controlling the shape of the OSL decay curve in quartz," *Radiat. Meas.*, vol. 29, pp. 65–79, 1998.

[59] B.W. Smith, M.J. Aitken, E.J. Rhodes, E.J. Robinson and D.M. Geldard, "Optical dating: methodological aspects," *Radiat. Prot. Dosim.*, vol. 17, pp. 229–233, 1986.

[60] A.G. Wintle, "Thermal quenching of thermoluminescence in quartz," *Geophys. J. Roy. Astron. Soc.*, vol. 41, pp. 107–113, 1975.

[61] R.M. Bailey, "Towards a general kinetic model for optically and thermally stimulated luminescence of quartz," *Radiat. Meas.*, vol. 32, pp. 17–45, 2001.

[62] R. Nanjundaswamy, K. Lepper and S.W.S. McKeever, "Thermal quenching of thermoluminescence in natural quartz," *Radiat. Prot. Dosim.*, vol. 100, pp. 305–308, 2002.

[63] J.S. Singarayer and R.M. Bailey, "Further investigations of the quartz optically stimulated luminescence components using linear modulation," *Radiat. Meas.*, vol. 37, pp. 451–458, 2003.

[64] V. Pagonis, C. Ankjærgaard, A.S. Murray, M. Jain, R. Chen, J. Lawless and S. Greilich, "Modelling the thermal quenching mechanism in quartz based on time resolved optically stimulated luminescence," *J. Lumin.*, vol. 130, pp. 902–909, 2010.

[65] A. Chruścińska, N. Kijek and S. Topolewski, "Recent development in the optical stimulation of luminescence," *Radiat. Meas.*, vol. 106, pp. 13–19, 2017.

This page intentionally left blank

## Chapter 7

# Time-resolved Luminescence: Progress in Development of Theory and Analytical Methods

Makaiko L. Chithambo

*Department of Physics and Electronics, Rhodes University*
*PO BOX 94, Grahamstown, 6140, South Africa*
*m.chithambo@ru.ac.za*

Time-resolved optical stimulation is an important method for measurement of optically stimulated luminescence. The aim of time-resolved optical stimulation is to separate the stimulation and emission of luminescence in time. The luminescence is stimulated from a sample using a short light pulse of constant intensity. The ensuing luminescence can be monitored either during stimulation in the presence of scattered stimulating light, or after the light-pulse. The time-resolved luminescence spectrum produced in this way can be resolved into components, each with a distinct lifetime. The lifetimes are linked to physical processes of luminescence. Time-resolved optical stimulation has thus been used to study dynamics of luminescence in various materials, particularly ones of interest in dosimetry such as quartz, feldspar, $\alpha$-$Al_2O_3$:C and BeO. This chapter will review the theory of time-resolved luminescence, look at the instrumentation involved and discuss advances in analytical methods of time-resolved luminescence spectra.

### 7.1. Introduction

Time-resolved optical stimulation has become established as one of the three principal methods for measurement of optically stimulated luminescence. Whereas in either continuous-wave or linearly-modulated stimulation methods, the light source is kept on

continuously, time-resolved optical stimulation relies on the use of a train of light pulses of constant intensity to separate in time the stimulation and emission of luminescence. The luminescence is stimulated using a short light pulse during which the measured signal consists usually of a monotonically increasing luminescence component and scattered stimulating light. After stimulation, the luminescence is measured over the background of a detector, say photomultiplier noise only, and decreases in intensity with time.

The measurement of time-resolved optically stimulated luminescence (TR-OSL) offers a number of attractions over the other methods of optical stimulation. In TR-OSL, the luminescence can be measured with a high signal-to-noise ratio over extended periods, as was exemplified using quartz [1]. In addition, since the stimulating light pulse is brief, only a negligible proportion of the trapped charge is sampled. This enables repetitive measurement of luminescence from the same sample without any significant decrease in luminescence intensity. This feature was noted previously with particular reference to $\alpha$-$Al_2O_3$:C [2] and has facilitated studies where multiple measurements on the same aliquot were required (e.g. [3, 4]). Time-resolved optical stimulation provides a means to determine luminescence lifetimes. The lifetimes are associated with charge transfer processes within the material, and as such aid to better understand the mechanisms involved in the emission of luminescence.

Time-resolved luminescence in dosimetry-related studies was first reported by Sanderson and Clark [5] on feldspar stimulated with a 10 ns pulse. They reported lifetimes of the order of hundreds of nanoseconds from alkali feldspars. Subsequently, the technique was applied on $\alpha$-$Al_2O_3$:C [2, 6–8], feldspars [1, 9, 10] and quartz [1, 11], all materials of interest in retrospective dosimetry. In their work, Markey *et al.* [2], showed two lifetime components from $\alpha$-$Al_2O_3$:C, a temperature-independent one of value 35 ms and a temperature-dependent lifetime extending to 545 ms. The studies on quartz identified a principal lifetime of about 40 $\mu$s from either synthetic quartz [10] or natural quartz [1, 11]. Recent studies on BeO [12], $YAlO_3$:$Mn^{2+}$ [13] and zircon [14] attest to the enduring interest in TR-OSL.

The aim of this chapter is to describe the theory, experimental and analytical methods for time-resolved optically stimulated luminescence. In particular, we outline models of TR-OSL and discuss advances in analytical methods based on lifetimes, luminescence intensity and luminescence throughput.

## 7.2. Measurement techniques

There are several methods for measurement of time-resolved optically stimulated luminescence. In this chapter, we describe only two, namely, time-correlated photon counting and the time-tag method.

### 7.2.1. *Time-correlated photon counting*

Time-correlated photon counting is a long established method for measurement of photon counts, as discussed in [15]. The principle for this type of measurement is that the luminescence intensity needs to be low enough to render the probability of detecting a luminescence photon in the measurement period negligible when the pulse repetition-rate is suitably high. This causes the luminescence intensity corresponding to stimulation either during or after the light pulse to be unsuitable for reliable analysis. In order to ameliorate against this drawback, a time-resolved luminescence spectrum is built up by summing spectra from multiple sweeps.

The stimulation of luminescence in this method may be illustrated using Fig. 1. Luminescence is emitted during a pulse of duration $t_w$ as well as between pulses. The correlation in time between the light pulse and the resultant luminescence photon is determined by a multichannel scaler. The multichannel scaler measures the number of events that arise during the time interval $t_i$ to $t_i + \Delta t$ as a function of time, where $\Delta t$ is the dwell-time. The events in question are the detection of luminescence photons. The signal is recorded over a time $t$ referred to as the dynamic range, which may be less than or equal to the *period* $P$. The dynamic range comprises an integral number of $n$ channels each of duration $\Delta t$ such that $t = n\Delta t$. In a measurement, the light pulse is on for a duration given by the product of the pulse width and the number of sweeps.

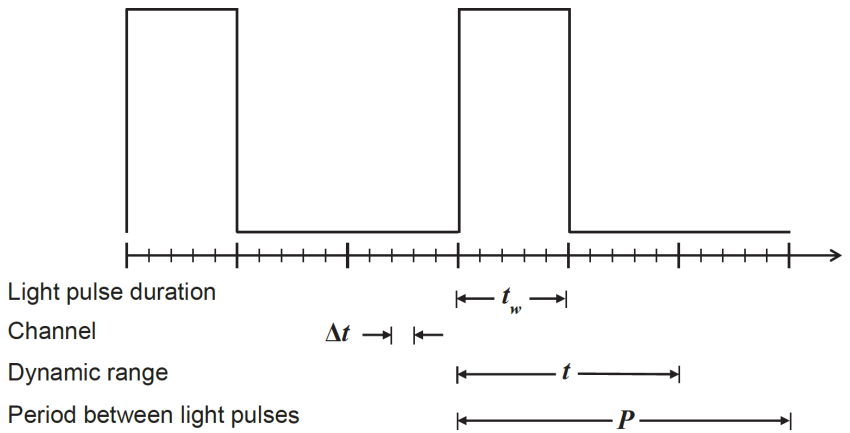


Fig. 1. A schematic diagram showing a luminescence stimulating light pulse of duration $t_w$ where the dynamic range $t$ is subdivided into an integral number of $n\Delta t$ channels [16].

Figure 2 shows an example of a measurement system for time-resolved luminescence [16]. The luminescence is detected by the photomultiplier tube (EMI 9635QA) whose signals, if above a set threshold, are processed by the timing filter amplifier (Ortec 474) and then fed into the constant fraction discriminator (Ortec 584) to enable their counting by the multichannel scaler (EG & G Ortec MCS-plus$^{TM}$). The multichannel scaler simultaneously triggers a set of light-emitting diodes and initiates a data-recording sweep in the computer. Once the sweep starts, the scaler records photon counts sequentially in its channels, with no dead-time between channels. The time-resolved spectrum measured in this way is a plot of cumulative photon counts against time for the dynamic range selected. An example of a time-resolved luminescence spectrum is shown in Fig. 3. The significance of the solid lines through data will be discussed later in the chapter.

### 7.2.2. *Time-tag mode*

The time-stamp or time-tag method is a type of time-correlated photon counting method [15]. The aim of this technique is to record information about every ensuing photon. The details stored include

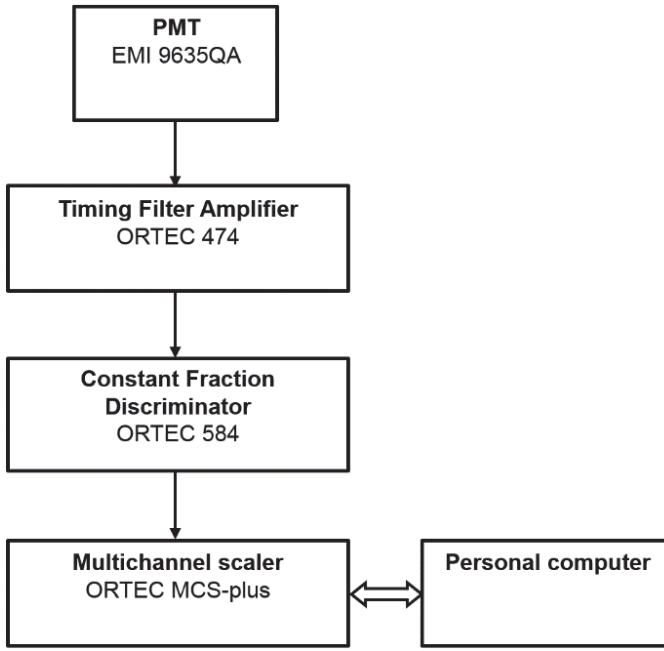


Fig. 2. An example of a pulsing system showing the arrangement for detection and measurement of time-resolved luminescence spectra [16].

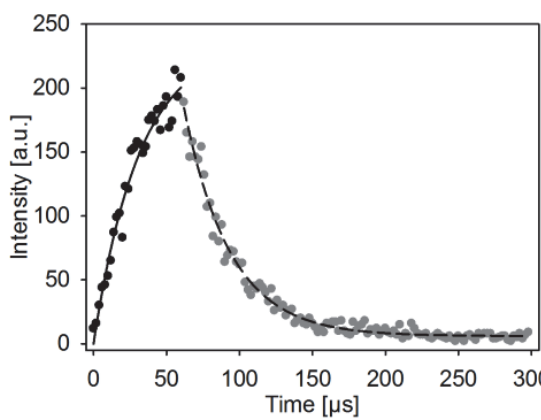


Fig. 3. Time-resolved luminescence from sedimentary quartz beta irradiated to 7 Gy and measured using a 60 $\mu$s pulse over $10^6$ sweeps [19].

the time of arrival since the start of the light pulse, and its time within the period. An example of such a system was described by Lapp *et al.* [17]. In their arrangement, a time marker is inserted in a buffer for each stimulation light pulse. The time of arrival of the luminescence photons during and after the stimulation pulses are each sequentially recorded in this buffer with respect to the time marker. Since for each light pulse only a few photons are emitted, the procedure is repeated many times over to obtain sufficient counts for analysis. The data read from the buffer can then be processed to produce a time-resolved spectrum.

### 7.2.3. *Other methods*

The methods summarized thus far are particular examples of pulsed optical stimulation. How the luminescence photons are detected and processed determines whether the luminescence is referred to as time-resolved luminescence or more generally, as pulsed optically stimulated luminescence and the two terms are used synonymously. An example of a general pulsed stimulation arrangement is exemplified by the system described by Markey *et al.* [2] where, instead of pulsing the light source, shutters were used to periodically intercept the stimulating light reaching the sample. The luminescence was measured during stimulation in the presence of the stimulating light, or in-between pulses as after-glow. The same method was used by Bulur and Göksu [7] except that in this case, the stimulating light was electronically triggered for a preset period.

## 7.3. Models of time-resolved luminescence

The principles of time-resolved luminescence spectra have been described using phenomenological models [18–20] and by a kinetics model based on simulation of experimental results e.g. [21, 22]. Although the methods have been applied on various materials, the discussion that follows will mostly draw on illustrative examples from experiments carried out on quartz and $\alpha$-$Al_2O_3$:C.

### 7.3.1. *Analytical model of time-resolved luminescence*

The model described by Chithambo [18, 19] is based on a simple case consisting of one electron trap with an initial electron concentration $N_i$ and one kind of recombination center. The model seeks to express charge movements during or after stimulation in terms of equations with a closed form solution.

If we set the probability of stimulation per unit time as $s$, and the decay constant giving the probability per unit time that a stimulated electron will produce luminescence as $\lambda$, then the rate of change of the number of stimulated electrons during stimulation can be written as

$$\frac{dN}{dt} = sN_i - \lambda N. \tag{1}$$

It follows that the time dependence of the number of stimulated electrons is

$$N(t) = \frac{sN_i}{\lambda}[1 - \exp(-\lambda t)]. \tag{2}$$

Since the luminescence, $L$, is produced as a result of radiative decay of stimulated electrons, one can write

$$dL(t) = \lambda N(t)dt. \tag{3}$$

By substituting Eq. (2) into Eq. (3), it can be shown that the rate of luminescence emission during pulsing is

$$l_1(t) = sN_i[1 - \exp(-\lambda t)]. \tag{4}$$

Equation (4) describes a saturating exponential from the start of stimulation at $t = 0$ and shows that during pulsed optical stimulation the rate of luminescent recombination increases approximately exponentially towards a limiting maximum.

In order to describe the emission of luminescence after a light pulse of duration $t_w$, we note that for $t > t_w$, $s = 0$. It readily follows from Eq. (3) that the time-dependence of luminescence emitted after

the light pulse is

$$l_2(t) = \lambda N(t_w)\exp[(-\lambda(t - t_w)], \tag{5}$$

where $N(t_w)$ is the number of stimulated electrons at time $t = t_w$. Equation (5) describes an exponential decay of the luminescence after the end of stimulation at time $t = t_w$.

The amount of luminescence produced during a stimulation light pulse of duration $t_w$ is found by integrating Eq. (3) to be

$$L_1 = sN_i t_w - \frac{sN_i}{\lambda}[1 - \exp(-\lambda t_w)]. \tag{6}$$

Similarly the luminescence emitted between the end of the pulse at $t_w$ to a time $t_2$ can be expressed as

$$L_2 = \frac{sN_i}{\lambda}[\exp(-\lambda t_w - 1)][\exp(-\lambda t_w) - \exp(-\lambda t_2)]. \tag{7}$$

When $t_2 \gg t_w$, Eq. (7) simplifies to

$$L_2 = \frac{sN_i}{\lambda}[1 - \exp(-\lambda t_w)]. \tag{8}$$

In practice, the period between light pulses is indeed usually much longer than the pulse width, that is, $t_2 \gg t_w$. As examples, Chithambo [23] reported measurements on quartz where the pulse width was 14 $\mu$s and the period between pulses was 286 $\mu$s or 95% of the dynamic range. In studies on $\alpha$-$Al_2O_3$:C, Pagonis *et al.* [24] used a pulse width of 0.5 s and an after-pulse detection time of 2.5 s or 83% of the dynamic range.

The amount of luminescence emitted after the end of the pulse, that is, $f_a = L_2/L_T$, where $L_T$ is the total integrated luminescence of the time-resolved luminescence spectrum, can be written as

$$f_a(t_w) = \frac{\tau}{t_w}\left[1 - \exp\left(-\frac{t_w}{\tau}\right)\right]. \tag{9}$$

Equation (9), which we define as the dynamic throughput, is instructive in demonstrating the influence of pulse width $t_w$ and lifetime $\tau$ on the amount of luminescence that can be measured under

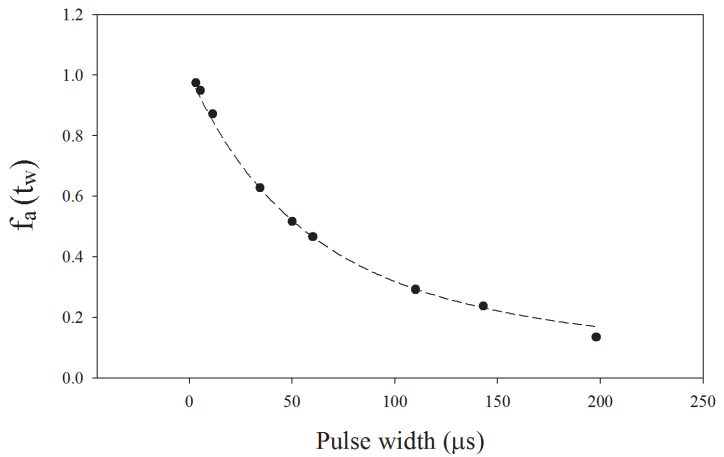


Fig. 4. The amount of luminescence emitted after the light pulse as a function of the pulse width for measurements made on annealed natural quartz [19].

pulsed stimulation. It can be deduced from Eq. (9) that, for a fixed lifetime, the amount of luminescence detected increases as the pulse width decreases. This fact is not influenced by the dynamic range and applies to any mode under which time-resolved luminescence is measured. Figure 4 shows the dynamic throughput for measurements made on quartz annealed at 800°C for 30 min and beta irradiated to 102 Gy before pulsed stimulation at 525 nm. The luminescence detected after stimulation as a proportion of the total signal increases from 44% to 97% when the pulse-width is changed from $2.5\tau$ to $0.11\tau$ for a lifetime of 31 $\mu$s. A further example concerns measurements on $\alpha$–$Al_2O_3$:C [25] where a pulse width of 300 ns was used. In each sweep, the luminescence was measured from 8 $\mu$s after the end of the pulse for 235 $\mu$s. It was noted that the best configuration for measurement was when both the pulse width and the acquisition time was less than the lifetime (about 36 ms). This is consistent with Eq. (9).

The implications of Eq. (9) as discussed, are valid for measurements made at a constant temperature and a fixed lifetime. In sections 7 and 8, we will extend the discussion to a more general situation when this is no longer the case.

### 7.3.2. *A description of pulsed luminescence based on change of the concentration of excited luminescence centers*

The preceding section discussed time-resolved luminescence in terms of the change in the concentration of stimulated electrons. An alternative approach reported by Yukihara and McKeever [20] uses the change in the concentration of excited luminescence centers. The concept is based on the fact that once a stimulated electron transits to a luminescence center, luminescence is not emitted immediately but rather after the excited luminescence center relaxes.

In this section, we expound on the idea above by considering the change with time of the concentration of excited luminescence centers $m^*$ during the initial light pulse, during subsequent pulses and, between light pulses. Analogous to Eq. (1), the concentration $m^*$ decreases due to relaxations, at a rate $\lambda$, and increases owing to stimulated electrons recombining at the luminescence centers. Assuming that the rate of recombination occurs at the same rate as the optical stimulation, one writes

$$\frac{dm^*}{dt} = -\lambda m^* - np, \tag{10}$$

where $p$ is the probability of optical stimulation of an electron from the electron trap to the conduction band and $n$ is the instantaneous concentration of trapped electrons. Since $dn/dt = -np$, Eq. (10) can be expressed as

$$\frac{dm^*}{dt} + \lambda m^* = n_o p e^{-pt}. \tag{11}$$

It is now helpful to consider the solutions of the linear first-order differential Eq. (11) in three cases, namely during the initial pulse of width $t_w$, during subsequent pulses, and between light pulses. If we assume that before any stimulation at all, there are no excited luminescence centers, that is, $m_i^* = 0$, the concentration of excited luminescence centers during stimulation will change with time as

$$m^* = \frac{n_o p}{(-p+\lambda)}(e^{-pt} - e^{-\lambda t}) \quad \text{pulse } j = 0;\ 0 \le t < t_w. \tag{12}$$

Since the luminescence intensity $I_{OSL} \propto \lambda m^*$, the time-dependent profile of the luminescence intensity should resemble that of Eq. (12). This equation describes a function that increases to a peak followed by a decrease. In the same way, the luminescence intensity should increase with optical stimulation, but must later decrease as the number of trapped electrons is depleted at extended stimulation times.

For subsequent pulses, $m_i^* \neq 0$, since not all excited centers can decay between pulses of finite duration. If we denote the concentration of excited states at the beginning of each subsequent pulse as $m_1^*$ then we find from Eq. (11) that

$$m^* = m_1^* e^{-\lambda t} + \frac{n_o p}{(-p+\lambda)}(e^{-pt} - e^{-\lambda t}) \quad \text{pulse } j \neq 0;\ 0 \leq t < t_w. \tag{13}$$

The profiles of Eqs. (12) and (13) are shown in Fig. (5). These are similar except that for Eq. (13), the initial intensity is offset by an amount $m_1^*$.

For the emission after the light pulse ($t \geq t_w$), $p = 0$ and since at $t = t_w$, $m^* = m_1^*$, it is found from Eq. (10) that

$$m^* = m_1^* e^{-\lambda(t-t_w)}. \tag{14}$$

Thus the luminescence after a light pulse of duration $t_w$ will decay exponentially. This is similar to Eq. (5) of the previous section.

Figure 5 shows simulated time-dependence of the luminescence intensity based on Eqs. (12), (13) and (14) for a dynamic range exceeding $4\tau$. Figure 5(a), for the predicted behavior during stimulation, shows that where the intensity is described by expressions of the form similar to Eqs. (12) and (13), it should go through a peak with time. If the light pulse is switched off before the peak is reached (Fig. 5b), the intensity will show a characteristic rise and fall if the pulse width is less than the lifetime. However, if the pulse width exceeds the lifetime, the intensity during stimulation will rise to some maximum and start to decrease before the onset of the exponential decay after the light pulse.

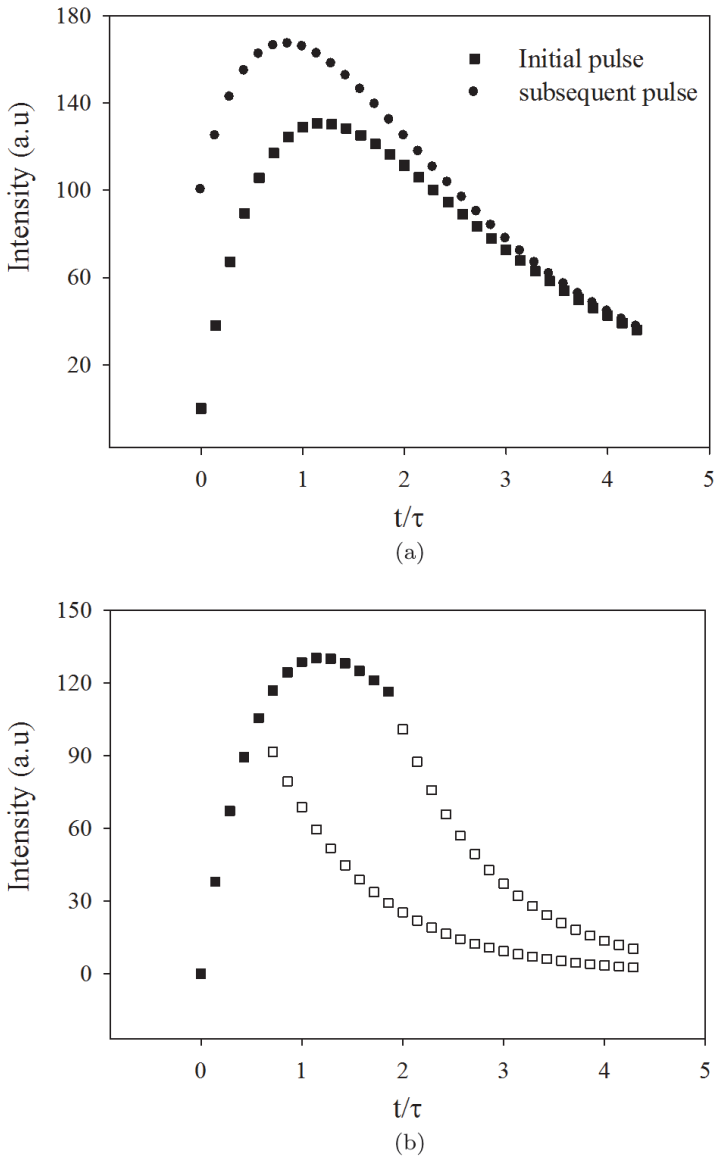


Fig. 5. Numerically simulated luminescence intensity based on Eqs. (12) and (13) during stimulation (a) The open symbols illustrate the decrease of luminescence after the light pulse (b).

### 7.4. Luminescence lifetimes

Experimentally, the lifetime as measured and discussed in this chapter denotes the delay between stimulation and emission of luminescence. The luminescence lifetimes may be associated with three possible physical mechanisms, namely, the time required to stimulate an electron from a trap $\tau_e$, the time $\tau_l$ for the electron to transit from the trap through the lattice to the recombination center, the lifetime of the excited state at the recombination center $\tau_f$, denoted throughout this chapter as simply $\tau$. In most cases, the dominant component is the relaxation time at the luminescence center ([3] and references therein).

With reference to Eqs. (4) and (5), lifetimes $\tau$ can be evaluated from either the portion of a time-resolved luminescence spectrum after the pulse by fitting exponential functions of the form

$$f(t) = Aexp\left(-\frac{t}{\tau}\right) + B, \tag{15}$$

or from the part during stimulation by fitting functions of the form

$$f(t) = D[1 - \exp(-t/\tau)], \tag{16}$$

where $t$ is time, $A$ and $D$ are scaling parameters and $B$ is a constant added to account for the background. The solid lines through data points during and after the light pulse in Fig. (3), giving respective lifetimes $\tau_d = 31.3 \pm 3.4\,\mu$s and $\tau_a = 31.6 \pm 0.8\,\mu$s are the best fits of Eqs. (16) and (15). The error $\Delta\tau$ in the lifetime reflects the scatter in data in the TR-OSL spectrum used to evaluate the lifetime. The lifetimes extracted from either portion of the time-resolved luminescence spectrum should be similar, since the recombination process responsible for luminescence is the same in both cases. If the lifetime has contributions from thermal excitation and radiative decay, it will be affected by temperature. This is discussed next.

#### 7.4.1. *The influence of measurement temperature on luminescence lifetimes*

When the Mott–Seitz configurational coordinate model for fluorescence [26] is modified for stimulated luminescence processes, the

distribution of luminescence lifetimes with temperature comprises radiative, phonon-assisted, and non-radiative terms as

$$\frac{1}{\tau} = \frac{1}{\tau_{rad}} + \gamma \coth\left(\frac{\hbar\omega}{kT}\right) + \nu \exp\left(\frac{-\Delta E}{kT}\right), \tag{17}$$

where $\tau$ is the lifetime of the excited state at the luminescence center, $\tau_{rad}$ is the radiative lifetime at absolute zero of temperature, $\gamma$ is a constant, $\omega$ is the phonon vibration frequency, $\hbar$ is the reduced Planck constant, $k$ is Boltzmann's constant, $\Delta E$ and $\nu$ are, respectively, the activation energy and frequency factor for non-radiative transitions [27, 28]. If the phonon-assisted transitions are negligible, Eq. (17) simplifies to

$$\tau = \frac{\tau_{rad}}{1 + Cexp(-\Delta E/kT)}, \tag{18}$$

where $C = \nu\tau_{rad}$.

Figure 6 shows some examples chosen to compare the theoretical form given in Eq. (18) with experimental results. Figure 6(a) shows the change of lifetimes with measurement temperature for quartz irradiated to 15 Gy. Measurements were made from 20 to 200°C (solid circles) and immediately thereafter from 200 to 20°C (open squares) [3]. In this example, the lifetimes are constant within $36 \pm 2\,\mu$s between 20 and 100°C but decrease to about $8\,\mu$s at 200°C. The dependence of lifetime with measurement temperature is independent of whether the measurements are made with the temperature increasing or decreasing. The data is satisfactorily fitted with Eq. (18) from which $\Delta E = 0.69 \pm 0.07$ eV (for measurement from 20 to 200°C) and $\Delta E = 0.67 \pm 0.05$ eV (for the run from 200 to 20°C) showing good consistency. Using $C = 8 \times 10^7$ from the fit, the frequency factor for the non-radiative process for quartz is calculated as $\nu = (2.2 \pm 0.1) \times 10^{12}\,\mathrm{s}^{-1}$.

Figure 6(b) shows an example from quartz annealed at 1000°C where the distribution of lifetimes with temperature cannot be described by Eq. (18), and simplifying assumptions were proposed to describe such a change [29].

Figure 6(c) shows yet another example that cannot readily be accounted for by using Eq. (18). This shows the change of lifetimes

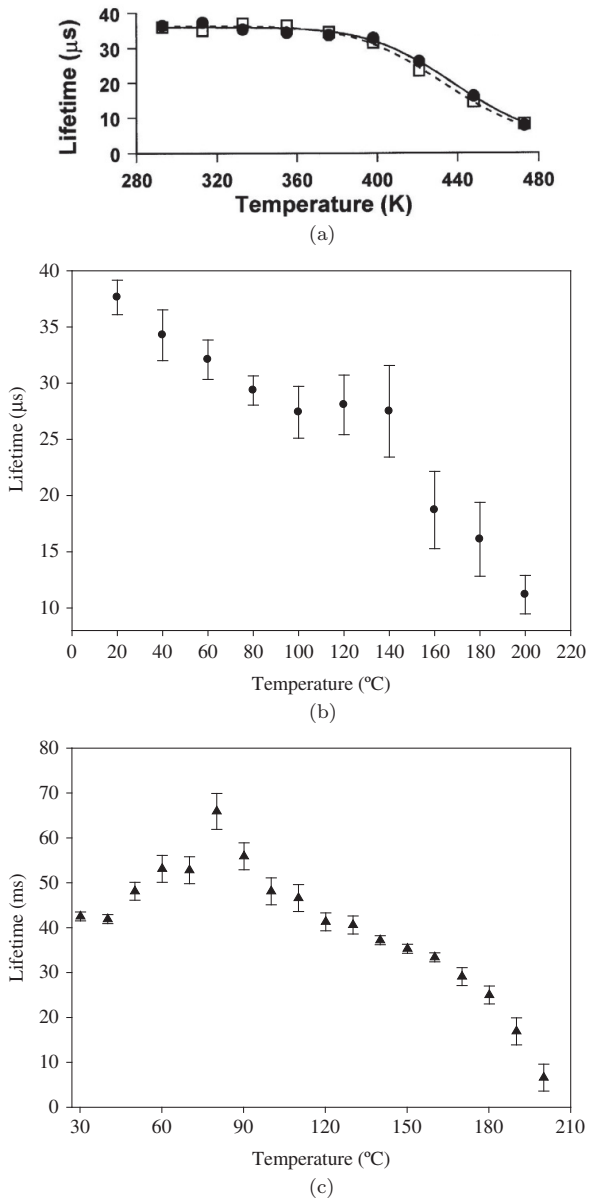


Fig. 6. The distribution of lifetimes with sample temperature from 20 to 200°C (solid circles) and from 200 to 20°C (open squares) in natural quartz [3]. Figures 6(b) and 6(c) show the same feature for quartz annealed at 1000°C [29] and in $\alpha$-$Al_2O_3$:C [30].

with temperature for a sample of $\alpha$-$Al_2O_3$:C irradiated to 1 Gy [30]. As Fig. 6(c) shows, the lifetimes go through a peak between 20 and 90°C. When similar measurements are made on another sample without shallow traps (as determined using thermoluminescence), the initial peak in lifetimes is less pronounced [30].

The cases of Figs. 6(b) and (c) show that the theoretical distribution of lifetimes with measurement temperature as given by Eq. (18) does not always apply to experimental data. Later in the discussion, we will describe alternative techniques for analyzing time-resolved spectra for thermal quenching, if Eq. (18) is inapplicable.

### 7.4.2. *The influence of annealing temperature on lifetimes in quartz*

When quartz is annealed beyond its first phase inversion temperature of 570°C, the sensitivity of its optically stimulated luminescence increases significantly beyond that monitored at room temperature [3, 31, 32]. This feature has motivated studies on the link between lifetimes and annealing temperature.

The relationship between lifetimes and annealing temperature in quartz was first systematically studied by Galloway [4] who proposed a model similar to the Schön-Klasens description, explained in detail by McKeever [33]. Figure 7 shows the dependence of lifetimes on annealing temperature for quartz annealed up to 900°C [34]. In this example, lifetimes are constant at about 33 $\mu$s up to about 600°C and then decrease steadily to 29 $\mu$s when the annealing temperature is increased to 900°C.

A schematic diagram of the model of Galloway [4] is shown in Fig. 8. The basic assumption is that annealing causes a transfer of holes between a non-radiative recombination center (R) and radiative ones. The change of lifetime from a higher value $\tau_H$ to a lower one $\tau_L$ with annealing temperature as shown in Figure 7 can be explained by transfer of holes between recombination centers (shown in Fig. 8 as $L_H$, $L_L$, $L_S$) with which lifetimes (say $\tau_H$, $\tau_L$, $\tau_S$) are associated where $\tau_H > \tau_L > \tau_S$. All luminescence centers contribute to the stimulated luminescence, but the value of the lifetime found will

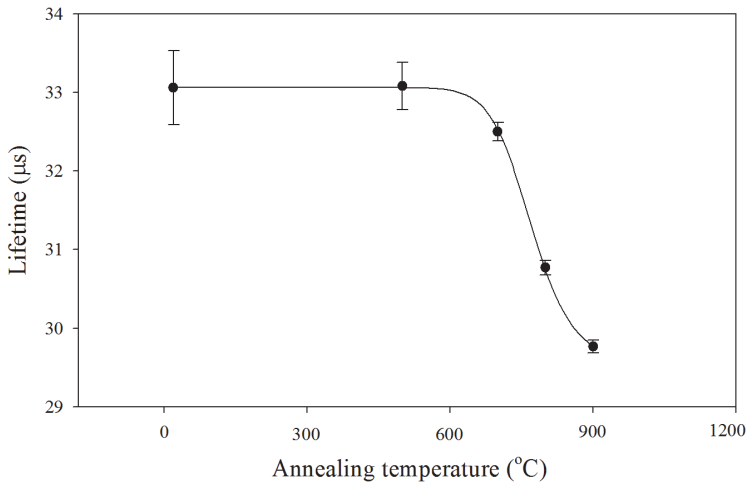


Fig. 7. The change of lifetimes with annealing temperature for quartz annealed up to 900°C [34].

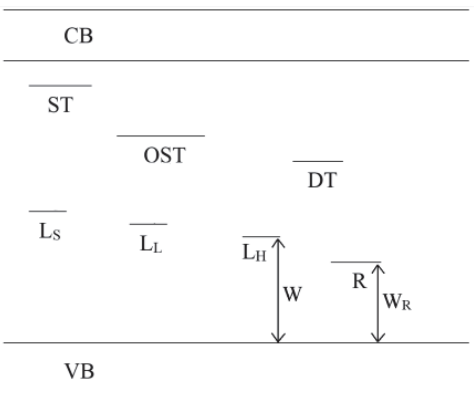


Fig. 8. The energy band model used to discuss luminescence lifetimes in quartz. Luminescence centers are labelled as $L_H$, $L_L$ and $L_S$ and the non-radiative center as R. The symbols ST, OST and DT stand for shallow electron traps, optically sensitive traps and deep traps (After Galloway [4]).

depend on which one of the centers is dominant. For completeness, Fig. 8 includes electron traps comprising shallow traps (ST), electron traps involved in optically stimulated luminescence (OST) and deep electron traps (DT).

The dependence of lifetime $\tau$ on annealing temperature T is modelled as

$$\tau = \tau_L + \frac{(\tau_H - \tau_L)}{1 + Cexp(-W/kT)}, \tag{19}$$

where $W$ is the activation energy above the valence band of the luminescence center from which holes involved in the luminescence process are thermally released [4] and all other parameters are as defined before. The line through the data in Fig. 7 is a fit of Eq. (19) giving $W = 2.14 \pm 0.01$ eV [34]. Other values in the literature for $W$ include $1.4 \pm 0.4$ eV [4] or the range 1.34–1.55 eV [35].

### 7.5. A simulation approach to description of time-resolved luminescence

Pagonis *et al.* [21] reported a model for TR-OSL based on computational simulations. Figure 9 shows a schematic diagram of the model, built on that of Galloway [4], comprising the main OSL trap and three recombination centers L1, L2, L3.

The charge movements during the stimulation pulse are as follows [21]:

$$\frac{dn_1}{dt} = -\lambda n_1 + A_n(N_1 - n_1)n_c, \tag{20}$$

$$\frac{dm_1}{dt} = -A_{m1}m_1n_c, \tag{21}$$

$$\frac{dm_2}{dt} = -A_{m2}m_2n_c, \tag{22}$$

$$\frac{dm_3}{dt} = -A_{m3}m_3n_c, \tag{23}$$

$$\frac{dn_c}{dt} = \frac{dm_1}{dt} + \frac{dm_2}{dt} + \frac{dm_3}{dt} - \frac{dn_1}{dt}. \tag{24}$$

The instantaneous luminescence $L$ is defined as

$$L = -\frac{dm_1}{dt} - \frac{dm_2}{dt} - \frac{dm_3}{dt}. \tag{25}$$

In these equations, $N_1$ and $n_1$ are the respective concentrations of electron traps and trapped electrons; $m_1$, $m_2$, and $m_3$ are the

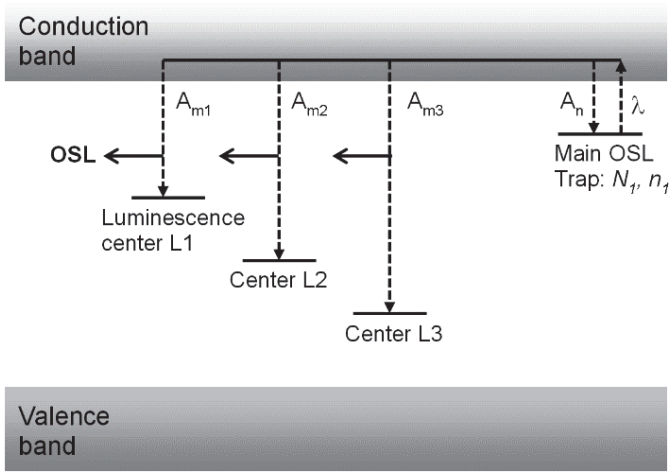


Fig. 9. A simulation based model for luminescence in quartz where all symbols are as explained in the text [21].

concentrations of holes at the recombination centers L1, L2, L3, and $n_c$ is the concentration of electrons in the conduction band.

Equation (20) describes the optical stimulation of electrons from the electron trap with probability $\lambda$ and retrapping with probability $A_n$. After stimulation, $\lambda$ equals zero. Equations (21–23) express transitions to the recombination centers with probabilities $A_{m1}$, $A_{m2}$ and $A_{m3}$ respectively. Equation (24) accounts for conservation of charge in the system. The assumption that all three recombination centers contribute to the observed luminescence is implicit in Eq. (25). As written, Eq. (25) implies that the three transitions have the same efficiency. If required, as Chithambo *et al.* [36] note, each term would otherwise have to be multiplied by an appropriate efficiency factor.

Figure 10 shows the results of running a simulation with the following set of parameters: $N_1 = 10^9\,\mathrm{cm}^{-3}$; $n_{10} = 10^9\,\mathrm{cm}^{-3}$; $A_n = 8 \times 10^{-6}\,\mathrm{cm}^3\,\mathrm{s}^{-1}$; $m_{10} = 5 \times 10^9\,\mathrm{cm}^{-3}$; $m_{20} = m_{30} = 0$; $A_{m1} = 6.1 \times 10^{-4}\,\mathrm{cm}^{-3}\,\mathrm{s}^{-1}$; $A_{m2} = 0$; $A_{m3} = 0$; $\lambda = 200\,\mathrm{s}^{-1}$ [21]. By setting $A_{m2}$ and $A_{m3}$ equal to zero, the results reflect the case of one dominant recombination center. The results of the simulation are a good match for the experimental data of Chithambo [19].

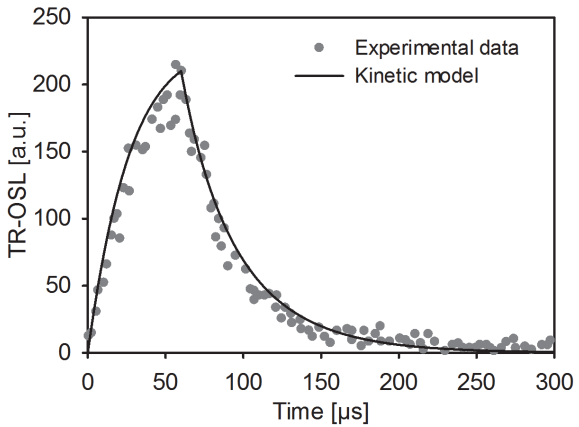


Fig. 10. A comparison of the model of Pagonis *et al.* [21] with experimental data of Chithambo [19].

### 7.5.1. *Analytical expressions for dependence of lifetimes on measurement temperature*

Pagonis *et al.* [24] described a model for thermal quenching in quartz based on an explanation of the same effect usually made using a configurational coordinate diagram [31]. The principle of this process is that electrons in an excited state can make either a direct radiative or an indirect thermally assisted non-radiative transition into the ground state of the recombination center.

Figure 11 shows the thermal quenching model of Pagonis *et al.* [24]. The main OSL electron trap is shown as level 1. In contrast with the earlier model [21], all other transitions are now localized at the recombination center. Electrons can transit from the conduction band, with probability $A_{CB}$, into the excited state of the recombination center (downward arrow 3). A radiative transition, with probability $A_R$, from the excited state into the ground state is labelled 5. In order to match the schematic of the configurational coordinate diagram, Pagonis *et al.* [24], set an additional excited state (level 3) to provide an alternative thermally assisted route (labelled 4) resulting in a radiationless transition (labelled 6). The probability of thermal excitation is modulated by the term $\exp(-\Delta E/kT)$ where $\Delta E$ is the activation energy for thermal quenching as before [33].

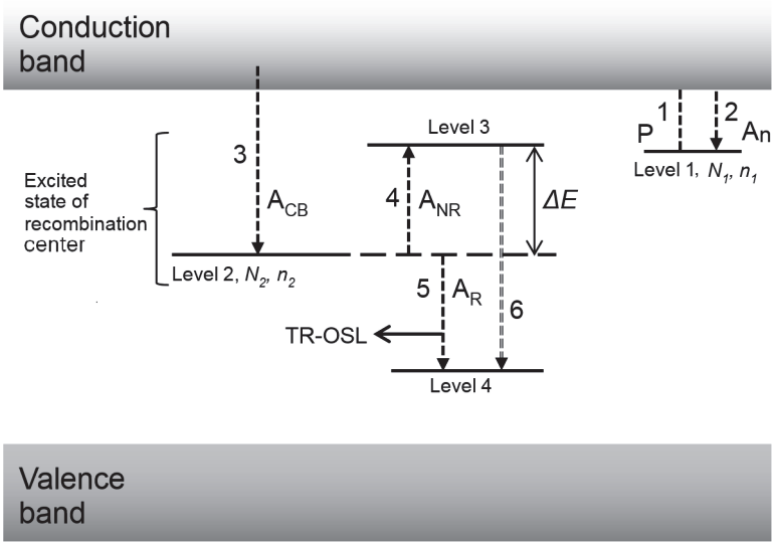


Fig. 11. The kinetic model of Pagonis *et al.* [24] developed to explain thermal quenching in quartz.

The charge movements are represented by the following expressions:

$$\frac{dn_1}{dt} = A_n n_c (N_1 - n_1) - n_1 P, \tag{26}$$

$$\frac{dn_c}{dt} = -A_n n_c (N_1 - n_1) + n_1 P - A_{CB} n_c (N_2 - n_2), \tag{27}$$

$$\frac{dn_2}{dt} = A_{CB} n_c (N_2 - n_2) - A_R n_2 - A_{NR} n_2 \exp\left(-\frac{\Delta E}{kT}\right), \tag{28}$$

where $N_1$ and $n_1$ are as defined before, $N_2$ and $n_2$ are the concentrations of electron traps and filled traps correspondingly in the excited level 2 of the recombination center, $A_n$ is the retrapping probability, and $P$ denotes the probability of optical excitation of electrons from the OSL trap and other parameters are as defined earlier.

Pagonis *et al.* [37] used equations (26–28) to derive analytical expressions for various aspects of TR-OSL. For example, from solutions of Eqs. (26, 27) and (28), the luminescence during the

stimulation pulse is found as

$$I(t) = A_R \frac{f}{A_R + A_{NR}\exp\left(-\frac{\Delta E}{kT}\right)} \times \left\{1 - \exp\left[-\left(A_R + A_{NR}\exp\left(-\frac{\Delta E}{kT}\right)t\right)\right]\right\}, \quad (29)$$

and after stimulation as

$$I(t) = A_R n_2(t_w)\left\{1 - \exp\left[-\left[A_R + A_{NR}\exp\left(-\frac{\Delta E}{kT}\right)\right](t - t_w)\right]\right\}. \quad (30)$$

Equation (29) shows that the TR-OSL intensity during stimulation can be described as a saturating exponential. In comparison, Eq. (30) shows that after pulsed-stimulation for a duration $t_w$, the luminescence decays as a simple exponential. These two expressions have the same form as Eqs. (4) and (5) in section 7.3.1. By comparing Eqs. (29) and (30) with Eqs. (4) and (5), it can be deduced that the lifetime $\tau$ can be written as

$$\tau = \frac{1/A_R}{1 + \frac{A_{NR}}{A_R}\exp(-\Delta E/kT)}. \quad (31)$$

This expression is similar to Eq. (18). Since from Eq. (18), $C = \nu\tau_{rad}$, it is deduced that $\nu \equiv A_{NR}$ and $\tau_{rad} = 1/A_R$ showing that the definitions of the dimensionless constant C from both formulations are consistent.

### 7.5.2. *Simulating the dependence of lifetimes on annealing temperature*

In order to describe the dependence of lifetimes on annealing temperature, Pagonis *et al.* [22] modified the model in Fig. 11 to now comprise two luminescence centers $L_H$ and $L_L$ and a hole reservoir R. By deriving expressions for the concentration of electrons in the excited states at the two luminescence centers and the concentration of holes at the non-radiative center R, it was shown that the

luminescence during stimulation could be written as

$$I_{ON}(t) = \frac{(A_R)_H g N_H}{\gamma_H}(1 - e^{-\gamma_H t}) + \frac{(A_R)_L g N_L}{\gamma_L}(1 - e^{-\gamma_L t}). \quad (32)$$

and after stimulation as

$$I_{OFF}(t) = (A_R)_H n_H(t_w) e^{-\gamma_H (t - t_w)} + (A_R)_L n_L(t_w) e^{-\gamma_L (t - t_w)}, \quad (33)$$

where $N_H$, $N_L$, $n_H$ and $n_L$ are each the concentrations of the total and filled electron traps in the two excited levels of the luminescence centers and $g$ is a constant. In particular, $n_H(t_w)$ and $n_L(t_w)$ are the concentrations at time $t = t_w$. The radiative transitions are defined by probabilities $(A_R)_H$ and $(A_R)_L$ which are related to luminescence lifetimes as $(A_R)_H = 1/\tau_H$ and $(A_R)_L = 1/\tau_L$, so that,

$$\gamma_H = (A_R)_H + (A_R)_H \exp(-(\Delta E)_H / kT), \quad (34)$$

and

$$\gamma_H = (A_R)_L + (A_R)_H \exp\left(-\frac{(\Delta E)_L}{kT}\right). \quad (35)$$

The constant $g$ is given by

$$g = \frac{A_{CB} n_1(0) P}{A_n(N_1 - n_1(0)) + A_{CB}(N_H + N_L)}, \quad (36)$$

where $(\Delta E)_H$ and $(\Delta E)_L$ are the activation energy for thermal quenching associated with recombination centers $L_H$ and $L_L$ respectively, and $n_1(0)$ is the initial concentration of trapped electrons and all other parameters are as defined before.

The dependence of the lifetimes on annealing temperature $T_A$ is encapsulated in the parameter $N_L$ as

$$N_L(T_A) = N_L + N_R(0)\left[1 - exp\left(-Bexp\left(-\frac{E_R}{kT_A}\right)\right)\right], \quad (37)$$

where $B$ is a constant, $N_R(0)$ represents the initial concentration of holes in the non-radiative recombination center and $E_R$ is the thermal activation energy for the non-radiative center, that is, the same as W in Eq. (19), and $N_L$ is the concentration of holes at

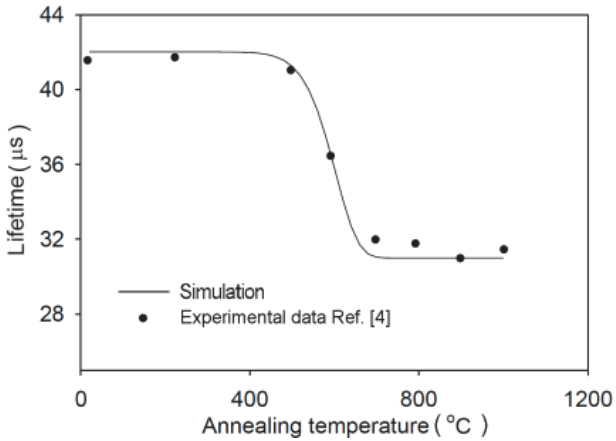


Fig. 12. Lifetimes developed using simulation [22] illustrated as the solid line compared with experimental data of Galloway [4].

the $L_L$ center in an unannealed sample. Using Eq. (32), Pagonis *et al.* [22] simulated the dependence of lifetimes on annealing temperature. Figure 12 shows a fit of the model (solid line) to the experimental data of Galloway [4] showing satisfactory agreement between model and experimental results.

### 7.6. Experimental evidence of multiple luminescence centers in heated quartz

The possibility that the emission of luminescence in annealed quartz might involve multiple luminescence centers [4] has been examined experimentally. Chithambo and Ogundare [38] studied the influence of measurement temperature on three separate lifetimes $\tau_H$, $\tau_L$ and $\tau_S$ associated with recombination centers $L_H$, $L_L$ and $L_S$ in quartz annealed up to 800°C. They found that the activation energy of thermal quenching associated with each of the centers $L_H$, $L_L$ and $L_S$ was unique at 0.64 eV, 0.72 eV and 0.84 eV respectively. Measurements of radioluminescence were then made on the same quartz as a way of monitoring any differences in emission bands due to annealing [22]. An emission band at ∼3.44 eV (360 nm) became significantly enhanced when the annealing temperature was increased to 500°C. A further increase in temperature caused the emission

intensity to decrease, but then a new band at ∼3.73 eV (330 nm) appeared for annealing in the range 600–700°C.

In another study [39], measurements on natural quartz from crystalline rocks with known thermal history showed examples where the lifetime component $\tau_H$ was dominant in metamorphic quartz, whereas the components $\tau_L$ and $\tau_S$ were present in plutonic quartz. The approximate provenance temperatures of the metamorphic and plutonic samples are 450–550 and 550–700°C.

The results summarized above are consistent with the interpretation that luminescence in quartz can be associated with multiple recombination centers and that whichever one is dominant depends on a number of factors, including the combination of annealing and measurement temperature.

## 7.7. The influence of measurement temperature on time-resolved luminescence intensity

The change of time-resolved luminescence intensity with measurement temperature can be described in various ways, such as by use of the intensity integrated over time-resolved spectra, or as the dynamic throughput. This section presents mathematical models for analyzing the throughput for thermal effects such as thermal assistance and thermal quenching.

### 7.7.1. *Dynamic throughput*

If the luminescence emitted during and after stimulation is denoted as $L_1$ and $L_2$ respectively, we define the dynamic throughput as the ratio of either $L_1$ or $L_2$ to the total integrated signal, $L_T$, i.e either $L_1/L_T$ or $L_2/L_T$ [18, 19]. This definition should not be mistaken for the ratio of luminescence emitted after stimulation to that emitted during pulsing ($L_2/L_1$) termed the efficiency by McKeever *et al.* [40]. The expression for the ratio $L_1/L_T$ is given in Eq. (9) and was developed using a simple model consisting of one electron trap and one kind of recombination center [18, 19]. As stated in section 7.3.1, we assume that since the stimulation pulse is brief, it causes only a negligible change in trapped charge and as such re-trapping is also

assumed to be negligible. If re-trapping is included in this model, the throughput can be expressed as

$$f_a(t_w) = \frac{1 - \exp[-(p_s + p_r)t_w]}{(p_s + p_r)t_w}, \tag{38}$$

where $p_s$ and $p_r$ are, respectively, the probability per unit time of stimulation and re-trapping. Equation (38) reduces to Eq. (9) when re-trapping is negligible. In practice, use of Eq. (38) in specific cases of the ratio $p_s/p_r$ requires numerical simulation but since this is not important for this discussion, it will not be explored.

The temperature dependence of the throughput was reported by Chithambo and Costin [41] in a study on $\alpha$-$Al_2O_3$:C. Here, we review the main elements of the theory. Measurements were made between 20 and 180°C on one sample irradiated only once to 10 Gy prior to use, and not irradiated again between measurements. Luminescence was stimulated using a 16 ms pulse width.

### 7.7.2. *Dynamic throughput and pulse-width*

Since the dynamic throughput relates the luminescence lifetime and pulse-width, there are two relevant cases to consider, namely $t_w > \tau$ or $t_w < \tau$. Bøtter-Jensen *et al.* [31] discussed this for measurements at room temperature. Chithambo and Costin [41] extended the description to account for a change in stimulation temperature.

#### 7.7.2.1. *Case 1: Lifetime greater than the pulse-width ($\tau > t_w$)*

Figure 13 shows the temperature dependence of the throughput ($L_1/L_T$) for measurements from 20 to 180°C and immediately thereafter from 180 to 20°C. The amount of luminescence emitted during stimulation increases from 17 to 22% between 20 and 70°C and then decreases to 3% at 180°C. Measurements made from 180 to 20°C (triangles) reproduce the pattern.

If the results of Fig. 13 are considered in terms of temperature only, the increase in intensity up to 40°C can be ascribed to contribution from shallow electron traps. The further increase in intensity thereafter up to 70°C can be accounted for by thermal

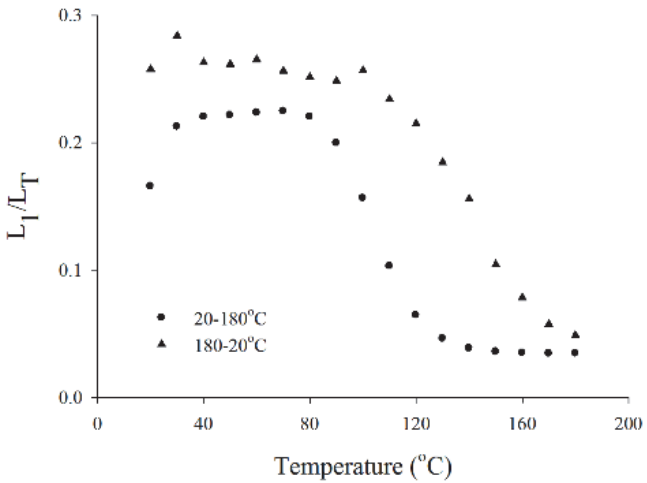


Fig. 13. The change of $L_1/L_T$ with sample temperature for measurements from 20 to 180°C (circles) and from 180 to 20°C (triangles) [41].

assistance to optical stimulation from the main electron trap. The decrease in intensity that then follows up to 180°C is deduced to result from thermal quenching. However, this explanation is sufficient if the lifetime is constant but not when it changes with measurement temperature.

The measurements in Fig. 13 were made using a pulse width of 16 ms. Since this is less than the relaxation lifetime of 35 ms at the luminescence center (the F-center) at room temperature, each pulse increases the concentration of excited luminescence centers relaxing after the pulse. Consequently, more luminescence is emitted after rather than during pulsed stimulation. Indeed, the throughput is less than 30% at any temperature, showing that any changes cannot be explained by thermal assistance and thermal quenching only.

#### 7.7.2.2. *Case 2: Lifetime less than the pulse-width ($\tau < t_w$)*

The reverse case where $\tau < t_w$, was studied in measurements using a 375 ms pulse and a 2000 ms dynamic range. Figure 14 shows the change of $L_2/L_T$ (open circles) and $L_1/L_T$ (solid circles) with sample temperature. The amount of signal emitted after pulsed stimulation

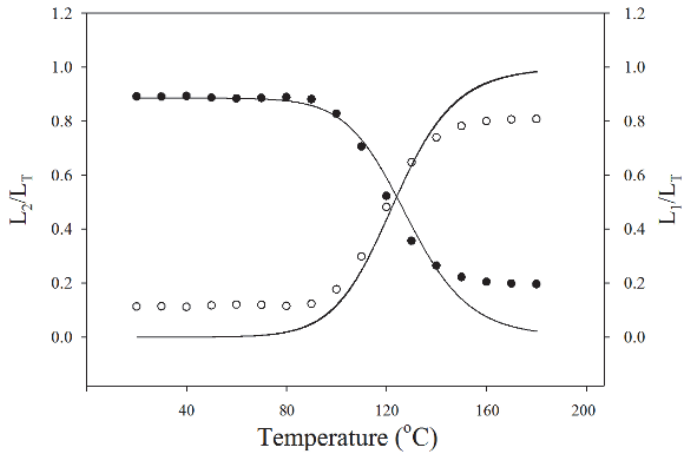


Fig. 14. The dependence of $L_2/L_T$ (open circles) and $L_1/L_T$ (solid circles) on sample temperature for measurements from 20 to 180°C. The solid lines are explained in the text [41].

is constant at about 11% between 20 and 90°C but increases to about 80% at 180°C. In comparison, about 89% of the signal is emitted during the pulse between 20 and 90°C, gradually decreasing to about 20% at 180°C.

Although the luminescence emitted after the pulse ($L_2/L_T$; open circles) increases with measurement temperature, it reaches a maximum of only about 80%, well below the ∼89% observed during stimulation. Regarding the proportion of luminescence emitted during stimulation ($L_1/L_T$; solid circles), this decreases with temperature to ∼20% which exceeds the initial value of 11% corresponding to $L_2/L_T$ for after stimulation. The importance of these results is discussed below.

### 7.7.3. *Dynamic throughput and lifetime*

Figures 13 and 14 show how the dynamic throughput is affected by whether the lifetime is more or less than the pulse width. This can be further explained by considering how the throughput is influenced by change in lifetime due to temperature. In Fig. 13 the lifetime remains longer than the pulse width, despite the lifetime

itself decreasing with sample temperature. The decrease in lifetime causes the concentration of luminescence centers relaxing after stimulation to increase. This thermally-induced effect, which leads to an increase in luminescence intensity, is not thermal assistance. On the other hand, the amount of luminescence emitted during stimulation decreases, an effect separate from any decrease due to thermal quenching.

### 7.7.4. *Analysis of the temperature-dependence of the throughput*

#### 7.7.4.1. *Analysis based on the luminescence intensity*

The purpose of this part is to describe the general dependence of the dynamic throughput on measurement temperature.

If for a given time-resolved spectrum, $I_i$ and $\tau_i$ are respectively, the amplitude and lifetime of the $i^{th}$ component, then its intensity can be expressed as

$$I(t) = \int_o^\infty I_i \exp(-t/\tau_i)dt = I_i\tau_i. \tag{39}$$

The intensity at any temperature $T$, for a lifetime $\tau_o$, is then $I(T) = I_i\tau_o$. Therefore the temperature-dependence of the luminescence intensity described in Eq. (39) is given by

$$f_1(T) = \frac{I(T)}{I_o} = \frac{1}{1 + Cexp(-\Delta E/kT)}. \tag{40}$$

Since $I(T)/I_o \leq 1$, we define $f_1(T)$ as the probability that excitations at temperature $T$ will produce luminescence. The probability of a non-radiative transition, $(1 - f_1(T))$, is then

$$f_2(T) = \frac{Cexp(-\Delta E/kT)}{1 + Cexp(-\Delta E/kT)}. \tag{41}$$

Equations (40) and (41), as probabilities, can be used to discuss the analysis of the throughput.

In Fig. 14, for which $t_w \gg \tau$ at all temperatures, the luminescence should mostly be emitted during stimulation. Therefore, the solid line through the data corresponding to this signal (solid circles) is

a fit of Eq. (40) giving $\Delta E = 1.12 \pm 0.01\,\text{eV}$ and $C = 1.2 \times 10^{14}$ from which $\nu = 3.3 \times 10^{15}\,\text{s}^{-1}$. In contrast, the line through the open symbols in Fig. 14 is a fit of Eq. (41) from which $\Delta E$ and C are $1.09 \pm 0.01\,\text{eV}$ and $C = 8.5 \times 10^{13}$ giving $\nu = 2.3 \times 10^{15}\,\text{s}^{-1}$. These compare well with literature values e.g. $\Delta E = 1.08 \pm 0.03$ eV [28]. Equations (40) and (41) do not account for retrapping. Thus although these expressions produce satisfactory results, they are only a good estimate for empirical behavior.

#### 7.7.4.2. *Analysis of the dynamic throughput in terms of lifetime*

Expressions for the throughput given in Eqs. (40) and (41) apply for emission after stimulation. Similarly, the throughput for emission during a light pulse at a given measurement temperature when retrapping is valid can be written as

$$f_{sr}(t_w) = \frac{(p_s + p_r)t_w - [1 - \exp(-(p_s + p_r))t_w]}{(p_s + p_r)t_w}, \tag{42}$$

and when retrapping is negligible as

$$f_s(t_w) = (1 - f_a(t_w)). \tag{43}$$

The temperature-dependence of $p_s$ and $p_r$ in Eqs. (42) and (43) are unknown and so their use may require numerical simulation. If retrapping were negligible, the throughput would only be affected by the temperature-dependence of lifetime as given in Eq. (18). In this case, the throughput after a pulse of width $t_w$ would depend on temperature as

$$f_a(\tau, T) = \frac{\tau_{rad}}{t_w}\left(\frac{1}{1 + Cexp(-\Delta E/kT)}\right) \times \left\{1 - exp\left[-\frac{t_w}{\tau_{rad}}(1 + Cexp(-\Delta E/kT))\right]\right\} \tag{44}$$

and during the light-pulse as

$$f_s(\tau) = \frac{[t_w(1 + Ce^{-\Delta E/kT})] - f_a(\tau, T)}{t_w(1 + Ce^{-\Delta E/kT})}, \tag{45}$$

where all symbols are as previously defined. Equations (44) and (45) are general and combine the change of luminescence intensity caused by de-excitations as well as the temperature-induced change in lifetimes.

## 7.8. Temperature dependence of luminescence intensity integrated over TR-OSL spectra

In this section, we discuss the methods of analyzing the luminescence intensity based on intensity integrated over TR-OSL spectra.

### 7.8.1. *Temperature dependence of the luminescence intensity during pulsed stimulation*

Figure 15 shows the change of $L_1$ with temperature between 20 and 200°C for $\alpha-Al_2O_3$:C [41]. We recall that the sample being referred to here was irradiated only once to 1 Gy before use and never irradiated again between pulsed stimulation at 16 ms per sweep. The intensity goes through a peak with measurement temperature.

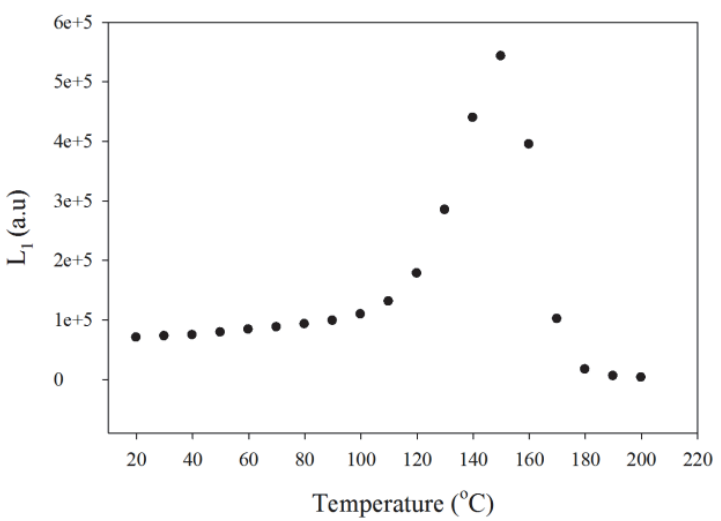


Fig. 15. The change of luminescence intensity during the pulse with measurement temperature [41].

Initially, the intensity increases with temperature at a slow rate up to ∼100°C but with a greater rate thereafter. This change of intensity reflects thermal assistance to stimulation of luminescence from shallow electron traps, and possibly a small amount of phototransfer from deep traps [42]. The similar change at higher temperatures up to about ∼150°C shows the same effect for the main peak. Figure 15 shows that the intensity increases with temperature at two distinct rates before the onset of thermal quenching. The measurements of Fig. 15 can be used to analyse the luminescence intensity for the influence of thermal assistance on the shallow and main electron traps separately, as will be discussed in section 7.8.2.

### 7.8.2. *Temperature dependence of luminescence intensity after pulsed stimulation*

Time-resolved luminescence from $\alpha$-$Al_2O_3$:C includes a second longer lifetime component in addition to the principal lifetime of 35 ms [2]. For this reason, the temperature dependence of the intensity after the light pulse cannot be studied by simply integrating the time-resolved spectrum as before, since this would subsume both lifetime components. In this case, the intensity may be studied by using the temperature dependence of the amplitudes A and B shown in Eq. (15). Figure 16 shows the change of A and B with temperature Between the two amplitudes, B is more intense and also goes through a peak with stimulation temperature. There is an initial decrease of intensity due to optical stimulation (Fig. 16b, inset) that is followed by the onset of increased intensity. Since the intensity increases with temperature at different rates, the behavior can be used to analyze luminescence for thermal assistance from the shallow and main electron trap separately.

#### 7.8.2.1. *Distinguishing thermal assistance at separate electron traps*

When the luminescence emission is subject to thermal assistance with an activation energy $E_a$, the overall probability of optical stimulation

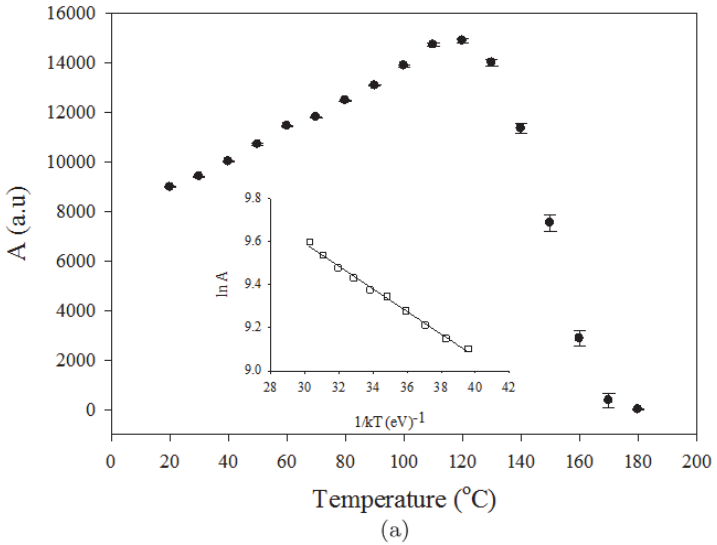


(a)

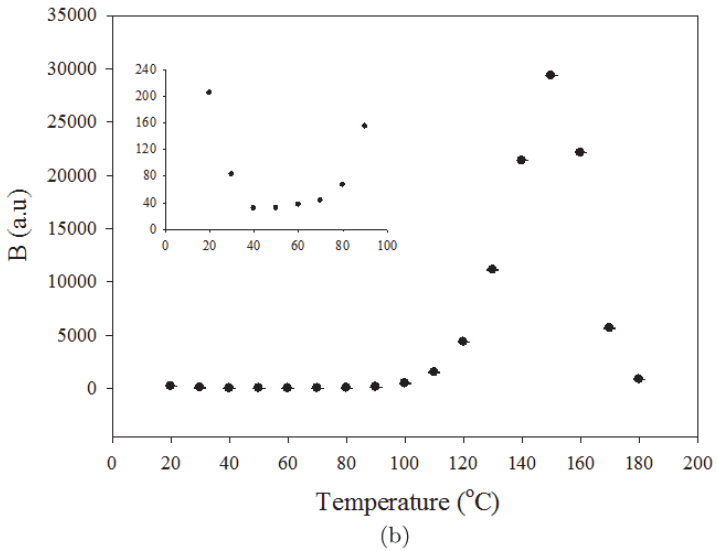


(b)

Fig. 16. The temperature dependence of amplitudes A (in (a)) and B (in (b)). The inset to part (a) shows a means to evaluate the activation energy for thermal assistance for the shallow trap. The inset in part (b) shows the initial change of intensity with temperature [41].

can be expressed for $n$ electron traps as

$$\frac{1}{\tau} = \left[\frac{1}{\tau_{rad}} + \nu exp\left(-\Delta E/kT\right)\right] \prod_{i}^{n} \exp(-E_{ai}/kT), \tag{46}$$

where $E_{ai}$ is the activation energy for thermal assistance for the $i^{th}$ electron trap, $n$ the number of electron traps contributing to the process and all other parameters are as defined before [41]. Using Eq. (46), it follows that the temperature-dependence of the luminescence intensity, where thermal assistance is relevant, can be written for $n$ electron traps as

$$I(T) = \frac{I_o \prod_i^n exp(-E_{ai}/kT)}{1 + Cexp(-\Delta E/kT)}. \tag{47}$$

Equations (46) and (47) imply that luminescence from different traps should be analyzed for thermal assistance separately. In practice, the luminescence associated with different electron traps cannot be isolated and simplifying assumptions become necessary to use Eq. (47).

In the rising edge of Fig. 15, at sufficiently low temperatures, thermal quenching can be neglected and for a particular electron trap, one can write from Eq. (47) that

$$I(T) = \kappa \exp(-E_a/kT), \tag{48}$$

where $\kappa$ is a constant. Therefore, the activation energy for thermal assistance corresponding to the $n^{\text{th}}$ trap can be determined from a plot of intensity $\ln I$ against $1/kT$ for temperatures where thermal assistance is dominant for that particular electron trap.

Examples of plots of $\ln I$ against $1/kT$ for measurements between 40 and 90°C (solid circles) corresponding to the shallow trap, as well as between 110 to 150°C (open squares) corresponding to the main trap in $\alpha$-$Al_2O_3$:C are shown in Fig. 17. The activation energy for thermal assistance $E_a$ was found for the shallow electron trap as $0.054 \pm 0.001$ eV and as $0.53 \pm 0.03$ eV for the main electron trap. If the combined intensities are used, the differences in response can no longer be perceptible and the activation energy evaluated will reflect the more dominant term. This can be demonstrated by applying

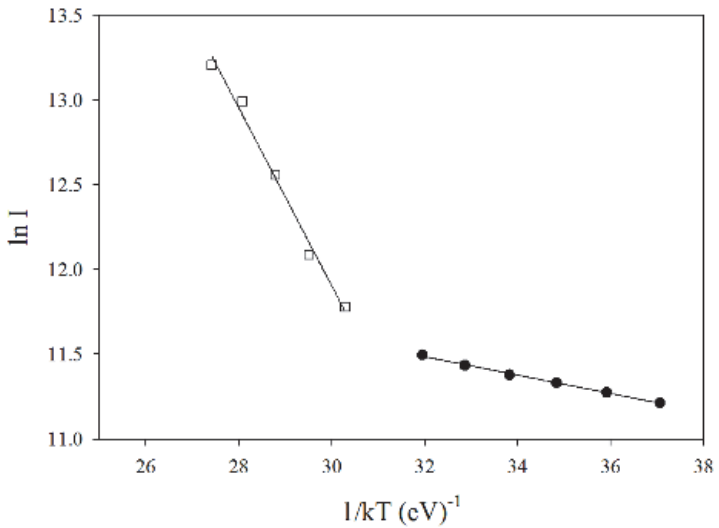


Fig. 17. Semi-logarithmic plots of intensity against sample temperature between 40 and 90°C (solid circles) and 110-150°C (open squares) corresponding to the shallow and main electron traps [41].

Eq. (48) to the data of Fig. 16(a) Here the activation energy for thermal assistance found (see inset for plot), that is, $0.053 \pm 0.001$ eV is for the shallow electron trap. The discussion in this section has therefore demonstrated how $E_a$ for the shallow and main electron traps can be distinguished.

## 7.9. Thermal quenching

### 7.9.1. *Analysis based on ratio of intensities*

The thermal quenching apparent in Fig. 15 can also be analyzed by applying the method based on use of the temperature-dependence of the area under an isothermal decay-curve [43]. If in a set of runs, a time-resolved spectrum is measured at a temperature where thermal quenching is most effective, then by definition, the corresponding intensity $\Phi_q$ will be related to values $\Phi_u$ obtained at temperatures where this is less of an effect as

$$\Phi_q = \Phi_u \eta(T), \tag{49}$$

where $T$ is the measurement temperature and $\eta(T)$ is the luminescence efficiency given by $1/(1+Cexp(-\Delta E/kT))$. Experimentally, $\Phi_q$ is chosen as the intensity corresponding to the highest measurement temperature $T'_q$ and $\Phi_u$ as intensities associated with all measurement temperatures $T'_u$ where $T'_u < T'_q$ and values of $\Phi_u$ are taken from the rising edge of the intensity-temperature graph. The intensities $\Phi_i (i = q, u)$ are the areas underneath the appropriate portion of a time-resolved spectrum. Although thermal quenching can be neglected at low temperatures; by definition, thermal assistance applies at all measurement temperatures. Therefore, one can write

$$\Phi_q = \frac{\Phi_u exp\left(-\frac{E_{ai}}{kT'}\right)}{1 + C\exp\left(-\frac{\Delta E}{kT'}\right)}, \tag{50}$$

where all parameters are as previously defined. After simplifying approximations, Eq. (50) can be written as

$$\frac{\Phi_q}{\Phi_u} \sim \frac{1}{C}\exp\left(\frac{\Delta E - E_a}{kT'}\right), \tag{51}$$

from which

$$\ln\left(\frac{\Phi_q}{\Phi_u}\right) = \frac{(\Delta E - E_a)}{kT'} + \gamma, \tag{52}$$

where $\gamma$ is a constant. Therefore, from a semi-logarithmic plot of $(\Phi_q/\Phi_u)$ against $1/kT'$, the activation energy for thermal quenching $\Delta E$ can be retrieved from the slope $(\Delta E - E_a)$ if $E_a$ is known. Figure 18 shows a plot of ln $(\Phi_q/\Phi_u)$ against $1/kT'$ for $\alpha$-$Al_2O_3$:C from which $\Delta E = 1.00 \pm 0.07$ eV. The value of $E_a$ used in the calculation of $(\Delta E - E_a)$ corresponds to the main trap (i.e $0.53 \pm 0.03$ eV, see section 7.8.2.1) because this is the one affected by thermal quenching at the temperatures used. The value of $\Delta E$ found compares favorably with $1.09 \pm 0.01$ eV and $1.12 \pm 0.01$ eV determined from Fig. 14 in the analysis of the dynamic throughput. The value is also consistent with others in the literature e.g. see refs. [28, 30, 44].

Another example using ratio of intensities was described for quartz exploiting the fact that thermal quenching becomes dominant

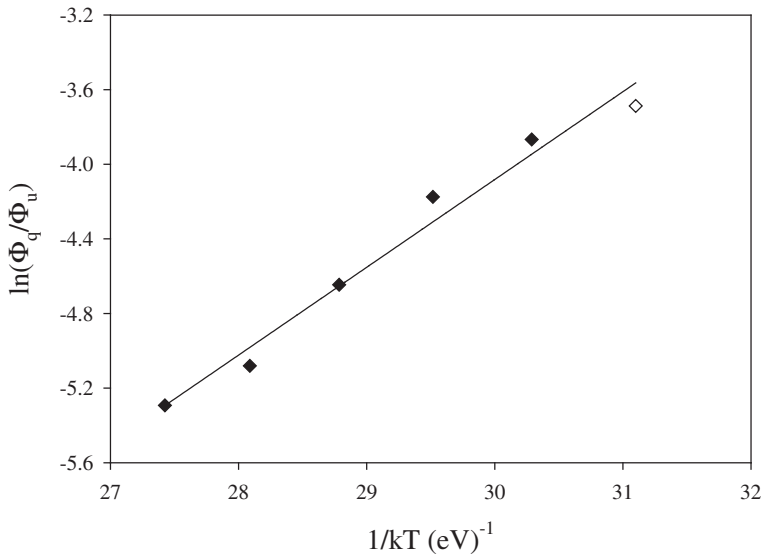


Fig. 18. A plot of ln $(\Phi_q/\Phi_u)$ as a function of $1/kT$ used to study thermal quenching in $\alpha$-$Al_2O_3$:C [41].

only at certain temperatures [3]. If an irradiated sample is exposed to light, the OSL intensity will decrease despite the measurement temperature. However, the decrease becomes pronounced in the presence of thermal quenching. Therefore the change of luminescence intensity with temperature can be described by using the ratio of intensities of luminescence stimulated from a sample under simultaneous optical stimulation and heating $(I_h)$ to that under optical stimulation only $(I_{uh})$. Figure 19(a) shows a plot of $I_h/I_{uh}$ against temperature of the heated sample. The data is shown fitted by the expression $I(T) = I_o/(1 + Cexp(-\Delta E/kT))$ giving $\Delta E = 0.63 \pm 0.07\,\text{eV}$ [3], a typical value for quartz e.g. ref. [31].

### 7.9.2. *Analysis based on temperature-dependence of TR-OSL intensity*

For a particular electron trap, it follows from Eq. (46) that

$$\tau = \frac{\tau_{rad} \exp\left(E_a/kT\right)}{1 + Cexp(-\Delta E/kT)}, \tag{53}$$

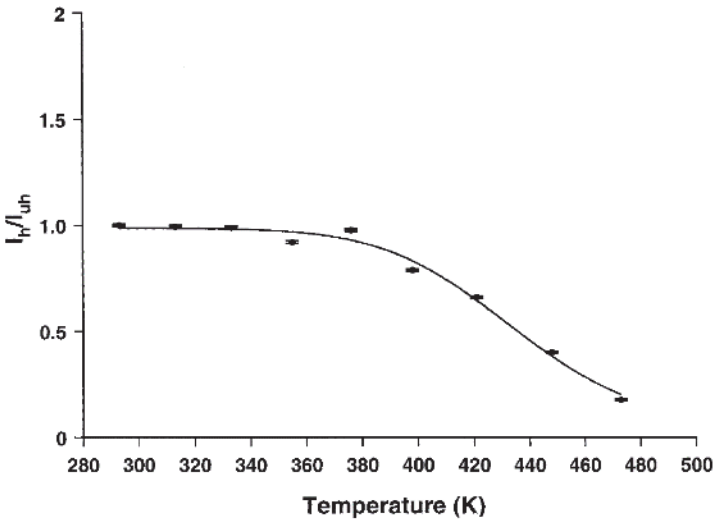


(a)

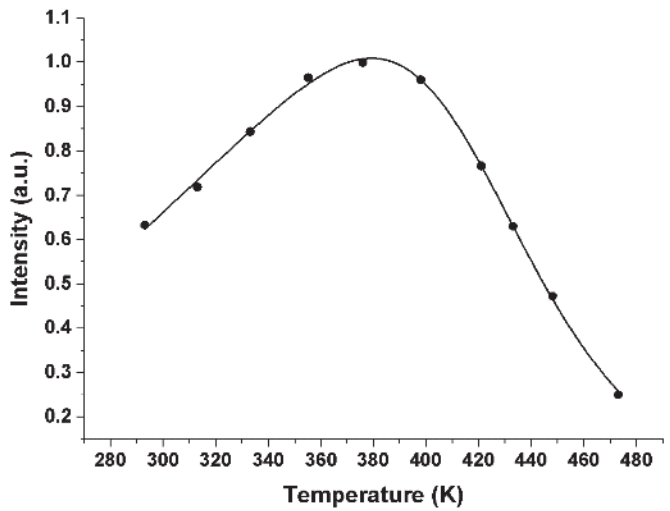


(b)

Fig. 19. A graph of $I_h/I_{uh}$ against temperature of the heated sample where $I_u$ is the intensity of the unheated sample and $I_h$ is the intensity of the sample measured at various temperatures (a) The temperature dependence of the intensity as a function of sample temperature in quartz (b). Figures 19(a) and (b) are reprinted from refs. [3] and [19] respectively.

which leads to

$$I(T) = \frac{I_o \exp\left(\frac{-E_a}{kT}\right)}{1 + Cexp(-\Delta E/kT)}. \tag{54}$$

Equation (54) can also be deduced directly from Eq. (47). For quartz, Eq. (54) has been useful where the intensity goes through a peak as a function of temperature as exemplified in Fig. 19(b). The increase in data is caused by thermal assistance to optical stimulation, and the subsequent decrease reflects the effect of thermal quenching. The parameters found from this fit are $\Delta E = 0.64 \pm 0.01\,\text{eV}$ and $E_a = 0.07 \pm 0.01\,\text{eV}$. Results from Eq. (54) can be used to corroborate calculations of the same parameters when determined using the temperature-dependence of lifetimes found from the same time-resolved spectra. By examining values of these activation energies in the literature, Chithambo [19] concluded that the values of $\Delta E$ depend on the emission wavelength, whereas those of $E_a$ are influenced by the stimulation wavelength.

## 7.10. Conclusion

This chapter has reviewed advances in the theory and analytical methods of time-resolved optical stimulation of luminescence. We have described three models for time-resolved optically stimulated luminescence. Two of the models seek to explain experimental results from a phenomenological view point, whereas the third approach relies on computational simulation of experimental results. A major use of time-resolved luminescence is study of dynamics of luminescence. Using examples drawn from quartz and $\alpha$-$Al_2O_3$:C, we have shown how kinetic analysis for various thermal effects such as thermal quenching and thermal assistance can be investigated from time-resolved spectra. The versatility of using the ratio of intensities, the intensity integrated from spectra as well as lifetimes, demonstrate some key advances in analytical methods for time-resolved spectra. Hopefully, this chapter will provide a motivation to interested readers to contribute in addressing some of the outstanding issues identified in the theories and limitations of analytical methods cited.

## References

[1] M.L. Chithambo and R.B. Galloway, "A pulsed light emitting diode system for stimulation of luminescence," *Meas. Sci. Technol.*, vol. 11, pp. 418–424, 2000.

[2] B.G. Markey, L.E. Colyott and S.W.S. McKeever, "Time-resolved optically stimulated luminescence from $\alpha$-$Al_2O_3$:C," *Radiat. Meas.*, vol. 24, pp. 457–463, 1995.

[3] M.L. Chithambo and R.B. Galloway, "On the slow component of luminescence stimulated from quartz by pulsed blue light emitting diodes," *Nucl. Instrum. Meth. B.*, vol. 183, pp. 358–368, 2001.

[4] R.B. Galloway, "Luminescence lifetimes in quartz: dependence on annealing temperature prior to beta irradiation," *Radiat. Meas.*, vol. 35, pp. 67–77, 2002.

[5] D.C.W. Sanderson and R.J. Clark, "Pulsed photostimulated luminescence of alkali feldspars," *Radiat. Meas.*, vol. 23, pp. 633–639, 1994.

[6] S.W.S. McKeever, M.S. Akselrod and B.G. Markey, "Pulsed optically stimulated luminescence dosimetry using $\alpha$-$Al_2O_3$:C," *Radiat. Prot. Dosim*, vol. 65, pp. 267–272, 1996.

[7] E. Bulur and H.Y. Göksu, "Pulsed optically stimulated luminescence from $\alpha$-$Al_2O_3$:C using green light emitting diodes," *Radiat. Meas.*, vol. 27, pp. 479–488, 1997.

[8] E. Bulur, H.Y. Göksu and W. Wahl, "Infrared (IR) stimulated luminescence from $\alpha$-$Al_2O_3$:C," *Radiat. Meas.*, vol. 29, pp. 625–638, 1998.

[9] R.J. Clark, I.K. Bailiff and M.J. Tooley, "A preliminary study of time-resolved luminescence in some feldspars," *Radiat. Meas.*, vol. 27, pp. 211–210, 1997.

[10] R.J. Clark and I.K. Bailiff, "Fast time-resolved luminescence emission spectroscopy in feldspars," *Radiat. Meas.*, vol. 29, pp. 553–560, 1998.

[11] I.K. Bailiff, "Characteristics of time-resolved luminescence in quartz," *Radiat. Meas.*, vol. 32, pp. 401–405, 2000.

[12] E. Bulur and B.E. Saraç, "Time-resolved OSL studies on BeO ceramics," *Radiat. Meas.*, vol. 59, pp. 129–138, 2013.

[13] Ya. Zhydachevskii, A. Luchechko, D. Maraba, N. Martynyuk, M. Glowacki, E. Bulur, S. Ubizskii, M. Berkowski and A. Suchocki, "Time-resolved OSL studies of $YAlO_3$:$Mn^{2+}$ crystals," *Radiat. Meas.*, vol. 94, pp. 18–22, 2016.

[14] E. Bulur, E. Kartal and B.E. Saraç, "Time-resolved OSL of natural zircon: A preliminary study," *Radiat. Meas.*, vol. 60, pp. 46–52, 2014.

[15] W. Becker, Advanced Time-Correlated Single Photon Counting Techniques, Berlin: Springer-Verlag, 2005.

[16] M.L. Chithambo, "A time-correlated photon counting system for measurement of pulsed optically stimulated luminescence," *J. Lumin.*, vol. 131, pp. 92–98, 2011.

[17] T. Lapp, M. Jain, C. Ankjærgaard and L. Pirtzel, "Development of pulsed stimulation and photon timer attachments to the RISØ TL/OSL reader," *Radiat. Meas.*, vol. 44, pp. 571–575, 2009.

[18] M.L. Chithambo, "The analysis of time-resolved optically stimulated luminescence. I: Theoretical considerations," *J. Phys. D.: Appl. Phys.*, vol. 40, pp. 1874–1879, 2007.

[19] M.L. Chithambo, "The analysis of time-resolved optically stimulated luminescence. II: Computer Simulations and Experimental Results," *J. Phys. D.: Appl. Phys.*, vol. 40, pp. 1880–1889, 2007.

[20] E.G. Yukihara and S.W.S. McKeever, Optically stimulated luminescence: Fundamentals and Applications, Chichester: Wiley, 2011.

[21] V. Pagonis, S.M. Mian, M.L. Chithambo, E. Christensen and C. Barnold, "Experimental and modelling study of pulsed optically stimulated luminescence in quartz, marble and beta irradiated salt," *J. Phys. D.: Appl. Phys.*, vol. 42, p. 055407, 2009.

[22] V. Pagonis, M.L. Chithambo, R. Chen, A. Chruścińska, M. Fasoli, S.H. Li, M. Martini and K. Ramseyer, "Thermal dependence of luminescence lifetimes and radioluminescence in quartz," *J. Lumin.*, vol. 145, pp. 38–48, 2014.

[23] M.L. Chithambo, "Dependence of the thermal influence on luminescence lifetimes from quartz on the duration of optical stimulation," *Radiat. Meas.*, vol. 37, pp. 167–175, 2003.

[24] V. Pagonis, C. Ankjærgaard, M. Jain and R. Chen, "Thermal dependence of time-resolved blue light stimulated luminescence in $\alpha$-$Al_2O_3$:C," *J. Lumin.*, vol. 136, pp. 270–277, 2013.

[25] M.S. Akselrod and S.W.S. McKeever, "A radiation dosimetry method using pulsed optically stimulated luminescence," *Radiat. Prot. Dosim.*, vol. 81, pp. 167–176, 1999.

[26] B. Di Bartolo, Optical Interactions in Solids, New York: Wiley, 1968.

[27] F. Agullo-Lopez, C.R.A. Catlow and P.D. Townsend, Point Defects in Materials, London: Academic Press, 1988.

[28] M.S. Akselrod, N. Agersnap Larsen, V. Whitley and S.W.S. McKeever, "Thermal quenching of F-center luminescence in $\alpha$-$Al_2O_3$:C," *J. Appl. Phys.*, vol. 84, pp. 3364–3373, 1998.

[29] M.L. Chithambo, "Luminescence lifetimes in natural quartz annealed beyond its second phase inversion temperature," *Radiat. Meas.*, vol. 81, pp. 198–204, 2015.

[30] M.L. Chithambo, A.N. Nyirenda, A.A. Finch and N.S. Rawat, "Time-resolved luminescence and spectral emission features of $\alpha$-$Al_2O_3$:C," *Physica. B: Condens. Matter.*, vol. 473, pp. 62–71, 2015.

[31] L. Bøtter-Jensen, S.W.S. McKeever and A.G. Wintle, Optically Stimulated Luminescence Dosimetry, Amsterdam: Elsevier, 2003.

[32] L. Bøtter-Jensen, N. Agersnap Larsen, V. Mejdahl, N.R.J. Poolton, M.F. Morris and S.W.S. McKeever, "Luminescence sensitivity changes in quartz as a result of annealing," *Radiat. Meas.*, vol. 24, pp. 535–541, 1995.

[33] S.W.S. McKeever, Thermoluminescence of Solids, Cambridge: Cambridge University Press, 1985.

[34] M.L. Chithambo, F.O. Ogundare and J. Feathers, "Principal and secondary luminescence lifetime components in annealed natural quartz," *Radiat. Meas.*, vol. 43, pp. 1–4, 2008.
[35] S. Fleming, Thermoluminescence Techniques in Archaeology, UK: Oxford University Press, 1979.
[36] M.L. Chithambo, C. Ankjærgaard and V. Pagonis, "Time-resolved luminescence from quartz: An overview of contemporary developments and applications," *Physica. B: Condens. Matter.*, vol. 481, pp. 8–18, 2016.
[37] V. Pagonis, J. Lawless, R. Chen and M.L. Chithambo, "Analytical expressions for time-resolved optically stimulated luminescence experiments in quartz," *J. Lumin.*, vol. 131, pp. 1827–1835, 2011.
[38] M.L. Chithambo and F.O. Ogundare, "Luminescence lifetime components in quartz: influence of irradiation and annealing," *Radiat. Meas.*, vol. 44, pp. 453–457, 2009.
[39] M.L. Chithambo, F. Preusser, K. Ramseyer and F.O. Ogundare, "Time-resolved luminescence of low sensitivity quartz from crystalline rocks," *Radiat. Meas.*, vol. 42, pp. 205–212, 2007.
[40] S.W.S. McKeever, M.S. Akselrod and B.G. Markey, "Pulsed optically stimulated luminescence dosimetry using $\alpha$-$Al_2O_3$:C," *Radiat. Prot. Dosim.*, vol. 65, pp. 267–272, 1996.
[41] M.L. Chithambo and G. Costin, "Temperature-dependence of time-resolved optically stimulated luminescence and composition heterogeneity of synthetic $\alpha$-$Al_2O_3$:C," *J. Lumin.*, vol. 182, pp. 252–262, 2017.
[42] M.L. Chithambo, C. Seneza and J.M. Kalita, "Phototransferred thermoluminescence of $\alpha$-$Al_2O_3$:C: Experimental results and empirical models," *Radiat. Meas.*, vol. 105, pp. 7–16, 2017.
[43] M.L. Chithambo, "A method for kinetic analysis and study of thermal quenching in thermoluminescence based on use of the area under an isothermal decay curve," *J. Lumin.*, vol. 151, pp. 235–243, 2014.
[44] A.N. Nyirenda, M.L. Chithambo and G.S. Polymeris, "On luminescence stimulated from deep traps using thermally-assisted time-resolved optical stimulation in $\alpha$-$Al_2O_3$:C," *Radiat. Meas.*, vol. 90, pp. 109–112, 2016.

# Chapter 8

# Thermoluminescent Dosimetry of Cosmic Radiation in Space

Paweł Bilski

*Institute of Nuclear Physics Polish Academy of Sciences*
*Radzikowskiego 152, 31-342 Kraków, Poland*
*pawel.bilski@ifj.edu.pl*

Thermoluminescent detectors (TLD) have been used in dosimetric measurements in space for over 50 years. They were — and still are, applied in all fields of operational dosimetry, as well as for various experimental works in orbit, being the detector of choice among passive systems. In the present chapter the problems related to the efficiency of TLDs to the complex radiation spectrum encountered in space and to its components (high energy ions) are discussed. The dependence of the relative efficiency on the linear energy transfer for the TL materials most frequently used in space is presented. Furthermore, various experiments and measurements carried out with TLDs in space over the last decades are reviewed.

## 8.1. Introduction

Thermoluminescent detectors (TLD) have been applied for the dosimetry of cosmic radiation nearly since the beginning of the space age. The first reported application of TLDs in measurements on Earth's orbit is the Mercury-8 mission in 1962, which was the third US manned orbital spaceflight [1]. In this flight an astronaut wore five polyethylene tubes containing LiF powder inside his spacesuit [2]. In fact it turned out that the dose accumulated in this short mission was too low to be registered by the not-very-sensitive TL measuring systems of those times. Nevertheless, TLDs were then included within

the personal dosimeters used in the next space program, Gemini, this time successfully providing astronauts' doses ranging from 10 to 80 millirads [2], as well as later in the Apollo program [3]. Similarly, TLDs were also used in early Russian space measurements [4], however little details are available about that. Since that time, TLDs (mostly LiF-based) were used probably in almost all human space missions, as well as in numerous unmanned experiments. Nowadays they are still widely applied in space measurements, being undoubtedly the detectors of choice among passive systems (together with track detectors). Their applications cover not only personal dosimetry of astronauts, but also dose mapping inside spacecrafts, phantom experiments and dosimetry for astrobiological experiments.

In this chapter we will review the most important recent experiments and measurements performed with TLDs in Earth orbit. Before that some issues related to the problem of the relative TL efficiency to the cosmic radiation spectrum will be discussed.

## 8.2. Influence of cosmic radiation spectrum on the response of TLDs

The cosmic radiation field is extremely complex and consists of a variety of particles with very broad energy and linear energy transfer (LET) range. Moreover, the spectrum varies with the solar cycle, altitude, latitude, as well as with the shielding thickness of a spacecraft. On the other hand, it is well known that TL efficiency is not constant, but depends on the radiation type and LET. In this situation an obvious question arises about the effective efficiency of TL detectors to this complex cosmic radiation spectrum. Until recent times, the exact answer to this question was not known, which may be somewhat surprising. It was generally accepted that TL detectors measure cosmic radiation doses "more or less" correctly and such vague knowledge had to suffice, mostly due to the lack of reliable experimental data. The situation began to change in the last decade, thanks to the better availability of high-energy ion beams for such investigations.

### 8.2.1. *Cosmic radiation field at low-earth orbit*

The main components of the cosmic radiation at the Earth's orbit are Galactic Cosmic Rays (GCR) and trapped protons in the Earth's radiation belts. GCR consist mainly of ionized nuclei, ranging from hydrogen to the heaviest elements. Figure 1 presents contributions of different GCR nuclei to the fluence, dose and dose equivalent [5]. The importance of heavier ions for biological effects is apparent, e.g., Fe (Z=26) is only 0.2% abundant but contributes about 20% of the dose equivalent [6]. The specific feature of GCR is the very high energy of particles, ranging up to $10^{20}$ eV, with a peak around 1 GeV/n. Consequently it is very penetrating and it is not possible to shield effectively against GCR. Moreover, shielding may actually increase the dose rate due to GCR, as illustrated in Fig. 2 [7]. A different situation occurs in the case of the trapped protons, which mostly have energies below 100 MeV and may be attenuated quite easily. The shielding thickness has also a great influence on the composition of the radiation field caused by GCR behind shielding, as presented in Fig. 3 [7]. For the lowest shielding thickness, the radiation field is

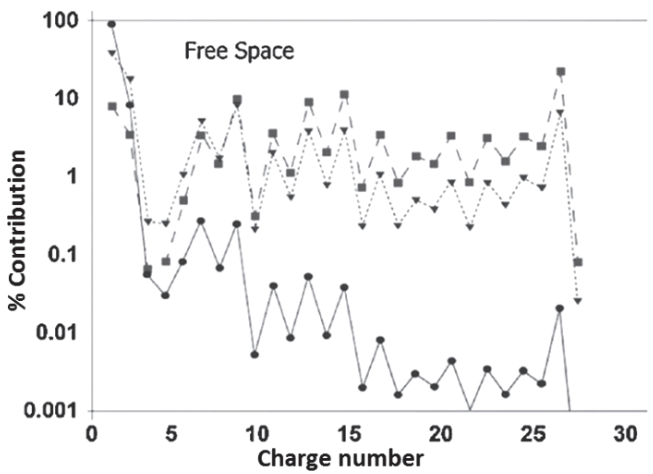


Fig. 1. Relative contributions from individual GCR elements for the particle flux (circles), dose (triangles) and dose equivalent (squares). Reprinted from Durante and Cucinotta [5].

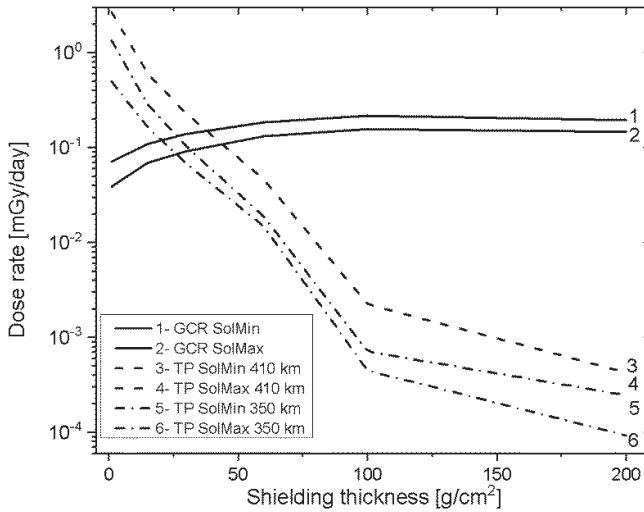


Fig. 2. Dose rates delivered by two components of the cosmic radiation spectrum: GCR and trapped protons (TP), vs. Al shielding thickness, calculated for two typical orbit altitudes and two solar cycle phases. Reprinted from Bilski *et al.* [7].

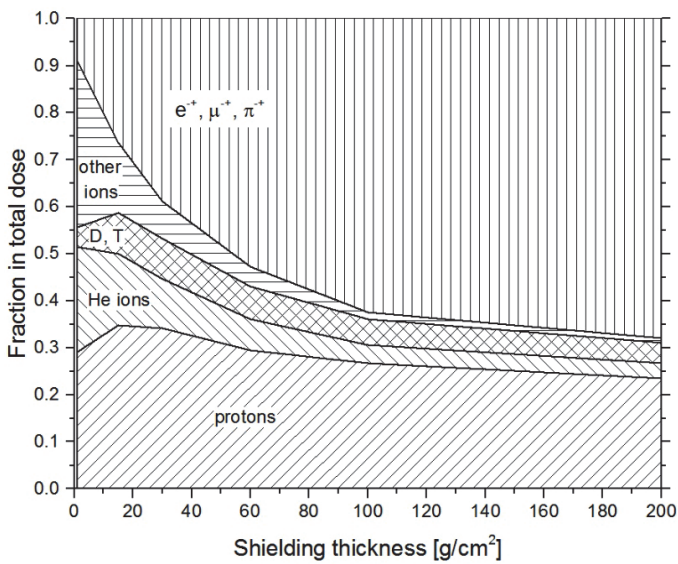


Fig. 3. Contribution of different particle types to the GCR dose vs. Al shielding thickness. Reprinted from Bilski *et al.* [7].

dominated by protons and other nuclei. With increasing thickness, the contribution of ions decreases and is replaced by lighter secondary particles: electrons, muons and pions of low LET. More details about the characteristics of the cosmic radiation field may be found e.g., in Refs. [4, 5, 8].

### 8.2.2. *TL efficiency to high-energy ions of TLD types used for space dosimetry*

The relative TL efficiency is usually defined as a TL signal per unit dose and unit mass for the given radiation type, divided by the same quantity for the reference gamma radiation (which is normally used for the calibration of TLDs):

$$\eta = \frac{(I/D)_k}{(I/D)_\gamma} \tag{1}$$

where: $\eta$ — the relative TL efficiency, $I$ — the intensity of the TL signal per unit mass, $D$ — the absorbed dose, $k$ — indicates the radiation under study. The relative efficiency not being equal to unity means, that the doses measured using the gamma calibration are underestimated (for $\eta < 1$) or overestimated (for $\eta > 1$).

The result of a TL measurement is a glow-curve, i.e. the TL signal plotted against temperature. Very often various peaks of a glow-curve show different relative TL efficiency, as illustrated in Fig. 4. Within this chapter, if not stated otherwise, we will discuss only the main TL peaks, i.e. those that are typically used for dosimetric measurements.

All thermoluminescent materials exhibit a dependence of the relative efficiency on the ionization density, which is a result of high local doses present in materials exposed to densely ionizing radiation (doses along heavy charged particles tracks), and non-linearity of TL characteristics at such high doses. More about the mechanism of this effect may be found e.g., in Refs. [9–11]. In the present chapter, we will review the experimental data on the dependence of $\eta$ on the radiation type and LET for TLD types used in space dosimetry.

The fact that TL efficiency for densely ionizing radiation is different from the TL efficiency for gamma-rays was known and studied already in 1960s [12]. Since then, knowledge on this subject

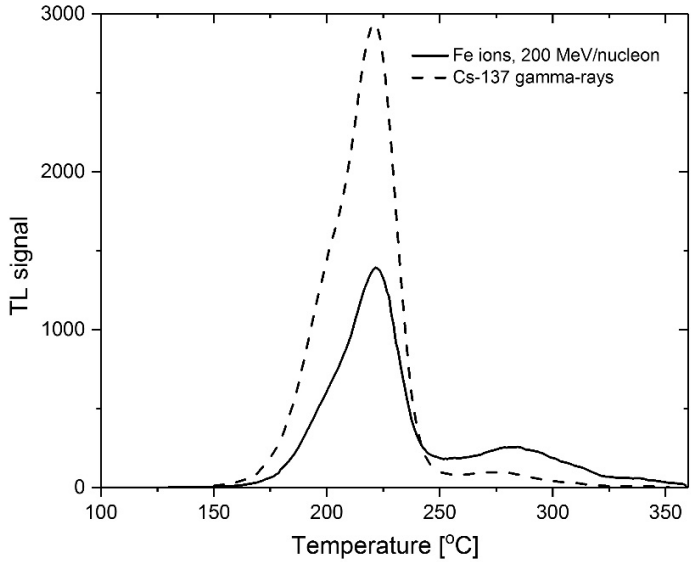


Fig. 4. Comparison of thermoluminescent glow-curves of LiF:Mg,Ti detectors irradiated with equal doses (50 mGy) of Cs-137 gamma-rays and iron ions. The main peak at 220°C exhibits the relative efficiency for iron ions lower than unity, while the high-temperature peaks, which extend above 250°C, higher than the unity.

has been gradually growing, but the number of investigations performed with high-energy ions, which are most relevant for cosmic radiation studies, was still limited. In the mid-1990s, a heavy ion accelerator (HIMAC) at the National Institute of Radiological Sciences in Chiba (Japan), capable of accelerating ions up to xenon and to energies up to 800 MeV/nucleon, was put into operation and shortly after applied to the TL efficiency studies [13]. In 2002, the project ICCHIBAN (Intercomparison of Cosmic rays with heavy ion Beams at NIRS) was initiated [14]. During the next years, the several subsequent ICCHIBAN sessions gathered practically all research teams involved in the space dosimetric measurements [15–17], producing a vast amount of data. After the completion of ICCHIBAN, research on radiation detectors at HIMAC was, and still is, continued within the numerous smaller projects. Another heavy-ion facility used for similar research was NASA Space Radiation Laboratory

at Brookhaven National Laboratory [18]. At the same time experimental capabilities were also increased by a rapid rise of proton (and carbon ion in much smaller number) radiotherapy facilities all over the world. All this has enabled a collection of a huge amount of good quality experimental data on TL efficiency to high-energy ions in the last 15 years, which greatly increased the status of current knowledge.

There are several types of TLDs that were applied for the dosimetry of cosmic radiation. Among them, undoubtedly the most widely used is LiF:Mg,Ti (similar to other areas of radiation dosimetry). At the beginning TLDs based on natural lithium were exploited, but since the Apollo program, isotopically enriched detectors have been often applied ($^{6}$LiF and $^{7}$LiF) in order to distinguish the signal from thermal neutrons [19]. LiF:Mg,Ti is also a TL material which attracted the most attention, with respect to investigations of the relative efficiency to heavy charged particles. The early results of these studies were reviewed by Horowitz [20, 21], while the more recent by Berger and Hajek [22]. Large collections of data can also be found in Refs. [23–29].

Figure 5a presents one of the most recent and most consistent sets of LiF:Mg,Ti efficiency data [7]. The most apparent observation is an overall trend of decreasing efficiency for the highest LET values, i.e., for the heavier ions. This trend, which is common among TLD types, is obviously of importance, as such ions deliver significant part of cosmic radiation dose and dose equivalent. For example, for iron ions, which are so important in GCR spectrum (Fig. 1), the relative efficiency drops down to about 0.4. Another interesting observation is the presence of separate functional branches for low-energy protons and helium ions (similar branches certainly do exist also for other ions and they are missing in the plot, due to the lack of experimental data). This presence means that the relative efficiency is not a unique function of LET. However, this effect has in fact small influence on the TL response to cosmic radiation, as the contribution of low-energy particles to the spectrum is less significant.

The third remarkable observation is that the efficiency is exceeding unity (up to 1.15) for H and He ions with LET between

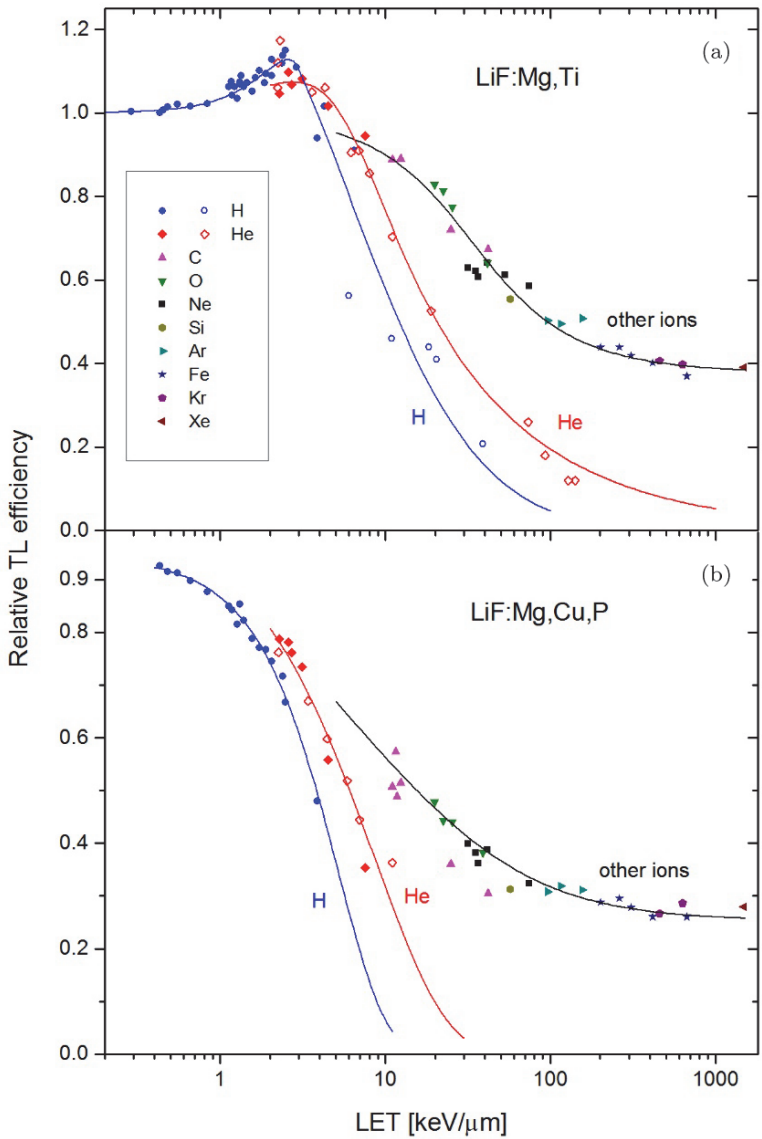


Fig. 5. Relative TL efficiency for the main peak area of (a) LiF:Mg,Ti and (b) LiF:Mg,Cu,P detectors to different ions. The lines represent fitted empirical functions *η(LET)* for protons, helium ions and the remaining ions. Reprinted from Bilski *et al.* [7].

approximately 1 keV/$\mu$m and 5 keV/$\mu$m. This effect is a result of supralinear dose-response of LiF:Mg,Ti and plays some role, as H and He in the mentioned LET range are quite abundant in the cosmic radiation field.

Figure 5b presents the efficiency data for LiF:Mg,Cu,P TL detectors. This type of TLDs is characterized by its high-sensitivity [30]. In space measurements LiF:Mg,Cu,P is often used together with LiF:Mg,Ti, because the usually observed difference of results between the two TLDs visualizes the presence of densely ionizing radiation. The reason of this difference lies in the relationship between $\eta$ and LET, as is illustrated in Fig. 5b. For LiF:Mg,Cu,P the relative efficiency is below unity even for protons of the highest energy. No increase of $\eta$ nor even a flat region is observed: $\eta$ decreases monotonically with increasing LET and this decrease is steeper than in the case of LiF:Mg,Ti.

Another type of TLD important for space dosimetry is $CaSO_4$:Dy. This material has been implemented in a TLD system (named *Pille*) developed especially for performing on board TL readouts [31]. Its main components are small vacuum bulbs made of glass containing a TL material attached to the surface of a resistive metal plate, which is heated electrically [32]. The special mechanical and electronic design of dosimeters and readers enable easy readout by astronauts themselves. The *Pille* system has proved to be very successful, thanks to its reliability and sensitivity. Since its development at the end of 1970, and after many upgrades, it is being used in numerous space missions. Besides *Pille* bulbs, $CaSO_4$:Dy is also used in a standard form [33].

Relative efficiency of $CaSO_4$:Dy to various ions is presented in Fig. 6. The number of available data points is much lower than in the case of LiF-based TLDs, therefore any conclusions on $\eta = \eta(LET)$ relationship are more uncertain. Nevertheless, the shape of this dependence seems to be similar to that of LiF:Mg,Ti, with one exception: $\eta$ for low-LET ions (H and He) is lower. Bearing in mind the importance of these particles in cosmic radiation spectrum, one may expect the value of $\eta$ of $CaSO_4$:Dy in space to be somewhat decreased compared to LiF:Mg,Ti.

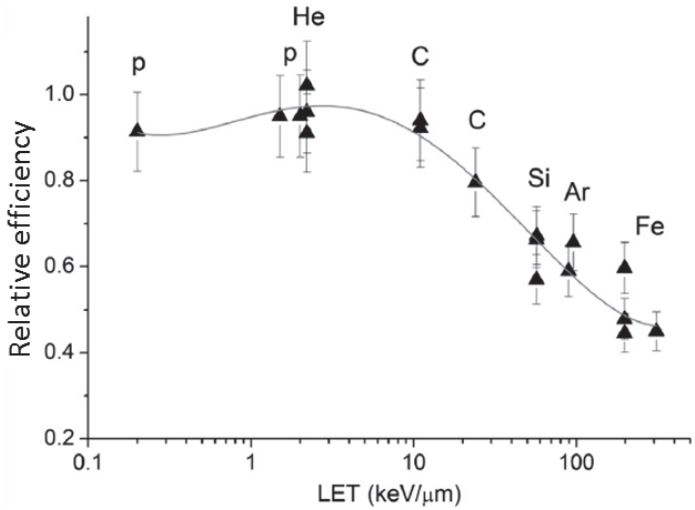


Fig. 6. Relative TL efficiency of $CaSO_4$:Dy to various high-energy ions. Reprinted from Ambrožová *et al.* [33].

Japanese scientists have developed a special dosimeter set dedicated to dose measurements in space called PADLES (PAssive Dosimeter for Life-science Experiments in Space) [34]. The thermoluminescent component of this set consists of $Mg_2SiO_4$:Tb detectors. Figure 7 presents the relative TL efficiency vs. LET for this material. In general $\eta = \eta(LET)$ relationship is again similar to that of LiF:Mg,Ti. The horizontal line drawn for LET up to 10 keV/$\mu$m indicates $\eta = 1$, but data points for helium ions suggest relative efficiency greater than unity in this LET range. More experimental data for helium ions and protons of intermediate energy would be needed to draw any firm conclusions.

Last among the TLDs frequently used for space dosimetry is $CaF_2$:Tm (TLD-300) [35–37]. The glow-curve of this material exhibits two distinct peaks (named usually peak 3 and peak 5), having different LET response. Relative efficiency of peak 3 decreases with increasing LET, while the efficiency of peak 5 first increases, reaching a maximum at ~30 keV/$\mu$m, and then decreases with LET (Fig. 8) [38]. For space dosimetry, only peak 5 is exploited, as peak 3 shows too much fading.

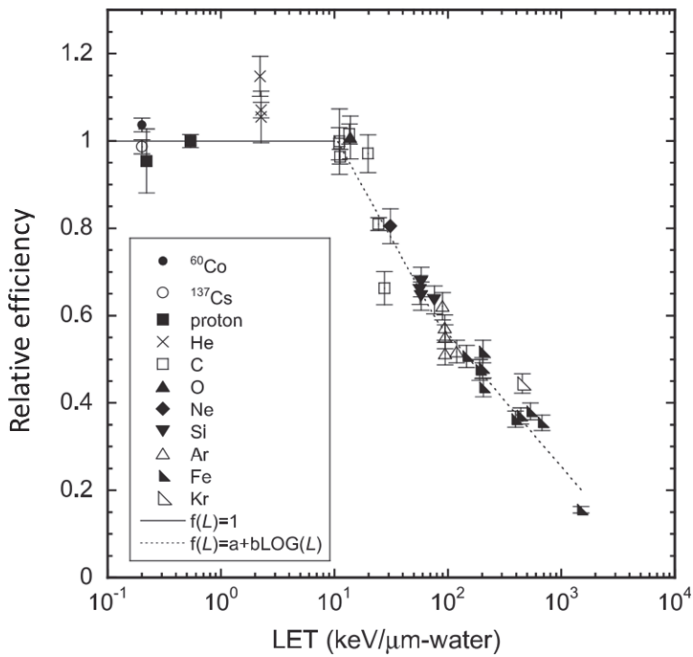


Fig. 7. Relative TL efficiency of $Mg_2SiO_4$:Tb to various high-energy ions. Reprinted from Tawara *et al.* [34].

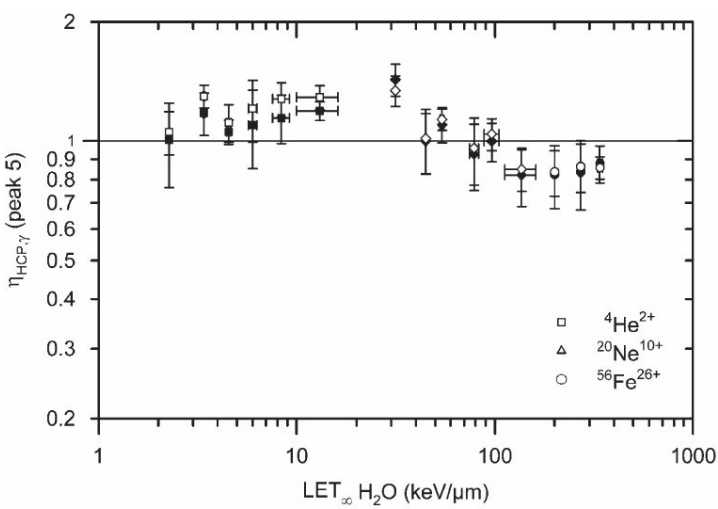


Fig. 8. Relative TL efficiency of $CaF_2$:Tm (peak 5) to various high-energy ions. Reprinted from Hajek *et al.* [38].

### 8.2.3. *TL efficiency to cosmic radiation spectrum*

In the previous section 8.2.2, we reviewed the experimental data on the relative TL efficiency to energetic ions, which are the most important components of the cosmic radiation. On the other hand, the radiation spectrum encountered in space is relatively well known and may be described, e.g. by means of computer simulations (see section 8.2.1). Folding these two characteristics — relative TL efficiency and cosmic radiation spectrum — one can arrive at a kind of *effective* TL efficiency, which will provide a description of TL response to this complex radiation field.

So far such analysis was attempted only for LiF-based TLDs [7, 39]. Figure 9 presents the results of the effective efficiency calculations, based on the experimental data from Fig. 5. The data are plotted against the shielding thickness, as this factor was found to have the strongest influence on TL efficiency, much stronger than the solar activity or the orbit altitude. The relative TL efficiency in

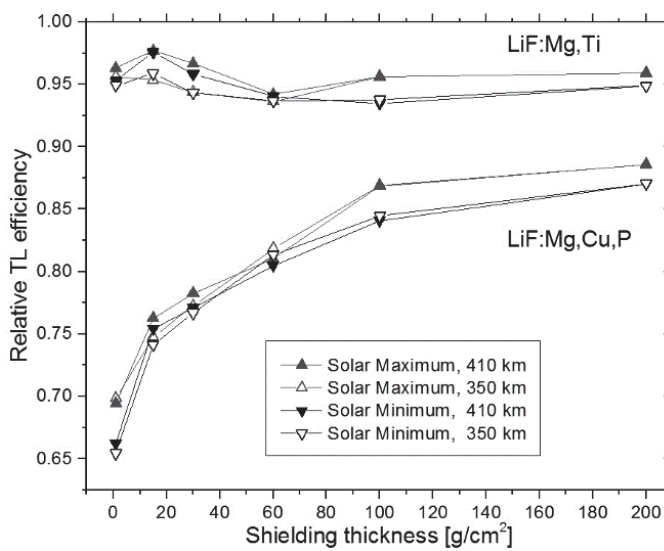


Fig. 9. Relative TL efficiency for cosmic radiation of LiF:Mg,Ti and LiF:Mg,Cu,P detectors vs. aluminum shielding thickness, calculated for various spaceflight conditions. Reprinted from Bilski *et al.* [7].

all studied cases was found to be lower than unity. For LiF:Mg,Ti detectors this under response is small, not exceeding about 5%. In the case of LiF:Mg,Cu,P the efficiency is much lower, ranging from about 0.65 to 0.88. Shielding thickness has particularly strong influence on LiF:Mg,Cu,P, whose efficiency increases monotonically with the increasing shielding. For LiF:Mg,Ti a weak maximum is observed for thickness of $15\,g/cm^2$, followed by a small decrease and then again an increase for the highest shielding thickness. This behavior may be explained by analyzing the TL efficiency separately for the two components of the spectrum: trapped protons and galactic cosmic radiation (Fig. 10). The TL efficiency for trapped protons at first increases with the shielding thickness. This is a result of the degradation of proton energy, which produces more protons with LET in the range 1–3 keV/$\mu$m, corresponding with the maximum of TL efficiency. For still greater thickness the efficiency declines, mostly

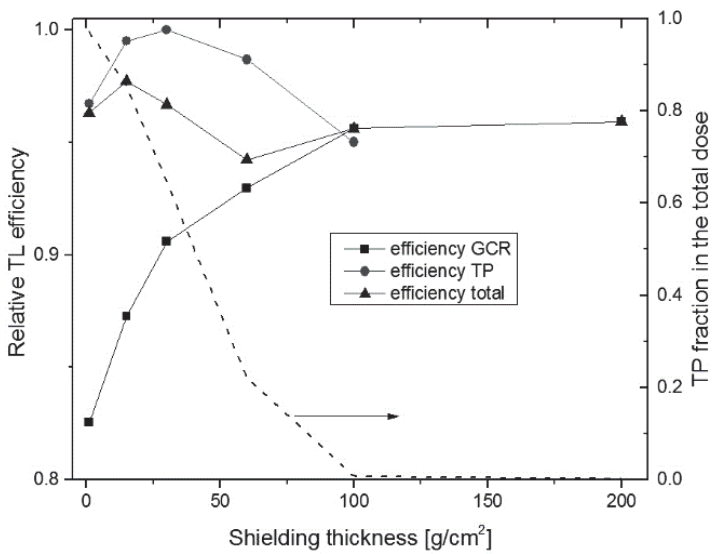


Fig. 10. The relative TL efficiency of LiF:Mg,Ti for galactic cosmic radiation (GCR) and trapped protons (TP) vs. aluminum shielding thickness (Solar maximum, altitude 410 km). The broken line illustrates dependence of trapped radiation contribution to the total dose on shielding thickness. Reprinted from Bilski *et al.* [7].

due to the reduction of protons in this LET range. For the highest shielding, the overall efficiency is dominated by the GCR efficiency, which is increasing monotonically with the shielding thickness. In the case of LiF:Mg,Cu,P the efficiency vs. LET relationship does not show any maximum for protons (Fig. 5b), therefore the efficiency for cosmic radiation increases monotonically with the shielding thickness.

The calculated under-response for LiF:Mg,Ti is practically negligible, therefore one can assume cosmic radiation doses measured on orbit with LiF:Mg,Ti detectors to be correct within a few percent of uncertainty. This good performance of LiF:Mg,Ti is obviously the result of $\eta > 1$ for intermediate energy protons, which are abundant within trapped radiation. However, one should keep in mind, that in the case of flights beyond the low-Earth orbit, almost the entire dose would be due to galactic radiation. In that case a significant under response may be expected at low shielding conditions.

As was mentioned, there were no analogous calculations for other TL materials so far. It may be expected that TLDs with $\eta = \eta(\mathrm{LET})$ characteristic similar to that of LiF, in general will also show similar effective efficiency to cosmic spectrum. However more quantitative evaluation requires detailed calculations and probably also more experimental data.

### 8.2.4. *Convolution of TLD and track etch detector results*

There is no passive detector capable of measuring over the whole cosmic radiation spectrum with constant efficiency; therefore, very often sets of different detectors are used in space measurements. In 1995 Doke [40] proposed a method of combining the results of TLDs and nuclear track detectors (NTD) for the determination of total absorbed dose and dose equivalent in space. The method was further developed and applied in numerous space missions and until now remains a standard for space dosimetry [4, 41–45]. It was also recommended by the US National Council on Radiation Protection and Measurements (NCRP) for operational dosimetry of astronauts [46].

TLDs and NTDs measure radiation almost in a complementary way. Nowadays almost entirely, polyallyl diglycol carbonate, known under the commercial name CR-39, is used as NTD. This material has a detection threshold of about 10 keV/$\mu$m (with some special techniques 5 keV/$\mu$m can be achieved), i.e., radiation of lower LET is not registered. Opposingly, TLDs exhibit efficiency close to unity of up to 10 keV/$\mu$m, whereas for higher LET the efficiency drops down as was discussed in section 8.2.2. However, TLD and NTD doses cannot be summed up directly. While the TL efficiency is decreased for LET $>$ 10 keV/$\mu$m, it is not equal to zero and therefore a part of the dose for this LET range would be counted twice. This may be corrected, providing that the approximate dependence of TL efficiency on LET is known. The mathematical procedure is as following:

$$D_{Lo} = D_{TLD} - \sum_i \eta(L_i) D_{NTD}(L_i) \Delta L_i \tag{2}$$

$D_{Lo}$ is the dose for LET $<$ 10 keV/$\mu$m, $D_{TLD}$ is the dose measured by a TL detector, $L_i$ is a discrete value of LET, $D_{NTD}$ is the dose measured by a track detector and $\eta$ is the relative TL efficiency for $L_i$. From NTD data one can obtain:

$$D_{Hi} = \sum_i D_{NTD}(L_i) \Delta L_i \tag{3}$$

$$H_{Hi} = \sum_i Q(L_i) D_{NTD}(L_i) \Delta L_i \tag{4}$$

$D_{Hi}$ is the dose for LET $\geq$ 10 keV/$\mu$m, $H_{Hi}$ is the dose equivalent for LET $\geq$ 10 keV/$\mu$m and $Q$ is the quality factor.

$$D_{total} = D_{Lo} + D_{Hi} \tag{5}$$

For LET $<$ 10 keV/$\mu$m $Q = 1$ is assumed, therefore one can write:

$$H_{total} = D_{Lo} + H_{Hi} \tag{6}$$

The average quality factor may be then calculated as:

$$\bar{Q} = \frac{H_{total}}{D_{total}} \tag{7}$$

It should be mentioned that besides the combination of TLDs and NTDs, which is a well-established method, some other techniques aimed at extracting information on LET and quality factor of cosmic radiation field have also been proposed. First among these methods is the high-temperature ratio (HTR) method, based on different LET responses of the main peak and high-temperature peaks of LiF:Mg,Ti TL glow-curve [47–49]. A similar approach was proposed also for the ratio of response of different detector types: e.g., LiF:Mg,Ti and LiF:Mg,Cu,P [50] or $Mg_2SiO_4$:Tb and RPL glass [51]. The HTR method was used for the analysis of results of several space experiments [49, 52, 53]. However, it was criticized as lacking a sound theoretical basis and as highly prone to error [54]. Later on it was demonstrated that in a general case of an unknown mixed radiation, like space radiation field, the HTR method produces erroneous values of an average LET [55]. However, HTR may be useful as a good qualitative indicator of the increased ionization density. It may also be quite successfully used for correcting a decreased TL efficiency for high LET radiation [56, 57]. Recently the LiF:Mg,Ti and LiF:Mg,Cu,P response ratio was proposed for the estimation of a local shielding thickness on board a spacecraft [7].

## 8.3. Review of TLD applications for cosmic radiation dosimetry

### 8.3.1. *Dose monitoring for the radiation protection of astronauts*

Measurements of doses for the purpose of radiation protection of astronauts is the main application of TLDs in space. TLDs are used both for personal dosimetry, when dosimeters are placed on astronauts' bodies, and for area monitoring, when dosimeters are distributed within a spacecraft. A broad review of dosimetric measurements in space including personal doses, since the earliest flights till the end of 1990s, was given by Benton and Benton [4]. Straube *et al.* [58] described the European crew personal dosimeter, which was relatively recently developed by the European Space Agency (ESA). It is based on a combination of TLDs (LiF:Mg,Ti) and track

detectors. Typically, three dosimeters per astronaut are in use: 1) for activities inside a spaceflight, 2) to be used during spacewalks (so-called Extra Vehicular Activity, EVA) — both worn at the torso — and 3) as reference in the sleeping quarters of astronauts. Similar passive systems (sometimes based only on TLDs) are used by US and Russian space agencies as well [59]. *Pille* dosimeters, described in section 8.2.2, are also applied for the measurements of personal doses of astronauts — including dosimetry during EVA, thanks to the possibility of an immediate readout in orbit [60].

Basically, identical or very similar detector configurations are used for area monitoring. These types of measurements, intended for dose mapping, are of importance, as the radiation field within a spacecraft may vary considerably due to differences in shielding. Dose mapping measurements with passive detector packages (always including TLDs) were performed during space shuttle flights and on the Mir orbital station [61–63]. They became of particular interest since the construction of the International Space Station (ISS), which is the largest space vehicle ever built. Many dosimetric projects were executed on board ISS, starting with DOSMAP in 2001 [64]. Nowadays area monitoring is performed continuously in various compartments of the ISS by different space authorities using the following passive, TLD based detector sets:

- USA (NASA): Radiation Area Monitor (RAM) [65]
- Russia (Institute of Biomedical Problems, IBMP): *Pille* [66]
- Japan (Japanese Space Agency, JAXA): PADLES [67]
- Europe (ESA): Passive Dosimeter Package (PDP) [37]

Area monitoring in the European ISS module Columbus is conducted within projects DOSIS (initially) and DOSIS-3D (presently), which were started in 2009 and are still continued. The results achieved so far were recently broadly reported by Berger *et al.* [37]. Within these projects PDP dosimeters are placed at 11 positions (always the same) inside Columbus for about 6-month exposure periods. Figure 11 presents the spatial and temporal variations of dose rates measured with $^{7}$LiF:Mg,Ti detectors. The reasons for temporal variations are changes in solar activity and orbit altitude, while for

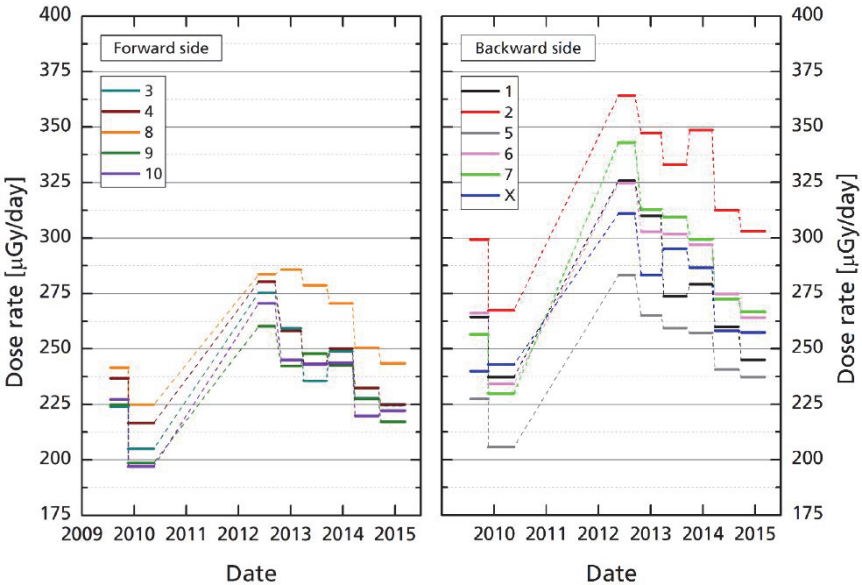


Fig. 11. Spatial and temporal variation of the dose rates measured with $^{7}$LiF:Mg,Ti TLDs at 11 different locations inside the Columbus module of the ISS during the DOSIS-3D experiment. Reprinted from Berger *et al.* [37].

spatial variations they are mainly due to different local shielding. DOSIS-3D project, being a large international collaboration, provides not only the data on dose distribution within the ISS, but also creates a unique opportunity for the comparison of various detector types in space radiation conditions. Table 1 presents a part of the results of this comparison: average response of different TLD types to cosmic radiation, with respect to that of $^{7}$LiF:Mg,Ti. These data clearly illustrate the influence of relative efficiency, as well as the presence of the neutron sensitive $^{6}$Li isotope.

### 8.3.2. *Phantom measurements in orbit*

Experimental approach to the estimation of radiation risk requires the determination of organ doses and of an effective dose. This can be achieved only by measurements within anthropomorphic phantoms, i.e., models of a human body. TLDs are the detectors of choice for this type of measurements, thanks to their small size.

Table 1. Response of various TLDs to cosmic radiation, normalized to $^{7}$LiF:Mg,Ti detector data, as measured during the DOSIS-3D experiment [37].

| Material | Ratio |
|---|---|
| $^{6}$LiF:Mg,Ti | 1.06 |
| $^{nat}$LiF:Mg,Ti | 1.06 |
| $^{6}$LiF:Mg,Cu,P | 0.90 |
| $^{7}$LiF:Mg,Cu,P | 0.87 |
| $CaF_2$:Tm | 1.01 |
| $CaSO_4$:Dy | 0.88 |
| $Al_2O_3$:C (TL) | 0.82 |

Phantom measurements in space are rare, because of limited possibilities of transporting large and heavy objects on orbit. The first phantom experiment in space was executed during 1989–1990: a head of Alderson Rando phantom was flown on three space shuttle flights (STS-28, STS-31, and STS-36) [68]. Exposure times were about 5 days. The head was equipped with a number of TLDs distributed in a 3 cm square grid. Unfortunately, the type of the TLDs used was not revealed in the publication. However, it seems likely that this could be LiF:Mg,Ti (TLD-100) with natural lithium isotopic composition, as most of the 'earlier' US TLD measurements used this type of phosphor.

During 1997–99 a spherical water-filled phantom with diameter 35 cm and special channels to accommodate TLDs, developed by the Institute of Biomedical Problems (IBMP) in Moscow, was flown on board Mir station [36]. The phantom was equipped with $^{7}$LiF:Mg,Ti and $^{6}$LiF:Mg,Ti detectors operated by the Technical University in Vienna. Three phases of the experiment were executed, with the exposure times ranging from 99 days to 271 days, which therefore is much longer than the previous phantom experiment. The TLDs were positioned at different depths in the phantom, allowing for the determination of depth–dose distributions.

In June 1998 NASA (in cooperation with the National Space Development Agency of Japan, NASDA), launched on the ninth

Shuttle-Mir mission the first phantom torso (named 'Fred') equipped with active and passive detectors (STS-91), with an aim of relating the skin dose to organ doses [69–71]. The exposure time was short, of about 10 days. The Alderson Rando phantom consisted of 34 equal slices from the head to the thigh. Each slice had a number of holes in a uniform grid pattern (total of 358) that were filled with four LiF:Mg,Ti chips. Additionally detector packages containing several TLD types ($Mg_2SiO_4$;Tb, BeO:Na, $Al_2O_3$, $^6$LiF:Mg,Ti, $^7$LiF:Mg,Ti, $CaF_2$:Mn) and track detectors, were located in positions of selected organs and on the phantom surface. The experiment allowed for the determination of organ doses and effective dose. The effective dose rate was found to be about 0.4 mSv/d, which was about 90% of the dose equivalent at the skin.

With the launching of the ISS (the first crew in year 2000) the opportunities of performing experiments in space were greatly enhanced. In January 2004, an unmanned spacecraft delivered a phantom equipped with a high number of TLDs to the ISS. This was the beginning of the project MATROSHKA (organized under auspices of ESA, led by German Aerospace Center, DLR and personally by Guenther Reitz), which turned out to be the biggest application of TLDs in space research ever carried out [72]. The phantom was again the Alderson Rando upper-torso with head, sliced into 33 sections, 2.54 cm thick. To enable a detailed dose mapping throughout the phantom torso, channels were drilled to accommodate a total number of about 5800 luminescence dosimeters located at equidistant points in 354 polyethylene tubes, which enabled the measurement of the depth distribution of absorbed dose to be determined in a 2.54 cm orthogonal grid (Fig. 12) [73]. Further TLDs and track detectors were placed in polyethylene boxes at positions of selected organs (eye, lung, stomach, kidney and intestines), as well as in the so-called 'poncho' covering the phantom. To evaluate skin doses, TLDs were distributed on the outer surface of the phantom. The experiment consisted of four phases (MTR-1, MTR-2A, MTR-2B, and MTR-Kibo), lasting about 1–1.5 year each, with the phantom located at various modules of the ISS. After each stage, the tubes with TLDs, as well as boxes with detectors,

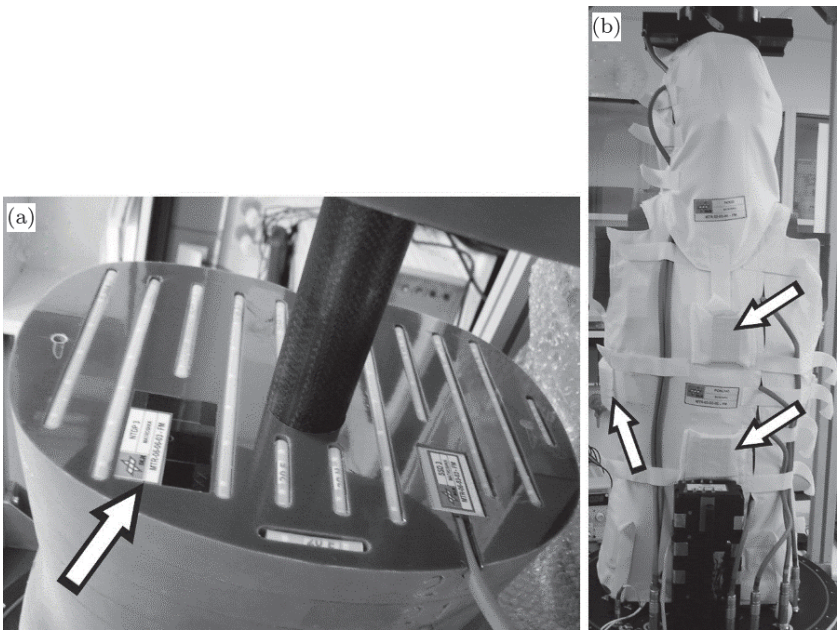


Fig. 12. MATROSHKA phantom: a) polyethylene tubes containing TLDs accommodated in a regular grid, b) whole phantom dressed in a 'poncho'. The arrows show detector boxes: (a) in position of stomach and (b) in the 'poncho'. Reprinted from Bilski *et al.* [28]

were disassembled by astronauts and returned to Earth for analysis, while a new set of detectors was launched into the orbit. Probably the most interesting part was the first phase (MTR-1), during which the phantom was mounted outside of the Zvezda module for 1.5 years. This is the first and the only phantom measurement outside a spacecraft so far, which simulated an astronaut during a spacewalk (EVA). The main part of the measurements was carried out using $^{7}$LiF:Mg,Ti and $^{6}$LiF:Mg,Ti operated by three institutions: Institute of Nuclear Physics (Kraków, Poland), German Aerospace Center (Cologne, Germany) and Technical University (Vienna, Austria). Several other TLD types were used, and several other research groups took part in the experiment [44]. The results of the MATROSHKA were published in a series of scientific papers [44, 45, 73, 74] and their main part is also downloadable from an on-line database [75].

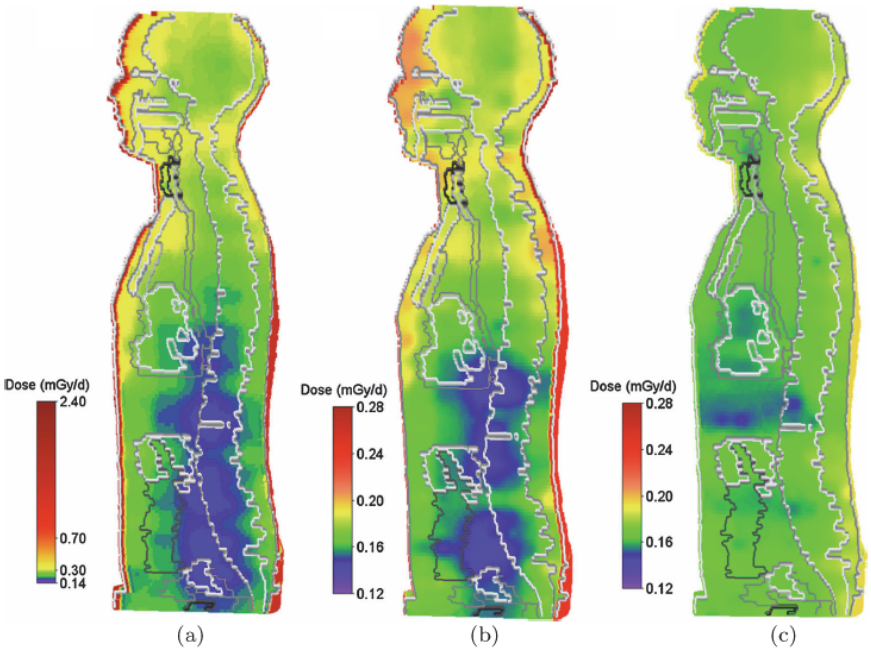


Fig. 13. Three-dimensional dose distribution calculated basing on the doses measured in a 2.5-cm orthogonal grid with $^{7}$LiF:Mg,Ti detectors during the MTR-1 (A), MTR-2A (B) and MTR-2B (C) missions (note different scales). Reprinted from Puchalska *et al.* [45].

Figure 13 presents dose distributions calculated based on the doses measured in a 2.5-cm orthogonal grid with TLDs, during three phases of the experiment. These results allowed for the determination of organ doses and effective doses. The interesting conclusion from these analyses was that, in case of an EVA, a personal dosimeter worn on an astronaut body overestimates the effective dose by more than a factor of 3 [45].

More or less simultaneously with the described MATROSHKA project, another phantom experiment (organized by IBMP in Russia), named MATROSHKA-R, was carried out [76]. The applied phantom was spherical, made of tissue equivalent plastic and was 35 cm in diameter. It was equipped with 20 rod-shaped containers for TLDs. They enabled the placement of TLDs at various depths

into the sphere, at the same time allowing easy retrieval of the detectors. Several measuring sessions were conducted, with the phantom located in different compartments of the ISS. LiF:Mg,Ti TLDs were mainly used, along with $CaSO_4$:Dy [77] and $Mg_2SiO_4$:Tb [78].

### 8.3.3. *Dosimetry for astrobiological experiments*

Since the beginning of the space age, biologists have been studying how living organisms respond to specific conditions of space, such as microgravity, cosmic radiation, vacuum, solar UV, etc. Biological experiments are often performed in open space in conditions of very low shielding. As the knowledge of the actual doses received by the studied samples is required, it is necessary to perform the dosimetric measurements at positions as close as possible to the biological specimens. TLDs are usually the best solution, thanks to their small size and low mass. Astrobiological investigations with application of TLDs, were conducted on board various spacecrafts: Apollo, Skylab, space shuttle, and unmanned satellites [79–81]. In most cases LiF:Mg,Ti detectors were utilized.

Among measurements carried out in recent times, one should mention the long-term experiments performed at the ISS: EXPOSE-E [82] and EXPOSE-R [83]. EXPOSE is an ESA research facility which can be attached to the external platforms of the ISS for long periods of time. The experiments performed with this facility lasted up to 2 years and housed a variety of organisms (from microorganisms to plant seeds) and organic chemical compounds (Fig. 14). Dosimetry was carried out with $^7$LiF:Mg,Ti and $^6$LiF:Mg,Ti detectors. Several experiments were also executed in the interior of the ISS, again with applications of various types of TLDs [84, 85]. Besides the utilization of the space station, other investigations are implemented using unmanned satellites [86, 87]. The design of some of them (e.g. BION and BIOPAN satellites) enables the opening of the experimental capsule on the orbit, in this way exposing samples to open space conditions [88, 89]. Due to the very low shielding (even 0.003 g/cm$^2$), the dose rate in such cases may reach several Gy per day. In addition to standard TLDs, special thin-layer LiF:Mg,Ti detectors were applied

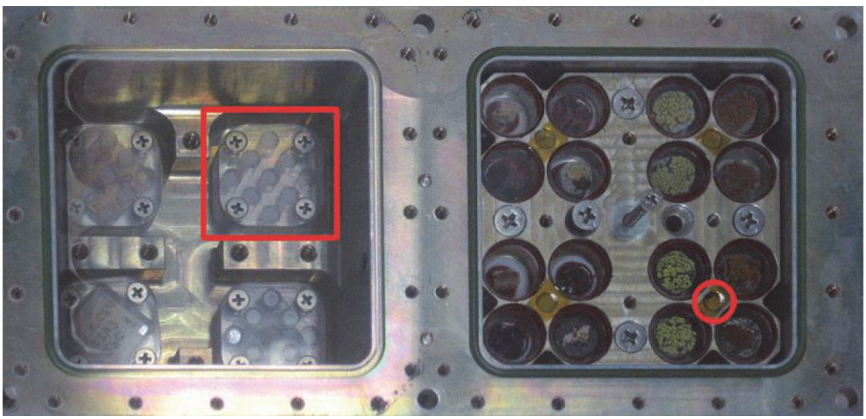

Fig. 14. Left: TLDs in acryl glass holders (red frame) installed beneath biological samples in a tray of the EXPOSE-E facility. Right: A red circle between biological samples indicates the position of one of several TLD stacks, which were used for measurements of the depth-dose distribution. Reprinted from Berger *et al.* [82].

in these measurements in order to account for the very steep dose gradient [88].

### 8.3.4. *Cosmic radiation in the atmosphere*

While the subject of this chapter concerns dosimetry in space, it may be worth mentioning briefly that TLDs were used for measurements of cosmic radiation not only in Earth orbit, but also in the atmosphere. Due to the shielding effects of the atmosphere and Earth magnetic field, cosmic radiation dose rates are much lower. Nevertheless, they are high enough to make it necessary to take into account the exposure of aircrew members due to cosmic radiation as part of the occupational exposure. While nowadays passive techniques are rarely used for aircrew dosimetry (which is now based mostly on the computational approach [90]), TLDs were applied for this purpose quite often in the past, when adequate measuring methods were only under development. Usually, LiF:Mg,Ti [91–94] detectors were the most commonly implemented ones. Among other types one can find LiF:Mg,Cu,P [95], $CaF_2$:Tm [96], $CaSO_4$:Dy, and $Li_2B_4O_7$ [97]. The highly sensitive $^7$LiF:Mg,Cu,P was successfully

used for measurements of doses even during single round-trip flights ($20-30\,\mu$Sv) [95]. $^{6}$LiF:Mg,Ti and $^{7}$LiF:Mg,Ti pairs were applied for the measurements of neutron doses, which provided quite reasonable results [93, 98], in spite of the very hard neutron energy spectrum. The same TLD types were employed in flight for passive neutron spectrometry with Bonner spheres [99] and for measurements inside an anthropomorphic phantom [100]. Finally, we may add that cosmic radiation was measured with TLDs not only at flight altitudes, but also on the ground level. This was achieved in locations where cosmic radiation dominates over the terrestrial radiation background: at high-mountains [101] and on the surface of a lake or sea [102, 103].

## 8.4. Concluding remarks

Thermoluminescent detectors have been used in dosimetric measurements in space for over fifty years. They were, and still are, applied in all fields of operational dosimetry, as well as for various experimental works in the orbit. Besides the small size that is always advantageous for space missions, the reason for such wide and successful applications may mostly be in their reliability, the feature that is of particular importance in the specific conditions of space applications. The long experience of their use in space resulted in the confidence in the data provided by TLDs. It is generally assumed that TLDs, in spite of their limitations, will in any case produce results that are at least approximately correct (which is not always true for some other more sophisticated instruments). The research performed in recent years for a better understanding of TLD characteristics relevant to space measurements enhances this confidence. In summary, while new technical developments may in future replace TLDs in some space applications, it seems certain that TLDs will still remain an important measuring tool.

## References

[1] C.S. Warren and W.L. Gill, *Radiation Dosimetry Aboard the Spacecraft of the Eighth Mercury-Atlas Mission (MA-8)*. 1964: NASA TN D-1862.

[2] R.G. Richmond, *Radiation Dosimetry for the Gemini Program*. 1972: NASA TN D-6695.

[3] J.V. Bailey, "Dosimetry during space missions," *IEEE Trans. on Nucl. Sci.*, vol. NS-23, 1976.
[4] E.R. Benton and E.V. Benton, "Space radiation dosimetry in low-Earth orbit and beyond," *Nucl. Instr. Methods B.*, vol. 184, pp. 255–294, 2001.
[5] M. Durante and F.A. Cucinotta, "Physical basis of radiation protection in space travel," *Rev. Mod. Phys.*, vol. 83, pp. 1245–1281, 2011.
[6] F.A. Cucinotta, H. Wu, M.R. Shavers and K. George, "Radiation dosimetry and biophysical models of space radiation effects," *Gravit. Space Biol. Bull.*, vol. 16, pp. 11–18, 2003.
[7] P. Bilski, D. Matthiä and T. Berger, "Influence of cosmic radiation spectrum and its variation on the relative efficiency of LiF thermoluminescent detectors — Calculations and measurements," *Radiat. Meas.*, vol. 88, pp. 33–40, 2016.
[8] G. Reitz, "Characteristic of the radiation field in low earth orbit and in deep space," *Z. Med. Phys.*, vol. 18, pp. 233–243, 2008.
[9] Y.S. Horowitz, O. Avila and M. Rodríguez-Villafuerte, "Theory of heavy charged particle response (efficiency and supralinearity) in TL materials," *Nucl. Instr. Methods B.*, vol. 184, pp. 85–112, 2001.
[10] Y. Horowitz, E. Fuks, H. Datz, L. Oster, J. Livingstone and A. Rosenfeld, "Mysteries of LiF TLD response following high ionization density irradiation: Glow curve shapes, dose response, the unified interaction model and modified track structure theory," *Radiat. Meas.*, vol. 46(12), pp. 1342–1348, 2011.
[11] P. Olko, P. Bilski, N.A. El Faramawy, H.Y. Göksu, J.L. Kim, R. Kopec and M.P.R. Waligorski, "On the relationship between dose-, energy- and LET-response of thermoluminescent detectors," *Radiat. Prot. Dosim.*, vol. 119, pp. 15–22, 2006.
[12] E. Tochilin, N. Goldstein and J.T. Lyman, "The quality and LET dependence of three thermoluminescent dosemeters and their potential use as secondary standards," in *2nd Int. Conf. on Luminescence,*. 1968, USAEC: Washington. pp. 424–437.
[13] H. Yasuda, "Glow Curve Analyses of $^{6}$LiF:Mg, Ti (TLD-600) and $^{7}$LiF:Mg, Ti (TLD-700) Exposed to High-Energy Heavy Ions," *J. Nucl. Sci. Technol.*, vol. 36(11), pp. 1105–1107, 1999.
[14] Y. Uchihori, K. Fujitaka, N. Yasuda and E. Benton, "Intercomparison of Radiation Instruments for Cosmic-ray with Heavy Ion Beams at NIRS (ICCHIBAN Project)," *J. Radiat. Res.*, vol. 43(S), pp. S81–S85, 2002.
[15] N. Yasuda, Y. Uchihori, E.R. Benton, H. Kitamura and K. Fujitaka, "The intercomparison of cosmic rays with heavy ion beams at NIRS (ICCHIBAN) project." *Radiat. Prot. Dosim.*, vol. 120, pp. 414–420, 2006.
[16] Y. Uchihori and E. Benton, eds. *Results from the first two intercomparison of dosimetric instruments for cosmic radiation with heavy ions beams at NIRS (ICCHIBAN 1&2).* HIMAC-078, 2004, NIRS: Chiba.
[17] Y. Uchihori and E. Benton, eds. *Results from the ICCHIBAN-3 and ICCHIBAN-4 experiments to intercompare the response of space radiation dosimeters.* HIMAC-128, 2008, NIRS: Chiba.

[18] J. Miller and C. Zeitlin, "Twenty years of space radiation physics at the BNL AGS and NASA Space Radiation Laboratory," *Life Sci. Space Res.*, vol. 9, pp. 12–18, 2016.
[19] G. Reitz, "Past and future application of solid-state detectors in manned spaceflight," *Radiat. Prot. Dosim.*, vol. 120, pp. 387–396, 2006.
[20] Y.S. Horowitz, "The theoretical and microdosimetric basis of thermoluminescence and applications to dosimetry," *Phys. Med. Biol.*, vol. 26, pp. 765–824, 1981.
[21] Y.S. Horowitz, "A unified and comprehensive theory of the TL dose response of thermoluminescent systems applied to LiF:Mg,Ti," in *Microdosimetric Response of Physical and Biological Systems to Low- and High-LET Radiations*, Y.S. Horowitz, ed. 2006, Elsevier: Amsterdam. pp. 75–202.
[22] T. Berger and M. Hajek, "TL-efficiency — Overview and experimental results over the years," *Radiat. Meas.*, vol. 43, pp. 146–156, 2008.
[23] O.B. Geiß, M. Krämer and G. Kraft, "Efficiency of thermoluminescent detectors to heavy charged particles," *Nucl. Instr. Methods B.*, vol. 142, pp. 592–598, 1998.
[24] E.R. Benton, A.L. Frank and E.V. Benton, "TLD efficiency of $^{7}$LiF for doses deposited by high-LET particles," *Radiat. Meas.*, vol. 32, pp. 211–214, 2000.
[25] P. Bilski, "Response of various LiF thermoluminescent detectors to high energy ions — Results of the ICCHIBAN experiment," *Nucl. Instr. Methods B.*, vol. 251(1), pp. 121–126, 2006.
[26] G. Massillon-JL, I. Gamboa-deBuen and M.E. Brandan, "TL response of LiF:Mg,Ti exposed to intermediate energy $^{1}$H, $^{3}$He, $^{12}$C, $^{16}$O and $^{20}$Ne ions," *J. Phys. D: Appl. Phys.*, vol. 40, pp. 2584–2593, 2007.
[27] P. Bilski and M. Puchalska, "Relative efficiency of TL detectors to energetic ion beams," *Radiat. Meas.*, vol. 45, pp. 1495–1498, 2010.
[28] P. Bilski, T. Berger, M. Hajek and G. Reitz, "Comparison of the response of various TLDs to cosmic radiation and ion beams: Current results of the HAMLET project," *Radiat. Meas.*, vol. 46, pp. 1680–1685, 2011.
[29] M. Sadel, P. Bilski, J. Swakon, M. Rydygier, T. Horwacik and A. Weber, "Comparative investigations of the relative thermoluminescent efficiency of LiF detectors to protons at different proton therapy facilities," *Radiat. Meas.*, vol. 82, pp. 8–13, 2015.
[30] P. Bilski, "Lithium Fluoride — from LiF:Mg,Ti to LiF:Mg,Cu,P," *Radiat. Prot. Dosim.*, vol. 100, pp. 199–203, 2002.
[31] S. Deme, I. Fehér, I. Apáthy, G. Reitz and Y. Akatov, "Twenty years of TLD measurements on board space vehicles by the Hungarian "Pille" system," *Radioact. Environ.*, vol. 7, pp. 916–925, 2005.
[32] I. Apáthy, S. Deme, L. Bodnár, A. Csöke and I. Héjja, "An On-Board TLD System for Dose Monitoring on the International Space Station," *Radiat. Prot. Dosim.*, vol. 84(1–4), pp. 321–323, 1999.
[33] I. Ambrožová, K.P. Brabcová, J. Kubančák, J. Šlegl, R.V. Tolochek, O.A. Ivanova and V.A. Shurshakov, "Cosmic radiation monitoring at

low-Earth orbit by means of thermoluminescence and plastic nuclear track detectors," *Radiat. Meas.*, 2016.

[34] H. Tawara, M. Masukawa, A. Nagamatsu, K. Kitajo, H. Kumagai and N. Yasuda, "Characteristics of $Mg_2SiO_4$:Tb (TLD-MSO-S) relevant for space radiation dosimetry," *Radiat. Meas.*, vol. 46(8), pp. 709–716, 2011.

[35] D. Zhou, E. Semones, R. Gaza, S. Johnson, N. Zapp, M. Weyland, R. Rutledge and T. Lin, "Radiation measured with different dosimeters during STS-121 space mission," *Acta Astronaut.*, vol. 64(4), pp. 437–447, 2009.

[36] T. Berger, M. Hajek, L. Summerer, N. Vana, Y. Akatov, V. Shurshakov and V. Arkhangelsky, "Austrian dose measurements onboard space station MIR and the International Space Station — overview and comparison," *Adv. Space Res.*, vol. 34(6), pp. 1414–1419, 2004.

[37] T. Berger, B. Przybyla, D. Matthiä, G. Reitz, S. Burmeister, J. Labrenz, P. Bilski, T. Horwacik, *et al.*, "DOSIS & DOSIS 3D: long-term dose monitoring onboard the Columbus Laboratory of the International Space Station (ISS)," *J. Space Weather Space Clim.*, vol. 6, p. A39, 2016.

[38] M. Hajek, T. Berger, R. Bergmann, N. Vana, Y. Uchihori, N. Yasuda and H. Kitamura, "LET dependence of thermoluminescent efficiency and peak height ratio of $CaF_2$:Tm," *Radiat. Meas.*, vol. 43, pp. 1135–1139, 2008.

[39] P. Bilski, "Calculation of the relative efficiency of thermoluminescent detectors to space radiation," *Radiat. Meas.* vol. 46, pp. 1728–1731, 2011.

[40] T. Doke, T. Hayashi, S. Nagaoka, K. Ogura and R. Takeuchi, "Estimation of dose equivalent in STS-47 by a combination of TLDs and CR-39", *Radiat. Meas.* vol. 24(1), pp. 75–82, 1995.

[41] D. Zhou, E. Semones, R. Gaza, S. Johnson, N. Zapp and M. Weyland, "Radiation measured for ISS-Expedition 12 with different dosimeters," *Nucl. Instr. Methods A.*, vol. 580(3), pp. 1283–1289, 2007.

[42] M. Hajek, T. Berger, N. Vana, M. Fugger, J.K. Pálfalvi, J. Szabó, I. Eördögh, Y.A. Akatov, *et al.*, "Convolution of TLD and SSNTD measurements during the BRADOS-1 experiment onboard ISS (2001)," *Radiat. Meas.*, vol. 43(7), pp. 1231–1236, 2008.

[43] D. Zhou, E. Semones, R. Gaza and M. Weyland, "Radiation measured with passive dosimeters in low Earth orbit," *Adv. Space Res.*, vol. 40(11), pp. 1575–1579, 2007.

[44] G. Reitz, T. Berger, P. Bilski, R. Facius, M. Hajek, V. Petrov, M. Puchalska, D. Zhou, *et al.*, "Astronaut's organ doses inferred from measurements in a human phantom outside the international space station," *Radiat. Res.*, vol. 171, pp. 225–235, 2009.

[45] M. Puchalska, P. Bilski, T. Berger, M. Hajek, T. Horwacik, C. Körner, P. Olko, V. Shurshakov, *et al.*, "NUNDO: A numerical model of a human torso phantom and its application to effective dose equivalent calculations for astronauts at the ISS," *Radiat. Environ. Biophys.*, vol. 53(4), pp. 719–727, 2014.

[46] NCRP, *Operational Radiation Safety Program for Astronauts in Low-Earth Orbit: A Basic Framework*. NCRP Report. 142. 2002, Bethesda.

[47] N. Vana, W. Schöner, M. Fugger and Y. Akatov, "Absorbed Dose Measurements and LET-Determination with TLDs in Space," *Radiat. Prot. Dosim.*, vol. 66, pp. 145–152, 1996.

[48] W. Schöner, N. Vana, M. Fugger and E. Pohn, "The Peak-Height Ratio (HTR)-Method for LET-Determination with TLDs and an Attempt for a Microdosimetric Interpretation," in *Proc. $20^{th}$ Symp. on Mcrodosim., Oxford,* 1997, pp. 411–414.

[49] T. Berger, M. Hajek, W. Schöner, M. Fugger, N. Vana, M. Noll, R. Ebner, Y. Akatov, *et al.*, "Measurement of the depth distribution of average LET and absorbed dose inside a water-filled phantom on board space station Mir," *Phys. Medica*, vol. 17 (Suppl. 1), pp. 128–130, 2001.

[50] P. Bilski, "Dosimetry of densely ionising radiation with three LiF phosphors for space applications," *Radiat. Prot. Dosim.*, vol. 120, pp. 397–400, 2006.

[51] H. Yasuda and K. Fujitaka, "Responses of TLD-$Mg_2SiO_4$:Tb and Radiophotoluminescent Glass to Heavy Charged Particles and Space Radiation," *Radiat. Prot. Dosim.* vol. 87(2), pp. 115–119, 2000.

[52] N. Vana, W. Schöner, M. Fugger, Y. Akatov and V. Shurshakov, "ADLET-Absorbed Dose and Average LET Determination with TLDs on the Space Station MIR During a Russian Long Term Flight," *Radiat. Prot. Dosim.*, vol. 66, pp. 173–177, 1996.

[53] T. Berger, M. Hajek, W. Schöner, M. Fugger, N. Vana, V. Akatov, V. Shurshakov, V. Arkhangelsky, *et al.*, "Application of the High-temperature Ratio Method for Evaluation of the Depth Distribution of Dose Equivalent in a Water-Filled Phantom on Board Space Station Mir," *Radiat. Prot. Dosim.*, vol. 100, pp. 503–506, 2002.

[54] Y.S. Horowitz, D. Satinger, E. Fuks, L. Oster and L. Podpalov, "On the Use of LiF:Mg,Ti Thermoluminescence Dosemeters in Space — A Critical Review," *Radiat. Prot. Dosim.*, vol. 106, pp. 7–24, 2003.

[55] P. Bilski, "On the correctness of the thermoluminescent high-temperature ratio (HTR) method for estimating ionisation density effects in mixed radiation fields," *Radiat. Meas.*, vol. 45, pp. 42–50, 2010.

[56] T. Berger, M. Hajek, M. Fugger and N. Vana, "Efficiency-Corrected Dose Verification with Thermoluminescence Dosemeters in Heavy-Ion Beams," *Radiat. Prot. Dosim.*, vol. 120, pp. 361–364, 2006.

[57] M. Hajek, T. Berger, M. Fugger, M. Fuerstner, N. Vana, V. Akatov, V. Shurshakov and V. Arkhangelsky, "BRADOS — Dose determination in the Russian Segment of the International Space Station," *Adv. Space Res.*, vol. 37, pp. 1664–1667, 2006.

[58] U. Straube, T. Berger, G. Reitz, R. Facius, C. Fuglesang, T. Reiter, V. Damann and M. Tognini, "Operational radiation protection for astronauts and cosmonauts and correlated activities of ESA Medical Operations," *Acta Astronaut.*, vol. 66, pp. 963–973, 2010.

[59] Y. Roed, D. Zhou, R. Gaza and N. Zapp, "Radiation measurements with passive detectors during recent Shuttle flights," *$14^{th}$ Workshop on Radiation Monitoring for International Space Station (WRMISS),* 2009; Dublin, Ireland, http://wrmiss.org/workshops/fourteenth/.

[60] I. Apáthy, S. Deme, I. Fehér, Y.A. Akatov, G. Reitz and V.V. Arkhanguelski, "Dose measurements in space by the Hungarian Pille TLD system," *Radiat. Meas.*, vol. 35(5), pp. 381–391, 2002.
[61] T. Doke, T. Hayashi, J. Kikuchi, S. Nagaoka, T. Nakano, S. Takahashi, H. Tawara and K. Terasawa, "Dose equivalents inside the MIR Space Station measured by the combination of CR-39 plates and TLDs and their comparison with those on Space Shuttle STS-79, -84 and -91 missions," *Radiat. Meas.*, vol. 35(5), pp. 505–510, 2002.
[62] G.D. Badhwar, "Radiation dose rates in Space Shuttle as a function of atmospheric density," *Radiat. Meas.*, vol. 30(3), pp. 401–414, 1999.
[63] G.D. Badhwar, W. Atwell, G. Reitz, R. Beaujean and W. Heinrich, "Radiation measurements on the Mir Orbital Station," *Radiat. Meas.* vol. 35(5), pp. 393–422, 2002.
[64] G. Reitz, R. Beaujean, E. Benton, S. Burmeister, T. Dachev, S. Deme, M. Luszik-Bhadra and P. Olko, "Space radiation measurements on-board ISS — the DOSMAP experiment," *Radiat. Prot. Dosim.*, vol. 116(1–4), pp. 374–379, 2005.
[65] E. Semones, M. Weyland, R. Rutledge, T. Shelfer, R. Gaza, D. Zhou, A. Johnson and N. Zapp, "Recent Radiation Monitoring Results: Expedition 10, 11 and STS-114", *$10^{th}$ Workshop on Radiation Monitoring for International Space Station (WRMISS)* 2005; Chiba, Japan, http://wrmiss.org/workshops/tenth/.
[66] I. Apáthy, Y.A. Akatov, V.V. Arkhangelsky, L. Bodnár, S. Deme, I. Fehér, A. Kaleri, I. Padalka, *et al.*, "TL dose measurements on board the Russian segment of the ISS by the "Pille" system during Expedition-8, -9 and -10," *Acta Astronaut.*, vol. 60(4), pp. 322–328, 2007.
[67] A. Nagamatsu, K. Murakami, K. Kitajo, K. Shimada, H. Kumagai and H. Tawara, "Area radiation monitoring on ISS Increments 17 to 22 using PADLES in the Japanese Experiment Module Kibo," *Radiat. Meas.*, vol. 59, pp. 84–93, 2013.
[68] A. Konradi, W. Atwell, G.D. Badhwar, B.L. Cash and K.A. Hardy, "Low earth orbit radiation dose distribution in a phantom head," *Int. J. Rad. Apl. Part D: Nucl. Tracks Rad. Meas.*, vol. 20(1), pp. 49–54, 1992.
[69] G.D. Badhwar, W. Atwell, F.F. Badavi, T.C. Yang and T.F. Cleghorn, "Space Radiation Absorbed Dose Distribution in a Human Phantom," *Radiat. Res.*, vol. 157, pp. 76–91, 2002.
[70] H. Yasuda, G.D. Badhwar, T. Komiyama and K. Fujitaka, "Effective Dose Equivalent on the Ninth Shuttle-Mir Mission (STS-91)," *Radiat. Res.*, vol. 154, pp. 705–713, 2000.
[71] H. Yasuda, "Effective Dose Measured with a Life Size Human Phantom in a Low Earth Orbit Mission," *J. Radiat. Res.*, vol. 50(2), pp. 89–96, 2009.
[72] G. Reitz and T. Berger, "The MATROSHKA facility — dose determination during an EVA," *Radiat. Prot. Dosim.*, vol. 120(1–4), pp. 442–445, 2006.
[73] T. Berger, P. Bilski, M. Hajek, M. Puchalska and G. Reitz, "The MATROSHKA Experiment: Results and Comparison from EVA (MTR-1)

and IVA (MTR-2A/2B) Exposure," *Radiat. Res.*, vol. 180, pp. 622–637, 2013.

[74] D. Zhou, E. Semones, D. O'Sullivan, N. Zapp, M. Weyland, G. Reitz, T. Berger and E.R. Benton, "Radiation measured for MATROSHKA-1 experiment with passive dosimeters," *Acta Astronaut.*, vol. 66, pp. 301–308, 2010.

[75] Online database of the MATROSHKA results. 2014; http://www.fp7-hamlet.eu/index.php/database/passive-data.

[76] V.A. Shurshakov, Y.A. Akatov, V.M. Petrov, V.V. Arkhangelsky, S.V. Kireeva, E.N. Yarmanova, A.Y. Kalery, V.I. Lyagushin, *et al.*, MATROSHKA-R experiment onboard the ISS: Current status and preliminary results. *$9^{th}$ Workshop on Radiation Monitoring for International Space Station (WRMISS)* 2004; Vienna, http://wrmiss.org/workshops/ninth/.

[77] I. Jadrníčková, K. Brabcová, Z. Mrázová, F. Spurný, V.A. Shurshakov, I.S. Kartsev and R.V. Tolochek, "Dose characteristics and LET spectra on and inside the spherical phantom onboard of ISS," *Radiat. Meas.*, vol. 45(10), pp. 1536–1540, 2010.

[78] A. Nagamatsu, K. Murakami, H. Tawara, K. Kitajo, K. Shimada, V. Petrov, V. Shurshakov, I. Nikolaev, *et al.*, "Space radiation dosimetery for the Matroshka-R #1 Experiment onboard the KIBO using PADLES from May–Sep. 2012 (Increment 31/32). *$18^{th}$ Workshop on Radiation Monitoring for International Space Station (WRMISS)* 2013; Budapest, http://wrmiss.org/workshops/eighteenth/.

[79] G. Reitz, H. Bücker, R. Beaujean, W. Enge, R. Facius, W. Heinrich, T. Ohrndorf and E. Schopper, "Dosimetric mapping inside BIORACK," *Adv. Space Res.*, vol. 6(12), pp. 107–113, 1986.

[80] H. Bücker, K. Baltshukat, R. Facius, G. Horneck, G. Reitz, M. Schäfer, J.U. Schott, R. Beaujean, *et al.*, "Advanced biostack: Experiment 1 ES 027 on spacelab-1," *Adv. Space Res.*, vol. 4(10), pp. 83–90, 1984.

[81] H. Bücker and G. Horneck, "The biological effectiveness of HZE-particles of cosmic radiation studied in the Apollo 16 and 17 Biostack experiments," *Acta Astronaut.*, vol. 2(3), pp. 247–264, 1975.

[82] T. Berger, M. Hajek, P. Bilski, C. Körner, F. Vanhavere and G. Reitz, "Cosmic radiation exposure of biological test systems during the EXPOSE-E mission," *Astrobiology.*, vol. 12(5), pp. 387–392, 2012.

[83] T. Berger, M. Hajek, P. Bilski and G. Reitz, "Cosmic radiation exposure of biological test systems during the EXPOSE-R mission," *Int. J. Astrobiol.*, vol. 14(1), pp. 27–32, 2014.

[84] O. Goossens, F. Vanhavere, N. Leys, P. De Boever, D. O'Sullivan, D. Zhou, F. Spurný, E.G. Yukihara, *et al.,* "Radiation dosimetry for microbial experiments in the International Space Station using different etched track and luminescent detectors," *Radiat. Prot. Dosim.*, vol. 120(1–4), pp. 433–437, 2006.

[85] F. Vanhavere, J.L. Genicot, D. O'Sullivan, D. Zhou, F. Spurný, I. Jadrníčková, G.O. Sawakuchi and E.G. Yukihara, "DOsimetry of BIological EXperiments in SPace (DOBIES) with luminescence (OSL and TL) and track etch detectors," *Radiat. Meas.*, vol. 43(2), pp. 694–697, 2008.

[86] F. Spurný and I. Votočková, "Depth dose behind thin shielding on the external surface of the Cosmos-2044 biosatellite," *Int. J. Rad. Apl. Part D: Nucl. Tracks Rad. Meas.*, vol. 20(1), pp. 171–173, 1992.

[87] G. Reitz, H. Bücker, R. Facius, M. Schäfer and R. Beaujean, "Dosimetric results of Cosmos 2044," *Int. J. Rad. Apl. Part D: Nucl. Tracks Rad. Meas.*, vol. 20(1), pp. 161–165, 1992.

[88] G. Reitz, R. Facius, P. Bilski and P. Olko, "Investigation of radiation doses in open space using TLD detectors," *Radiat. Prot. Dosim.*, vol. 100, pp. 533–536, 2002.

[89] R. de la Torre, L.G. Sancho, G. Horneck, A.d.l. Ríos, J. Wierzchos, K. Olsson-Francis, C.S. Cockell, P. Rettberg, *et al.*, "Survival of lichens and bacteria exposed to outer space conditions — Results of the Lithopanspermia experiments," *Icarus.*, vol. 208(2), pp. 735–748, 2010.

[90] J.F. Bottollier-Depois, P. Beck, B. Bennett, L. Bennett, R. Butikofer, I. Clairand, L. Desorgher, C. Dyer, *et al.*, "Comparison of codes assessing galactic cosmic radiation exposure of aircraft crew," *Radiat. Prot. Dosim.*, vol. 136, pp. 317–323, 2009.

[91] D.T. Bartlett, L.G. Hager, D. Irvine and M. Bagshaw, "Measurements on Concorde of the Cosmic Radiation Field at Aviation Altitudes," *Radiat. Prot. Dosim.*, vol. 91(4), pp. 365–376, 2000.

[92] T. Horwacik, P. Bilski, P. Olko, F. Spurný and K. Turek, "Investigations of doses on board commercial passenger aircraft using CR-39 and thermoluminescent detectors," *Radiat. Prot. Dosim.*, vol. 110, pp. 377–380, 2004.

[93] P. Bilski, P. Olko and T. Horwacik, "Air-crew exposure to cosmic radiation on board of Polish passenger aircraft," *Nukleonika.*, vol. 49, pp. 77–83, 2004.

[94] M. Hajek, T. Berger and N. Vana, "A TLD-based personal dosemeter system for aircrew monitoring," *Radiat. Prot. Dosim.*, vol. 110(1–4), pp. 337–341, 2004.

[95] F. Verhaegen and A. Poffijn, "Air Crew Exposure on Long-haul Flights of the Belgian Airlines," *Radiat. Prot. Dosim.*, vol. 88, pp. 143–148, 2000.

[96] M. Hajek, T. Berge, W. Schöner, L. Summerer and N. Vana, "Dose Assessment of Aircrew using Passive Detectors," *Radiat. Prot. Dosim.*, vol. 100(1–4), pp. 511–514, 2002.

[97] F. Spurný, O. Obraz, F. Pernicka, I. Votockova, K. Turek, V.D. Nguyen, O. Vojtisek, V. Starostova, *et al.*, "Dosimetric Characteristics of Radiation Fields on Board Czechoslovak Airlines' Aircraft as Measured with Different Active and Passive Detectors," *Radiat. Prot. Dosim.*, vol. 48, pp. 73–77, 1993.

[98] P. Bilski, M. Budzanowski, B. Marczewska and P. Olko, "Response of TL Dosemeters to Cosmic Radiation on Board Passenger Aircraft," *Radiat. Prot. Dosim.*, vol. 100, pp. 549–552, 2002.

[99] M. Hajek, T. Berger and N. Vana, "Passive in-flight neutron spectrometry by means of Bonner spheres," *Radiat. Prot. Dosim.*, vol. 110(1–4), pp. 343–346, 2004.

[100] T. Berger, M. Meier, G. Reitz and M. Schridde, "Long-term dose measurements applying a human anthropomorphic phantom onboard an aircraft," *Radiat. Meas.*, vol. 43(2), pp. 580–584, 2008.

[101] M. Hajek, T. Berger, W. Schöner and N. Vana, "Analysis of the neutron component at high altitude mountains using active and passive measurement devices," *Nucl. Instr. Methods A.*, vol. 476(1), pp. 69–73, 2002.

[102] M. Budzanowski, B. Burgkhardt, P. Olko, W. Pessara and M.P.R. Waligorski, "Long-term investigation on self-irradiation and sensitivity to cosmic rays of TL detectors types TLD-200, TLD-700, MCP-N and new phosphate glass dosemeters," *Radiat. Prot. Dosim.*, vol. 66, pp. 135–138, 1996.

[103] M. Budzanowski, P. Bilski, L. Bøtter-Jensen, A. Delgado, P. Olko, J.C. Saez-Vergara and M.P.R. Waligorski, "Comparison of LiF:Mg,Cu,P (MCP-N, GR-200) and $Al_2O_3$:C TL Detectors in Short-Term Measurements of Natural Radiation," *Radiat. Prot. Dosim.*, vol. 66, pp. 157–160, 1996.

This page intentionally left blank

# Chapter 9

# Luminescence Measurements for Retrospective Dosimetry

Stephen W.S. McKeever and Sergey Sholom

*Oklahoma State University, Department of Physics*
*145 PS, Stillwater, OK 74078*
*stephen.w.mckeever@okstate.edu, sergey.sholom@okstate.edu*

This Chapter deals with applications of luminescence dosimetry (both TL and OSL) for determination of doses obtained due to a nuclear or radiological accident, or possible nuclear terrorist attack. The properties of many different materials that demonstrate radiation-induced TL or OSL signals, and therefore may be used for recovering accidental doses, are described. Depending on the stability of these signals, materials may be used as retrospective dosimeters (if the signals are stable over periods of months/years and the sensitivity of the material is enough for recovering doses of about 100 mGy), or as emergency dosimeters (for materials with potentially unstable signals, but with sensitivity enough to measure doses of about 1-2 Gy within several days of the exposure). Retrospective dosimetry techniques exploit mainly the properties of quartz from different building materials as well as ceramics, while the list of materials that can be used for emergency dosimetry is much wider and includes different paper and plastic cards, banknotes, items of clothing and shoes, as well as components of personal electronic devices.

## 9.1. Introduction

### 9.1.1. *Short historical overview of luminescence techniques in dating and dosimetry*

Two luminescence techniques are currently used in archeological dating and retrospective/emergency dosimetry, namely Thermoluminescence and Optically-Stimulated Luminescence (TL and OSL,

respectively). Originally, both were developed for dating of archeological samples, but then were promptly adapted for retrospective dose assessment.

The principles of TL dating techniques have been summarized in [1] and several review papers. For dose reconstruction, the TL technique was used for the first time by Ichikawa et al. [2], who measured typical roof tiles to assess the A-bomb doses in Hiroshima and Nagasaki. The era of OSL dating/dosimetry was opened by the pioneering paper by Huntley *et al.* [3]. The OSL method became very popular since the so-called single-aliquot regenerative-dose (SAR) protocol was developed and formalized [4], which allowed the significant reduction of the amount of the sample required for dose reconstruction and improvement in the accuracy of the reconstructed doses. During the last few decades, retrospective luminescence dosimetry was successfully applied to reconstruct the doses due to Chernobyl Nuclear Power Plant accident in Ukraine [5], Semipalatinsk Nuclear Tests in Kazakhstan [6, 7], and radioactive contamination of the Techa River in Russia [8, 9]. More details about these results will be given below.

### 9.1.2. *The role of luminescence measurements among different dosimetric techniques*

A classification of different dose reconstruction techniques can be found in recent reviews [10–12]. It is commonly accepted that all retrospective dosimetry techniques can be divided into either biological or physical. The latter include electron paramagnetic resonance (EPR) dosimetry with teeth and nails, as well as luminescence dosimetry techniques with many different materials. In general, biological techniques work with soft human tissue, EPR with hard tissues while luminescence techniques are applied to materials that were located in the vicinity of people during accidental exposure.

### 9.1.3. *Materials available for dose reconstruction using luminescence measurements*

The most popular material in retrospective luminescence dosimetry is quartz located in bricks or ceramics, i.e. materials that were

annealed at high temperature during the manufacturing process. These materials could be used for dose reconstruction with any TL or OSL technique. Quartz from unfired construction materials like concrete or silicate bricks has also been tested as a possible dosimetric material [13, 14] but its practical application remains limited. Other building materials like gypsum wallboard, schist and clay, as well as some minerals like feldspar have also been tested with luminescence dosimetry techniques [15–18], but they demonstrated significant fading of the corresponding TL/OSL signals and might be only used a short time after exposure, i.e. in emergency dose reconstruction.

Much more choice exists for materials that could be found on/near an individual. Usually such materials demonstrate unstable TL/OSL responses and therefore can be used only for emergency dosimetry. The list of such materials includes the components of mobile phones or other electronic devices, as well as different plastics and paper cards, elements of clothing and shoes [19–21]. Some less common materials like silicate dust could also be used [22, 23] as potential emergency dosimeters.

### 9.1.4. *Requirements for dose reconstruction techniques using luminescence materials*

There is no single material that can be used in all dose reconstruction cases, and because of this much effort has been applied to find and test new materials as possible retrospective dosimeters. Any such new material should satisfy the following requirements:

— For potential retrospective dosimeters, radiation-induced TL/OSL signals should be stable over a period of months/years; for prospective emergency dosimeters, such signals need not be stable, as long as a proper fading correction procedure is available.
— Minimum detectable doses should be as low as about 100 mGy for retrospective dosimetry; a similar detection limit is needed for emergency dosimeters, to enable them to reliably distinguish doses in the range 1-2 Gy for samples measured within several days after exposure. (This is necessary for triage of the large

number of individuals expected to be affected during a radiation-related accident or nuclear terrorism attack.)
— The material should be widely spread.
— The doses reconstructed using such material should be relatable to the doses received by individuals.

## 9.2. Luminescence dose reconstruction months (years) after an accident (retrospective OSL/TL dosimetry)

Dose reconstruction was used for the first time for A-bomb victims in Hiroshima and Nagasaki, and at that time researchers used a term "A-bomb dosimetry". With time, the number of radiation-related accidents has increased, and a more common term "retrospective dosimetry" was introduced. In general, this term means any dose reconstruction fulfilled after exposure to some ionizing radiation dose. Historically, dose reconstruction techniques have been developed and applied to persons or objects exposed a long time prior to dose measurement, which assumes the use of stable radiation-induced markers (over a time period of years). To distinguish between this case and dosimetry a short-time after exposure, we will keep using "retrospective dosimetry" (in a narrow sense of this term) for dosimetry with stable radiation-induced markers aimed to reconstruct doses months/years after exposure, and will use "emergency dosimetry" for dose reconstruction undertaken within several days after exposure. We will discuss two main luminescence dosimetry techniques only, i.e. thermoluminescence and optically stimulated luminescence.

### 9.2.1. *Peculiarities of retrospective luminescence dosimetry techniques*

Because retrospective dosimetry, in the narrow sense of this term, is applied to samples that were accidentally exposed years in the past, it measures the so-called cumulative dose of the sample $D_{cum}$:

$$D_{cum} = D_{acc} + D_{bg} \tag{1}$$

where $D_{acc}$ is an accidental dose (the quantity that is sought) and $D_{bg}$ is a background (BG) dose to the sample. $D_{bg}$, in turn, consist of several components. For example, for quartz included in fired building materials (red bricks and ceramics), $D_{bg}$ may be expressed as:

$$D_{bg} = (\dot{D}_{\gamma} + \dot{D}_{\alpha} + \dot{D}_{\beta} + \dot{D}_{cosm}) * A \tag{2}$$

where $\dot{D}_{\gamma}$, $\dot{D}_{\alpha}$ and $\dot{D}_{\beta}$ are gamma, alpha and beta dose rates from natural radionuclides of the building material, $\dot{D}_{cosm}$ is the dose rate due to cosmic rays and $A$ is the age of the sample. Thus, the accidental component of the dose can be found from the following expression:

$$D_{acc} = D_{cum} - (\dot{D}_{\gamma} + \dot{D}_{\alpha} + \dot{D}_{\beta} + \dot{D}_{cosm}) * A \tag{3}$$

$D_{cum}$ in Eq. (3) is determined using TL or OSL. For samples with quartz, it could be one of the available TL techniques (either high-temperature TL or the pre-dose method [24–26]), or the OSL technique usually employed using the SAR protocol [27]. Components of the BG dose are calculated/measured through separate approaches, which will not be discussed here.

Dose $D_{acc}$ determined using Eq. (3) is the dose to the quartz grains, which has to be converted to the accidental dose of individuals. This is not a trivial problem, and some sophisticated approaches have been proposed to resolve this issue [28, 29].

### 9.2.2. *Retrospective TL dosimetry with different materials*

#### 9.2.2.1. *Red bricks*

Red bricks remain the most popular material used in dose reconstruction with quartz. TL glow curves of quartz from red bricks may have a few TL peaks; usually the 110°C and 210°C peaks are used for dose assessment with the pre-dose or high temperature TL technique, respectively [30].

#### 9.2.2.2. *Ceramics*

Ceramics include many different materials, but samples of porcelain have mainly been used for dose reconstruction [31–33]. For porcelain, the pre-dose technique applied to thin slices (200–300 $\mu$m thick) cut from the sample is the preferred TL technique [33]. This technique allows measurement of doses as low as 100 mGy, or even less [31].

#### 9.2.2.3. *Other materials*

Bailiff and Mikhailik [14] tested the possibility of using calcium silicate bricks for retrospective dosimetry. During the manufacturing process, these bricks are annealed at a relatively low temperature (200°C), which is enough to remove charges from traps associated with the 210°C peak in quartz and therefore this peak may be used for dose reconstruction. It should be noted that the results reported by Bailiff and Mikhailik [14] were obtained on calcium silicate bricks from the former Soviet Union, and the properties of such bricks may vary from those manufactured elsewhere. In general, the TL properties of bricks manufactured in different countries may vary due to differences in the technology of manufacturing.

Afouxenidis *et al.* [16] investigated the TL and OSL properties of natural schist, which is a metamorphic rock, composed mainly of quartz and muscovite and used as a building stone in many countries. For the natural samples of schist, the TL glow curve demonstrates a peak at about 275°C while a complex TL glow curve is observed in exposed samples (this glow curve was deconvoluted into 6 individual peaks; four of the most prominent of them (located at 110, 225, 275 and 350°C) were studied in detail). The 275°C peak was found to be highly sensitized, but three residual peaks demonstrated linear responses in the range 1–100 Gy (1–50 Gy for the 110°C peak) and could be used in retrospective dosimetry.

Many other materials such as mortar, render, concrete and clay [17, 34] have also been tested as possible retrospective TL dosimeters, but the obtained results did not satisfy the desired requirements.

### 9.2.3. *Retrospective OSL dosimetry with different materials*

#### 9.2.3.1. *Red bricks*

As was already mentioned, quartz from red bricks is not only a well-known retrospective TL dosimeter, but also could be used as an OSL material. Retrospective OSL dosimetry with quartz became very popular after the development of the single-aliquot regenerative-dose (SAR) protocol [4], which allowed a significant reduction of time and effort required for the reconstruction of a single dose. An example of the OSL curves and corresponding dose response curve obtained with the SAR protocol for a sample of brick quartz is shown in Fig. 1.

In this example, an OSL signal $L_i$ recorded after exposure to some regenerative dose in the range 0–14 Gy is normalized by using the OSL signal $T_i$ recorded after exposure to a test dose. The exposure to the test dose was applied after each measurement of $L_i$. The $L_i$ signal is recorded, for this specific brick at 80°C, after a preheat at

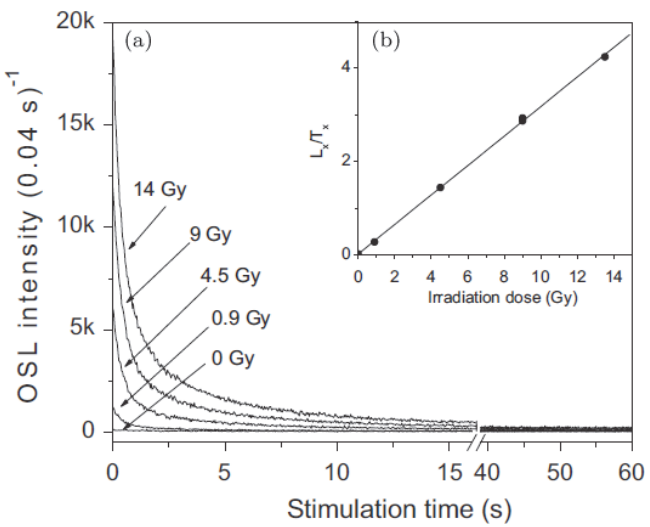


Fig. 1. (a) OSL decay curves for different doses. (b) Dose response curves derived using the initial 1 s integration interval from these curves [35].

180°C for 10 s to remove an unstable component of the OSL signal. The $T_i$ signal is also acquired at 80°C, but after a sample preheat at 120°C. Before each regeneration dose, the sample is bleached at 280°C for 40 s to remove all residual charges from shallow and medium-deep traps.

The above-described SAR protocol was developed especially for quartz from Japanese bricks [35], which demonstrates a TL peak at 80°C (but does not have a TL peak at 110°C). The SAR protocol for quartz from red bricks from other countries may be different, due to the variability in the properties of the quartz [36, 37].

#### 9.2.3.2. *Ceramics*

Ceramics may include, in addition to quartz, several other minerals. For example, porcelain may contain mullite, cristobalite and aluminum oxide [31]. For this reason, porcelain samples demonstrate significant inter- and intra-sample variability of OSL signals. It was suggested [18] that just the $Al_2O_3$ component is responsible for the enhanced OSL sensitivity in some porcelain samples. For samples with low sensitivity, a so-called OSL-pre-dose technique has been proposed [38], which exploits the phenomenon that OSL sensitivity of porcelain samples (i.e. the response to a test dose) depends on the total accumulated dose (pre-dose), and increases after sample heating to 675°C. The minimum detectable dose (MDD) with this technique was found to be as low as 40 mGy.

#### 9.2.3.3. *Other materials*

Feldspar is an OSL-sensitive mineral with a wider dose response than quartz [18], but it suffers from so-called anomalous fading [39], which makes this material unacceptable for dose reconstruction.

Gypsum wallboard (drywall) has been tested as a possible OSL dosimeter [15]. The strong natural signal was found to interfere with the radiation-induced signal. However, the natural signal almost disappeared if the OSL was recorded at low stimulation power ($0.35\,mW\,cm^{-2}$). The SAR protocol was optimized to study the gypsum samples [15]. A dose as low as 0.5 Gy could be determined with freshly exposed samples; however, the radiation-induced signal (RIS)

decayed with time after exposure, which limits its application in retrospective dosimetry.

Thomsen *et al.* [40] tested the possibility of using quartz from concrete blocks (an unfired building material with potentially a high natural dose) for retrospective OSL dosimetry. They analyzed the reconstructed doses using many (thousands) of single quartz grains and found that concrete blocks have enough quartz grains that were well-bleached in the past by solar radiation. With the developed single-grain dose analysis, they were able to reconstruct doses as low as ∼50–100 mGy using the concrete blocks.

Cement of different types has been tested with the OSL technique by Göksu *et al.* [34]. It was concluded that the OSL sensitivity of hydrated cement is not enough to use this material in retrospective dosimetry.

As was mentioned above, Afouxenidis *et al.* [16] investigated natural schist with both TL and OSL techniques. In the OSL part of the study, they observed both a signal from feldspar (using infrared-light stimulation) and quartz (using blue-light stimulation). OSL signals were recorded at 125°C after a preheat at 180°C for 10 s. The OSL response was linear in the range 1–100 Gy, which suggests that the schist could be used in retrospective dosimetry.

### 9.2.4. *Application of the retrospective luminescence dosimetry for past accidents*

#### 9.2.4.1. *A-bomb dose reconstruction in Japan*

A-bomb doses have been reconstructed using TL measurements of quartz extracted from roof tiles collected at different distances from the corresponding hypocenters [41–43]. They were used to improve previous dose calculation systems (which have historical names T65D and DS86). As a result, the last dose calculation system (DS02) has very good coincidence with corresponding TL doses (see Fig. 2) and provides accurate dose assessments to the A-bomb victims.

#### 9.2.4.2. *Chernobyl NPP accident*

In the case of the Chernobyl Nuclear Power Plant (NPP) accident, retrospective luminescence dosimetry has been used to verify the

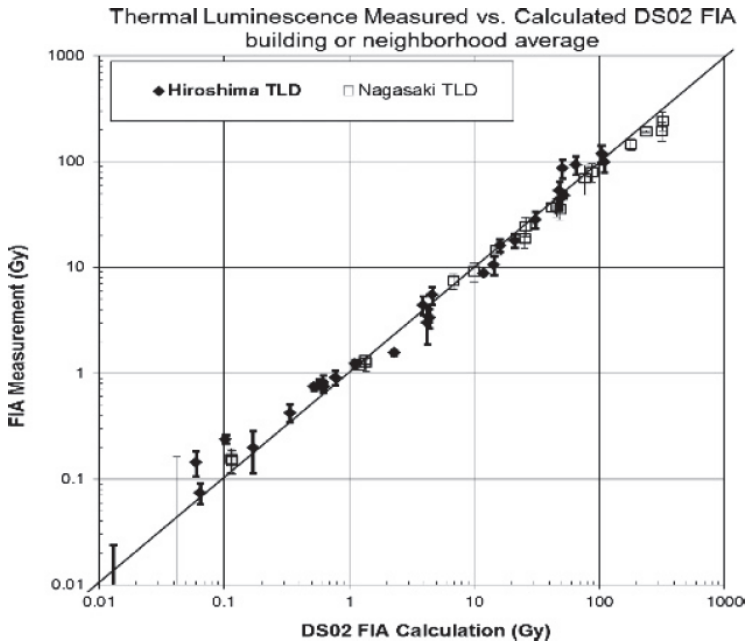


Fig. 2. Comparison of measured values (TL) with DS02 calculated values of free-in-air (FIA) absorbed dose from gamma-rays at 1 m above ground at Hiroshima and Nagasaki [44].

doses provided by computational modeling for inhabitants of territories contaminated by radioactive fallout [5, 45]. Quartz extracted from the red bricks was mainly used with both TL and OSL. Dosimetry with red bricks has an additional advantage because it allows not only the determination of the total cumulative doses, but also allows estimates of the effective energy of the radiation beam. This is obtained through measurement of the dose profile (i.e. a dependence of accidental dose as a function of depth from the wall surface of a brick). An example of such dose profile is shown in Fig. 3 for a brick collected in Zaborie, Russia. An average (over data from several different laboratories) dose profile is compared with that calculated for $^{137}$Cs uniformly distributed in the soil; a good coincidence is seen which confirms that just this isotope contributed in the main to the cumulative accidental dose, and the contribution from the short-lived radionuclides, which were present

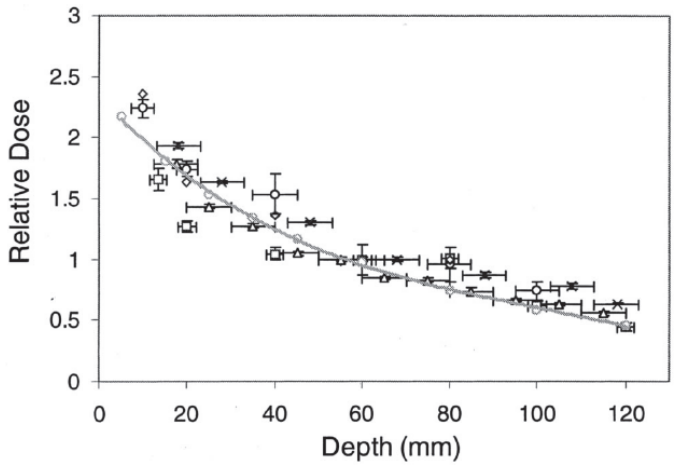


Fig. 3. Comparison of experimental and calculated relative depth-dose profiles for a brick from Zaborie, Russia. The experimental results were corrected on the natural background dose. The solid line is an interpolated curve fitted to the calculated values obtained from Monte Carlo simulations assuming a uniform distribution of $^{137}$Cs in soil to a depth of $5\,\mathrm{g\,cm^{-2}}$ [5].

in the Chernobyl radioactive fallout during the first days/weeks after accident, was not significant.

Luminescence doses were reconstructed for two different settlements (Vesnianoje in Ukraine and Zaborie in Russia) and compared with doses calculated using two different models. Good agreement between luminescence and calculated doses was seen, which confirms the appropriateness of the developed models.

### 9.2.4.3. *Techa river residents*

Although the main contamination of the Techa river by the liquid radioactive waste from the Mayak Production Association (a plutonium production plant located in the Southern Urals in Russia) occurred between 1947–1956, the dose reconstruction studies started only in the 1990s. Several papers reported luminescence doses obtained with both TL and OSL using quartz from red bricks collected from some settlements alongside the Techa river (see Refs. [8, 9, 46–48]). A few versions of the Techa River Dosimetry System (TRDS) have been developed and verified against doses obtained

Table 1. Comparison of the integral air kerma at the Techa shoreline derived from luminescence studies of bricks in Metlino and Muslyumovo and those assumed in the Techa River Dosimetry System (TRDS) (2016 version) [9].

| Location, Time Period | Building | Wall orientation | Air kerma (Gy) [95% CI] | |
|---|---|---|---|---|
| | | | Estimated from doses in brick | Assumed TRDS-2016 |
| Metlino, 7 km from release site, 1949–1956 | Mill | SW | 23 [15–32] | 21 [11–42] |
| | Church | WSW | 28 [15–36] | |
| | | SSW | 22 [17–28] | |
| | | SSE | 48 [36–58] | |
| Muslyumovo, 78 km from release site, 1949–2007 | Mill | W | 2.2 [0.2–1.5] | 1.9 [0.9–3.8] |

CI = confidence interval.

with independent dose reconstruction techniques, including luminescence. Table 1 shows the results of comparison of the luminescence doses and those obtained with TRDS-16, which is the latest version of TRDS. Quite fair agreement is observed between two doses, which validates the use of TRDS-16 for calculation of the doses of Techa river basin inhabitants.

#### 9.2.4.4. *Semipalatinsk nuclear test site*

According to Takada *et al.* [49], 459 nuclear tests were conducted in the former Soviet Union between 1949 and 1989 at the Semipalatinsk Nuclear Test Site (SNTS), but the most significant consequences were obtained from the test on August 29$^{th}$, 1949. Fallout from this test formed a narrow plume that covered Dolon and some other settlements in Kazakhstan and Russia [6]. Luminescence dose reconstruction was undertaken for these settlements using quartz from red bricks [6, 7, 49]. Fallout-related doses obtained with luminescence techniques were in the range from $<25$ mGy for settlements Bol'shaya Vladimirovka, Izvestka and Laptev Log to $475 \pm 110$ mGy for Dolon. The obtained results clearly confirmed

the strong heterogeneity in fallout dose distribution, as well as demonstrated that reconstruction of the SNTS dose distribution is possible with luminescence techniques. (Dose reconstruction with calculation techniques, which use the contemporary measurements of radionuclides concentration in soil, can be a problem because most of the radionuclides in the fallout were short-lived and are absent in the soil now. The calculation techniques do not work very well in the case of SNTS.)

### 9.2.5. *Future directions for retrospective luminescence dosimetry*

In retrospective luminescence dosimetry with quartz, feldspar is considered as a contaminant and should be separated from the quartz to avoid an additional uncertainty in the dose estimation, due to anomalous fading of the signal from feldspar. For samples of red bricks and tiles, quartz and feldspar grains are usually separated using their difference in density, and the whole procedure of separation takes 2–3 days [50]. In the case of samples of porcelain, density separation is quite difficult due to the small size of the mineral grains and, therefore, thin slices cut from a core drilled from a sample are usually used. To reduce the contribution from feldspar to the cumulative OSL signal, the samples are bleached with infra-red light, before recording of the blue-light stimulation OSL [51].

To overcome the above problems, Denby *et al.* [51] proposed separation of the signals from quartz and feldspar using their difference in OSL lifetime. This could be achieved by using the pulsed optically stimulated luminescence (POSL) technique, wherein the sample is stimulated by a short pulse, but the OSL is recorded after the end of the pulse. This technique is illustrated in Fig. 4, where plot **a** shows POSL responses of pure quartz and feldspar, while plot **b** is the response from the mixture of two minerals. It is seen in this figure that the feldspar signal decays mostly during a few $\mu$s after the pulse is off while the quartz signal decays much more slowly. In the case of a mixture of the two minerals, proper gating of the photomultiplier tube (for counting during the time marked as "Quartz Contribution" in plot **b**) allows the significant reduction (up to 98.4%, according to

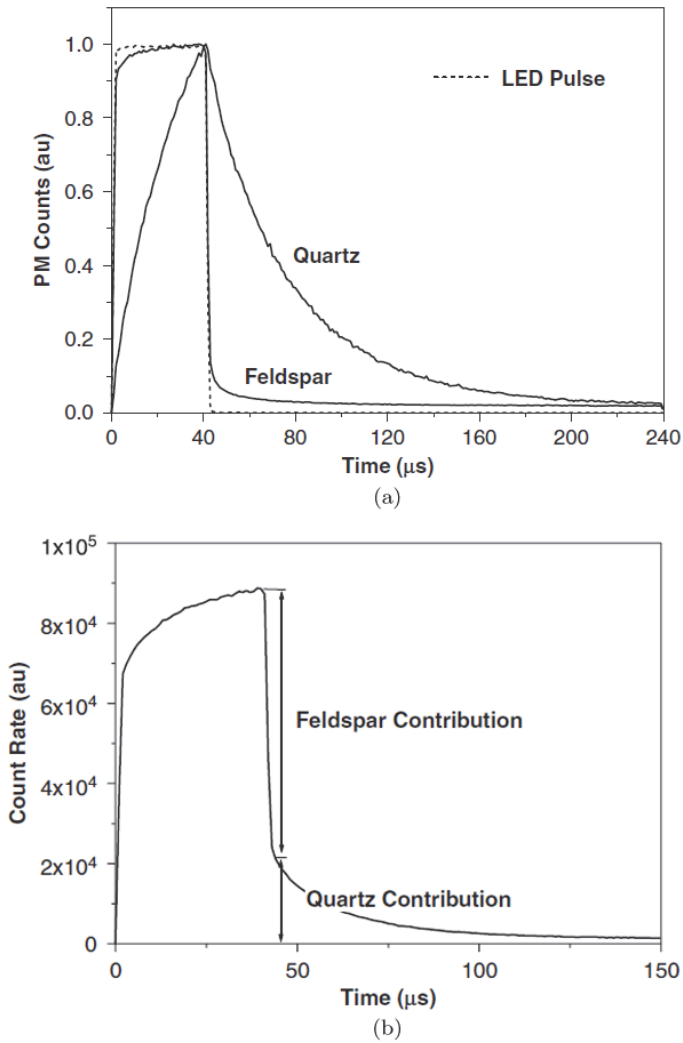


Fig. 4. Time resolved responses (under pulsed stimulation) of pure quartz and feldspar (a) and a mixed quartz feldspar sample (b) [51].

Denby *et al.* [51]) of the contribution from feldspar to the cumulative OSL signal of the mixed sample.

The POSL technique has been studied in several follow-up papers (see e.g. [52] and references therein). Kim *et al.* [53, 54] proposed a modification of the POSL technique for quartz, i.e. the so-called

single aliquot additive dose (SAAD)-POSL method, which accounts for the partial bleaching of the sample during optical stimulation to the short pulse (this is important to obtain the correct dose response curve with the single aliquot using an additive dose technique). They tested the SAAD-POSL method on the core disc samples extracted from red bricks, tiles and porcelain and estimated the minimum detectable dose as low as 0.01 Gy. Additionally, the time required for reconstruction of one dose was as short as 2 h. However, the fading test revealed that values of the reconstructed doses decreased by 5–42% if dose reconstruction with SAAD-POSL method was conducted two weeks after exposure, which indicates that there is still a contribution from an unstable component to the cumulative POSL signal (probably from other minerals like $Al_2O_3$ that may be present in the ceramic samples).

## 9.3. Luminescence dose reconstruction days/weeks after an accident (emergency OSL/TL dosimetry)

Retrospective reconstruction of dose in a time period of days or weeks after exposure requires a number of different considerations, compared to dose reconstruction months or years after exposure. An obvious consideration is that the stability of the signal to be measured does not have to be as great as that measured a long time after the event. Metastable signals can be tolerated, as long as enough of the signal remains at the time of measurement for reliable usage, and that fading of the signal during the period between exposure and measurement can be mathematically described and accounted for accurately and confidently.

A further consideration is that the period immediately following a radiological incident, possibly involving mass casualties, is likely to be chaotic. Apart from triage and treatment of physically injured trauma victims, rapid assessment of radiological exposure is paramount. With a focus only on radiation exposure we may say that there are likely to be three broad categories of radiation casualty following an incident, namely: (i) those for whom the dose is so high that medical intervention is unlikely to produce a

favorable outcome; (ii) those for whom timely medical intervention can produce beneficial results; and (iii) those for whom the exposure was so low that there is no immediate health threat and treatment for exposure can be safely delayed, or may even be unnecessary. The latter category includes those who are often referred to as the "worried well". The key, then, is to be able to perform rapid dose assessment (i.e. a "radiation triage") on casualties, in order to identify the important middle category. Furthermore, this needs to be done on what may be many thousands (even hundreds of thousands) of people. Additionally, it is obvious that the vast majority of those exposed, or potentially exposed, will not have been wearing a conventional personal radiation dosimeter.

As a result of these considerations the focus of luminescence dosimetry research in short-term emergency radiation dosimetry has been to find common-place materials that might confidently be expected to be found on any individual and that can provide the basic characteristics needed for use as reliable and rapid radiation dosimeters.

### 9.3.1. *Peculiarities of emergency luminescence dosimetry techniques*

In order to identify victims and categorize them as groups (i), (ii) or (iii) above, the chosen measurement parameter is absorbed dose. (See, Refs. [12, 55, 56] for a more detailed discussion.) In the search for common-place materials that may act as emergency OSL or TL dosimeters three properties are paramount: (a) Dose response (signal versus dose), with linearity being desirable; (b) sensitivity (signal per unit dose) and a sufficiently low minimum detectable dose (MDD); (c) fading characteristics, with fading slow enough (say, over one week) and mathematically defined, so that corrections for fading may be applied. In this regard, research has focused on components from personal electronics, plastic and paper goods (e.g. credit cards, banknotes), and clothing (including shoes). Additional materials studied include common vitamin tablets and household items (e.g. table salt).

### 9.3.2. *Emergency OSL dosimetry with different materials*

#### 9.3.2.1. *Surface-mount resistors from phones and other personal electronic devices*

Surface-mount resistors (SMRs) have been the subject of most research. This is because the substrate of these components is alumina ($Al_2O_3$), a material that is well-known as a TL and (particularly) an OSL dosimeter when grown as a single crystal with carbon as a dopant. The latter enhances the creation of oxygen vacancies (F-centers) within the crystal matrix, leading to strong luminescence emission [57]). Alumina in electronic components, however, is grown under very different conditions to those of commercial $Al_2O_3$ TL/OSL dosimeters and markedly different dosimetry properties result.

Initial pioneering work on the use of SMRs as potential OSL dosimeters is described by Inrig *et al.* [58] in which examinations of the dose response, sensitivity, and fading properties of the OSL signal from these components are described. Figure 5 illustrates a typical TL glow curve and OSL decay curves, while Fig. 6 shows the corresponding dose response for OSL for a set of SMRs from a mobile phone. This early work indicated that the dose response was linear and that the MDD was <10 mGy, sufficient for emergency dosimetry applications. However, unlike its commercial counterpart this form of alumina exhibited significant fading of the TL and OSL signals after irradiation. Following earlier authors [39] the fading is termed "anomalous" and is described by a decay function [58, 59]:

$$I = I_c \left[1 - \frac{g}{100} \log_{10}\left(\frac{t}{t_c}\right)\right] \tag{4}$$

where $I$ is the OSL intensity at time $t, I_c$ is the corrected OSL intensity at $t = t_c$, and $g$ is the percent decrease in intensity per decade. For the samples studied in Inrig *et al.* [58] $g$ was found to be ∼23.7% per decade for a preheat temperature of 160°C. Later studies by the same authors [59] showed much lower $g$-value of 7.3–10.6% per decade, for pre-heating temperatures up to 260°C. These results were interpreted as a combination of thermal and

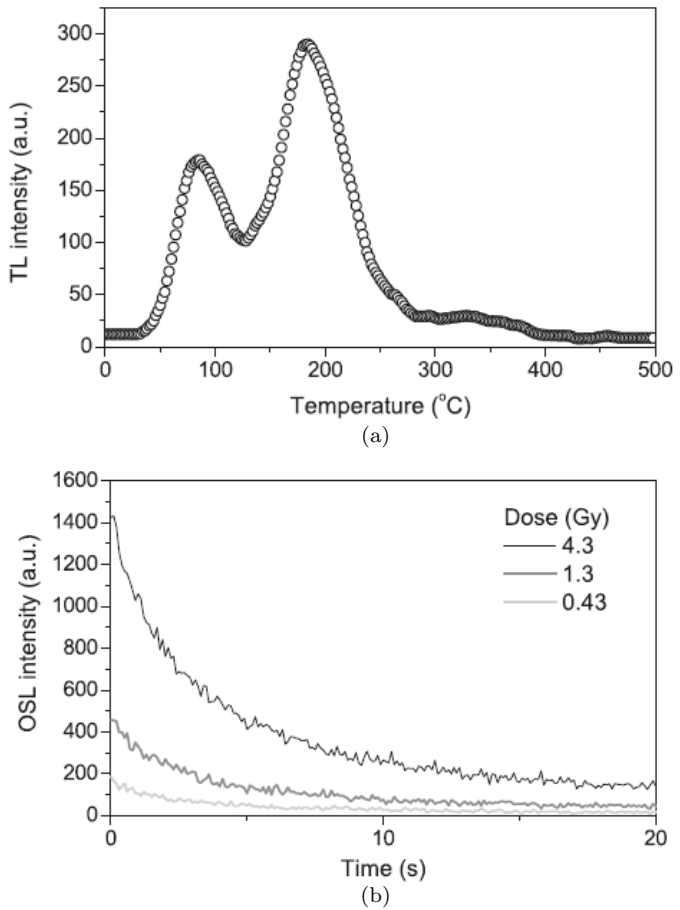


Fig. 5. (a) TL glow curves and (b) OSL decay curves for SMRs extracted from a mobile phone [58].

athermal (anomalous) fading for the low-temperature preheats, but anomalous only for the higher temperature preheats [59]. Other authors [60, 61] could not describe the fading using Eq. (4) and instead found that the fading could be described as the sum of multiple exponentials, plus a constant, for example:

$$\frac{I(t)}{I(0)} = \sum_i \alpha_i e^{-\beta_i t} + k \tag{5}$$

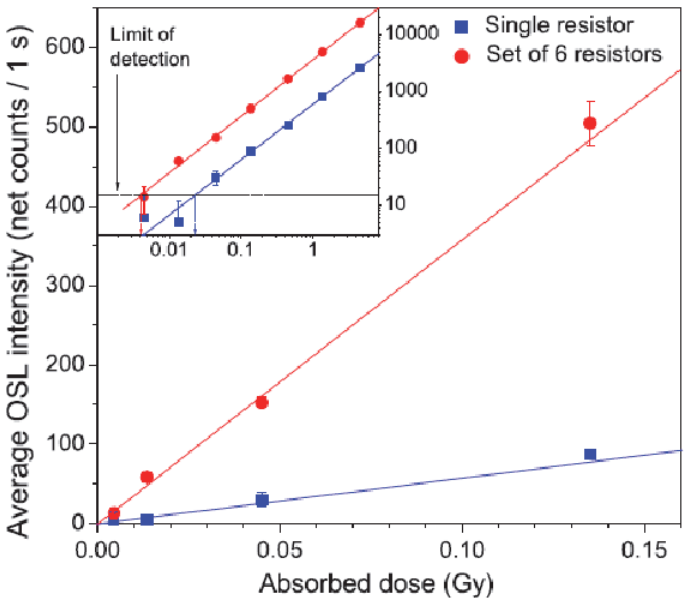


Fig. 6. OSL dose response curves from SMRs [58].

where $I(t)$ is the signal at time $t$ and $I(0)$ is the signal at time zero (i.e. immediately after the irradiation); $\alpha_i$, $\beta_i$ and $k$ are constants; and $i = 1 \ldots 5$. The discrepancy between the fading observed in Ref. [60] and Ref. [61] and others may be a variable contribution to the fading from thermal decay processes [62].

Alumina is the standard substrate material in a wide array of microelectronic applications, including surface mount devices. Usually produced in the alpha- phase, it is generally available in standard 96%–96.5% grade for general electronics, or 99.6% for higher frequency applications. The composition of the SMRs used in Inrig *et al.* [59] were listed as 97% $Al_2O_3$ and 3% $SiO_2$, while others [63] state that the composition is 96% $Al_2O_3$ and 4% $SiO_2$. SEM elemental analysis of the alumina substrates from some more-modern SMRs [64] reveals the expected dominance of Al and O, although no trace impurities could be detected by this method. Also of interest is the observation that the substrate for electronic inductors, also primarily alumina, reveals amounts of Si and some Ba.

Commercial OSL dosimetry-grade $Al_2O_3$ has strong luminescence emission near 420 nm for both TL and OSL, corresponding to the relaxation of excited F-centers. In contrast SMR-grade alumina reveals its maximum TL emission in the red region of the spectrum, as illustrated in Fig. 7, where a main TL emission is seen at a temperature of ∼160°C with a peak emission occurring at a wavelength around 695 nm. Similar data are shown in Lee *et al.* [66] where emission near 700 nm is reported along with a lower intensity, broad emission in the region of 300 nm to 480 nm. The cause of the 695 nm emission is uncertain, but since chromium is a common impurity in alumina it may be the broadened R-line from $Cr^{3+}$ ions [67]. With the assumption that OSL involves the same emitting centers and therefore also emits primarily in the red part of the spectrum, then one immediate suggestion from this is that enhanced OSL sensitivity may be achieved with the use of

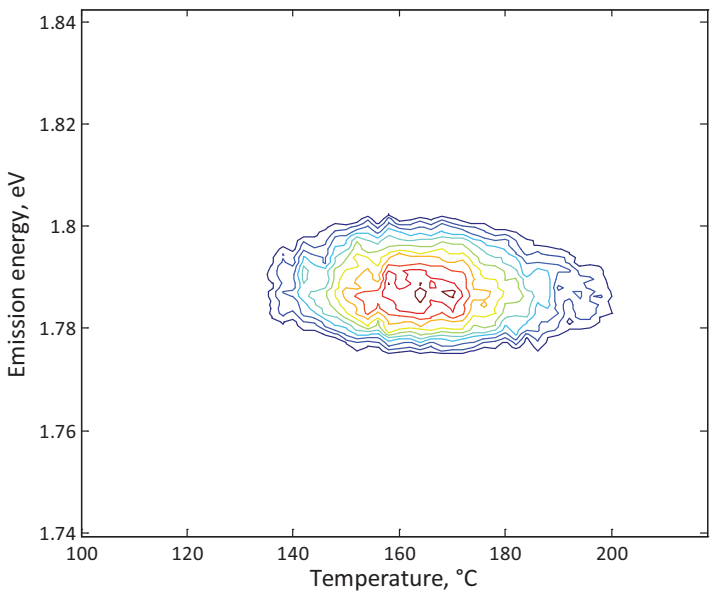


Fig. 7. TL emission spectrum from SMRs following a dose of 20 kGy. The emission peaks at ∼695 nm. The spectra have been corrected for the wavelength response of the detection system (spectrometer plus CCD detector) and for a constant energy bandwidth [65].

red-sensitive photodetectors (for example, a photomultiplier tube with an S-20 photocathode) rather than the more usual visible-UV sensitive detectors. The observation that the emitting centers are entirely different from those in crystalline, carbon-doped $Al_2O_3$ is not entirely unexpected, due to the amorphous nature of the SMR alumina substrate and the different method of production.

Similarly, the distribution of trapping centers in SMRs is quite different from that of crystalline $Al_2O_3$:C. Both TL and OSL curve shapes have been examined [68] and it was concluded that the trapping centers are distributed in energy. This is consistent with expectation for an amorphous, non-crystalline material. The observation of a continuous distribution of trapping centers for OSL (and TL) [68] leads naturally to the question of the optimum wavelength for stimulation of the OSL emission. Following Inrig *et al.* [58, 59] most work has used 470 nm blue-LEDs to generate the OSL (so-called "blue-OSL", or BSL) [63, 68–74]. Generally, the research has confirmed the fading behavior of the OSL signal and the effects of various pre-heat treatments on the OSL signal shape, sensitivity and stability. A preheat of 120°C for 10 s seems to be the best compromise between stability and sensitivity [68] with variable fading rates being observed with the use of different pre-heat treatments [73]. All observations confirm a linear OSL response with dose, with MDDs of the order of tens-hundreds of mGy.

A laboratory intercomparison was conducted with BSL from SMRs, using the experience and lessons learned from the above-mentioned research [75]. In the intercomparison two pre-heat protocols were adopted, termed "fast-mode" (no preheat, OSL measurement at room temperature for 30 s) and "full-mode" (10 s at 120°C, OSL measurement at 100°C for 30 s). The fast-mode was proposed for fast, triage measurements while the full-mode was proposed for detailed dose assessment during follow-up. Fading correction protocols were prescribed using the fading formula in Eq. (4). The result of the intercomparisons revealed that both the fast- and full-modes were able to classify the dose absorbed into the categories <1 Gy, 1-2 Gy and >2 Gy, with success rates of ∼90% for the fast mode and ∼70% for the full mode.

Recently, the use of violet stimulation (405 nm) has been proposed for OSL (termed VSL) [64]. VSL and BSL measurements were compared, with both being performed either at 40°C with a preheat (125°C hold for 10 s), or at 125°C without a preheat. VSL and BSL results (dose response, fading, sensitivity) were found to be comparable, but VSL demonstrated better stability and sensitivity. A difficulty was found with VSL due to a non-negligible zero-dose signal that interfered with the low-dose, dose-response curve. This requires further study.

Infra-red stimulation has also been found to induce a measurable OSL signal (termed IRSL). BSL and IRSL from various SMRs were compared by Bassinet *et al.* [71] where it was noted that the IRSL signal was weak-to-nonexistent, and the authors concentrated on dosimetry analysis using BSL only. However, a study at Oklahoma State University (unpublished) of IRSL from SMRs as a function of pre-heat temperature, reveals that a maximum in the IRSL sensitivity can be achieved for a preheat temperature of 160°C. Figure 8 shows the fading of the IRSL signal with time after irradiation, indicating a much more stable signal than either BSL or VSL (i.e. approximately 20% in the first 24 hrs followed by a slow reduction for longer delay times). Back-to-back comparisons between BSL and IRSL indicate an MDD of ∼tens of mGy for BSL and ∼hundreds of mGy for IRSL. Thus, although the sensitivity (using a PMT

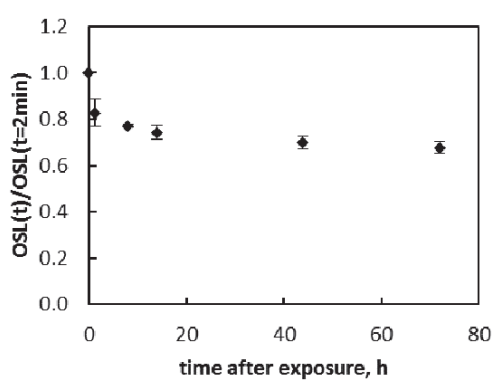


Fig. 8. Fading of the IRSL signal from SMRs with time after irradiation.

with a bi-alkali photocathode) of IRSL is considerably less than BSL, sufficient sensitivity is available for emergency dosimetry, with considerably less fading of the signal. As noted above, however, it is possible that the IRSL sensitivity may be improved using a PMT with a red-sensitive photocathode.

The photon energy dependence of BSL from SMRs shows the expected response for photon energies below ~300 keV, peaking around 100 keV [63], using $^{137}$Cs as a reference source.

#### 9.3.2.2. *Integrated circuits from phones and other personal electronic devices*

One disadvantage of using SMRs for dosimetry is that these devices are very small, and the size of these components has decreased in modern phones with respect to older models. As a result, multiple SMRs are required per measurement and there exists the practical difficulty of extracting the devices from the circuit board. However, this problem is obviated with integrated circuits (ICs), which are among the largest components on a printed circuit board and easy to extract. Here the interest is in the black epoxy encapsulation, not the active semiconductor material within the IC. Since this material is black, a lower OSL/TL sensitivity might be expected compared to a collection of SMR samples. However, as discussed below, experience has shown that the sensitivity is sufficient for emergency dosimetry. Recent scanning electron microscope analysis of the epoxy covering a typical IC [76] reveals the presence of Si, O and some Al, which is interpreted as demonstrating the existence of $SiO_2$ and $Al_2O_3$ phases. It is speculated that the luminescence signal originates from these phases.

Several research groups have examined both TL and OSL from these devices [71, 72, 76–78]. One undesirable property of BSL from ICs is a sensitivity change with reuse. One manifestation of this property is a non-linear dose-response curve. A long OSL measurement time of up to 600 s was found to remove the sensitivity change resulting in a linear dose response [78]. Alternatively (e.g. Ref. [76]), a small test dose can be used along with a shorter OSL measurement period, to normalize the sensitivity such that a linear

dose response may be attained by plotting normalized OSL versus dose.

The main blue-light stimulated OSL centers from ICs are stable up to approximately 110°C. Dependence on pre-heat temperature is minimal. OSL from these materials can also be stimulated by infrared stimulation (IRSL). Stimulation times are much longer (∼100 s) and the sensitivity is less than for BSL, but it is still adequate for emergency dosimetry. Measurements at OSU reveal that the MDD for BSL is 130–250 mGy and 240–740 mGy for IRSL. Advantages of IRSL over BSL, however, include no sensitivity change with re-use, and no observed fading of the signal, at least up to 3 days after exposure. The fading of BSL versus IRSL are compared in Fig. 9, using a pre-heat of 160°C for the IRSL signal.

#### 9.3.2.3. *Other electronic components*

In addition to SMRs and ICs, inductors, resonators and capacitors from various types of electronic device have also been examined, including smart phones, USB memory sticks, electronic chips in credit cards, ID cards and SIM cards [12, 79, 80]. Both TL and OSL have been studied. Inductors, resonators and capacitors from electronic devices also have alumina substrates; they demonstrated a variety of different dose responses, including linear and a saturating exponential [68].

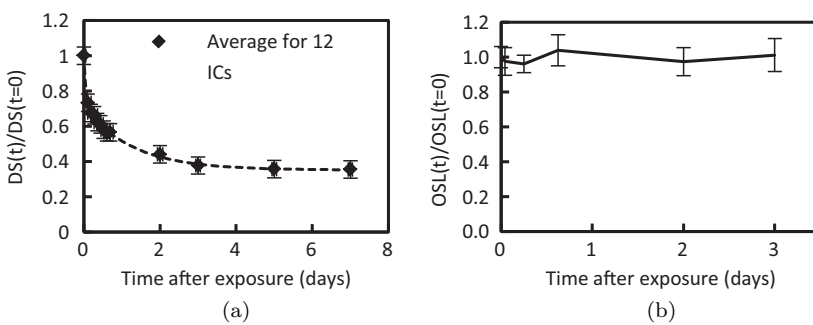


Fig. 9. (a) Fading of BSL, and (b) fading of IRSL from ICs. The BSL fading can be described as the sum of two exponentials, whereas little or no fading is observed with IRSL.

Capacitors also show a pre-irradiation, 'native' signal, which is about 10% of the 1.2 Gy induced signal. Most OSL studies have used blue-light stimulation, but recently VSL studies of inductor substrates have shown a higher sensitivity with linear dose dependence, but with similar fading characteristics [64]. The MDD for all materials, whether monitored using TL or OSL, seems to be in the range of tens of mGy to ∼hundreds of mGy for IRSL [72, 73], depending on sensitivity and the degree of fading.

In general, silicate minerals are sensitive TL/OSL materials. Thus, the silicate powders embedded in the epoxy resin covering electronic chip modules, as used in modern credit cards, ID cards, SIM cards, etc., have been the focus of attention for emergency dosimetry. TL, IRSL and BSL have each been examined, with mixed results. TL and IRSL each show a pre-irradiation 'native' signal, and in addition IRSL exhibits low sensitivity [81–83]. The native signal is speculated to be due to UV-curing of the epoxy, with the size of this signal dependent upon the curing temperature [84, 85]. Despite the native signals, the MDD with BSL is estimated at around a few 10 s mGy.

#### 9.3.2.4. *Display and protective glasses from mobile phones*

Perhaps the most obvious component of a mobile phone that has potential for dosimetry is the large glass display, especially as used in modern smart phones. Generally, the glasses can be divided into the actual display glass, and the protective or touchscreen glass above it. The display glass is the substrate for the liquid crystal display (LCD) unit, or other types of display unit. Both the protective/touchscreen glass and the display glass can be found in most modern smartphones and can be separated for individual use using common tools, as described, for example, by Discher and Woda [86].

Most luminescence studies to date on smart phone glass have focused on TL. The rationale for this is that, clearly, the glass will have been exposed to light, either externally from sunlight or room light, or internally from the display itself. Thus, OSL may be a questionable method to employ, whereas TL may be resistant, to some degree, to light exposure.

The shape of the TL glow curve from the display and protective glass is variable, depending on the origin of the glass and the spectral window used. TL emission spectra for two types of protective glass, known as Gorilla® glass, are shown in Fig. 10. Other published spectra for display glass are similar [87].

When TL from display glass is measured in a spectral window of 290–370 nm (U-340 filter) four categories of glass can be distinguished from their TL glow curve shape [86], as shown in Fig. 11. Category A is for alkali-aluminosilicate glass, categories B and C are from boron-silicate glasses, and category D from soda-lime glasses. The aforementioned Gorilla® glass is an alkali-aluminosilicate. Other glass manufacturers sell similar alkali-aluminosilicate glasses for the protective glass covers in smartphones under a variety of commercial names (e.g. Dragontail®, and others). Alkali-aluminosilicate glasses are also the most sensitive [88].

When measured in the spectral window from 530–630 nm (with a Schott OG530 and HA03 filters) the glow curve shape changes [87, 89] and it should be emphasized that the characteristic glow

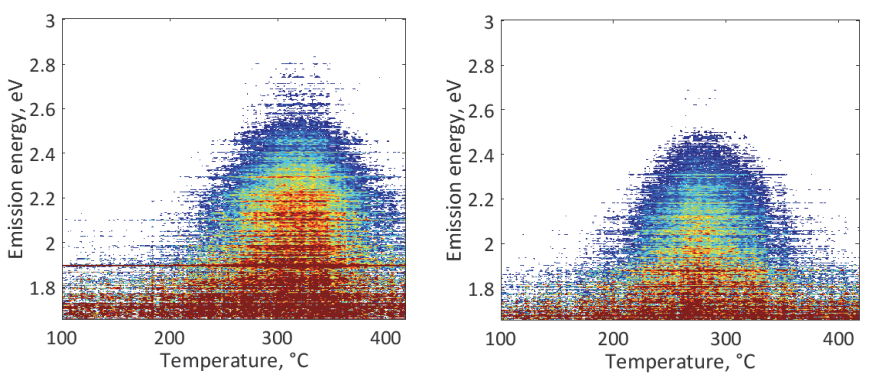


Fig. 10. TL emission spectra from two types of protective Gorilla® glass, expressed in eV: (a) From an iPhone 6+ (dose 10 kGy); the TL emission peaks at ∼310°C and ∼650 nm. (b) From a Samsung Galaxy S6 (dose 10 kGy); the TL emission peaks at ∼260°C and ∼720 nm. The data have been corrected for the wavelength response of the spectrometer and for a constant energy bandwidth [65].

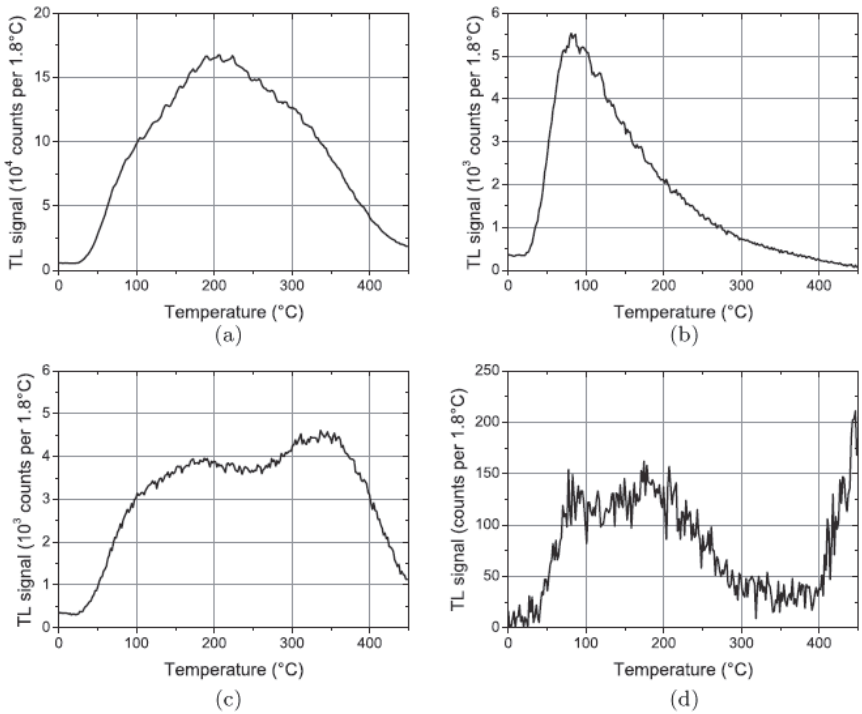


Fig. 11. The four categories of display glass as found when the TL is monitored in the emission window of 290–370 nm (i.e. with a U-340 filter) [86].

curves shown in Fig. 11 are only observed if measured under the conditions described.

A confounding problem with use of TL from protective and display glasses is the observation of a zero-dose (native) signal from unexposed glasses [86, 87, 89–91]. The size of this signal can vary widely from manufacturer to manufacturer and is believed to be caused by UV curing of the thin-film transistor (TFT) structure on the display glass, and curing of the adhesives used to glue the various layers together during manufacture. In untreated glasses, this native signal can be, typically, equivalent to several hundred mGy and adversely affects the MDD that can be obtained. However, it has been demonstrated that either etching of the glass surface [90] or mechanically grinding the surface [91] reduces or removes

the native signal, indicating that it is a surface effect. If glasses are treated in this fashion, the MDD can be reduced to several tens of mGy. The strength of the native signal is of course unknown prior to measurement and a universal mean value, with associated confidence limits, is often used and subtracted from the measured signal following the accident dose [86].

Fading of the TL signal is reported by several research groups [86, 87, 91]. All demonstrate a logarithmic decay function. A measurable signal is observed after approximately 2 weeks, although correction for fading is required.

When stored in an illuminated environment, e.g. natural sunlight or typical room light, some additional decay (faster) of the signal becomes apparent [86, 91]. Pre-illumination of the glass has been recommended by some authors — e.g. Discher and Woda, [86] and Mrozik *et al.* [89] — in an effort to account for this optically unstable TL component. (It is noted that the rear display glass is the least affected by external light exposure or internal display light exposure [91].) Illumination with 470 nm blue light, after irradiation and before heating, is recommended for all glasses by some authors [86] but others note that the optimum wavelength depends on the glass, with 470 nm being optimum for some and 302 nm for others [89]. Exposure time for optimum results depends on the power of the illumination source, but 100 s is typical. Efforts to apply pre-illumination to account for realistic light exposure scenarios have yielded mixed results. In particular, some studies have shown that the procedure leads to an underestimation of the applied dose [88]. TL signals (corrected for fading) are seen to follow a linear behavior with dose, enabling accident doses as low as a few hundred mGy to be determined, within acceptable error limits [12].

A modification to the TL technique is phototransferred TL. Here, the conventional TL glow curve is first recorded by heating to the desired temperature and, upon cooling to room temperature, the sample is then exposed to light (usually UV light) for a fixed period. On subsequent re-heating of the sample, a second TL curve is obtained which, like the original TL, is proportional to the dose originally received by the material. The cause of this signal

is the phototransfer of electrons from deep traps which were not emptied during the initial heating, to those traps that were emptied during recording of the initial TL curve. Thus, the signal is termed phototransferred TL, or PTTL.

There are several potential advantages to using the PTTL signal rather than the TL signal in emergency dosimetry of glasses — and several disadvantages. Firstly, the PTTL curve provides a signal for potential "second evaluation" of unknown absorbed dose, after the first evaluation using TL. Secondly, that component of fading that may be due to thermal processes will be circumvented since the traps probed in PTTL are very deep and not subject to thermal fading. In addition, since the technique is probing an entirely different set of traps from those that yield the initial TL signal, they will not necessarily undergo athermal or anomalous fading, for example, via tunneling. An obvious disadvantage, however, is the need for a much longer processing time to arrive at the final dose. Additionally, PTTL signals are usually much weaker that their TL counterparts, and thus a reduced sensitivity may be expected.

Each of these attributes was examined for PTTL from protective Gorilla® glass from smartphones [92]. Samples for PTTL are prepared in the same way as for TL measurements [86, 92] but after recording the initial TL the specimens are exposed to 365 nm light for varying periods at room temperature before re-heating. The PTTL signal so-obtained depends on the duration of the UV exposure, the temperature to which the sample is initially heated during TL, and the original absorbed dose. The PTTL signal is linear versus dose (up to ∼20 Gy) and exhibits minimal fading following the initial exposure (over several days). However the sensitivity is low, allowing an MDD of 100 mGy to as high as 5 Gy for some glass samples. A potentially confounding signal is a TL signal that is directly induced during the UV exposure. This signal appears along with the PTTL signal during second heating. However, a method to account for this using a pre-heat procedure has been proposed [92]. Overall, this multistep process is time consuming, but in cases where fading is a problem preventing dose evaluation by TL, or in cases were a second dose evaluation is needed, it may prove to be a useful procedure.

9.3.2.5. *Plastic and paper cards*

A study of the OSL from plastic cards (credit cards, ID cards, driver's licenses, etc.) [19, 20] revealed some potential for these types of personal objects to be used as dosimeters in emergency situations. Plastic cards are commonly 100% polyvinylchloride (PVC), but some are made from ABS (acrylonite butadiene styrene) or from mixtures such as 60% PVC and 40% polyester. A wide variety of, thicknesses, colors, etc. are available. Initial experiments (and, so far, the only ones available in the published literature [20]) used 470 nm stimulation (i.e. BSL) and the emission was detected in the UV spectral region using a U-340 filter. BSL emission wavelengths are as yet unreported.

BSL curves vary widely from card to card in both intensity for a given dose and in curve shape, with some readout times being quite long, up to ∼100 s, while others are much shorter. Furthermore, as with many other materials, there exists a significant native signal in some cards, particularly 60% PVC/40% polyester cards, but this too is variable in BSL shape and intensity. Many cards, especially 100% PVC, do not exhibit a native signal. The native BSL signal can be accounted for by using the entirely different BSL curve shape observed for these materials, compared to the radiation-induced BSL curve shape. Alternatively, it was also observed that Green OSL GSL (i.e. OSL stimulated with 530 nm light), did not exhibit a strong native signal, but the intensity of the GSL signal was reduced compared to BSL.

The BSL signal from these materials was also observed to fade significantly, with both 'fast' (49% in 1 hour) and 'moderate' (21% in 1 hour) fading rates observed. The decays observed were monotonic and thus corrections for fading are possible. The dose response was linear for all plastic cards examined, and MDDs of between 8 mGy and 1.5 Gy were observed. Reconstructed doses following the administration of a known laboratory dose, could be retrieved after correction for fading up to 7 days after the exposure, with an uncertainty of ±20% [20].

Paper business cards demonstrate strong OSL when stimulated at 470 nm and monitored in the UV range, with coated cards being much more sensitive than uncoated cards [19]. Confounding features

include the appearance of a "zero-dose" or native signal with some business cards (but not all). The native signal is observed to have a substantially different BSL decay curve shape when compared to the radiation-induced signal. As a result, a mathematical procedure has been proposed to account for and subtract the native signal from an exposed sample [19, 20]. Once this procedure is performed, a linear dependence of the BSL intensity versus dose is observed, with an MDD of between ~40 mGy and ~1.0 Gy [19]. Fading of the signal, however, is an additional problem, with an observed ~50% reduction over the first 2 days, followed by relative stability over a total period of 3 weeks when stored in the dark. Although this is a relatively moderate degree of fading, when stored under typical room lighting the fading is much more rapid such that the signal disappears over several hours. Nevertheless, correction for the fading is quite straightforward and, once corrected, the MDD for a sample of card that had been stored in the dark for 24 hrs was observed to be ~50 mGy to ~2.0 Gy [19]. The BSL properties (sensitivity and fading) are also variable from card to card, requiring calibration of each sample before a dose can be estimated.

#### 9.3.2.6. *Banknotes*

Other ubiquitous materials likely to be found on most people include banknotes and coins. Banknotes are normally manufactured from cotton, or cotton and linen mixtures, which are examples of cellulose polymers. A study of the sensitivities of the BSL from banknotes of various denominations and currencies [20] revealed sufficient sensitivity for potential use in emergency dosimetry. As with paper business cards, some notes revealed a native signal that must be accounted for in order for these materials to be used in dosimetry. Fortunately, the native BSL curve shape is again different from the radiation-induced curve shape, and the native signal can thus be subtracted using the same mathematical procedure as noted above for business cards [20].

Further examination of both the native signal and the radiation-induced signal from banknotes (Polish zloty) showed that the intensity distribution over the surface of the banknotes was highly

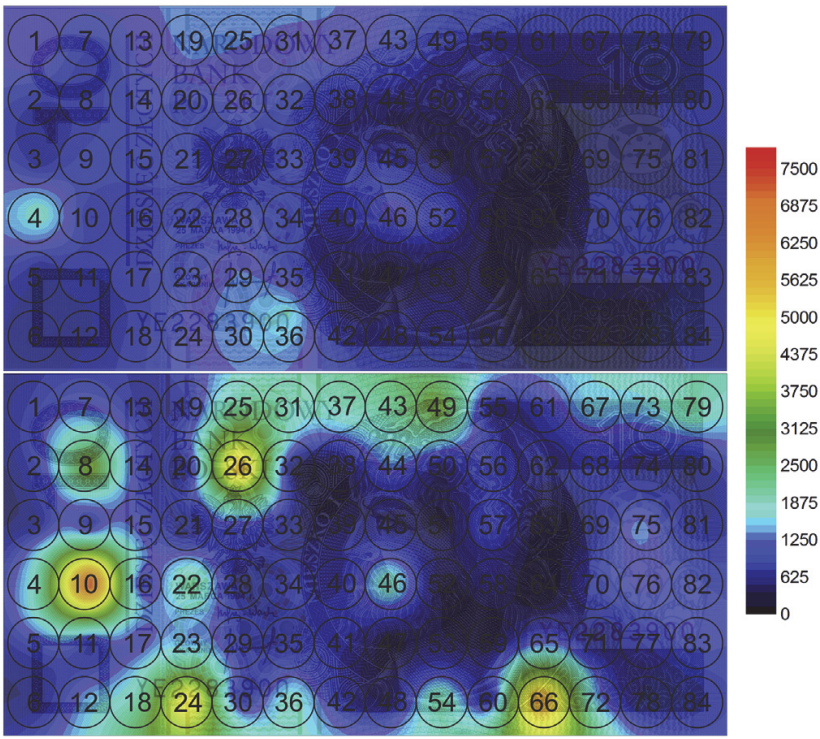


Fig. 12. Maps of the variation in intensity of BSL emission from a Polish 10-zloty note. Top: No irradiation. Bottom: After 1 Gy beta irradiation [93].

varied [93]. High intensity spots were observed, but the position of these spots was not consistent from banknote to banknote. Examples of the intensity variation over the surface of a 10-zloty note are shown in Fig. 12. Similar observations were made for US dollar and 5-euro banknotes. The implication from this is that each part of a banknote to be used in dosimetry must be individually calibrated.

Fading of the OSL signal is also observed, with most occurring over the first 2 days, with relative stability after that. The dose response is linear.

### 9.3.2.7. *Other materials*

Other common polymer materials that might be used as emergency dosimeters include modern clothing fabrics and shoes, and these too

have been examined for their TL and OSL dosimetry properties [20, 94]. Materials examined include polyester, rubber, polypropylene, nylon, spandex, hemp, silk, cotton, rayon, and some combinations. OSL can be stimulated using both blue- and green-light stimulation (BSL and GSL).

As with other similar materials, a significant and variable native signal was observed. This can be accounted for by making use of the different OSL decay curve shape for the native signal compared to the radiation-induced signal [20]. A set of mixed polyester fabrics was studied in Bossin *et al.* [94] using both BSL and IRSL. The native signal was found to be negligible under IR stimulation, while a strong radiation-induced signal could be measured quite easily, characterized by a linear dose response. All fabric specimens fade rapidly after irradiation, with the fading dependent on the amount of oxygen in the environment [94]. This suggests that they may be impractical for emergency dosimeters.

Tooth enamel and dental ceramics have been the target of several OSL studies with a view to establishing emergency dosimetry techniques. Early studies focused on TL rather than OSL, but they were hampered by the presence of triboluminesence and chemiluminescence [95, 96] prompting the use of OSL in order to avoid heating the sample [97]. IRSL, GSL, BSL and UV-stimulated OSL were all observed from deproteinated tooth enamel [97, 98] and the MDD was found to vary between 1.5 and 4 Gy [99–101]. However, these MDD values were only obtained using high sensitivity apparatus and multiple extracted teeth. The goal of *in-vivo* dosimetry is not yet possible due to the very low sensitivity observed.

By performing the OSL measurement on extracted teeth at elevated temperature (250°C) it is possible to increase the sensitivity [102]. This makes it possible to monitor the emission spectrum from tooth enamel, which is observed to peak at ∼412 nm, when stimulated at 354 nm [102].

Fading of the signal is strong, requiring correction for fading, which in turn increases the MDD [103]. In contrast the EPR signature ($CO_2^-$ radicals) from the same material (hydroxyapatite) is stable. In a comparative study OSL and EPR were nevertheless able to

determine the same delivered dose, once correction for OSL fading was performed [104].

Several authors have focused on the use of dental repair ceramics, instead of the dental enamel itself. Repair ceramics come in a wide variety of chemical forms, including alumina-, zirconia-, feldspathic- and glass-based materials. OSL and TL properties have been studied [63, 105–109]. Fading is observed, but is mathematically describable and therefore correctable. The sensitivity is high such that MDD values of mGy to tens of mGy are possible. Finally, unlike tooth enamel, the fading and sensitivity properties are insensitive to moisture [108]. These combined properties suggest that dental repair materials may be suitable for development and a target for emergency dosimetry.

Common medicines are found in many households and have thus been examined as potential OSL dosimeters. Several are known to exhibit strong OSL and/or TL signals after irradiation [110] although it is not known which component of the drug (binding material, dye, preservative, flavoring, etc.) generates the luminescence signal. EPR and OSL studies of a variety of vitamin types showed that several could be used as sensitive OSL dosimeters using a pre-heat to reduce the fading of the signal [111]. However, other OSL studies have found that some medicines do not exhibit substantial fading, allowing dosimetry without the need for fading correction [112]. Further study is necessary before overall conclusions can be drawn, but there is some potential with such materials.

Desiccants are found in many households and have been the subject of several TL and OSL studies. Common desiccants consist of silica gel, morillonite clay or activated charcoal [113]. Linear dose response and varied amounts of fading were observed, with some materials exhibiting low to no fading, with a MDD of between 8 and 450 mGy, adequate for emergency dosimetry.

Common household salt, a ubiquitous material found in most homes and some workplaces, has long been suggested as an emergency dosimeter using OSL owing to its high sensitivity [114–119]. Sensitivity changes lead to supralinearity of the dose response and require normalization of the OSL signal to obtain a linear response [115]. MDD values of a few mGy are reported. Fading is caused

by thermally induced loss of charge from shallow traps and can be decreased (to a few percent over several weeks) by pre-heating to remove this unstable component [115, 116]. Most researchers have studied BSL only. It has also been suggested as a neutron dosimeter via neutron activation of $^{23}$Na via the reaction $^{23}\mathrm{Na}(\mathrm{n},\gamma)^{24}\mathrm{Na}$, leading ultimately to gamma emission from $^{24}$Mg following beta decay of the $^{24}$Na nucleus [119]. Thus, there is potential of this material as a dosimeter in neutron accidents.

Dust is also ubiquitous and likely to be found everywhere leading to several efforts to use TL or OSL from dust as an emergency dosimeter. Either dust collected from the environment (cupboards, foodstuffs, etc.) or from personal objects (clothes, jewelry, tobacco, money, etc.) has been examined (see, for example, [20, 120–124]). The primary constituents of interest for luminescence dosimetry are the silicate minerals present in dust, especially quartz and feldspar with most studies focusing on the TL properties, although some OSL measurements — both BSL from dust on coins [20] and IRSL from tobacco dust [124] — are also reported. In general, non-mineral components have to be removed from the collected dust by various washing procedures. A recent work [124] examined the emission spectra of dust found in tobacco, revealing primary TL emissions near 745 nm, 560 nm, 440 nm and 410 nm, which the authors conclude is characteristic of feldspar. As expected for feldspathic materials, significant fading is observed. This requires correction to obtain the correct dose. A problem with all such measurements, however, is the necessary separation of the background natural dose; dust has likely been exposed to natural background irradiation over a lengthy period, and collected samples may not be fully reset before the accident dose is delivered.

## 9.4. Conclusions

Many different materials demonstrate radiation-induced TL or OSL signals and therefore may be used for accident dosimetry. Depending on the stability of these signals, materials may be used as retrospective dosimeters (if the signals are stable over months or years and

the sensitivity of the material is enough to determine doses of about 100 mGy). Or, they may be used as emergency dosimeters (using potentially unstable signals but with the possibility to correct for fading, and with a sensitivity high enough to measure the doses of about 1-2 Gy several days after exposure). Retrospective dosimetry techniques exploit mainly the properties of quartz from different building materials and ceramics, while the list of materials potentially useful for emergency dosimetry includes paper and plastic cards, banknotes, clothing and shoes, and components of electronic devices.

## References

[1] M.J. Aitken, Thermoluminescence Dating, London: Academic Press, 1985.
[2] Y. Ichikawa, T. Higashimura and T. Sidei, "Thermoluminescence dosimetry of gamma rays from atomic bombs in Hiroshima and Nagasaki," *Health Phys.*, vol. 12, pp. 395–405, 1966.
[3] D.J. Huntley, D.I. Godfrey-Smith and T.L.W. Thewalt, "Optical Dating of Sediments," *Nature*, vol. 313, pp. 105–107, 1985.
[4] A.S. Murray and A.G. Wintle, "Luminescence dating of quartz using an improved single-aliquot regenerative-dose protocol," *Radiat. Meas.*, vol. 32, pp. 57–73, 2000.
[5] I.K. Bailiff, V.F. Stepanenko, H.Y. Göksu, *et al.*, "Comparison of retrospective luminescence dosimetry with computational modeling in two highly contaminated settlements downwind of the Chernobyl NPP," *Health Phys.*, vol. 86, pp. 25–41, 2004.
[6] I.K. Bailiff, V.F. Stepanenko, H.Y. Göksu, *et al.*, "The application of retrospective dosimetry in areas affected by fallout from the Semipalatinsk Nuclear Test Site: an evaluation of potential," *Health Phys.* vol. 87, pp. 625–641, 2004.
[7] V.F. Stepanenko, M. Hoshi, M. Yamamoto, *et al.*, "International intercomparison of retrospective luminescence dosimetry method: sampling and distribution of the brick samples from Dolon' village, Kazakhstan," *J. Radiat. Res.* vol. 47 (Suppl. A), pp. A15–A21, 2006.
[8] H.Y. Göksu, M.O. Degteva, N.G. Bougrov, *et al.*, "First international intercomparison of luminescence techniques using samples from the Techa River valley," *Health Phys.*, vol. 82, pp. 94–101, 2002.
[9] M.M. Hiller, C. Woda, Bougrov, *et al.*, "External dose reconstruction for the former village of Metlino (Techa River, Russia) based on environmental surveys, luminescence measurements, and radiation transport modelling," *Radiat. Environ. Biophys.*, vol. 56, pp. 139–159, 2017.
[10] A.E. Ainsbury, E. Bakhanova, J.F. Barquinero, *et al.*, A., "Review of retrospective dosimetry techniques for external ionizing radiation exposures," *Radiat. Prot. Dosim.*, vol. 147, pp. 573–592, 2011.

[11] E. Ainsbury, C. Badie, S. Barnard, *et al.*, "Integration of new biological and physical retrospective dosimetry methods into EU emergency response plans – joint RENEB and EURADOS inter-laboratory comparisons," *Int. J. Radiat. Biol.* vol. 93, pp. 99–109, 2017.

[12] I.K. Bailiff, S. Sholom and S.W.S. McKeever "Retrospective and emergency dosimetry in response to radiological incidents and nuclear mass-casualty events: A review," *Radiat. Meas.*, vol. 94, pp. 83–139, 2016.

[13] H.Y. Göksu and I.K. Bailiff "Luminescence dosimetry using building materials and personal objects," *Radiat. Prot. Dosim.*, vol. 119, pp. 413–420, 2006.

[14] I.K. Bailiff and V.B. Mikhailik "The use of calcium silicate bricks for retrospective dosimetry," *Radiat. Meas.*, vol. 38, pp. 91–99, 2004.

[15] J.W. Thompson, K.E. Burdette, E.L. Inrig, *et al.*, "Optically stimulated luminescence dosimetry with gypsum wallboard (drywall)," *Radiat. Prot. Dosim.*, vol. 141, pp. 1–9, 2010.

[16] E.C. Afouxenidis, G.S. Stefanaki, A. Polymeris, *et al.*, "TL/OSL properties of natural schist for archaeological dating and retrospective dosimetry," *Nucl. Instr. Meth. Phys. Res. A*, vol. 580, pp. 705–709, 2007.

[17] F.S. Olise, S.B. Ola and F.A. Balogun, "Characterisation of clay samples from minerals — rich deposits for thermoluminescence applications," *Journal of King Saud University — Science*, vol. 30, pp. 158–167, 2018.

[18] L. Bøtter-Jensen and S.W.S. McKeever, "Optically stimulated luminescence dosimetry using natural and synthetic materials," *Radiat. Prot. Dosim.*, vol. 65, pp. 273–280, 1996.

[19] S. Sholom, R. DeWitt, S.L. Simon, *et al.*, Emergency optically stimulated luminescence dosimetry using different materials," *Radiat. Meas.*, vol. 46, pp. 1866–1869, 2011.

[20] S. Sholom and S.W.S. McKeever, "Emergency OSL dosimetry with commonplace materials," *Radiat. Meas.*, vol. 61, pp. 33–51, 2014.

[21] S. Sholom and S.W.S. McKeever, "Developments for emergency dosimetry using components of mobile phones," *Radiat. Meas.*, vol. 106, pp. 158–167, 2017.

[22] E. Bortolin, C. Boniglia, S. Della Monaca, *et al.*, "Silicates collected from personal objects as a potential fortuitous dosimeter in radiological emergency," *Radiat. Meas.*, vol. 46, pp. 967–970, 2011.

[23] S. Della Monaca, P. Fattibene and E. Bortolin, "A thermoluminescence study of mineral silicates extracted from herbs in the dose range 0.5–5 Gy," *Radiat. Meas.*, vols. 53–54, pp. 74–79, 2013.

[24] I.K. Bailiff, "The pre-dose technique," *Radiat. Meas.*, vol. 23, pp. 471–479, 1994.

[25] E.H. Haskell, P.L. Kaipa and M.E. Wrenn, "Environmental and accident dosimetry using the pre-dose TL technique," *Nucl. Track.*, vol. 10, pp. 513–516, 1994.

[26] I.K. Bailiff, L. Bøtter-Jensen, V. Correcher, *et al.*, "Absorbed dose evaluations in retrospective dosimetry: methodological developments using quartz," *Radiat. Meas.*, vol. 32, pp. 609–613, 2000.

[27] L. Bøtter-Jensen, S. Solongo, A.S. Murray, *et al.*, "Using the OSL single-aliquot regenerative-dose protocol with quartz extracted from building materials in retrospective dosimetry," *Radiat. Meas.*, vol. 32, pp. 841–845, 2000.
[28] I.K. Bailiff, "The development of retrospective luminescence dosimetry for dose reconstruction in areas downwind of Chernobyl," *Radiat. Prot. Dosim.*, vol. 84, pp. 411–419, 1999.
[29] R. Meckbach and P. Jacob, "Gamma exposures due to radionuclides deposited in urban environments. Part II: location Factors for different deposition patterns," *Radiat. Prot. Dosim.* vol. 25, pp. 181–190, 1988.
[30] E.H. Haskell, "Retrospective accident dosimetry using environmental materials," *Radiat. Meas.*, vol. 21, pp. 87–93, 1993.
[31] I.K. Bailiff, "Retrospective dosimetry with ceramics," *Radiat. Meas.*, vol. 27, pp. 923–941, 1997.
[32] D. Stoneham, I.K. Bailiff, L. Brodski, *et al.*, "TL accident dosimetry measurements on samples from the town of Pripyat," *Nucl. Tracks Radiat. Meas.*, vol. 21, pp. 195–200, 1993.
[33] D. Stoneham, "Accident dosimetry using porcelain: TL analysis of low dose samples," *Radiat. Meas.* vol. 24, pp. 499–505, 1995.
[34] H.Y. Göksu, I.K. Bailiff and V.B. Mikhailik, "New approaches to retrospective dosimetry using cementitious building materials," *Radiat. Meas.*, vol. 37, pp. 323–327, 2003.
[35] H. Fujita, M. Jain and A.S. Murray, "Retrospective dosimetry using Japanese brick quartz: a way forward despite an unstable fast decaying OSL signal," *Radiat. Meas.*, vol. 46, pp. 565–572, 2011.
[36] D. Banerjee, L. Bøtter-Jensen and A.S. Murray, "Retrospective dosimetry: preliminary use of the single-aliquot regeneration (SAR) protocol for the measurement of quartz dose in young house bricks," *Radiat. Prot. Dosim.*, vol. 84, pp. 421–426, 1999.
[37] A.K. Singh, S.N. Menon, S.Y. Kadam, *et al.*, "OSL studies of local bricks for retrospective dosimetric application," *Nucl. Instr. Meth. Phys. Res. B*, vol. 383, pp. 14–20, 2016.
[38] S. Hübner and H.Y. Göksu, "Retrospective Dosimetry using the OSL-predose Effect in Porcelain," *Appl. Radiat. Isot.*, vol. 48, pp. 1231–1235, 1997.
[39] D.J. Huntley and M. Lamothe, "Ubiquity of anomalous fading in K feldspars and the measurement and correction for it in optical dating," *Can. J. Earth Sci.*, vol. 38, pp. 1093–1106, 2001.
[40] K.J. Thomsen, M. Jain, L. Bøtter-Jensen, *et al.*, "Variation with depth of dose distributions in single grains of quartz extracted from an irradiated concrete block," *Radiat. Meas.*, vol. 37, pp. 315–321, 2003.
[41] Y. Ichikawa, T. Nagatomo, M. Hoshi, *et al.*, "Thermoluminescence dosimetry of $\gamma$ rays from the Hiroshima bomb at distances of 1.27 to 1.46 kilometers from the hypocentre," *Health Phys.*, vol. 52, pp. 443–451, 1987.
[42] M. Hoshi, S. Sawada, Y. Ichikawa, *et al.*, "Thermoluminescence dosimetry of gamma-rays from the Hiroshima atomic-bomb at distances 1.91–2.05 km from the hypocentre," *Health Phys.*, vol. 57, pp. 1003–1008, 1989.

[43] T. Nagatomo, M. Hoshi and Y. Ichikawa, "Thermoluminescence dosimetry of the Hiroshima atomic-bomb gamma-rays between 1.59 km and 1.63 km from the hypocentre," *Health Phys.*, vol. 69, pp. 556–559, 1995.

[44] G.D. Kerr, S.D. Egbert, I. Al-Nabulsi, *et al.*, "Workshop report on atomic bomb dosimetry-review of dose related factors for the evaluation of exposures to residual radiation at Hiroshima and Nagasaki," *Health Phys.*, vol. 109, pp. 582–600, 2015.

[45] I.K. Bailiff, V.F. Stepanenko, H.Y. Göksu, *et al.*, "Retrospective luminescence dosimetry: development of approaches to application in populated areas downwind of the Chernobyl NPP," *Health Phys.*, vol. 89, pp. 233–246, 2005.

[46] N. Bougrov, A. Baturin, H.Y. Göksu, *et al.*, "Investigations of thermoluminescence dosimetry in the Techa River Flood Plain: analysis of the new results," *Radiat. Prot. Dosim.*, vol. 101, pp. 225–228, 2002.

[47] V. Taranenko, R. Meckbach, M.O. Degteva, *et al.*, "Verification of external exposure assessment for the upper Techa riverside by luminescence measurements and Monte Carlo photon transport modeling," *Radiat. Environ. Biophys.*, vol. 42, pp. 17–26, 2003.

[48] C. Woda, P. Jacob, A. Ulanovsky, *et al.*, "Evaluation of external exposures of the population of Ozyorsk, Russia, with luminescence measurements of bricks," *Radiat. Environ. Biophys.*, vol. 48, pp. 405–417, 2009.

[49] J. Takada, M. Hoshi, T. Nagatomo, *et al.*, "External doses for residents near Semipalatinsk nuclear test site," *J. Radiat. Res.*, vol. 40, pp. 337–344, 1999.

[50] R.B. Hayes and S. Sholom, "Retrospective imaging and characterization of nuclear material," *Health Phys.*, vol. 113, pp. 91–101, 2017.

[51] P.M. Denby, L. Bøtter-Jensen, A.S. Murray, *et al.*, "Application of pulsed OSL to the separation of the luminescence components from a mixed quartz/feldspar sample," *Radiat. Meas.*, vol. 41, pp. 774–779, 2006.

[52] M.L. Chithambo, C. Ankjærgaard and V. Pagonis, "Time-resolved luminescence from quartz: An overview of contemporary developments and applications," *Physica B*, vol. 481, pp. 8–18, 2016.

[53] M.J. Kim, Y.J. Lee, J.I. Lee, *et al.*, "Fast assessment of retrospective dosimetry using the SAAD-POSL method with core disc samples from building materials," *Radiat. Meas.*, vol. 71, pp. 490–493, 2014.

[54] M.J. Kim, Y.J. Lee, J.I. Lee, *et al.*, "Fading test using the SAAD-POSL method for retrospective accidental dosimetry of building materials," *Radiat. Phys. Chem.*, vol. 116, pp. 373–376, 2015.

[55] M.E. Rea, R.M. Gougelet, Nicolalde, *et al.*, "Proposed triage categories for large-scale radiation incidents using high-accuracy biodosimetry methods," *Health Phys.*, vol. 98, pp. 136–144, 2010.

[56] A. Jaworska, E.A. Ainsbury, P. Fattibene, *et al.*, "Operational guidance for radiation emergency response organizations in Europe for using biodosimetric tools developed in EU MULTIBIODOSE project," *Radiat. Prot. Dosim.*, vol. 164, pp. 165–169, 2014.

[57] E.G. Yukihara and S.W.S. McKeever, Optically Stimulated Luminescence: Fundamentals and Applications, Chichester: Wiley, 2011.
[58] E.L. Inrig, D.I. Godfrey-Smith and S. Khanna, "Optically stimulated luminescence of electronic components for forensic, retrospective, and accident dosimetry," *Radiat. Meas.*, vol. 43, pp. 726–730, 2008.
[59] E.L. Inrig, D.I. Godfrey-Smith and C.L. Larsson, "Fading corrections to electronic component substrates in retrospective accident dosimetry," *Radiat. Meas.*, vol. 45, pp. 608–610, 2010.
[60] K. Beerten, F. Reekmans, W. Schroeyers, *et al.*, "Dose reconstruction using mobile phones," *Radiat. Prot. Dosim.*, vol. 144, pp. 580–583, 2011.
[61] J.S. Eakins, L.G. Harper, E. Kouroukla, *et al.*, The PHE fortuitous dosimetry capability based on optically stimulated luminescence of mobile phones," *Radiat. Prot. Dosim.*, vol. 170, pp. 412–415, 2016.
[62] E.C. Kouroukla, I.K. Bailiff and I. Terry, "Emergency dosimetry using ceramic components in personal electronic devices," *Int. J. Modern Phys: Conf. Series*, vol. 27, pp. 1460155-1–1460155-10, 2014.
[63] D. Ekendahl and L. Judas, "Retrospective dosimetry with alumina substrate from electronic components," *Radiat. Prot. Dosim.*, vol. 150, pp. 134–141, 2012.
[64] C. Bassinet, S. Kreutzer, N. Mercier, *et al.*, Violet stimulated luminescence signal from electronic components for radiation accident dosimetry," *Radiat. Meas.*, vol. 106, pp. 431–435, 2017.
[65] Y. Wang and P.D. Townsend, "Potential problems in collection and data processing of luminescence signals," *J. Lumin.*, vol. 142, pp. 202–211, 2013.
[66] J.I. Lee, H. Kim, J.L. Kim, *et al.*, "Thermoluminescence of chip inductors and resistors in new generation mobile phones for retrospective accident dosimetry," *Radiat. Meas.*, vol. 105, pp. 26–32, 2017.
[67] A. Pillonnet, C. Garapon, C. Champeaux, *et al.*, "Fluorescence of $Cr^{3+}$ doped alumina optical waveguides prepared by pulsed laser deposition and sol-gel method," *J. Lumin.*, vols. 87–89, pp. 1087–1089, 2000.
[68] C. Woda, S. Greilich and K. Beerten, "On the OSL curve shape and preheat treatment of electronic components from portable electronic devices," *Radiat Meas.*, vol. 45, 746–748, 2010.
[69] D. Ekendahl, B. Bulanek and L. Judas, "Comparative measurements of external radiation exposure using mobile phones, dental ceramics, household salt and conventional personal dosimeters," *Radiat. Meas.*, vol. 72, pp. 60–66, 2015.
[70] K. Beerten, C. Woda and F. Vanhavere "Thermoluminescence dosimetry of electronic components from personal objects," *Radiat. Meas.*, vol. 44, pp. 620–625, 2009.
[71] C. Bassinet, F. Trompier and I. Clairand "Radiation accident dosimetry on electronic components by OSL," *Health Phys.*, vol. 98, 440–445, 2010.
[72] A. Pascu, S. Vasiliniuc, M. Zeciu-Dolha, *et al.*, "The potential of luminescence signals from electronic components for accident dosimetry," *Radiat. Meas.*, vol. 56, pp. 384–388, 2013.

[73] J.I. Lee, I. Chang, A.S. Pradhan, *et al.*, "On the use of new generation mobile phone (smart phone) for retrospective accident dosimetry," *Radiat. Phys. Chem.*, vol. 116, pp. 151–154, 2015.
[74] J.I. Lee, I. Chang, J.L. Kim, *et al.*, "Dose re-estimation using thermoluminescence of chip inductors and resistors following the dose estimation by using optically stimulated luminescence readout for retrospective accident dosimetry," *Radiat. Meas.*, vol. 90, pp. 257–261, 2016.
[75] C. Bassinet, C. Woda, E. Bortolin, *et al.*, "Retrospective radiation dosimetry using OSL from electronic components: results of an inter-laboratory comparison," *Radiat. Meas.*, vol. 71, pp. 475–479, 2014.
[76] A. Mrozik, B. Marczewska, P. Bilski, *et al.*, "OSL signal of IC chips from mobile phones for dose assessment in accidental dosimetry," *Radiat. Meas.*, vol. 98, pp. 1–9, 2017.
[77] S. Sholom and S.W.S. McKeever, "Emergency OSL/TL dosimetry with integrated circuits from mobile phones," *Proc. SPIE*, vol. 9213, 921319-1–021319-10, 2014.
[78] S. Sholom and S.W.S. McKeever, "Integrated circuits from mobile phones as possible emergency OSL/TL dosimeters," *Radiat. Prot. Dosim.*, vol. 170, pp. 398–401, 2016.
[79] A.S. Pradhan, J.L. Lee and K.L. Kim, "Use of ubiquitous materials for the estimation of accidental exposures," *J. Med. Phys.*, vol. 37, pp. 121–123, 2012.
[80] K. Beerten and F. Vanhavere, "The use of a portable electronic device in accident dosimetry," *Radiat. Prot. Dosim.*, vol. 131, pp. 509–512, 2008.
[81] H.Y. Göksu "Telephone chip-cards as individual dosemeters," *Radiat. Meas.*, vol. 37, pp. 617–620, 2003.
[82] V.K. Mathur, J.H. Barkyoumb, E.G. Yukihara, *et al.*, "Radiation sensitivity of memory chip module of an ID card," *Radiat. Meas.*, vol. 42, pp. 43–48, 2007.
[83] J.H. Barkyoumb and V.K. Mathur, "Epoxy encapsulant as serendipitous dosimeters during radiological/nuclear events," *Radiat. Meas.*, vol. 43, pp. 841–844, 2008.
[84] C. Woda and T. Spöttl "On the use of OSL of wire-bonded chip card modules for retrospective and accident dosimetry," *Radiat. Meas.*, vol. 44, pp. 548–553, 2009.
[85] C. Woda, I. Fieldler and T. Spöttl, "On the use of OSL of chip card modules with molding for retrospective and accident dosimetry," *Radiat. Meas.*, vol. 47, pp. 1068–1073, 2012.
[86] M. Discher and C. Woda, "Thermoluminescence of glass displays from mobile phones for retrospective and accident dosimetry," *Radiat. Meas.*, vols. 53–54, pp. 12–21, 2013.
[87] M. Discher and C. Woda, "Thermoluminescence emission spectrometry of glass display in mobile phones and resulting evaluation of the dosimetric properties of a specific type of display glass," *Radiat. Meas.*, vol. 71, pp. 480–484, 2014.

[88] M. Discher, E. Bortolin and C. Woda "Investigations of touchscreen glasses from mobile phones for retrospective and accident dosimetry," *Radiat. Meas.*, vol. 89, pp. 44–51, 2016.
[89] A. Mrozik, B. Marczewska, P. Bilski, *et al.*, "Investigation of thermoluminescence properties of mobile phone screen displays as dosimeters for accidental dosimetry," *Radiat. Phys. and Chem.*, vol. 104, 88–92, 2014.
[90] M. Discher, C. Woda and I. Fiedler "Improvement of dose determination using glass display of mobile phones for accident dosimetry," *Radiat. Meas.*, vol. 56, pp. 240–243, 2013.
[91] C. Bassinet, N. Pirault, M. Baumann, *et al.*, "Radiation accident dosimetry: TL properties of mobile phone screen glass," *Radiat. Meas.*, vol. 71, pp. 461–465, 2014.
[92] S.W.S. McKeever, R. Minniti and S. Sholom "Phototransferred thermoluminescence (PTTL) dosimetry using Gorilla® glass from mobile phones," *Radiat. Meas.*, vol. 106, pp. 423–430, 2017.
[93] A. Mrozik, D. Kulig, B. Marczewska, *et al.*, "Dose estimation based on OSL signal from banknotes in accident dosimetry," *Radiat. Meas.*, vol. 101, pp. 1–6, 2017.
[94] L. Bossin, I.K. Bailiff and I. Terry "Luminescence characteristics of some common polyester fabrics: Application to emergency dosimetry," *Radiat. Meas.*, vol. 106, pp. 436–442, 2017.
[95] M. Jasińka and T. Niewiadomski, "Thermoluminescence of biological materials," *Nature*, vol. 227, pp. 1159–1160, 1970.
[96] C. Christoudlides and J.H. Fremlin, "Thermoluminescence of biological materials," *Nature*, vol. 232, pp. 257–258, 1971.
[97] D.I. Godfrey-Smith and B. Pass, "A new method of retrospective radiation dosimetry: optically stimulated luminescence in dental enamel," *Health Phys.*, vol. 72, pp. 744–749, 1997.
[98] E.G. Yukihara, S.W.S. McKeever and S.L. Simon "Investigation on the potential of the Optically Stimulated Luminescence (OSL) from dental enamel for retrospective assessment of radiation exposure," *Radiat. Meas.*, vol. 42, pp. 1256–1260, 2007.
[99] D.I. Godfrey-Smith, "Towards *in vivo* OSL dosimetry of human tooth enamel," *Radiat. Meas.*, vol. 45, pp. 854–858, 2008.
[100] R. DeWitt, D.M. Klein, E.G. Yukihara, *et al.*, "Optically stimulated luminescence (OSL) of tooth enamel and its potential use in post-irradiation exposure triage," *Health Phys.*, vol. 98, pp. 432–439, 2010.
[101] Ü.R. Yüce, N. Meriç, O. Atakol, *et al.*, "Dose response of hydrazine-deproteinated tooth enamel under blue light stimulation," *Radiat. Meas.*, vol. 45, pp. 797–800, 2010.
[102] A. Soni, D.R. Mishra, G.S. Polymeris, *et al.*, "OSL and thermally assisted OSL response in dental enamel for its possible application in retrospective dosimetry," *Radiat. Environ. Biophys.*, vol. 53, pp. 763–774, 2014.
[103] S. Sholom, R. DeWitt, S.L. Simon, *et al.*, "Emergency dose estimation using optically stimulated luminescence from human tooth enamel," *Radiat. Meas.*, vol. 46, pp. 778–782, 2011.

[104] S. Sholom and M.F. Desrosiers, "EPR and OSL emergency dosimetry with teeth: A direct comparison of two techniques," *Radiat. Meas.*, vol. 71, pp. 494–497, 2014.

[105] J.E. Davies, "On the use of dental ceramics as a possible second-line approach to accident irradiation dosimetry," *Radioprotection*, vol. 14, pp. 89–97, 1979.

[106] I.K. Bailiff, V. Correcher, A. Delgado, *et al.*, "Luminescence characteristics of dental ceramics for retrospective dosimetry: A preliminary study," *Radiat. Prot. Dosim.*, vol. 101, pp. 519–524, 2002.

[107] I. Veronese, A. Galli, M.C. Cantone, *et al.*, "Study of TSL and OSL properties of dental ceramics for accidental dosimetry applications," *Radiat. Meas.* vol. 45, pp. 35–41, 2010.

[108] T. Geber-Bergstand, C. Berhardsson, S. Mattsson, *et al.*, "Retrospective dosimetry using OSL of tooth enamel and dental repair materials irradiated under wet and dry conditions," *Radiat. Environ. Biophys*, vol. 51, pp. 443–449, 2012.

[109] D. Ekendahl, L. Judas and L. Sukupova, "OSL and TL retrospective dosimetry with a fluorapatite glass-ceramic used for dental restoration," *Radiat. Meas.*, vol. 58, pp. 138–144, 2013.

[110] N.A. Kazakis, N.C. Tsirliganis and G. Kitis, "Preliminary thermoluminescence and optically stimulated luminescence investigation of commercial pharmaceutical preparations towards the drug sterilization dosimetry," *Appl. Radiat. Isot.*, vol. 9, pp. 79–91, 2014.

[111] S. Sholom and S.W.S. McKeever, "Emergency EPR and OSL dosimetry with table vitamins and minerals," *Radiat. Prot. Dosim.*, vol. 172, pp. 139–144, 2016b.

[112] S.N. Menon, A.K. Singh, S.Y. Kadam, *et al.*, "OSL studies of commonly available medicines for their use as retrospective dosimeters," *Radiat. Meas.*, vol. 101, pp. 7–12, 2017.

[113] T. Geber-Bergstrand, C. Bernhardsson, M. Christiansson, *et al.*, "Desiccants for retrospective dosimetry using optically stimulated luminescence (OSL)," *Radiat. Meas.* vol. 78, pp. 17–22, 2015.

[114] R.M. Bailey, G. Adamiec and E.J. Rhodes, "OSL properties of NaCl relative to dating and dosimetry," *Radiat. Meas.*, vol. 32, pp. 717–723, 2000.

[115] D. Ekendahl and L. Judas, "NaCl as a retrospective and accident dosemeter," *Radiat. Prot. Dosim.*, vol. 145, pp. 36–44, 2011.

[116] K.J. Thomsen, L. Bøtter-Jensen and A.S. Murray, "Household and workplace chemicals as retrospective luminescence dosemeters," *Radiat. Prot. Dosim.*, vol. 101, pp. 515–518, 2002.

[117] C. Bernhardsson, M. Christiansson, S. Matsson, *et al.*, "Household salt as a retrospective dosemeter using optically stimulated luminescence," *Radiat. Environ. Biophys.*, vol. 48, pp. 21–28, 2009.

[118] A. Timar-Gabor and O. Trandafir, "On optically stimulated luminescence properties of household salt as a retrospective dosemeter," *Radiat. Prot. Dosim.*, vol. 155, pp. 404–409, 2013.

[119] D. Ekendahl, P. Rubovic, P. Žlebčík, *et al.*, "Dosimetry with salt in mixed radiation fields of photons and neutrons," *Radiat. Protect. Dosim.*, vol. 178(3), pp. 329–332, 2018.

[120] A. Wieser, Y.H. Göksu, D.F. Regulla, *et al.*, "Limits of retrospective accident dosimetry by EPR and TL with natural materials," *Radiat. Meas.*, vol. 23, pp. 509–514, 1994.

[121] Y.H. Göksu, D.F. Regulla, B. Hietel, *et al.*, "Thermoluminescent dust for identification of irradiated spices," *Radiat. Prot. Dosim.*, vol. 34, pp. 319–322, 1990.

[122] S. Della Monaca, E. Bortolin, P. Fattibene, *et al.*, "A retrospective dosimetry method based on luminescence measurements of food seasonings," *Radioprotection*, vol. 43, p. 190, 2008.

[123] E. Bortolin, C. Boniglia, S. Della Monaca, *et al.*, "Is dust a suitable material for retrospective personal dosimetry?" *Radiat. Meas.*, vol. 45, pp. 753–755, 2010.

[124] J.A. Ademola, C. Woda and E. Bortolin, "Thermoluminescence investigations on tobacco dust as an emergency dosimeter," *Radiat. Meas.*, vol. 104, pp. 13–21, 2017.

## Chapter 10

# TL/OSL Dating

Sheng-Hua Li* and Bo Li†

*Department of Earth Sciences
The University of Hong Kong, Pokfulam Road
Hong Kong, China
shli@hku.hk

†Centre for Archaeological Science
School of Earth & Environmental Sciences
University of Wollongong, Wollongong
NSW 2522, Australia
bli@uow.edu.au

TL/OSL dating has been developed rapidly since it was proposed about 60 years ago. TL dating was mainly applied in fired or heated materials, where the luminescence clock was reset when they were last heated, while OSL dating has been primarily applied to sediments in which the clock was reset to zero when they were last exposed to sunlight. TL/OSL dating has its advantages over other dating methods in both age range and material range, so that it can determine ages that cannot be achieved with other radiometric dating methods. This chapter describes the practical aspects of TL/OSL dating. Commonly used minerals and protocols are described. Dating techniques and methodologies are presented and outlined, and developments in recent years are discussed.

## 10.1. Introduction

The development of nuclear sciences in the 1950s greatly accelerated the study of ionizing radiation dosimetry. Thermoluminescence (TL) signals from dosimeters were used for measuring the ionizing radiation doses. In searching for natural dosimeters, some rock minerals

have shown similar features to TL dosimeters. Their TL signals increase with the accumulated dose, and the signals are stable over thousands years or longer. Such natural dosimeters have then been regarded as chronometers, based on the assumption that the annual irradiation dose (or environmental dose rate) from natural ionizing radiation surrounding the dosimeters is constant. This idea has been successfully applied in dating pottery and heated archaeological and geological materials [1].

Materials composed of minerals, such as pottery, tile and brick, were fired during their manufacturing process. Such a high temperature would cause the trapped electrons in the defects of the minerals to be ejected. After the burial of these archaeological samples, they were exposed to ionizing radiation emitted by the decay of the radioactive elements within the samples and the surrounding materials, e.g. Potassium-40 ($^{40}$K), Rubidium-87 ($^{87}$Rb), and the isotopes in the decay series of Thorium (Th) and Uranium (U). The radiation resulted in creation of free electrons and subsequent trapping of these electrons in the defects inside mineral lattices. Due to the long half-life of these radioactive isotopes, the annual radiation received by the minerals over the geological time of interest can be considered as constant. Since the TL signal is proportional to the number of trapped charges (or the accumulated dose) in the mineral lattice, the TL intensity emitted from the minerals is proportional to the time since they were fired.

In practice, the 'natural' TL signal was measured by heating the samples to a high temperature, e.g. 500°C, during which the TL signal could be recorded through a photomultiplier. Such signals are then compared with those created from a range of known laboratory irradiations. In such a way, the amount of the radiation accumulated during the natural process, the so-called paleodose (P) or equivalent dose ($D_e$) (in units of Gy), is equivalent to the amount of laboratory dose that is able to produce the same TL signal intensity. The TL age A is derived from a simple equation:

$$D_e = \int_0^A \dot{D}(t)dt \tag{1}$$

Table 1. Dose rate conversion factors for U, Th and K. Data from Guérin *et al.* [4].

| Concentration | Dose rate conversion factor (Gy/ka) | | |
|---|---|---|---|
| | alpha | beta | gamma |
| 1 ppm, Uranium | 2.795 | 0.1457 | 0.1116 |
| 1 ppm, Thorium | 0.738 | 0.0227 | 0.0479 |
| 1%, Potassium | | 0.798 | 0.249 |

where $\dot{D}(t)$ is the environmental dose rate as a function of time t. If $\dot{D}$ is constant, the age equation is reduced to $A = D_e/\dot{D}$. The determination of $D_e$ is based on the measurements of the TL signal from the minerals. The environmental dose rate is estimated from analysis of the concentrations of radioactive elements (mainly U, Th and K) in the sample itself and its surroundings, and then converting them into dose rates according to published conversion factors (Table 1). Apart from the radiation particles emitted from the surrounding radioactive elements, a minor component of environmental dose rate is contributed by the cosmic ray flux, which can be estimated based on the elevation, latitude, longitude and burial depth of the sample [2]. The environmental dose rate can also be estimated directly by inserting sensitive artificial dosimeters in the sampling position for a period (e.g., several months or years) and measuring the accumulated doses stored in the dosimeters.

Basic techniques and relevant dosimetry fundamentals associated with TL dating were developed in the 1950–1970s. In the 1960s, TL dating was first introduced to date young geological sediments (e.g. [3]), based on resetting of TL signal by sunlight bleaching. However, TL signals cannot be bleached completely even after prolonged sunlight exposures, which results in a residual dose prior to deposition. This residual brought in uncertainties and difficulties for TL dating of sediments, especially for fluvial or colluvial samples that might be briefly bleached before deposition.

It was not until the middle 1980s that the optically stimulated luminescence (OSL) technique was introduced for dating sediments, which allows directly measuring signals associated with

light-sensitive traps only. The use of OSL for dating sediments (also called optical dating) was introduced in the 1980s using a green laser for stimulation [5]. Following that, the use of infrared stimulated luminescence (IRSL) for K-feldspar was introduced by Hütt *et al.* [6]. Since the OSL signal can be bleached quickly and completely by sunlight, it has become the dominant technique for dating sediments [7].

For luminescence dating to be applicable to geological and archaeological samples, some prerequisites must be met in order to obtain reliable ages. These include:

(1) The measured luminescence signals must be stable over a period equivalent to or longer than the age of the sample. This is largely controlled by the sample's storage temperature (e.g., in burial soil) and trap parameters associated with the luminescence signal. For example, the signals should be stable over tens of millions years to avoid significant age underestimation when attempting to date sediments of one million years old. The stability of a signal is dependent on the trap depth (activation energy) of the associated electron traps. The stability of OSL signals is not as straightforwardly distinguished as TL signals, because it can be affected by several light-sensitive traps with different trap depths (or thermal stabilities). Hence, in practice, a preheat after irradiation is commonly applied to remove any unstable signals and to avoid age underestimation.
(2) The luminescence signals must not be in saturation, a situation in which the signals stop increasing with irradiation dose. The growth of luminescence signals with dose is usually described by a saturating exponential function. In general, quartz OSL signal usually gets saturated at $\sim 100 - 400$ Gy, which places its upper dating limit to less than $\sim 200$ ka unless the environmental dose rates are exceptionally low (e.g., $< 1$ Gy/ka).
(3) The environmental dose rate, or annual dose, did not change with time through the burial period of the sample. Because the environmental dose rate is mainly contributed by the surrounding radioactive elements (mainly U, Th and $^{40}$K), it is

affected by many factors. For example, change of burial conditions (e.g., ground water movement) may result in disequilibrium in the U and Th decay chains. Chemical weathering may also induce the movement of $^{40}$K. Other factors, such as change of ground water level or change of burial depths, may also affect the environmental dose rate. Hence, validating the equilibrium in U and Th decay chains and reliably assessing effective water content are crucial for dating, especially for samples from geochemically active conditions. To deal with this problem, special techniques such as isochron dating and subtraction dating have been developed [8, 9]. These techniques utilize the radiation dose contributed from the radioactive elements (mainly $^{40}$K and $^{87}$Rb) inside the lattice of K-rich feldspars, which are unaffected by the external changes. The isochron age is calculated from the differences in the equivalent doses and internal dose rates of quartz and/or K-feldspar grains extracted from the same sample.

(4) A 'zeroing' event resets the luminescence signals to zero or a known constant level, and this event must relate closely to the age of the samples. For example, manufacturing pottery is such an event which resets the luminescence signals to zero. Hence, the ages of pottery are the times since they were manufactured or fired. Similar heating events can be applied to lava baked layers, burnt flints, etc. Sunlight bleaching is the resetting event for OSL dating. When minerals are exposed to sunlight prior to deposition, their OSL signals can be effectively zeroed in a short time ranging from a few seconds to several hours. Therefore, luminescence age of a sediment is the time since it was last exposed to sunlight. Another zeroing event is the crystallization of the minerals, in which case the luminescence age is the time since the mineral crystalized or re-crystalized.

The commonly applied natural dosimeters (minerals) for luminescence dating are quartz and feldspars. Other minerals, such as zircon, calcite, flint, etc., have also been used but less commonly. Quartz and feldspars are the most commonly occurring natural minerals on earth, so they are usually present in most objects with a high abundance.

Therefore, luminescence dating has advantages in dating targets over other radiometric dating methods. Apart from that, luminescence dating has an age range that cannot be covered by the other dating methods. It can be applied beyond the oldest limit of radiocarbon dating ($\sim$50,000 years) and below the youngest limits of many other radiometric dating methods. The age range and material range make luminescence dating play an important role in archaeological and geological studies.

Because quartz and feldspars have different luminescence properties, e.g., thermal stability, saturation dose level and sunlight bleaching rate, they have their own advantages and disadvantages in dating. First, quartz has the advantages in having fast and complete bleaching of its OSL signals, while the signals from feldspars usually require much longer time (several hours or more) to be bleached. Hence, quartz is more suitable than feldspar for dating sediments that were briefly exposed to sunlight. Second, K-feldspar has advantages in its IRSL signals having higher saturating doses than the OSL signals of quartz (Fig. 1), so K-feldspar is in theory suitable for dating older samples. However, the luminescence signals from feldspar suffer from a malign effect, so-called anomalous fading

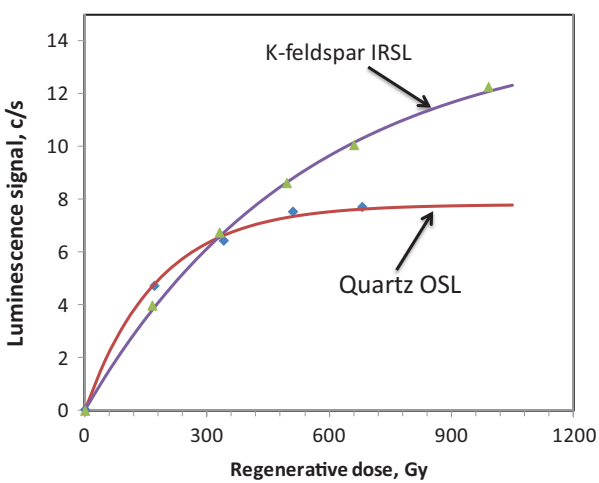


Fig. 1. Typical dose response curves of quartz OSL and K-feldspar IRSL.

[10, 11] — a phenomenon of leaking trapped charges at a much faster rate than expected from kinetic considerations, which may result in significant age underestimation. Another difference between quartz and K-feldspar is the internal dose rate. Different from the negligible internal radioactivity in quartz, sand-sized K-feldspar grains have a considerable internal beta dose rate from the radioactive decay of $^{40}$K and $^{87}$Rb inside the grains. Hence, K-feldspar grains suffer less from the effect of variations in the external dose rate (from beta, gamma and cosmic radiation, including any changes in water content).

## 10.2. $\mathbf{D_e}$ measurement procedures

In luminescence dating, $D_e$ is estimated by comparing the TL/OSL signals induced by natural irradiation with those created by laboratory irradiation. In practice, the samples are subjected to a preheat at an elevated temperature for a period prior to OSL measurement, to remove any thermally unstable signals e.g. [12, 13]. Such a preheat procedure is also necessary for transferring charges from shallow traps into the deep traps, a process occurring during the natural process [14]. Several techniques have been developed for estimation of $D_e$, including multiple-aliquot, single-aliquot and single-grain techniques.

### 10.2.1. *Multiple-aliquot technique*

The multiple 'aliquot' — each composed of several hundred or thousand grains — technique was originally developed for TL dating [1, 7]. Two methods have been developed: additive-dose and regenerative-dose methods. The additive-dose method was firstly used in 1960s for TL dating [15]. In this method, the natural sample is divided into several groups, and then each of the groups is given a different laboratory dose (including a zero dose for measuring the natural signal, N). The TL or OSL signals from these sub-samples are then measured and plotted against the corresponding laboratory doses ($\beta_1, \beta_2, \beta_3 \ldots$) to establish an additive-dose growth curve. The $D_e$ value will then be estimated by extrapolating the curve to a background level (Fig. 2a). The additive-dose method works best

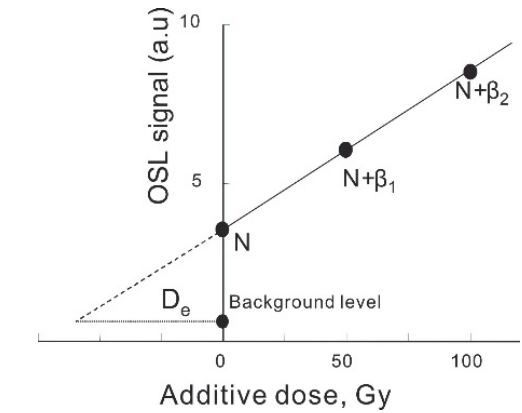


(a)

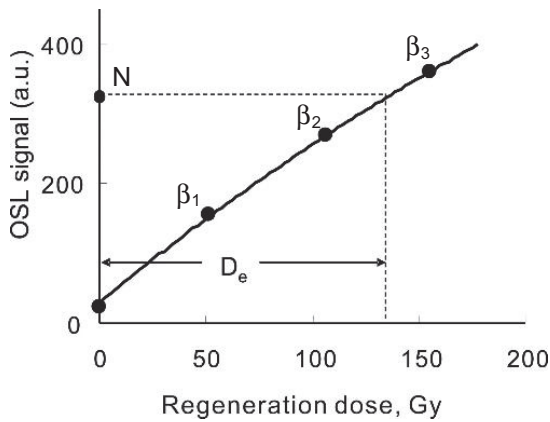


(b)

Fig. 2. Illustrations of the additive-dose method (a) and regeneration method (b) Each data point represents the average of a group of aliquots treated in the same way.

when the TL or OSL signal lies on the linear part of the dose response curve (DRC). However, it may introduce a significant error because of an inappropriate use of a fitting function, if the samples have $D_e$ values in the non-linear range of DRC.

To overcome the problem of the additive-dose method and to deal with non-linear DRC, the regenerative-dose method was proposed [16]. In this method, the aliquots of natural samples are first

measured to observe the natural signals. After that, they are given different laboratory doses to regenerate luminescence signals. A DRC is then obtained by plotting the regenerated signals against the corresponding regenerative doses. The $D_e$ can be calculated from the horizontal intersection of the natural signal level and the DRC (Fig. 2b). The advantage of this method is that it avoids the problem of extrapolation. Hence, it can be applied to samples whose $D_e$ are in the non-linear response region. The drawback of this method, however, is that it becomes inaccurate if there is a significant sensitivity change between the measurement of the natural signal and the regeneration signals, which has been commonly observed as a result of bleaching, preheating or laboratory irradiation, e.g. [14].

One of the most critical drawbacks of the multiple-aliquot methods is that all aliquots are assumed to behave identically in terms of luminescence sensitivity and their corresponding dose response. However, this assumption is usually not valid, especially for quartz [17–19]. In addition, a large number of aliquots are necessary to obtain a single $D_e$ value. Given its drawbacks compared to the single-aliquot method, the multiple aliquot technique appears to have been abandoned for nearly two decades. It is not until recently that several studies have demonstrated its special merit for dating samples that are not suitable for single-aliquot method (see next section). Lu *et al.* [20] proposed a modified multiple-aliquot regenerative-dose (MAR) method for quartz OSL, in which a test dose signal ($T_x$) is used to normalize the inter-aliquot differences in the quartz OSL signals. The sensitivity-corrected natural signal ($L_n/T_n$) was then projected onto the DRC established using the sensitivity-corrected regenerative-dose signal ($L_x/T_x$) obtained using multiple aliquots. This new MAR method was successfully applied to their quartz samples and produced reliable ages up to ∼130 ka. More recently, Li *et al.* [21] proposed an improved MAR method for IRSL dating of feldspar, based on the concept of the regenerative-dose normalization (re-normalization) procedure, developed by Li *et al.* [22–24] for establishing a standardized growth curve (SGC). They demonstrated that this method does not only maintain the advantages of the multiple-aliquot method over the single-aliquot method, but also overcomes

the difficulty of normalizing the inter-aliquot scattering, and, hence, may be applied routinely for $D_e$ determination for feldspars.

### 10.2.2. *Single-aliquot technique*

Given the problems encountered in the multiple-aliquot technique and the non-destructive nature of the OSL measurement, several single-aliquot methods based on repeated measurements on the same aliquot have been proposed [5]. Compared to the multiple-aliquot technique, the single-aliquot technique has the following advantages:

(1) A single $D_e$ value can be obtained from one single aliquot, so it allows the assessment of the $D_e$ variation among different aliquots from the same sample, which is useful for detecting samples that were either insufficiently bleached prior to their burial [25, 26] or suffer from post-depositional mixture or bioturbation.
(2) Normalization is not needed since all measurements are conducted on the same aliquot. Hence, the problem of inter-aliquot variation has been avoided, and higher precision can be achieved than in the multiple-aliquot method.
(3) Only a small amount of material is needed to obtain a single $D_e$ value.

#### 10.2.2.1. *Single-aliquot additive-dose method*

The single-aliquot additive-dose method (SAAD) method was firstly proposed by Duller (1991) for measuring feldspar IRSL, and it was later developed by others e.g. [27–30]. In this method, a single aliquot was first preheated and then given a short exposure (0.1 s) to IR stimulation (so-called 'short shine') in order to minimize the optical depletion of IRSL signals. It was then given a laboratory dose prior to another preheat and short shine being conducted again. Such a cycle of dose, preheat and short shine was repeated several times to establish an additive DRC. The signal loss due to the preheat and short shine through the sequence was corrected for using a decay factor, which is obtained by repeating the preheat and short shine without dosing several times. The $D_e$ value can be estimated by extrapolating the corrected growth curve (Fig. 3a).

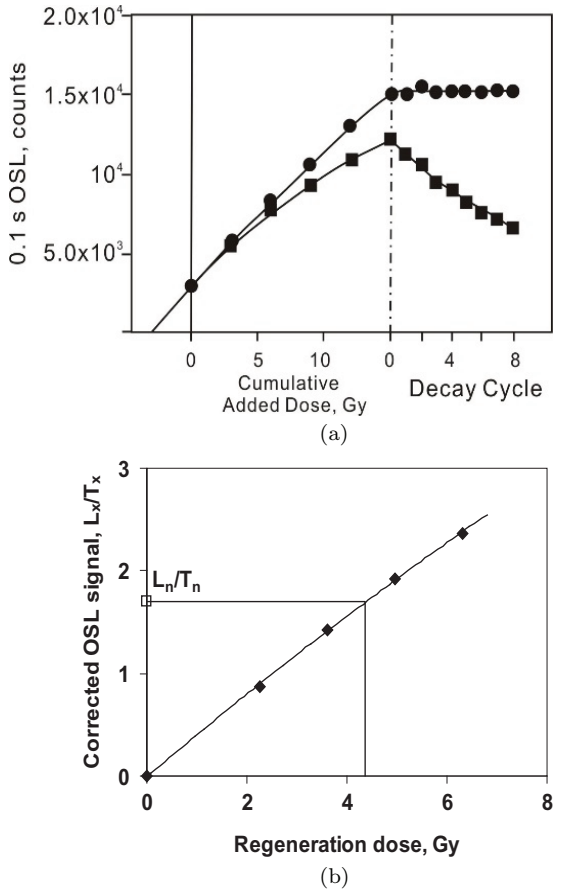


Fig. 3. (a) Example of the SAAD method. The filled squares are the measured OSL signal. The filled circles are decay-corrected signal. The last eight data points are obtained from preheat and short shine measurement cycles without giving any dose (data from Murray *et al.* [28]). (b) Example of the SAR method. The full diamonds are the sensitivity-corrected regenerative-dose OSL signals ($L_x/T_x$). The empty square is the sensitivity-corrected natural OSL signal ($L_n/T_n$)

One of the drawbacks of the SAAD method is that it is assumed that there are no sensitivity changes during the whole measurement procedure; this is, however, unlikely for most samples, especially for quartz whose sensitivity has a large dependence on dosing and preheating [14]. Another drawback of this method is that the correction

factor (i.e., decay rate) measured at the end of the sequence may not be the same as those for the previous cycles. Finally, extrapolation is used in this method, which may result in a large error if the $D_e$ value lies in the non-linear range of DRC. The SAAD method was systematically investigated by Stokes *et al.* [31] for dating quartz, and a 64% failure rate was reported.

10.2.2.2. *Single-aliquot regenerative-dose method*

Although introduced in early 1990s [32], the application of the single-aliquot regeneration method has been hampered by sensitivity changes occurring during the measurement process. It was not until the late 1990s that a breakthrough was made for the development of a reliable procedure, so-called 'single-aliquot regenerative-dose' (SAR) procedure [33–35]. An outline of the SAR protocol is given in Table 2. The key feature of this procedure is the means of monitoring and correcting for the sensitivity changes that accompanied the repeated measurement cycles, which is achieved by measuring a test dose signal ($T_n$ or $T_x$) following each measurement of natural and regeneration signals ($L_n$ or $L_x$). DRC can then be constructed using the sensitivity-corrected OSL signal ($L_x/T_x$) from the regeneration doses, and $D_e$ is estimated from the interception of sensitivity-corrected natural signal ($L_n/T_n$) on the DRC (Fig. 3b).

In the SAR protocols, a zero dose is usually measured to check the extent of 'recuperation' — expressed as the ratio between the sensitivity-corrected signal for zero dose and the natural signal — caused by retrapping of charges from thermally unstable and optically insensitive traps to optically sensitive OSL traps as a result of preheat [7, 36]. Murray and Wintle [35] have suggested that the recuperation should not exceed 5 %. Apart from measuring the zero dose, a repeat dose taken to be the same as one of the non-zero doses, is also measured to check the robustness of sensitivity change correction. If the sensitivity is well corrected, the ratio between the sensitivity-corrected signals for the two identical doses — so-called 'recycling ratio' — should be statistically indistinguishable. Murray and Wintle [35] suggested that a recycling ratio within the range of $1.0 \pm 0.1$ should be acceptable.

Table 2. The single-aliquot regenerative-dose (SAR) protocol.

| Step | Treatment | Observed |
|---|---|---|
| 1 | Regenerative dose, $D_i^a$ | |
| 2 | Preheat | |
| 3 | OSL measurement | $L_n$ or $L_x$ |
| 4 | Test dose, $D_t$ | |
| 5 | Preheat or cut-heat | |
| 6 | OSL measurement | $T_n$ or $T_x$ |
| 7 | Return to step1 | |

[a]For the 'natural' sample, i = 0 and $D_0 = 0$. The whole sequence is repeated for several regenerative doses including a zero dose and a repeat dose.

The suitability of the SAR protocol is usually tested by checking if there is any dependence of $D_e$ upon preheat temperatures, the so-called preheat plateau test [33, 35]. This can be done by measuring the $D_e$ values using a range of preheat temperatures in step 2 (Table 2). A preheat temperature within a 'plateau' region where there is no systematic change in $D_e$ values, is considered as appropriate. In addition to the preheat plateau test, the accuracy of $D_e$ can be tested using a dose recovery experiment [33, 34]. This test involves giving a known laboratory dose to the grains whose natural signals have been bleached (either using sunlight or laboratory light sources) prior to any significant thermal treatment. This given dose is then treated as an 'unknown' dose and measured using the SAR protocol. Failure in a dose recovery test is an indication that the SAR procedure is likely to be unreliable. However, a success in dose recovery does not necessarily guarantee a reliable determination of natural dose, because of the distinctive differences between laboratory irradiation and natural irradiation, such as dose rate, trapping possibility, retrapping of electrons and competition among different traps e.g. [37–39].

The SAR protocol had originally been proposed for quartz OSL, but it was subsequently applied to IRSL and post-IR IRSL (pIRIR) measurements of feldspars [40–42]. The SAR procedure has now been widely applied in optical dating of sediments [43–48].

### 10.2.3. *Single-grain technique*

In the multiple and single aliquot techniques, up to hundreds or thousands grains are mounted on the same disc and measured simultaneously. The results obtained are thus a mean (or weighted mean) of all the grains, and any information on the variability among individual grains is absent. For this reason, the single-grain technique has been developed [18, 34, 49]. With the advance of luminescence instrumentation, single-grain measurements can be conducted using automated Risø luminescence readers equipped with a green laser (532 nm) and/or an IR laser [50] for precisely locating and stimulating individual grains. Sand-sized mineral grains can be mounted onto a single grain disc, such as gold-plated aluminum discs drilled with 100 holes and each 300 $\mu$m in diameter and 300 $\mu$m deep [51], where each grain hole can hold one grain of $180 - 212\,\mu$m in diameter or several grains of smaller sizes.

Compared to the multiple-grain techniques (i.e., single aliquot or multiple aliquot methods), the single-grain technique has several advantages:

(1) The variability and distribution pattern of single-grain $D_e$ values provides information about the extent to which the grains were sufficiently bleached prior to deposition, and it can also provide insights into post-depositional mixture or bioturbation that can affect the stratigraphic integrity of a deposit.
(2) It can provide detailed information on the variation in luminescence behaviors among individual grains [52], such as thermal stabilities [53] and anomalous fading [54], which may ultimately influence the reliability of $D_e$ estimation.
(3) It is possible to identify and reject poorly behaved grains with aberrant luminescence characteristics that may result in erroneous $D_e$ value.

Therefore, the single-grain technique is especially useful to deal with complex depositional environments, which are usually associated with archaeological sites. In fact, the development of single-grain dating has been largely motivated by dating key archaeological

sites [18, 19, 49, 55, 56]. One of the key findings from single-grain analysis is that the luminescence characteristics of individual grains are highly variable, so that some of the grains are unsuitable for $D_e$ determination [17, 19, 34, 57, 58]. A series of criteria has been proposed to identify and discard the 'aberrant' grains and to allow $D_e$ determination based on only the 'well-behaved' grains [13, 59]. There are three groups of commonly applied criteria:

(1) signal-related criteria:
   (a) whether test-dose response for the natural dose ($T_n$) is more than 3 sigma above the background (BG) [59]
   (b) relative standard error of $T_n$ [60]
   (c) fast ratio of $T_n$ [61]

(2) growth-curve-related criteria:
   (a) recycling ratio [13]
   (b) IR-depletion ratio [62]
   (c) recuperation [13]
   (d) goodness of fit [63]
   (e) shape of growth curve [64, 65]
   (g) thermo-depletion ratio [53]

(3) $D_e$-related criteria:
   (a) methods used for $D_e$ determination (interpolation or extrapolation)
   (b) relative standard error of $D_e$

Among the above criteria, the proportion of grains being rejected by each of them is highly variable from sample to sample. In many cases, 80% or more of the measured grains could be rejected, and most of them are usually rejected by the signal-related criteria (i.e., the measured signals are too dim to be reliably measured).

Another crucial step involved with single-grain measurements is statistical analysis, since a large number of $D_e$ values are usually obtained, and each of these $D_e$ values may vary significantly in their values and associated uncertainties. Therefore, a variety of statistical 'age' models were developed to identify and combine the $D_e$ values for the population of grains related most closely to the

event of interest [34, 66, 67]. These include the Central Age Model (CAM) for calculating the weighted mean $D_e$ by taking account of any overdispersion for samples fully bleached by sunlight at the time of deposition and not mixed subsequently, the Minimum Age Model (MAM) for samples that may have been partially or heterogeneously bleached prior to deposition, and Finite Mixture Model (FMM) for dealing with samples with discrete $D_e$ components (e.g., samples with post-depositional mixture).

## 10.3. Recent advances

Over the last decade, attempts have been made to extend the time range of optical dating, focusing on exploiting a variety of light-sensitive and stable traps that are saturated at higher doses. Multiple methods involving measuring different kinds of signals in different ways have been proposed, including thermally-transferred OSL (TT-OSL) and violet stimulated luminescence (VSL) from quartz, post-IR IRSL, pulsed-IRSL and radioluminescence from feldspar. These techniques have their own advantages and disadvantages, so they may be applied in different situations but are not universally applicable to all samples.

### 10.3.1. *Post-IR IRSL dating of feldspars*

The anomalous fading phenomenon has hampered the application of luminescence dating of feldspar for many years. Recent progress in understanding anomalous fading of feldspar has raised the prospect of isolating a non-fading IRSL component for dating feldspars. This is based on the observation that the initial part of the IRSL decay curve has a higher anomalous fading rate than that for the later part (Fig. 4) [42]. This observation implies that the IRSL signal observed at the initial stimulation is mainly a result of tunneling recombination of spatially close donor-acceptor pairs, while the signal observed at the later part is the result of recombination of spatially distant donor-acceptor pairs [68]. Hence, by first bleaching the feldspar grains using IR photons at 50°C and then measuring the pIRIR signal at an elevated temperature ($> 200$°C), it is possible to

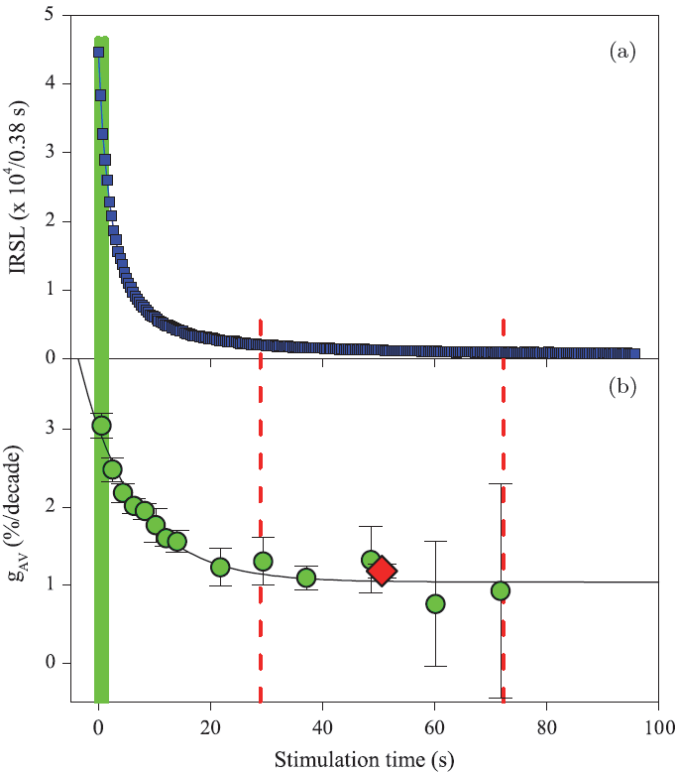


Fig. 4. (a) Typical IRSL decay curve (at 50°C) from K-feldspar. (b) Anomalous fading rate, expressed as g-value (i.e., calculated as the percentage loss of signal when stored in dark at room temperature per decade of time) [1], plotted as a function of stimulation time. Figure from Thomsen *et al.* [42].

preferentially sample the charges from the traps that suffer less from fading. Different versions of pIRIR procedures have been developed, including a two-step [69, 70] and a multiple elevated temperature (MET) post-IR IR stimulation procedure [71].

#### 10.3.1.1. *Two-step pIRIR procedure*

The two-step pIRIR method [42] involves an IRSL bleach at a lower temperature (T1) and a subsequent IR stimulation at a higher temperature (T2) (Table 3). Since then, different versions of the pIRIR method using different combinations of IR stimulation

Table 3. The two-step pIRIR and multi-elevated-temperature pIRIR (MET-pIRIR) protocols.

| | Two-step pIRIR protocol | | MET-pIRIR protocol | |
|---|---|---|---|---|
| Step | Treatment | Observed | Treatment | Observed |
| 1 | Regenerative dose, $D_i^a$ | | Regenerative dose, $D_i^a$ | |
| 2 | Preheat[b] | | Preheat[b] | |
| 3 | IRSL at T1 for 200 s | $L_{x(50)}$ | IRSL at 50°C for 100 s | $L_{x(50)}$ |
| 4 | IRSL at T2 for 200 s | $L_{x(T)}$ | IRSL at 100°C for 100 s | $L_{x(100)}$ |
| 5 | Test dose, $D_t$ | | IRSL at 150°C for 100 s | $L_{x(150)}$ |
| 6 | Preheat[b] | | IRSL at 200°C for 100 s | $L_{x(200)}$ |
| 7 | IRSL at T1°C for 200 s | $T_{x(50)}$ | IRSL at 250°C for 100 s | $L_{x(250)}$ |
| 8 | IRSL at T2°C for 200 s | $T_{x(T)}$ | IRSL at 300°C for 100 s | $L_{x(300)}$ |
| 9 | IR at 325°C for 40 s | | Test dose, $D_t$ | |
| 10 | Return to step 1 | | Preheat[b] | |
| 11 | | | IRSL at 50°C for 100 s | $T_{x(50)}$ |
| 12 | | | IRSL at 100°C for 100 s | $T_{x(100)}$ |
| 13 | | | IRSL at 150°C for 100 s | $T_{x(150)}$ |
| 14 | | | IRSL at 200°C for 100 s | $T_{x(200)}$ |
| 15 | | | IRSL at 250°C for 100 s | $T_{x(250)}$ |
| 16 | | | IRSL at 300°C for 100 s | $T_{x(300)}$ |
| 17 | | | IR at 325°C for 100 s | |
| 18 | | | Return to step 1 | |

[a]For the 'natural' and sunlight-bleached samples, $i = 0$ and $D_0 = 0$. The whole sequence is repeated for several regenerative doses including a zero dose and a repeat dose.
[b]For the pIRIR(50, 225) method [70], the preheat temperature is 250°C. For the pIRIR(50, 290) [69] and MET-pIRIR method [72], the preheat temperature is 320°C.

temperatures (expressed as 'pIRIR(T1, T2)') have been proposed. Buylaert *et al.* [70] first tested the pIRIR(50, 225) procedure and found that the fading rate of the $pIRIR_{225}$ signal is significantly smaller than for the 50°C IRSL signal. However, fading correction is still needed, albeit the uncertainty associated with fading correction is largely reduced. Thiel *et al.* [69] proposed a modified pIRIR procedure to further reduce the anomalous fading, which adopted a higher preheat temperature (320°C) and a higher temperature for measuring the pIRIR signal at (T2 = 290°C) (pIRIR(50, 290)). They claimed that, although a small fading rate (∼1.1 %/decade)

was observed, the $pIRIR_{290}$ signal of their loess sample does not suffer from anomalous fading, deduced from the observation that the natural pIRIR(50, 290) signal is consistent with the saturation level of the laboratory dose response curve.

The $pIRIR_{290}$ method was subsequently applied in a number of studies, many of which produced reliable ages without fading correction [73]. However, recent studies suggest that the $pIRIR_{290}$ signal from some samples may still suffer from significant fading (Fig. 5a), especially for samples from volcanic regions [74]. It is therefore suggested that a laboratory fading test should be routinely conducted to check the reliability of pIRIR dating.

#### 10.3.1.2. *Multi-step pIRIR procedure*

Different from the two-step pIRIR procedure, Li and Li [75] proposed a modified pIRIR procedure (Table 3) involving multiple IR stimulations at different stimulation temperatures, so-called multiple-elevated-temperature pIRIR (MET-pIRIR) procedure. It was based on the observation that a non-fading IRSL signal may be isolated by progressively increasing the stimulation temperature from 50 to 300°C in steps of 50°C, suggesting that the MET-pIRIR protocol can achieve a non-fading component. The reliability of this protocol was tested using various sedimentary samples from Northern China deposited in the last ∼300 ka [73], and the MET-pIRIR ages obtained at 200 and 250°C are consistent with independent or quartz OSL age.

An advantage of the MET-pIRIR protocol over the two-step pIRIR protocol is that the anomalous fading can be demonstrated in an Age–Temperature (A–T) plot, in which the ages are plotted against IR stimulation temperatures (Fig. 5b). In such plot the age or $D_e$ usually increases with the stimulation temperature, and a plateau can be reached at higher temperatures (e.g. above 200°C [71] or above 250°C for older samples [76]), indicating that a non-fading component was isolated at elevated temperatures. An absence of a plateau may, in turn, indicate that a non-fading signal may not be isolated. Another advantage of the A-T plot is that it can be used as an indicator of insufficiently bleached samples, because the pIRIR

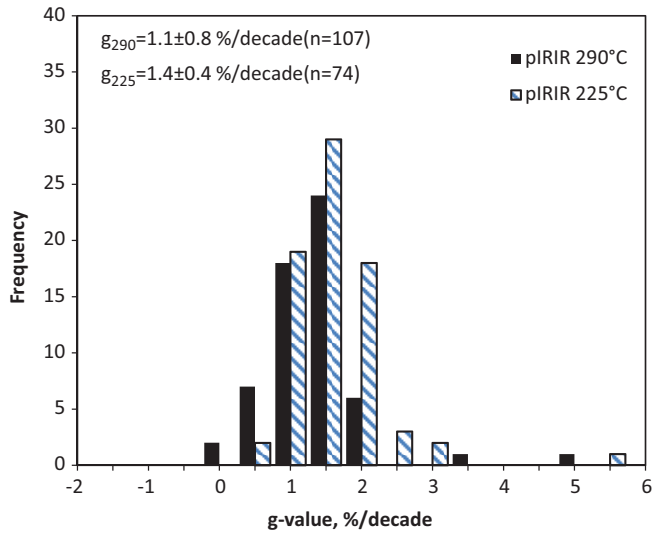


(a)

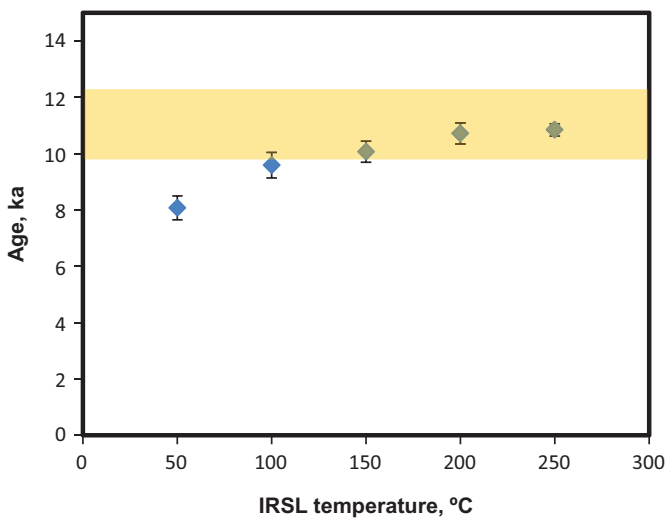


(b)

Fig. 5. (a) A summary of the g-values measured using pIRIR(50, 290) and pIRIR(50, 225) methods (modified from Li *et al.* [73]). (b) An example of A-T plot for the MET-pIRIR signals from sample SY3 (data from Li and Li [71]). The yellow band represents the quartz OSL age, which is considered as reliable.

signals obtained at higher temperatures are more difficult to bleach than the low temperature signals.

### 10.3.2. *IR-RF dating of feldspars*

Different from the most commonly applied techniques of TL and OSL, where luminescence signals are stimulated after irradiation, an alternative way of dose measurement is called infrared-radiofluorescence (IR-RF) or radioluminescence (RL). This is the emission of infrared photons at 1.44 eV (855 nm) (rather than stimulation by infrared photons) during the process of irradiation ($\beta$-, $\gamma$-irradiation, or X-rays) [77, 78]. The IR-RF of feldspars was explained as being the result of luminescent transition of electrons into optically active traps, so it allows a direct determination of trapped electrons [79]. Because only electron traps are involved in the IR-RF process, it has advantages over the TL/OSL method that involves both traps and luminescence centers. Another main advantage of IR-RF is that laboratory fading tests (storage over periods of several months at room temperature) demonstrated that it does not suffer from anomalous fading [80], so it can potentially produce reliable ages without fading correction.

$D_e$ measurement using IR-RF is achieved using a procedure similar to the single-aliquot regenerative dose (SAR) procedure [81, 82], which involves 3 main measurement steps: (1) irradiation on top of the natural dose to measure the IR-RF signal, (2) optical bleaching (using solar simulator) to empty the traps, and (3) a second irradiation is performed to measure IR-RF from regenerative dose. The intensity of IR-RF is proportional to the density of empty traps, so in contrast to the TL/OSL signal where the signal intensity grows with radiation dose, the IR-RF signal decays in intensity as a function of dose.

The SAR IR-RF procedure usually yields two curves, one is the natural signal and the second is the regenerated signal. $D_e$ can be calculated either by fitting a stretched exponential function to the regenerated signal and projecting the natural signal onto the fitted curve [81], or by sliding both curves onto each other [82, 83].

Despite its great potential for overcoming anomalous fading, the study and application of IR-RF for dating has been limited due to the lack of commercial instruments capable of measuring it. It is not until recently that commercial instruments from luminescence instruments companies (Risø and Freiberg Instruments) provided optional function for IR-RF measurements [83, 84]. Previous studies focused on testing the IR-RF method using samples that were independently dated with other methods, and both agreement and disagreement with independent ages were reported [82, 83]. Therefore, systematic studies on the IR-RF, in terms of thermal and athermal stability, bleachability, sensitivity change and reproducibility, are yet to be conducted to establish a reliable dating protocol.

### 10.3.3. *TT-OSL dating on quartz*

The thermally transferred OSL (TT-OSL) signal refers to the signal measured by first emptying the OSL traps and then heating the sample to an elevated temperature to thermally transfer electrons from deeper and light insensitive traps into the empty OSL traps. It is sometimes also referred to as recuperated OSL (ReOSL). Two types of TT-OSL have been defined: recuperation and basic transfer [7]. The former refers to the charges originally trapped in the main OSL traps, which are transferred into a refuge trap by light exposure and then recycled into the OSL traps again by an additional heating, so this signal is dose-dependent. The basic transfer refers to the charges that are originally from light-insensitive traps and are transferred into the OSL traps; it is thus unsuitable for dating sediments.

Utilizing TT-OSL signal for dating quartz was firstly proposed by Wang *et al.* [86], who found that the TT-OSL signal of silt-sized quartz grains extracted from Chinese loess continued to grow to many thousands of Gy (Fig. 6b), much higher than that of the OSL signal of the same sample (which saturated at a few hundred Gy) (Fig. 6a), enabling them to date back to the Brunhes/Matuyama (B/M) boundary (∼780 ka).

The TT-OSL dating technique was originally based on a multiple aliquot regenerative dose procedure [86, 87]. For each of the natural

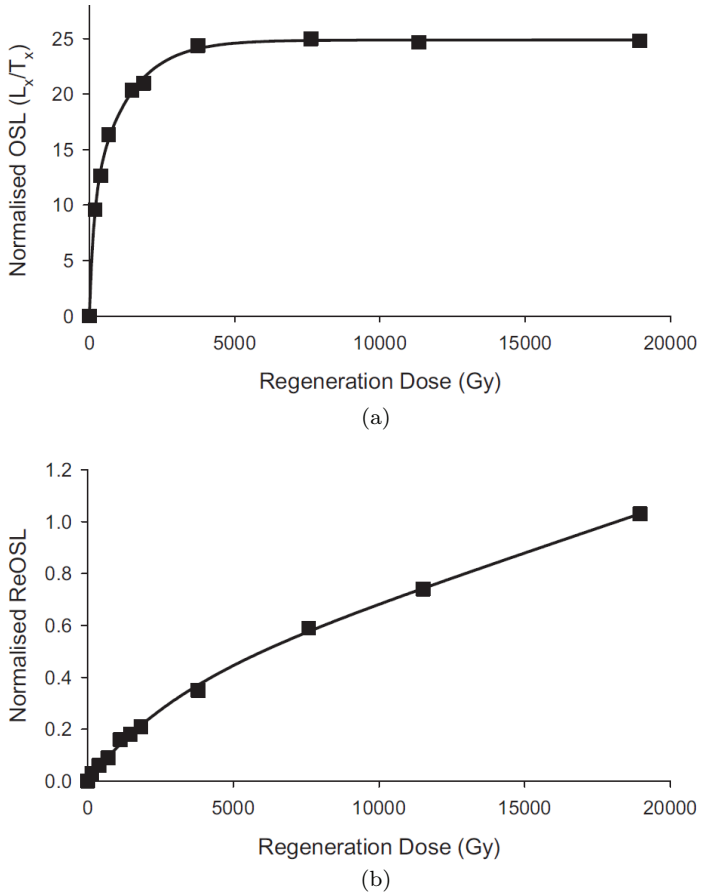


Fig. 6. Dose response curves for a sample of quartz extracted from Luochuan, China. (a) OSL signal measured using a multiple aliquot regenerative dose procedure; (b) TT-OSL measured using a multiple aliquot regenerative dose procedure. Figure from Duller and Wintle [85].

and regeneration points, two measurement stages are involved (Table 4). In the first stage, the main OSL signal is removed using a blue bleaching or BLSL measurement (step 3). After that, the sample is heated to 260°C for 10 s (step 4) to thermally transfer charges from light insensitive traps into the empty OSL traps, before the resulting TT-OSL signal ($L_{TT\text{-}OSL}$) is measured (step 5). This signal is corrected for sensitivity change by measuring the test dose OSL

Table 4. TT-OSL dating protocol of Wang *et al.* (2006a).

| Step | Treatment | Observed | Purpose |
|---|---|---|---|
| Stage 1 | | | |
| 1 | Dose | | |
| 2 | Preheat at 260°C, 10 s | | |
| 3 | BLSL at 125°C, 270 s | | Empty OSL traps |
| 4 | Preheat at 260°C, 10 s | | Thermally transfer charges into OSL traps |
| 5 | BLSL at 125°C, 90 s | $L_{TT\text{-}OSL}$ | Measure TT-OSL signal |
| 6 | Test dose | | |
| 7 | Preheat at 220°C, 20 s | | |
| 8 | BLSL at 125°C, 90 s | $T_{TT\text{-}OSL}$ | Measure test dose signal |
| Stage 2 | | | |
| 9 | Annealing to 300°C, 10 s | | Thermally transfer remnant TT-OSL signals |
| 10 | BLSL at 125°C, 90 s | | Remove remnant TT-OSL signals |
| 11 | Preheat at 260°C, 10 s | | Thermally inducing basic-transferred OSL signals |
| 12 | BLSL at 125°C, 900 s | $L_{BT\text{-}OSL}$ | Measuring BT-OSL intensity |
| 13 | Test dose | | |
| 14 | Preheat at 220°C, 20 s | | |
| 15 | BLSL at 125°C, 90 s | $T_{BT\text{-}OSL}$ | Measure test dose signal for BT-OSL |

signal (step 8, $T_{TT\text{-}OSL}$). Since this TT-OSL signal is expected to be composed of both recuperation and basic transfer — the former is dose dependent and the latter is not — the basic transfer OSL signal needs to be measured and then subtracted from the TT-OSL signal. In stage 2, the basic transfer signal is measured. Firstly, the sample is heated to 300°C for 10 s to thermally transfer any recuperated OSL remaining after stage 1. Then a procedure similar to stage 1 is repeated to measure the basic transfer ($L_{BT\text{-}OSL}$) and corresponding test dose signal ($T_{BT\text{-}OSL}$). The sensitivity corrected recuperated OSL signal can then be calculated using the following equation:

$$\mathrm{ReOSL} = \frac{L_{\mathrm{TT\text{-}OSL}}}{T_{\mathrm{TT\text{-}OSL}}} - \frac{L_{\mathrm{BT\text{-}OSL}}}{T_{\mathrm{BT\text{-}OSL}}} \tag{2}$$

Since the initial development, different versions of these procedures have been proposed and applied to date sediments from various geological settings (see Duller and Wintle [85] for a detailed review of different procedures). Although this technique is very encouraging, the applicability appears to be highly sample and procedure dependent. For example, several studies have suggested that the TT-OSL signal is thermally unstable, which may result in significant age underestimation [88–90]. Another issue of concern is the bleachability of the TT-OSL signal. For example, Jacobs *et al.* [91] found that it would take ∼26 and ∼50 weeks of continuous exposure to direct sunlight to reset the ReOSL and BT-OSL signals for their samples from South Africa, which significantly restricts the range of possible applications of this method.

### 10.3.4. *VSL dating of quartz*

Conventional methods for determining $D_e$ for quartz are based on OSL signals stimulated by blue or green light, i.e., blue-light stimulated luminescence (BLSL) or green-light stimulated luminescence (GLSL). The main traps responsible for BLSL and GLSL have been shown to be associated with the 325°C TL peak [92]. They are also the most optically sensitive traps in quartz, e.g., the initial component (or the 'fast component' [93]) can be bleached down to a negligible level by sunlight in a time as short as tens of seconds. However, the main components of BLSL and GLSL typically saturate at a dose less than ∼200 Gy [34], placing an upper limit of dating using quartz for less than 200 ka, unless the dose rates in sedimentary environments are exceptionally low.

In contrast to the fast-bleaching component that can be sampled by stimulating blue or green light, Jain [94] demonstrated that stimulating quartz using violet light (405 nm) can probe deeper traps associated with the 375°C TL peak [95] that are not accessible by blue or green light. More importantly, the violet stimulated luminescence (VSL) from quartz appeared to grow with dose up to 1,000 Gy or more [95], which has a great potential for increasing the dating range using quartz.

Table 5. VSL protocols for quartz.

| Step | a [94] | b [95] | c [97] |
|---|---|---|---|
| 1 | Regenerative dose | Regenerative dose | Regenerative dose |
| 2 | Preheat 340°C, 10 s | BLSL 280°C, 100 s | Preheat 300°C, 100 s |
| 3 | BLSL 125°C, 100 s | VSL 125°C, 100 s | BLSL 125°C, 100 s |
| 4 | VSL 50°C, 500 s | Test dose | VSL 30°C, 500 s |
| 5 | Test dose | BLSL 270°C, 100 s | Test dose |
| 6 | Cutheat 340°C, 1 s | VSL 125°C, 100 s | Cutheat 290°C, 100 s |
| 7 | BLSL 125°C, 100 s | VSL 280°C, 200 s | BLSL 125°C, 100 s |
| 8 | VSL 50°C, 500 s | Repeat steps 1–7 | VSL 30°C, 500 s |
| 9 | BLSL 500°C, 100 s | | VSL 380°C, 200 s |
| 10 | Repeat steps 1–9 | | Repeat steps 1–9 |

Several procedures have been proposed to measure VSL from quartz, and these are summarised in Table 5. A common feature of these procedures is that the VSL is measured after a BLSL to remove the main OSL component. The first version of the VSL procedure has been proposed by Jain [94], which involves a high preheat temperature at 340°C for 10 s to remove the unstable component that is supposed to correspond to one of the slow components (S3) in BLSL [96]. However, this procedure was subsequently shown to yield large sensitivity changes between the measurements of the natural signal and the following test dose signal, resulting in either large under- or overestimations in $D_e$. To overcome this problem, Ankjærgaard *et al.* [95] combined the blue bleaching and preheat by using a blue bleach (BLSL) at 280°C, which can remove the unstable OSL S3 component and avoid a stringent preheat. This procedure was tested using 9 samples from Netherlands and yielded ages consistent with independent age controls. However, this procedure was subsequently found to be likely to result in significant changes in sensitivity and decay curve shape [97]. As a result, a moderate preheat at 300°C for 100 s was proposed, before the measurement of post-BLSL VSL [97]. The application of this procedure in dating of a palaeosol sequence in Israel and Chinese loess resulted in severe age underestimations [97, 98]. Ankjærgaard *et al.* [98] suggested that this underestimation is due to the change of trapping probability as a

result of the high preheat temperature used. In order to overcome this problem, they proposed a multi-aliquot additive-dose (MAAD) protocol, in which a young sample from the same site is divided into several groups: one group is used to measure natural signals, and the other groups are given different doses in addition to the natural dose to establish an additive dose growth curve. Because the doses are given before any thermal treatment, the trapping probability is expected to be comparable to natural irradiation. The MAAD protocol successfully produced chronology consistent with independent age control for Chinese loess samples up to ∼0.6 Ma [98].

In conclusion, the VSL signal has been shown to have great potential for extending the upper dating range of quartz, but it remains to be tested using more samples from other regions.

### 10.3.5. *Pulsed-IRSL dating of feldspars*

Pulsed-IRSL is the luminescence observed by stimulating in a pulsed way, which is also called time-resolved IRSL (TR-IRSL). The signal is observed during and between short pulses of stimulation (each pulse stimulation could be as short as several $\mu$s) using infrared photons. It has been observed that different traps from different minerals may have different decay rates in their pulsed-stimulated luminescence, which offers a way to distinguish different signals from the same mineral or different minerals. For example, pulsed stimulation offers a means of separating the quartz and feldspar OSL signals for samples that contain both minerals, as the TR-OSL decay of quartz is much slower than that of feldspar [99]. The time-resolved signals from feldspar have been found to be able to separate less-fading signals, as first proposed by Sanderson and Clark (1994). It was observed that different parts of the pulsed OSL signal of feldspar have different fading rates, and anomalous fading might be avoided by selecting those parts of the signal that do not fade [68, 100].

Tsukamoto *et al.* [101] conducted a systematic study on the pulsed-IRSL signal from several samples from Germany and Japan. For each measurement of pulse stimulation, they used a pulse of 100 $\mu$s ('on'-time) and a period between two stimulation pulses of 400 $\mu$s ('off'-time). Such pulsed stimulation was conducted repeatedly

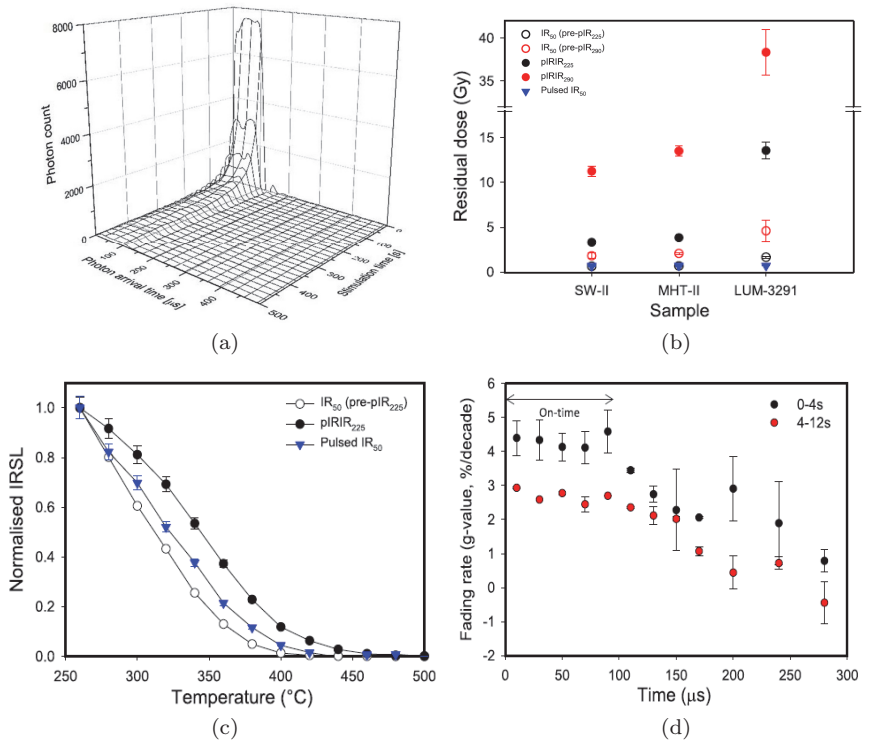


Fig. 7. (a) An example of 3D time resolved IRSL curve of sample MHT-II measured at 50°C for 500 s. (b) Residual doses after 4 h bleaching with a solar simulator for $IR_{50}$ (pre-$pIRIR_{225}$), IR50 (pre-$pIRIR_{290}$), $pIRIR_{225}$, $pIRIR_{290}$ and pulsed IRSL signals. (c) Pulsed annealing test of the IR50 (pre-$pIRIR_{225}$), $pIRIR_{225}$ and pulsed IRSL signals for 0–4s signal integration. (d) Fading rate (g-value) of the two different integration limits, 0–4s and 4–12s of the pulsed-IRSL decay curve for sample MHT-II. Figures are from Tsukamoto *et al.* [101].

for 500 s (corresponding to 1 million IR pulses) until the pulsed-IRSL signals reach a negligible level (Fig. 7a). They tested the bleachability, thermal stability and anomalous fading of pulsed-IRSL based on a SAR procedure, in which the samples were preheated at 250°C for 60 s and stimulated at 50°C for 500 s. By comparing with $pIRIR_{225}$ and $pIRIR_{290}$ signals from the same samples, they found that the pulsed-IRSL has negligible residual doses (Fig. 7b) and similar thermal stabilities (Fig. 7c). More importantly, it was

observed that a non-fading signal could be obtained for signals from the middle part of the decay curve (4–12s) at around ∼200 $\mu$s (∼100 $\mu$s during the off-time) (Fig. 7d). Therefore, compared to the conventional pIRIR signals, the pulsed-IRSL signal is not only able to achieve a non-fading signal, but also offers advantages in dating young samples given much smaller residual doses. However, the technique is yet to be tested using a range of samples of different age ranges and different regions.

In summary, among the techniques described in this chapter, single aliquot and single grain techniques are the most widely applied in OSL dating of sediments. The new techniques developed in recent years have shown advantages and disadvantages, but they are not universally applicable and some of them are still to be tested in different archaeological and geological settings.

## References

[1] M.J. Aitken, "Thermoluminescence Dating," London, Academic press, 1985.

[2] J.R. Prescott and J.T. Hutton, "Cosmic-ray contributions to dose rates for luminescence and ESR dating — large depths and long-term time variations," *Radiation Measurements*, vol. 23, pp. 497–500, 1994.

[3] G.V. Morozov, *The relative dating of Quaternary Ukrainian sediments by the thermoluminescence method*. In *8th International Quaternary Association Congress*. 1968. Paris: U.S. Geological Survey Library, Washington, D.C.

[4] G. Guérin, N. Mercier and G. Adamiec, "Dose-rate conversion factors: update," *Ancient TL*, vol. 29, pp. 5–8, 2011.

[5] D.J. Huntley, D.I. Godfrey-Smith and M.L.W. Thewalt, "Optical dating of sediments," *Nature*, vol. 313, pp. 105–107, 1985.

[6] G. Hütt, I. Jaek and J. Tchonka, "Optical dating: K-feldspars optical response stimulation spectra," *Quaternary Science Reviews*, vol. 7, pp. 381–385, 1988.

[7] M.J. Aitken, "An Introduction to Optical Dating," Oxford, Oxford University Press, 1998.

[8] J.C. Vogel, A.G. Wintle and S.M. Woodborne, "FOCUS: Luminescence dating of coastal sands: Overcoming changes in environmental dose rate," *Journal of Archaeological Science*, vol. 26, pp. 729–733, 1999.

[9] B. Li, S.H. Li, A.G. Wintle and H. Zhao, "Isochron dating of sediments using luminescence of K-feldspar grains," *Journal of Geophysical Research-Earth Surface*, vol. 113, pp. F02026 (1–15), 2008.

[10] A.G. Wintle, "Anomalous fading of thermoluminescence in mineral samples," *Nature*, vol. 245, pp. 143–144, 1973.
[11] N.A. Spooner, "The anomalous fading of infrared-stimulated luminescence from feldspars," *Radiation Measurements*, vol. 23, pp. 625–632, 1994.
[12] S.H. Li, "Removal of the thermally unstable signal in optical dating of K-feldspar," *Ancient TL*, vol. 9, pp. 26–29, 1991.
[13] A.G. Wintle and A.S. Murray, "A review of quartz optically stimulated luminescence characteristics and their relevance in single-aliquot regeneration dating protocols," *Radiation Measurements*, vol. 41, pp. 369–391, 2006.
[14] A.G. Wintle and A.S. Murray, "Luminescence sensitivity changes in quartz," *Radiation Measurements*, vol. 30, pp. 107–118, 1999.
[15] M.S. Tite, "Thermoluminecent dating of ancient ceramics: a reassessment," *Archaeometry*, vol. 9, pp. 155–169, 1966.
[16] A.G. Wintle and D.J. Huntley, "Thermoluminescence dating of ocean sediments," *Canadian Journal of Earth Sciences*, vol. 17, pp. 348–360, 1980.
[17] G.A.T. Duller, L. Bøtter-Jensen and A.S. Murray, "Optical dating of single sand-sized grains of quartz: sources of variability," *Radiation Measurements*, vol. 32, pp. 453–457, 2000.
[18] R.G. Roberts, R.F. Galbraith, J.M. Olley, H. Yoshida and G.M. Laslett, "Optical dating of single and multiple grains of quartz from jinmium rock shelter, northern Australia, part 2, Results and implications," *Archaeometry*, vol. 41, pp. 365–395, 1999.
[19] Z. Jacobs, G.A.T. Duller and A.G. Wintle, "Optical dating of dune sand from Blombos Cave, South Africa: II — single grain data," *Journal of Human Evolution*, vol. 44, pp. 613–625, 2003.
[20] Y.C. Lu, X.L. Wang and A.G. Wintle, "A new OSL chronology for dust accumulation in the last 130,000 yr for the Chinese Loess Plateau," *Quaternary Research*, vol. 67, pp. 152–160, 2007.
[21] B. Li, Z. Jacobs and R.G. Roberts, "An improved multiple-aliquot regenerative-dose (MAR) procedure for post-IR IRSL dating of K-feldspar," *Ancient TL*, vol. 35, pp. 1–10, 2017.
[22] B. Li, R.G. Roberts, Z. Jacobs and S.H. Li, "Potential of establishing a 'global standardised growth curve' (gSGC) for optical dating of quartz from sediments," *Quaternary Geochronology*, vol. 27, pp. 94–104, 2015.
[23] B. Li, R.G. Roberts, Z. Jacobs, S.H. Li and Y.J. Guo, "Construction of a 'global standardised growth curve' (gSGC) for infrared stimulated luminescence dating of K-feldspar," *Quaternary Geochronology*, vol. 27, pp. 119–130, 2015.
[24] B. Li, Z. Jacobs and R.G. Roberts, "Investigation of the applicability of standardised growth curves for OSL dating of quartz from Haua Fteah cave, Libya," *Quaternary Geochronology*, vol. 35, pp. 1–15, 2016.
[25] S.H. Li, "Optical Dating — Insufficiently Bleached Sediments," *Radiation Measurements*, vol. 23, pp. 563–567, 1994.
[26] S.H. Li, "Identification of well-bleached grains in the optical dating of quartz," *Quaternary Science Reviews*, vol. 20, pp. 1365–1370, 2001.

[27] R.B. Galloway, "Equivalent dose determination using only one sample: Alternative analysis of data obtained from infrared stimulation of feldspars," *Radiation Measurements*, vol. 26, pp. 103–106, 1996.

[28] A.S. Murray, R.G. Roberts and A.G. Wintle, "Equivalent dose measurement using a single aliquot of quartz," *Radiation Measurements*, vol. 27, pp. 171–184, 1997.

[29] S.H. Li, M.Y. Tso, K.E. Westaway and G. Chen, "Choice of the most appropriate thermal treatment in optical dating of quartz," *Radiation Protection Dosimetry*, vol. 84, pp. 495–498, 1999.

[30] J.F. Zhang, S.H. Li and M.Y.W. Tso, "Improvement of the equivalent dose determination using aliquots of potassium feldspar," *Radiation Measurements*, vol. 33, pp. 65–71, 2001.

[31] S. Stokes, A.E.L. Colls, M. Fattahi and J. Rich, "Investigations of the performance of quartz single aliquot D-E determination procedures," *Radiation Measurements*, vol. 32, pp. 585–594, 2000.

[32] G.A.T. Duller, "Equivalent dose determination using single aliquots," *Nuclear Tracks and Radiation Measurements*, vol. 18, pp. 371–378, 1991.

[33] A.S. Murray and R.G. Roberts, "Measurement of the equivalent dose in quartz using a regenerative-dose single-aliquot protocol," *Radiation Measurements*, vol. 29, pp. 503–515, 1998.

[34] R.F. Galbraith, R.G. Roberts, G.M. Laslett, H. Yoshida and J.M. Olley, "Optical dating of single and multiple grains of quartz from Jinmium rock shelter, northern Australia, part 1, Experimental design and statistical models," *Archaeometry*, vol. 41, pp. 339–364, 1999.

[35] A.S. Murray and A.G. Wintle, "Luminescence dating of quartz using an improved single-aliquot regenerative-dose protocol," *Radiation Measurements*, vol. 32, pp. 57–73, 2000.

[36] M.J. Aitken and B.W. Smith, "Optical dating — recuperation after bleaching," *Quaternary Science Reviews*, vol. 7, pp. 387–393, 1988.

[37] R.M. Bailey, "Towards a general kinetic model for optically and thermally stimulated luminescence of quartz," *Radiation Measurements*, vol. 33, pp. 17–45, 2001.

[38] R.M. Bailey, "Paper I — simulation of dose absorption in quartz over geological timescales and its implications for the precision and accuracy of optical dating," *Radiation Measurements*, vol. 38, pp. 299–310, 2004.

[39] R.M. Bailey, S.J. Armitage and S. Stokes, "An investigation of pulsed-irradiation regeneration of quartz OSL and its implications for the precision and accuracy of optical dating (Paper II)," *Radiation Measurements*, vol. 39, pp. 347–359, 2005.

[40] J. Wallinga, A. Murray and A. Wintle, "The single-aliquot regenerative-dose (SAR) protocol applied to coarse-grain feldspar," *Radiation Measurements*, vol. 32, pp. 529–533, 2000.

[41] B. Li and S.H. Li, "Luminescence dating of K-feldspar from sediments: A protocol without anomalous fading correction," *Quaternary Geochronology*, vol. 6, pp. 468–479, 2011.

[42] K.J. Thomsen, A.S. Murray, M. Jain and L. Bøtter-Jensen, "Laboratory fading rates of various luminescence signals from feldspar-rich sediment extracts," *Radiation Measurements*, vol. 43, pp. 1474–1486, 2008.

[43] S. Stokes, S. Ingram, M.J. Aitken, F. Sirocko, R. Anderson and D. Leuschner, "Alternative chronologies for Late Quaternary (Last Interglacial-Holocene) deep sea sediments via optical dating of silt-sized quartz," *Quaternary Science Reviews*, vol. 22, pp. 925–941, 2003.

[44] O.B. Lian and R.G. Roberts, "Dating the Quaternary: progress in luminescence dating of sediments," *Quaternary Science Reviews*, vol. 25, pp. 2449–2468, 2006.

[45] F. Preusser, M.L. Chithambo, T. Götte, M. Martini, K. Ramseyer, E.J. Sendezera, G.J. Susino and A.G. Wintle, "Quartz as a natural luminescence dosimeter," *Earth-Science Reviews*, vol. 97, pp. 184–214, 2009.

[46] R.G. Roberts, Z. Jacobs, B. Li, N.R. Jankowski, A.C. Cunningham and A.B. Rosenfeld, "Optical dating in archaeology: thirty years in retrospect and grand challenges for the future," *Journal of Archaeological Science*, vol. 56, pp. 41–60, 2015.

[47] A.S. Murray and J.M. Olley, "Precision and accuracy in the optically stimulated luminescence dating of sedimentary quartz: a status review," *Geochronometria*, vol. 21, pp. 1–16, 2002.

[48] A.G. Wintle, "Luminescence dating: where it has been and where it is going," *Boreas*, vol. 37, pp. 471–482, 2008.

[49] R. Roberts, M. Bird, J. Olley, R. Galbraith, E. Lawson, G. Laslett, H. Yoshida, R. Jones, R. Fullagar, G. Jacobsen and Q. Hua, "Optical and radiocarbon dating at Jinmium rock shelter in northern Australia," *Nature*, vol. 393, pp. 358–362, 1998.

[50] L. Bøtter-Jensen, C.E. Andersen, G.A.T. Duller and A.S. Murray, "Developments in radiation, stimulation and observation facilities in luminescence measurements," *Radiation Measurements*, vol. 37, pp. 535–541, 2003.

[51] L. Bøtter-Jensen, E. Bulur, G.A.T. Duller and A.S. Murray, "Advances in luminescence instrument systems," *Radiation Measurements*, vol. 32, pp. 523–528, 2000.

[52] Z. Jacobs and R.G. Roberts, "Advances in optically stimulated luminescence dating of individual grains of quartz from archeological deposits," *Evolutionary Anthropology*, vol. 16, pp. 210–223, 2007.

[53] A.C. Fan, S.H. Li and B. Li, "Observation of unstable fast component in OSL of quartz," *Radiation Measurements*, vol. 46, pp. 21–28, 2011.

[54] M. Lamothe and M. Auclair, "The fadia method: a new approach in luminescence dating using the analysis of single feldspar grains," *Radiation Measurements*, vol. 32, pp. 433–438, 2000.

[55] C.S. Henshilwood, F. d'Errico, R. Yates, Z. Jacobs, C. Tribolo, G.A.T. Duller, N. Mercier, J.C. Sealy, H. Valladas, I. Watts and A.G. Wintle, "Emergence of modern human behavior: Middle Stone Age engravings from South Africa," *Science*, vol. 295, pp. 1278–1280, 2002.

[56] Z. Jacobs, R.G. Roberts, R.F. Galbraith, H.J. Deacon, R. Grün, A. Mackay, P. Mitchell, R. Vogelsang and L. Wadley, "Ages for the Middle Stone Age of Southern Africa: Implications for Human Behavior and Dispersal," *Science*, vol. 322, pp. 733–735, 2008.

[57] H. Yoshida, R.G. Roberts, J.M. Olley, G.M. Laslett and R.F. Galbraith, "Extending the age range of optical dating using single 'supergrains' of quartz," *Radiation Measurements*, vol. 32, pp. 439–446, 2000.

[58] K.J. Thomsen, A.S. Murray and L. Bøtter-Jensen, "Sources of variability in OSL dose measurements using single grains of quartz," *Radiation Measurements*, vol. 39, pp. 47–61, 2005.

[59] Z. Jacobs, G.A.T. Duller and A.G. Wintle, "Interpretation of single grain $D_e$ distributions and calculation of $D_e$," *Radiation Measurements*, vol. 41, pp. 264–277, 2006.

[60] M. Ballarini, J. Wallinga, A.G. Wintle and A.J.J. Bos, "A modified SAR protocol for optical dating of individual grains from young quartz samples," *Radiation Measurements*, vol. 42, pp. 360–369, 2007.

[61] A.T. Madsen, G.A.T. Duller, J.P. Donnelly, H.M. Roberts and A.G. Wintle, "A chronology of hurricane landfalls at Little Sippewissett Marsh, Massachusetts, USA, using optical dating," *Geomorphology*, vol. 109, pp. 36–45, 2009.

[62] G.A.T. Duller, "Distinguishing quartz and feldspar in single grain luminescence measurements," *Radiation Measurements*, vol. 37, pp. 161–165, 2003.

[63] K. Douka, Z. Jacobs, C. Lane, R. Grün, L. Farr, C. Hunt, R.H. Inglis, T. Reynolds, P. Albert, M. Aubert, V. Cullen, E. Hill, L. Kinsley, R.G. Roberts, E.L. Tomlinson, S. Wulf and G. Barker, "The chronostratigraphy of the Haua Fteah cave (Cyrenaica, northeast Libya)," *Journal of Human Evolution*, vol. 66, pp. 39–63, 2014.

[64] K.J. Thomsen, A.S. Murray, J.P. Buylaert, M. Jain, J.H. Hansen and T. Aubry, "Testing single-grain quartz OSL methods using sediment samples with independent age control from the Bordes-Fitte rockshelter (Roches d'Abilly site, Central France)," *Quaternary Geochronology*, vol. 31, pp. 77–96, 2016.

[65] Y.-J. Guo, B. Li, J.-F. Zhang, B.-Y. Yuan, F. Xie and R.G. Roberts, "New ages for the Upper Palaeolithic site of Xibaimaying in the Nihewan Basin, northern China: implications for small-tool and microblade industries in north-east Asia during Marine Isotope Stages 2 and 3," *Journal of Quaternary Science*, vol. 32, pp. 540–552, 2017.

[66] R.G. Roberts, R.F. Galbraith, H. Yoshida, G.M. Laslett and J.M. Olley, "Distinguishing dose populations in sediment mixtures: a test of single-grain optical dating procedures using mixtures of laboratory-dosed quartz," *Radiation Measurements*, vol. 32, pp. 459–465, 2000.

[67] R.F. Galbraith and R.G. Roberts, "Statistical aspects of equivalent dose and error calculation and display in OSL dating: An overview and some recommendations," *Quaternary Geochronology*, vol. 11, pp. 1–27, 2012.

[68] M. Jain and C. Ankjaergaard, "Towards a non-fading signal in feldspar: insight into charge transport and tunnelling from time-resolved optically stimulated luminescence," *Radiation Measurements*, vol. 46, pp. 292–309, 2011.

[69] C. Thiel, J.P. Buylaert, A. Murray, B. Terhorst, I. Hofer, S. Tsukamoto and M. Frechen, "Luminescence dating of the Stratzing loess profile (Austria) — testing the potential of an elevated temperature post-IR IRSL protocol," *Quaternary International*, vol. 234, pp. 23–31, 2011.

[70] J.P. Buylaert, A.S. Murray, K.J. Thomsen and M. Jain, "Testing the potential of an elevated temperature IRSL signal from K-feldspar," *Radiation Measurements*, vol. 44, pp. 560–565, 2009.

[71] B. Li and S.-H. Li, "Luminescence dating of K-feldspar from sediments: a protocol without anomalous fading correction," *Quaternary Geochronology*, vol. 6, pp. 468–479, 2011.

[72] B. Li and S.H. Li, "Luminescence dating of Chinese loess beyond 130 ka using the non-fading signal from K-feldspar," *Quaternary Geochronology*, vol. 10, pp. 24–31, 2012.

[73] B. Li, Z. Jacobs, R.G. Roberts and S.-H. Li, "Review and assessment of the potential of post-IR IRSL dating methods to circumvent the problem of anomalous fading in feldspar luminescence," *Geochronometria*, vol. 41, pp. 178–201, 2014.

[74] B. Li, R.G. Roberts, A. Brumm, Y. Guo, B. Hakim, M. Ramli, M. Aubert, R. Grün, J.-x. Zhao and E.W. Saptomo, "IRSL dating of fast-fading sanidine feldspars from Sulawesi, Indonesia," *Ancient TL*, vol. 34, pp. 1–13, 2016.

[75] B. Li and S.H. Li, "Luminescence dating of K-feldspar from sediments: A protocol without anomalous fading correction," *Quaternary Geochronology*, vol. 6, pp. 468–479, 2011.

[76] B. Li and S.-H. Li, "Luminescence dating of Chinese loess beyond 130 ka using the non-fading signal from K-feldspar," *Quaternary Geochronology*, vol. 10, pp. 24–31, 2012.

[77] T. Trautmann, A. Dietrich, W. Stolz and M.R. Krbetschek, "Radioluminescence dating: A new tool for quaternary geology and archaeology," *Naturwissenschaften*, vol. 86, pp. 441–444, 1999.

[78] T. Schilles and J. Habermann, "Radioluminescence dating: the IR emission of fefdspar," *Radiation Measurements*, vol. 32, pp. 679–683, 2000.

[79] T. Trautmann, M.R. Krbetschek, A. Dietrich and W. Stolz, "The basic principle of radioluminescence dating and a localized transition model," *Radiation Measurements*, vol. 32, pp. 487–492, 2000.

[80] M.R. Krbetschek, T. Trautmann, A. Dietrich and W. Stolz, "Radioluminescence dating of sediments: methodological aspects," *Radiation Measurements*, vol. 32, pp. 493–498, 2000.

[81] G. Erfurt and M.R. Krbetschek, "Studies on the physics of the infrared radioluminescence of potassium feldspar and on the methodology of its application to sediment dating," *Radiation Measurements*, vol. 37, pp. 505–510, 2003.

[82] M. Frouin, S. Huot, S. Kreutzer, C. Lahaye, M. Lamothe, A. Philippe and N. Mercier, "An improved radiofluorescence single-aliquot regenerative dose protocol for K-feldspars," *Quaternary Geochronology*, vol. 38, pp. 13–24, 2017.

[83] J.P. Buylaert, M. Jain, A.S. Murray, K.J. Thomsen and T. Lapp, "IR-RF dating of sand-sized K-feldspar extracts: A test of accuracy," *Radiation Measurements*, vol. 47, pp. 759–765, 2012.

[84] D. Richter, A. Richter and K. Dornich, "Lexsyg — A new system for luminescence research," *Geochronometria*, vol. 40, pp. 220–228, 2013.

[85] G.A.T. Duller and A.G. Wintle, "A review of the thermally transferred optically stimulated luminescence signal from quartz for dating sediments," *Quaternary Geochronology*, vol. 7, pp. 6–20, 2012.

[86] X.L. Wang, Y.C. Lu and A.G. Wintle, "Recuperated OSL dating of fine-grained quartz in Chinese loess," *Quaternary Geochronology*, vol. 1, pp. 89–100, 2006.

[87] X.L. Wang, A.G. Wintle and Y.C. Lu, "Thermally transferred luminescence in fine-grained quartz from Chinese loess: Basic observations," *Radiation Measurements*, vol. 41, pp. 649–658, 2006.

[88] G. Adamiec, G.A.T. Duller, H.M. Roberts and A.G. Wintle, "Improving the TT-OSL SAR protocol through source trap characterisation," *Radiation Measurements*, vol. 45, pp. 768–777, 2010.

[89] B. Li and S.H. Li, "Studies of thermal stability of charges associated with thermal transfer of OSL from quartz," *Journal of Physics D: Applied Physics*, vol. 39, pp. 2941–2949, 2006.

[90] M.S. Chapot, H.M. Roberts, G.A.T. Duller and Z.P. Lai, "Natural and laboratory TT-OSL dose response curves: Testing the lifetime of the TT-OSL signal in nature," *Radiation Measurements*, vol. 85, pp. 41–50, 2016.

[91] Z. Jacobs, R.G. Roberts, T.J. Lachlan, P. Karkanas, C.W. Marean and D.L. Roberts, "Development of the SAR TT-OSL procedure for dating Middle Pleistocene dune and shallow marine deposits along the southern Cape coast of South Africa," *Quaternary Geochronology*, vol. 6, pp. 491–513, 2011.

[92] N.A. Spooner, "On the optical dating signal from quartz," *Radiation Measurements*, vol. 23, pp. 593–600, 1994.

[93] J.S. Singarayer and R.M. Bailey, "Further investigations of the quartz optically stimulated luminescence components using linear modulation," *Radiation Measurements*, vol. 37, pp. 451–458, 2003.

[94] M. Jain, "Extending the dose range: Probing deep traps in quartz with 3.06 eV photons," *Radiation Measurements*, vol. 44, pp. 445–452, 2009.

[95] C. Ankjærgaard, M. Jain and J. Wallinga, "Towards dating Quaternary sediments using the quartz Violet Stimulated Luminescence (VSL) signal," *Quaternary Geochronology*, vol. 18, pp. 99–109, 2013.

[96] M. Jain, A.S. Murray and L. Bøtter-Jensen, "Characterisation of blue-light stimulated luminescence components in different quartz samples: implications for dose measurement," *Radiation Measurements*, vol. 37, pp. 441–449, 2003.

[97] C. Ankjærgaard, B. Guralnik, N. Porat, A. Heimann, M. Jain and J. Wallinga, "Violet stimulated luminescence: geo- or thermochronometer?," *Radiation Measurements*, vol. 81, pp. 78–84, 2015.

[98] C. Ankjærgaard, B. Guralnik, J.P. Buylaert, T. Reimann, S.W. Yi and J. Wallinga, "Violet stimulated luminescence dating of quartz from Luochuan (Chinese loess plateau): Agreement with independent chronology up to ∼600 ka," *Quaternary Geochronology*, vol. 34, pp. 33–46, 2016.

[99] P.M. Denby, L. Bøtter-Jensen, A.S. Murray, K.J. Thomsen and P. Moska, "Application of pulsed OSL to the separation of the luminescence components from a mixed quartz/feldspar sample," *Radiation Measurements*, vol. 41, pp. 774–779, 2006.

[100] S. Tsukamoto, P.M. Denby, A.S. Murray and L. Bøtter-Jensen, "Time-resolved luminescence from feldspars: New insight into fading," *Radiation Measurements*, vol. 41, pp. 790–795, 2006.

[101] S. Tsukamoto, R. Kondo, T. Lauer and M. Jain, "Pulsed IRSL: A stable and fast bleaching luminescence signal from feldspar for dating Quaternary sediments," *Quaternary Geochronology*, vol. 41, pp. 26–36, 2017.

## Chapter 11

# Fundamentals of Luminescence Photo- and Thermochronometry

Benny Guralnik* and Reza Sohbati†

*Soil Geography and Landscape group and the Netherlands Centre for Luminescence dating, Wageningen University
P.O. Box 47, 6700AA Wageningen, The Netherlands
benny.guralnik@gmail.com

†Center for Nuclear Technologies, Technical University of Denmark
DTU Risø Campus, DK-4000 Roskilde, Denmark
resih@dtu.dk

With its classic applications rooted in archaeology and sedimentology, the field of luminescence dating has, in the past decade, experienced a remarkable bloom of innovation and novel applications in Earth science. In the field of *thermochronometry*, luminescence has begun to successfully complement mainstream noble-gas and fission-track techniques, by constraining thermal histories of bedrock at low temperatures ($<100^{\circ}$C) over previously inaccessible timescales ($<10^5$ years). In the field of surface exposure dating (hereafter: *photochronometry*), luminescence has been put on a solid theoretical footing similar to that of cosmogenic nuclide techniques, and can now be used to determine the duration ($<10^5$ years) and degree of rock surface preservation on unprecedented spatial (millimeter) scales. In this chapter, we present a uniform mathematical description of luminescence photo- and thermochronometers, highlighting the close theoretical similarity between the two. We first introduce and discuss key theoretical concepts (partial retention, apparent age, and system closure), and demonstrate them using familiar luminescence signals obeying simple first-order reaction kinetics. We then proceed to show how these concepts may be deployed for reconstructing past environmental conditions (static or variable), involving temperature or light. We conclude the chapter by discussing some of the current methodological conundrums, including the description of non-first-order

reaction kinetics, the incorporation of quantum mechanical tunneling effects, and the utilization of multi-signal luminescence systems.

## 11.1. Introduction

### 11.1.1. *Earth surface dynamics*

The majority of luminescence dating applications in archaeology and geoscience have insofar focused on quantifying time durations, over which certain minerals have been *shielded from* external light and/or elevated temperature [1]. During such periods, a fraction of the energy released by the environmental ionizing radiation becomes stored in the crystalline lattice of certain minerals, in the form of metastable electric charge. This charge includes electrons and holes that get temporarily trapped in oppositely-charged lattice defects and impurities. When exposed to sufficiently bright light and/or sufficiently elevated temperature, trapped charge can remobilize and recombine, thus emptying the traps. Given the general reversibility of trapped charge accumulation, luminescence ages have been most often associated with *the last event of shielding* of archaeological or geological materials from light (e.g. sediment burial) and/or heat (e.g. cooling of fired bricks or pottery). The recent arrival of luminescence dating into the fields of *thermochronometry* [2] and *surface exposure dating* [3], marks a paradigm shift in regard to its utilization in Earth science. Whereas traditionally luminescence dating would only be seen as a proxy to obtain a mineral's *shielding duration from* light/temperature, recent developments have enabled researchers to quantify a mineral's *exposure duration to* light/temperature. In such applications, a luminescence age is more than just a time span: it simultaneously constrains the paleo-environmental condition of choice (light/temperature), as well as the timescale over which the reconstructed time-averaged condition applies [4].

Thermochronometry, a broad subdiscipline that radiated out of geochronology by the late 1960's, seeks to quantitatively reconstruct time-temperature histories of geologic materials [5]. Progressive rock cooling typically accompanies erosion of landscape and/or uplift of mountains, while progressive rock heating is a common phenomenon

in subsiding basins or subducting tectonic plates. By measuring present-day concentrations of specific pairs of radionuclides and their products (e.g. $^{40}$K and $^{40}$Ar, $^{238}$U and fission tracks, etc.) in a variety of natural minerals, and by constraining their nuclear half-lives (if relevant) and rates of annealing or diffusion through the crystalline lattice at different temperatures, it is possible to reconstruct a detailed thermal history of a rock, spanning over broad ranges of geological times and temperatures. Ultimately, the comparison of spatial age data with coupled thermochronological and geothermal models enables researchers to characterize and quantify large-scale dynamics of the Earth's crust ($\sim 10^3$–$10^4$ m and $\sim 10^5$–$10^9$ a scales) [5].

Surface exposure dating, which radiated from geochronology by the late 1980's, addresses similar geodynamic questions yet on much smaller spatial and temporal scales [6]. The methodology owes to the existence of high-energy cosmic rays, whose particles cascade through the atmosphere, collide with common elements within the uppermost meters of the Earth's surface, and produce distinct nuclides (e.g. $^{3}$He, $^{10}$Be, etc.) at quantifiable rates. By measuring the present-day concentrations of cosmogenic nuclides in geological materials and estimating local cosmic ray fluxes and their attenuation in matter, it is possible to reconstruct the residence time of rocks at, or away from, the Earth's surface [6], resolving the finer and more recent dynamics of the Earth's crust ($\sim 10^0$–$10^2$ m, and $\sim < 10^6$ a scales) in comparison to the above mentioned thermochronometric methods.

In the past decades fruitful interdisciplinary exchange between thermochronometry and surface exposure dating has given rise to some fascinating methodological cross-overs such as detrital thermochronology [7] and cosmogenic paleothermometry [8], as well as to auxiliary techniques aiming to bridge the temporal gap between the two [9]. It seems that the versatility of trapped charge (whose accumulation is due both to radioactive decay and cosmic rays, and whose stability is often both temperature-dependent and light-sensitive), presents a further opportunity for a methodological fusion between classical thermochronometry and surface exposure dating. Specifically, this chapter demonstrates that through only minor

adjustments, the very same (or vastly similar) luminescence systems can be deployed to constrain the most recent (typically $<10^5$ a) Earth surface conditions at low temperatures ($<100°$C), and their dynamics over a broad range of spatial scales ($10^{-3}$–$10^3$ m).

For methodological nomenclature, we adopt the familiar term *luminescence thermochronometry* [2], to denote a system comprising of a multitude of radioactive parents (chiefly $^{238}$U, $^{234}$Th, and $^{40}$K), one or several radiation-damage product(s) (typically, electrons trapped in certain types of lattice defects), and an extended interpretative scheme, capable of accounting for luminescence signal saturation and/or athermal loss [e.g. 4, 10]. In the lack of an umbrella term for the various applications of luminescence dating to constrain the cumulative exposure of geological [11–13] or archaeological [14] material to daylight, we introduce by analogy the term *luminescence photochronometry*, to signify the utilization of luminescence techniques to quantify the exposure histories of various materials to visible or near-visible light photons (comprising the typical daylight spectrum).

### 11.1.2. *Basics of luminescence photo- and thermochronometry*

The accumulation and loss of trapped electrons with time $t$ (s) in a natural mineral can usually be described by the rate equation:

$$dn/dt = A(N - n) - Kn \tag{1}$$

where $N$ (cm$^{-3}$) is the number density of electron traps of a certain type, and $n$ (cm$^{-3}$) is the number density of electrons trapped in them [15]. Eq. (1) corresponds to the simplest description of concurrent accumulation and loss within a trapped-charge system [2, 10], and classifies as first-order reaction kinetics. Due to the experimental difficulty in measuring absolute densities of traps and trapped electrons, we will often operate with the more easily quantifiable *fraction of filled traps*, denoted as $\hat{n} = n/N$ (unitless). Conceptually analogous to the daughter/parent ratio in isotope geochemistry [10], $\hat{n}$ will also be occasionally referred to as "concentration".

The trapping coefficient $A$ ($s^{-1}$) in Eq. (1) governs the rate at which free electrons enter (or populate) empty traps. It is usually defined as the ratio of the environmental ionizing dose rate $\dot{D}$ (Gy $s^{-1}$), to the material's characteristic (or "saturation") dose $D_0$ (Gy) [15]:

$$A = \dot{D}/D_0. \tag{2}$$

The detrapping coefficient $K$ ($s^{-1}$) in Eq. (1) similarly governs the rate at which trapped electrons escape (depopulate) their host traps. This coefficient is typically related to the environmental conditions, either via the Arrhenius law [15]:

$$K = s \exp(-E/k_B T). \tag{3}$$

or the Beer-Lambert law [11]:

$$K = \sigma \varphi_0 \exp(-\mu z). \tag{4}$$

Note that both laws utilize the same functional form $K \sim e^{-x}$, differing only in parametrization. For thermal loss at a temperature $T$ (K), reparametrized as a scaled reciprocal temperature $1/k_B T$ (where $k_B$ is Boltzmann's constant), the governing kinetic parameters of $K$ are the thermal activation energy $E$ (eV), and the escape frequency factor $s$ ($s^{-1}$). For optical loss within a homogeneous medium at depth $z$ (mm), $K$ is governed by the light attenuation coefficient $\mu$ ($mm^{-1}$), the photoionization cross section $\sigma$ ($cm^2$), and the incident photon flux $\varphi_0$ ($cm^{-2}\,s^{-1}$). For convenience, we refer to systems where $K = 0$ as "closed", and to those with $K > 0$ as "leaky" [10].

### 11.1.3. *Scope of this chapter*

The treatment presented here is limited to two mutually-exclusive cases of pure thermochronometry (systems affected by thermal loss), and pure photochronometry (systems undergoing optical loss). Noting that temperature is an implicit variable in the latter, and that modelling of simultaneous thermal and optical losses is possible [16, 17], we are however unaware of any Earth science applications

that utilize these loss pathways independently. Thus, the treatment of composite *photo-thermochronometers* remains a future challenge.

Since the highest derivative in Eq. (1) is $dn/dt$, Eq. (1) is a first-order differential equation; since $dn/dt$ is linearly proportional to both $n$ and $N - n$, Eq. (1) represents first-order reaction kinetics. These orders should not be confused; while first-order differential equations dominate luminescence theory, higher reaction orders are not uncommon [18]. Although real-life luminescence behavior may noticeably depart from first-order reaction kinetics (Sec. 4), the latter is sufficiently robust to approximate nearly all key luminescence behavior in common dosimeters. Thus, while the presented analytical solutions apply to first-order reaction kinetics only, all key concepts have been defined universally (regardless of reaction order), and are applicable to any luminescence system.

This chapter includes both previously published material, as well as new work. Accepted definitions of luminescence age and closure are reviewed, while the concepts of partial retention zone and system opening/resetting are presented here for the first time in the luminescence literature. A central aim of this chapter is to demonstrate that all concepts originating in thermochronometry can be easily applied to photochronometry and vice versa.

## 11.2. Systems under constant environmental conditions

### 11.2.1. *General solution*

The analytical solution of Eq. (1) with constant $A$ and $K$ is given by:

$$\hat{n}_{A,K}(t) = \hat{n}_0 e^{-(A+K)t} + (1 + K/A)^{-1}[1 - e^{-(A+K)t}]. \qquad (5)$$

in which $\hat{n}_0$ is the fraction of filled traps at $t = 0$ [cf. 10, 15]. Equation (5) establishes a key relationship between the fraction of filled traps ($\hat{n}$), time ($t$), and fixed environmental conditions ($A, K$). This relationship lies at the core of interpreting not only systems where $A$ and $K$ have been constant, but also those where $A$ and $K$ might have evolved through time.

### 11.2.2. *Secular equilibrium*

At very long times $t \gg (A+K)^{-1}$, Eq. (5) reduces to:

$$\hat{n}_{SS} = \hat{n}(t \to \infty) = (1 + K/A)^{-1}. \tag{6}$$

where $\hat{n}_{SS}$ is the fraction of filled traps at *steady-state*, a condition that onsets at long times when $K/A$ remains fixed. The condition in Eq. (6) is also known as a *secular equilibrium*; secular (*lat.* for temporary), because if $K/A$ were to change, $\hat{n}$ would be instantaneously set back into motion according to:

$$\hat{n}_{A,K}(t) = (1 + K_0/A_0)^{-1} e^{-(A+K)t} + (1 + K/A)^{-1}[1 - e^{-(A+K)t}].$$

where $A_0$ and $K_0$ are the former environmental conditions, and $(A+K)^{-1}$ the mean lifetime of system re-equilibration at the new $A$ and $K$. Equation (6) can be used both for forward modelling (to predict steady-state trap populations for known $K/A$), or inverse modelling (to reconstruct time-averaged $K/A$ from an observed $\hat{n}$). Note that since the re-equilibration lifetime is unaffected by former conditions ($A_0$ and $K_0$), extrapolation of a reconstructed $K/A$ back in time is only meaningful over a few (typically <5) mean lifetimes.

Two reference luminescence depth profiles in bedrock, believed to be in secular equilibrium [4, 13], are shown in Fig. 1 (the data in Fig. 1d corresponds to $\hat{n} \approx (n/N)_{nat}/(n/N)_{SS\ at\ 0^\circ K}$ in the original publication; see Table S8 in [4]). Juxtaposition of the optical (Fig. 1a) and thermal (Fig. 1d) luminescence profiles accentuates the sharp difference between the characteristic spatial scales of optical and thermal loss (the vertical axis of Figs. 1d-f corresponds to ~3.5 km). Furthermore, since light attenuates with depth, while ambient temperature increases further underground, the profiles in Fig. 1a,d mirror each other. The continuous curves in Fig. 1 have been regressed through data via Eq. (6). When loss predominates ($K/A \to \infty$), $\hat{n}_{SS}$ asymptotes to 0, and when loss is relatively negligible ($K/A \to 0$), $\hat{n}_{SS}$ asymptotes to 1. The corresponding environmental parameters $A$ and $K$ are shown in Fig. 1b,e. Notably, the concentration $\hat{n}_{SS}$ exhibits its greatest range of variation ($0.1 \leq \hat{n}_{SS} \leq 0.9$) when $K$ and $A$ fall within the same order of magnitude ($10^{-1} \leq K/A \leq 10^{1}$). To estimate how rapidly

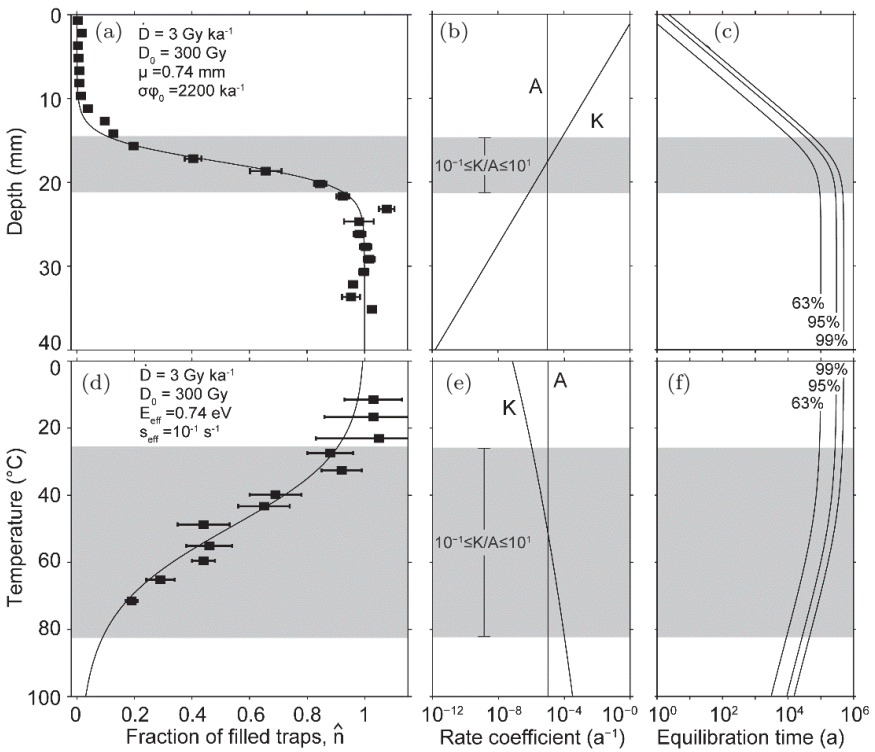


Fig. 1. Experimental (squares) and theoretical (lines) fractions of filled traps as observed within the top of a glacial boulder (XJ64-1) in Tibet [13] (a), and within the top of the KTB borehole [4] (d). Panels (b,e) show the electron trapping ($A$) and detrapping ($K$) coefficients; the transition between an accumulation-driven and loss-driven behavior occurs when $A$ and $K$ are within the same order of magnitude (grey regions). Panels (c,f) show the timescales, necessary to achieve 63%, 95% and 99% of secular equilibrium (see text).

each $\hat{n}_{SS}$ could have been achieved, the durations for attaining 63%, 95% and 99% of secular equilibrium are shown in Fig. 1c,f. Since both exponential terms in Eq. (5) share the same lifetime, these equilibration timescales are invariant of the starting conditions, and are simply given by multiples of 1, 3 and 5 of $(A+K)^{-1}$. Note that a near-saturated signal $\hat{n}_{SS} \sim 1$ corresponds to the longest possible equilibration lifetime $\sim A^{-1}$, while progressively shorter lifetimes are required to attain lower values of $\hat{n}_{SS}$.

A match between an observed luminescence profile and its predicted secular equilibrium (Fig. 1a,d) may provide useful paleo-environmental information. For the quartzite boulder in Pamir (Fig. 1a–c), the luminescence depth profile limits the boulder's erosion rate within the past ∼30 ka, thus providing valuable input for calculation of a more precise $^{10}$Be age [13]. For the top ∼2.5 km of the German KTB borehole (Fig. 1d–f), the luminescence depth profile enables to safely extrapolate its modern geothermal gradient (∼28°C km$^{-1}$) over the last ∼50 ka, a timescale which is inaccessible by any mainstream noble gas and fission track method [4].

### 11.2.3. *Partial retention*

To extend the treatment to transient systems where accumulation and loss are not necessarily counterbalanced, we invoke the concept of *Partial Retention Zone* (PRZ) [5], which characterizes the behavior of a leaky system through its comparison to a time-equivalent yet closed-system analogue. Formally, partial retention can be defined as a fraction ($0 \leq x \leq 1$) between concentrations in a leaky and an analogous closed system, accumulated over the same time period $t$:

$$x = \frac{n(t)}{n_{K=0}(t)}. \tag{7}$$

Substitution of Eq. (5) into both the numerator and denominator in Eq. (7), and setting $K = 0$ in the latter, yields:

$$x = \frac{\hat{n}_0 e^{-(A+K)t} + (1 + K/A)^{-1}[1 - e^{-(A+K)t}]}{\hat{n}_0 e^{-At} + [1 - e^{-At}]}. \tag{8}$$

In the general case, Eq. (8) should be numerically solved for $K$ (for arbitrarily-chosen $x$, $t$, $A$ and $\hat{n}_0$), and the resultant $K$ converted into $T = E/k_B \ln(s/K)$ or $z = \mu^{-1} \ln[\sigma\varphi_0/K]$ via Eqs. (3–4). While some convenient simplifications of Eq. (8) may be derived, including $K = -\ln(x)/t$ for $A = 0$, and the recursive formula $K = A \{[1 - e^{-(A+K)t}]/x\,(1 - e^{-At}) - 1\}$ for $A > 0$ and $\hat{n}_0 = 0$, we stress that in the general case of arbitrary parameters in Eq. (8), a numerical solution is likely unavoidable. To demonstrate Eq. (8) and discuss

conventional choices for $x$, $t$, $A$ and $\hat{n}_0$, we continue with our reference photo- and thermochronometers from Fig. 1, and demonstrate their various partial retention zones in Fig. 2.

Given the multitude of variables in Eq. (8), the PRZ can be visualized in a variety of ways, most commonly as a function of $t$ for a given $x$ (Fig. 2a,c), or as a function of $x$ for a given $t$ (Fig. 2b,d). Due to the exponent in Eqs. (3–4), the storage time $t$ must be explored across many orders of magnitude (Figs. 2a,c).

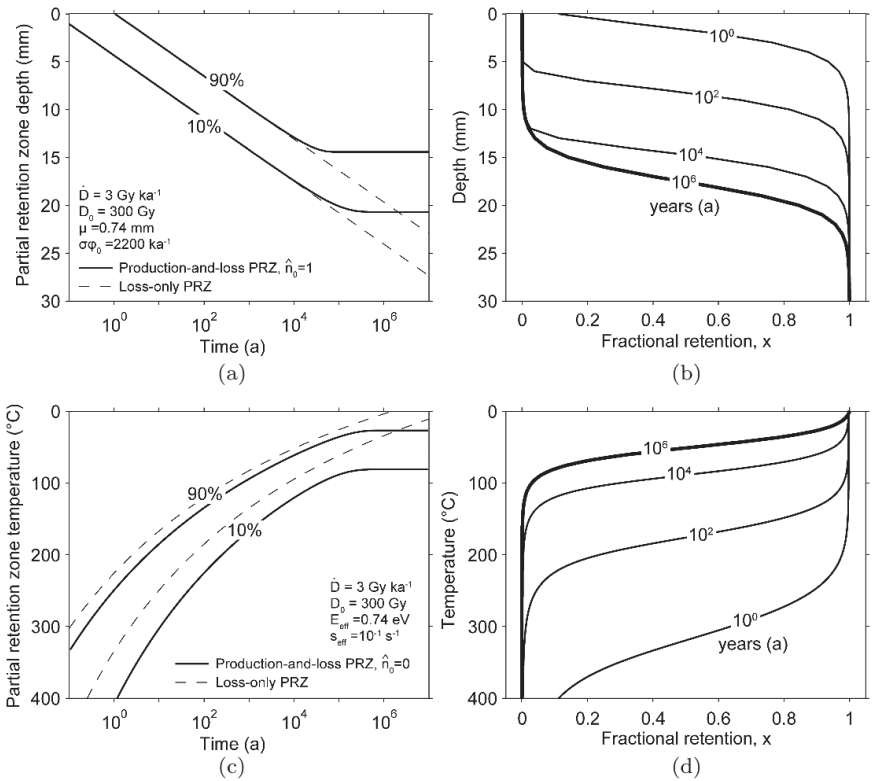


Fig. 2. (a,c) Partial Retention Zone (PRZ) contours of 10% and 90%, for the photo- and thermochronometers from Fig. 1. Solid and dashed lines represent production-and-loss PRZ and the loss-only PRZ, respectively (see text). Panels (b,d) show continuous partial retention profiles (Eq. 8) for some representative times. Note that at $10^6$ a, the profiles are indistinguishable from steady-state (cf. Fig. 1a,d).

Conventionally, $x = 10\%$ and $x = 90\%$ are chosen to represent loss-driven and accumulation-driven behavior, respectively [5]. The choice of $\hat{n}_0$ and $A$ is more arbitrary, and depends on the geological scenario. In photochronometry, where the electron traps that come into interaction with daylight are typically field-saturated, the baseline assumption is $\hat{n}_0 = 1$ (Fig. 2a,b) [13, 14]. In thermochronometry, where rocks often cool from an initially high temperature, the default would be $\hat{n}_0 = 0$ (Fig. 2c,d) [10]. Obviously, alternative $\hat{n}_0$ can be assigned, depending on the circumstances. Finally, the choice of whether or not to neglect $A$ gives rise to a further nomenclature distinction. The *production-and-loss PRZ* ($A > 0$, solid lines in Fig. 2) is of relevance to continuous and monotonic geological processes, e.g. long-term exhumation or cooling. The *loss-only PRZ* ($A = 0$, dashed lines in Fig. 2) is of relevance to abrupt events during which accumulation can be neglected, e.g. a short and intense pulse of erosion or a catastrophic heating. Note that at long times ($>10^4$ a), the two types of PRZ diverge (Fig. 2a), because for $A > 0$ and $t \to \infty$ Eq. (8) asymptotes to a constant $K = A(x^{-1}-1)$. Comparison of the latter expression to Eq. (6) reveals that $\hat{n}_{SS} = x$, and thus the $10^{-1} \leq K/A \leq 10^{1}$ range in Fig. 1 coincides with the 10%–90% production-and-loss PRZ. By analogy, the 10%–90% production-and-loss PRZ of a transient system can be imagined to bracket the range, where the time-averaged effects of accumulation ($A$) and loss ($K$) are within one order of magnitude.

### 11.2.4. *Apparent age*

Not a single introductory text on luminescence dating [e.g. 19, 20] goes without the classic "luminescence age equation", written as:

$$\text{Age (a)} = \frac{\text{Equivalent dose (Gy)}}{\text{Dose rate (Gy a}^{-1})} = \frac{D_e}{\dot{D}}, \tag{9}$$

in which $\dot{D}$ remains as before, and $D_e$ (Gy) is a laboratory dose which artificially produces the same luminescence response, as that which has been acquired naturally. In contrast to Eq. (9), our operational definition of luminescence age is obtained by rearranging Eq. (5) into

[cf. 10, 21]:

$$t = (A + K)^{-1} \ln \left[ \frac{\hat{n}_0 - (1 + K/A)^{-1}}{\hat{n}_{obs} - (1 + K/A)^{-1}} \right], \tag{10}$$

in which $\hat{n}_{obs}$ denotes the observed fraction of filled traps, and all other variables remain as before. Results reported using "age equations" (e.g. Eqs. 9, 10) are usually referred to as "model" or "apparent" ages, reminding the practitioner that the strong dependence of age on the selected age model implies that calculated ages may not always correspond to actual events occurring in the past.

The comparison of Eqs. (9) and (10) highlights three key issues: (i) "age" is an abstract notion; here, it involves an extrapolation of a testable model to convert measurable physical quantities into an immeasurable length of time, (ii) different studies may operate with different age definitions, none of them being "right" or "wrong", and (iii) under certain assumptions, substantially different age definitions may become identical. For example, consider two special cases of Eq. (10), each suppressing a different rate coefficient:

$$t_{K=0} = A^{-1} \ln[(\hat{n}_0 - 1)/(\hat{n}_{obs} - 1)], \tag{11a}$$

$$t_{A=0} = K^{-1} \ln(\hat{n}_0/\hat{n}_{obs}). \tag{11b}$$

A closer inspection of Eqs. (9) and (11a) reveals that the two are identical, if the equivalent dose is defined as $D_e = D_0 \ln[(\hat{n}_0 - 1)/(\hat{n}_{obs} - 1)]$, while $A$ expanded into $\dot{D}/D_0$ (Eq. 2). In the lack of $\dot{D}$ in Eq. (11b), an identity between Eq. (9) and (11b) is impractical. The latter observation highlights that Eq. (10) can be seen as a generalization of Eq. (9), applicable to both closed and leaky systems.

### 11.2.5. *Relating apparent age to time and constant environmental conditions*

The default definition of "apparent age" in luminescence dating is obtained by assuming zero inheritance and zero loss ($\hat{n}_0 = 0$, $K = 0$)

in Eq. (10):

$$t_{app} = -A^{-1} \ln(1 - \hat{n}_{obs}). \tag{11c}$$

Requiring minimal assumptions, Eq. (11c) is the baseline age model across a wide range of geological scenarios. By using Eq. (11c) to interpret trapped electrons that have accumulated in a system, which in reality is leaky (Eq. 5 with $\hat{n}_0 = 0$, $K > 0$), we arrive at a key relationship between time $t$ and the apparent age $t_{app}$ [cf. 21]:

$$t_{app}(K,t) = -A^{-1} \ln\{1 - (1 + K/A)^{-1}[1 - e^{-(A+K)t}]\}, \tag{12a}$$

$$t(K,t_{app}) = -(A + K)^{-1} \ln[1 - (1 + K/A)(1 - e^{-At_{app}})], \tag{12b}$$

$$K(t_{app},t) = A\{[1 - e^{-(A+K)t}]/[1 - e^{-At_{app}}] - 1\}. \tag{12c}$$

Unlike Eqs. (12a,b), Eq. (12c) is recursive; rapid convergence is typically reached for an initial guess of $K_{guess} = t_{app}^{-1}$ [22]. While an extended treatment (coupling of Eqs. 5 and 11a to account for $\hat{n}_0 \geq 0$) is certainly possible, it will not be considered here. Given the novelty of Eqs. (12a–c) in the luminescence dating literature [21], we demonstrate some of their valuable uses below.

Figure 3a shows the evolution of apparent age (as predicted by Eq. 12a) in a quartz Optically Stimulated Luminescence (OSL) thermochronometer (kinetic parameters from [23]), stored at various environmental temperatures, while Fig. 3b further focuses on the evolution of the apparent age at 30°C. At short times, when thermal loss is still negligible, the apparent age asymptotes to time itself ($t_{app} \rightarrow t$, 1:1 line in Fig. 3b). At infinitely long times, the apparent age asymptotes to a constant reflecting the relative magnitudes of $A$ and $K$ ($t_{app} \rightarrow A^{-1} \ln(1 + A/K)$, horizontal line in Fig. 3b). To quantify the transition of apparent age from one asymptote to another, we utilize a relative 10% threshold which, while arbitrary, is nevertheless comparable to current uncertainties both in luminescence dating [24] and in OSL-thermochronometry [25]. For storage at 30°C, the apparent age remains synchronous with time (within 10%) up to ~100 ka (point A in Fig. 3b), thus enabling to utilize the system as a "chronometer" up to this point. From ~200 ka and onwards (point B in Fig. 3b), the apparent age enters

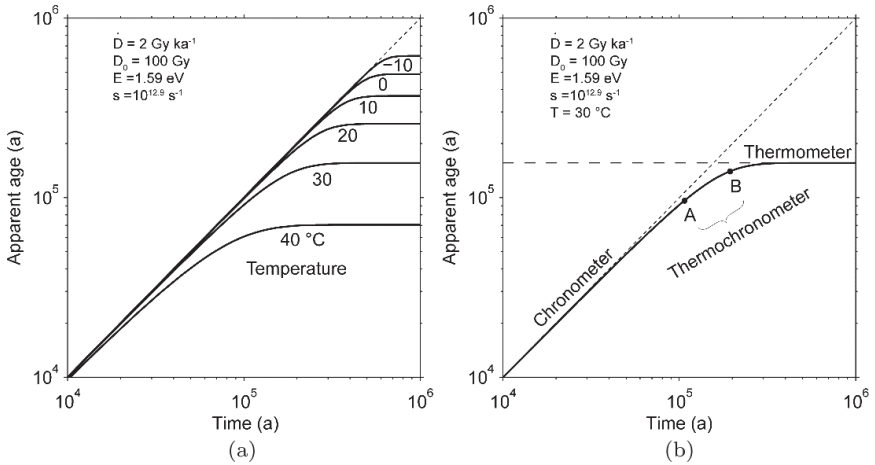


Fig. 3. (a) Age evolution in a leaky OSL thermochronometer (kinetic parameters from [23]), held at different temperatures, predicted by Eq. (12a). (b) subdivision of a selected curve from (a) into regions of system susceptibility to time (prior to point A), temperature (beyond point B), and combined effect of time and temperature (between points A and B). When the system behaves as a chronometer, the age evolution asymptotes to the 1:1 line; when the system behaves as a thermometer, the apparent age asymptotes to a constant value.

within 10% of its thermal secular-equilibrium value, thus stipulating to use the system as a "thermometer".

Between points A and B, the system should be equally affected both by time and temperature, and thus represents a "thermochronometer", capable of recording variations of temperature with time. By looking at Fig. 3a, it becomes clear that the transition from a "chronometer" to a "thermometer" behavior occurs at different times for different storage temperatures — the higher the environmental temperature, the earlier the transition.

Figure 4 demonstrates how Eq. (12b) can be applied to correct an age underestimate (filled circle) using well-constrained environmental conditions. The sample in question is a fault gouge from the San Andreas fault, likely to have been flash-heated during the largest historical earthquake at this site (the $M_w$ 7.9 Fort Tejon, 1857 AD). The reported luminescence apparent age (139 ± 12 a, as of 2010) underestimates the Fort Tejon event by ∼9% [26], and although the

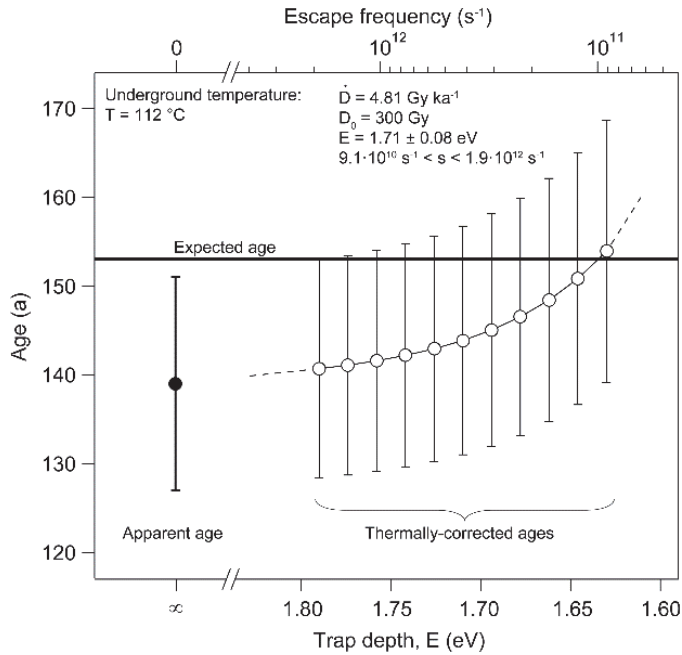


Fig. 4. Apparent (filled circle), and thermally-corrected (open circles; Eq. 12b) feldspar $IRSL_{50}$ ages from a 3.1-km deep (112°C) fault gouge sample, San Andreas Fault Observatory at Depth (US) [26]. Kinetic parameters are adopted from [27, 28].

age is based on only a few weighted points, we assume that this age is correct. To evaluate whether the sample's ambient temperature (112°C at 3.1 km underground), justifies a thermal correction via Eq. (12b), we adopt the nominal kinetic parameters of the feldspar $IRSL_{50}$ signal (Infra-Red Stimulated Luminescence, measured at 50°C; [27]), assume the characteristic covariance $E \propto \log s$ [28], and apply Eq. (12b) to obtain thermally-corrected ages (open circles in Fig. 4). Since the propagated uncertainties of thermally-corrected ages do overlap with the expected age (horizontal line in Fig. 4), a thermal correction of the raw results using Eq. (12b) seems to be justified in this case.

Finally, to demonstrate how Eq. (12c) can be used to extract meaningful environmental paleotemperatures, we revisit two

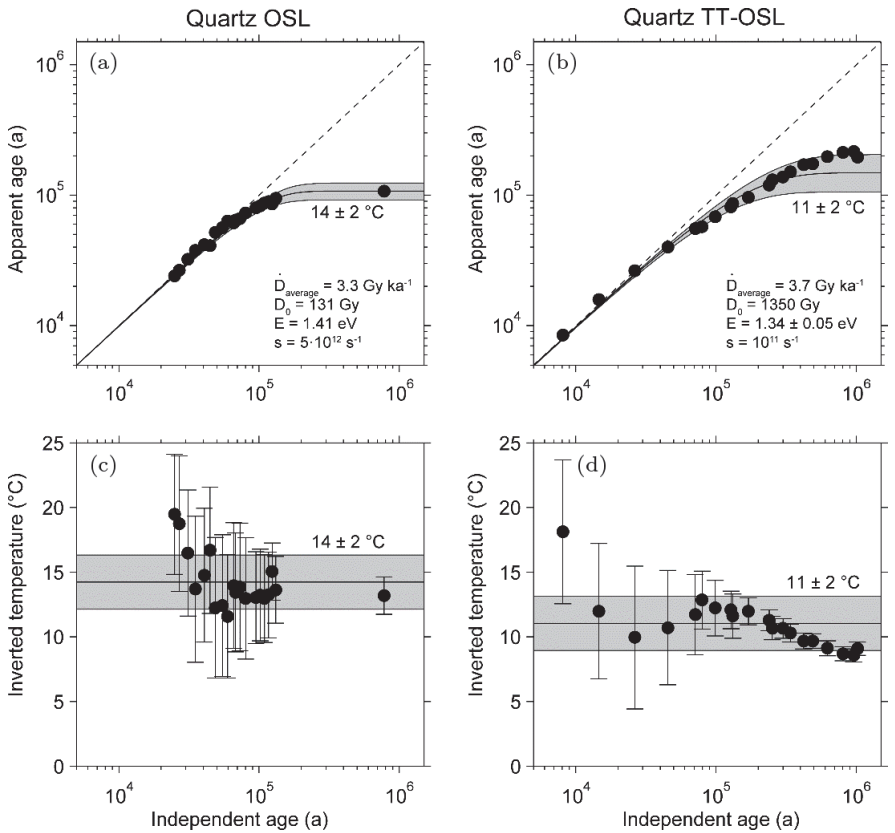


Fig. 5. Apparent quartz OSL (a) [29], and TT-OSL (b) [30] ages, reported at Luochuan (Loess Plateau, China), exhibit characteristic thermochronometric behavior when plotted against independent age control (cf. Fig. 3). The mismatch between luminescence ages and their independent estimates is translated into environmental paleotemperature via Eqs. (12c) and (3), and is shown in (c–d). The average paleotemperatures of both systems (solid lines and grey bands in c–d) can accurately predict most of the apparent ages (Eq. 12a; solid lines and grey bands in a–b).

independent luminescence chronologies [29, 30] from the classic loess-paleosol sequence at Luochuan (China). In Fig. 5a,b the luminescence ages of quartz OSL [29], and quartz TT-OSL [30] (Thermally-Transferred OSL), are plotted against their independent

age constraints (determined by marine isotope stage proxies). The characteristic transition from chronometry to thermometry in both luminescence systems (cf. Figs. 3 and 5), invites to consider whether meaningful paleotemperatures can be extracted from these progressive age mismatches. Using system-specific [29] or sample-specific [30] kinetic parameters, each pair of an apparent luminescence age and its independent age has been converted into paleotemperature via Eq. (12c), and plotted in Fig. 5c,d. The average paleotemperatures of $14\pm2$°C (OSL) and $11 \pm 2$°C (TT-OSL) are only a few degrees above (i) the modern mean annual temperature at the site (9.1°C, [31]), and (ii) independent paleotemperature estimations [e.g. 32] (furthermore, this slight skew to higher temperature is both expectable and accountable for, as will be shown in Sec. 3.1). The fact that two well-established leaky luminescence systems, whose saturation doses and thermal stabilities differ by orders of magnitude [29, 30], yield mutually overlapping average palaeotemperatures, provides a compelling case for these systems' utilization for environmental paleothermometry. Further efforts should address a key question of whether the temporal trends in paleotemperature as a function of time in Fig. 5b,d correspond to a meaningful signal or just noise.

To conclude Sec. 2, the assumption of constant environmental conditions should be the null hypothesis in photo- and thermochronometry, and is accepted as the default interpretation of luminescence intensity in naturally-occurring minerals (Eqs. 10–11). This assumption is justifiable when e.g. a thermally-corrected age (Eq. 12b) or a reconstructed paleotemperature (Eq. 12c) agrees well with their independent estimates. Since temperature is omnipresent, the relevance of Eqs. (12) to almost any reported luminescence age is self-evident; whether or not Eqs. (12) are also of use in photochronometry remains to be seen. It should be remembered that while the default assumption of constant environmental conditions may lead to acceptable and plausible results, alternative scenarios including variable environmental conditions (Sec. 3) and anomalous signal loss (Sec. 4.2) should be considered as well.

## 11.3. Systems under variable environmental conditions

### 11.3.1. *Periodic fluctuations of environmental conditions*

The simplest scenario, in which a luminescence photo- or thermochronometer can be affected by variable environmental conditions, involves the case of diurnal, seasonal, or inter-annual variations in e.g. temperature, water content, light intensity, etc. In Sec. 2.5 we successfully inverted the departure of two luminescence chronologies [29, 30] from their independent age constraints into an effective environmental paleotemperature of 11–14°C at Luochuan. To explain why the latter result overestimates the modern mean annual temperature at the site (9.1°C) by a few degrees, we proceed to discuss how cyclic variations in environmental conditions can and should be taken into account.

A common approach is to avoid solving Eq. (1) with time-dependent rate coefficients, but instead, to obtain *effective* rate coefficients [8, 15], corresponding to the time-averaged values of $A$ and $K$:

$$A_{\mathit{eff}} = t^{-1} \int_0^t A(t')dt', \quad K_{\mathit{eff}} = t^{-1} \int_0^t K(t')dt', \tag{13}$$

where $t$ is time over which the rate coefficient is integrated, and $t'$ is a dummy integrating variable. The key point is that, since $A$ and $K$ are not necessarily linear functions of their corresponding environmental parameters (e.g. $\dot{D}$, $\varphi_0$, $T$), *effective* parameters may not necessarily coincide with the *average* parameters.

To show how effective environmental parameters are derived, and quantify their offset from environmental averages, we consider seasonal variations in soil temperature, soil moisture and incident light flux at Mt. Gonglushan (China) [33], only ∼100 km away from Luochuan. The average annual temperature at Mt. Gonglushan is $\bar{T}$ = 9.3°C (Fig. 6a), essentially identical to that in Luochuan (9.1°C). To find the effective temperature $T_{\mathit{eff}}$, at which the net annual loss of the luminescence signal would have been the same

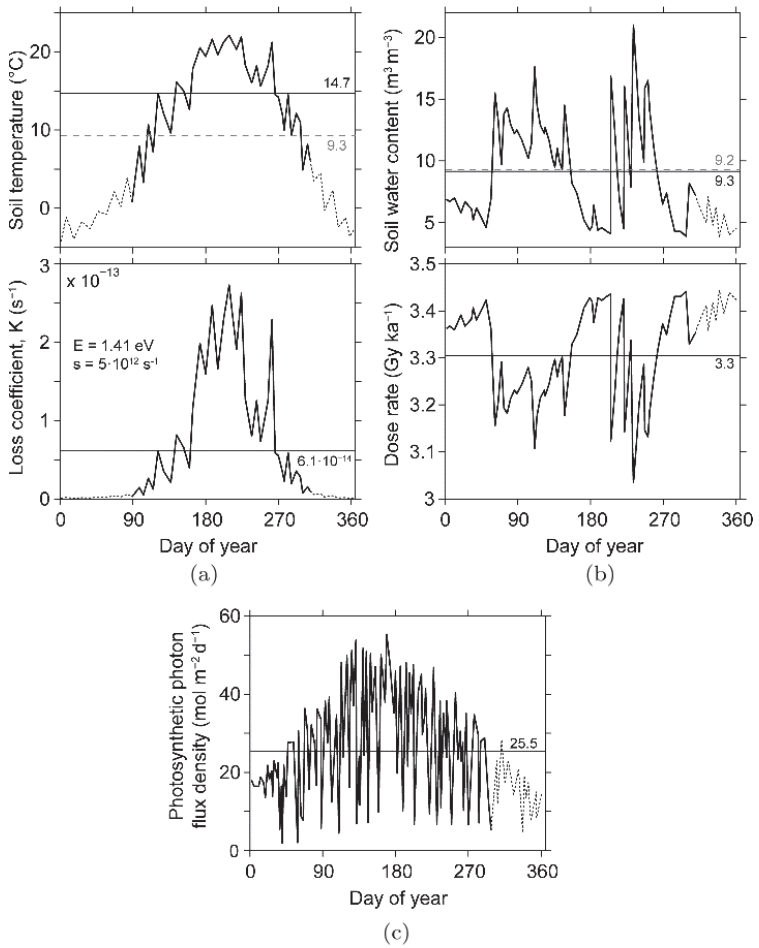


Fig. 6. Seasonal variations in soil temperature (a) soil water content (b) and photosynthetically-active radiation (c) in the vicinity of Luochuan (China), measured over the course of 2010 [33] (solid lines) or extrapolated (dotted lines). Lower panels demonstrate how these environmental fluctuations affect (the constituents of) the corresponding rate coefficients. Dashed and solid horizontal lines correspond to average and effective environmental parameters, respectively.

as under actual fluctuating temperature, we equate the effective and the time-averaged loss coefficients [15]:

$$K_{\mathit{eff}} = se^{-E/k_B T_{\mathit{eff}}} = st^{-1} \int_0^t e^{-E/k_B T(t')} dt'.$$

and solve for $T_{eff}$. For the OSL system, the calculated $T_{eff} = 14.7°\mathrm{C}$ is in perfect agreement with this system's inferred $14 \pm 2°\mathrm{C}$ paleotemperature at Luochuan (Sec. 2.5). As noted by [15], paleotemperatures extracted from luminescence thermochronometers will always exceed mean environmental temperatures; the influence of short-lived thermal maxima on $T_{eff}$ is governed by the Arrhenius parameters in the loss coefficient $K$ (Eq. 3).

To demonstrate how fluctuating environmental conditions are nonlinearly imprinted on the trapping coefficient $A$, we consider the influence of variable soil moisture on the effective annual dose rate $\dot{D}$. Assuming negligible contribution from alpha particles, and applying standard dose rate conversion factors to beta and gamma radiation [19], we equate the effective and the time-averaged dose rates:

$$\begin{aligned}\dot{D}_{eff} &= \left[\frac{\dot{D}_{\beta,dry}}{1+1.25W_{g,eff}} + \frac{\dot{D}_{\gamma,dry}}{1+1.14W_{g,eff}}\right] \\ &= t^{-1}\int_0^t \left[\frac{\dot{D}_{\beta,dry}}{1+1.25W_g(t')} + \frac{\dot{D}_{\gamma,dry}}{1+1.14W_g(t')}\right] dt'.\end{aligned}$$

where $\dot{D}_{\beta,dry} = 2.35$ Gy ka$^{-1}$ and $\dot{D}_{\gamma,dry} = 1.20$ Gy ka$^{-1}$ are dry beta and gamma dose rates characteristic of Luochuan deposits [29, 30], and $W_g$ (kg kg$^{-1}$) is the gravimetric water content (w.c., converted from volumetric w.c. in Fig. 6b via a loess bulk density of 1.5 Mg m$^{-3}$). Solving for $W_{g,eff}$, and converting back into volumetric w.c., we obtain $W_{v,eff} = 9.2\%$ which, although negligibly different from the average water content $\bar{W}_v = 9.3\%$, does further demonstrate that the effect of fluctuating environmental parameters on the rate coefficients in Eq. (1) is not necessarily linear, indicating the need for a calculation of effective rate coefficients as outlined above. An exception to this may be the incident light flux $\varphi_0$ (Fig. 6c): since $\varphi_0$ is a pre-exponential factor of $K$ (Eq. 4), the average and the effective photon fluxes should be one and the same, i.e. $\bar{\varphi}_0 = \varphi_{0,eff} = t^{-1}\int_0^t \varphi_0(t')dt'$.

### 11.3.2. *Monotonic change of environmental conditions*

Continuous cooling (heating) of rock in thermochronometry can often be described via an increase (decrease) of the reciprocal temperature with time:

$$1/T(t) = 1/T_0 + t/(\tau E/k_B), \tag{14}$$

in which $\tau$ (s) is a time constant, $\tau > 0$ for cooling and $\tau < 0$ for heating [10, 34]. Similarly, the increase (decrease) of a crystal's depth from the rock's surface, due to sedimentation (erosion) can be formulated as:

$$z(t) = z_0 + t/(\tau\mu), \tag{15}$$

in which $\tau > 0$ for sedimentation and $\tau < 0$ for erosion [13]. When Eqs. (14, 15) are coupled with their corresponding loss coefficients (Eqs. 3, 4), one obtains $K = se^{-E/k_BT_0 - t/\tau}$ or $K = \sigma\varphi_0 e^{-\mu z_0 - t/\tau}$, both further reducible to $K(t) = K_0 e^{-t/\tau}$. To incorporate such $K$ into Eq. (1), we rewrite the latter as a set of coupled differential equations:

$$\begin{aligned} dn/dt &= A(N-n) - Kn, \\ dK/dt &= -K/\tau, \end{aligned} \tag{16}$$

which provided $A > 0$ and $K > 0$ are amenable to the analytical solution [10, 13]:

$$\hat{n} = \begin{cases} \tau A(\tau K)^{\tau A} e^{\tau K} \Gamma(-\tau A, \tau K) & \\ \quad -\tau A(\tau K)^{\tau A} e^{\tau K} \Gamma(-\tau A, \tau K_0), & \tau > 0, \\ M(1, 1-\tau A, \tau K) & \\ \quad -(K_0/K)^{-\tau A} e^{-\tau K_0 + \tau K} M(1, 1-\tau A, \tau K_0), & \tau < 0, \end{cases} \tag{17}$$

wherein $\Gamma(a, z)$ is the upper incomplete gamma function, and $M(a, b, z)$ Kummer's confluent hypergeometric function [35]. Depending on further assumptions (if relevant), the second right-hand-side terms in Eq. (17) may be dropped [10, 13]. Clearly, $\tau$ governs the lifetime over which $K$ changes by a factor of $e$.

To translate $\tau$ into a more tangible, linear rate of change, one can take the derivative of Eqs. (14, 15) in respect to time [34], obtaining:

$$\begin{aligned} dT/dt &= -T^2/(\tau E/k_B), \\ dz/dt &= 1/(\tau\mu). \end{aligned} \tag{18}$$

Figure 7 shows selected transient (solid lines) and steady-state profiles ($|\tau| \to \infty$, dashed lines) predicted by Eq. (17) for the

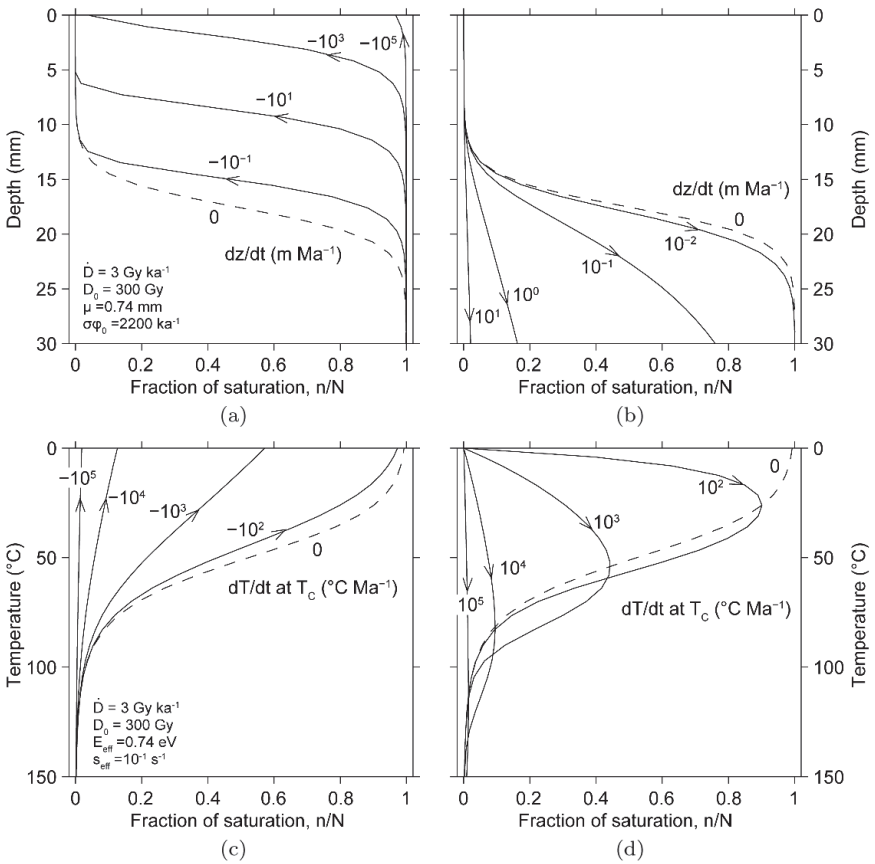


Fig. 7. Transient profiles in a luminescence photochronometer (a–b) and thermochronometer (c–d) from Figs. 1–2, subjected to an exponential growth (a,d) or decay (b,c) of the loss coefficient ($K$) with time (Eqs. 16–17). The linear cooling/heating rates in (c–d) are calculated in the vicinity of the closure temperature (Sec. 3.3) of each corresponding cooling history.

reference photo- and thermo-chronometer shown in Figs. 1, 2. The modelled luminescence systems evolve along solid profile lines, in the direction marked by the arrows. Note that at sufficiently slow rates, the transient profile becomes barely distinguishable from the steady-state profile (dashed curves in Fig. 7). Note that the curves in Figs. 7b and 7c are mirroring, due to the identical assumption of $\hat{n}_0 = 0$. The difference in curve shape across Figs. 7a and 7d discloses different starting conditions, i.e. $\hat{n}_0 = 1$ for a photochronometer being exhumed [13], and $\hat{n}_0 = 0$ for a (sedimentary) thermochronometer being buried [22].

### 11.3.3. *System closure, opening, and resetting*

The concept of system closure [10, 34] links the apparent age of a cooling thermochronometer (eroding photochronometer) to its corresponding environmental paleotemperature (paleodepth). Mathematically, closure involves an extension of the treatment in Sec. 2.5 ($K = const$) to the case of $K(t) = K_0 e^{-t/\tau},\ \tau > 0$. To understand "closure" on an intuitive level, consider Fig. 8a, where each of the 150 random monotonic time-temperature (t-T) paths drives an OSL thermochronometer (Eqs. 1–3 with kinetic parameters from [23]) to an arbitrarily-chosen final concentration of $\hat{n} = 0.73$. To estimate the t-T "bottleneck" that all systems reaching $\hat{n} = 0.73$ seem to have passed through, we can construct an "average" thermal history (thick black curve in Fig. 8a), and read off the temperature (55°C) at the apparent age of the system (66 ka). Note that beyond the apparent age, even storage at $T = \infty$ would not have inhibited the system to subsequently attain $\hat{n} = 0.73$, and thus the "average" cooling history at all times preceding the apparent age is ill-defined, and should not be calculated at all.

In Fig. 8b, the thermal bottleneck is calculated analytically (grey area), while only three end-member t-T paths are further considered [36]: (i) an instantaneous cooling 66 ka ago from $T_0 = \infty$ to the present-day $T_P = 0$°C, (ii) an infinitely long isothermal storage at $T = 41$°C, and (iii) a monotonic cooling from $T_0 = \infty$ to $T_P = 0$°C as given by Eq. (14) with a time constant $\tau = 5.8$ ka. It is scenarios (i) and (iii) that the concept of closure temperature combines. Closure

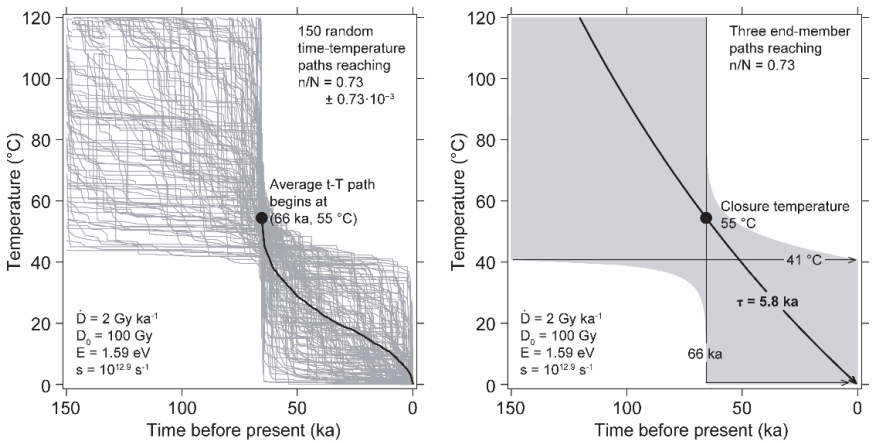


Fig. 8. Random monotonic paths (a) and simplified end-member scenarios (b), evolving to an apparent age of ∼66 ka in a quartz OSL thermochronometer (kinetic parameters from [23]). The thermal bottleneck, through which all scenarios must pass, is well characterized by the closure temperature, formally defined as "the temperature of the system at the time, represented by its apparent age" [34].

temperature ($T_C$) is "the temperature of the system at the time, represented by its apparent age" [34]. Using Eq. (21) to obtain $T_C = 55°\mathrm{C}$, closure temperature can thus be perceived as the analytical counterpart of the empirical "earliest average temperature" derived via Monte-Carlo simulations of random cooling paths in Fig. 8a.

To derive an exact expression for closure temperature in a system obeying first-order reaction kinetics [10], we equate the concentration of a *monotonically-cooled* leaky system (Eq. 17 with $\tau > 0$), to that of an *isothermal* leaky system, held at the final cooling temperature of the former (Eq. 5 with $\hat{n}_0 = 0$):

$$\begin{aligned} &\tau A(\tau K_P)^{\tau A} e^{\tau K_P}[\Gamma(-\tau A, \tau K_P) - \Gamma(-\tau A, \tau K_0)] \\ &\quad = (1 + K_P/A)^{-1}[1 - e^{-(A+K_P)t}], \end{aligned} \tag{19}$$

where $K_0$ and $K_P$ are the loss coefficients at the initial ($T_0$) and final ($T_P$) temperatures of cooling. Solving Eq. (19) for time, and substituting the resultant $t_{app}$ and its input parameters $T_P$, $T_C$ and $\tau$

into Eq. (14), we obtain:

$$1/T_P = 1/T_C + t_{app}/(E\tau/k_B). \tag{20}$$

which after some rearrangement, reduces to [10]:

$$T_C = \left\{ \frac{1}{T_P} + \frac{k_B/E}{\tau A + \tau K_P} \cdot \ln \left[ 1 - \frac{\tau A + \tau K_P}{(\tau K_P)^{-\tau A} e^{-\tau K_P}} \right. \right. \\ \left. \left. \times \left( \Gamma(-\tau A, \tau K_P) - \Gamma(-\tau A, \tau K_0) \right) \right] \right\}^{-1}. \tag{21}$$

While Eq. (21) is valid only for first-order systems (note, that the parameter $A$ here appears as $-\lambda$ in [10]), Eq. (20) is the broader definition of closure temperature, applicable to any luminescence system regardless of its kinetics.

To complement closure, the concepts of system *opening* and *resetting* [37] address systems that undergo continuous heating or burial. To derive the relevant expression, we compare the concentrations of a *monotonically-heating leaky* system with $K(t) = K_0 e^{-t/\tau}$, $\tau < 0$, and its equivalent *closed* system. Starting from the definition of the PRZ (Eq. 7), and substituting Eq. (17) with $\tau < 0$ into the numerator, and Eq. (5) with $K = 0$ in the denominator, we obtain:

$$x = \frac{M(1,\ 1 - \tau A, \tau K) - (K_0/K)^{-\tau A} e^{-\tau K_0 + \tau K} M(1,\ 1 - \tau A, \tau K_0)}{1 - (1 - \hat{n}_0) e^{-At}}. \tag{22}$$

Unlike system closure, to which the apparent age of the system is fundamental [34], the definitions of opening and resetting are arbitrary, and do not depend on age at all [37]. By convention, a system "opens" when its concentration drops to below $x = 99\%$ of an equivalent closed system, and "resets" at $x = 1\%$ [37].

Figure 9 revisits the reference thermochronometer (Figs. 1, 2, and 7) and depicts its closure, opening, and resetting at two different cooling/heating rates ($|dT/dt| = 1000°\text{C Ma}^{-1}$ in Fig. 9a–b, and $100°\text{C Ma}^{-1}$ in Fig. 9c–d). A central message of Fig. 9 is that closure does *not* necessarily have to coincide with the effective onset of concentration growth. Indeed, for $dT/dt = -1000°\text{C Ma}^{-1}$, the relative concentration at $T_C$ is 20% (0.11/0.57) of its final value;

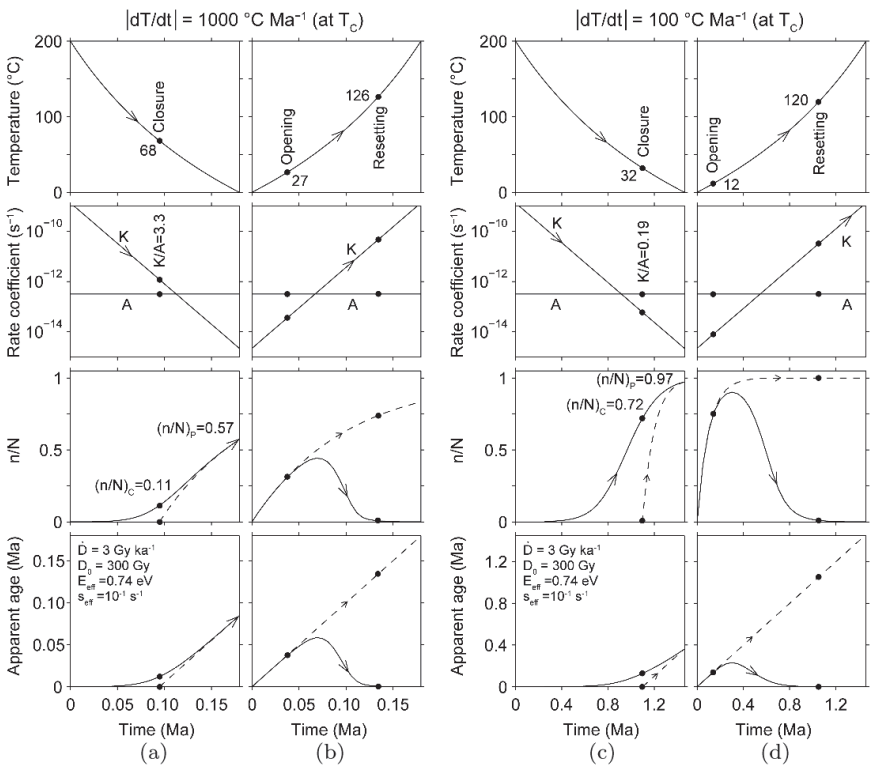


Fig. 9. Closure (a,c) and opening/resetting (b,d) in a luminescence thermochronometer (Figs. 1, 2, 7), subjected to cooling (a,c) and heating (b–d) rates of 1000 (a–b) and 100 (c–d)°C Ma$^{-1}$, respectively. Shown are the evolution of temperature with time (Eq. 14; top row), the rate coefficients (Eqs. 3–4; second row), the concentration (Eq. 17; third row), and apparent age (Eq. 11c; bottom row). Dashed lines represent the behavior of an equivalent closed system (the right-hand-side term in Eq. 19, or the denominator in Eq. 22).

yet for −100°C Ma$^{-1}$, this ratio rises to 74% (0.72/0.97). This emphasizes that in leaky and/or saturating systems, effective closure may correspond to non-negligible concentration. While counter-intuitive, this does not conflict with Dodson's definition of closure [10], and on the contrary, enables to apply the closure formalism to systems with limited product storage space and/or everlasting leaky state [10]. As evident from Fig. 8a, caution must be taken not to extrapolate monotonic histories beyond a point where past

conditions diverge into a field of infinite possibilities. Finally, while Sec. 3.3 has been written mainly with thermochronometry in mind, only minor adaptations are needed to obtain expressions for closure, opening, and resetting depth in photochronometry.

## 11.4. Beyond a single, first-order system

### 11.4.1. *Non-first-order kinetics*

Proportionality of the electron trapping and detrapping rates to the number of empty and filled traps, respectively (Eq. 1; first-order reaction kinetics) is a robust assumption and hence the accepted default in all trapped charge dating applications [2, 10]. However, laboratory experiments often reveal some degree of deviation from first-order behavior. In particular, the ubiquity of slower-than-exponential kinetics (i.e. processes that start as first-order reactions but progressively become slower and slower) accentuates the need for adaptations and/or alternatives to the first-order kinetics model, especially when extrapolation over geological timescales is necessary.

A simple mathematical extension to Eq. (1), known as the General Order Kinetics (GOK) model, enables to capture the progressive departure from first-order behavior via:

$$dn/dt = A(N - n)^{\alpha} - Kn^{\beta}, \tag{23}$$

where $\alpha \geq 1$ and $\beta \geq 1$ are unitless kinetic orders [38]. For $\alpha = \beta = 1$, Eq. (23) reduces to Eq. (1), while higher orders slow down the accumulation and loss, often in line with experimental behavior (Fig. 10). The advantage of GOK is that it describes the system with a single rate equation as before, and has reasonable physical interpretations of the additional model parameters, i.e. the exponents $\alpha$ (e.g. Coulomb repulsion [38]) and $\beta$ (e.g. electron retrapping [18]). However, since $\alpha$ and $\beta$ are not directly relatable to any actual physical quantities, GOK is rarely viewed as a physically-driven formulation. Furthermore, in the general case, Eq. (23) is a "stiff" differential equation requiring a numerical solution with adequate step-size adjustment throughout the integration.

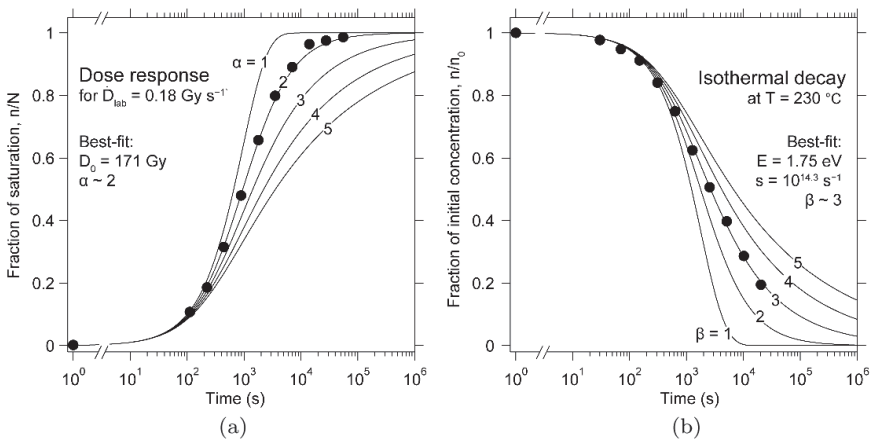


Fig. 10. The effect of kinetic orders ($\alpha$ and $\beta$ in Eq. (23) [38]) on the rates of electron trapping (a) and thermal detrapping (b), in a representative sample (19B) from the KTB borehole (Germany) [4]. Note, that the experimental data (filled circles) align along kinetic orders of 2 (a) and 3 (b), respectively. See text for alternative interpretation of these data.

As an alternative to the GOK model, one can instead hypothetically divide the electron traps into a continuum of subpopulations $i$, each governed by first-order kinetics but with its own parameters $A_i$, $K_i$ and $N_i$ [e.g. 39]:

$$dn_i/dt = A_i(N_i - n_i) - K_i n_i, \quad n/N = \sum_i n_i \Big/ \sum_i N_i. \tag{24}$$

For example, a similarly good fit (not shown) to the experimental data in Fig. 10 can be obtained via a continuum of first-order systems with a Gaussian distribution of the kinetic parameters [40, 41], specifically $D_0 = 10^{2.5\pm0.5}$ Gy (Fig. 10a) and $E = 1.81 \pm 0.08$ (Fig. 10b). The advantage of using the trap continuum in Eq. (24) is that each subsystem has simple analytical solutions; the disadvantage is that trap breakdown into discrete and non-interacting subpopulations is often difficult to justify and/or confirm physically, while taking such interactions into account would greatly increase the complexity of the problem.

To conclude, the two common approaches to address non-first order kinetics (Eqs. 23, 24) must be regarded as complementary, each

with its own benefits and drawbacks, while hybrid models may offer a potential compromise [4]. Most importantly, it must be recognized that neither approach addresses the complex luminescence behavior to the full. Finally, despite the important quest for adapting and perfecting the kinetic models, adequate first-order analogues should not be overlooked. In fact, first-order systems can often provide acceptable approximations of real system behavior via "effective" kinetic parameters that are not necessarily physically comprehensive, but are nevertheless capable of describing complex systems sufficiently. Such is the case with the reference thermochronometer in Figs. 1, 2, 7 and 9, which is a robust first-order equivalent of a highly non-first-order system as rigorously explored in [4].

### 11.4.2. *Athermal loss*

Recombination of trapped electrons with their nearest-neighboring holes via quantum mechanical tunneling [42] (also known as *anomalous fading* [43]), is a ubiquitous athermal process that takes place in complex and/or disordered crystalline lattices, e.g. feldspar or volcanic quartz [44, 45]. The fact that this process may compete with optical and/or thermal losses, implies that it can potentially bias photo- and thermochronometry results if unaccounted for [46]. In luminescence dating, two contrasting ways to account for anomalous fading are: (i) detailed physical modelling of its effects [e.g., 39, 42], or (ii) avoiding its effects altogether by electron trap subsampling [47, 48]. While both approaches have been validated, the following example is set to demonstrate the severe effect of unaccounted anomalous fading on thermochronological results.

For the exercise, we return to the Luochuan locality (Sec. 2.5), and consider yet another luminescence age dataset from the Loess Plateau, obtained using the $IRSL_{50}$ signal in K-feldspar [47]. Adopting the nominal kinetic parameters of K-feldspar $IRSL_{50}$ [27], and assuming purely thermal losses, we use Eq. (12c) to convert each pair of independent and luminescence age into a corresponding environmental paleotemperature (Fig. 11a,c). Unlike in Sec. 2.5, the inverted temperatures are all unreasonably high ($81 \pm 3$°C). Recognizing that the persistence of simmering near-surface temperatures during

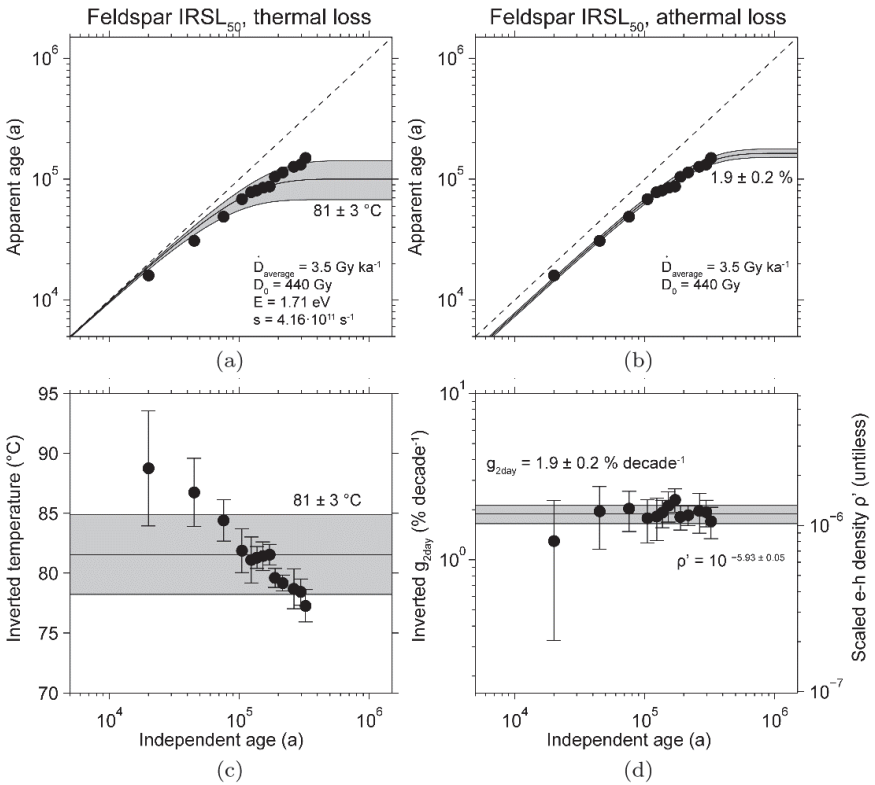


Fig. 11. (a–b) Apparent ages of the K-feldspar $IRSL_{50}$ signal from the Luochuan type section, plotted against independent age control [47]. Explaining the observed age underestimations via thermal loss (cf. Fig. 5) yields unrealistic environmental temperatures (c); discarding the paleotemperature reconstruction, and reconsidering the losses to have been solely governed by anomalous fading, yields far more plausible results (d).

the late Quaternary is highly unlikely, we seek an alternative explanation for the departure of luminescence ages from their independent constraints, and evaluate a purely athermal loss of signal. Involving a power-law loss with time [42], the accumulation of trapped electrons under continuous anomalous fading can be modelled via a continuum of first-order sub-systems [39, 42], i.e. Eq. (24) with:

$$N(r') = 3r'^2 \exp(-r'^3), \quad K(r') = s \exp(-\rho'^{-1/3} r') \qquad (25)$$

where $r'$ and $\rho'$ (both dimensionless) are the scaled electron-hole separation distance and hole density, respectively. Fitting Eqs. (24, 25) to the data in Fig. 11b yields a best-fit scaled electron-hole density $\rho' = 10^{-5.93}$ (equivalent to $g_{2days} = 1.9\%$/decade [39]), which is in agreement with the laboratory observation that $IRSL_{50}$ in these minerals fades [47], and possibly even provides a more realistic estimate of fading than its laboratory measurement [49]. Furthermore, the fit to the data (Fig. 11b) is far more adequate than that in Fig. 11a, further discarding the paleotemperature interpretation considered earlier as improbable. Note that no temperature can be inferred from the fit in Fig. 11b,d; the age discrepancy between K-feldspar $IRSL_{50}$ ages and independent chronometry is purely due to athermal loss of signal; maximum possible temperatures can be obtained [4], but are of little interest for the present example.

To conclude, Sec. 4.2 illustrates that a failure to account for anomalous fading can result in a gross misinterpretation of past environmental conditions. For current practices of combining thermal and athermal losses, the reader is referred to [4, 50, 51]; the utilization of combined optical and athermal losses [16, 17] is yet to be undertaken.

### 11.4.3. *Inversion of multi-signal systems*

Shortly after thermoluminescence dating was introduced to the scientific community [52], it has been proposed that discernible luminescence subsignals within the same rock (or mineral) may hold a record of a continuous exposure history [53]. However, almost 60 years would pass before both the luminescence theory and the accompanying methodology would be sufficiently mature to enable routine extraction and quantification of such histories. Here, we revisit two recent studies [12, 50] that pioneer the utilization of a suite of luminescence signals with varying optical (thermal) stabilities for constraining a common and continuous optical (thermal) exposure history. This brief re-analysis invokes many of the previously introduced concepts, and thus provides a concluding demonstration on how theory developed in Secs. 1–3 meets some of the real-life questions arising in geology [50] and physical geography [12].

Figure 12a presents multi-signal thermochronometric data from a single rock (NB124) collected in the vicinity of Namche Barwa (Tibet) [50]. This unique geological setting is among the fastest-eroding regions worldwide and feeds a long-standing debate on the interactions between climate and tectonics. Surely not the final say in the dispute, the luminescence thermochronometry study [50] is nonetheless noteworthy for placing multiple unprecedented constraints on the thermal histories of the analyzed rocks on a <0.1 Ma timescale, generally inaccessible by mainstream thermochronometers [5]. Given two marginally different feldspar mineralogies (K-feldspar vs. Na-rich K-feldspar), and four distinguishable luminescence signals in each, there is a total of eight presumably independent systems sharing the same thermal history. In the case of a continuous cooling scenario, older apparent ages ($t_{app}$) may be expected for signals with higher thermal stability. This is exactly what has been observed in practice: the obtained $t_{app}$ and their corresponding closure temperatures $T_C$ align along a clear cooling trend in the 100–50 ka and 80–50°C range (Fig. 12a). A simple regression of

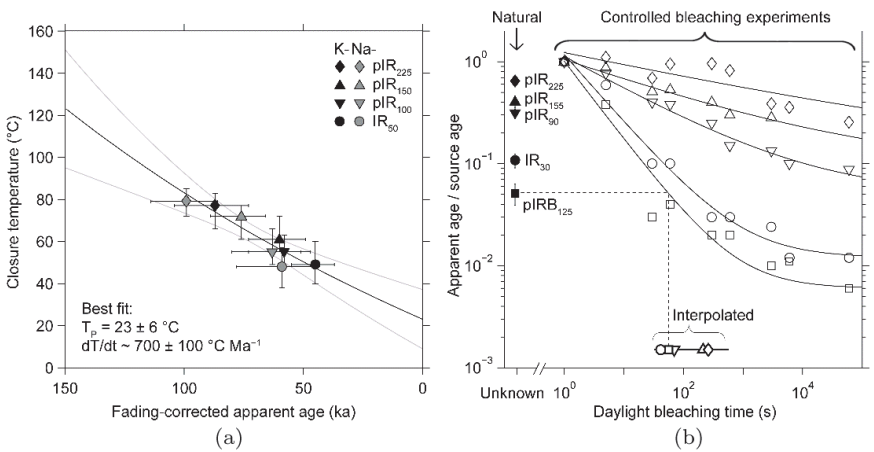


Fig. 12. Utilization of multi-signal systems in thermo- and photochronometry. (a) The recent cooling pathway of sample NB124 (Namche Barwa, [50]) as constrained by eight individual apparent ages and closure temperatures. (b) The daylight exposure duration of sample ZM-07-A1 (De Zandmotor, The Netherlands [12]) as constrained by the intersection of five individual apparent ages.

Eq. (14) through the $(t_{app}, T_C)$ data in Fig. 12a yields a cooling rate of $\sim 700 \pm 100$°C Ma$^{-1}$ (essentially the same as in [50]); the intercept of the regressed cooling history predicts a modern surface temperature of $23 \pm 6$°C — high, but not unreasonable. In combination with other data, the high cooling rate of NB124 has been used to question the notion of a spatially-fixed locus of tectonic uplift at Namche Barwa and to support a rivalling theory of a northward migration of regional tectonic deformation [50].

Figure 12b presents multi-signal photochronometric data from a multimineral sand sample (quartz and feldspar) originating from De Zandmotor ("the sand engine"), a coastal mega-nourishment project at the shore of Delftland coast, southwest of the city The Hague (The Netherlands) [12]. De Zandmotor consists of $\sim 22$ Mm$^3$ of fluvial sand, dredged from the sea bottom (offshore Rhein deposits) and redistributed along a 2.5 km long coastal stretch; it is a pilot project of the new Dutch coastal protection scheme, set to mitigate the effects of a future sea-level rise and more frequent storm activity. The luminescence dating of the parent material ($\sim$43 ka) and of the redistributed (progressively younger) sands was aimed at constraining the modes (e.g. aerial vs. water-lain redeposition) and the timing (continuous vs. storm-related) of coastal sediment dynamics, ultimately providing insight into the efficiency of the new coastal nourishment strategy. The apparent ages of five luminescence signals in sample ZM-07-A1, normalized to their corresponding values in the parent material, are shown as filled symbols in Fig. 12b. In analogy with Sec. 2.5, where we converted age deficits into storage temperatures, here we can similarly convert an age deficit into a cumulative duration of exposure to daylight. Open symbols in Fig. 12b illustrate the rates at which the luminescence signals of the parent material reduced with progressive exposure to daylight in monitored open-air conditions outside of the laboratory. The interpolation of the natural luminescence signals of ZM-07-A1 (filled symbols) onto signal decay curves regressed through the laboratory bleaching data (curves and open symbols, respectively), follows the same methodology as in [50], and constrains the cumulative daylight exposure of sample ZM-07-A1 to $10^{2.0 \pm 0.5}$ s, i.e. 0.5–5 minutes of effective daylight. Given

∼700–800 meters separating the location where the source sand has been dumped, and the location of sample ZM-07-A1 whereto the sand has naturally drifted, the relatively short effective daylight exposure (0.5–5 minutes) points at two possibilities, i.e. either (i) a continuous sub-aerial sand drift underwater (where daylight is attenuated), or (ii) an abrupt semi-aerial sand redeposition during a few storm events. Further insight into the governing process could possibly be gained via controlled luminescence bleaching experiments underwater.

An even bigger multitude of presumably discrete luminescence subsignals (e.g. in feldspar thermoluminescence [54, 55]), each offering a unique thermal or photosensitive "bottleneck" that the natural luminescence system can be traced through (cf. Fig. 8), may eventually retire some of the analytical tools presented in Secs. 1–3. Specifically, one could bypass analytics altogether by generating random exposure histories (e.g. Fig. 8a), predicting the resultant trap subpopulations (e.g. Eq. 1–3), and finally assessing which of those exposure histories predict the observations within an agreed-upon threshold [50, 51]. Conceptually similar to the interpretation of continuous degassing spectra of $^{40}Ar/^{39}Ar$ or $^{4}He/^{3}He$ [5], such numerical methods are able to address not only smooth continuous processes, but also periods of acceleration or deceleration in signal loss. Such non-linear scenarios could occur due to a non-smooth time-temperature history (e.g. during a complex erosion history [56]), or due to secular changes in light intensity (e.g. following hemispheric dispersal of volcanic ash, filtering certain light wavelengths for long periods). While such numerical approaches would not be limited by simplistic assumptions of constant environmental conditions (Eqs. 5, 12c) or constant rates of their change (Eqs. 14, 15), they do require far more rigorous sensitivity tests in comparison to analytical solutions. For example, in thermochronometry it would be critical to evaluate which parts of the reconstructed cooling curve are constrained by which luminescence subsignals and whether the independence of these subsignals is experimentally justifiable. In photochronometry it would be of critical importance to demonstrate that the effects of charge redistribution across the different trap subpopulations during

progressive light exposure are either negligible or can be accounted for. To conclude, it appears that for a meaningful and successful interpretation in both photo- and thermochronometry, numerical and analytical methods should go hand-in-hand rather than compete with each other.

## 11.5. Summary and outlook

Luminescence photo- and thermochronometry are relatively new subdisciplines in the domain of trapped charge dating. Historically, each has been shaped after and influenced by its closest field in Earth science, namely cosmogenic nuclide dating [6], and noble-gas thermochronometry [5], respectively. While the mathematical treatment of both photo- and thermochronometry essentially reduces to the very same equations (Secs. 1–4), slightly different practices have emerged in each field. For example, in thermochronometry, a single hand-specimen is typically treated as an individual entity and assigned a single apparent age and closure temperature [4, 10], unless multiple signals are targeted [50]. On the other hand, in photochronometry it is more common to subdivide a hand-specimen into multiple subsamples, constructing a depth profile and calculating a common age to all points [13, 14]. In thermochronometry, one typically calibrates the kinetic parameters in the laboratory [4]; in photochronometry, via "field" calibration [13, 14]. The list of differences goes on, but most of them merely reflect common practices rather than highlight some inbuilt restrictions. In most cases, analytical practices can be easily exchanged between the two fields (e.g. assignment of individual ages per each surface exposure depth, or derivation of a common age for a thermochronometry profile). This has been the objective of this chapter — to highlight the parallels between the two techniques and stimulate a fruitful technological transfer and an open dialogue between the two.

## Acknowledgements

We are indebted to K. Hippe, M. M. Tremblay, F. Herman, G. E. King, and P. G. Valla for insightful reviews that greatly improved

this work. J. Q. G. Spencer, M. S. Chapot, B. Li, and T. Reimann are thanked for discussions regarding their data, revisited in Figs. 4, 5, 11, and 12. BG was supported by the Netherlands Organization for Scientific Research (NWO) Veni grant 863.15.026.

## References

[1] A.G. Wintle, "Luminescence dating: where it has been and where it is going," *Boreas*, vol. 37, pp. 471–482, 2008.

[2] G.E. King, B. Guralnik, P.G. Valla and F. Herman, "Trapped-charge thermochronometry and thermometry: A status review," *Chem. Geol.*, vol. 446, pp. 3–17, 2016.

[3] R. Sohbati, "Luminescence, Rock Surfaces," *Encyclopedia Sci. Dating Methods*, pp. 485–488, 2015.

[4] B. Guralnik, M. Jain, F. Herman, C. Ankjærgaard, A.S. Murray, P.G. Valla, F. Preusser, G.E. King, R. Chen, S.E. Lowick, M. Kook and E.J. Rhodes, "OSL-thermochronology of feldspar from the KTB Borehole, Germany," *Earth Planet. Sci. Lett.*, vol. 423, pp. 232–243, 2015.

[5] P.W. Reiners and T.A. Ehlers, *eds.* "Low-Temperature Thermochronology: Techniques, Interpretations, Applications," *Rev. Mineral. Geochem.*, vol. 58, 2005.

[6] T.J. Dunai, "Cosmogenic Nuclides: Principles, concepts and applications in the Earth surface sciences," *Cambridge University Press*, 2010.

[7] J.I. Garver, M.T. Brandon, M. Roden-Tice and P.J. Kamp, "Exhumation history of orogenic highlands determined by detrital fission-track thermochronology," *Geol. Soc. London Spec. Pub.*, vol. 154, pp. 283–304, 1999.

[8] M.M. Tremblay, D.L. Shuster and G. Balco, "Cosmogenic noble gas paleothermometry," *Earth Planet. Sci. Lett.*, vol. 400, pp. 195–205, 2014.

[9] C. Glotzbach, "Deriving rock uplift histories from data-driven inversion of river profiles," *Geology*, vol. 43, pp. 467–470, 2015.

[10] B. Guralnik, M. Jain, F. Herman, R.B. Paris, T.M. Harrison, A.S. Murray, P.V. Valla and E.J. Rhodes, "Effective closure temperature in leaky and/or saturating thermochronometers," *Earth Planet. Sci. Lett.*, vol. 384, pp. 209–218, 2013.

[11] R. Sohbati, M. Jain and A.S. Murray, "Surface exposure dating of non-terrestrial bodies using optically stimulated luminescence: A new method," *Icarus*, vol. 221, pp. 160–166, 2012.

[12] T. Reimann, P.D. Notenboom, M.A. De Schipper and J. Wallinga, "Testing for sufficient signal resetting during sediment transport using a polymineral multiple-signal luminescence approach," *Quat. Geochron.*, vol. 25, pp. 26–36, 2015.

[13] R. Sohbati, J. Liu, M. Jain, A.S. Murray, D. Egholm, R.B. Paris and B. Guralnik, "Centennial- to millennial-scale hard rock erosion rates deduced from luminescence-depth profiles," *Earth Planet. Sci. Lett.*, (in press).

[14] M.S. Chapot, R. Sohbati, A.S. Murray, J.L. Pederson and T.M. Rittenour, Constraining the age of rock art by dating a rockfall event using sediment and rock-surface luminescence dating techniques, *Quat. Geochron.*, vol. 13, pp. 18–25, 2012.

[15] C. Christodoulides, K.V. Ettinger and J.H. Fremlin, "The use of TL glow peaks at equilibrium in the examination of the thermal and radiation history of materials," *Mod. Geol.*, vol. 2, pp. 275–280, 1971.

[16] M. Jain, B. Guralnik and M.T. Andersen, "Stimulated luminescence emission from localized recombination in randomly distributed defects," *J. Phys. Condens. Matter*, vol. 24, p. 385402, 2012.

[17] M. Jain, R. Sohbati, B. Guralnik, A.S. Murray, M. Kook, T. Lapp, A.K. Prasad, K.J. Thomsen and J.P. Buylaert, "Kinetics of infrared stimulated luminescence from feldspars," *Radiat. Meas.*, vol. 81, pp. 242–250, 2015.

[18] S.W.S. McKeever and R. Chen, "Luminescence models," *Radiat. Meas.*, vol. 27, pp. 625–661, 1997.

[19] M.J. Aitken, *Thermoluminescence Dating*, London, Academic Press, 1985.

[20] G.A.T. Duller, "Luminescence Dating: guidelines on using luminescence dating in archaeology," *English Heritage*, 2008.

[21] J. Liu, A.S. Murray, J.P. Buylaert, M. Jain, J. Chen and Y. Lu, "Stability of fine-grained TT-OSL and post-IR IRSL signals from a ca. 1 Ma sequence of aeolian and lacustrine deposits from the Nihewan Basin (northern China)," *Boreas*, vol. 45, pp. 703–714, 2016.

[22] G.L. Gong, S.H. Li, W.D. Sun, F. Guo, B. Xia and B.F. Lü, "Quartz thermoluminescence — another potential paleo-thermometer for studies of sedimentary basin thermal history," *Chin. J. Geophys.*, vol. 53, pp. 103–112, 2010.

[23] A.S. Murray and A.G. Wintle, "Isothermal decay of optically stimulated luminescence in quartz," *Radiat. Meas.*, vol. 30, pp. 119–125, 1999.

[24] A.G. Wintle and A.S. Murray, "A review of quartz optically stimulated luminescence characteristics and their relevance in single-aliquot regeneration dating protocols," *Radiat. Meas.*, vol. 41, pp. 369–391, 2006.

[25] B. Guralnik, C. Ankjærgaard, M. Jain, A.S. Murray, A. Müller, M. Wälle, S.E. Lowick, F. Preusser, E.J. Rhodes, T.-S. Wu, G. Mathew and F. Herman, "OSL-thermochronometry using bedrock quartz: a note of caution," *Quat. Geochron.*, vol. 25, pp. 37–48, 2015.

[26] J.Q. Spencer, J. Hadizadeh, J.P. Gratier and M.L. Doan, Dating deep? Luminescence studies of fault gouge from the San Andreas Fault zone 2.6 km beneath Earth's surface, *Quat. Geochron.*, vol. 10, pp. 280–284, 2012.

[27] A.S. Murray, J.P. Buylaert, K.J. Thomsen and M. Jain, "The effect of preheating on the IRSL signal from feldspar," *Radiat. Meas.*, vol. 44, pp. 554–559, 2009.

[28] K. Héberger, S. Kemény and T. Vidóczy, "On the errors of Arrhenius parameters and estimated rate constant values," *Int. J. Chem. Kinetics*, vol. 19, pp. 171–181, 1987.

[29] Z.-P. Lai and A. Fan, "Examining quartz OSL age underestimation for loess samples from Luochuan in the Chinese Loess Plateau," *Geochronometria*, vol. 41, pp. 57–64, 2014.
[30] M.S. Chapot, H.M. Roberts, G.A.T. Duller and Z.P. Lai, "Natural and laboratory TT-OSL dose response curves: Testing the lifetime of the TT-OSL signal in nature," *Radiat. Meas.*, vol. 85, pp. 41–50, 2016.
[31] A. Bronger and T. Heinkele, "Micromorphology and genesis of paleosols in the Luochuan loess section, China: pedostratigraphic and environmental implications," *Geoderma*, vol. 45, pp. 123–143, 1989.
[32] H. Jiamao, L. Houyuan, W. Naiqin and G. Zhengtang, "The magnetic susceptibility of modern soils in China and its use for paleoclimate reconstruction," *Studia Geophysica et Geodaetica*, vol. 40, pp. 262–275, 1996.
[33] W.Y. Shi, J.G. Zhang, M.J. Yan, N. Yamanaka and S. Du, "Seasonal and diurnal dynamics of soil respiration fluxes in two typical forests on the semiarid Loess Plateau of China: Temperature sensitivities of autotrophs and heterotrophs and analyses of integrated driving factors," *Soil Biol. Biochem.*, vol. 52, pp. 99–107, 2012.
[34] M.H. Dodson, "Closure temperature in cooling geochronological and petrological systems", *Contrib. Mineral. Petrol.*, vol. 40, pp. 259–274, 1973.
[35] M. Abramowitz and I.A. Stegun, "Handbook of Mathematical Functions with Formulas, Graphs, and Mathematical Tables (Vol. 55)," *National Bureau of Standards, U.S. Government Printing Office*, 1964.
[36] T.S. Wu, M. Jain, B. Guralnik, A.S. Murray and Y.G. Chen, "Luminescence characteristics of quartz from Hsuehshan Range (Central Taiwan) and implications for thermochronometry," *Radiat. Meas.*, vol. 81, pp. 104–109, 2015.
[37] E. Gardés and J.M. Montel, "Opening and resetting temperatures in heating geochronological systems," *Contrib. Mineral. Petrol.*, vol. 158, pp. 185–195, 2009.
[38] B. Guralnik, B. Li, M. Jain, R. Chen, R.B. Paris, A.S. Murray, S.H. Li, V. Pagonis, P.G. Valla and F. Herman, "Radiation-induced growth and isothermal decay of infrared-stimulated luminescence from feldspar," *Radiat. Meas.*, vol. 81, pp. 224–231, 2015.
[39] R.H. Kars, J. Wallinga and K.M. Cohen, "A new approach towards anomalous fading correction for feldspar IRSL dating-tests on samples in field saturation," *Radiat. Meas.*, vol. 43, 786–790, 2008.
[40] D.J. Huntley, M.A. Short and K. Dunphy, "Deep traps in quartz and their use for optical dating," *Canad. J. Phys.*, vol. 74, pp. 81–91, 1996.
[41] R. Lambert, G.E. King, P.G. Valla, F. Herman, "Investigating thermal kinetic processes of feldspar for the application of luminescence thermochronometry," *Radiat Meas.* (in revision).
[42] D.J. Huntley, "An explanation of the power-law decay of luminescence," *J. Phys. Condens. Matter*, vol. 18, p. 1359, 2006.
[43] A.G. Wintle, "Anomalous fading of thermoluminescence in mineral samples," *Nature*, vol. 245, pp. 143–144, 1973.

[44] R. Visocekas, C. Barthou and P. Blanc, "Thermal quenching of far-red $Fe^{3+}$ thermoluminescence of volcanic K-feldspars," *Radiat. Meas.*, vol. 61, pp. 52–73, 2014.

[45] C. Thiel, S. Tsukamoto, K. Tokuyasu, J.P. Buylaert, A.S. Murray, K. Tanaka and M. Shirai, "Testing the application of quartz and feldspar luminescence dating to MIS 5 Japanese marine deposits," *Quat. Geochron.*, vol. 29, pp. 16–29, 2015.

[46] P.G. Valla, S.E. Lowick, F. Herman, J.D. Champagnac, P. Steer and B. Guralnik, Exploring $IRSL_{50}$ fading variability in bedrock feldspars and implications for OSL thermochronometry, *Quat. Geochron.*, vol. 36, pp. 55–66, 2016.

[47] B. Li and S.-H. Li, "Luminescence dating of K-feldspar from sediments: a protocol without anomalous fading correction," *Quat. Geochron.*, vol. 6, pp. 468–479, 2011.

[48] J.P. Buylaert, M. Jain, A.S. Murray, K.J. Thomsen, C. Thiel and R. Sohbati, "A robust feldspar luminescence dating method for Middle and Late Pleistocene sediments," *Boreas*, vol. 41, pp. 435–451, 2012.

[49] B. Li, Z. Jacobs, R.G. Roberts, and S.H. Li, "Review and assessment of the potential of post-IR IRSL dating methods to circumvent the problem of anomalous fading in feldspar luminescence," *Geochronometria*, vol. 41, pp. 178–201, 2014.

[50] G.E. King, F. Herman, R. Lambert, P.G. Valla and B. Guralnik, "Multi-OSL-thermochronometry of feldspar," *Quat. Geochron.*, vol. 33, pp. 76–87, 2016.

[51] G.E. King, F. Herman and B. Guralnik, "Northward migration of the eastern Himalayan syntaxis revealed by OSL thermochronometry," *Science*, vol. 353, pp. 800–804, 2016.

[52] F. Daniels, C.A. Boyd and D.F. Saunders, "Thermoluminescence as a research tool," *Science*, vol. 117, pp. 343–349, 1953.

[53] F.G. Houtermans, E. Jäger, M. Schön and H. Stauffer, "Messungen der thermolumineszenz als mittel zur untersuchung der thermischen und der strahlungsgeschichte von natürlichen mineralien und geisteinen," *Ann. Phys.*, vol. 20, pp. 283–292, 1957.

[54] N.D. Brown, E.J. Rhodes and T.M. Harrison, "Using thermoluminescence signals from feldspars for low-temperature thermochronology," *Quat. Geochron.*, vol. 42, pp. 31–41, 2017.

[55] R.H. Biswas, F. Herman, G.E. King and J. Braun, "Thermoluminescence of feldspar as a multi-thermochronometer to constrain the temporal variation of rock exhumation in the recent past," *Earth Planet. Sci. Lett.* (in review).

[56] F.M. Richter, O. Lovera, T.M. Harrison and P. Copeland, Tibetan tectonics from $^{40}Ar/^{39}Ar$ analysis of a single K-feldspar sample. *Earth Planet. Sci. Lett.*, vol. 105, pp. 266–278, 1991.

This page intentionally left blank

# Chapter 12

# Medical Applications of Luminescent Materials

Larry A. DeWerd*, Cliff Hammer* and Stephen Kry†

*Department of Medical Physics
Medical School, University of Wisconsin
Madison, WI, USA
ladewerd@wisc.edu
†Department of Radiation Physics
The University of Texas MD Anderson Cancer Center
Houston, TX

Luminescent materials have long been an integral part of radiation measurement with a long history of investigation and wide range of applications. This chapter will explore the processes affecting the applications of the luminescent materials in the fields of Health and Medical Physics, and will focus on the two primary luminescent materials and their methodologies in use today: thermoluminescent dosimeters (TLD) and optically stimulated luminescent dosimeters (OSLD). Discussion will include dosimeter types, expected precision and accuracy, dosimeter limitations, proper handling techniques and readout systems used for each dosimeter. Calibrations, corrections, general and specific use considerations as well as precision-enhancing procedures will also be discussed in order to establish best practices for optimum measurement results. The end of the chapter will apply these processes and develop an example of a best uncertainty budget. This chapter is meant to provide the reader with the information necessary to successfully implement their own luminescent-dosimeter system.

## 12.1. Introduction

The use of luminescent materials for the purpose of radiation measurement has an extensive history in the fields of Health and Medical

Physics. Some of the major uses of luminescent materials include personnel and environmental dose monitoring (Health Physics), as well as therapy and diagnostic ionizing radiation measurements (Medical Physics). A "dosimeter" is the common name for these radiation (dose) measurement materials. The two major types of luminescent dosimeters are Thermoluminescent Dosimeters (TLD) and Optically Stimulated Luminescent Dosimeters (OSLD.) TLDs have been studied more extensively and have a longer history of use. The processes for accurate TLD measurement are well established and have been implemented for decades. While OSLDs are relatively newer, much work has been done in recent years to characterize and improve the accuracy of OSLD measurements. Historical use of both of these types of detector have been based on passive dosimetry methods, where irradiation of the dosimeter and read-out of the signal are done at separate times. Recently, however, use of luminescent materials as scintillators has been investigated in therapy applications to provide real-time dosimetry. The most promising of the scintillators are organic based, because their absorption properties are similar to tissue. At higher energies, the scintillators display a Cerenkov effect that must be accounted for. Although scintillators show much promise, they will not be dealt with in this chapter, due to their relatively newer application as dosimeters.

All luminescent processes are dependent on impurities and the defect structure of the material. Other chapters in this book deal with these topics in detail. This chapter will deal with the characteristics, applications and handling procedures for precise use of TLDs and OSLDs. There are many phosphors used for luminescence dosimetry both for TLD and OSLD. However, the fundamental processes discussed in this chapter would be applicable in modified form for any luminescent material. The process for each of these parameters will be explored for the major types of dosimeters used for medical applications. The two specific formulations discussed will be LiF:Mg,Ti for TLDs (known as TLD-100 commercially) and $Al_2O_3$:C for OSLD (nanoDot).

Both OSLDs and TLDs are extensively used today in Health Physics. The accuracy needed for most Health Physics dosimetric

applications, such as personnel dosimetry, is generally 10–20%. The majority of these measurements are low dose and require a sensitive dosimeter. A "badge" is the common terminology for the dosimeter in these applications. These badges are used for a set amount of time, typically monthly or quarterly, and sent back to the company providing the service for readout and analysis. The emphasis for Health Physics badges is on the efficiency of their use, including automatic readout procedures.

This chapter will focus on the medical dosimetry applications of these materials, since great care must be taken in each case to obtain the precision needed. Diagnostic measurements, such as measurements during a mammographic exam or quality control procedures, require a higher accuracy of at least 10%. When TLDs or OSLDs are used for Diagnostic applications, an account for energy dependence of the signal is typically warranted, unless the dosimeters are calibrated with a beam energy very similar to that used experimentally. Energy dependence is a substantial factor if the dosimeters are calibrated at a high energy, such as $^{60}$Co and then used to measure dose in Diagnostic x-ray beams. TLDs can over-respond relative to $^{60}$Co by up to a factor of 1.4 at low energies (Nunn *et al.* [1]) while OSLDs can have an overresponse as high as 3.5 (Gasparian *et al.* [2]). Energy response investigations and applications will be discussed in more detail later in this chapter.

The most precise and accurate dosimetry application is for therapy measurements, requiring accuracies of 5% or less. Beam quality variations have only a small impact on the response of either TLD or OSLD irradiated with Megavoltage beams; across different MV beam energies, the response varies by less than a 3% compared to $^{60}$Co. (Mobit *et al.* [3]). However, for the high precision requirements of therapy applications, other corrections must also be managed. Most notably, non-linearity in the dose response is substantial compared to the uncertainty budget, particularly for OSLD, where a 5% over-response of the detector occurs at a dose of $\sim$5 Gy (compared to a calibration dose of 1 Gy, Omotayo *et al.* [4]).

Other challenges and limitations of luminescent dosimeters may be relevant in the case of specific applications. The form factor

can be very important for therapy applications, especially for small fields. With therapeutic treatment fields becoming smaller, the need for equally small dosimeters has become a necessity for accurate measurements. Further discussion on field size limitations will be addressed later in this chapter.

## 12.2. Crystal growth for TLD and OSLD

The intent of this section is to provide a general overview of the process of crystal growth, in order to give context for the various TLD and OSLD dosimeter form factors. After crystal growth, there are processes necessary to get useable dosimeters.

When TLD crystals are grown, such as LiF with impurities, the process is well known and outlined below. For the standard LiF:Mg,Ti formulation, the crystal seed is pulled from the melt, which has a specific concentration of magnesium and titanium impurities. The standard concentration is 200 ppm of Mg and 20 ppm of Ti. The magnesium and titanium concentrate on opposite ends of the boule. Thus, when the boule is complete, the concentration of the impurities is not constant across the crystal, causing the corresponding TL sensitivity to vary considerably. Therefore, a section within the center of the boule is ground into powder and mixed to achieve greater uniformity. This powder can be used directly or can be pressed into a solid format, such as an extruded solid or by depositing it on a surface, such as Teflon or other plastic sheeting. The powder can be compressed into a solid form, commonly an extruded solid, in the form of either rods, chips (commonly 3.2 mm × 3.2 mm × 0.89 mm) or cubes (1 mm on a side). Considering that this powder is pressed into these forms, it is not surprising that there would be some dissolution if directly placed in tissue. This, combined with the toxicity (albeit mild) of lithium, (McKinlay [5]) means that the dosimeters should be bagged and sealed before placing them in tissue.

OSLDs are commercially available only in solid form (discs and strips) and consist of only one material for medical applications: $Al_2O_3$:C, and essentially is available only as a single product called

the nanoDot$^{TM}$. A similar deposition process as above is used for OSL dosimeters, where the aluminum oxide crystal is grown with carbon impurities. This crystal is ground into a relatively uniform powder, fixed onto a plastic tape, which is then punched into discs that are mounted into light-tight plastic cassettes. The useable and readable disc area of the nanoDot$^{TM}$ is 4 mm in diameter, and is 0.2 mm thick. Because the powder is embedded in a tape layer and because of the high chemical stability of $Al_2O_3$ crystals, OSLDs are not damaged by submersion (for short periods of time) in water (Ref. [6]). Futhermore, because they are non-toxic, they could be placed directly in tissue (although good sterilization procedures would still involve bagging and sealing them).

## 12.3. Precision and accuracy of luminescence signal

Consistent dosimeter handling and treatment methodology is crucial for obtaining precision in the output of the luminescence signal. When using TL as a medical dosimeter, high accuracy and precision are both necessary. Accuracy can be defined as the closeness to the conventional true value (or the absolute correct value) as determined by a primary laboratory. Accuracy is best determined through a traceable ionization chamber that has a quantity that is traceable to a primary laboratory. Precision is defined as the reproducibility of the values and is determined through repeated measurements. The accuracy and precision of the dose determination with luminescent dosimeters largely depend on consistent and proper handling procedures, as well as individual dosimeter characterization. This can be obtained through dose-response investigations and the use of a repeatable, exact methodology. Before this can be achieved, an understanding of how to best handle and treat the dosimeters is essential.

## 12.4. Dosimeter handling and treatment

Dosimeter handling is very important and can affect the results desired. Non-uniform processes in handling of the dosimeters can result in increased uncertainty and errors.

### 12.4.1. *General handling guidelines for TLDs*

Handling of TLDs covers the manipulation of the solid materials or powder, up to and including their placement on the reader. Each aspect of these procedures must be carefully addressed. For example, a decrease in TL signal can result from scratches on the surface, which can affect the optical characteristics of the TLD (DeWerd, [7]). The surface of the TLD is also susceptible to contamination from skin oil and other chemicals. For these reasons, it is recommended that vacuum tweezers and latex/nitrile gloves be used when handling TLDs directly. Whether TLDs are used for research or clinical purposes, precautions should be taken to avoid surface contamination. This could include ensuring any phantom is clean, or sealing the TLDs in plastic bags when placing them on a patient.

The defect structure of the TL dosimeter is also of importance, especially as it affects the glow curve of the material. It has been shown in the past (Grant and Cameron [8]) that the trapping defects in LiF:Mg, Ti (TLD 100) responsible for peak 2 are dipole clusters and for peak 5 are three dipoles (trimer clusters). These defect clusters have been elaborated upon by Horowitz in a number of publications (for example, see Mahajna *et al.* [9]).

#### 12.4.1.1. *TLD annealing techniques*

The behavior of TLD phosphor traps is dependent on annealing time and environmental conditions. Use of appropriate TLD annealing and readout protocols allow for high reproducibility. The phosphors' defects can migrate through the crystal structure at room temperature prior to irradiation. This defect migration causes unpredictable changes in the radiation sensitivity of the TLDs. Annealing TLDs at high temperatures prior to irradiation serves to reset the defect structure and to release any currently trapped electrons and holes from their traps. Despite the use of regimented annealing protocols, the thermoluminescent signal can still change following irradiation at room temperature. Consequently, a waiting period between irradiation and readout is often recommended (Liang and DeWerd, [10]). During this waiting period, the short-lived peaks

are allowed to decay to insignificant levels while the long-lived peaks remain relatively stable due to their longer half-lives. An alternative method of minimizing the effect of the short-lived, low-energy traps is to clear them prior to readout using a low-temperature anneal.

The standardized handling and annealing process for TLD-100 use implemented at the University of Wisconsin-Madison Medical Radiation Research Center (UWMRRC) is given below. TLDs are always handled with vacuum tweezers to avoid scratching or introducing debris onto the dosimeters, as can be done by the use of metal tweezers (DeWerd, [7]). The annealing process includes heating the TLDs at 400°C for 1 hour in an aluminum holder, followed by quick cooling to room temperature on an aluminum block for 20–30 minutes, and then heating at 80°C for 24 hours followed by cooling to room temperature on an aluminum block for 20–30 minutes. TLDs are always read at least 24 hours after exposure to allow for sufficient decay of any residual short-lived, low-energy traps. The 400°C anneal empties all trap centers in the phosphor, while the 80°C annealing step redistributes the trap centers from Mg-dipoles to Mg-trimers throughout the crystalline structure. This 80°C anneal thus reduces the presence of the short-lived traps. An alternative to using the 80°C anneal methodology used at the UWMRRC is to instead anneal at 100°C pre-irradiation for 2 hours and pre-readout for 10 to 15 minutes. This causes the peak 2 traps to be emptied of any electrons, with the trap structure remaining in place, as illustrated in Fig. 1. Figure 1 shows the typical glow curve for LiF:Mg, Ti without annealing, with the 400°C anneal with 24 hours at 80°C and the remainder of the low temperature peaks after doing the 100°C anneal as described above. This last option can cause an inaccuracy in the integrated readout because of fading of the low temperature peaks. Shorter times for the 80°C anneal have been investigated and are not recommended. For example, if the 80°C annealing process is shortened to 9 hours instead of 24 hours, there is a 3.9% error in the integrated signal (Dhar *et al.* [11]).

Some precautions when using powder would be to make sure the batch of powder is well mixed. The batch is usually weighed out and put in capsular form. When reading the samples, uniform

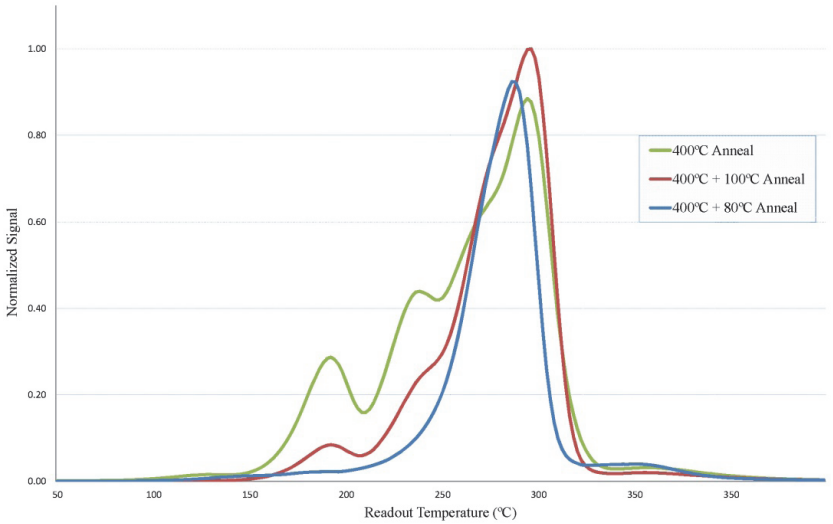


Fig. 1. Glow curves after various annealing processes.

batches need to be put on a planchet reader. A nitrogen atmosphere is maintained to eliminate surface effects on the TLD dosimeter (Cameron *et al.* [12]).

While TLDs can only be read out once per irradiation, they can be reused for additional irradiations and readouts indefinitely, so long as proper and consistent annealing methods are used. The exception to this would be if the TLDs were irradiated to a significantly high dose (>20 Gy). When given a dose of this magnitude, usual annealing methods are not sufficient to clear all the high-temperature traps, resulting in residual signal. In this case, either the TLDs should not be reused or methods such as glow-curve analysis and deconvolution to eliminate any interfering signals should be used for the dose determination.

### 12.4.1.2. *TLD sorting procedure*

TL response sensitivity of 1000 chips can be ±25%. The TLD chips can be sorted into groupings of narrower sensitivity range based upon repeatability and/or magnitude of response after a series of low-dose irradiations and readouts. In addition to use of strict annealing and

readout parameters, selection of a set of "high-performance" TLDs for radiation dose determination is used. This technique involves the selection of a specified number of TLDs from a large batch, based on the magnitude and reproducibility of their response. Although TLDs may have the same nominal dimensions, individual chips respond differently per unit dose from one another. Individual TLD sensitivities, termed "chip factors," are used to characterize the unique response of each TLD after being irradiated to the same dose level. Chip factors can be determined before the experimental cycle, or by using the average of chip factors determined before and after the experimental cycle using calibration sources, such as $^{137}$Cs or $^{60}$Co. The TLDs are irradiated to a known dose in a uniform field and the chip factor for each TLD, $k_{s,i}$, is determined. Three cycles of annealing-irradiation-readout of the TLDs are performed for all the TLDs in the initial batch. The average chip factors and standard deviation of each individual chip are determined. A subset of chips can be selected from the initial batch of TLDs based on an established selection criteria, such as response agreement within 1% ($k = 1$), and a small standard deviation (i.e. 1–2%).

#### 12.4.1.3. *Fading*

As discussed earlier, annealing techniques must be used in order to mitigate the spontaneous electron loss of low-temperature traps that cause fading of the overall thermoluminescence signal. While annealing takes care of most fading issues, it does not do so completely. Depending on the annealing method used, TLDs will still have signal fading of up to several percent over the first 24 hours. For this reason, it is recommended that users wait 24 hours post-irradiation before reading out TLDs. Additionally, there is long-term fading of the order of 1% per month (Luo [13]) that should be taken into account when reading out TLDs that were irradiated at different times.

### 12.4.2. *Handling guidelines for OSLD*

Like TLD, consistent and proper handling of OSLD is necessary to achieve optimal precision and accuracy. In some ways, OSLDs are

easier to manage than TLD, since the active volume is not normally open to the environment, so the risk of scratching the detector or contaminating it with oils from the skin are negligible. Physical handling of the detector is therefore simple. On the other hand, the detector is sensitive to ambient light. Fortunately, nanoDots are housed in a light-tight case. And even if the detector is exposed to ambient room light, the signal loss is only a few percent per minute (Jursinic [14]), so short accidental exposures to ambient light are likely not a concern. A major advantage of OSL dosimetry is that the read-out process liberates only a small fraction (typically <0.1%) of the trapped signal, depending on the stimulation conditions such as power, time and wavelength. This means that the detector can be re-read repeatedly, providing an additional level of assurance on the obtained value. The decrease in signal after each reading may need to be considered, depending on the number of readings.

#### 12.4.2.1. *OSLD bleaching techniques*

Thermal treatments to anneal OSLD are neither effective, requiring temperatures in excess of 600°C (Yukihara *et al.* [15]), nor are they practical as the nanoDots are manufactured in plastic casings that would melt. However, because they are sensitive to light, OSLDs can have their signal removed through the analogous process of bleaching. Bleaching involves exposing the dosimeter to a light source for a prolonged period of time to release residual trapped electrons and holes after read-out.

The bleaching process is, unfortunately, complicated by the nature of the traps. The OSL signal will decrease in an exponential-like fashion as the trapping centers are emptied. In the case of practical OSL materials, the OSL curve is not a single exponential because there are also multiple trapping centers. Simplistically, OSLD can be considered to have three distinct trap depths; these are classified as shallow traps (that spontaneously empty generally within the first 8 minutes after irradiation), dosimetric traps that are stable at room temperature but can be readily emptied by optical stimulation (during read-out or bleaching), and deep traps that require substantial energy to empty. Even after the read-out or

bleaching process, these deep traps remain filled. This is a problem because, as total dose history increases, even with bleaching, the distribution of available traps changes because the deep traps become progressively more filled. Because the deep traps are not emptied, the detector does not return to its original (pre-irradiated) condition after bleaching. The progressive (and essentially permanent) filling of deep traps means not only that the sensitivity of the detectors changes with accumulated dose, but so does also the supralinearity of the detectors (Jursinic [14]; Yukihara and McKeever [16], Reft [6], Mrčela, *et al.* [17], Jursinic [18], Omotayo [4]). Additionally, after bleaching of the detector but before it is used again, filled deep traps will spontaneously empty into shallower traps, meaning that for detectors with a large dose history there will be a background signal that will continue to grow with time (Jursinic [18]). Because of the host of complications, best practice is to avoid reusing these dosimeters beyond a cumulative dose of 10 Gy.

Compared to the annealing process for TLD, the bleaching process for OSLD has a major advantage and a major disadvantage compared to annealing TLDs. The advantage is that the process is simple — the OSLDs need simply be exposed to light for several hours after use. No equipment or heating or timing cycles are necessary. The disadvantage is that the bleaching process is imperfect, in that it can only be applied to these dosimeters until they have received a cumulative dose of 10 Gy.

The standardized process for nanoDot use implemented at the Imaging and Radiation Oncology Core (IROC) Houston office, based at The University of Texas MD Anderson Cancer Center is as follows. After irradiation, at least 10 minutes are allowed to elapse before OSLDs are read, so that shallow traps can spontaneously empty. After read-out, the OSLDs are opened and placed on a clear tray between an upper and lower bank of LED lights. These lights are covered with UV shields to prevent any stimulation. The OSLDs are bleached for 24 hours, after which a small sample of the bleached dots are spot-checked to ensure that their signal is consistent with a background signal (i.e., to check that the dosimeters are fully bleached). For each detector (identified with the bar code that is

included on nanoDots), the dose history is tracked. Detectors are discarded once their accumulated dose reaches 10 Gy.

#### 12.4.2.2. *OSLD sorting procedure*

Even if OSLDs had a uniform sensitivity per unit mass, it is impossible to measure the active mass of the OSLD, because of the tape into which the powder is embedded and the plastic casing that encompasses the entire detector. It is therefore no surprise that each OSLD has a distinct sensitivity, and that sensitivities across a batch of nanoDots vary by 10% or more (Mrčela *et al.* [17], Dunn *et al.* [19]). To achieve acceptable precision in OSLD measurements therefore, the relative element sensitivity must be taken into account.

To manage the relative element sensitivity and achieve the highest precision, the $k_{s,i}$ of each detector should be determined and applied. Determination of this value follows an identical process as for TLD. A group of dosimeters are irradiated to a low but uniform dose (e.g., 250 mGy). This allows easy determination of the relative sensitivity of each detector, as well as the inverse of this relative sensitivity which is the correction factor. Fortunately, for OSLD, because each has a unique bar code, each specific detector can easily have its own element sensitivity correction factor (with an associated uncertainty of $<1\%$, at the $k = 1$ level).

Another option is often employed in clinical practice, which provides poorer precision but is less work to implement. For an increased detector cost, the vendor will provide the element sensitivity correction for purchased nanoDots. This avoids the step of determining the element sensitivity correction factor, but the manufacturer-specified $k_{s,i}$ has a stated uncertainty of $\pm 2.8\%$ ($k = 1$).

#### 12.4.2.3. *Fading*

Unlike with TLD, no annealing or pre-heating cycles are available to mitigate spontaneous electron loss from low-temperature traps. These shallow traps are, fortunately, almost completely emptied within $\sim$10 minutes after irradiation (during which period these detectors should not be read) (Reft [6]). The remaining dosimetric traps will experience some spontaneous electron loss at room

temperature. This long-term fading of the order of 1% per month should be taken into account when reading out OSLDs that were irradiated at substantially different times.

## 12.5. Reader

The readout device is an important part of the process. The reproducibility of the readout directly affects the final value for the dose determination. TL/OSL readers stimulate the detector using either heat or light, and monitor the resultant luminescence with a photo-multiplier tube (PMT), which converts the luminescence into "counts" or current. More detailed reviews of luminescent readers and readout processes are available in the literature (Chen and McKeever [20], Bøtter-Jensen *et al.* [21], Bøtter-Jensen *et al.* [22], Yukihara and McKeever [16]).

### 12.5.1. *TLD readers*

TLD readers are of two basic types: the automatic reader and the single chip or powder reader. A very simplified reader is described in the original book on TLD by Cameron *et al.* [12] The single TLD reader is generally called the planchet reader. A TLD readout system, or simply a TLD reader, includes a mechanism to heat a TLD phosphor and to detect the light emitted during the thermoluminescence process. A simplified schematic diagram is given in Fig. 2.

#### 12.5.1.1. *Planchet reader*

A basic TLD reader system consists of a planchet for holding and heating the TLD, a photomultiplier tube (PMT) to detect the thermoluminescence light emission and convert it into an electrical signal linearly proportional to the detected photon fluence, and an electrometer for recording the PMT signal as a charge or current. (See Fig. 2). The TLD phosphor to be measured is placed in the heater pan at room temperature and then heated while the emitted light is measured with a PMT. Nitrogen gas is flowing to prevent surface effects from the TLD. The TLD is then cooled quickly using

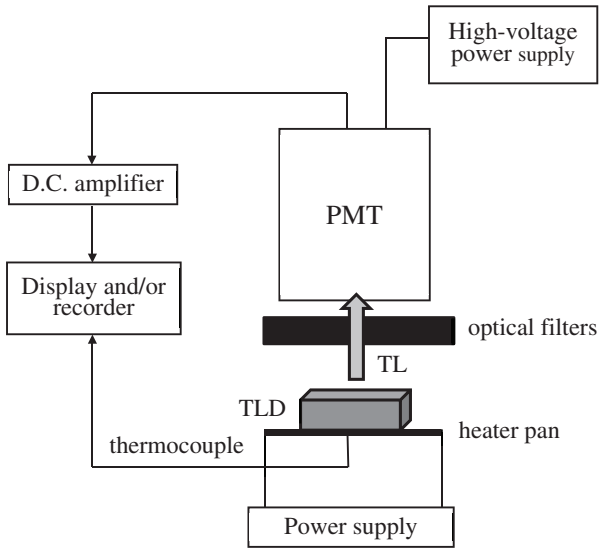


Fig. 2. Simple schematic of TLD reader.

nitrogen gas to bring the internal temperature back down to room temperature.

The majority of planchet readers read single dosimeters, with the TLDs being read and then replaced on the planchet. There is an automated TLD planchet reader made by REXON in Beachwood, Ohio. This reader uses a Bar Code to keep track of the TLD. The majority of automated readers are hot Nitrogen gas readers, which will be described in Section 12.5.1.2 below.

### 12.5.1.2. *Nitrogen gas reader*

An alternative system for reading out TLDs replaces the simple planchet with nitrogen gas as the means for heating the TLD. In this automated system, TLDs are loaded up into a carousel disk that can hold up to 50 individual TLDs. Once inserted into the TLD reader, the TLDs are lifted out of the carousel individually by a vacuum pick into a compartment where hot nitrogen gas is introduced to heat up the TLD to the desired temperature. Again, a PMT is used to detect and amplify the thermoluminescence emission.

There are several advantages to an automated system. Instead of an operator being manually involved for each TLD readout and being present for the entirety of the readout process, the automated reader only requires the user to load the carousel and start the readout process. The user need not be present for the entire readout process, as the reader will automatically read out each TLD in sequence. The user needs only be present to start the read and to remove/unload the carousel after the readout. This process results in a potentially much lower time commitment in terms of manual labor than the standard single read planchet reader.

While the majority of readers use nitrogen to cool the TLD after readout, there is an additional advantage to using the nitrogen gas to heat the TLD. The hot nitrogen flow helps reduce surface effects. In addition, the use of the gas for heating avoids the infrared emission of the planchet, which would have to be subtracted from the TL signal if it is significant. A purer signal results from the hot nitrogen gas reader.

#### 12.5.1.3. *The time-temperature profile*

The magnitude of TLD light output emitted during the readout process depends on the heating rate, maximum heating temperatures, and length of heating time at certain temperatures. A consistent set of readout parameters should be used to allow for a fair comparison of results from multiple readout sessions. The readout parameters consist of the preheat temperature, the heating rate, and the maximum temperature. The combination of these parameters is called the time-temperature profile (TTP). Most commercial TLD readers allow the users to define the TTPs. One typical TTP used in commercial TLD readers involves rapidly heating the TLDs through the unstable-trap region (preheat), ignoring light emission until a preset temperature range, and then recording the light emission in the temperature range that sufficiently covers the glow peak of dosimetric interest. The light emission measured over the temperature range of interest is recorded with units of charge. Following the light emission measurement period, the TLD may be kept at the maximum heat temperature, or heated further to release any remaining charge from deeper traps.

TLD research at the UWMRRC typically involves use of a TTP that includes a preheat temperature of 50°C, a heating rate of 15°C/s from 50°C to the maximum temperature of 350°C. An investigation of the effect of readout parameters on the TLD-100 response was performed by Liang and DeWerd [10]. They evaluated the effect of different heating rates and maximum readout temperatures on TLD light output. The maximum readout temperatures ranged from 240°C to 380°C and heating rates ranged from 2°C/s to 30°C/s. They found that a maximum readout temperature of 240°C is too low to show the complete glow curve. When the $T_{\max}$ is higher than 320°C, the high temperature peaks (peak 6, 7) appear and can affect the integral area of the glow curve. Different heating rates do not change the dose response very much. However, the signal to background (noise) ratio decreases noticeably when the heating rate is lower than 5°C/s, which makes the low heating rate impractical. Higher heating rates result in an increase in the glow peak temperature, which requires a higher maximum readout temperature. The results showed that TLD dose response when using the integral area under the glow curve is strongly dependent on the readout parameters, indicating that consistent and appropriate readout parameters are required to minimize the uncertainty.

12.5.1.4. *PMT sensitivity and linearity*

The PMT detects and amplifies the signal that is released from the TLDs and is usually assumed to behave linearly. If the PMT does not amplify the signal in a linear fashion, the relationship between TLD light output and PMT output must be characterized, so that light output data can be properly corrected. Bartol and DeWerd [23] examined the performance of the PMT for the Harshaw Company model 5500 automated hot-gas TL reader in use at the UWMRRC. This investigation found an overresponse of the PMT with increasing magnitude of TL dosimeter light output. This was accomplished with measurement of the difference for the same dose using neutral density filters. Thus, the light intensity was reduced and this signal was compared with the PMT response to increased light. The supralinear response was taken into account leaving only the PMT

response difference. The reader needs to be aware that the overall supralinear response consists of both TLD and PMT components. This investigation led to the recommended application of a PMT nonlinearity correction to TLD light output data, discussed later in this chapter. If these corrections are not applied, the uncertainty caused by the reader can increase significantly at higher doses when a dynamic range is used. In addition, the dark current reading also must be accounted for; however, this quantity is generally very small and does not contribute a great deal to the uncertainty. This PMT phenonmenon has been included in multiple peer-reviewed publications, for example in DeWerd *et al.* [24].

### 12.5.2. *OSLD readers*

Figure 3 shows the basic elements of an OSLD reader, although other orientations of the key components are possible. OSLDs can be read-out using light, either of constant intensity (continuous-wave technique) or variable intensity (pulsed-wave technique). The OSL decay curve is also affected by the type of stimulation light (broadband vs. monochromatic), its intensity, and its duration. Increasing the stimulation intensity increases the initial OSL signal, but signal loss occurs faster as a result (with the same integral

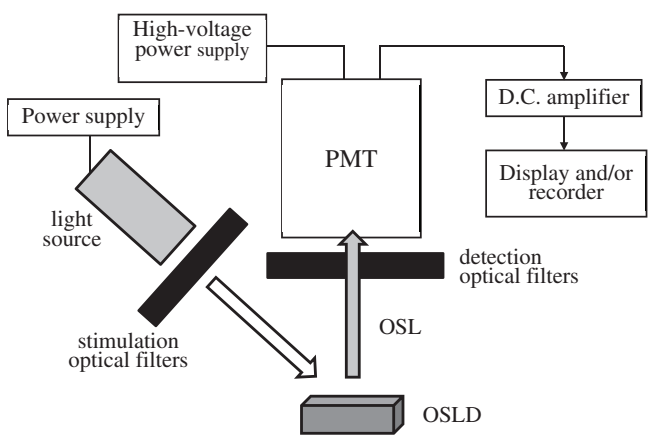


Fig. 3. Basic elements of an OSLD reader.

signal for a long-readout time). In practice, most commercial readers stimulate the detector for a short period of time (e.g., 1 s), so that only a fraction of the trapped charge is released.

Orientations of the light source and detector other than that shown in Fig. 3 may also be used (such as transmission instead of reflection). A light source such as a laser, light-emitting diode (LED), or broadband lamp is used for stimulation. Optical filters are typically used in front of the light source to select specific stimulation wavelengths and to block wavelengths that overlap with those of the OSL signal. Optical filters are also used in front of the PMT to block the stimulation light while transmitting the OSL signal. In the case of an $Al_2O_3$:C dosimeter, stimulation is typically performed using green light from a laser or LED (~525 nm), with the emission band in the blue (~420 nm) (Jursinic [14], Yukihara and McKeever [16]).

#### 12.5.2.1. *Types of OSLD readers*

OSLD readers are much the same as TLD readers in that they are comprised of a source of stimulation and a PMT. The light source can be a laser, light-emitting diode (LED), or broadband lamp as shown in Fig. 3.

The illumination process in OSLD readers can be implemented in one of two main ways. First, the light source can be on continuously during the read-out process (continuous-wave technique) and the signal is recorded continuously during the stimulation time. Filtration is relied upon to separate the stimulation and emission light. Second, the light source can be pulsed during the read-out process (pulsed-wave technique). If a pulsed-wave technique is used, the stimulation is comprised of a series of short pulses of light, with read-out done during the periods when the stimulation source is off. This approach provides a slightly better signal-to-noise (background) ratio, but does not substantially impact the practical use or precision of the system (Akselrod and McKeever [25]).

#### 12.5.2.2. *Count rate*

Typical output from an OSLD readout is the number of counts. As the detector is illuminated, the count rate decreases as the number

of traps that remain filled decreases. The OSL signal decreases in an exponential-like fashion as the trapping centers are emptied. In reality, this is not a single exponential because there are multiple different trapping centers. In practice, this issue is not of great concern. Commercial readers stimulate the detector for a short period of time (e.g., 1 s), and the net number of counts over that second are reported. The shape of the underlying exponential decay is barely sampled, because so small a fraction of the trapped charge is released. However, the interplay of the different trap types does affect fading, reuse, and read-out of OSLDs.

## 12.6. Best practice recommendations

The purpose of this section is to give standard practices that are suggested for the best and preferred results. Consistent procedures produce consistent results.

### 12.6.1. *Best practice for TL dosimetry*

Consistency is very important for good TL dosimetry results, with consistent procedures producing consistent results. It is important to always do the same operation each time of readout.

#### 12.6.1.1. *TLD reader and linearity*

Due to the heating rate dependence of TLD signals, the reproducibility of the heating profile is critical to consistent TL dosimetry. In addition to a reproducible heating profile, the stability of other components of the reader system is also important. For example, the PMT sensitivity must remain stable and the optical components of the system must remain clean. It is recommended that routine cleaning and maintenance of the system is performed. Users are encouraged to follow the guidelines provided by the manufacturer of their particular reader system. Additionally, ensuring the integrity of TL measurements requires periodic quality assurance (QA) to be performed on the reader system.

A robust reader QA protocol is essential for obtaining best accuracy and precision. It is recommended that such a protocol include

verification and testing of overall reader response and repeatability. This would include periodic testing of reader response to a single dose, such as is done when sorting and determining a chip factor. A simple way to achieve this is to use a "gold" setof TLDs that are irradiated to the same dose and read out repeatedly over time and used only for this QA purpose. Standard deviation of response over time is correlated with overall reader stability, while definitive trends in response would warrant further investigation. Long-term tracking of the PMT noise and reference light readings that accompany most TLD readouts is another useful tool for determining the health of the reader system's PMT. If the noise readings increase, it could indicate that some contaminant or condensation build-up is present within the PMT enclosure. Decreasing reference light readings over time would indicate a loss of overall sensitivity of the PMT and may warrant repair or replacement. An increase in reference light readings is not expected and would warrant further investigation.

As discussed earlier, the PMT's response has been found to be non-linear to increasing light output. Internal investigations at the UWMRRC have found that while this non-linear response is relatively stable for a particular PMT, each individual PMT has its own unique non-linear response that must be determined. Separate characterization of response over light output should be performed for every unique PMT used, whether it is for different readers or when replacing an old PMT with a new one. A method for characterizing and tracking this non-linear response would be to again use a "gold" set of TLDs that are irradiated to a dynamic dose range of interest (i.e. 100 mGy to 10 Gy). The readout value (nC) per dose (Gy) would be determined for each dose point. This nC/Gy value would then be normalized to one of the lower dose values (i.e. 100 mGy) to determine the relative response of the combination of the TLDs and the PMT for increasing doses. It is expected that the relative response will over-respond as signal increases. For example, 1.00 Gy should have a higher nC/Gy relative to 100 mGy, with the overresponse disparity increasing as dose/signal increases. As the same "gold" TLDs are used for every reading, any changes in overresponse over time can be attributed primarily to the PMT. It

is important to note that while each individual PMT exhibits its own unique non-linear response, it has been found internally at the UWMRRC that this individual response is relatively consistent over time. Significant changes in the over-response (i.e. >5%) between testing is not expected and would warrant further examination.

12.6.1.2. *TLD calibration*

Several corrections must be applied to raw TLD readings to obtain the fully corrected TLD light output. These corrections include a PMT nonlinearity correction, an individual TLD sensitivity correction (chip factor), and background subtraction. Descriptions of the PMT nonlinearity correction and individual TLD sensitivity corrections have already been discussed. Subtracting the signal measured from several unirradiated TLDs, which have been annealed following the same procedure as the experimental TLDs, typically performs the background subtraction. This operation eliminates the background radiation and TLD reader noise component of the TLD signal. The fully corrected TLD reading (in nC), $M_i$, for each TLD measurement was calculated using the following equation:

$$M_i = \frac{M_{raw,\,i}\, k_{PMT}}{k_{s,i}} - M_{bkgd} \tag{1}$$

where $M_{raw}$ is the raw reading (in nC) obtained from the TLD reader, $k_{PMT}$ is the PMT nonlinearity correction coefficient, $k_{s,i}$ is the individual TLD sensitivity correction factor or chip factor, and $M_{bkgd}$ is the average value of the corrected readings for a set of unirradiated TLDs. After obtaining $k_{s,i}$ (in nC), a calibration must be applied to obtain the TLD measured air kerma or dose. This calibration involves relating the corrected nC to a dose traceable to a primary laboratory.

TLDs are often calibrated in $^{60}$Co or $^{137}$Cs reference beams. At the UWMRRC, the $^{60}$Co or $^{137}$Cs reference beams are traceable to the National Institute of Standards and Technology (NIST). Traceability to a primary laboratory allows for standardization of measurement quantities, which is necessary to minimize experimental

uncertainties and to allow for equal comparisons of the results of independent investigations. A dose in the linear range of the TLD intrinsic linearity function is used for the calibration, because for a given photon energy the TL output is directly proportional to the absorbed dose in this range. This dose must be verified with a well-calibrated reference instrument, such as an ionization chamber. If x-ray beams are involved and calibration is done with a high-energy irradiator such as $^{60}$Co or $^{137}$Cs reference beams, an energy response correction needs to be made (Nunn *et al.* [1]).

After correcting the TLD raw readings with the PMT nonlinearity correction, chip factor correction, and background subtraction correction, the fully corrected reading can be converted to air kerma or dose to TLD (or other media, such as water) through the use of a calibration coefficient. The method of determining calibration coefficients depends on many factors including the irradiation source type and the quantity of interest (air kerma vs. dose to TLD, or dose to water). Typical calibration methodology involves irradiation of calibration TLDs to a known level of air kerma or dose, followed by TLD readout. The calibration coefficient, $N_{bq}$, for a specific beam quality can be determined with the following equations:

$$N_{bq} = \frac{K_c}{TL_{cal}} \tag{2}$$

or

$$N_{bq} = \frac{D_c}{TL_{cal}} \tag{3}$$

where $K_c$ and $D_c$ are the known air kerma or dose given to the calibration TLDs and $TL_{cal}$ is the fully corrected TL reading of the calibration TLDs. After the calibration coefficient of the TLDs is determined, the air kerma or dose measured by TLDs irradiated with the source for which the calibration coefficient applies can be calculated from the product of the calibration coefficient and the fully corrected reading of the experimental TLDs. The uncertainty in this calibration now includes the added uncertainty of obtaining traceability to a primary laboratory.

### 12.6.2. *Best practice for OSLD*

#### 12.6.2.1. *OSLD reader considerations*

Light output, as relevant for OSLD reading, is generally easier to manage than the temperature requirements of the heating cycle associated with TLD. Nevertheless, proper QA and maintenance of OSLD readers is essential to achieve precision.

Reader stability at IROC has been found to be on the order of ±1.2% (coefficient of variation). That is, from day to day, the variation in the response of a typical OSLD reader is relatively small. However, long term drift in the reader sensitivity has also been observed on the order of 15%, highlighting the need for monitoring of the reader performance. As a starting point for reader QA, manufacturer recommendations should be followed to monitor and track the stability of the light source and the PMT. In addition to this, a critical overall evaluation of an OSLD reader is to use a "gold" OSLD; also known as a constancy dosimeter. Constancy dosimeters are dosimeters irradiated to a known dose and/or a range of known doses and provide the opportunity to conduct periodic testing of reader response. A major advantage of OSLD is that each reading of the dosimeter only releases a small fraction of a percent of the trapped signal (as described by the signal depletion). This means that a single set of constancy dosimeters can be maintained and read repeatedly on a periodic basis to verify the response of the reader. The constancy dosimeters need only be corrected for depletion and fading, and then can be used for an extended period of time (typically up to a year).

Fading is described in section 12.4.2.3. Depletion is the signal lost per reading and can be easily determined during reader commissioning by repeatedly reading an OSLD (e.g., 50 times) and fitting the signal versus reading number to determine the change. Depletion is a function of the reader and can vary by a factor of 2 or more between different readers.

#### 12.6.2.2. *Calibration OSLDs*

Calibration of OSLD follows the same conceptual approach as for TLD above, but there are specific differences that must be accounted for, as described in this section.

Because OSLD lose only a small fraction of their stored signal with each reading, they can, and should, be read repeatedly (e.g. 3 times). Repeated reading of the OSLD allows for a quick check on the consistency of the readings. This average reading can be corrected for depletion for optimal precision. Additionally, the signal from an unirradiated "background" OSLD can be subtracted to correct for any background dose. And as described above, to account for the different sensitivities of each detector, the signal should be corrected by the element sensitivity correction factor. The raw signal $M_{raw}$ (in counts), is then converted to a corrected count rate by the following equation, for the i$^{\text{th}}$ dosimeter read $J$ times:

$$M_{corr} = k_{s,i}\left[\frac{\sum_j (M_{raw,j,i} k_d^{j-1})}{J} - M_{bkg}\right] \tag{4}$$

However, unless the OSLDs are being used to measure a very low dose, the background signal is likely to be negligible. Similarly, unless a large number of readings are taking place, the depletion correction is likely to be negligible. Therefore, the above equation reduces simply to:

$$M_{corr,i} = k_{s,i} \cdot \overline{M_{raw,i}} \tag{5}$$

Dose (or air kerma) can then be calculated from the corrected reading based on the calibration factor and a correction for intrinsic non-linearity of the dosimeter:

$$D = M_{corr} \times N \times k_L \tag{6}$$

The calibration coefficient ($N$) relates measured counts to dose. Most often the calibration will be of the form $N_{D,w}$ relating counts to a dose in water, because this is the most common dosimetric assessment in medical applications and because this metric is most easily traceable to a primary standard. However, an identical formalism can be used to relate counts from the detector to dose in another media, or kerma; one needs only have a traceable standard established for those other conditions.

While LiF TLDs exhibit a relatively large range of dose over which their response is linear, this is not the case for $Al_2O_3$:C OSLDs, which

show non-linearity effects in their dose response at 1 Gy or lower (Omotayo *et al.* [4]). This supralinearity in dose response can exceed 10% at 10 Gy, and therefore must be accounted for in order to achieve reasonable accuracy through correcting for the dosimeter response at the dose level of the experimental OSLD as compared to the dose level of the calibration OSLD. This is done through the linearity correction $k_L$. The non-linearity can be accounted for by either generating an analytic functional form for the correction, which can then be applied to any dose, or by generating a calibration curve as a function of dose, so the non-linearities are already incorporated into the calibration curve.

Linearity has only been studied in the dosimeter itself for OSLD. No study has examined any nonlinearity of the PMT in an OSLD reader, an effect that was described for TLD readers above. However, there is no reason to think that OSLD PMTs would behave differently than PMTs from TLD readers. Therefore, this issue should be carefully reviewed during system calibration.

Other corrections may be necessary, such as a correction for angular dependence, depending on the relative orientation of the detector in the calibration condition and the experimental setup. Because the shape of the OSLD has such a high aspect ratio, there is approximately a 2% difference in detector response (at 6 MV) between an en-face irradiation and an edge-on irradiation (Lehmann *et al.* [26]). As with all corrections, this one is minimized by ensuring that the calibration and experimental conditions are the same.

### 12.6.3. *Energy dependence for TLD and OSLD*

TLDs and OSLDs are often used to measure sources with photon energies that differ from the calibration beam photon energies. A common example of this is the measurement of low-energy photon-emitting brachytherapy sources, with TLDs that have been calibrated with high-energy photon-emitting sources such as $^{60}$Co or 4–6 MV x-rays. In cases such as this, when TLDs or OSLDs are calibrated with high-energy photon sources, but measurements are made using a lower energy beam, an energy dependence correction must be applied to accurately determine the dose delivered. The

energy dependence corrections must be applied to account for the change in the response of the TLD/OSLD as a function of photon energy. The magnitude of these energy dependence corrections depends on the phosphor type, the phosphor manufacturer, and the photon energies involved. The energy dependence is comprised of two components, termed the absorbed-dose energy dependence and the intrinsic energy dependence (Nunn *et al.* [1], DeWerd *et al.* [27] and Davis *et al.* [28]). The absorbed-dose energy dependence $f(Q)$, describes the relationship between the dose to the TLD/OSLD and the dose to another medium, as a function of photon beam quality. The absorbed-dose energy dependence can be calculated directly through Monte Carlo simulations based on the relative cross sections of the different media. The following equation gives this relationship:

$$f(Q) = \frac{D_{med}(Q)}{D_{TLD}(Q)} \tag{7}$$

where $D_{med}$ is the dose to the medium of interest, $D_{TLD}$ is the dose to the TLD (or OSLD) and $Q$ is the photon beam quality. There is another component to the energy dependence of luminescent detectors: the intrinsic energy dependence $k_{bq}(Q)$. The intrinsic energy dependence describes the relationship between the detector light output and the dose to the detector material as a function of photon beam quality. The TLD intrinsic energy dependence was investigated by Davis *et al.* [28] and Nunn *et al.* [1]. Davis *et al.* [28] investigated the thermoluminescence response using Monte Carlo calculations, and found that there is a greater response than that predicted by Monte Carlo alone. This was shown by Nunn *et al.* [1], who determined the relative intrinsic energy dependence of TLD-100, as the ratio of the measured relative TLD light output per unit air kerma and the calculated relative dose-to-TLD per unit air kerma. The measured and calculated results for a photon beam of quality $Q$ are normalized to their respective results for $^{60}$Co. The absorbed-dose energy dependence can be calculated directly through Monte Carlo simulations. The intrinsic energy dependence, $k_{bq}(Q)$, accounts for the relationship between the TLD light output and the dose to TLD as a function of photon energy, and is given by the

following equation:

$$k_{bq}(Q) = \frac{D_{TLD}(Q)}{M_{TLD}(Q)} \tag{8}$$

where $D_{TLD}$ is the dose to the TLD (or OSLD) and $M_{TLD}$ is the detector signal. Investigators have arrived at conflicting conclusions about the magnitude of the TLD intrinsic energy dependence. The investigation of Das *et al.* [29] yielded results that suggest that the TLD intrinsic energy dependence does not change with photon energy; however, these results had large uncertainties that may have obscured changes that would have otherwise been observed. The investigations of Davis *et al.* [28], Nunn *et al.* [1], Tedgren *et al.* [30], Reed *et al.* [31], Scarboro *et al.* [32] all yielded results that suggest that the TLD intrinsic energy dependence changes with photon energy, with a difference ranging from 7% to 13% at photon energies in the energy range of $^{125}$I and $^{103}$Pd brachytherapy sources relative to $^{60}$Co. Their results had lower experimental uncertainties (compared to those of Das *et al.* [29]) and ultimately provide more definitive evidence that the intrinsic energy dependence changes with photon energy.

OSLD nanoDots have a higher effective atomic number than LiF-based TLD, and therefore have a more pronounced energy dependence. However, studies to date have found no indication that OSLD exhibits any intrinsic energy dependence (Gasparian *et al.* [2], Scarboro *et al.* [33]). Therefore, while the overall energy dependence is more pronounced (substantially so at kV energies), the energy dependence is captured with Monte Carlo or cavity theory.

## 12.7. Clinical use considerations

This section reviews specific clinical applications of TLDs/OSLDs, focusing on the challenges and special considerations that may be necessary. Both the TLDs and OSLDs are considered together in these following sections because the approaches to manage them for clinical use are very similar.

### 12.7.1. *Field size limitations*

As clinical applications become more and more often dependent on small fields (in IMRT or SRS/SBRT treatments), the applicability of TL dosimetry or OSL dosimetry is an important consideration. Small radiation fields pose challenges in dosimetry because the lack of lateral charged particle equilibrium, observed at the edge of all treatment fields, comprises a large portion of the small field. Consequently, the small field is non-uniform, and may not have lateral charged particle equilibrium even on central axis. The physical size of the detector becomes a limiting factor for appropriate use. To prevent volume averaging effects and avoid complicated small field corrections because of the non-uniform field, the detector must not just fit within the field, the outer edge of the detector should be within the field edge by the lateral charge particle equilibrium range (TRS 483 [34]). Complicating matters is the fact that small fields are often not uniform throughout due to scatter. Additional factors, such as shape of field and measurement location, add to the complexity of obtaining accurate and precise small field measurements. In general, the smaller the dosimeter compared to the field, the more accurate is the measurement. Repeated measurements are important for obtaining good precision.

TLDs come in many different sizes and shapes but this section will focus on two primary form factors: TLD chips and TLD microcubes. TLD chips have a nominal size of 3.2 mm × 3.2 mm × 0.89 mm. Due to their size, caution is needed when using them in fields smaller than 1.5 cm. Great care must be taken to ensure that the TLD chip is placed in the center of the field, and multiple measurements for each setup should be taken to determine the precision that can be expected. To determine best overall accuracy in these small-field measurements, TLD results should be compared with other measurements, such as diodes, radiochromic film, and/or Monte Carlo simulations.

TLD microcubes are 1 $mm^3$ and have been used in smaller fields than TLD chips. Accurate and precise measurements have been taken with microcubes in linear accelerator stereotactic radiosurgery (SRS)

fields as small as 5 mm × 5 mm. Use in even smaller fields is possible, as long the aforementioned steps are taken to ensure the best results possible. As field sizes get smaller and less uniform, it is important to remember that any calculated dose from microcubes will be an average dose over the 1 mm × 1 mm area of the dosimeter.

The generally used OSL dosimeters (nanoDots) for medical application consist of 4 mm discs of detector encapsulated in a $1 \times 1\,cm^2$ plastic case. The larger size of these detectors makes them less well suited for small field measurements than TLD, and notable uncertainty in the measured output factors was seen for fields smaller than $2 \times 2\,cm^2$ (Phan [35]). Small field measurements are also complicated because of the air gaps present in the nanoDot structure. These air gaps impact the electronic equilibrium and can affect the measurement by several percent (Charles *et al.* [36]). As a final consideration, the active volume in the nanoDot detector is not centered in the plastic case, requiring careful alignment of the detector to the radiation field.

### 12.7.2. *Out-of-field measurements*

The standard TLD formulation TLD-100 is not recommended for out-of-field measurements for energies 15 MV and higher, due to a substantial over-response to the neutrons present in the beams (Kry *et al.* [37]). For out-of-field measurements with energies lower than 15 MV, TLD-100 may be used. For any out-of-field measurements, it is important to consider the effective energy at the point of measurement, as the majority of radiation present outside of fields is due to scatter, and therefore at a lower energy than that of the primary source (Edwards and Mountford [38], Scarboro *et al.* [32]). To account for both the medium-dependent and intrinsic energy dependence for this lower-energy beam, measurements are required. Such evaluations have been conducted in the literature for a range of scenarios, and correction factors from these references may be appropriate, depending on the desired accuracy of the specific situation (Scarboro *et al.* [32]). Any difference in effective energy between that of the calibration and measurement TLDs

should be accounted for by applying an energy-response correction as described earlier in section 12.6.1.3. Once applied, the energy-response correction enables accurate out-of-field measurements.

OSLDs can also be used for out-of-field applications. These detectors do not over-respond to neutrons, so OSLDs can be used for out of field dosimetry of any beam energy. However, like TLDs, OSLDs will over-respond to the softer spectrum found outside the treatment field. A range of conditions and corresponding correction factors are similarly available in the literature (Scarboro *et al.* [33]). While TLD over-respond by 4–12% (Scarboro *et al.* [32]), OSLDs over-respond more, by 10–25% (Scarboro *et al.* [33]).

### 12.7.3. *Surface dose measurements*

Measuring dose on the surface of a patient or phantom introduces added complexity to obtaining accurate results. Use of buildup (bolus) is recommended when using TLDs or OSLDs, to avoid the high dose gradient prevalent at the surface. It is important to keep in mind that dose measurements from TLDs are the average of the dose over the thickness of the TLD. For TLD-100 chips and microcubes, this equates to the average dose over 0.89 mm or 1 mm of the TLD (equating to 2.2 mm to 2.5 mm of water). Even at higher energies, where the average can be taken as the dose to the center of the TLD, the difference between the surface and water equivalent effective measurement depth must be accounted for. This difference can cause substantial additional uncertainty due to the steep dose gradients at the surface, often being more than 10% different over a 1 mm span (Lamb and Blake [39] and Kry *et al.* [40]). The magnitude of these gradients falls off quickly with depth, making accurate dosimetry more easily obtainable. Different energies require proportional buildup to get into this more gradual dose-gradient region. When performing surface dose measurements without buildup, it is recommended that all measurements are verified with another dosimeter designed for surface dosimetry (e.g., parallel plate or extrapolation chamber), or Monte Carlo simulations.

Similar considerations are warranted for OSLDs. Considering the plastic casing, the air gap, and the OSLD disc, the nanoDot has

an effective point of measurement that is 0.8 mm below the front surface of the plastic case (Zhuang and Olch [41]). Because the active volume is a very thin disc, there is little concern for averaging over the dose gradient in the depth direction. While the use of bolus to provide buildup greatly facilitates surface dosimetry using OSLDs, the very precise effective point of measurement for nanoDot dosimeters has allowed very high quality surface dosimetry to be performed relatively easily, even without the application of buildup (Zhuang and Olch [41]).

### 12.7.4. *Brachytherapy/low energy measurements*

As with surface dose measurements, brachytherapy and other low-energy measurements have added complexity. To achieve the best results, several factors must be accounted for. Dose gradients throughout the thickness of the TLD again are problematic, as low energies have a steep gradient in medium. Related to this effective dose drop off is the position of the TLD relative to the source of radiation. Angular dependence becomes an issue whenever the TLD is in an orientation other than perpendicular to the source, as any angle other than 90° will cause an effective increase in the depth the radiation must travel through the TLD. This can cause additional dose averaging issues. The final consideration when using TLDs for low-energy measurements is the effective energy at the point of measurement. The prevalence of scatter radiation in the measurement field will cause a change in the overall effective energy relative to the primary source. This means that the energy dependence will depend not only on the radiation source, but also on the geometry of the phantom. The effective energy of the radiation beam at the point of measurement can be calculated via Monte Carlo simulations or other means; however, for TLDs the full energy correction can only be determined with measurement.

These issues also manifest themselves for applications of OSLDs to brachytherapy and other low energy sources. OSLDs are well suited to the steep gradients involved, because they have a very thin active volume (provided the face of the disc is oriented towards the source). However, OSL dosimetry is more problematic than TL

dosimetry in terms of angular dependence and energy dependence. Because of its disc form and the non-uniform plastic case, there is a 4% difference in detector response between en-face and edge-on irradiation (Sharma and Jursinic [42]). Variations in energy can also substantially impact the measured dose. Difference in filtration between $^{192}$Ir source models and beam hardening between 2 cm depth in water and 10 cm depth in water, can produce differences of several percent in the measured response per dose (Casey *et al.* [43], Sharma and Jursinic [42]). Similarly, for CT scans the nominal kV energy, presence of a bow-tie filter, and even the size of the phantom and scan extent can all impact detector response by several percent (LaVoie *et al.* [44], Ding and Malcolm [45], Scarboro *et al.* [46]).

### 12.7.5. *Additional Precision-enhancing techniques*

When not in use, a TLD reader's internal components are at or near room temperature (with the exception of the PMT, which is kept at a cooler temperature via nitrogen-gas cooling). As TLDs start to be read out, this internal temperature rises due to the introduction of hot nitrogen gas. For this reason, it is recommended that a "warm up" procedure is followed before reading out any TLDs of interest. This can be achieved by reading out "dummy" TLDs before each reading of import. For example, the UWMRRC reads out a carousel filled with 50 dummy TLDs to get the reader up to a more uniform reading temperature.

Another technique for improving read-out precision is to add fiducials to the TLDs, to track orientation during readout. Tracking dosimeter orientation in this manner has little effect on TLD chip reproducibility, but was shown to improve microcube precision by approximately 1.5% (daRosa, *et al.* [47]). The common technique used at the UWMRRC is to mark the edge of the microcubes with graphite (pencil) and place them in the same orientation in the carousel or planchet for every read out.

Reading of OSLD also requires precise and consistent procedures in order to achieve optimal precision. Specific considerations for optimal reading precision depend on the nature of the reader and its use, and may not be obvious. For example, readers dedicated to

the nanoDot detector are surprisingly sensitive to the consistency of the mechanical opening of the cassette, and to the alignment of the active volume with the optical engine of the reader. Some of these OSLD readers use a rotary knob to control opening of the cassette. The torque with which the knob is turned can impact the reading obtained (1–2%). A source of even greater uncertainty is the holder or drawer of the nanoDot reader that holds the detector during the reading process. It is possible for this holder to position the detector slightly differently between subsequent readings, which can manifest as differences in signal by several percent. The holder/drawer should be rigorously tested to ensure it provides consistent signal (when corrected for depletion) for repeated readings of several detectors. Issues such as these should be evaluated for any OSLD reader, and consistent procedures should be implemented to maximize precision.

## 12.8. Uncertainty analysis for TL and OSL readings

The uncertainty procedures are outlined in the Guide to the Expression of Uncertainty in Measurement (GUM) report ([48]) and summarized by NIST (Taylor and Kuyatt [49]). There are two types of uncertainty categories: Type A uncertainty and Type B uncertainty. In this section, both the Type A and Type B uncertainties are discussed, specifically for TLD or OSLD dose determinations. For detector measurements, Type A uncertainties are evaluated by statistical methods and arise from the reproducibility of the readings of the detector. TLD/OSLD readings show statistical fluctuations such that a TLD/OSLD will not give the same reading over the course of multiple irradiations, even if all irradiation and readout conditions are consistent. Typical reading reproducibility has been reported to be as good as about 0.3% (1 standard deviation) for TLD-100 chips and about 0.6% (1 standard deviation) for TLD-100 microcubes (Luo, [10]) and about 0.8% for OSLD (including uncertainty in the estimation of $k_{s,i}$) (Alvarez *et al.* [50]). Reproducibility results vary based on the type of reader and details such as the heating profile. For TLDs reproducibility has been found to improve if individual dosimeters are oriented in the reader in a consistent manner from

measurement to measurement. As discussed earlier, this may be facilitated by marking a portion of the TLD with a pencil and orienting this marked portion the same way every time the TLD is read. Identifying dosimeter orientation in this way has little effect on chip reproducibility, but was shown to improve microcube reproducibility by about 1.5% (Luo [13]). A similar issue exists for OSLD; physical positioning of the active element in the light source must be consistent in order to achieve precise results. Instability in the physical positioning can introduce uncertainty in excess of 5% into the measured signal.

The uncertainty in TLD readings can be reduced if the TLD sorting is performed to select a set of TLDs with a similar element sensitivity. Similarly, for optimal precision, the element sensitivity of each OSLD must be identified and applied through a $k_{s,i}$ correction.

The other quantities for dosimetric uncertainty are Type B uncertainties, which involve determinations from scientific judgment or experience with the measurement equipment. Part of the Type B uncertainty would be positioning if phantom measurements were being made, or set-up reproducibility when irradiating calibration TLDs.

Sources of uncertainty for the corrected TLD readings are the reproducibility of the TLDs, the potential PMT linearity correction and the reader stability. For the TLD reproducibility, the Type A uncertainty was determined from the statistical uncertainty of the TLD calibrations. The uncertainty for the PMT linearity correction is greater for higher doses, where larger corrections are applied. For low dose energy dependence and calibration coefficient measurements, the uncertainty is determined by comparing measurements with and without the linearity correction applied. For patient and phantom measurements, however, the PMT linearity correction may be larger, because of other sources of uncertainty. Reader stability was determined to be a negligible source of uncertainty since it could not be determined independently from, and is assumed to be included in, the TLD reproducibility. For the calibration coefficient measurements, the sources of uncertainty are TLD reproducibility, air-kerma rate determination, TLD positioning, PMT linearity correction, reader

stability, and field uniformity. For the calibration coefficient Monte Carlo simulations, the sources of uncertainty are the MC statistical uncertainty, the photon spectrum and cross sections used, and the simulation geometry. The air-kerma rate determination components of the uncertainty budgets come from the UWMRRC's uncertainty budget for each source. Several components make up the TLD intrinsic energy dependence uncertainty included in Table 1 for a 60 kVp x-ray beam. A detailed uncertainty budget for the energy dependence would be necessary in the event two energies are necessary for calibration, as would be the case for HDR $^{192}$Ir. The TLD measured and MC calculated components would be necessary, especially if a brachytherapy source was under consideration. Careful analysis of all parameters involved in the thermoluminescent process is necessary. Table 1 should be considered as indicative only and includes most of the relative parameters as discussed here. This chapter and the analysis given here are only suggestive; the reader must understand that the laboratory must do its own uncertainty analysis for its own conditions.

For OSLD, the sources of uncertainty include the corrected readings and the OSLD reproducibility (for the experimental OSLDs as well as the calibration OSLDs). Uncertainty in the traceable dose to the primary laboratory used to determine the calibration coefficient is also included. There is also type B uncertainty in the

Table 1. Suggestive uncertainty analysis for TLD reading at 60 kVp x-rays.

| | Relative Standard Uncertainty (%) | |
|---|---|---|
| Parameter | Type A | Type B |
| TLD Reproducibility | 1.5 | |
| Air Kerma rate determination | | 0.64 |
| Traceability to Primary Lab | | 1.0 |
| Energy response | 0.5 | 0.5 |
| PMT nonlinearity | | 0.10 |
| Reader stability | | 0.01 |
| Total uncertainty ($k = 1$) | 2.04 | |
| Expanded uncertainty ($k = 2$) | 4.08 | |

correction factors that are determined for the detector, including corrections for energy dependence, non-linearity, and fading. These uncertainties are shown in Table 2 for a 6 MV beam based on a cobalt calibration. They are based on the IROC experience as detailed in Alvarez *et al.* [50]. The uncertainties in the correction factors assume that the calibration and experimental conditions are very similar (i.e., with a similar beam energy, to a similar dose level, and at a similar time). Therefore these are the residual uncertainties associated with necessary correction factors, assuming that the correction factors themselves have been minimized (i.e., were made close to unity by experimental design). Larger uncertainties would be associated with less controlled situations.

Tables 1 and 2 should be considered only as sample uncertainty budgets. These budgets reflect the uncertainties achieved by UWMRRC and IROC with extensive experience in the use of these dosimeters. Less experienced programs and less experienced operators should expect to see a higher uncertainty. In general, careful analysis of all parameters involved in the luminescent process, as established in any particular environment, is necessary to fully understand and quantify the associated measurement uncertainty for those specific conditions. These uncertainties are also the uncertainty associated with the dosimeter itself. The uncertainty associated with specific clinical measurements, such as in vivo patient measurements,

Table 2. Suggestive uncertainty analysis for OSLD readings in a 6 MV beam.

| | Relative Standard Uncertainty (%) | |
|---|---|---|
| Parameter | Type A | Type B |
| Reproducibility | 0.8 | |
| Calibration dose | | 0.64 |
| Calibration reproducibility | 0.8 | |
| Energy response | | 0.9 |
| Non linearity correction | | 0.3 |
| Fading correction | | 0.1 |
| Total uncertainty ($k = 1$) | 1.6 | |
| Expanded uncertainty ($k = 2$) | 3.2 | |

may be much higher because of other clinical and patient-related sources of uncertainty (Riegel *et al.* [51]).

## 12.9. Conclusion

This chapter has attempted to explain the concepts involved in the TL dosimetry and OSL dosimetry processes for Medical Applications. Maintaining consistent methodologies and procedures is necessary for accurate, precise measurements. When using the described methodologies, measurements with TLDs and/or OSLDs can be achieved with less than a 5% expanded uncertainty. Attention needs to be paid to any variations from the suggested procedures discussed, as any deviation can lead to an increase in total uncertainty.

While TLDs and OSLDs are theoretically very similar, there are many practical differences that make one or the other advantageous for different applications. Users wishing to implement one program or the other should carefully consider the pros and cons of each system relative to their needs.

## Acknowledgments

We would like to thank all the staff and students involved in the UW MRRC and IROC dosimetry programs. We especially want to thank Jennifer Hull for helping us with the reader figures. We also would like to thank all the customers of the UW ADCL whose calibrations provide student funding.

## References

[1] A.A. Nunn, S.D. Davis, J.A. Micka and L.A. DeWerd, "LiF:Mg,Ti TLD response as a function of photon energy for moderately filtered x-ray spectra in the range of 20–250 kVp relative to $^{60}$Co," *Medical Physics*, vol. 35, pp. 1859–1869, 2008.

[2] P.B.R. Gasparian, F. Vanhavere and E.G. Yukihara, "Evaluating the influence of experimental conditions on the photon energy response of $Al_2O_3$:C optically stimulated luminescence detectors," *Radiation Measurements*, vol. 47, pp. 243–249, ISSN 1350-4487, 2012.

[3] P. Mobit,E. Agyingi and G. Sandison, "Comparison of the energy-response factor of LiF and $Al_2O_3$ in radiotherapy beams," *Radiation Protection Dosimetry*, vol. 119, pp. 497–499, https://doi.org/10.1093/rpd/nci676, 2006.

[4] A.A. Omotayo, J.E. Cygler and G.O. Sawakuchi, "The effect of different bleaching wavelengths on the sensitivity of $Al_2O_3$:C optically stimulated luminescence detectors (OSLDs) exposed to 6 MV photon beams," *Medical Physics*, vol. 39, no. 9, pp. 5457–5468, 2012.

[5] A.F. McKinlay, Thermoluminescence dosimetry. Bristol, UK, Adam Hilger Ltd., 1981.

[6] C.S. Reft, "The energy dependence and dose response of a commercial optically stimulated luminescent detector for kilovoltage photon, megavoltage photon, and electron, proton, and carbon beams," *Medical Physics*, vol. 36, no. 5, pp. 1690–1699, 2009. Erratum: *Medical Physics*, vol. 39, no. 9, p. 5788, 2012.

[7] L.A. DeWerd, "Handling technique for thermoluminescent dosimeters," *Health Physics*, vol. 31, pp. 525–526, 1976.

[8] R.M. Grant and J.R. Cameron, "Effects of pre-irradiation annealing on the thermoluminescence and dielectric loss of LiF:Mg," *J. Appl. Phys.*, vol. 37, p. 3791, 1966.

[9] L. Oster, Y.S. Horowitz and N. Issa, "Identification of competitive trapping centers in irradiated LiF:Mg,Ti (TLD-100) via optical absorption studies," *Radiat. Effs. and Defects in Solids*, vol. 146, pp. 243–249, 1998.

[10] Q. Liang and L.A. DeWerd, "The influence of readout parameters on the TL dose response of TLD-100," *Medical Physics*, vol. 36, p. 2585, 2009.

[11] A. Dhar, L.A. DeWerd and T.G. Stoebe, "Effects of annealing and cooling processes on thermoluminesence of LiF (TLD100)," *Health Physics*, vol. 25, pp. 427–433, 1973.

[12] J.R. Cameron, N. Suntharalingam and G.N. Kenney, Thermoluminescent Dosimetry, Madison, WI: University of Wisconsin Press, 1968.

[13] L.Z. Luo, "Extensive fade study of Harshaw LiF TLD materials, In Radiation Measurements, vol. 43, Issues 2–6, 2008, Pages 365–370, ISSN 1350–4487," https://doi.org/10.1016/j.radmeas.2007.11.069.

[14] P.A. Jursinic, "Characterization of optically stimulated luminescent dosimeters, OSLDs, for clinical dosimetric measurements," *Medical Physics*, vol. 34, no. 12, pp. 4594–4604, 2007.

[15] E.G. Yukihara, R. Gaza, S.W.S. McKeever and C.G. Soares, "Optically stimulated luminescence and thermoluminescence efficiencies for high-energy heavy charged particle irradiation in $Al_2O_3$:C," *Radiation Measurements*, vol. 38, no. 1, pp. 59–70, 2004.

[16] E.G. Yukihara and S.W. McKeever, "Optically stimulated luminescence (OSL) dosimetry in medicine," *Physics in Medicine and Biology* vol. 53, no. 20, pp. R351–379, 2008.

[17] I. Mrčela, T. Bokulić, J. Izewska, M. Budanec, A. Fröbe and Z. Kusić, "Optically stimulated luminescence in vivo dosimetry for radiotherapy: physical characterization and clinical measurements in $^{60}$Co beams," *Physics in Medicine and Biology*, vol. 56, no. 18, pp. 6065–6082, 2011.

[18] P.A. Jursinic, "Changes in optically stimulated luminescent dosimeter (OSLD) dosimetric characteristics with accumulated dose," *Medical Physics*, vol. 37, no. 1, pp. 132–140, 2010.

[19] L.J. Dunn, J. Lye, J. Kenny, J. Lehmann, I. Williams and T. Kron, "Commissioning of optically stimulated luminescence dosimeters for use in radiotherapy," *Radiation Measurements*, vol. 51–52, pp. 31–39, 2013.

[20] R. Chen and S.W.S. McKeever, "Theory of thermoluminescence and related phenomena," Singapore; River Edge, N.J., World Scientific, 1997.

[21] L. Bøtter-Jensen, S.W.S. McKeever and A.G. Wintle, Optically Stimulated Luminescence Dosimetry, Amsterdam, Boston, London: Elsevier, 2003.

[22] L. Bøtter-Jensen, K.J. Thomsen and M. Jain, "Review of optically stimulated luminescence (OSL) instrumental developments for retrospective dosimetry," *Radiation Measurements*, vol. 45, nos. 3–6, pp. 253–257, 2010.

[23] L. Bartol and L.A. DeWerd, "Characterization of thermoluminescent dosimeter reader precision and artifacts," *Medical Physics*, vol. 35, p. 2796, 2008.

[24] L.A. DeWerd, Q. Liang, J.L. Reed and W.S. Culberson, "The use of TLDs for brachytherapy dosimetry," *Radiat. Meas.*, vol. 71, pp. 276–281, 2014, doi:10.1016/j.radmeas.2014.05.005.

[25] M.S. Akselrod and S.W.S. McKeever, "A radiation dosimetry method using pulsed optically stimulated luminescence," *Radiation Protection Dosimetry*, vol. 81, no. 3, pp. 167–175, 1999.

[26] J.L. Lehmann, J.L. Dunn, J.E. Lye, J.W. Kenny, A. Alves, A. Cole, A. Asena, T. Kron and I.M. Williams, "Angular dependence of the response of the nanoDot OSLD system for measurements at depth in clinical megavoltage beams," *Medical Physics*, vol. 41, no. 6, p. 061712, 2014.

[27] L.A. DeWerd, L.J. Bartol and S.D. Davis, "Chapter 24: Thermoluminescence dosimetry," *Proceedings of the AAPM Summer School*, pp. 815–840, 2009.

[28] S.D. Davis, C.K. Ross, P.N. Mobit, L. Van der Zwan, W.J. Chase and K.R. Shortt, "The response of LiF thermoluminescence dosemeters to photon beams in the energy range from 30 kV x rays to 60Co gamma rays," *Radiation Protection Dosimetry*, vol. 106, no. 1, pp. 33–43, 2003.

[29] R.K. Das, Z. Li, H. Perera and J.F. Williamson, "Accuracy of Monte Carlo photon transport simulation in characterizing brachytherapy dosimeter energy-response artefacts." *Physics in Medicine and Biology*, vol. 41, pp. 995–1006, 1996.

[30] A.C. Tedgren, A. Hedman, J. Grindborg and G.A. Carlsson, "Response of LiF:Mg,Ti thermoluminescenct dosimeters at photon energies relevant to the dosimetry of brachytherapy (<1 MeV)," *Medical Physics*, vol. 38, pp. 5539–5550, 2011.

[31] J.L. Reed, B.E. Rasmussen, S.D. Davis, J.A. Micka and L.A. DeWerd, "The intrinsic energy dependence of LiF:Mg,Ti thermoluminescent dosimeters for $^{125}$I and $^{103}$Pd brachytherapy sources relative to $^{60}$Co," *Medical Physics*, vol. 41, pp. 122103-1–122103-11, 2014.

[32] S.B. Scarboro, D.S. Followill, R.M. Howell and S.F. Kry, "Variations in photon energy spectra of a 6 MV beam and their impact on TLD response," *Medical Physics*, vol. 38, no. 5, pp. 2619–2628, 2011.

[33] S.B. Scarboro, D.S. Followill, J.R. Kerns, R.A. White and S.F. Kry, "Energy response of optically stimulated luminescent dosimeters for non-reference

measurement locations in a 6 MV photon beam," *Physics in Medicine and Biology*, vol. 57, no. 9, pp. 2505–2515, 2012.

[34] Dosimetry of Small Static Fields Used in External Beam Radiotherapy. IAEA Technical Reports Series No. 483. International Atomic Energy Agency, 2017.

[35] C. Pham, "Characterization of OSLDs for use in small field photon beam dosimetry." University of Texas Thesis, 2013.

[36] P.H. Charles, S.B. Crowe, T. Kairn, J. Kenny, J. Lehmann, J. Lye, L. Dunn, B. Hill, R.T. Knight, C.M. Langton and J.V. Trapp, "The effect of very small air gaps on small field dosimetry," *Physics in Medicine and Biology*, vol. 57, pp. 6947–6960, 2012.

[37] S.F. Kry, M. Price, D. Followill, F. Mourtada and M. Salehpour, "The use of LiF (TLD-100) as an out-of-field dosimeter," *Journal of Applied Clinical Medical Physics*, vol. 8, pp. 169–175, doi:10.1120/jacmp.v8i4.2679, 2007.

[38] C.R. Edwards and P.J. Mountford, "Near surface photon energy spectra outside a 6 MV field edge," *Physics in Medicine and Biology*, vol. 49, no. 18, pp. N293–301, 2004.

[39] A. Lamb and S. Blake, "Investigation and modelling of the surface dose from linear accelerator produced 6 and 10 MV photon beams," *Physics in Medicine & Biology*, vol. 43, pp. 1133–1146, 1998.

[40] S.F. Kry, S.A. Smith, R. Weathers and M. Stovall, "Skin dose during radiotherapy: a summary and general estimation technique," *Journal of Applied Clinical Medical Physics*, vol. 13, no. 3, pp. 20–34, 2012.

[41] H. Zhuang and A.J. Olch, "Validation of OSLD and a treatment planning system for surface dose determination in IMRT treatments," *Medical Physics*, vol. 41, no. 8, p. 081720, 2014.

[42] R. Sharma and P.A. Jursinic, "In vivo measurements for high dose rate brachytherapy with optically stimulated luminescent dosimeters," *Medical Physics*, vol. 40, no. 7, p. 071730, 2013.

[43] K.E. Casey, P. Alvarez, S.F. Kry, R.M. Howell, A. Lawyer and D.S. Followill, "Development and implementation of a remote audit tool for high dose rate (HDR) Ir-192 brachytherapy using optically stimulated luminescence dosimetry" *Medical Physics*, vol. 40, no. 11, p. 112102, 2013.

[44] L.M. Lavoie, Ghita, L. Brateman and M. Arreola, "Characterization of a commercially-available, optically-stimulated luminescent dosimetry system for use in computed tomography," *Health Physics*, vol. 101, no. 3, pp. 299–310, 2011.

[45] G.X. Ding and A.W. Malcolm,"An optically stimulated luminescence dosimeter for measuring patient exposure from imaging guidance procedures," *Physics in Medicine and Biology*, vol. 58, no. 17, pp. 5885–5897, 2013.

[46] S.B. Scarboro, D. Cody, P. Alvarez, D.S. Followill, L. Court, F. Stingo, D. Zhang, M. McNitt-Gray and S.F. Kry, "Characterization of the nanoDot OSLD dosimeter in CT," *Medical Physics*, vol. 42, no. 4, pp. 1797–1807, 2015.

[47] L. A. R. da Rosa, D.F. Regulla and U.A. Fill, "Reproducibility study of TLD-100 micro-cubes at radiotherapy dose level," *Applied Radiation Isotopes*, vol. 50, pp. 573–577, 1999.

[48] Evaluation of measurement data — Guide to the expression of uncertainty in measurement, *International Organization for Standardization* (*ISO*), Joint Committee for Guides in Metrology (JCGM 100, 2008) (corrected version 2010, http://www.bipm.org/utils/common/documents/jcgm/JCGM_100_2008_E.pdf).

[49] B.N. Taylor and C.E. Kuyatt, Guidelines for Evaluating and Expressing the Uncertainty of NIST Measurement Results, Technical Note 1297, National Institute of Standards and Technology, 1994.

[50] P. Alvarez, S.F. Kry, F. Stingo and D.S. Followill, "TLD and OSLD dosimetry systems for remote audits of radiotherapy external beam calibration," *Radiation Measurements*, vol. 106, p. 412, 2017.

[51] A.C. Riegel, Y. Chen, A. Kapur, L. Apicello, A. Kuruvilla, J.A. Rea, A. Jamshidi and L. Potters, "In vivo dosimetry with optically stimulated luminescent dosimeters for conformal and intensity-modulated radiation therapy: a 2-year multicenter cohort study," *Practical Radiation Oncology*, vol. 7, pp. 135–144, 2017.

This page intentionally left blank

# Author Index

This page intentionally left blank

# Subject Index